WCAP 9183

Copy

PWR FLECHT SKEWED PROFILE LOW FLOODING RATE TEST SERIES EVALUATION REPORT

Westinghouse Nuclear Energy Systems

WCAP 9183

NRC-2

NRC-W-EPRI Cooperative Research and Development Report

LOCA LIBRARY COPY

PWR FLECHT SKEWED PROFILE LOW FLOODING RATE TEST SERIES EVALUATION REPORT

G. P. Lilly
H. C. Yeh
C. E. Dodge
S. Wong

November 1977

APPROVED L E Hochreiter
L. E. Hochreiter
Safeguards Development

APPROVED A P Suda
A. P. Suda
Project Engineer

Program Jointly Funded by Westinghouse and USNRC Under Contract At (49-24)-0178

WESTINGHOUSE ELECTRIC CORPORATION
Nuclear Energy Systems
P. O. Box 355
Pittsburgh, Pennsylvania 15230

LEGAL NOTICE

This report was prepared as an account of Government-sponsored work. Neither the United States, nor the Commission, nor any person acting on behalf of the Commission:

A. Makes any warranty or representation, expressed or implied, with respect to the accuracy, completeness, or usefulness of the information contained in this report, or that the use of any information, apparatus, method, or process disclosed in this report may not infringe privately owned rights; or

B. Assumes any liabilities with respect to the use of, or for damages resulting from the use of any information, apparatus, method, or process disclosed in this report.

As used in the above, "person acting on behalf of the Commission" includes any employe or contractor of the commission, or employe of such contractor, to the extent that such employe or contractor of the Commission, or employe of such contractor prepares, disseminates, or provides access to, any information pursuant to his employment with such contractor.

ACKNOWLEDGMENTS

The authors wish to acknowledge the contributions of the following persons toward completion of this report: K. M. Beatty, J. V. Savani, M. A. Emery, R. A. Russman for the writing of data analysis programs, running these programs to obtain the analyzed data, and presenting the data for the report; E. R. Rosal for his help in interpreting the test results, Dr. J. O. Cermak for suggesting a method to correlate the heat transfer data, and to C. E. Conway who prepared the bundle post-test mechanical data.

TABLE OF CONTENTS

TABLE OF CONTENTS (cont)

TABLE OF CONTENTS (cont)

LIST OF ILLUSTRATIONS

LIST OF ILLUSTRATIONS (cont)

LIST OF ILLUSTRATIONS (cont)

LIST OF ILLUSTRATIONS (cont)

LIST OF ILLUSTRATIONS (cont)

LIST OF ILLUSTRATIONS (cont)

LIST OF TABLES

SECTION 1
INTRODUCTION

1-1. GENERAL INFORMATION

The FLECHT Low Flooding Rate Skewed Power shape tests is the second test series designed to expand the earlier FLECHT forced flooding rate data base for lower flooding rates. That set of tests employed a cosine axial power shape while the skewed power shape tests has an axial power shape which is skewed to the top of the test bundle. The cosine test results and associated data analysis are reported in references 1 and 2, respectively. The data from the skewed axial profile tests is reported in reference 3. This report presents the evaluation, analysis, and model development efforts which have been performed on the skewed axial data.

1-2. SKEWED AXIAL TEST SERIES OBJECTIVES

The overall objective of the FLECHT low flooding rate test program has been to obtain heat transfer data useful for calculating the reflooding behavior of a PWR core following a postulated loss-of-coolant accident. The behavior of the emergency core coolant (ECC) with respect to the mass stored and mass flow leaving the core during reflood is also needed for this purpose. The capability for meeting this latter need, has been made possible with the improved hardware and instrumentation of the cosine tests.

The other main objective of the FLECHT low flooding rate test program is to provide valid data which can be used to verify/develop mechanistic reflood models. This effort was first performed on the cosine data and is reported in WCAP-8838. This report continues and expands upon that effort.

1. Rosal, E. R., et al. FLECHT Low Flooding Rate Cosine Test Series Data Report WCAP-8651 December, 1975.
2. Lilly, G. P., et al. PWR FLECHT Cosine Low Flooding Rate Series Evaluation Report WCAP-8838, March 1977.
3. Rosal, E. R., et al. FLECHT Low Flooding Rate Skewed Test Series Data Report WCAP 9108, May 1977.

1-3. SPECIFIC OBJECTIVES

Specific objectives for the skewed axial power shape test series are as follows:

- Provide heat transfer coefficient and core mass effluent data at flooding rates near one in./sec
- Supplement parametric effects studied in the original FLECHT program such as:
  1. Low cladding temperature
  2. Low subcooling at low flooding rates
  3. Peak rod power
  4. Variable forced flooding rate
  5. Radial power gradients
  6. Housing behavior
- Provide data for reflood heat transfer model development
- Repeat original FLECHT tests with new instrumentation and data processing techniques
- Perform repeat tests to demonstrate data reproducibility
- Perform tests which overlap with existing cosine data to assess the effect of power shape.

1-4. DATA EVALUATION AND ANALYSIS OBJECTIVES

The objectives followed in evaluating and analyzing the low flooding rate skewed axial profile data were:

- Present skewed profile parametric effects and compare/contrast with cosine axial power shape effects.
- Apply the data for calculation of bundle average flow properties at several axial positions in the bundle and use these properties to help identify heat transfer mechanisms which are important in reflood heat transfer. Perform these calculations for both the skewed and cosine power shapes.
- Compare the mass effluent fraction model developed in WCAP-8838 with the skewed axial profile data and resolve any differences.

- Develop an empirical heat transfer correlation which will predict the heat transfer during reflooding for different axial power shapes.

1-5. REPORT ORGANIZATION

Section 2 presents a brief discussion of test hardware procedures and instrumentation. Sections 3 through 6 present the results of the data evaluation and model development.

Section 3 presents parametric effects on heat transfer, temperature transients and bundle mass effluent. Parameters included are:

- Flooding rate
- Peak power
- Pressure
- Subcooling
- Initial clad temperature
- Initial flooding rate (variable flooding rate)

Also, in section 3, a number of special effects tests were analyzed and evaluated. These included:

- The effect of hot and cold channels on heat transfer and bundle effluent mass flow
- Data repeatability within the present test series with comparisons to the cosine low flooding rate data
- Gravity reflooding tests with the skewed axial profile
- An evaluation and analysis of the skewed axial profile tests which overlapped with the cosine power tests.

Section 4 presents the results of the calculation of the bundle average mass flow and quality at several locations within the bundle. Both the actual nonequilibrium and equilibrium qualities are calculated and are compared where possible with the cosine axial profile data. In addition, a model is used to predict radiation to vapor, radiation to droplets, and wall surface radiation such that the convective portion of the total wall heat flux can be obtained.

Section 5 compares the mass effluent model, developed in reference 1, to the skewed axial profile data.

---

1. Lilly, G. P., et al. PWR FLECHT Cosine Low Flooding Rate Series Evaluation Report WCAP-8838, Mar. 1977.

Section 6 develops the logic for a new empirical FLECHT heat transfer correlation which can predict the heat transfer above the quench front for both the cosine and skewed axial power shapes.

An evaluation of the physical state of the rod bundle, crud formation, and surface roughness is included in appendix H. Photographs of the heater rod crud and post-test measurements of the housing are also presented.

SECTION 2
TEST DESCRIPTION

2-1. INTRODUCTION

This chapter is designed to provide sufficient facility and test information to permit a clear understanding of the data evaluations and analyses in subsequent chapters. For the user of the data, detailed descriptions of the test facility instrumentation, test procedures and test matrix are contained in the data report, WCAP-9108.[1]

2-2. TEST FACILITY

Basically, the test facility is similar to the facility used for earlier FLECHT forced flooding tests. A number of refinements have been made to improve the data obtained from each test. A schematic of the facility appears in figure 2-1.

The principal components of the facility include:

- A pressurized, temperature-controlled water supply to provide forced flooding of the test bundle.
- Flow control valve and flow metering devices to set flooding rate to the bundle.
- The test section consists of:
    1. A thin circular housing which contained 105, 12-foot heater rods,
    2. Six guide tube thimbles, eight metal filler rods, and one ANC level transducer.
- Separators and collection tanks for removing and measuring the liquid in the test section effluent.
- Orifice for metering test section effluent vapor flow.
- Pressure control valve for maintaining test section pressure.

---

1. Rosal, E.R., et al. FLECHT Low Flooding Rate Skewed Test Series Data Report WCAP-9108 May 1977.

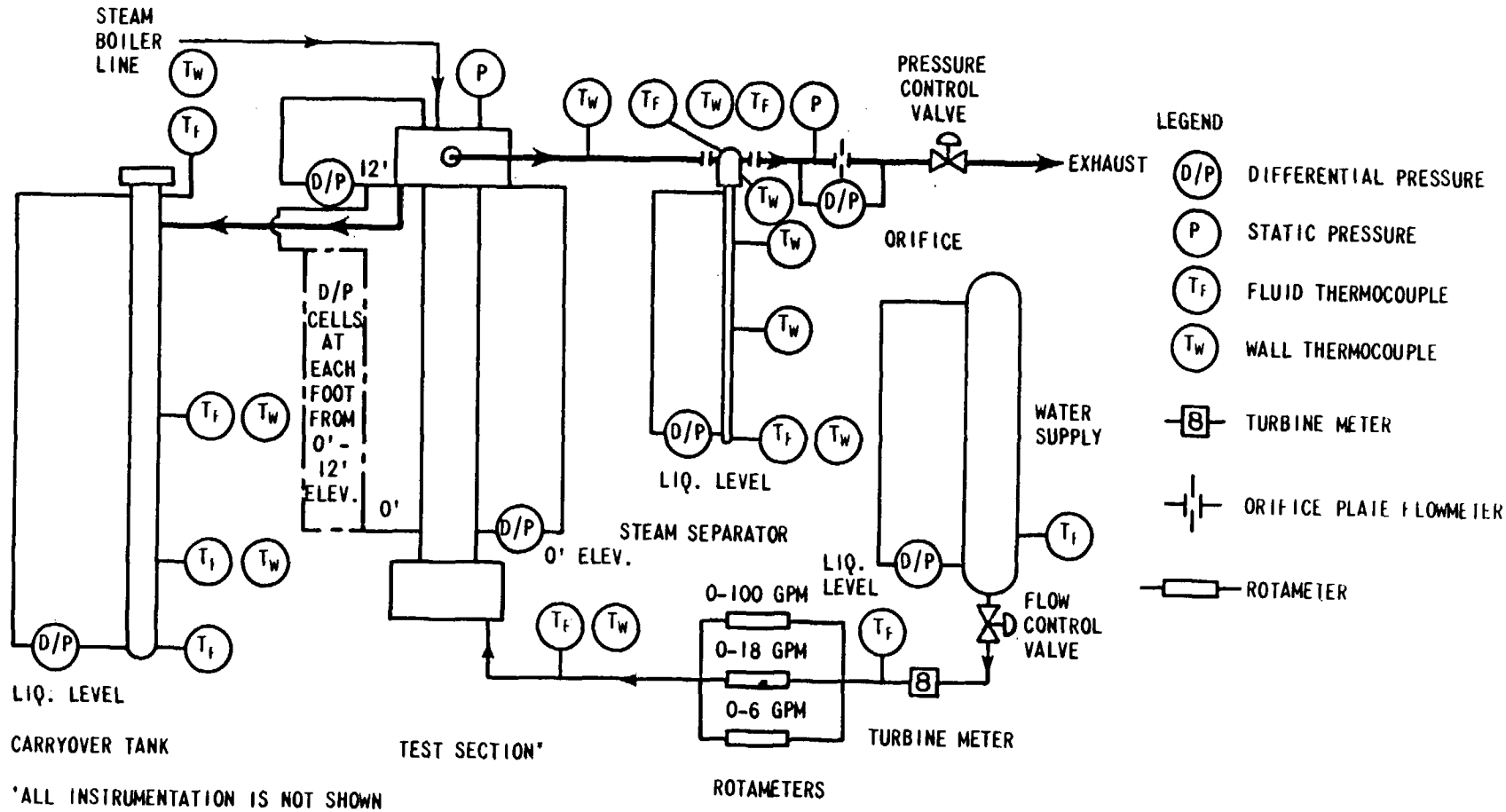

Figure 2-1. FLECHT Low Flooding Rate Test Configuration

The axial power shape used in this test series had the peak power location at the ten-foot elevation. The actual power shape used is shown in figure 2-2.

The principal improvements in instrumentation over previous FLECHT forced flooding tests include:

- More extensive thermocouple instrumentation in the rod bundle so that bundle energy release can be calculated. Rod bundle thermocouple instrumentation is presented in figure 2-3.
- Bundle housing pressure drop data every foot of elevation which permits determination of instantaneous mass storage in the bundle and the bundle void fraction distribution.
- Close coupled separator and liquid collection tank for determining the amount of liquid in test section effluent.
- Effluent vapor flow measurement to perform bundle mass balance at the test section exit.

In addition to these improvements, the volume of the entrainment separator was increased by a factor of five for high flooding rate tests, a steam probe was installed at the test section exit pipe, and a Vee-ball pressure control valve was added to the exhaust line. These improvements are discussed in detail in reference 1. The behavior of the thin-walled circular housing has been evaluated and analyzed and is also discussed in detail in reference 1.

It was the general conclusion that the use of the thin-walled housing was helpful and acted to minimize nontypical housing effects and did result in improved heat transfer and mass entrainment data.

2-3. TEST PROCEDURE

A detailed test procedure is given in the data report WCAP-9108.[1] Very simply, a typical test proceeds as follows:

- Temperature in the water supply tank is set at the desired level.
- Rod bundle housing is heated to the desired temperature level and temperature profile by pulsing power to the rod bundle.
- The housing lower plenum is filled to the bottom of the rod's heated length.
- The test section is pressurized to the desired test pressure using the pressurizer.

---

1. Rosal, E. R., et al. FLECHT Low Flooding Rate Skewed Test Series Data Report WCAP 9108, May 1977.

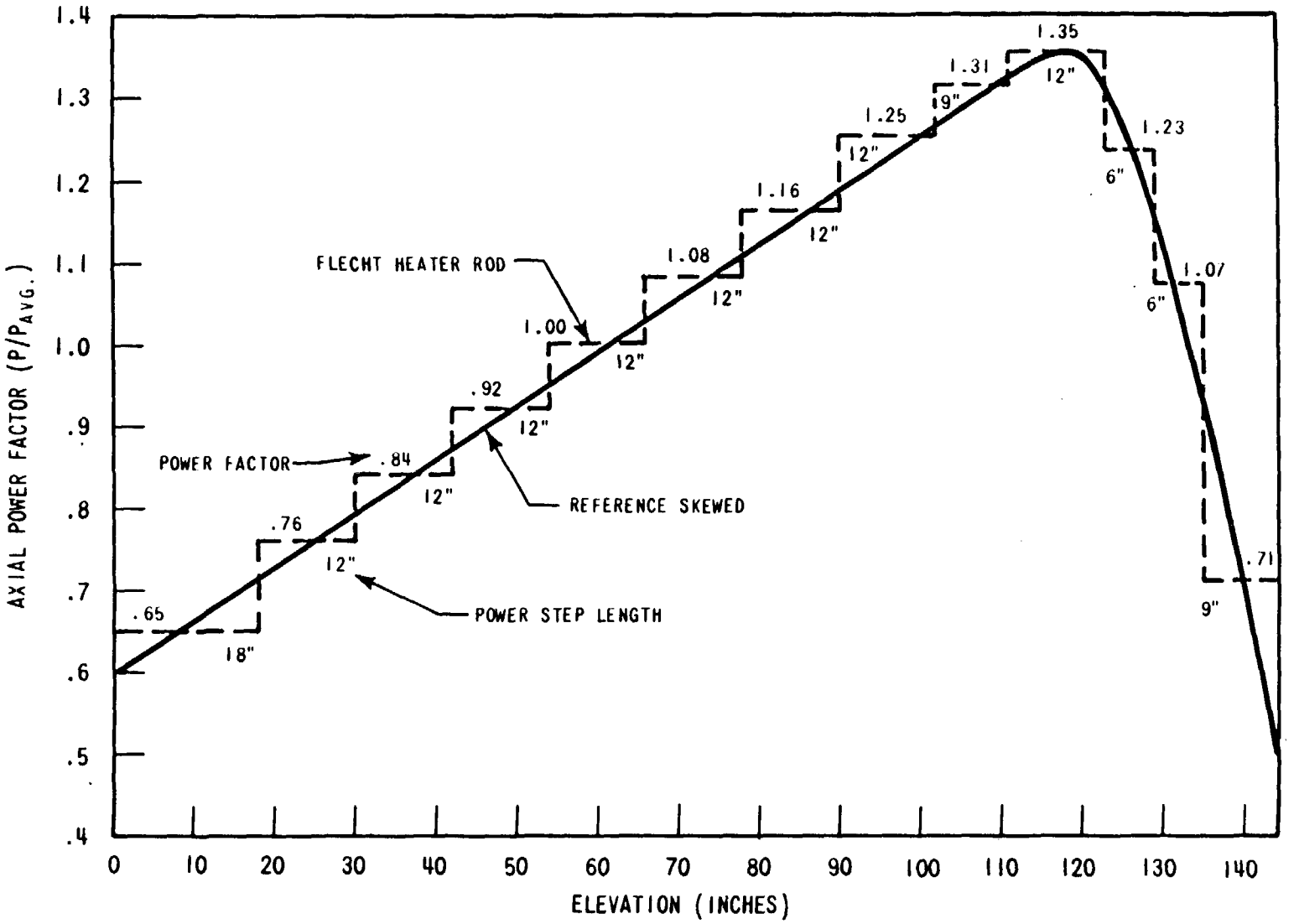

Figure 2-2 FLECHT - Low Flooding Rate Test Skewed Axial Power Profile

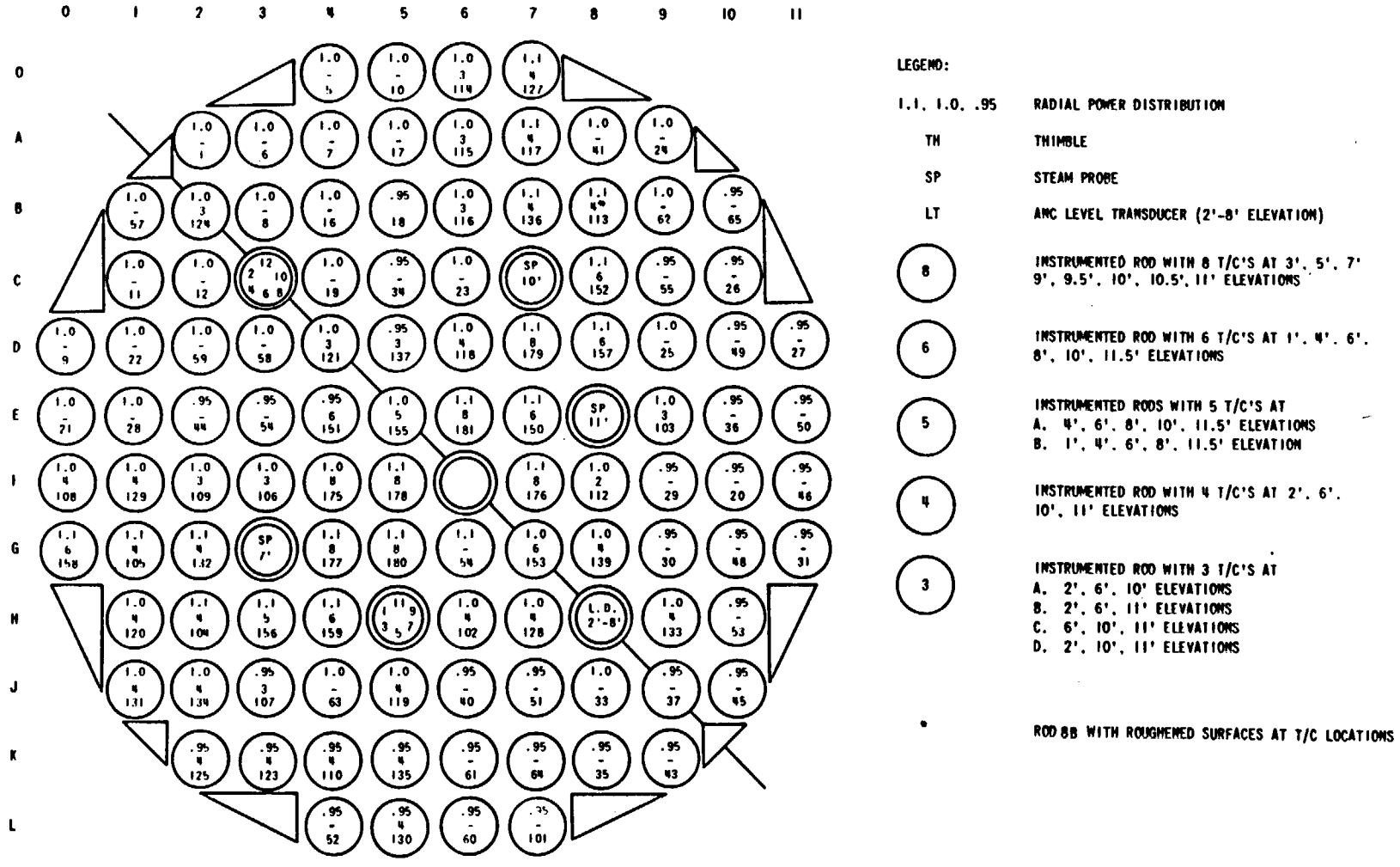

Figure 2-3. FLECHT - Low Flooding Rate Tests – Skewed Axial Power Profile Bundle Instrumentation

- The stream probe valves are opened and flow is established.
- Power to the bundle is turned on and all rods begin to heat up; when any two rods reach the preset initial cladding temperature, bundle flooding and power decay are initiated automatically.
- After the bundle has quenched completely, the test is terminated.

2-4. TEST MATRIX

Table 2-1 lists all the valid runs made in the low flooding rate test series. The runs are ordered by test matrix number.[1] The table gives run conditions hot spot location, maximum temperature, turnaround time, and quench time; also given are bundle quench time and location of failed rods.

For examining different parametric effects, groups of runs where only one parameter is varied are of interest. The test matrix has been regrouped with the single parameter variation identified and the range of parameters in section 3. The nominal reference conditions for the reference tests used for detailed analysis is given in section 4.

---

1. Last two digits on run number are the matrix number.

TABLE 2-1
FLECHT-LOW FLOODING RATE SKEWED TEST-SERIES-RUN SUMMARY DATA

Run Conditions								Results							
Test Matrix (Rev. 4) No.	Run No.	Upper Plenum Pressure (psia)	Rod Initial Clad Temp at 10-ft Elev. (°F)	Rod Peak Power (kw/ft)	Flooding Rate (in./sec)	Coolant Temp. (°F)	Bundle Radial Power Profile	Hottest Rod T/C & Elev. (No.-ft)	$T_{initial}$ (°F)	$T_{max.}$ (°F)	ΔT_{rise} (°F)	t_{turn} (sec)	t_{quench} (sec)	$t_{bundle\ quench}$ (sec)	Disconnected Rod Location
Constant Flooding Rate															
01	13001[a]	39	1600	0.7	5.7	126	Uniform	5F 9.5	1601	1635	34	5	114	139	4A 1F
	17201[b]	40	1630	0.7	6.0	127	Uniform	5D 10	1630	1648	18	2	108	122	4A 1F 7E 7F 9H
02	12102[a]	40	1614	0.7	3.0	126	Uniform	5F 9.5	1616	1675	59	7	174	203	4A 1F
	17302[b]	40	1628	0.7	3.0	127	Uniform	5D-10	1628	1697	69	8	208	239	4A 1F 7E 7F
03	11003	40	1595	0.7	1.5	127	Uniform	5F 9.5	1595	1684	89	20	321	377	4A 1F
	11103	40	1595	0.7	1.5	128	Uniform	5F 9.5	1601	1686	85	20	341	397	4A 1F
	13303	41	1600	0.7	1.5	126	Uniform	5F 9.5	1601	1719	118	25	367	428	4A 1F 9F
04	13404	41	1603	0.7	1.0	127	Uniform	7H 10	1545	1890	345	139	498	582	4A 1F
05	15305	40	1603	0.7	0.8	127	Uniform	7H 10	1550	2034	484	158	620	674	4A 1F 7L 9A
06	15606	40	1528	0.7	0.7	127	Uniform	6D-10	1525	2191	666	205	791	870	4A 1F 9A
Pressure at Coolant Flooding Rate															
07	12907[a]	20	1602	0.7	6.0	91	Uniform	5F-9.5	1602	1636	34	4	119	152	4A 1F
	17407[b]	20	1626	0.7	5.8	93	Uniform	5D-10	1626	1654	28	3	128	155	4A 1F 7E 7F
08	13508	21	1599	0.7	1.54	91	Uniform	5F-9.5	1601	1693	92	12	536	624	4A 1F
09	13609	21	1600	0.7	1.0	87	Uniform	5K 10	1580	1803	223	121	723	844	4A 1F
10	16110	20	1617	0.7	0.8	96	Uniform	7H-10	1549	1933	384	165	883	978	4A 1F
11	13711	60	1609	0.7	1.0	152	Uniform	5F-10	1565	1916	351	117	418	467	4A 1F
ΔT Subcooling Effect															
12	13812	41	1604	0.7	1.0	184	Uniform	5K-10	1579	1701	122	48	818	1039	4A 1F
13	15713	40	1607	0.7	1.0	165	Uniform	7H-10	1531	1784	253	103	604	675	4A-1F
14	13914	21	1605	0.7	1.0	223	Uniform	5K-10	1579	1701	122	48	818	1039	4A 1F
Low Initial T_{clad} Temp. Effect															
15	12515	39	1002	0.7	1.5	126	Uniform	6E 10	984	1443	459	108	314	375	4A 1F
16	12816	40	507	0.7	1.5	126	Uniform	7B 10	493	1168	636	124	302	325	4A 1F
17	12617	20	507	0.7	1.5	89	Uniform	7A 10	475	1260	785	187	491	568	4A 1F

TABLE 2-1 (cont)

FLECHT-LOW FLOODING RATE SKEWED TEST-SERIES RUN SUMMARY DATA

Run Conditions								Results							
Test Matrix (Rev. 4) No.	Run No.	Upper Plenum Pressure (psia)	Rod Initial Temp. at 10 ft Elev. (°F)	Rod Peak Power (kw/ft)	Flooding Rate (in./sec)	Coolant Temp. (°F)	Bundle Radial Power Profile	Hottest Rod T/C & Elev. (No. ft)	$T_{initial}$ (°F)	T_{max} (°F)	ΔT_{rise} (°F)	t_{turn} (sec)	t_{quench} (sec)	$t_{bundle\ quench}$ (sec)	Disconnected Rod Location
Rod Peak Power Effect															
18	11618	41	1618	0.45	1.5	126	Uniform	5F 9.5	1618	1663	45	10	241	278	4A 1F
19	11719	41	1001	0.45	1.5	126	Uniform	8D 10	984	1196	212	63	193	220	4A 1F
20	12720	40	508	0.45	1.5	126	Uniform	2H 10	491	913	422	85	176	192	4A 1F
21	11821	20	507	0.45	1.64	85	Uniform	2H 10	484	905	421	108	238	268	4A 1F
22	16022	40	1636	1.0	1.5	128	Uniform	7H 10	1563	1856	293	84	524	593	4A 1F 5G
Radial Power Effect															
23	15423	40	1606	0.8	1.0	126	FLECHT	7E 10	1541	1901	359	143	524	574	4A 1F 7D
Overlap Cosine Tests															
24	11524	40	837	0.373	0.8	126	FLECHT	5F 10	819	1269	450	146	256	276	4A 1F
25	11225	41	954	0.464	1.5	126	FLECHT	4G 10	942	1154	211	64	180	199	4A 1F
26	11326	60	950	0.604	2.0	152	FLECHT	7B 10	949	1125	176	40	127	140	4A 1F
27	13127	40	955	0.464	6.0(5 sec) 0.8(onward)	126	FLECHT	8C 10	928	1239	310	109	261	287	4A 1F
28	11428	20	916	0.464	1.0	90	FLECHT	5F 10	897	1316	419	146	379	480	4A 1F
29	12329[a]	18	918	0.610	5.9	166	FLECHT	5F 9.5	918	966	48	6	152	186	4A 1F
	17579[b]	18	917	0.552	6.0	167	Uniform	5F 9.5	917	947	30	5	115	136	4A 1F 7F 7F
Variable Step Flow Effect															
30	14230	32	1208	0.7	1.5(100 sec) 0.5(onward)	151	Uniform	4E 10	1157	1648	491	295	835	980	4A 1F
31	14331	32	1204	0.7	1.55(100 sec) 1.0(onward)	151	Uniform	2H 10	1152	1517	365	133	561	621	4A 1F
32	15132	39	1555	0.7	6.0(5 sec) 0.8(onward)	127	Uniform	7H 10	1552	1921	370	164	558	639	4A 1F 7L 9A
33	15233	19	1553	0.7	6.0(5 sec) 0.8(onward)	89	Uniform	7H 10	1549	1798	249	148	811	935	4A 1F 7L 9A
34	15034	21	1609	0.7	6 - 0.8 (15 sec) 0.8(onward)	86	Uniform	3F 10	1534	1690	156	155	803	923	4A 1F 7L 9A
35	14935	20	804	0.7	1.0	86	Uniform	4E 10	786	1488	1102	273	723	846	4A 1F 7L 9A

TABLE 2-1 (cont)

FLECHT-LOW FLOODING RATE SKEWED TEST SERIES RUN SUMMARY DATA

Run Conditions								Results							
Test Matrix (Rev. 4) No.	Run No.	Upper Plenum Pressure (psia)	Rod Initial Temp at 10-ft Elev. (°F)	Rod Peak Power (kw/ft)	Flooding Rate (in./sec)	Coolant Temp. (°F)	Bundle Radial Power Profile	Hottest Rod T/C & Elev. (No.-ft)	$T_{initial}$ (°F)	T_{max} (°F)	ΔT_{rise} (°F)	t_{turn} (sec)	t_{quench} (sec)	$t_{bundle\ quench}$ (sec)	Disconnected Rod Location
Repeatability															
36	17136	40	1638	0.7	1.0	133	Uniform	7H-10	1572	1892	320	123	460	516	4A 1F 7E 7F
Hot and Cold Channel Effect															
37	15937	40	1625[a] 482[b]	0.7[a] 0.45[b]	1.5	128	Hot/Cold Channels	5D-10	1627	1819	192	41	230	285	4A 1F
38	15838	41	966	0.55	1.5	126	Uniform	5D-10	966	1265	299	86	213	286	4A 1F
Gravity Reflood					Injection Rate lbs/sec										
40	16340	40	950	0.55	11.3(14 sec) 1.4(onward)	125	Uniform	5D-10	950	1009	59	41	110	175	4A 1F
41	16741	40	1626[a] 568[b]	0.7[a] 0.45[b]	11.4(14 sec) 1.45(onward)	127	Hot/Cold Channels	5D-10	1627	1681	54	8	149	200	4A 1F 7E 7F
42	16642	21	1609[a] 433[b]	0.7[a] 0.45[b]	12.6(14 sec) 1.44(onward)	94	Hot/Cold Channels	5D-10	1609	1659	50	7	226	291	4A 1F 7E 7F
43	16543	20	672	0.455	11.8(14 sec) 1.42(onward)	160	Uniform	5D-10	662	740	78	30	43	117	4A 1F 7E
Transient Tests					Flooding Rate in./sec										
44	16844	40→ 20	1629	0.7	6.0(5 sec) 0.8(onward)	127	Uniform	4F-10	1597	1914	317	205	636	751	4A 1F 7F 7F 10J
45	16945	40	1632	0.7	6.7(5 sec) 0.8(onward)	127→ 262	Uniform	7H-10	1561	1997	377	152	622	680	4A 1F 7E 7F
46	17046	40→ 20	1632	0.7	6.0(5 sec) 0.8(onward)	127→ 262	Uniform	4F-10	1543	1995	452	134	668	798	4A 1F 7F 7F
Additional Overlap Cosine Tests															
47	14647	21	1610	0.17	1.0	89	FLECHT	5F 9.5	1611	1672	61	18	382	424	4A 1F 9A 7I
48	14548	41	1611	0.216	1.0	127	FLECHT	5F 9.5	1611	1634	23	13	241	261	4A 1I

a. Hot Channel

b. Cool Channel

SECTION 3
PARAMETRIC EFFECTS

3-1. INTRODUCTION

This section is a qualitative presentation of the effects of the principal test parameters. No attempt has been made to analyze the causes of the observed trends. A detailed quantitative analysis of heat transfer mechanisms and their effects is treated in section 4.

Trends in temperature rise and quench time are also compared with the cosine test results. Comparison of skewed and cosine power shapes for the same test conditions indicate that the skewed profile is less severe than the cosine; that is, for the same test conditions including peak power, the skewed profile usually results in lower temperature rises than the cosine power shape.

Parametric effects examined are flooding rate, pressure, subcooling, initial cladding temperature, peak power, and initial flooding rate for variable flooding rate tests. Table 3-1 presents the range of parameters and relevant runs used for each comparison. The effect of each parameter on heat transfer, temperature transients, and mass effluent fractions are presented. Temperature rise and quench time trends are then compared with cosine results. For these latter comparisons, the test conditions are usually not the same. However, the main purpose of these comparisons is to examine the trends with each parameter, rather than the absolute values of temperature rise or quench time. In particular, the quench times plotted for the skewed tests are 10-foot values while for cosine, the 6-foot values are plotted. This typically results in much longer quench times for the skewed tests.

Time-integrated values of mass effluent fractions are presented as a function of time rather than the instantaneous values. Fluctuations in the instantaneous values during a run tends to obscure the small run-to-run differences in mass effluent fraction. On the figures, Γ_{out} versus time is plotted. The parameter Γ_{out} is defined as follows

$$\Gamma_{out}\ (t) = \frac{M_{in}\ (t) - M_{st}\ (t)}{M_{in}\ (t)} \qquad (3\text{-}1)$$

TABLE 3-1

PARAMETRIC EFFECTS, SUMMARY OF
RUN NUMBERS AND RANGE OF PARAMETERS

Parameter Studied	Reference Value	Parameter Values	Run Numbers
Flooding Rate (in./sec)	0.8, 1.0, 1.5	0.6, 0.8, 1.0, 1.5, 3, 6	15606, 15305, 13404 13303, 12102, 13001
Pressure[b] (psia)	40	20, 40, 60	13609, 13404, 13711
Initial Cladding[a] Temp. (°F)	1600	500, 1000, 1600	12816, 12515, 13303
Subcooling[b] (°F)	140	5, 80, 140	15713, 13812, 13404
Peak Power[a] (kw/ft)	0.7	0.45, 0.7, 1.0	11618, 13303, 16022
Initial Flooding[c] Rate (Variable Flooding Rate Runs) (in./sec)	0.8	0.8; 6(5), 0.8 on[c] 6→0.8(15), 0.8 on[d]	15305, 15132 15034

a. 1.5 in./sec flooding rate

b. 1.0 in./sec flooding rate

c. 6 in./sec flooding rate for 5 sec, 0.8 in./sec after 5 sec

d. Flow ramped from 6 to 0.8 in./sec in first 15 sec, 0.8 in./sec after 15 sec

where

M_{in} (t) = Total mass injected up to time t. (lbm)

M_{st} (t) = Total mass stored in the bundle up to time t. (lbm)

It will be noted that some of the Γ_{out} curves tend to large values early in time. On physical grounds Γ_{out} must be zero at time zero since mass must enter the bundle some finite time increment before it leaves the bundle. The large values of Γ_{out} in the first 10 to 20 seconds of the runs are artifacts of the uncertainty in the mass balance measurements and definition of Γ_{out} which, by equation (3-1), becomes indefinite at time zero.

The heat transfer and temperature transient curves presented in the following discussion represent averages of all the rod thermocouples in the central 6 x 6 array of the bundle shown in figure 3-1. All the tests used to study parametric effects were run with uniform radial power distribution; that is, all rods had the same power.

3-2. FLOODING RATE EFFECT

An abundant amount of data is available on the effect of flooding rate with a cosine power shape.[1] In WCAP-8838 it was shown that temperature rise and quench time trends were consistent among all the cosine data. Figures 3-2 and 3-3 reproduce figures from WCAP-8838 showing these effects. The skewed data have been added to these figures.

Figure 3-2 for temperature rise shows that the skewed data exhibit the same trend as the cosine data of increasing temperature rise with decreasing flooding rate. This trend is expected. The surprising result of this plot shows that temperature rises of the skewed data are generally lower than the cosine data for the same flooding rate. This is true even in the cases where the peak conditions and run parameters are identical. This result indicates that the skewed power distribution is a less severe case than a cosine power distribution.

Figure 3-3 shows the quench times versus flooding rate. For this parameter, skewed data show longer quench times for the peak power location than the cosine data at the same conditions. This is expected due to the 50 percent higher elevation of the peak power locations for the skewed shape. Trends of quench time with flooding rate are the same for both power shapes.

Figures 3-4 and 3-5 present the variation of heat transfer coefficient and peak temperatures at the 10-foot elevation versus time for the sequence of runs in which only flooding rate was varied. The figures show the expected orderly increase in heat transfer at all times as flooding rate increases. Temperatures show more rapid turnaround and increasingly lower peak temperatures as flooding rate is increased.

1. Lilly, G. P., et al. PWR FLECHT Cosine Low Flooding Rate Series Evaluation Report WCAP-8838, Mar. 1977.

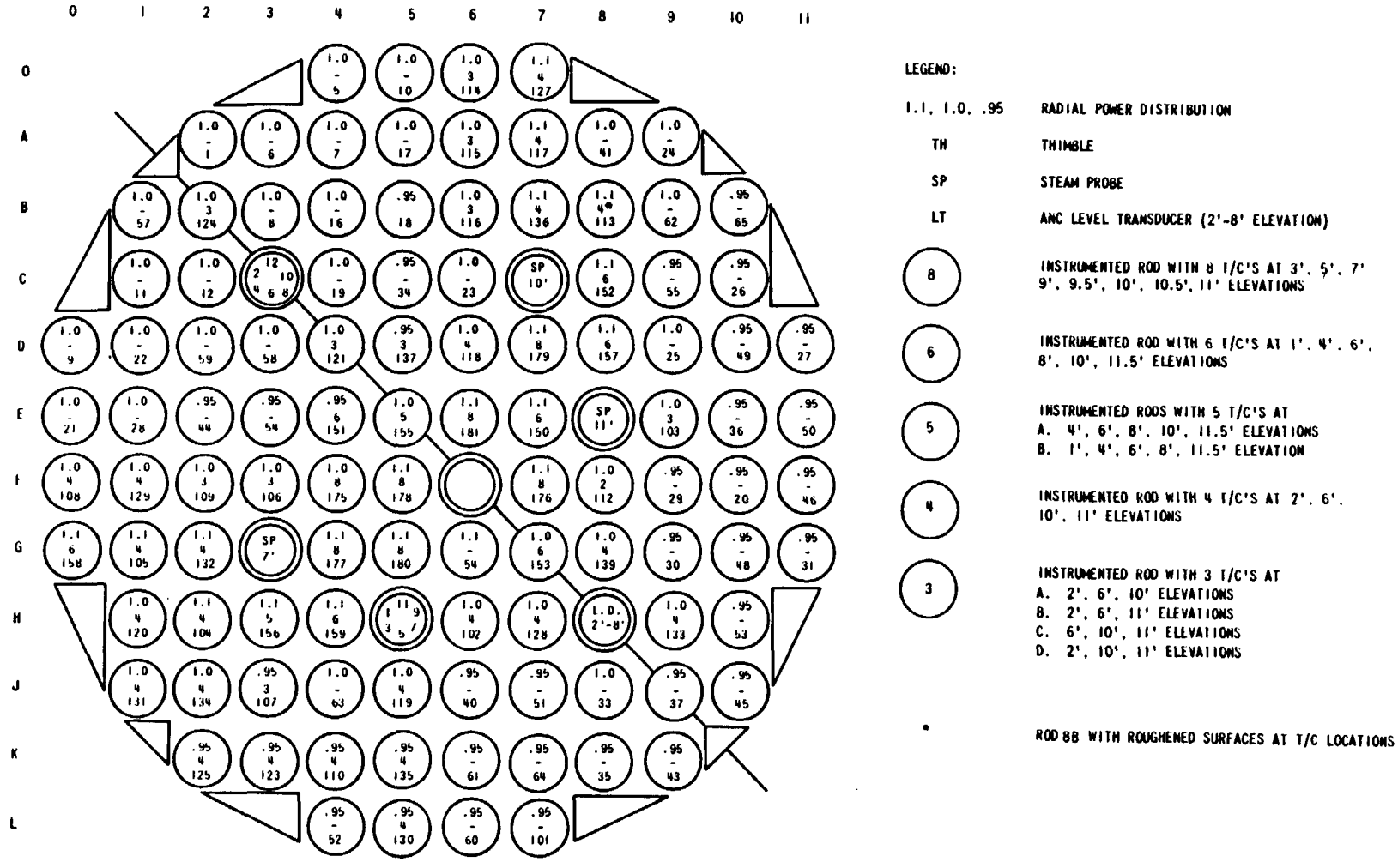

Figure 3-1. FLECHT - Low Flooding Rate Tests – Skewed Axial Power Profile Bundle Instrumentation

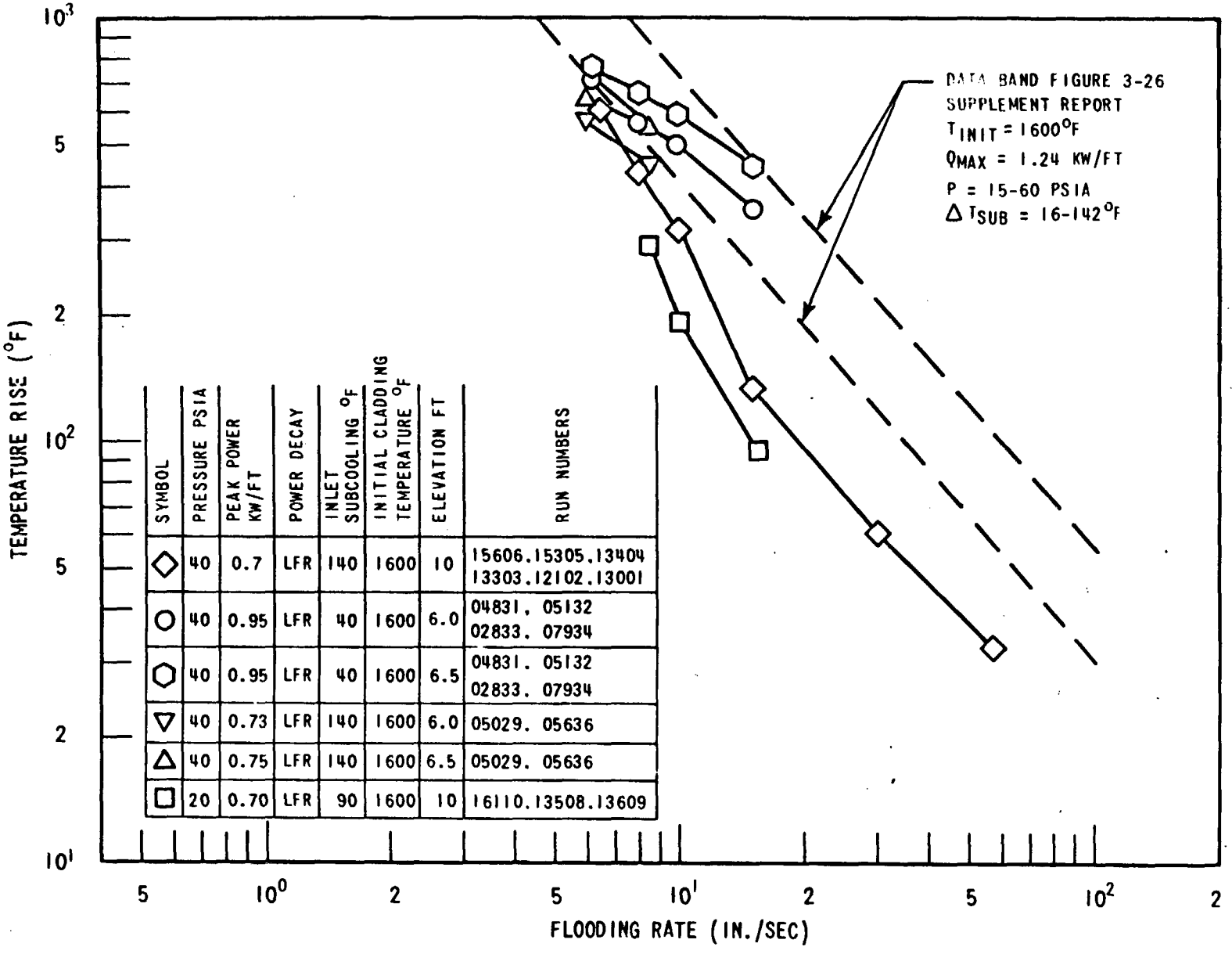

Figure 3-2. Comparison of Old and New FLECHT Data for Temperature Rise at Low Flooding Rates

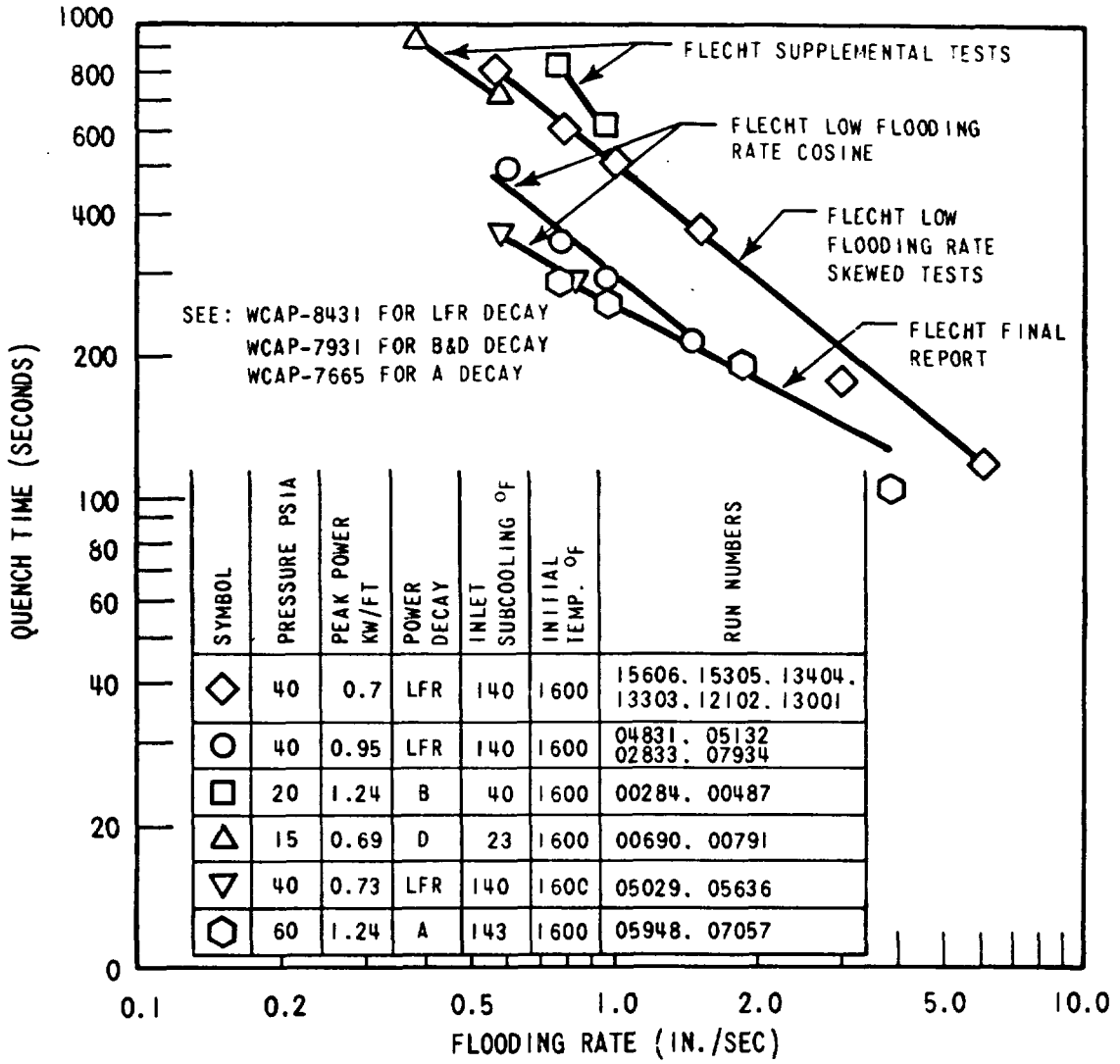

SYMBOL	PRESSURE PSIA	PEAK POWER KW/FT	POWER DECAY	INLET SUBCOOLING °F	INITIAL TEMP. °F	RUN NUMBERS
◇	40	0.7	LFR	140	1600	15606, 15305, 13404, 13303, 12102, 13001
○	40	0.95	LFR	140	1600	04831, 05132 02833, 07934
□	20	1.24	B	40	1600	00284, 00487
△	15	0.69	D	23	1600	00690, 00791
▽	40	0.73	LFR	140	1600	05029, 05636
⬡	60	1.24	A	143	1600	05948, 07057

Figure 3-3. Comparison of Previous and Present FLECHT Data for Quench Time at Low Flooding Rates

RUN NUMBERS	15606-15305-13404-13303-12102-13001
PRESSURE	40 PSIA
INITIAL CLADDING TEMPERATURE	1600°F
PEAK POWER	0.7 KW/FT
SUBCOOLING	140°F
INJECTION RATE	VARIABLE

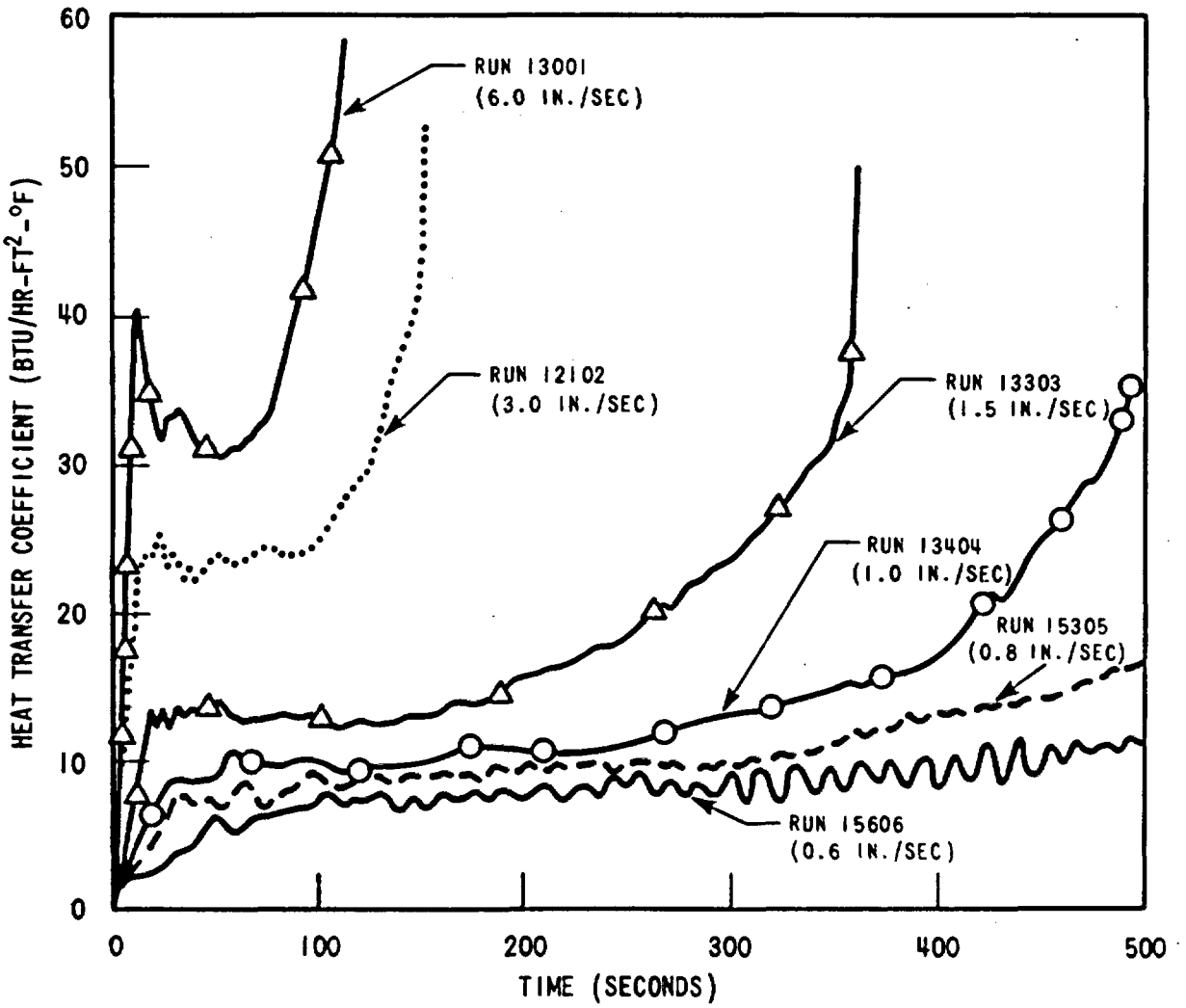

Figure 3-4. Flooding Rate Effect on Heat Transfer Coefficient (10 FT)

RUN NUMBERS	15606-15305-13404-13303 12102-13001
PRESSURE	40 PSIA
INITIAL CLADDING TEMPERATURE	1600°F
PEAK POWER	0.7 KW/FT
SUBCOOLING	140°F
INJECTION RATE	VARIABLE

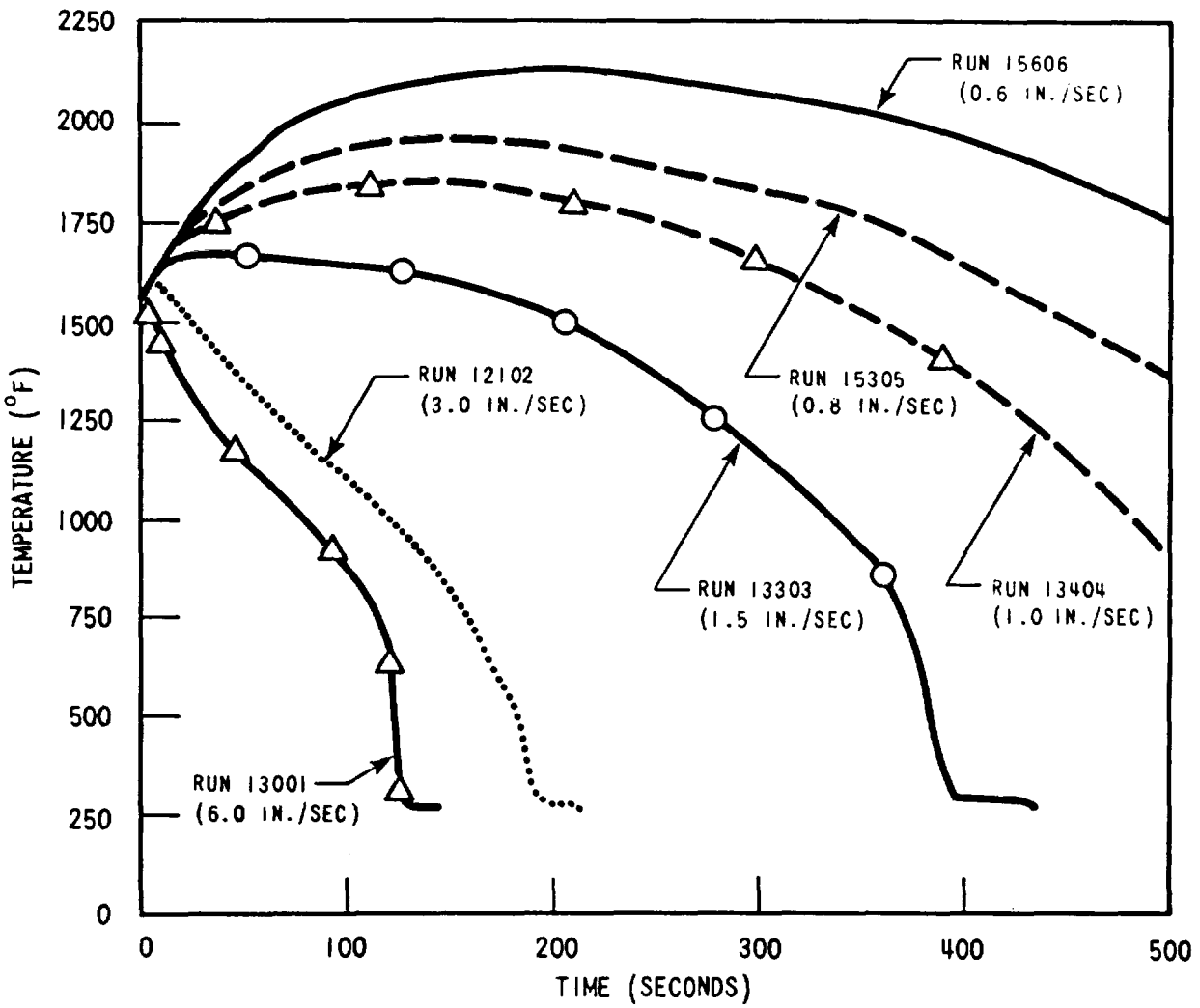

Figure 3-5. Flooding Rate Effect on Cladding Temperature (10 FT)

Figure 3-6 presents the variation of time-integrated mass effluent fraction versus time. The higher the flooding rate, the more rapidly the mass effluent fraction approaches its asymptotic value. This is expected due simply to the accelerated pace of events in higher flooding rate runs. The same trend was observed for the cosine tests (WCAP-8838).[1] Of course, the principal effect of increasing flooding rate is to proportionately increase the mass flow above the quench front with the mass effluent fraction exerting only a secondary influence. Mass effluent fraction plots were not included for the high flooding rate runs as the mass balance for these runs was not as good as tests at lower flooding rates.

3-3. PRESSURE EFFECT

Pressure and subcooling were two parameters which showed opposite trends with respect to temperature rise for skewed and cosine power shapes. Trends of quench time were the same for all parameters for both power shapes.

Figure 3-7 presents temperature rise and quench time plots versus pressure for both cosine and skewed power shapes. Temperature rise is seen to increase with pressure for the skewed tests and decrease with pressure for the cosine. The skewed trend is consistent for several different flooding rates. The trend of the low flooding rate cosine data was also consistent with previous cosine data as shown in WCAP-8838.

Figures 3-8 and 3-9 present the heat transfer coefficient and temperature transients for the sequence of skewed power tests at 1.0 in./sec. The temperature transient for 20 psi is somewhat uncharacteristic of most temperature curves. It rises rapidly with other curves then abruptly becomes flat for a long period of time. The heat transfer which causes this shows an abrupt rise early in time and then gradually decreases until shortly before quench.

Figure 3-10 displays the effect of pressure on integrated mass effluent fraction. The low pressure tests show a higher carryout early in time. This same effect was observed for the cosine tests. This trend could be expected, since lower pressures will lead to higher void formation for the same steam generation. This will tend to reduce storage below the quench front.

It is believed that the earlier entrainment in the 20 psia tests establishes a minimum heat transfer coefficient which will result in halting the cladding temperature rise. Separate calculations indicate that an h value of 8-10 Btu/hr-ft^2-°F will be sufficient to prevent cladding

---

1. Lilly, G. P., et al. PWR FLECHT Cosine Low Flooding Rate Series Evaluation Report WCAP-8838, Mar 1977.

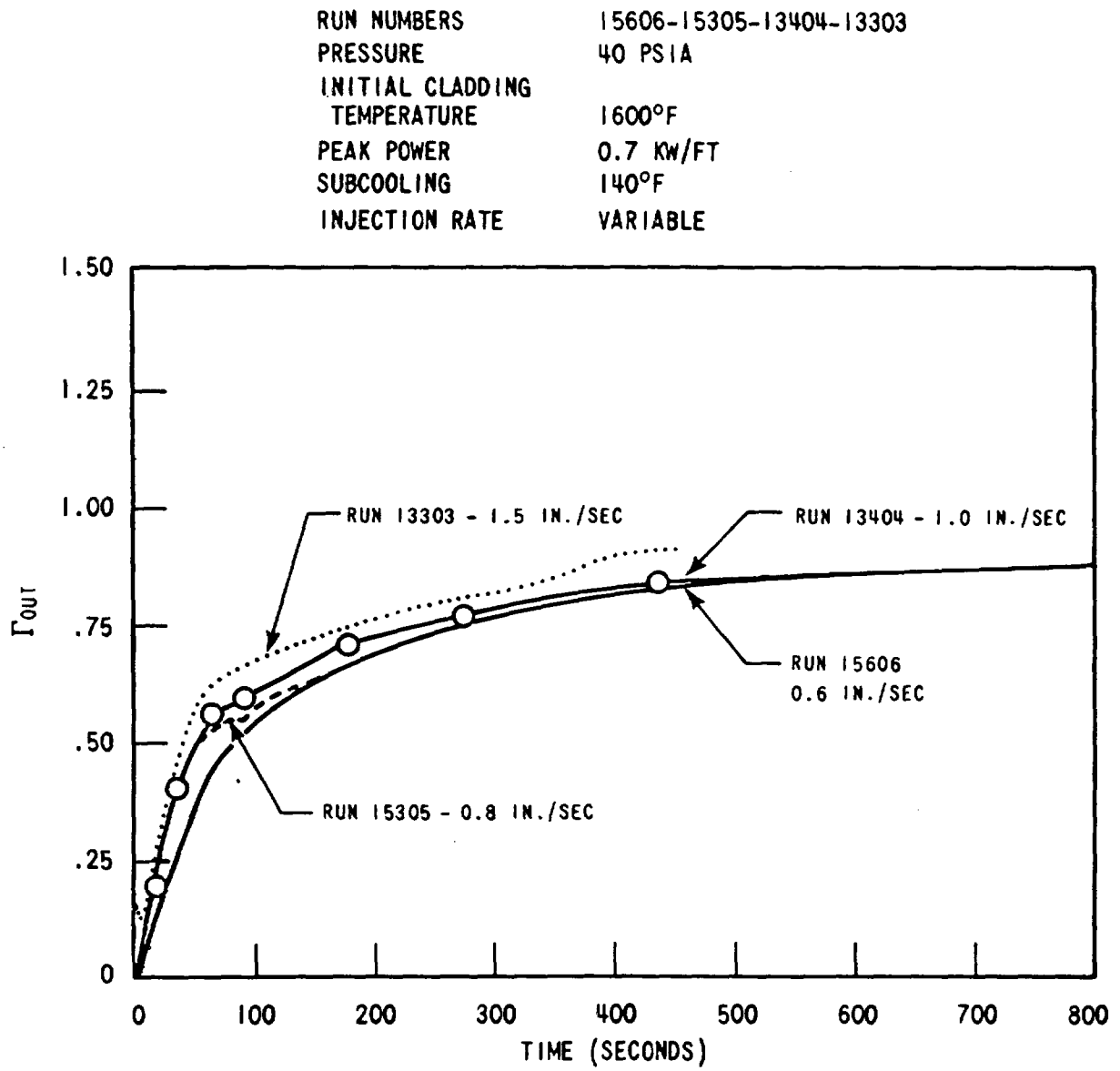

Figure 3-6. Flooding Rate Effect on Mass Effluent Fraction (Low Flooding Rates)

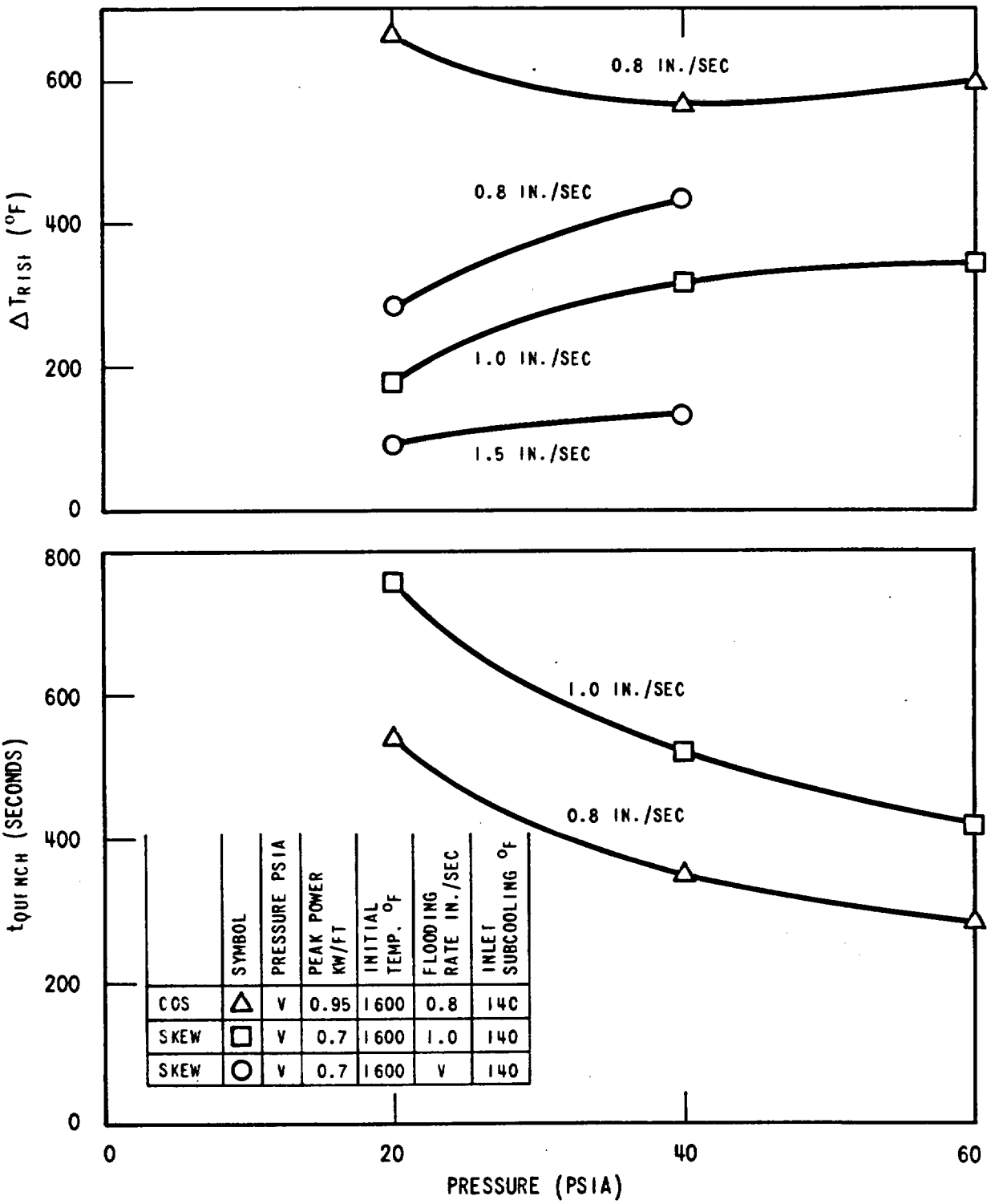

Figure 3-7. Pressure Effect on Temperature Rise and Quench Time

RUN NUMBERS	13609-13404-13711
PRESSURE	VARIABLE PSIA
INITIAL CLADDING TEMPERATURE	1600°F
PEAK POWER	0.7 KW/FT
SUBCOOLING	140°F
INJECTION RATE	1.0 IN./SEC

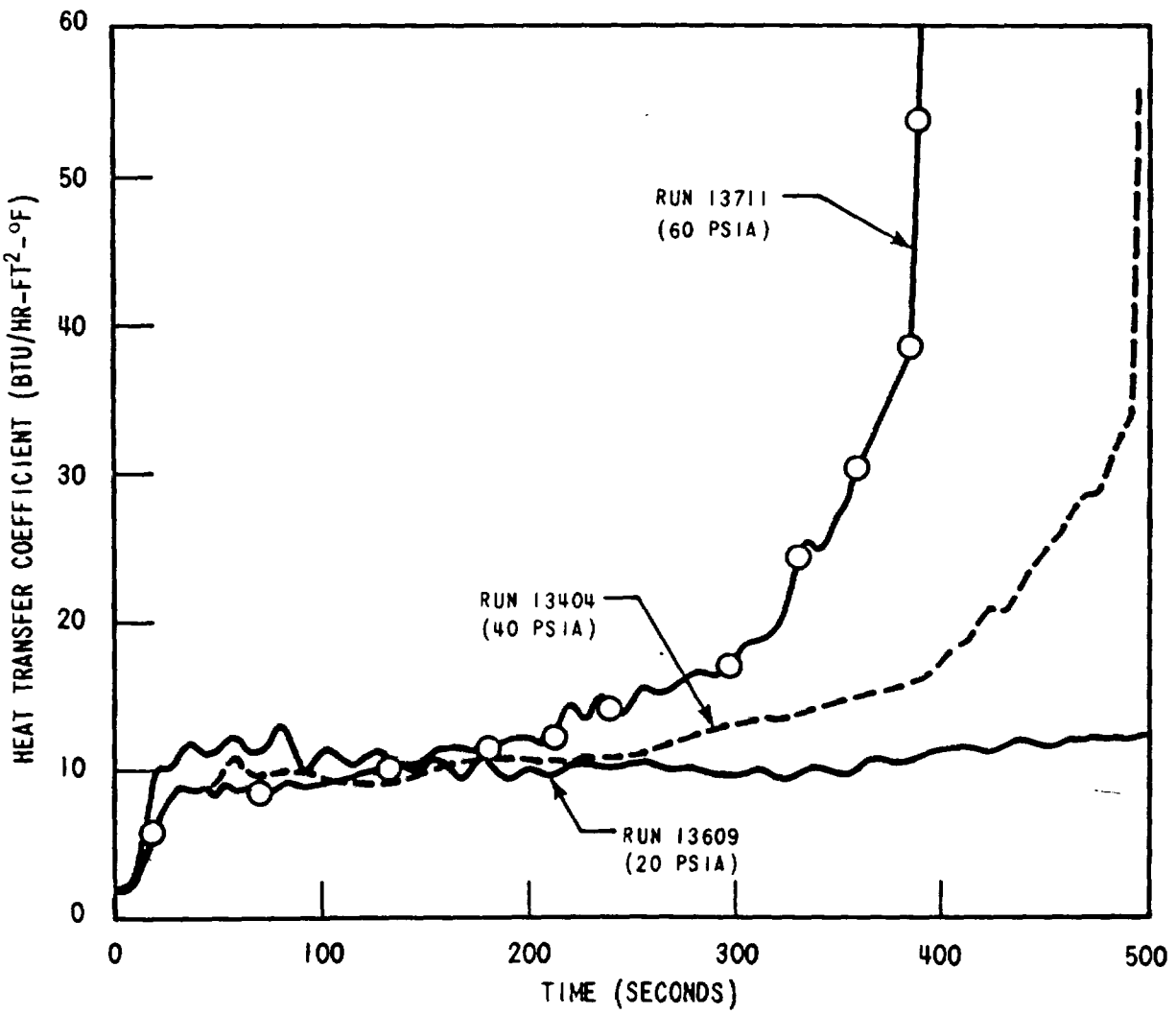

Figure 3-8. Pressure Effect on Heat Transfer Coefficient (10 FT)

RUN NUMBERS	13609-13404-13711
PRESSURE	VARIABLE PSIA
INITIAL CLADDING TEMPERATURE	1600°F
PEAK POWER	0.7 KW/FT
SUBCOOLING	140°F
INJECTION RATE	1.0 IN./SEC

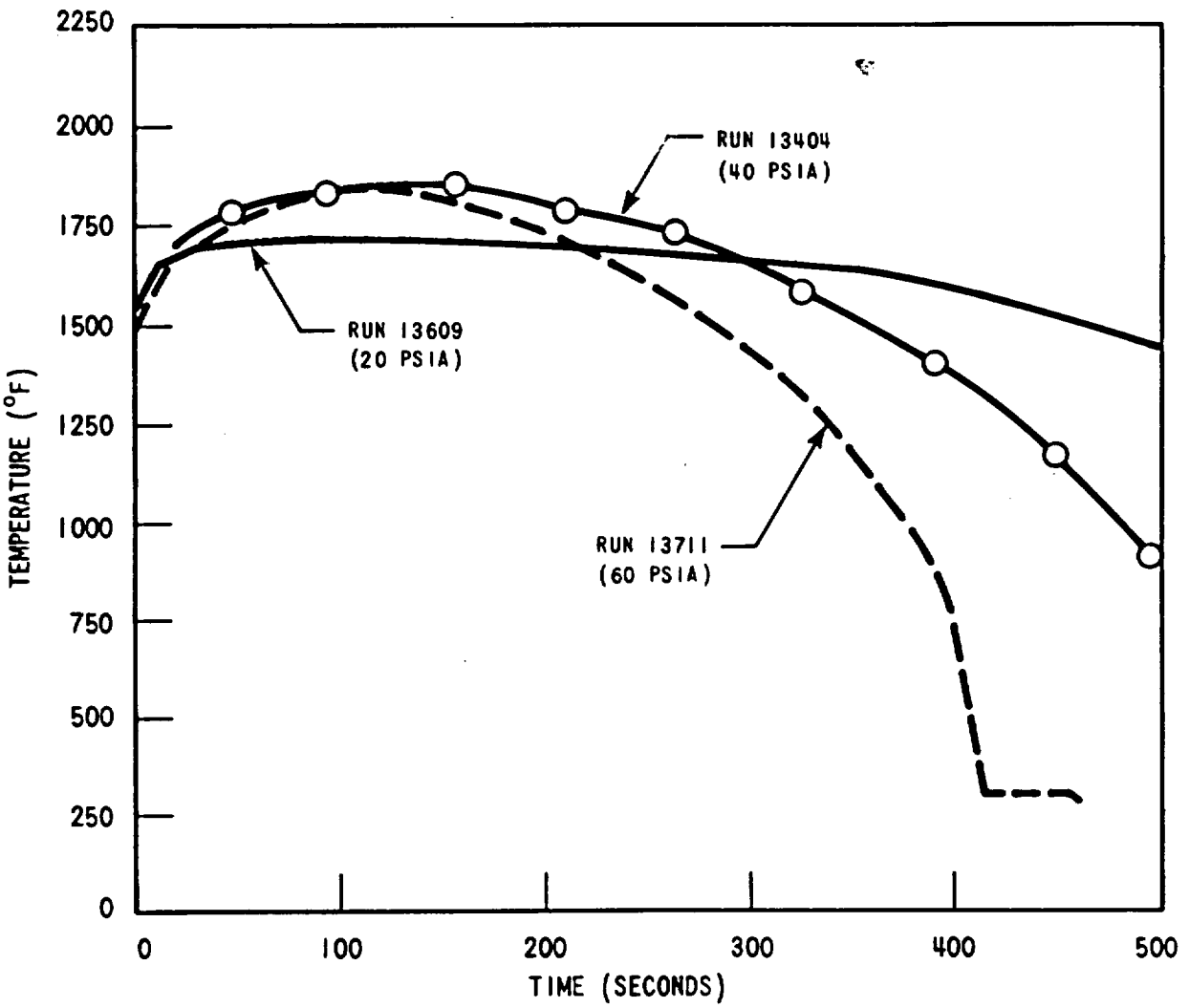

Figure 3-9. Pressure Effect on Cladding Temperature (10 FT)

RUN NUMBERS	13609-13404-13711
PRESSURE	VARIABLE PSIA
INITIAL CLADDING TEMPERATURE	1600°F
PEAK POWER	0.7 KW/FT
SUBCOOLING	140°F
INJECTION RATE	1.0 IN./SEC

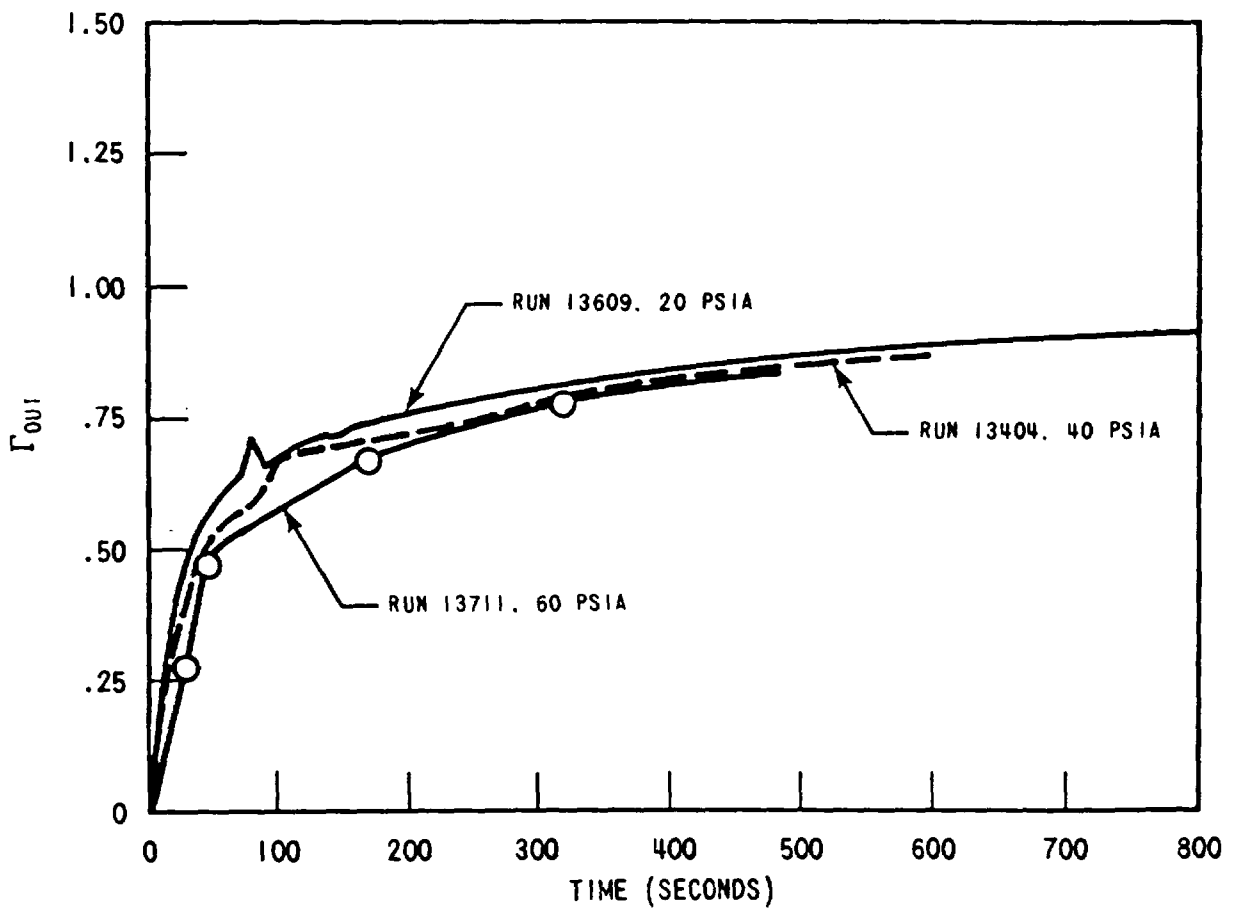

Figure 3-10. Pressure Effect on Mass Effluent Fraction

temperature increases at the rod peak power used in these tests. The same trend of a flat temperature response at lower pressures was also observed in the low flooding rate cosine tests (WCAP-8838) as again the rod heat transfer reached a minimum value for halting the cladding temperature rise.

3-4. SUBCOOLING EFFECT

The effect of subcooling on temperature rise for the cosine tests was a very weak effect and heat transfer coefficients were virtually identical well past turnaround time. Figure 3-11 shows that the effect of subcooling is somewhat stronger and in the opposite direction for the skewed power shape. Figures 3-12 and 3-13 show higher heat transfer and much more rapid turnaround for the lowest value of subcooling.

The integrated carryout fraction, Figure 3-14 shows a marked increase with decreased subcooling. This was also observed for the cosine tests and is to be expected since the lower subcooling means more vapor generation for the same heat input.

3-5. INITIAL CLADDING TEMPERATURE EFFECT

Initial cladding temperature effects for skewed power shape parallel closely the trends observed for the cosine tests. These effects are basically higher temperature rises and shorter quench times as seen in figure 3-15. Heat transfer coefficients, shown in figure 3-16, are difficult to interpret because of the wide variation in wall-to-saturation temperature differences. Differing wall temperature (figure 3-17) and mass effluent fractions (figure 3-18) could be expected to have quite different heat transfer mechanisms.

With regard to the mass effluent fraction, the delay in carryout for the lower cladding temperatures is to be expected. The lower temperatures mean less skewed energy and hence less vapor formation and liquid entrainment. Therefore, the solid water level (or the saturation line), will penetrate further into the bundle for lower cladding initial temperature early in time.

3-6. ROD PEAK POWER EFFECT

Predictably, decreasing peak power decreases both temperature rise and quench time. This is shown in figure 3-19 for both cosine and skewed power shapes. For the cosine tests, heat transfer to turnaround time is negligibly affected by peak power. For the skewed tests, the higher powers show higher heat transfer before turnaround (figure 3-20). The power effect still dominates however, leading to higher temperature rises for higher power (figure 3-21).

The mass effluent fractions (figure 3-22) increase with power. The lower powers lead to lower void formation below the quench front and hence more storage below the quench front. The quench front also moves faster at low power.

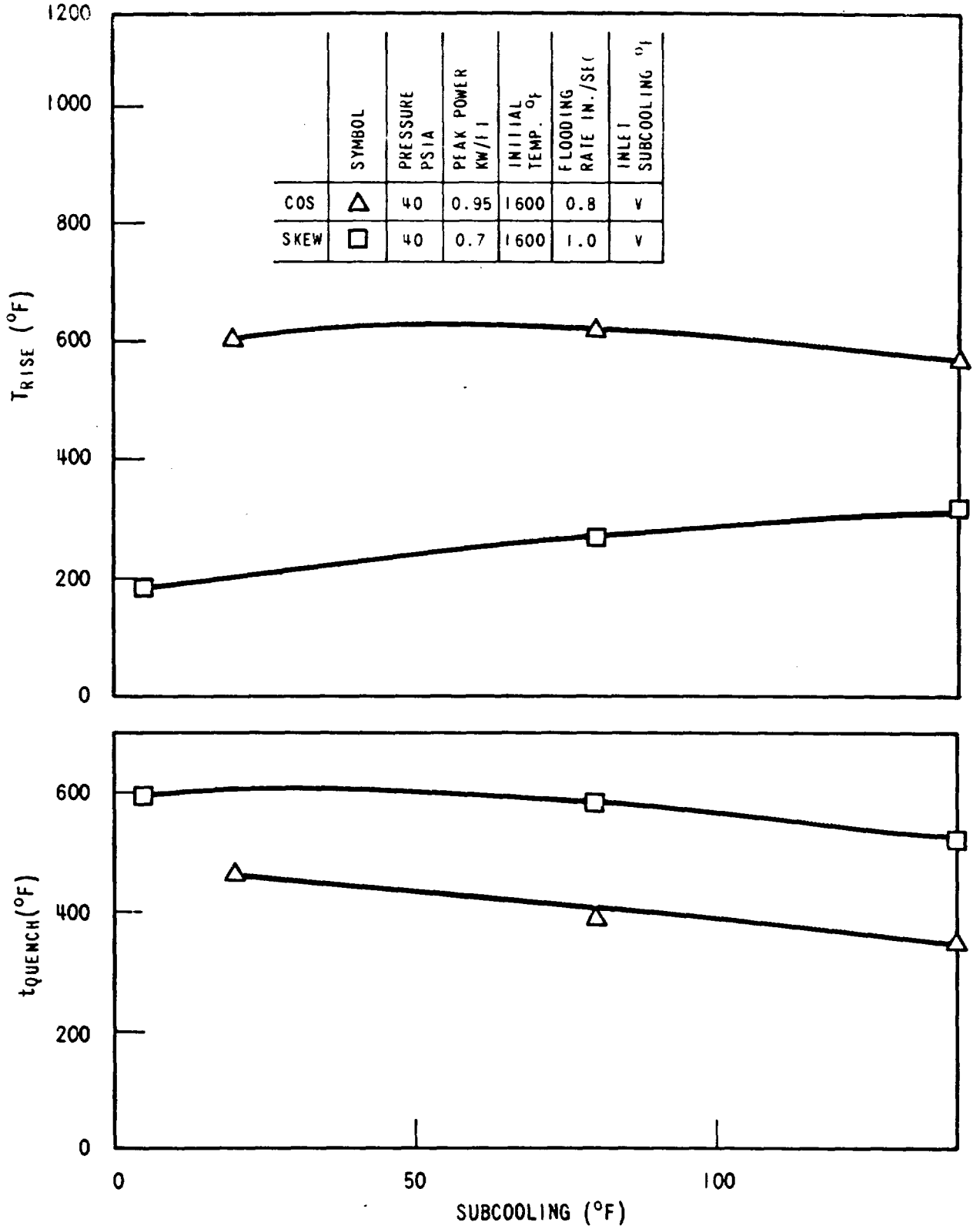

Figure 3-11. Subcooling Effect on Temperature Rise and Quench Time

RUN NUMBERS	15713-13812-13404
PRESSURE	40 PSIA
INITIAL CLADDING TEMPERATURE	1600°F
PEAK POWER	0.7 KW/FT
SUBCOOLING	VARIABLE °F
INJECTION RATE	1.0 IN./SEC

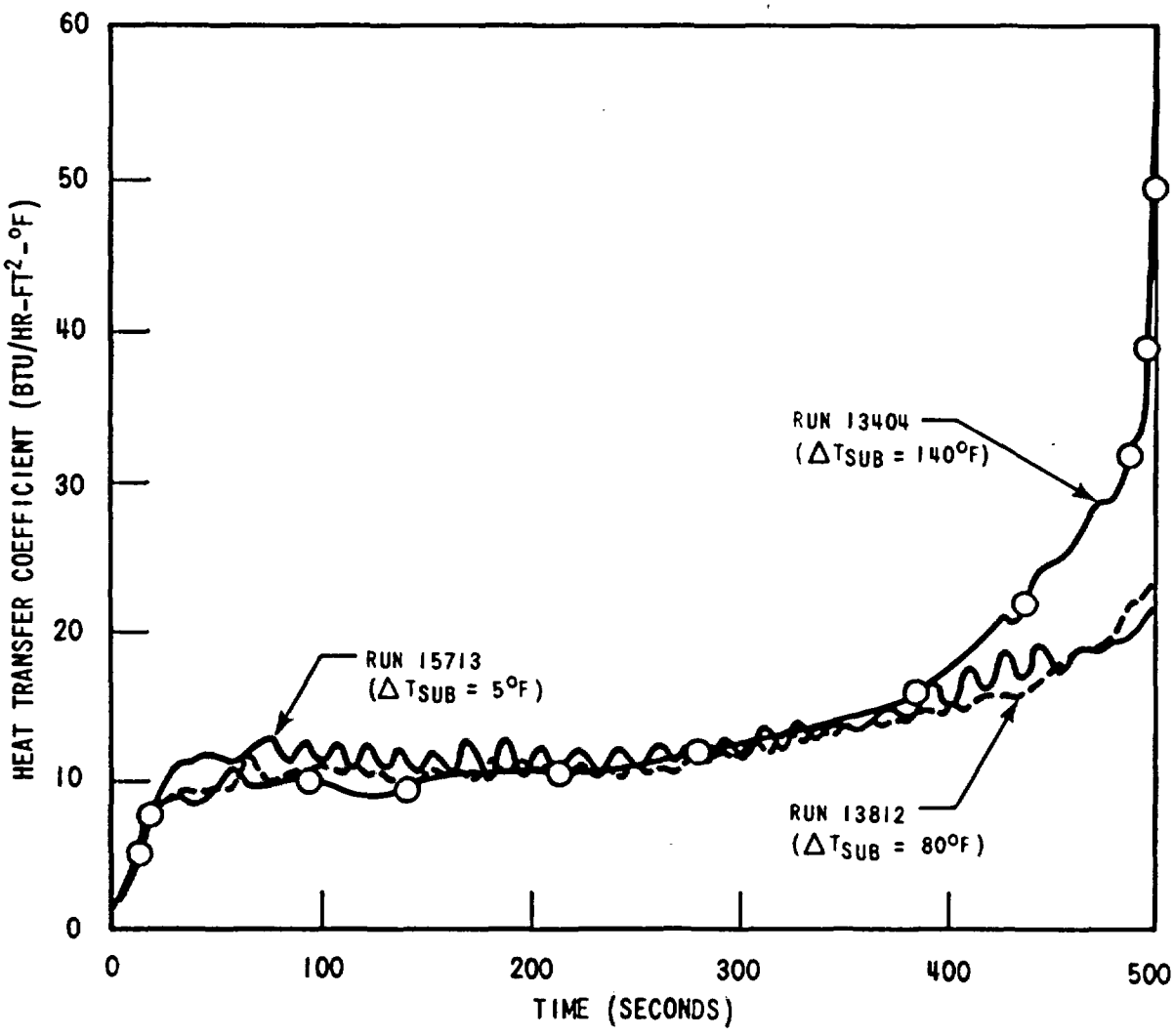

Figure 3-12. Subcooling Effect on Heat Transfer Coefficient (10 FT)

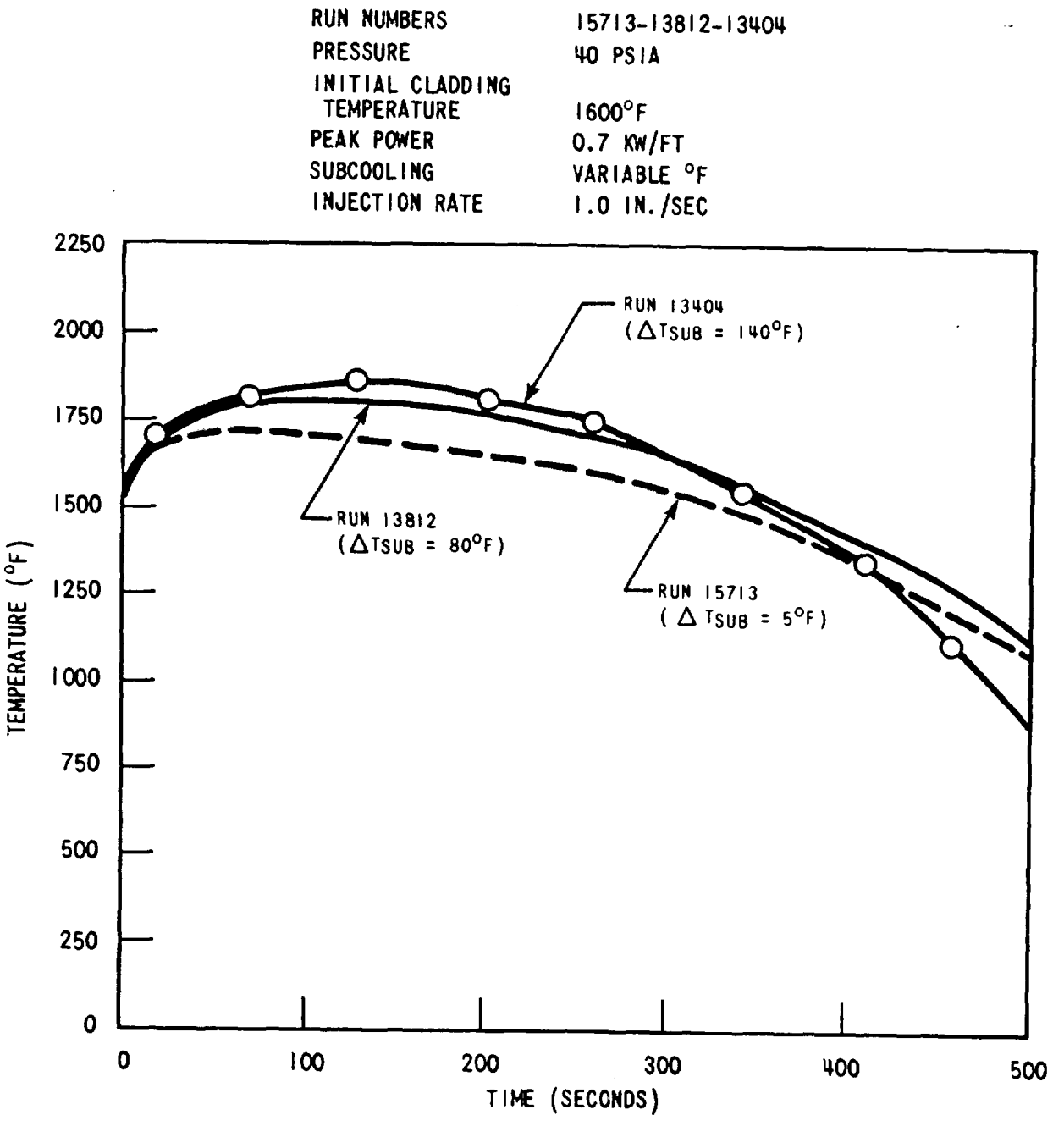

Figure 3-13. Subcooling Effect on Cladding Temperature (10 FT)

RUN NUMBERS	15713-13812-13404
PRESSURE	40 PSIA
INITIAL CLADDING TEMPERATURE	1600°F
PEAK POWER	0.7 KW/FT
SUBCOOLING	VARIABLE °F
INJECTION RATE	1.5 IN./SEC

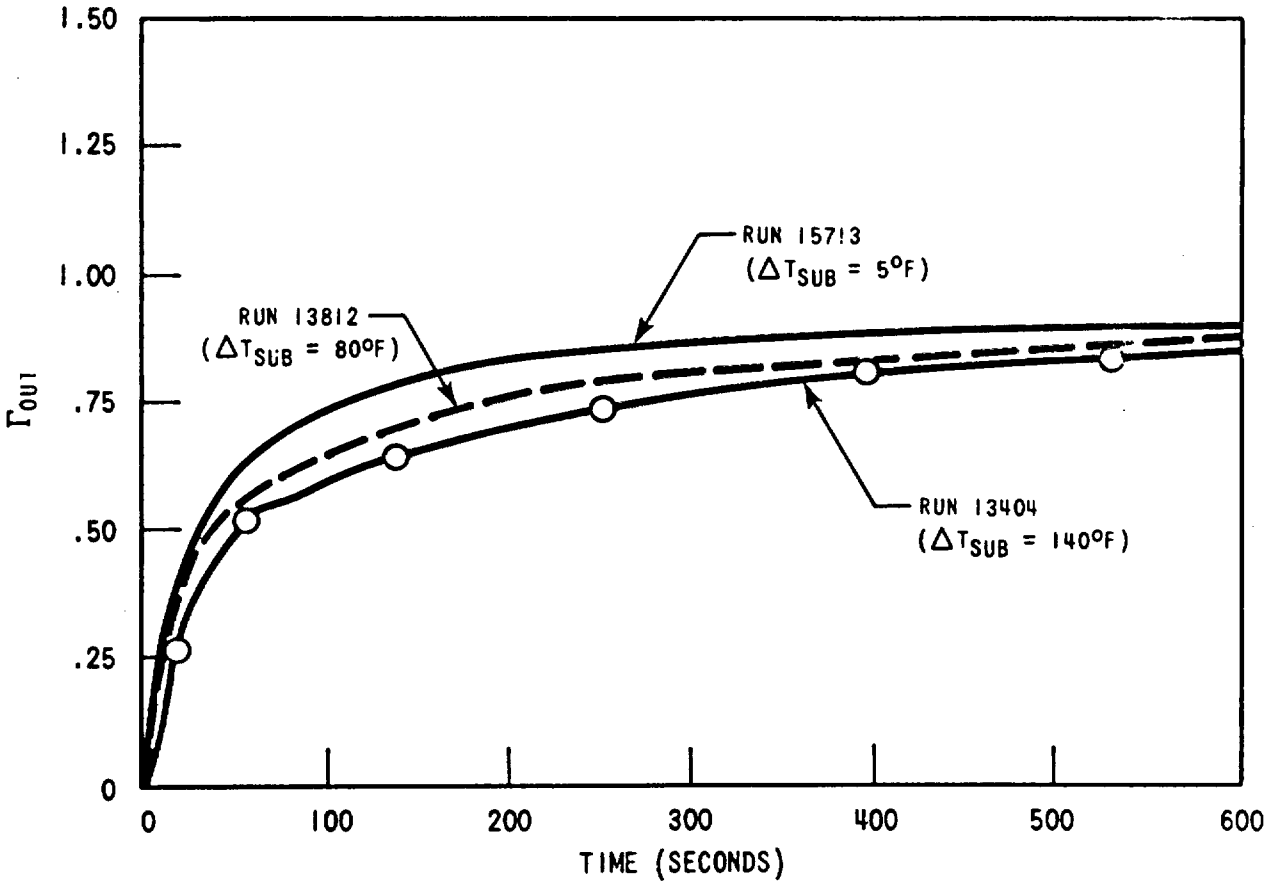

Figure 3-14. Subcooling Effect on Mass Effluent Fraction

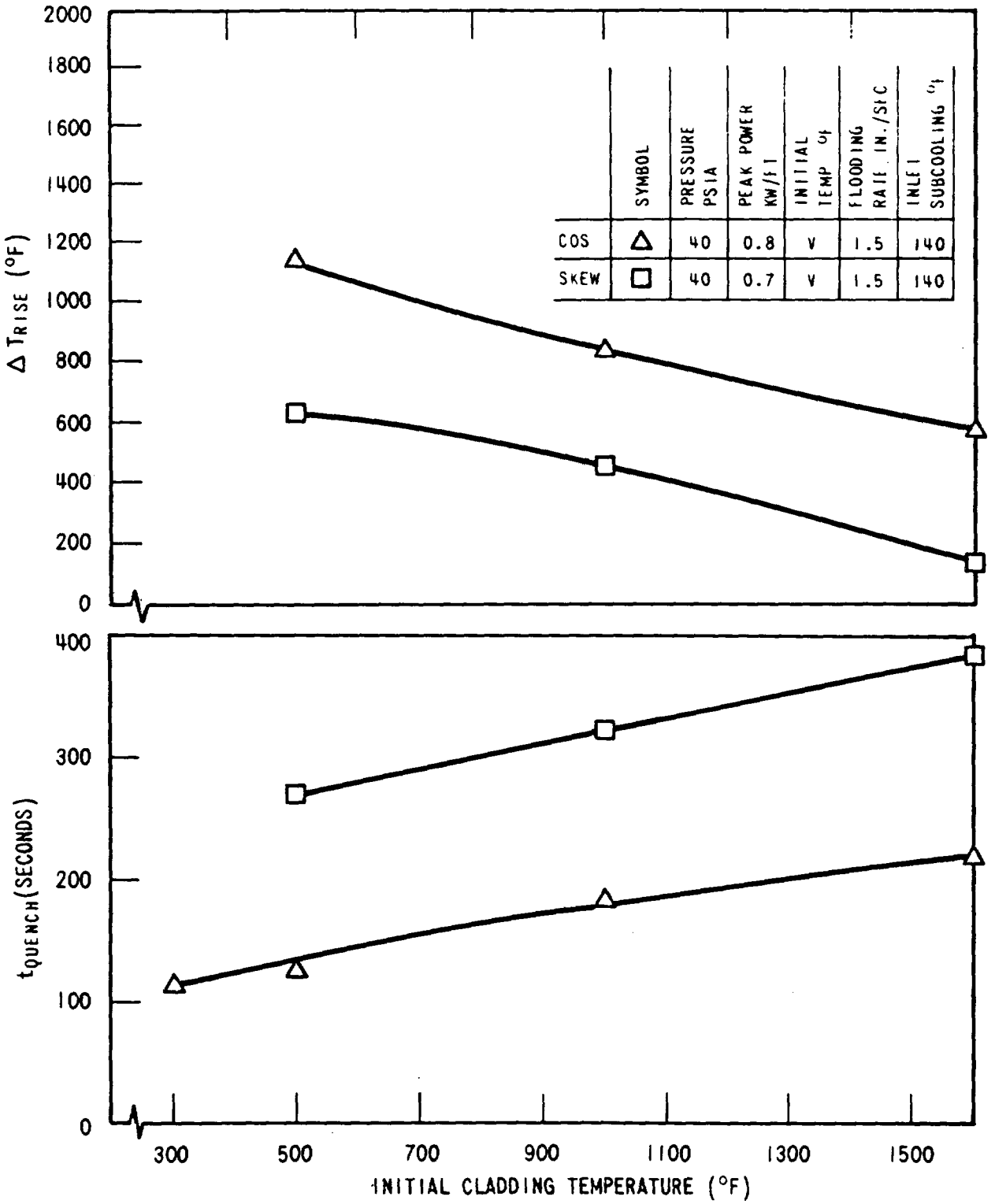

Figure 3-15. Initial Cladding Temperature Effect on Temperature Rise and Quench Time

RUN NUMBERS	13303-12515-12816
PRESSURE	40 PSIA
INITIAL CLADDING TEMPERATURE	VARIABLE °F
PEAK POWER	0.7 KW/FT
SUBCOOLING	140°F
INJECTION RATE	1.5 IN./SEC

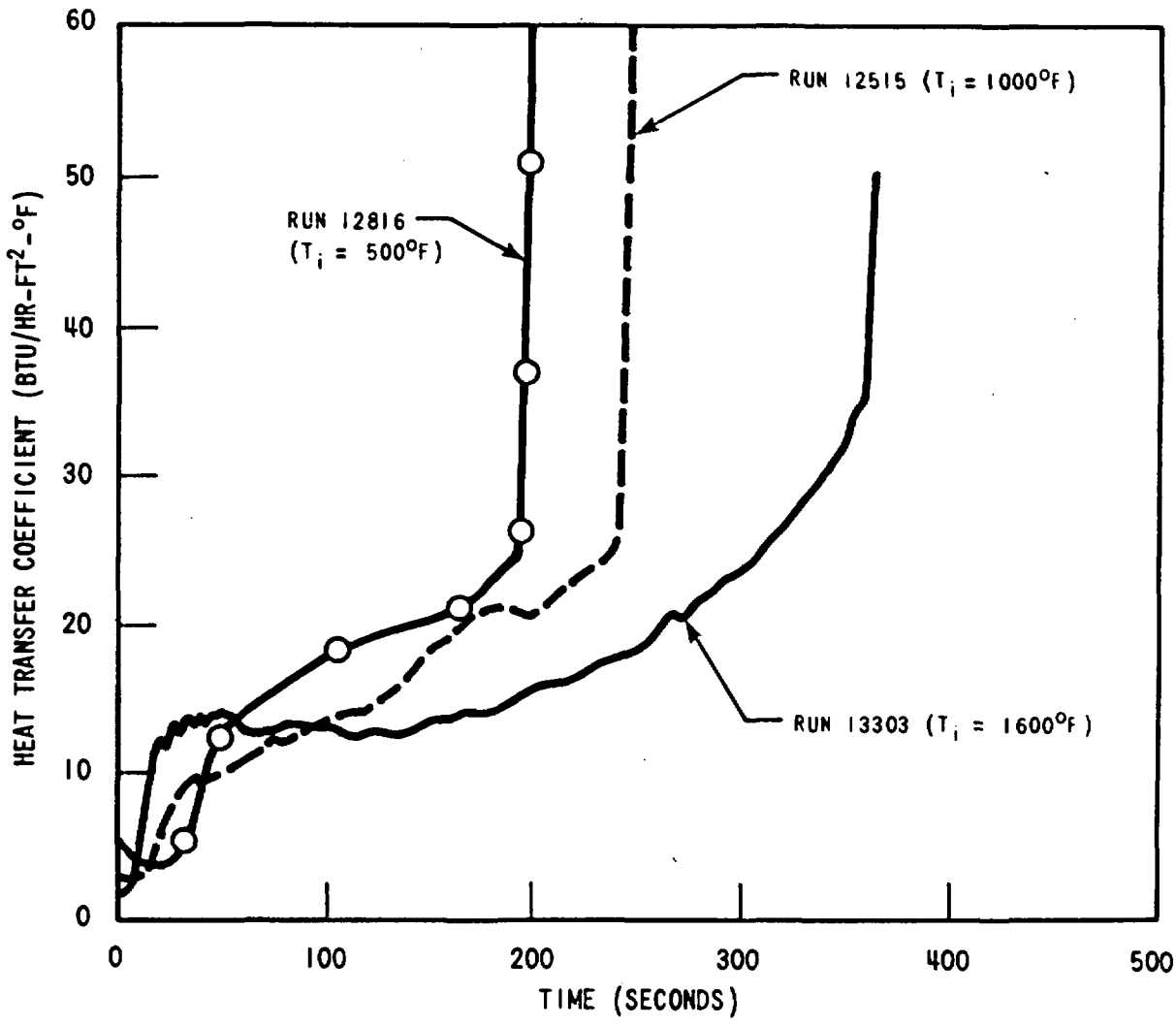

Figure 3-16. Initial Cladding Temperature Effect on Heat Transfer Coefficient (10 FT)

RUN NUMBERS	13303-12515-12816
PRESSURE	40 PSIA
INITIAL CLADDING TEMPERATURE	VARIABLE °F
PEAK POWER	0.7 KW/FT
SUBCOOLING	140°F
INJECTION RATE	1.5 IN./SEC

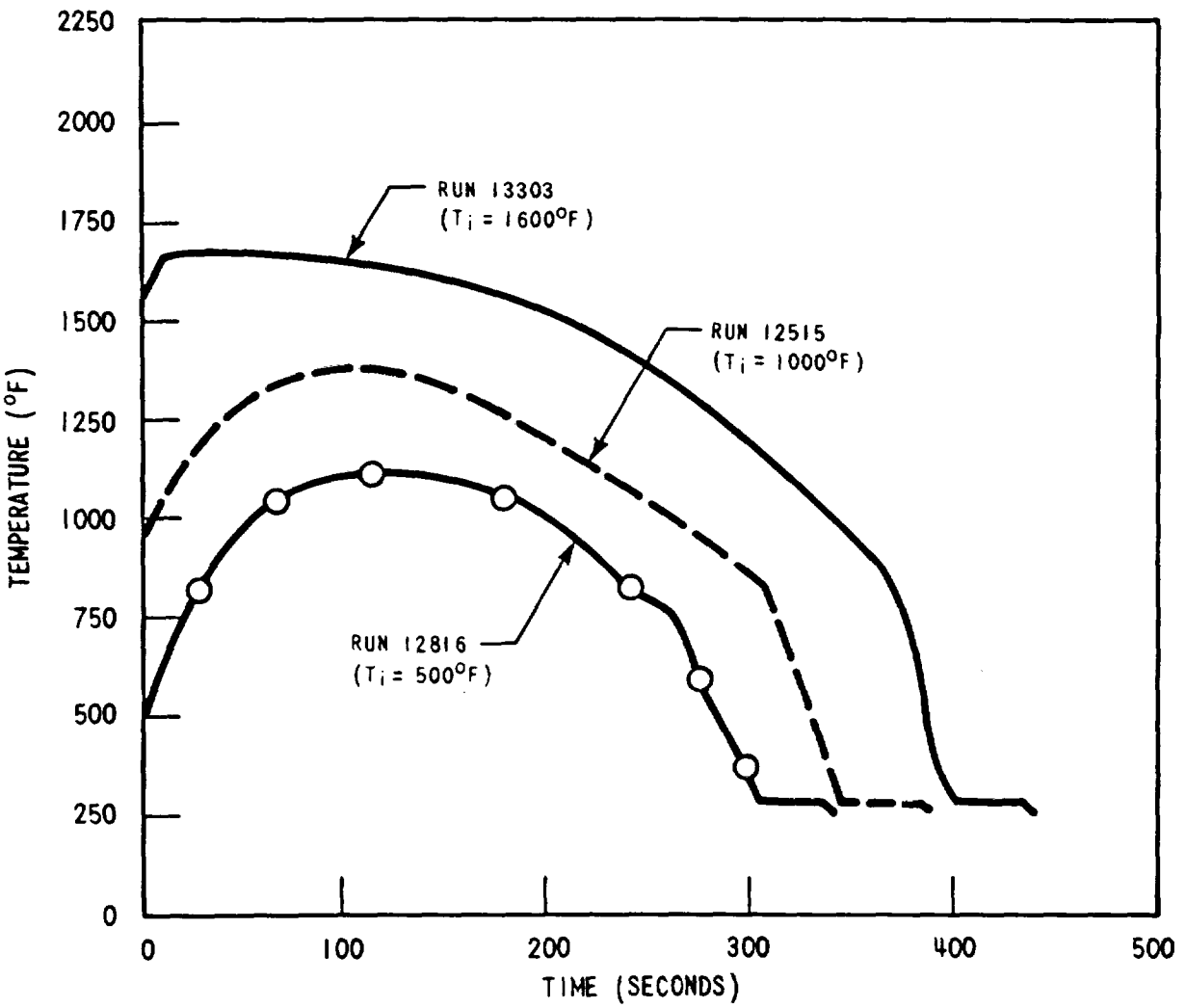

Figure 3-17. Initial Cladding Temperature Effect on the Cladding Temperature Itself (10 FT)

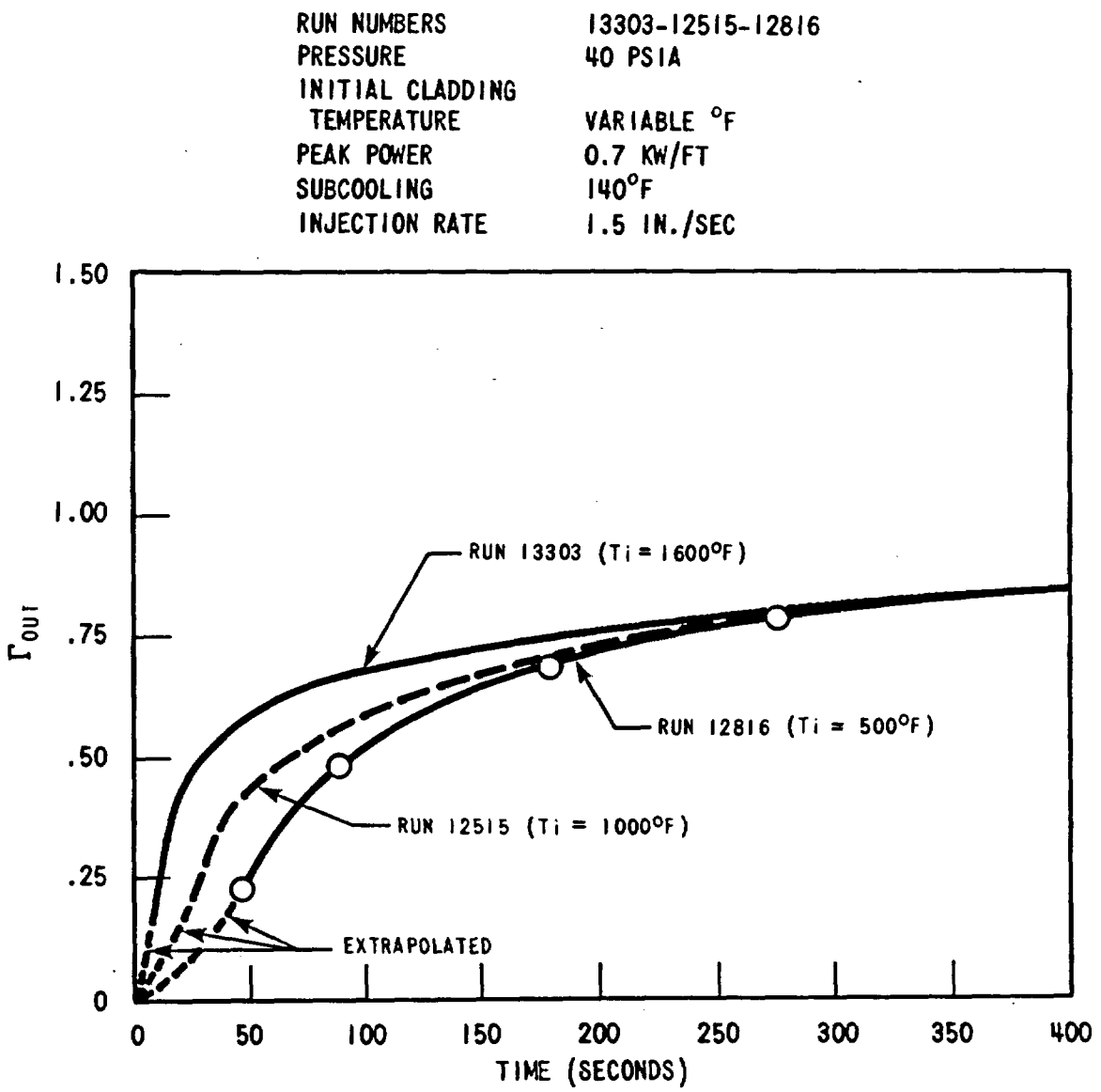

Figure 3-18. Initial Cladding Temperature Effect on Mass Effluent Fraction

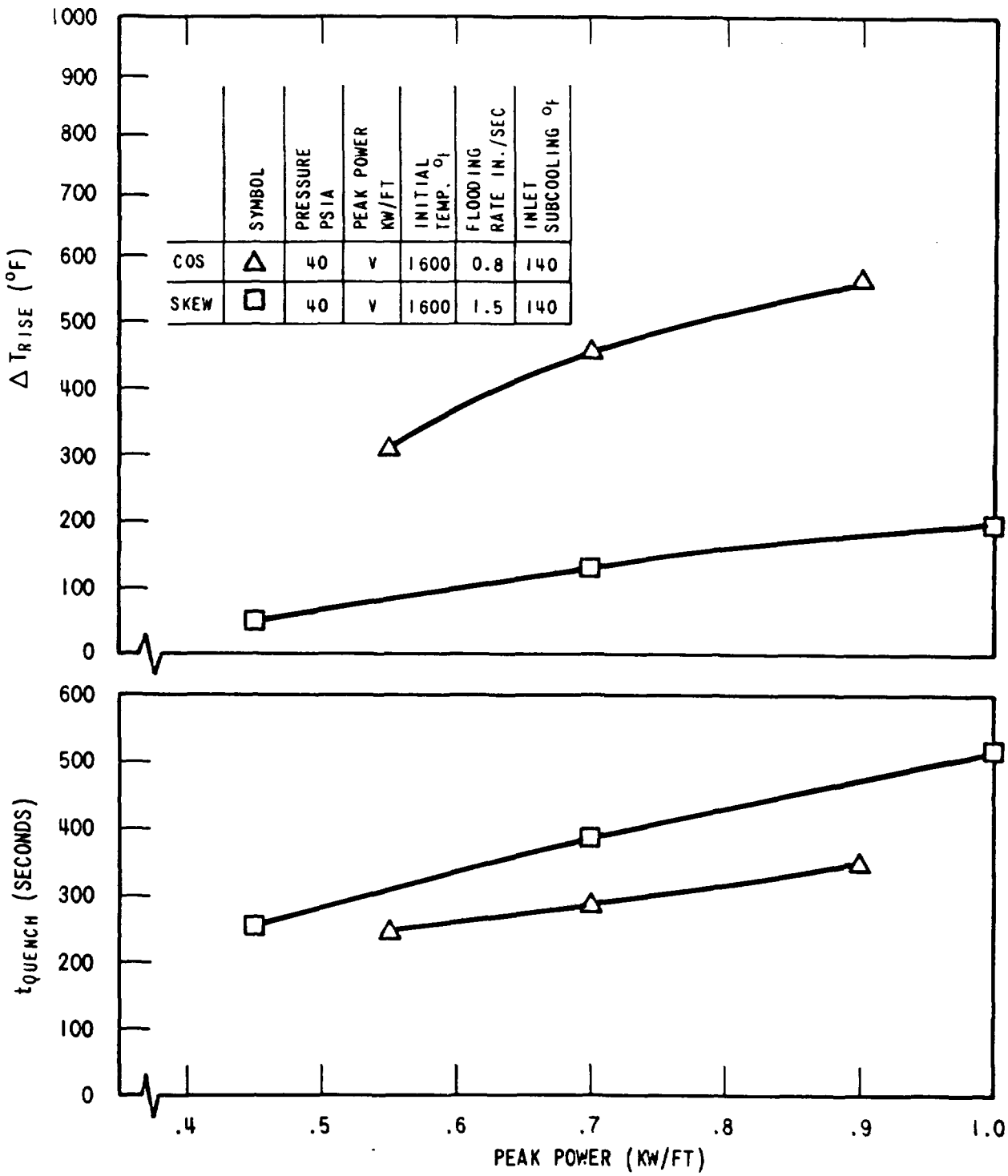

Figure 3-19. Power Effect on Temperature Rise and Quench Time

RUN NUMBERS	16022-13303-11618
PRESSURE	40 PSIA
INITIAL CLADDING TEMPERATURE	1600°F
PEAK POWER	VARIABLE KW/FT
SUBCOOLING	140°F
INJECTION RATE	1.5 IN./SEC

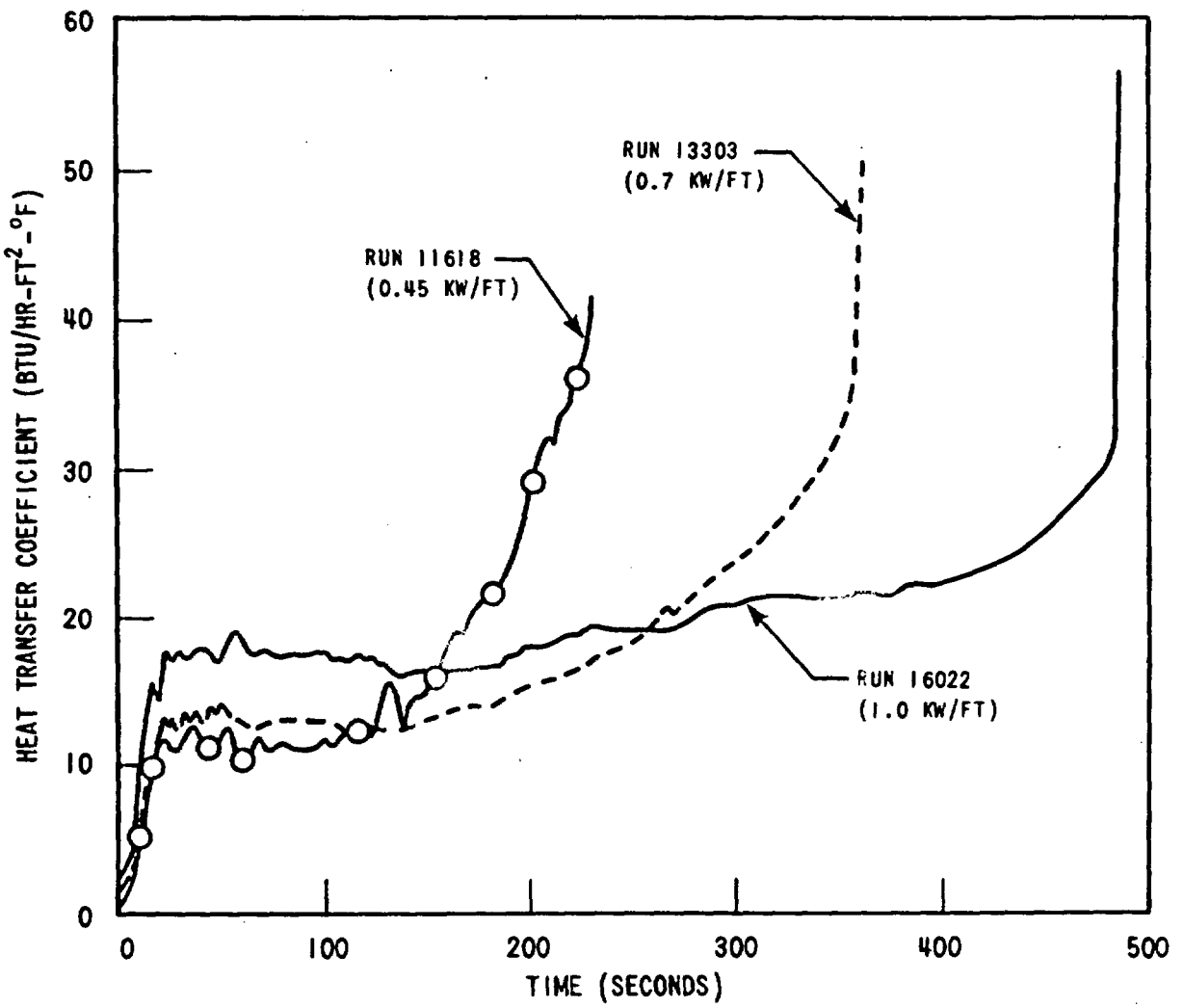

Figure 3-20. Power Effect on Heat Transfer Coefficient (10 FT)

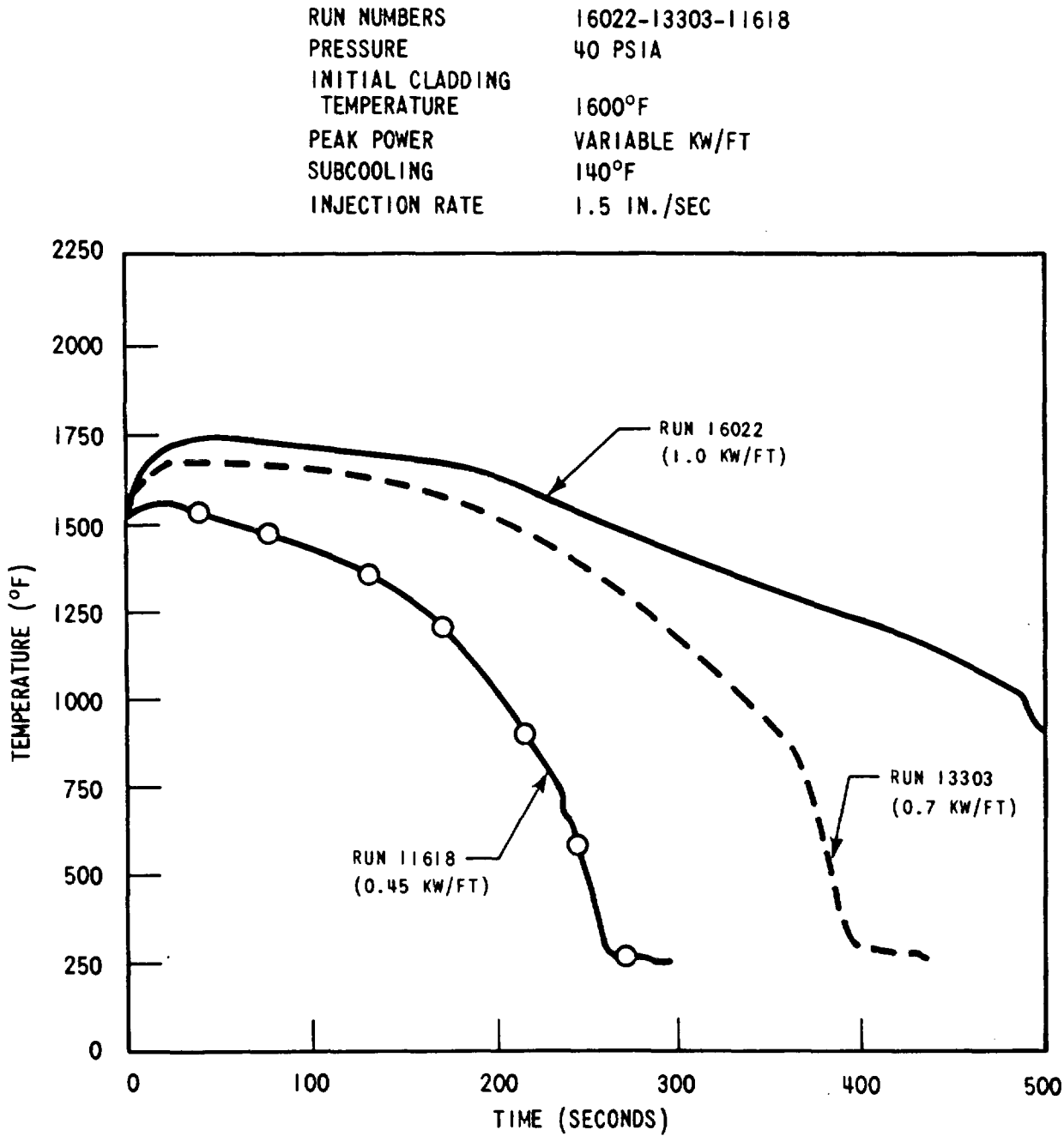

Figure 3-21. Power Effect on Cladding Temperature (10 FT)

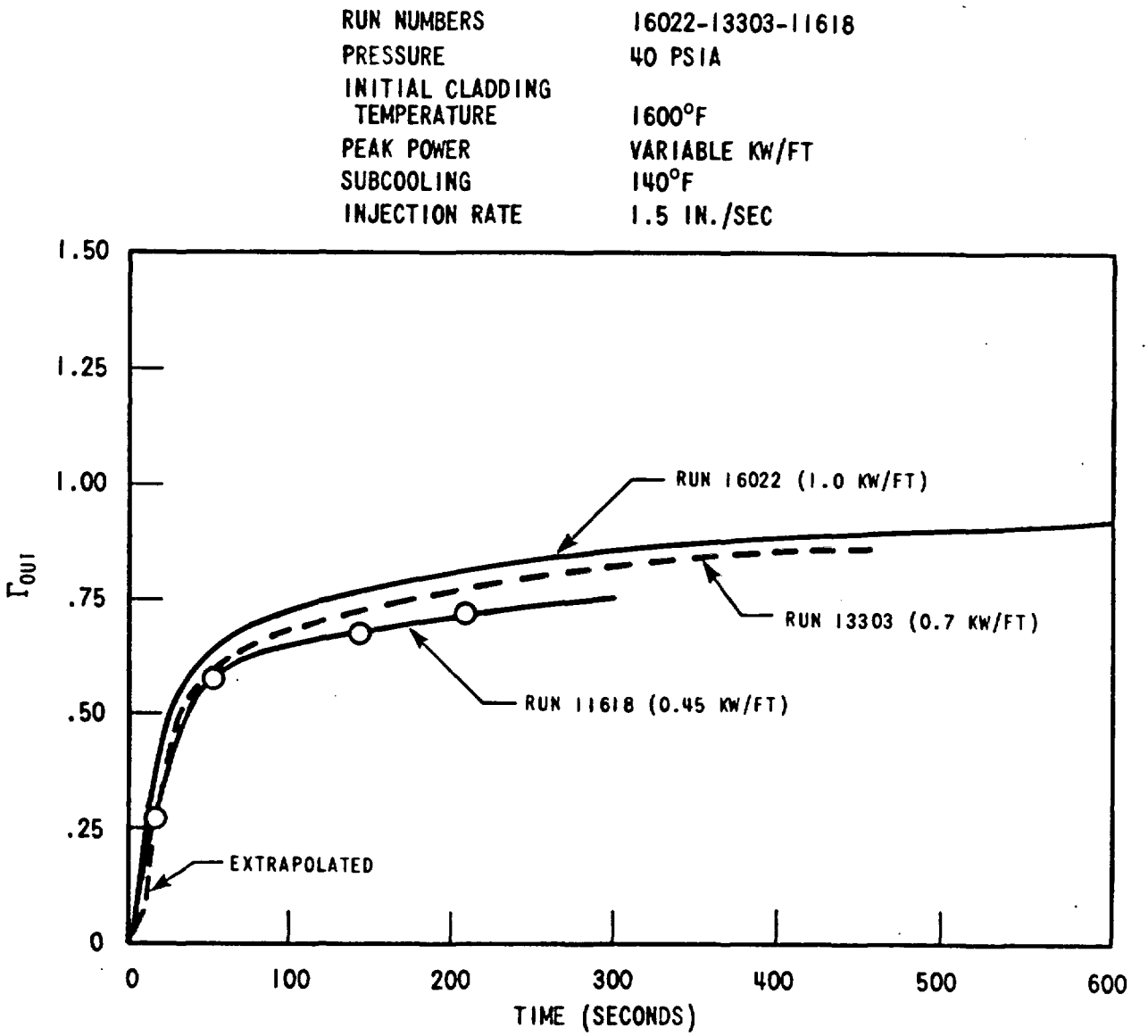

Figure 3-22. Power Effect on Mass Effluent Fraction

3-7. VARIABLE FLOODING RATE EFFECT

The variable flooding rate tests examine the effect of an initial period of high flooding rate on an otherwise constant low flooding rate run. The typical pattern used for flooding rate was a constant high initial flooding rate for 5 seconds followed by a step down to 0.8 in./sec for the remainder of the run. One run was made with an initial flooding rate of 6 in./sec, which was ramped down to 0.8 in./sec over a period of 15 seconds.

The step variable flooding rate tests indicate that temperature rise and quench times decrease as increasing amounts of water are injected in the initial period. This is displayed in figure 3-23, where the amount of water in the initial period is directly proportional to the initial flooding rate. The decrease of temperature rise and quench times is observed for both skewed and cosine tests. Heat transfer coefficients and temperature transients for the skewed tests are presented in figures 3-24 through 3-27. Figures 3-26 and 3-27 include the run with the ramped initial flooding rate. This particular ramp has more total injection than a constant 6 in./sec for 5 seconds and exhibits a smaller temperature rise and shorter quench time.

Figures 3-28 and 3-29 show the integrated mass effluent fraction for the skewed step and ramp variable flooding rates. A high proportion of the water injected in the initial period is carried out of the bundle and is responsible for the improved heat transfer.

3-8. RADIAL POWER GRADIENT

Unlike all previous test series, the skewed tests were run predominantly with equal power to all rods (uniform radial power distribution). This was done to simplify the data analysis. Previous test series used the FLECHT power distribution which simulated actual rod-to-rod power differences that would be encountered in an operating PWR assembly. In figure 3-1, the rods in the bundle are labeled 1.1, 1.0, or 0.95 indicating their power relative to average bundle power in the FLECHT power distribution. As noted however, most runs were made with all rods operating in the 1.0 mode.

One uniform power distribution run in the skewed series was repeated using the FLECHT power distribution. Results of these two tests are compared in this section to identify any differences. Figure 3-30 compares the average heat transfer coefficient for all the 1.1 rods in the central 6 x 6 array. For the uniform power test (13404) these rods were run in the 1.0 mode. Average bundle power was the same for the two runs. Thus, the power to these two groups of rods differed by ten percent.

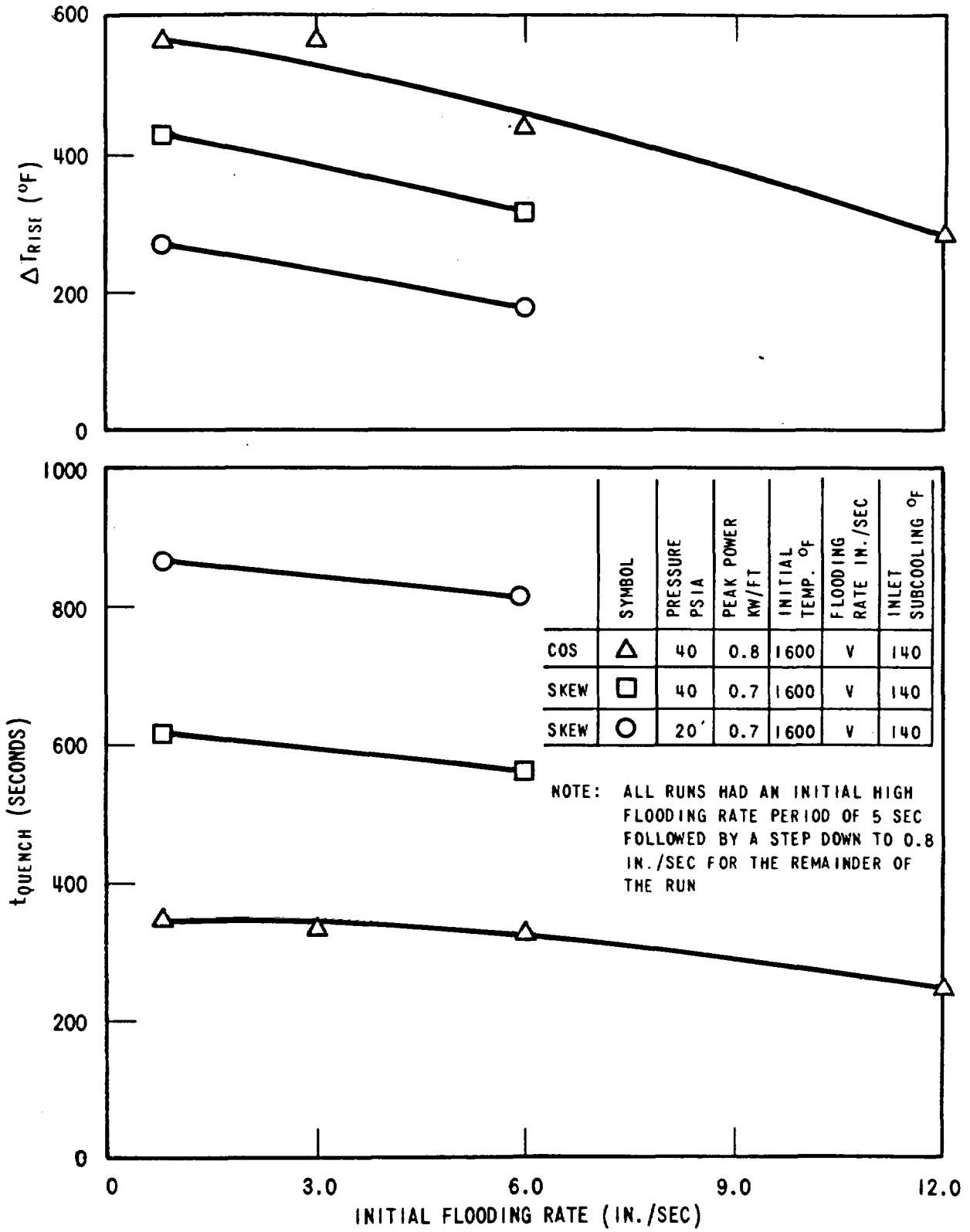

Figure 3-23. Initial Flooding Rate Effect on Temperature Rise and Quench Time

RUN NUMBERS	15132-15305
PRESSURE	40 PSIA
INITIAL CLADDING TEMPERATURE	1600°F
PEAK POWER	0.7 KW/FT
SUBCOOLING	140°F
INJECTION RATE	VARIABLE

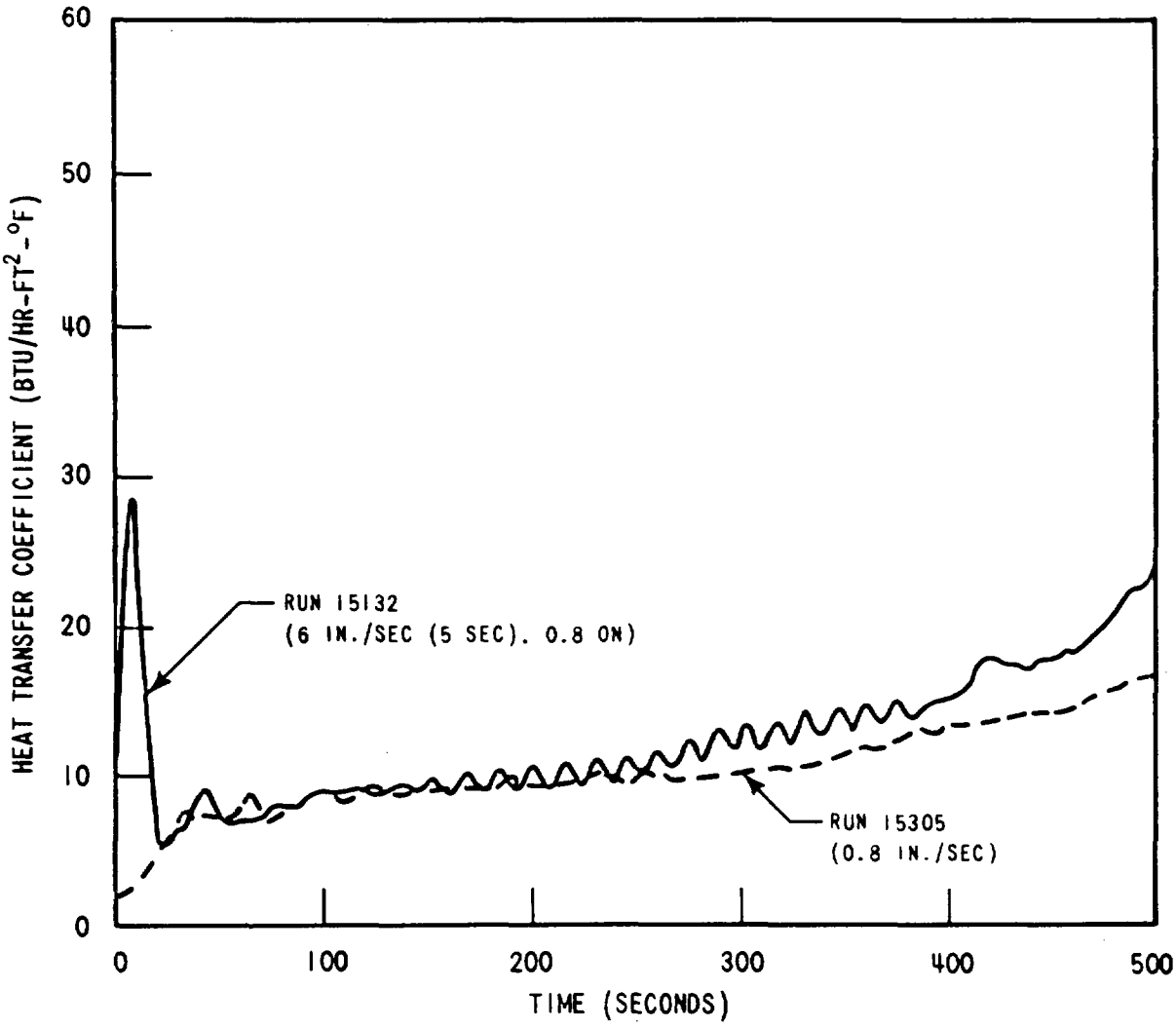

Figure 3-24. Initial Flooding Rate Effect on Heat Transfer Coefficient (10 FT)

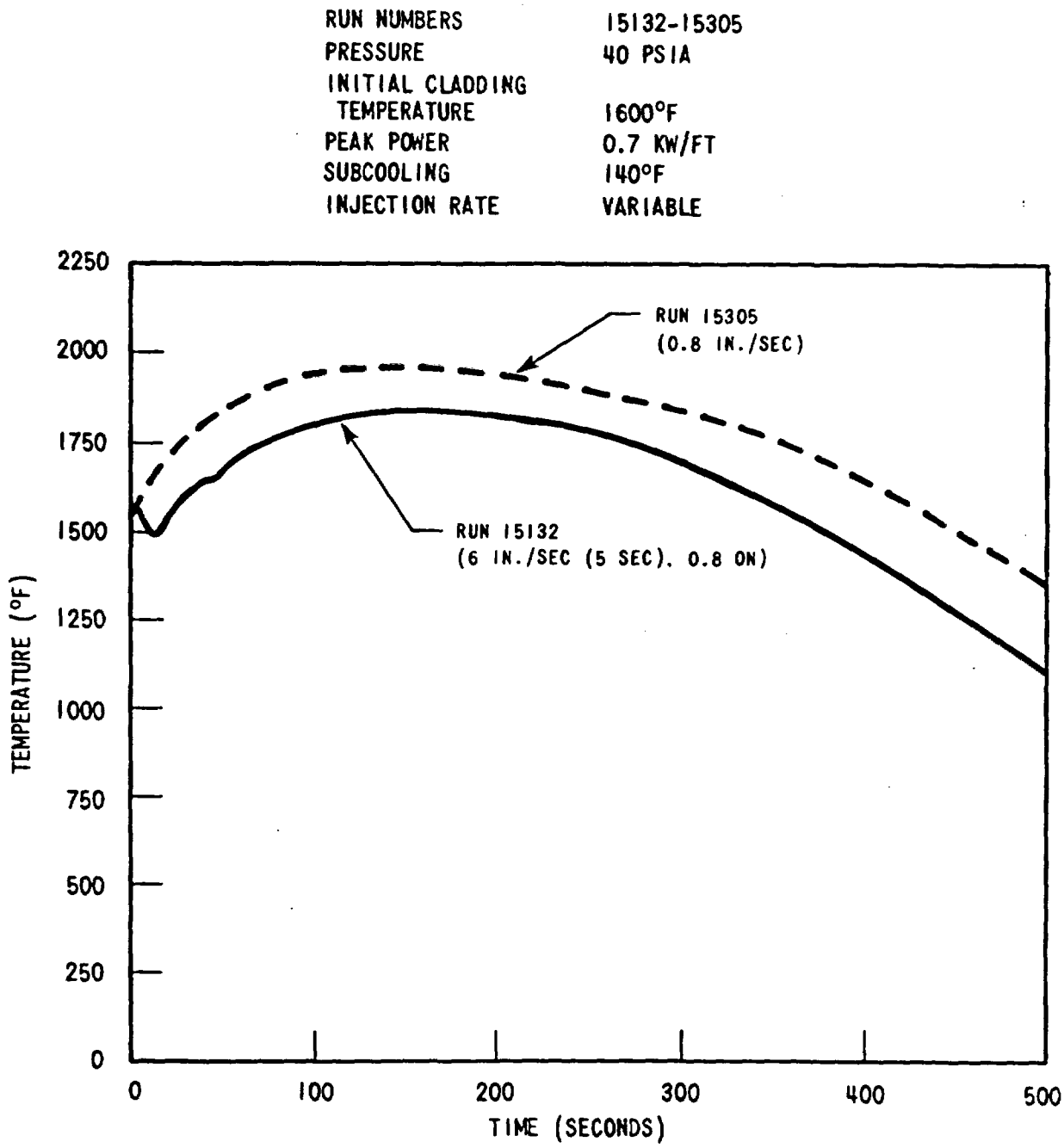

Figure 3-25. Initial Flooding Rate Effect on Temperature (10 FT)

RUN NUMBERS	16110-15233-15034
PRESSURE	20 PSIA
INITIAL CLADDING TEMPERATURE	1600°F
PEAK POWER	0.7 KW/FT
SUBCOOLING	140°F
INJECTION RATE	VARIABLE

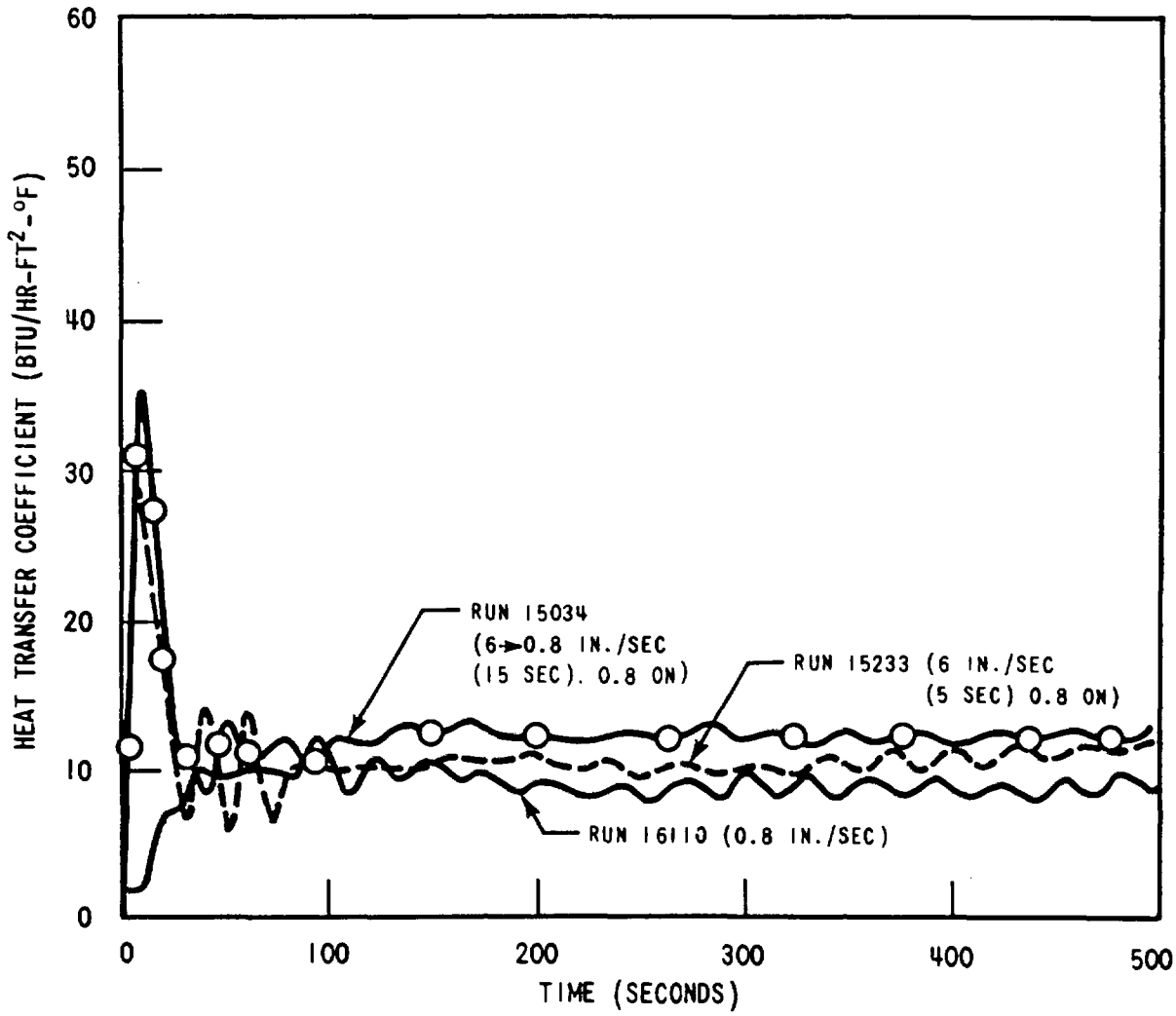

Figure 3-26. Initial Flooding Rate Effect on Heat Transfer Coefficient (10 FT)

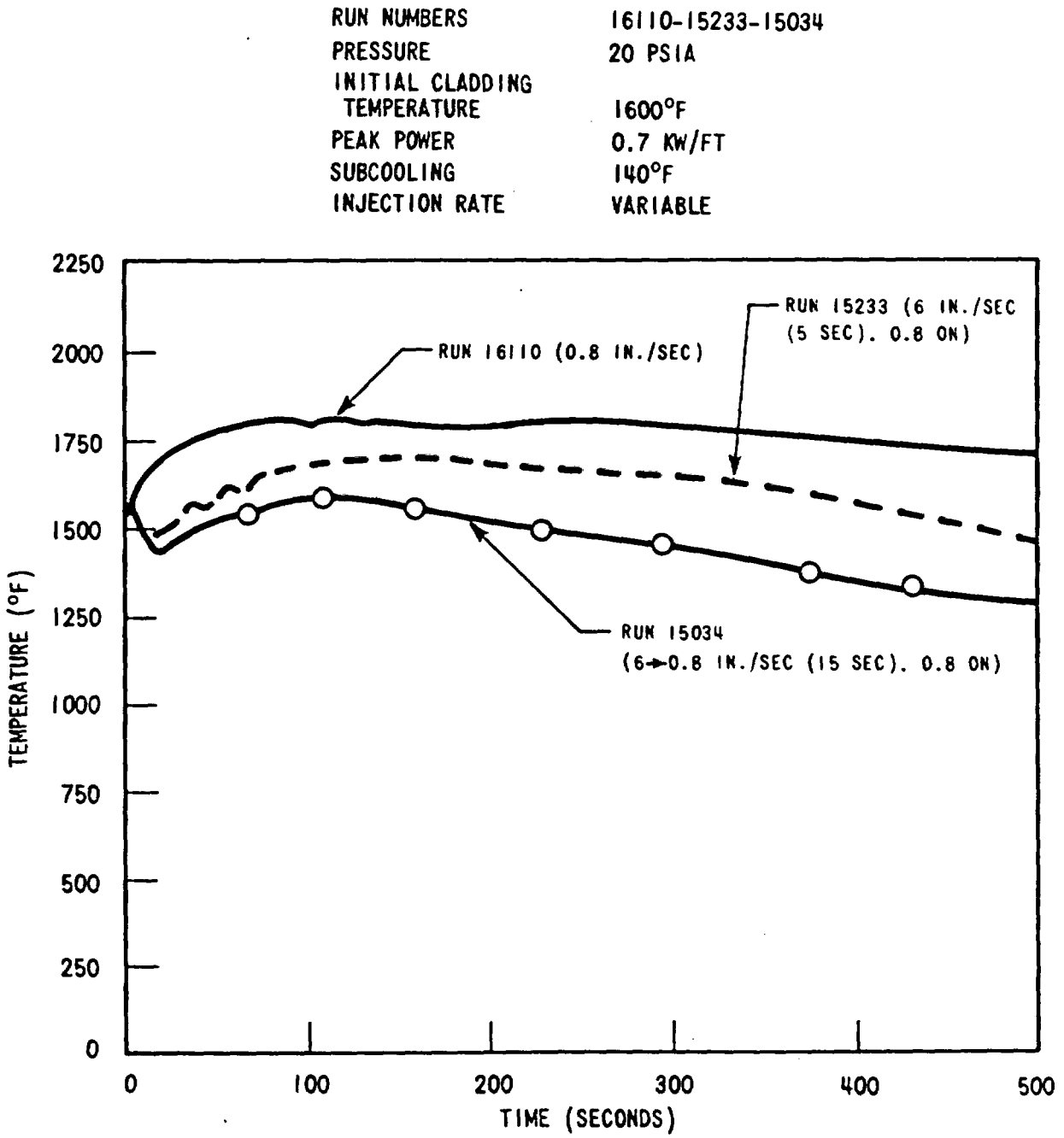

Figure 3-27. Initial Flooding Rate Effect on Cladding Temperature (10 FT)

RUN NUMBERS	15137-15305
PRESSURE	40 PSIA
INITIAL CLADDING TEMPERATURE	1600°F
PEAK POWER	0.7 KW/FT
SUBCOOLING	140°F
INJECTION RATE	VARIABLE

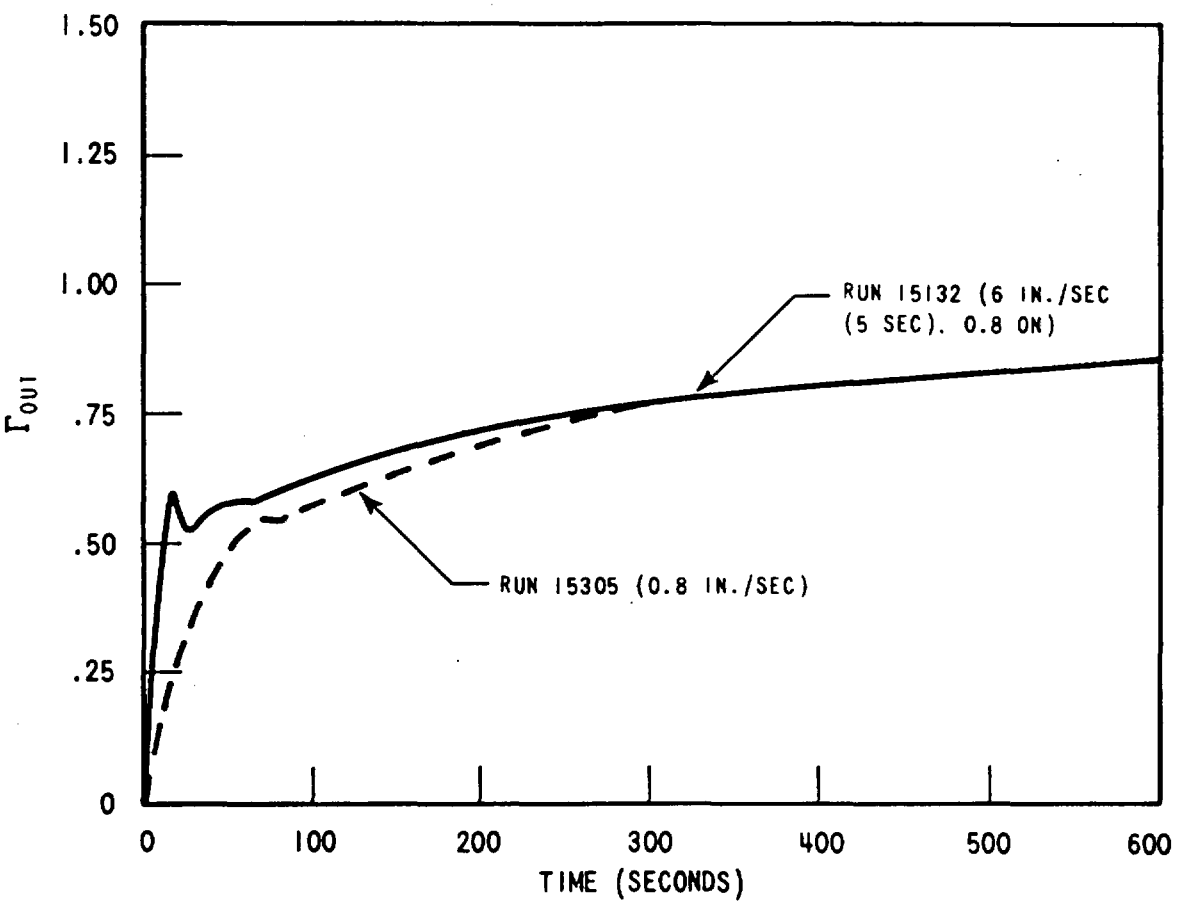

Figure 3-28. Initial Flooding Rate Effect on Mass Effluent Fraction (40 PSIA)

RUN NUMBERS	16110-15233-15034
PRESSURE	40 PSIA
INITIAL CLADDING TEMPERATURE	1600°F
PEAK POWER	0.7 KW/FT
SUBCOOLING	140°F
INJECTION RATE	VARIABLE

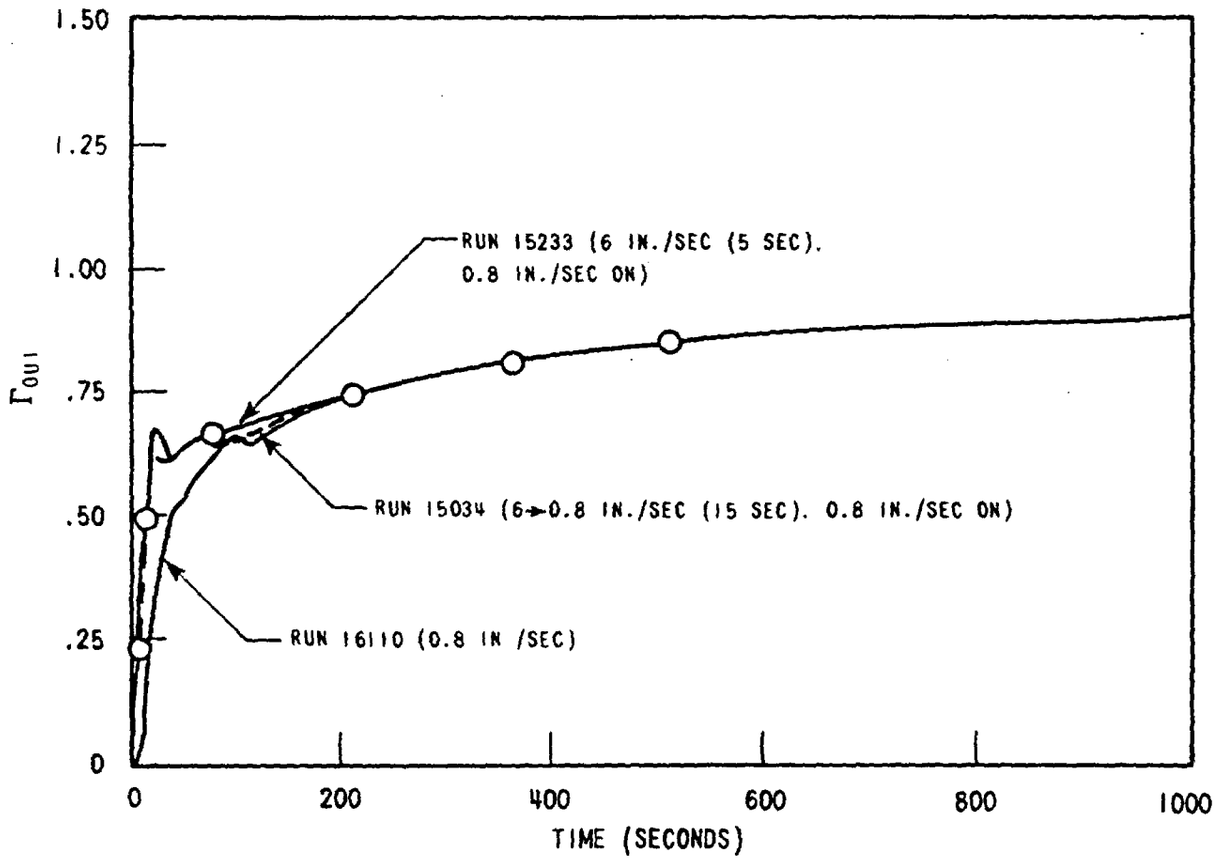

Figure 3-29. Initial Flooding Rate Effect on Mass Effluent Fraction (40 PSIA)

RUN NUMBERS	13404-15423
PRESSURE	40 PSIA
INITIAL CLADDING TEMPERATURE	1600°F
PEAK POWER	VARIABLE KW/FT
SUBCOOLING	140°F
INJECTION RATE	1.0 IN./SEC

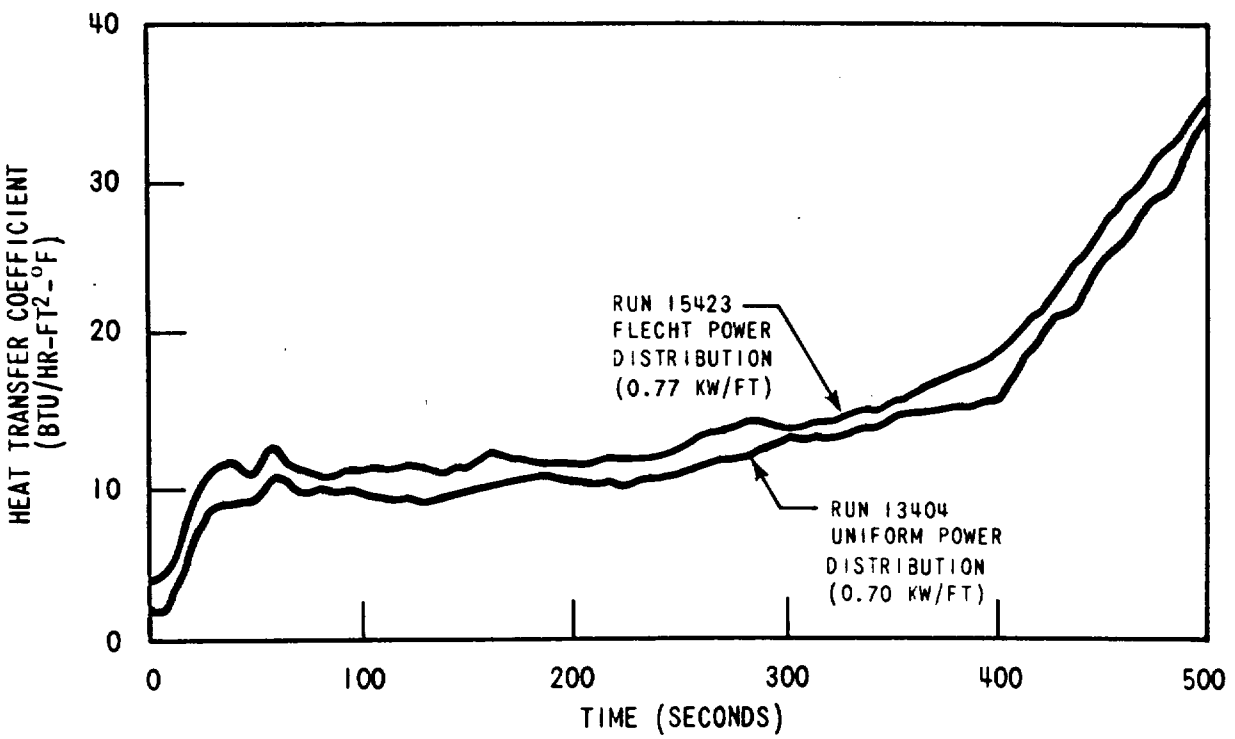

Figure 3-30. Heat Transfer Coefficients for Central 1.1 Power Zone Rods

The heat transfer coefficient for the FLECHT distribution is consistently 15 percent higher than for the uniform distribution. A substantial power effect was observed for the skewed tests (figure 3-20); however, one might expect this to be a bundle average effect. Average bundle power might, for example, affect the flow conditions above the quench front and consequently affect the heat transfer. One possible explanation is that the 1.1 powered rods tend to be clustered around the thimbles. This may lead to some local (radial) change in flow conditions above the quench front which predominantly affects the 1.1 rods. This is somewhat corroborated when the 1.0 power zone rods are examined (figure 3-31). For these rods, the power and heat transfer are identical for the uniform and FLECHT radial power distributions.

The mass effluent fraction quench progression plots for these two runs were essentially coincident for these two runs. This is expected in light of the equal bundle average powers for the two cases.

3-9. HOT AND COLD CHANNELS TESTS

Most FLECHT initial test conditions simulate one small segment of a reactor core at the start of reflood following a hypothetical LOCA. A significant radial variation of both peak power and initial cladding temperature could be expected across a PWR core under these circumstances. The small FLECHT bundle cannot fully simulate these radial variations. It is of interest, however, to examine the effect of large power and initial cladding temperature gradients in the FLECHT rod bundle. One test in the matrix was run with about 40 percent of the rods at typical hot rod conditions and the remaining 60 percent at power and initial temperature conditions typical of what could be expected in a peripheral assembly. Hot and cold zones are pictured in figure 3-32.

A parallel test was run with the same average bundle power and initial cladding temperature, but with uniform distribution across the bundle. Test conditions for these two runs are given in table 3-2. A third run with the same test conditions as the hot rods in the hot/cold test is also included in table 3-2, and will be used for some comparisons.

RUN NUMBERS	13404-15423
PRESSURE	40 PSIA
INITIAL CLADDING TEMPERATURE	1600°F
PEAK POWER	VARIABLE KW/FT
SUBCOOLING	140°F
INJECTION RATE	1.0 IN./SEC

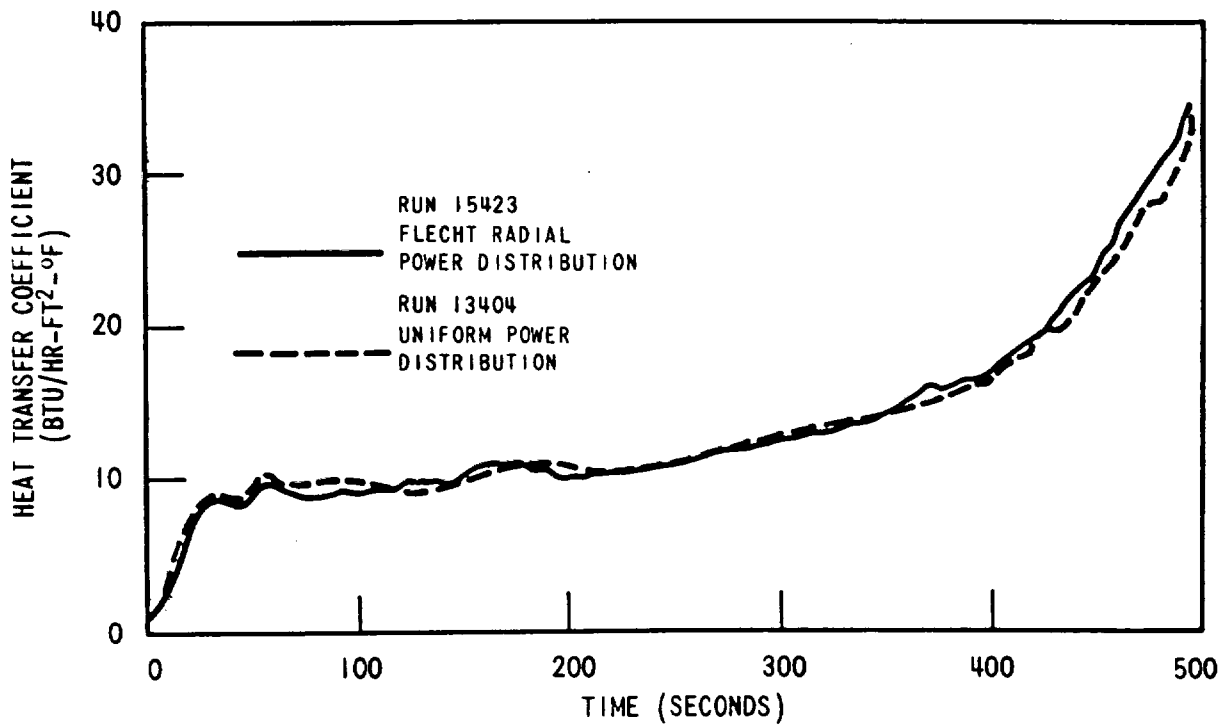

Figure 3-31. Heat Transfer Coefficients for Central 1.0 Power Zone Rods

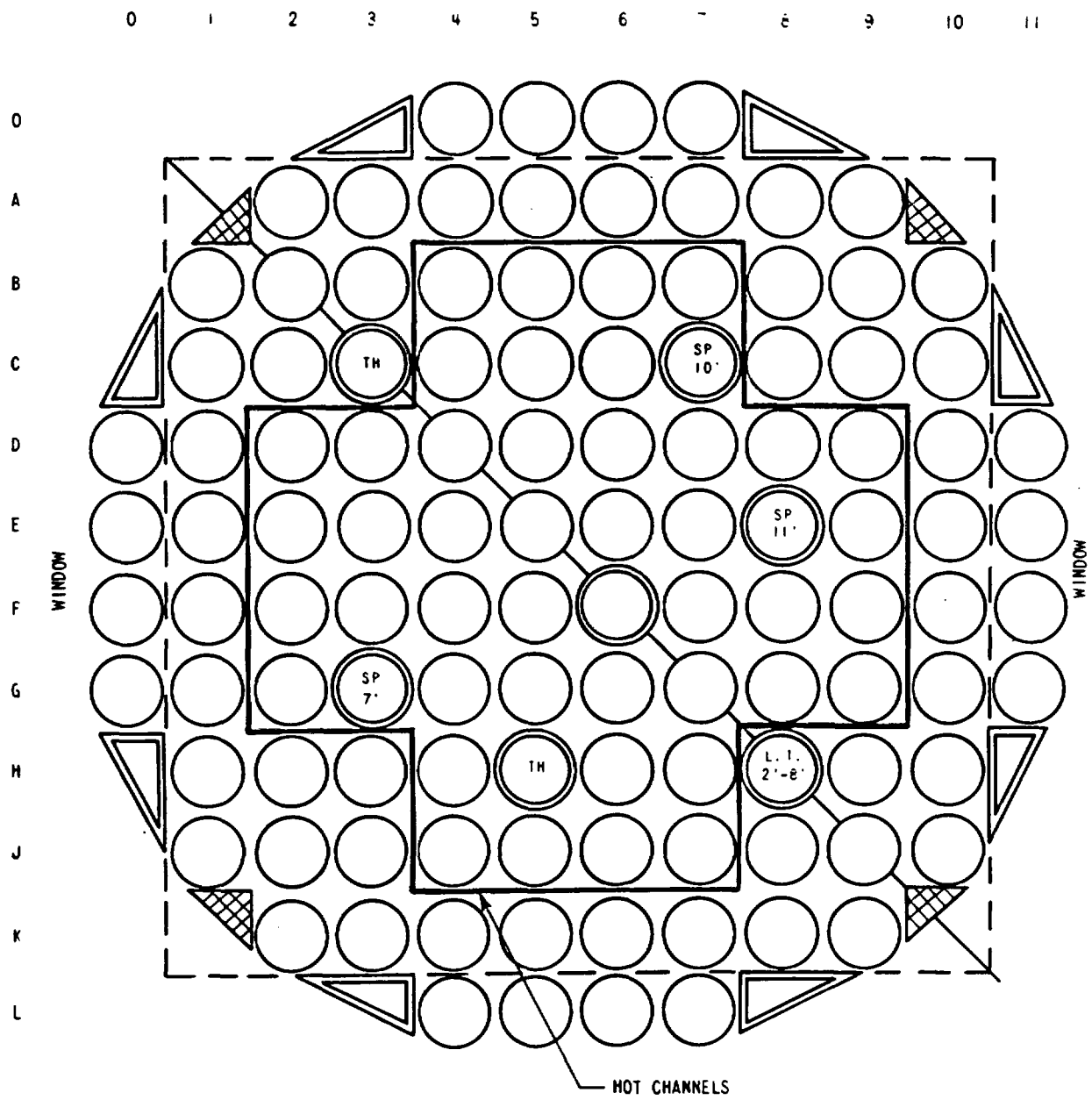

Figure 3-32. Hot and Cold Channel Test Configuration

TABLE 3-2
RUNS USED FOR HOT AND COLD CHANNEL
TEST COMPARISONS

Run Number	15838	15937			13303
		Avg	Cold	Hot	
Pressure (psia)	40	40	40	40	40
Initial Cladding Temp (°F)	966	959	482	1626	1600
Rod Peak Power (kw/ft)	0.55	0.55	0.45	0.7	0.7
Flooding Rate (in./sec)	1.5	1.5	1.5	1.5	1.5
Subcooling (°F)	140	140	140	140	140

The principal effect of lower power and initial cladding temperature is to reduce the mass effluent fraction. This could aid reflooding in a gravity reflood situation. The simplest approach for calculating mass effluent fraction when hot and cold channels are present is to assume the bundle is at an average power and initial cladding temperature. A test of this approach is to compare the mass effluent fraction for runs 15937 and 15838, which have the same average power and initial cladding temperatures as those listed in table 3-2. This is done in figure 3-33 for both integrated (equation 3-1) and instantaneous mass effluent fraction. Instantaneous mass effluent fraction is given by

$$\Gamma = \frac{\dot{M}_{in} - \dot{M}_{st}}{\dot{M}_{in}} \qquad (3\text{-}2)$$

where

$\dot{M}_{in}$ = injection flow rate (lbm/sec)

$\dot{M}_{st}$ = rate of storage in bundle (lbm/sec)

From figure 3-33 it can be seen that the mass effluent fractions are substantially equal, although the hot and cold channel test showed slightly higher and less steady mass effluent fractions early in time. A similar comparison made for the cosine tests is reproduced from WCAP-8838 in figure 3-34.[1] Mass effluent fractions are seen to be virtually identical.

1. Lilly, G. P., et al. PWR FLECHT Cosine Low Flooding Rate Series Evaluation Report WCAP-8838, Mar. 1977.

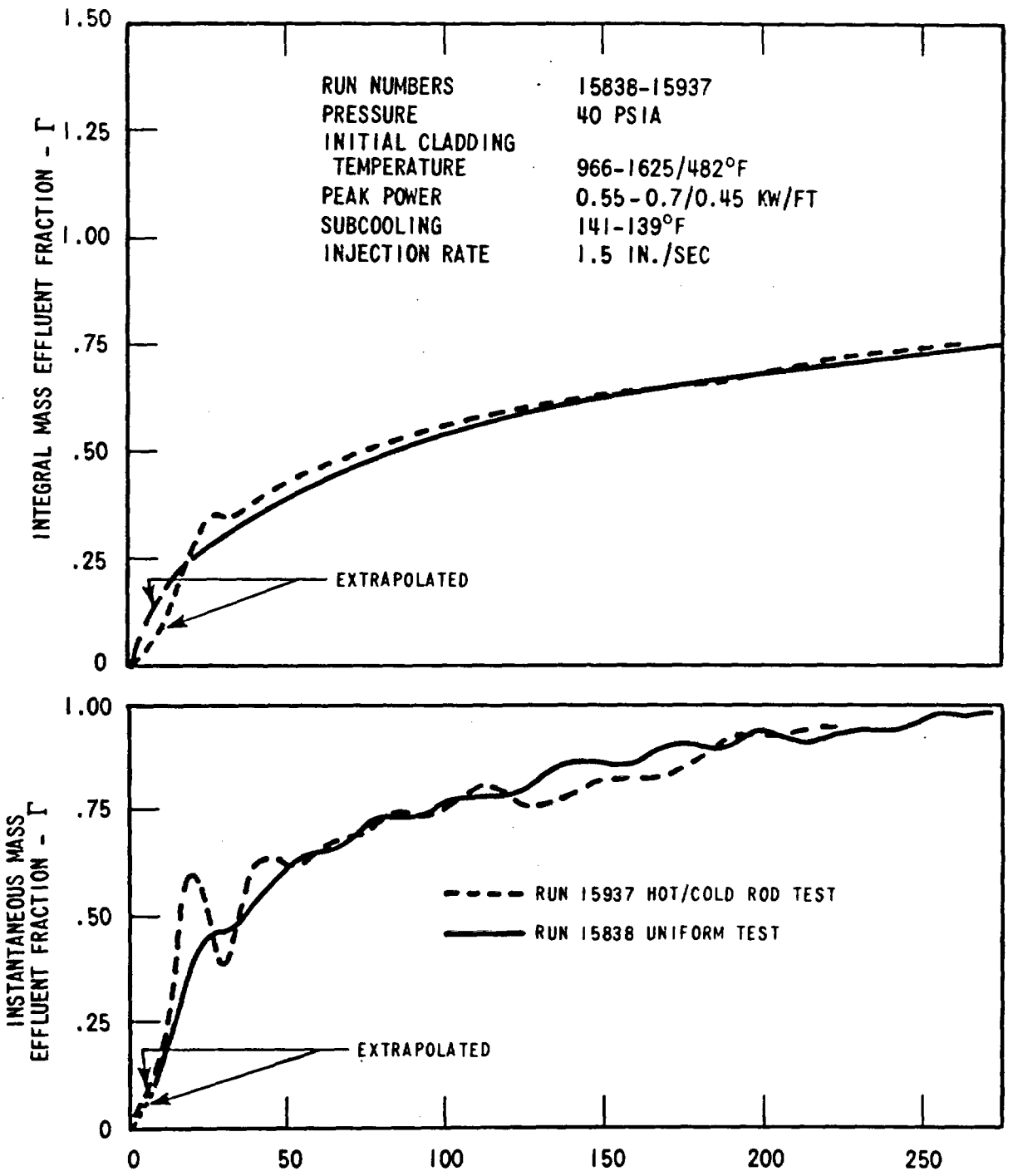

Figure 3-33. Comparison of Mass Effluent Fraction for Uniform and Hot/Cold Rod Tests

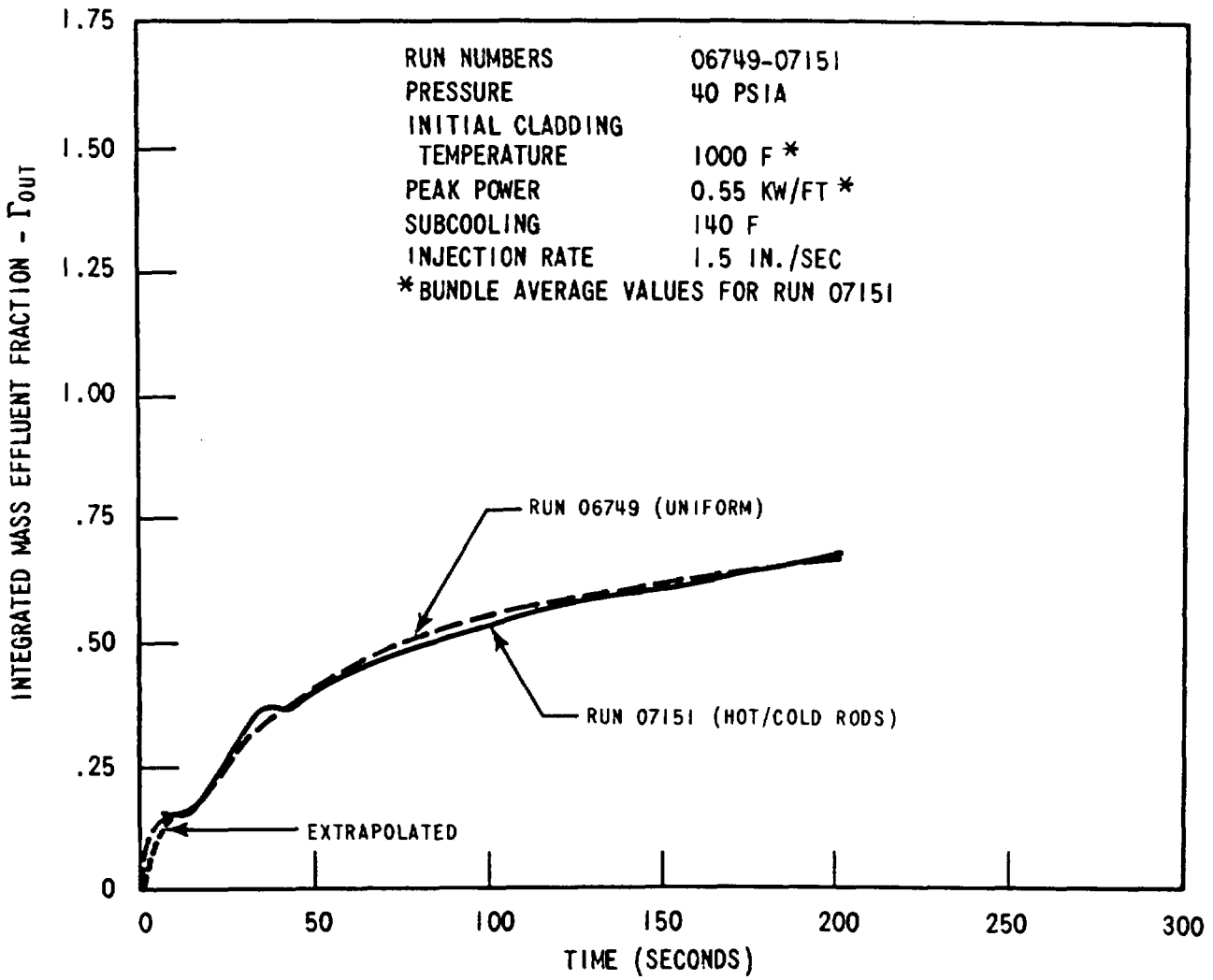

Figure 3-34. Comparison of Integrated Mass Effluent Fraction for Cosine Runs With Uniform and Hot/Cold Rods

The conclusion to be drawn from the above comparisons is that the use of average bundle conditions provides a reasonable means of estimating mass effluent fraction when large power and temperature differences are present.

From table 3-2, it is seen that test conditions for the hot rods of Run 15937 are the same as those for all rods in Run 13303, which were run at uniform conditions. Figure 3-35 compares heat transfer and temperature transients for rod 6E at 10 feet for these two runs. The lower bundle power and average initial temperature is seen to dominate. The hot rod in Run 15937 shows a much more rapid rise in heat transfer and earlier quench. This is consistent with similar comparisons made in WCAP-8838. It is also consistent with the trend of decreased quench times with lower values of stored and generated energy.

3-10. DATA REPEATABILITY

Eight runs listed in table 3-3 can be used to evaluate data repeatability within the skewed test series. Also included is one comparison from the low flooding rate cosine series reported in WCAP-8838. Average values of initial rod temperature, quench time, turnaround time, temperature rise, and maximum temperature were calculated differently at the peak power location depending upon the radial power profile as follows:

- Uniform: simple average of all valid thermocouple data within the inner 6 x 6 array
- FLECHT: simple average of all valid thermocouple data on 1.1 rods within the inner 6 x 6 array.

Although the computational mechanics are different, the underlying philosophy of comparison is consistent. Both techniques evaluate hot zone data within the test section at the peak power location.

Percentage variations in turnaround time, quench time, and temperature rise were calculated by the following formula for both skewed runs found in table 3-4 and for cosine runs found in table 3-5 of WCAP-8838.

$$\% \text{ Variation} = 100\% \left[\frac{\text{maximum recording} - \text{minimum recording}}{\text{minimum recording}} \right]$$

The range of variation has been tabulated for both cosine and skewed data.

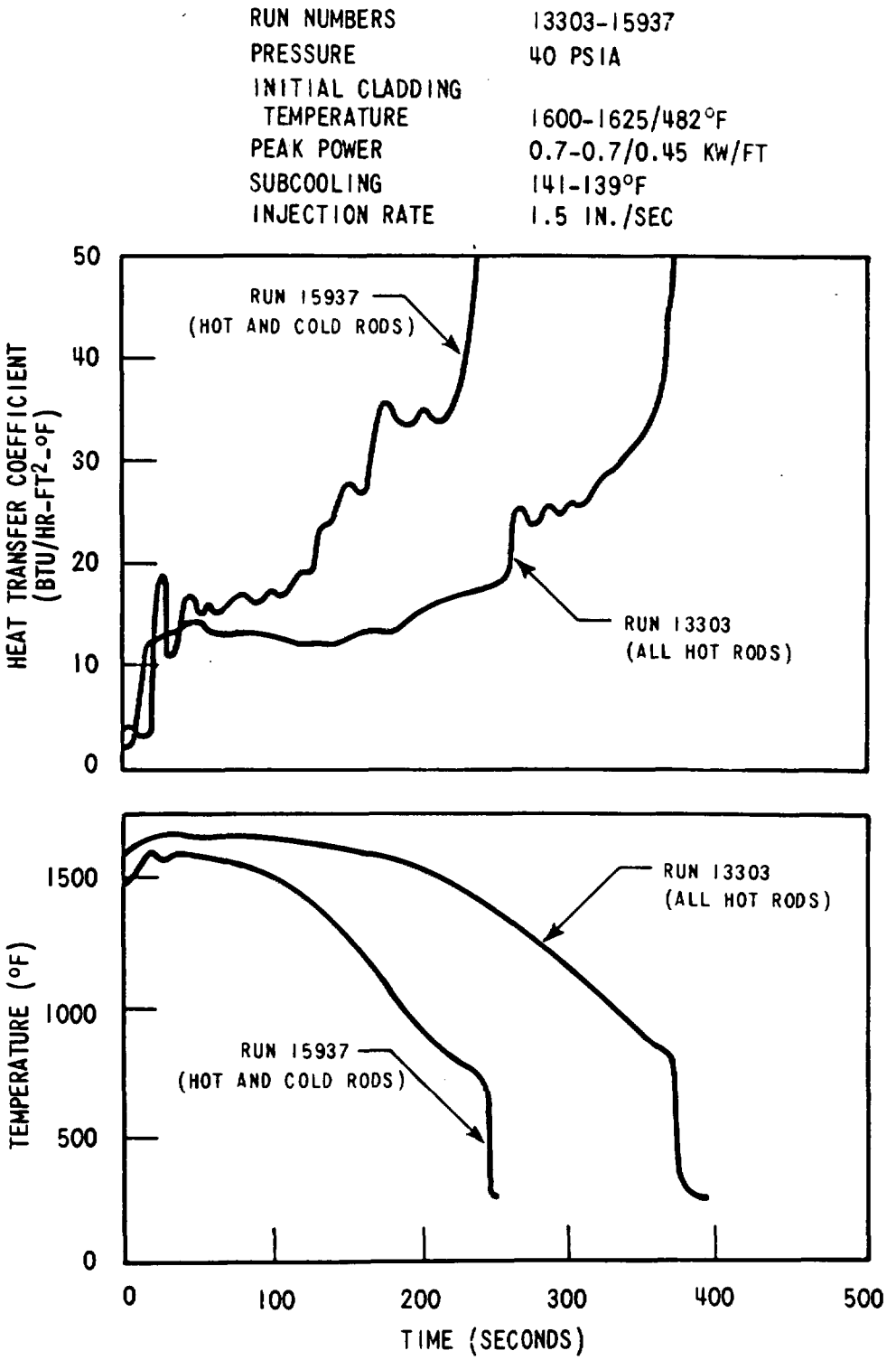

Figure 3-35. Heat Transfer and Temperature Transients for Runs 13303 and 15937 (Hot Rod) – Rod 6E, 10 FT

TABLE 3-3
SUMMARY OF DATA REPEATABILITY FOR COSINE AND SKEWED TESTS

Run No.	Upper Plenum Pressure	Average Initial Rod Temp At Peak Power Location (°F)	Rod Peak Power (kw/ft)	Flooding Rate (in./sec)	Coolant Temp. (°F)	Bundle Radial Power Profile	Quench Time (sec)	Turnaround Time (sec)	Temp. Rise (°F)	Max. Temp. (°F)	Power Decay	Test Series	Comparison
04748	40	1559.5	0.95	1.51	131	FLECHT	207.4	66.7	338.9	1898.4	LFR	Cosine	I
04831	40	1560.3	0.95	1.50	125	FLECHT	210.3	69.5	350.5	1910.8	LFR	Cosine	
13303	41	1545.3	0.7	1.5	126	Uniform	384	35.8	132.6	1676	LFR	Skewed	II
11003	40	1541.9	0.7	1.5	127	Uniform	337.4	23	98.1	1640	LFR	Skewed	
17136	40	1562.8	0.7	1.0	133	Uniform	453	120.3	284.3	1847.1	LFR	Skewed	III
13404	41	1543.6	0.7	1.0	127	Uniform	518.4	143	315.3	1859	LFR	Skewed	
12102	40	1550.6	0.7	3.0	126	Uniform	179.2	7.2	60.2	1610	LFR	Skewed	IV
17302	40	1550.7	0.7	3.0	127	Uniform	196.7	8.2	70.1	1615	LFR	Skewed	
12907	20	1557.5	0.7	6.0	91	Uniform	131.7	4.0	34.3	1578.6	LFR	Skewed	V
17407	20	1520.8	0.7	5.8	93	Uniform	128.7	4.8	29	1561.7	LFR	Skewed	

TABLE 3-4
VARIATION IN TEMPERATURE RISE,
TURNAROUND AND QUENCH TIMES

Quantity	Range of Variation (%)					
	Minimum		Mean		Maximum	
	Skewed	Cosine	Skewed	Cosine	Skewed	Cosine
Temperature Rise	16.4	3.2	20.6	8.4	35.2	19
Quench Time	2.3	2.4	10.0	10.7	14.4	35.7
Turnaround Time	13.9	2.2	27.0	15.9	55.6	50

This analysis indicates that for cosine and skewed repeatability tests, more scatter might be expected in the skewed data than in the cosine data, particularly for turnaround time and temperature rise. There is no apparent reason for this increased data scatter. Further examination of table 3-5 in WCAP-8838 shows that the average variation in cosine quench time data is 4.7 percent neglecting Comparison IV which happens to be a 6-in./sec test. Skewed data at 6 in./sec do not show the large quench-time variation as that of the cosine data. Neglecting the 6-in./sec cosine comparison, which appears to be well outside the average tolerances, quench time repeatability for skewed tests is not as good as for cosine tests. The general conclusion to be drawn is that differences in quench time, turnaround time, and temperature rise within repeated skewed runs are greater than those for the cosine power profile tests. Run conditions were re-evaluated for several of the skewed and cosine pairs without finding any effects in parameters such as flooding rate, failed rods, or pressure control. This might account for the differences in repeatability between skewed and cosine series tests. However, the skewed tests, unlike cosine tests, had a peak power power location higher in the bundle and was subject to quenching from both directions. Much more scatter is observed in quench times of 10-foot skewed versus 6-foot cosine data. The effect of double-ended quench is likely to contribute to the variation in skew repeatability found above.

Examples of average 10-foot heat transfer and temperature profiles for three skewed 40 psia repeat runs are found as figures 3-36, 3-37, and 3-38, corresponding to Comparison

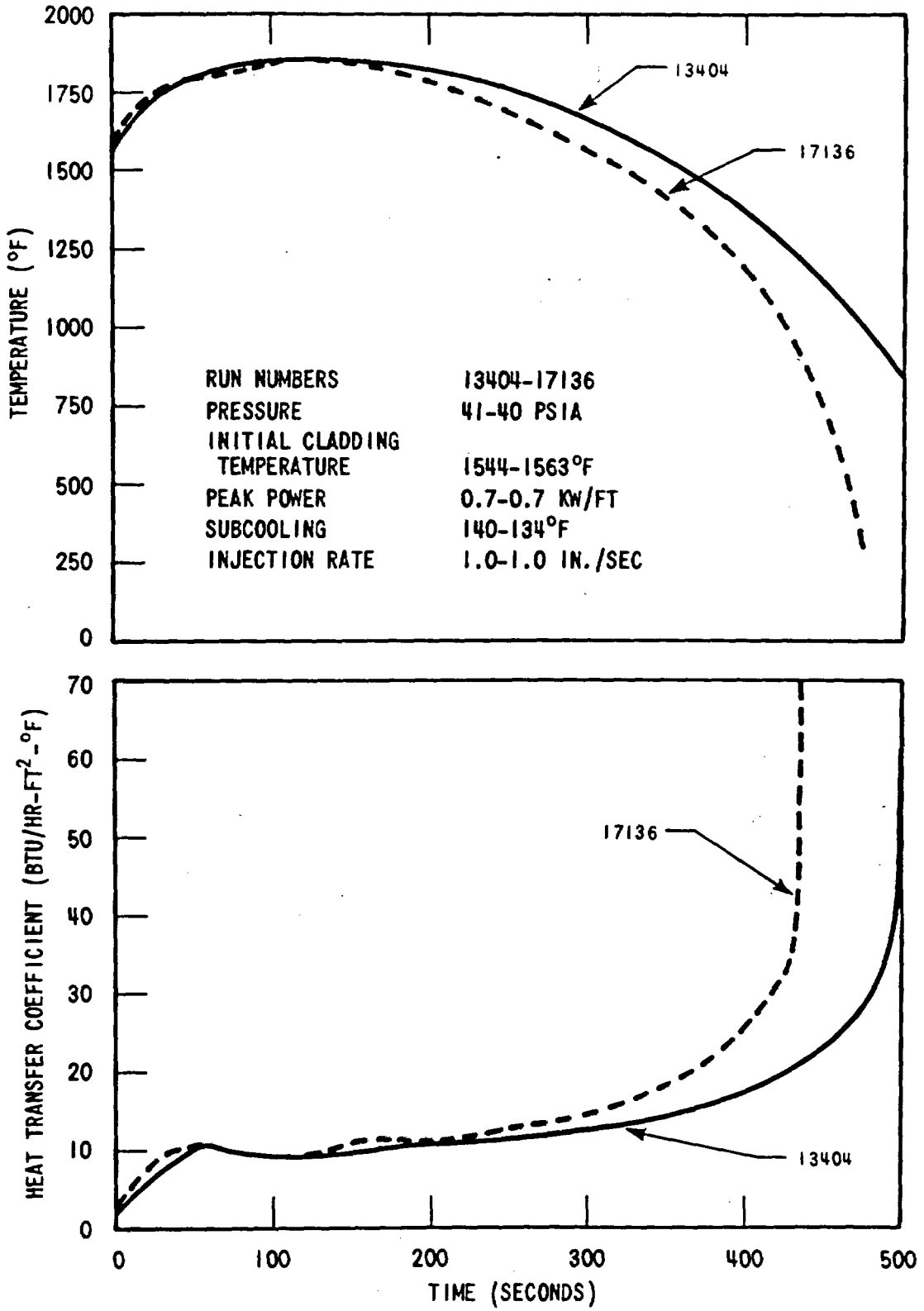

Figure 3-36. Data Repeatability – Average 10 FT Temperature and Heat Transfer Versus Time for Runs 17136 and 13404

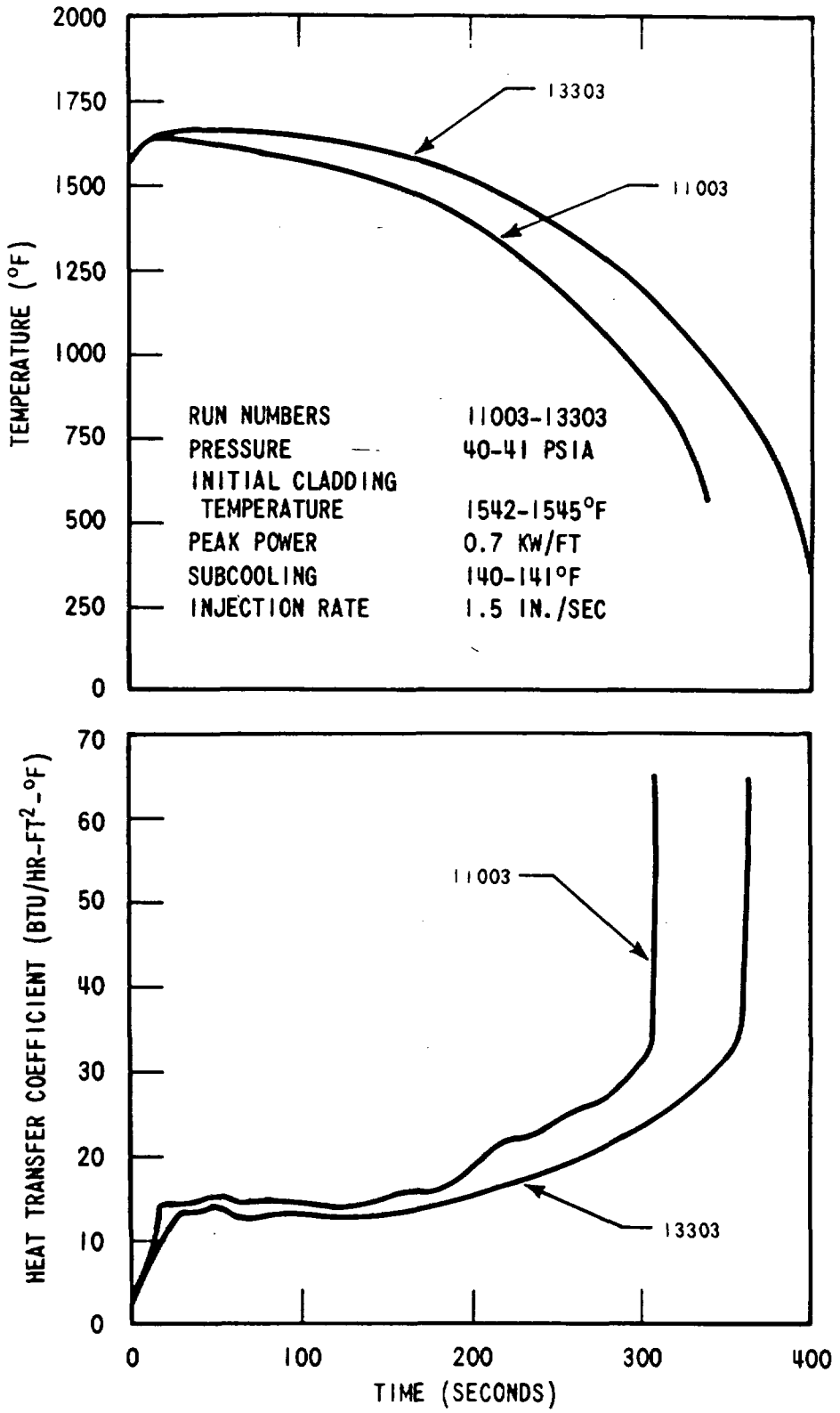

Figure 3-37. Data Repeatability – Average 10 FT Temperature and Heat Transfer Versus Time for Runs 11003 and 13303

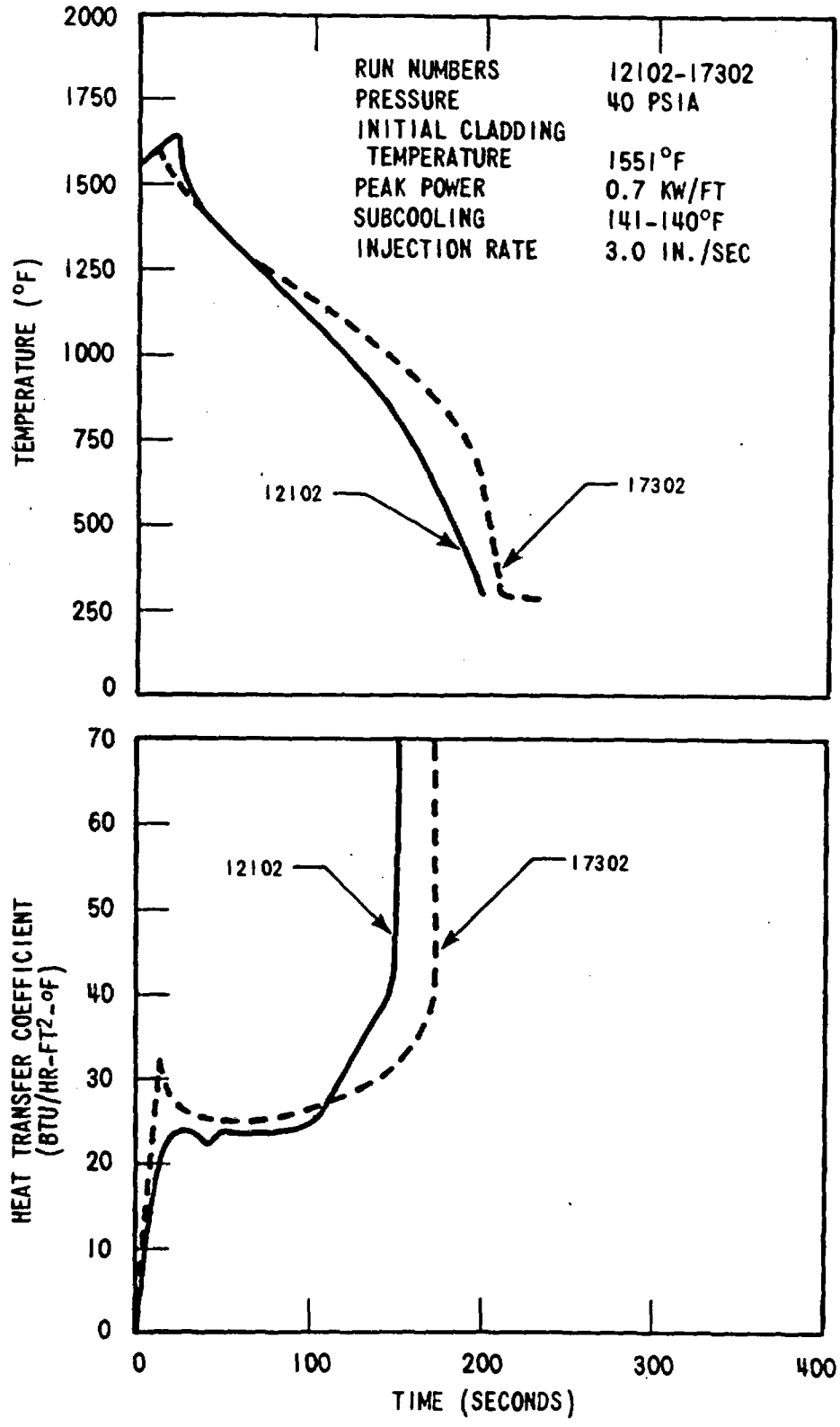

Figure 3-38. Data Repeatability – Average 10 FT Temperature and Heat Transfer Versus Time for Runs 12102 and 17302

groups II, III and IV in table 3-3. Note that these tests have similar run conditions except for flooding rates. Figure 3-39 is a plot of heat transfer and temperature transient for the repeat 20 psia tests of Comparison group IV.

Comparison of other "duplicate" skewed runs within the test matrix for data repeatability were not made for the following reasons:

Run	Reason	
11103	Cold Housing Effect	
12329	FLECHT Radial Power Profile	Different Radial
17529	Uniform Radial Power Profile	Power Profile

3-11. TRANSIENT TESTS

Several tests in the skewed matrix were run with time-varying test parameters. In two tests, pressure and subcooling were ramped downward separately. In a third test, ramp decrease in pressure and subcooling were combined. The pressure ramps were from 40 to 20 psi and the subcooling was ramped from 140°F to 5°F. The ramps were spread over the duration of the run. The principal usefulness of these tests lies in a data base for use in model verification. In this section, the transient tests will be examined qualitatively by comparing them to some of the fixed parameter tests.

Table 3-5 lists the transient tests which were made along with the fixed test condition runs used for comparison. All tests were performed with variable flooding rates; i.e. an initial flooding rate of 6 in./sec for 5 sec, followed by a steady 0.8 in./sec.

3-12. TRANSIENT PRESSURE

Figure 3-40 shows the pressure versus time ramp for Run No. 16844. Figure 3-41 compares this test with constant condition tests at pressures corresponding to the endpoints of the ramp. The transient test is initially at 40 psia and follows the 40 psia constant pressure test, Run No. 15132. Later in time, as the pressure approaches 20 psia, the temperature trace tends toward a more gradual slope characteristic of the 20 psia constant pressure run. The heat transfer transients, figure 3-42, are somewhat confused early in time but show the ramped pressure test falling between the 40 and 20 psia constant pressure runs. In summary, the qualitative behavior of the ramped pressure test shows no unexpected trends.

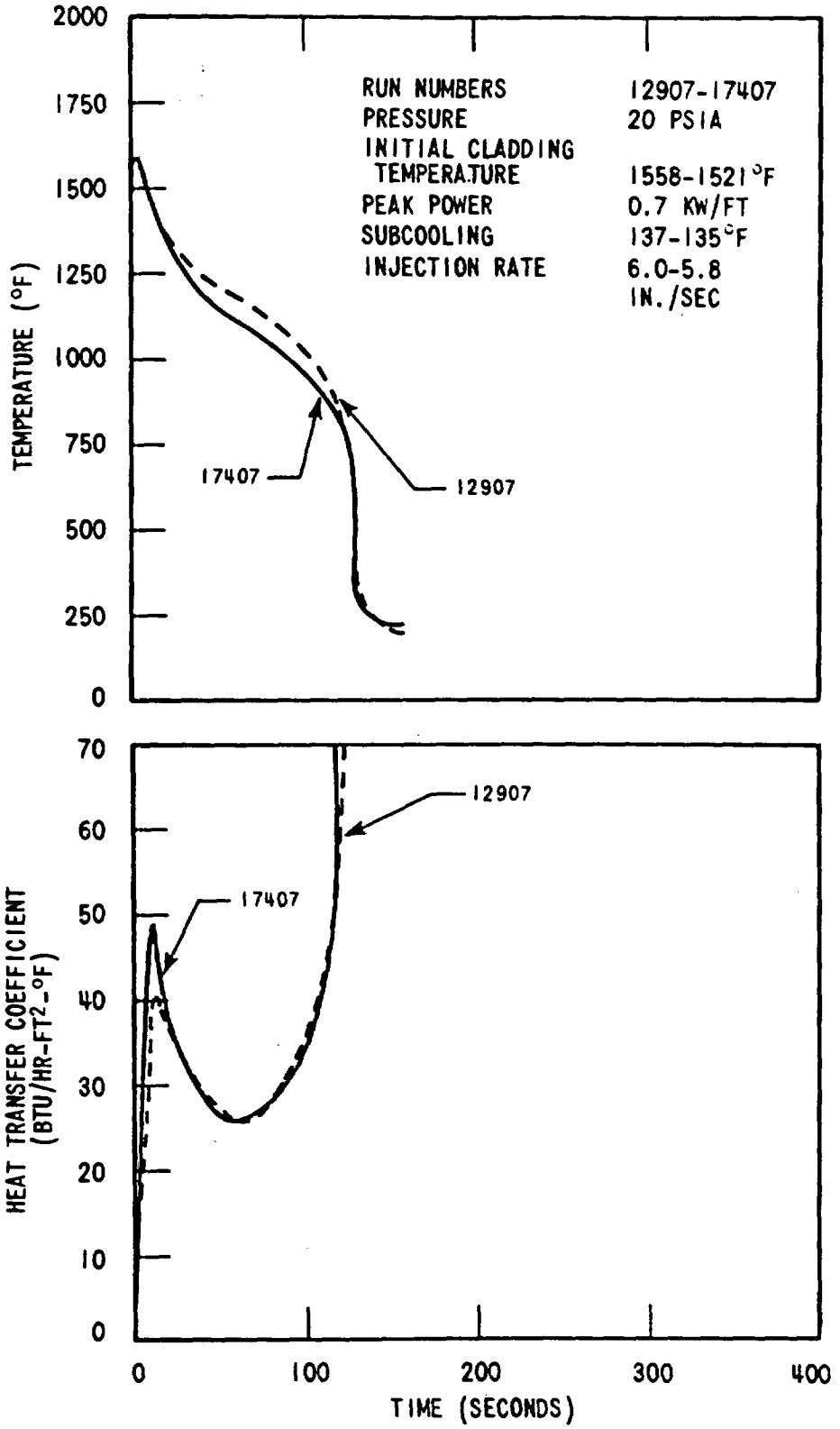

Figure 3-39. Data Repeatability – Average 10 FT Temperature and Heat Transfer Versus Time for Runs 12907 and 17407

RUN NUMBERS	16844
PRESSURE	40 → 20 (RAMP) PSIA
INITIAL CLADDING TEMPERATURE	1600°F
PEAK POWER	0.7 KW/FT
SUBCOOLING	140°F
INJECTION RATE	6.0 (5 SEC) 0.8 (ONWARD) IN./SEC

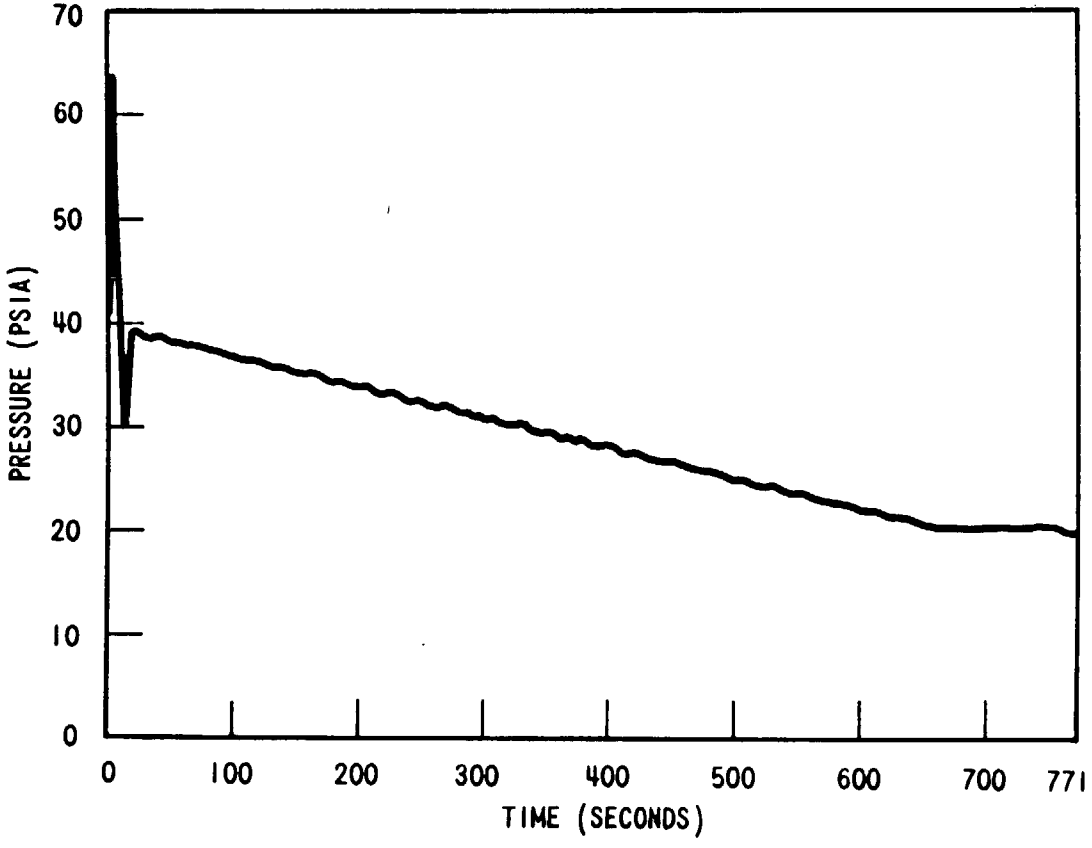

Figure 3-40. Upper Plenum Pressure Versus Time for Run 16844

RUN NUMBERS	15132-15233-16844
PRESSURE	VARIABLE PSIA
INITIAL CLADDING TEMPERATURE	1600°F
PEAK POWER	0.7 KW/FT
SUBCOOLING	140°F
INJECTION RATE	6.0 (5 SEC) 0.8 (ONWARD) IN./SEC

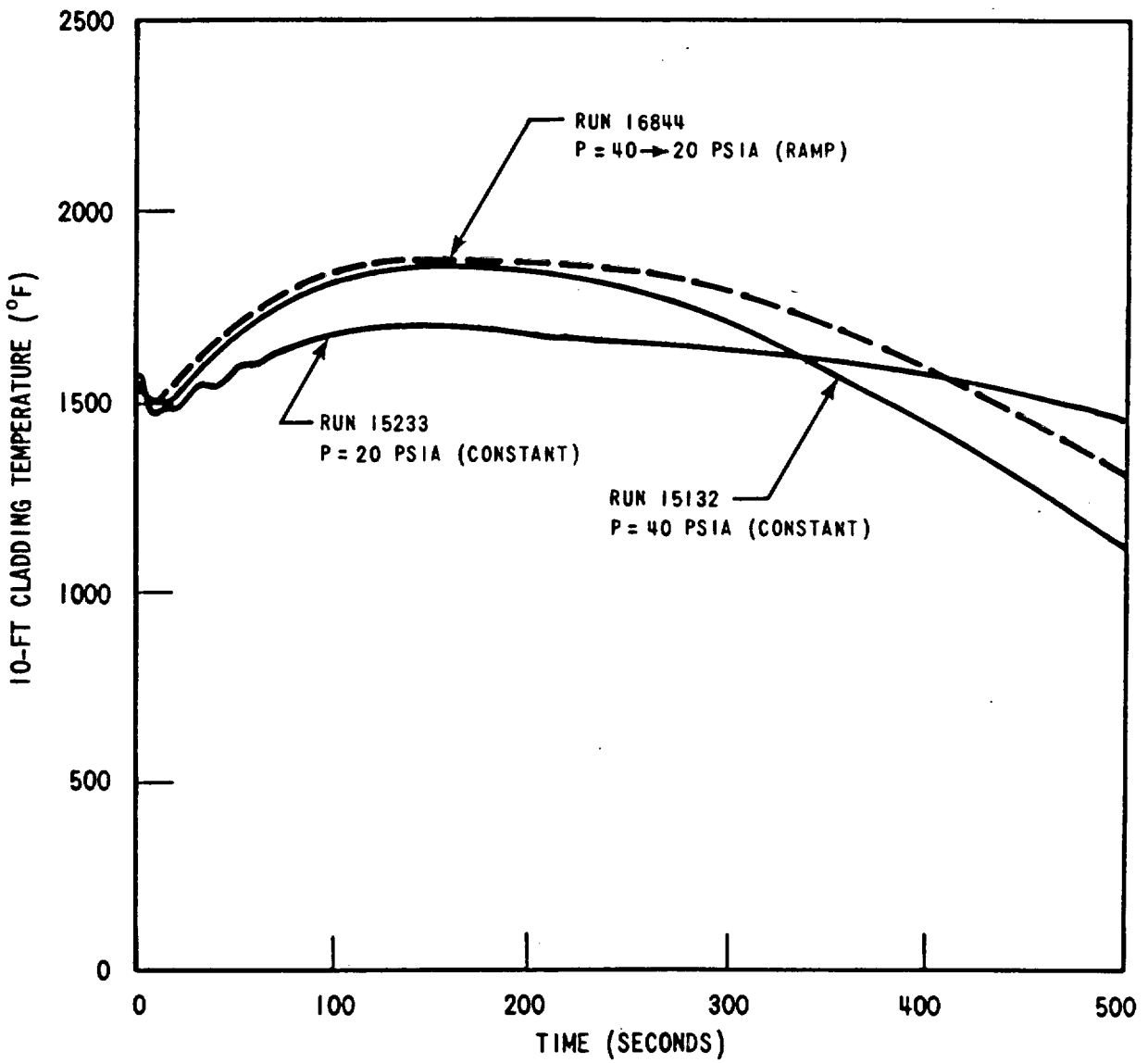

Figure 3-41. Comparison of Variable Pressure Test with Fixed Pressure Tests – 10 FT Clad Temperature

RUN NUMBERS	15132-15233-16844
PRESSURE	VARIABLE PSIA
INITIAL CLADDING TEMPERATURE	1600°F
PEAK POWER	0.7 KW/FT
SUBCOOLING	140°F
INJECTION RATE	6.0 (5 SEC) 0.8 (ONWARD) IN./SEC

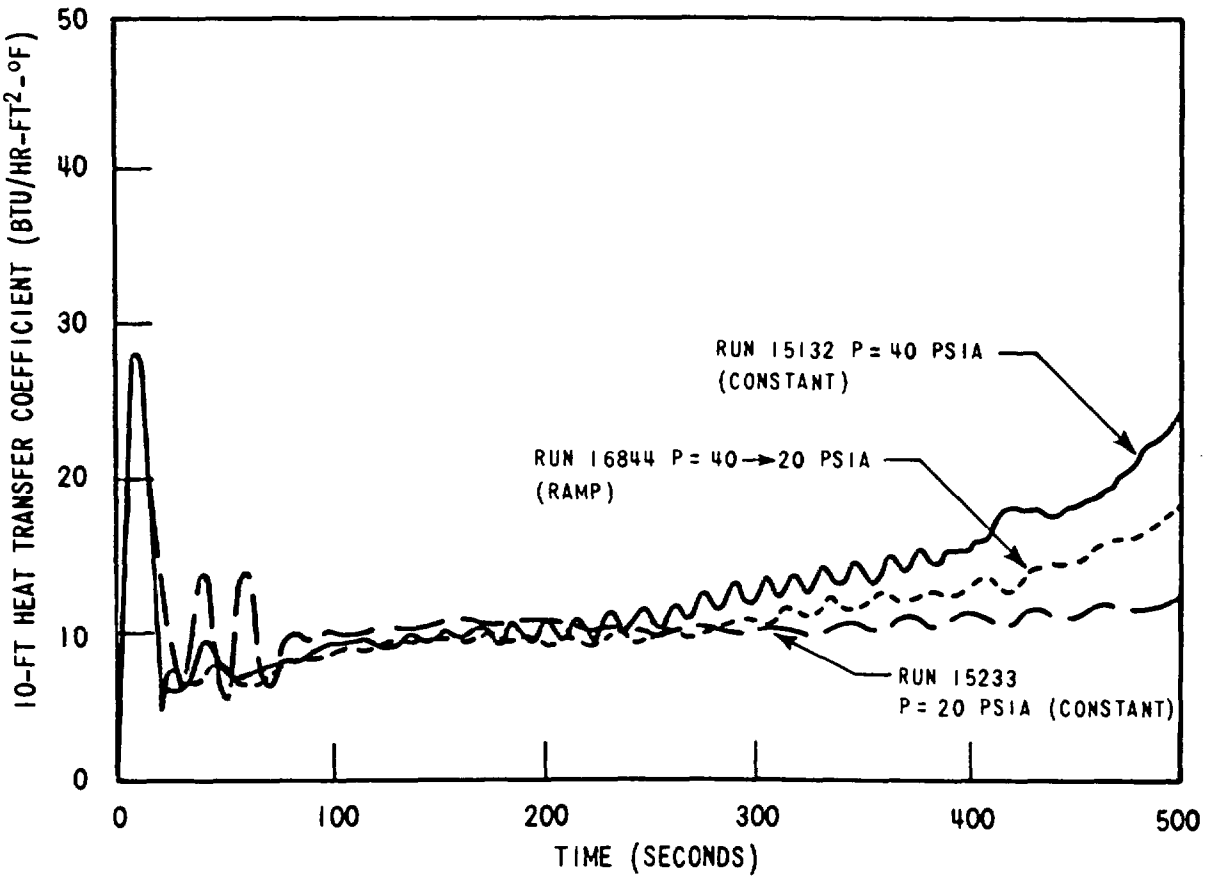

Figure 3-42. Comparison of Variable Pressure Test with Fixed Pressure Test — 10 FT Heat Transfer Coefficient

TABLE 3-5
NOMINAL TEST CONDITIONS FOR TRANSIENT TESTS AND REFERENCE RUNS

Run Number	Pressure (psia)	Flooding Rate (in./sec)	Initial Clad Temp(°F)	Peak Power (kw/ft)	Subcooling (ΔT-°F)	Remarks
15132	40	6.0 (5 sec) 0.8 onward	1600	0.7	140	Fixed test conditions
15233	20	6.0 (5 sec) 0.8 onward	1600	0.7	140	Fixed test conditions
16844	40→20 ramp	6.0 (5 sec) 0.8 onward	1600	0.7	140	Transient pressure test
16945	40	6.0 (5 sec) 0.8 onward	1600	0.7	140→5 ramp	Transient subcooling test
17046	40→20 ramp	6.0 (5 sec) 0.8 onward	1600	0.7	140→5	Combined transient subcooling and pressure test

3-13. SUBCOOLING TRANSIENT

The subcooling effect in the fixed parameter tests showed no significant effect on heat transfer. The heat transfer coefficient comparisons shown in figure 3-43 for most of the run indicate no significant difference between the constant 140° subcooling run and the ramped subcooling run. The differences in initial heat transfer spikes appear to be due to differences in initial injection rates. The subcooling for both runs was the same for this initial period. Variation of coolant temperature is shown at the top of figure 3-43. The injection flows and effluent steam flows are plotted for the initial 20 seconds of both runs in figure 3-44. Both injection and effluent steam flows are higher for the constant subcooling run. This explains the increased heat transfer spike early in time for this run. The increased injection flow early in time could also be expected to accelerate the quench time. This is manifested in a slightly higher heat transfer coefficient late in the run. Figure 3-45 shows the corresponding temperature transients for the constant and variable subcooling tests. The principal effect is seen to be the different behavior in the first 10 to 20 seconds of the run. If it were not for the temperature difference of 20 seconds, both temperature traces would be quite similar.

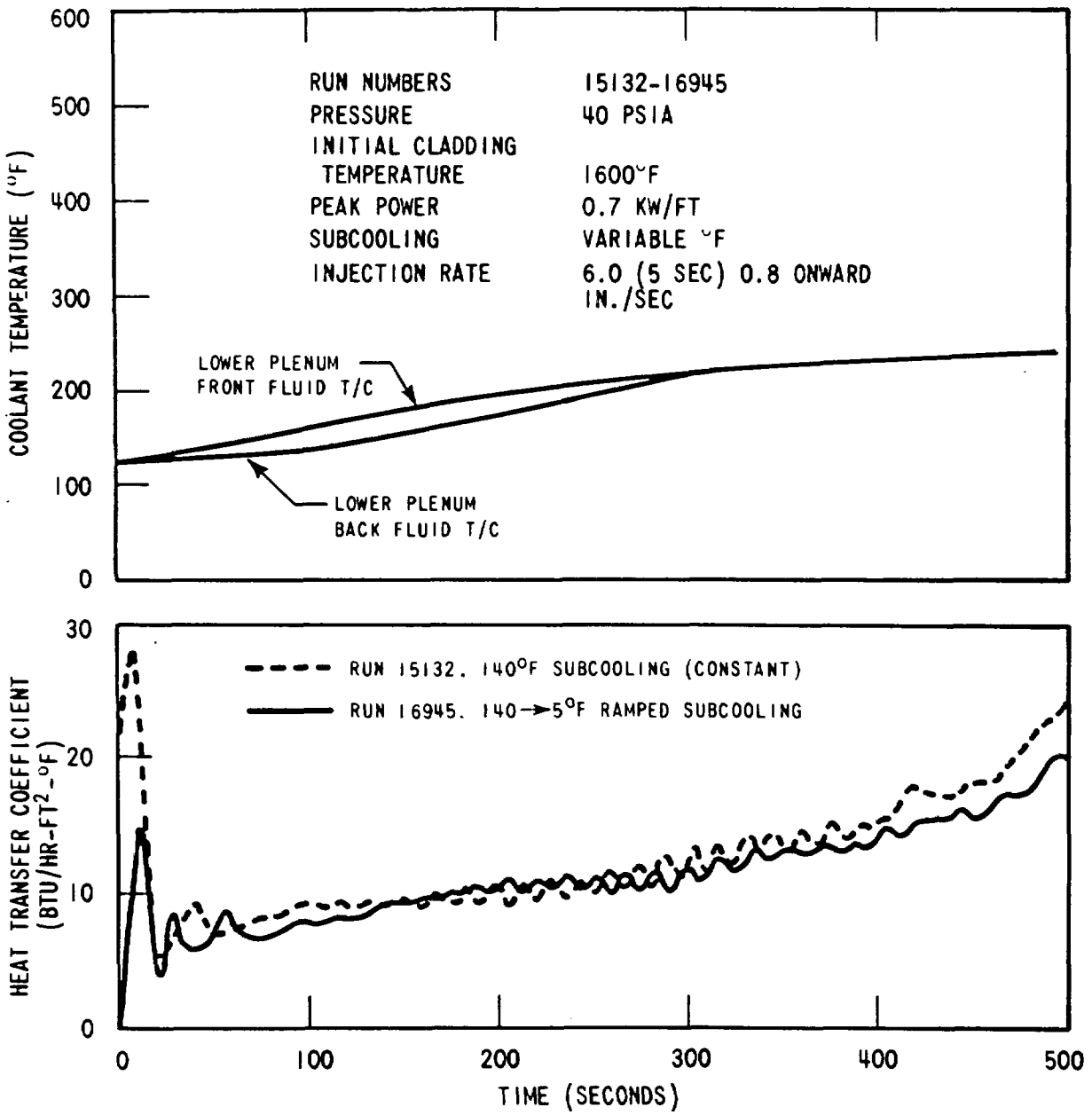

Figure 3-43. Heat Transfer Coefficients for Constant and Variable Subcooling

RUN NUMBERS	15132-16945
PRESSURE	40 PSIA
INITIAL CLADDING TEMPERATURE	1600°F
PEAK POWER	0.7 Kw/FT
SUBCOOLING	VARIABLE °F
INJECTION RATE	6.0 (5 SEC) 0.8 (ONWARD) IN./SEC

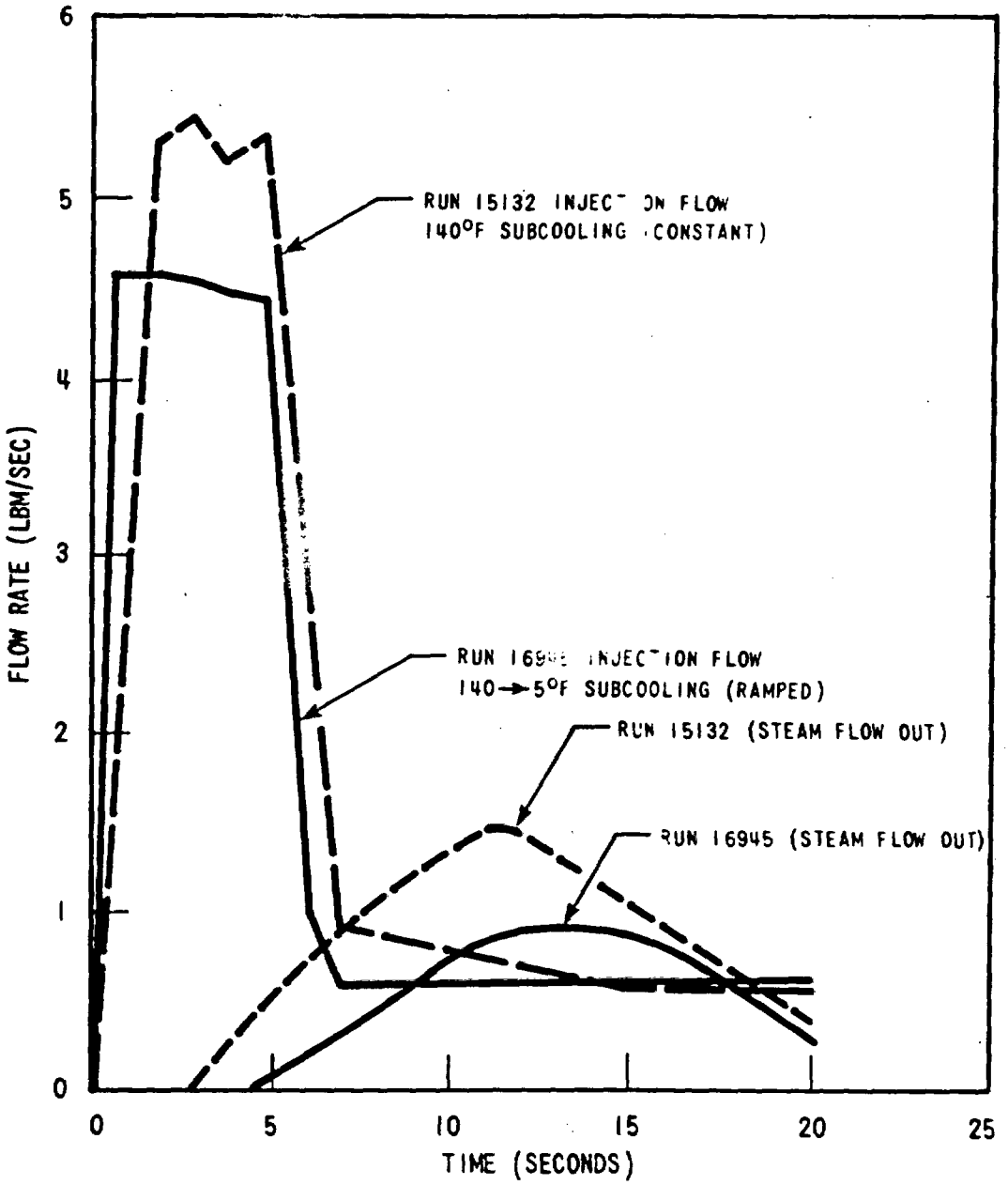

Figure 3-44. Injection and Exhaust Orifice Flows for Constant (15132) and Variable (16945) Subcooling Test

RUN NUMBERS	15132-16945
PRESSURE	40 PSIA
INITIAL CLADDING TEMPERATURE	1600°F
PEAK POWER	0.7 KW/FT
SUBCOOLING	VARIABLE °F
INJECTION RATE	6.0 (5 SEC) 0.8 (ONWARD) IN./SEC

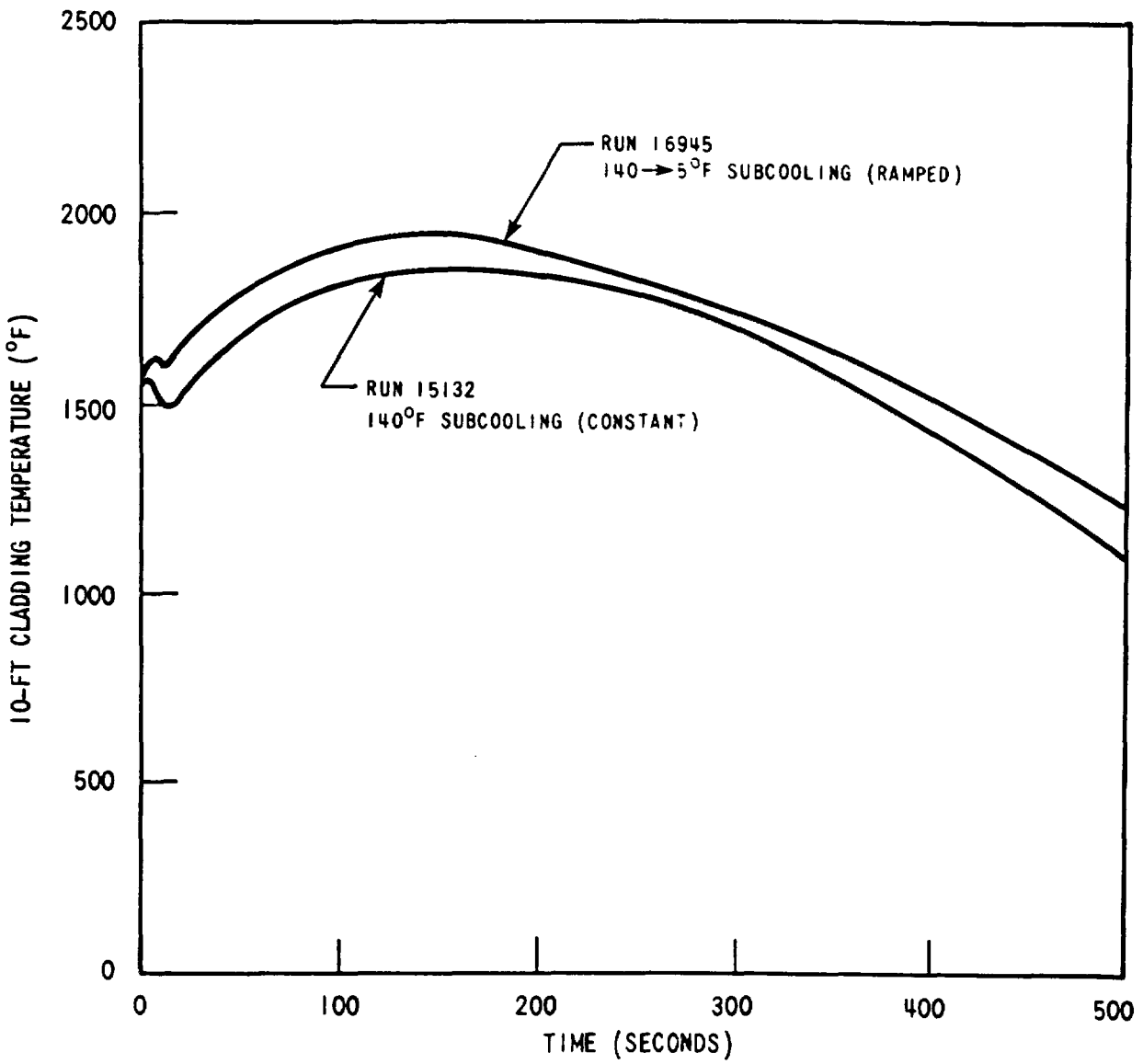

Figure 3-45. Cladding Temperature Transients for Constant and Variable Subcooling

3-14. COMBINED PRESSURE AND SUBCOOLING TRANSIENT

Since the effect of subcooling is a minor one, the combined subcooling and pressure transient test (Run No. 17046) could be expected to give results quite similar to the pressure transient test (Run No. 16844). Factors apparently unrelated to the transients caused these runs to be different such that no conclusion on the above hypothesis could be drawn.

Figures 3-46 and 3-47 show the pressure and coolant temperature transients for Run No. 17046. These transients are the same as the pressure transient for Run No. 16844 (figure 3-40) and the subcooling transient for Run No. 16945 (figure 3-43).

Figure 3-48 shows a comparison of the heat transfer coefficient for the two tests with pressure transients. Nominal run conditions for these tests are identical (see table 2-1) except for the variable subcooling in Run No. 17046, which was shown by the previous section to be a minor effect. Some differences in heat transfer coefficient are evident. First, the initial peak typically present with the initial high flooding rate is missing from Run No. 17046. Second, the heat transfer coefficient later in time for Run No. 17046 is somewhat higher than the constant subcooling test, Run No. 16844.

The absence of the initial peak cannot be attributed to the transients since the peak occurs in the first 20 seconds. No significant change in subcooling or pressure has occurred during this short time. The primary cause of the absence of the expected high peak in heat transfer is not certain. Injection flows for both runs are quite similar early in time, as shown in figure 3-49. Orifice effluent flows, however, are quite different and much lower for the run with the low initial peak heat transfer.

The other difference evident from figure 3-48 is the large heat transfer for the variable subcooling test. This appears to be due to one, or both, of two factors, neither directly related to the transient nature of the test.

The heat transfer coefficient for the variable subcooling test (Run No. 17046) has a much larger oscillatory component later in time than the constant subcooling test (Run No. 16844). This is also evident in the exhaust orifice flow rate, as shown for these two runs in figures 3-50 and 3-51. These oscillations may have contributed to an increased level of heat transfer late in time. The oscillations may simply be characteristic of the system when combined low subcooling and low pressure occur. The heat transfer coefficient for Run No. 13914, which had both low subcooling (5°F) and low pressure (20 psia), showed some significant regular oscillations, seen in figure 3-52.

RUN NUMBERS	17046
PRESSURE	40 → 20 (RAMP) PSIA
INITIAL CLADDING TEMPERATURE	1600°F
PEAK POWER	0.7 KW/FT
SUBCOOLING	140 → 5 (RAMP) °F
INJECTION RATE	6.0 (5 SEC) 0.8 (ONWARD) IN./SEC

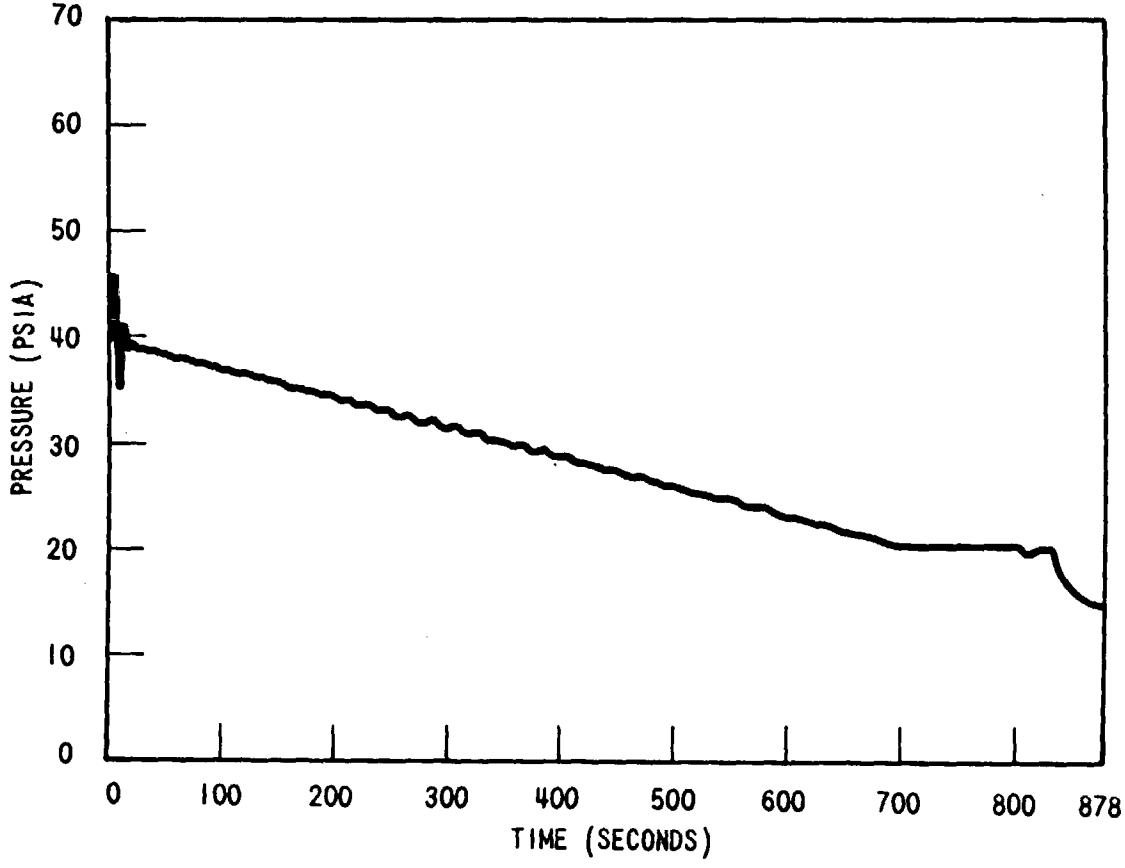

Figure 3-46. Upper Plenum Pressure Versus Time for Run 17046, Combined Pressure and Subcooling Transient Test

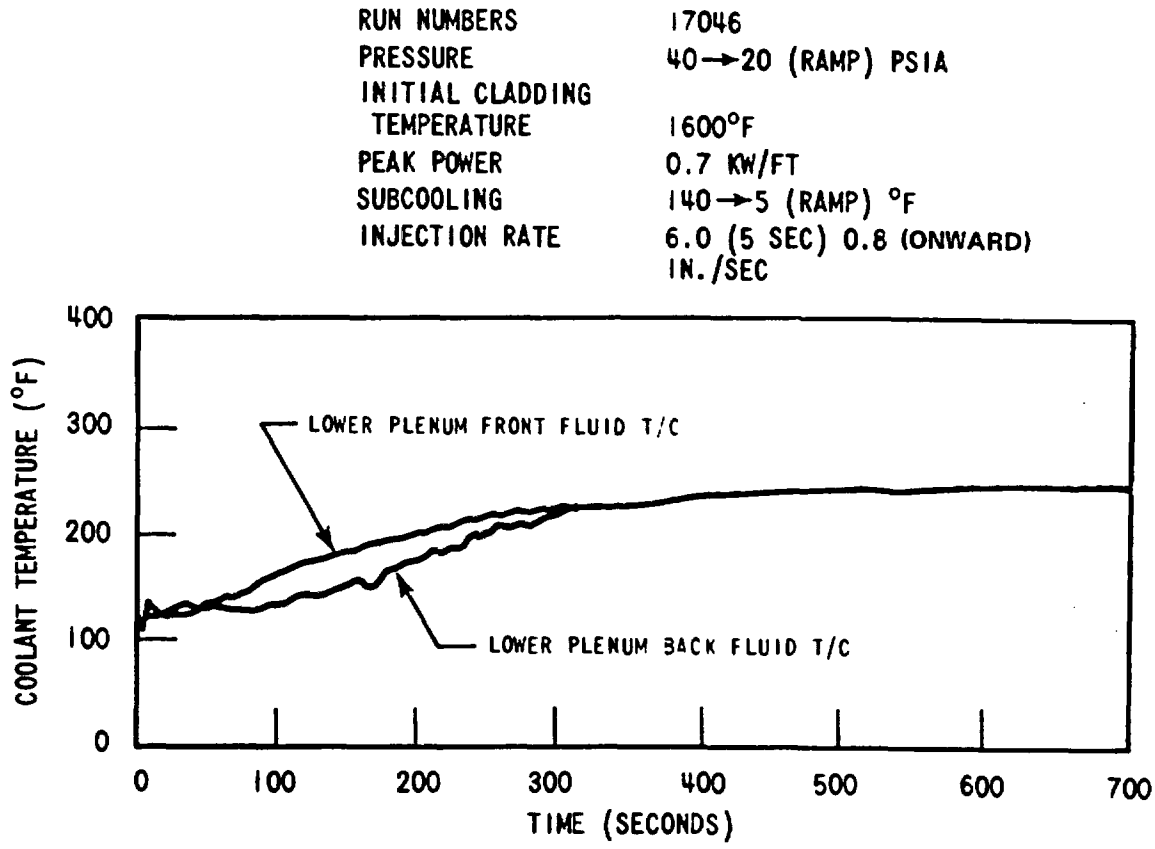

Figure 3-47. Coolant Temperature Versus Time for Run 17046, Combined Pressure and Subcooling Transient Test

RUN NUMBERS	16844-17046
PRESSURE	40→20 (RAMP) PSIA
INITIAL CLADDING TEMPERATURE	1600°F
PEAK POWER	0.7 KW/FT
SUBCOOLING	140-140→5 (RAMP) °F
INJECTION RATE	6.0 (5 SEC) 0.8 (ONWARD) IN./SEC

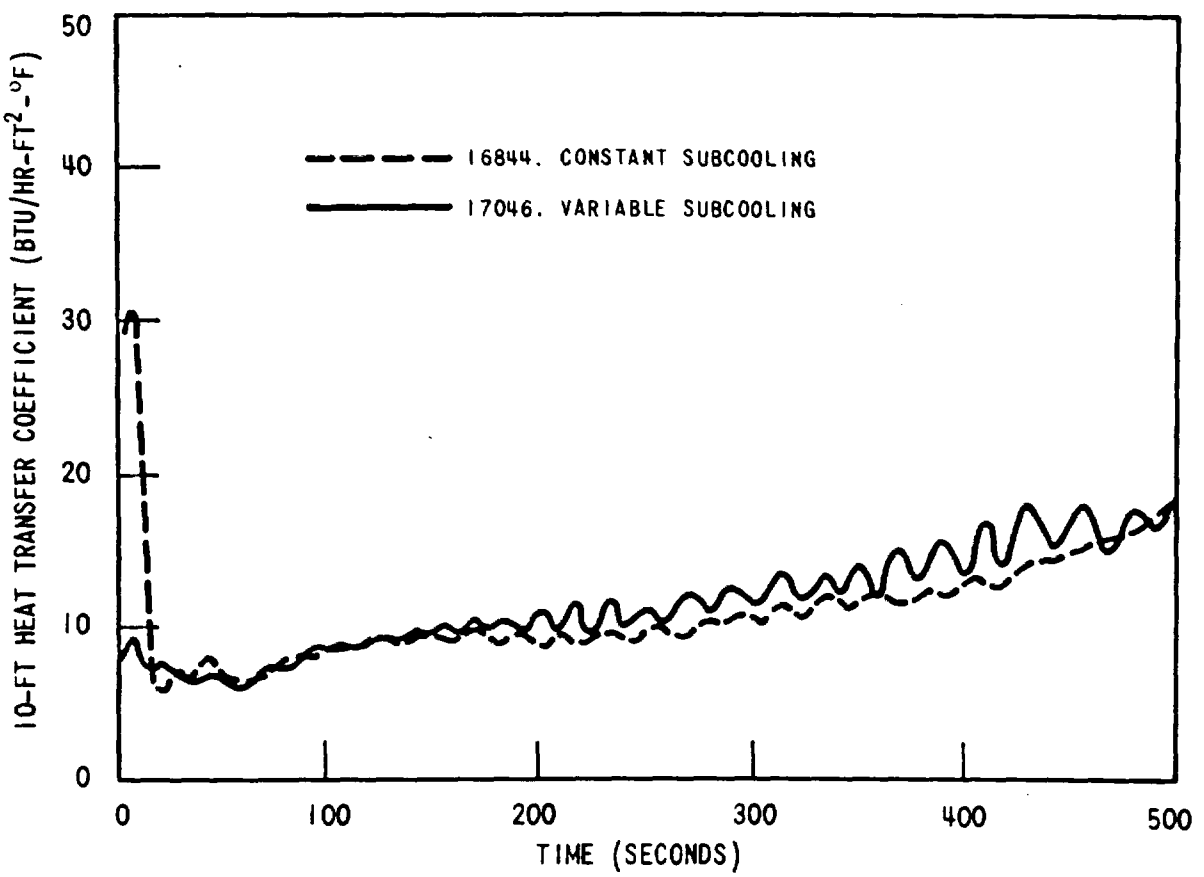

Figure 3-48. Comparison of Heat Transfer Coefficients for Pressure Transient Tests

RUN NUMBERS	16844-17046
PRESSURE	40→20 (RAMP) PSIA
INITIAL CLADDING TEMPERATURE	1600°F
PEAK POWER	0.7 KW/FT
SUBCOOLING	140-140→5 (RAMP) °F
INJECTION RATE	6.0 (5 SEC) 0.8 (ONWARD) IN./SEC

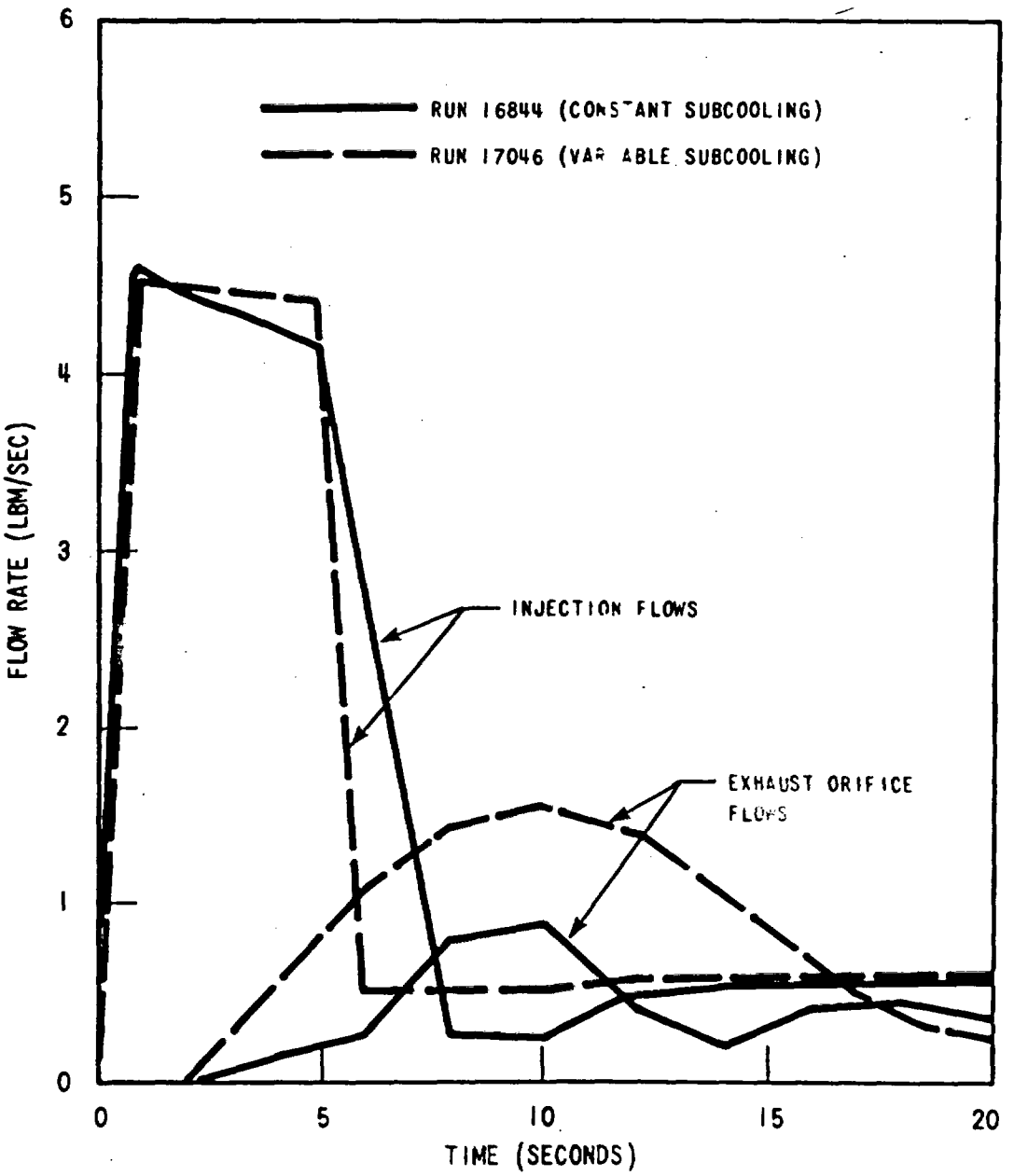

Figure 3-49. Injection and Exhaust Orifice Flow Rates for Runs 16844 and 17046

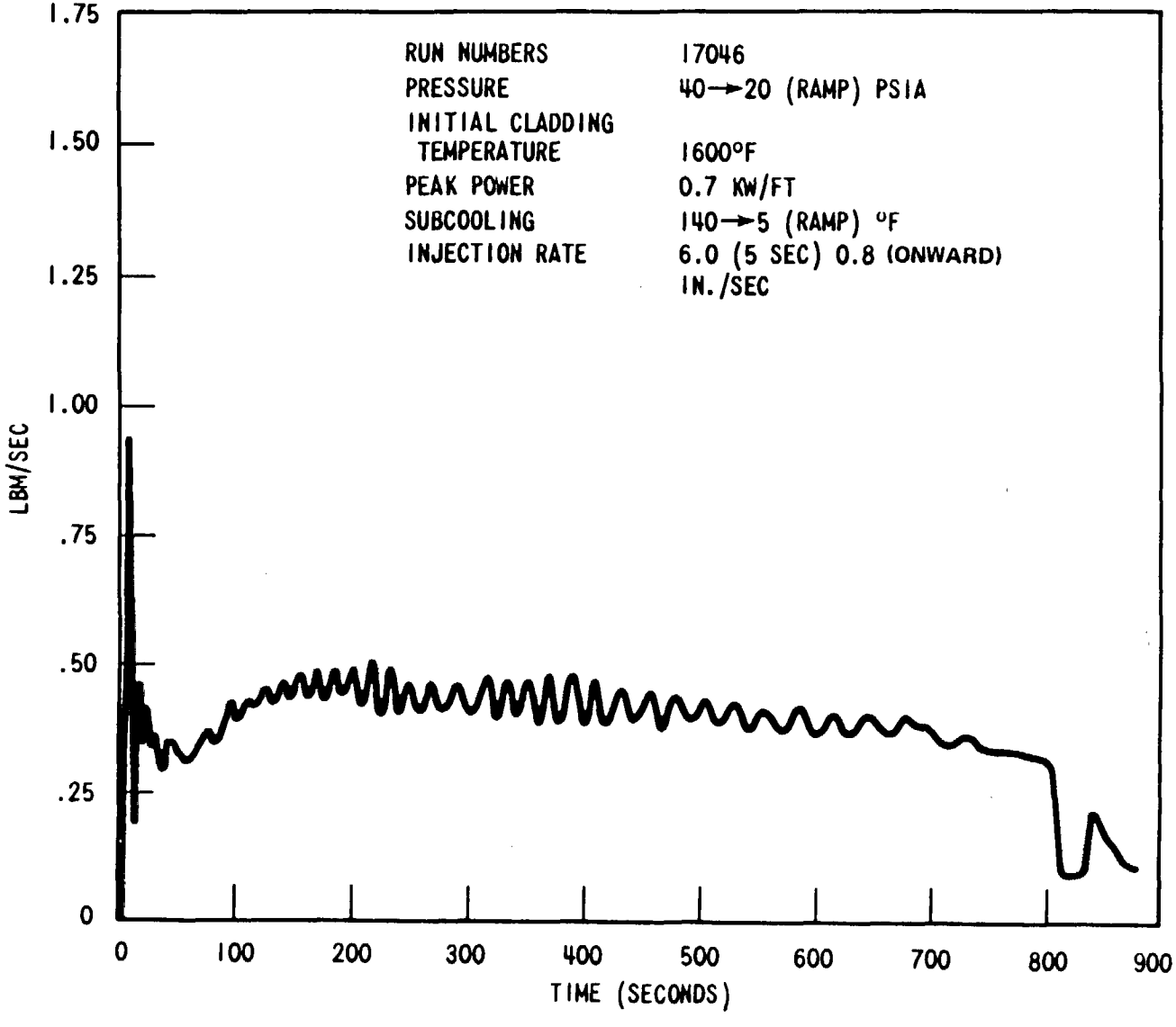

Figure 3-50. Exhaust Orifice Flow for Run 17046, Variable Subcooling

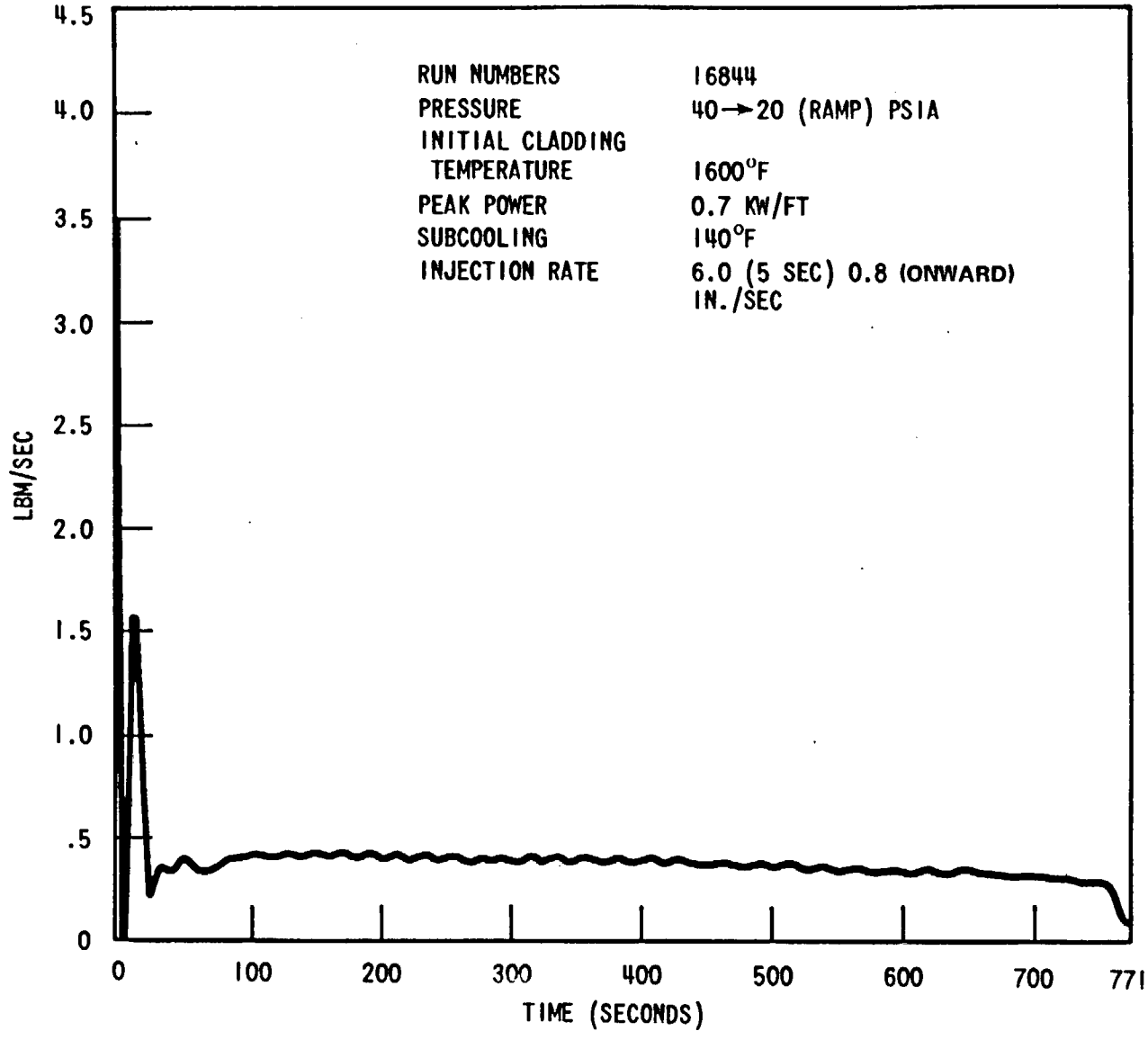

Figure 3-51. Exhaust Orifice Flow for Run 16844, Constant Subcooling

RUN NUMBERS	13914
PRESSURE	21 PSIA
INITIAL CLADDING TEMPERATURE	1605°F
PEAK POWER	0.7 KW/FT
SUBCOOLING	5°F
INJECTION RATE	1.0 IN./SEC

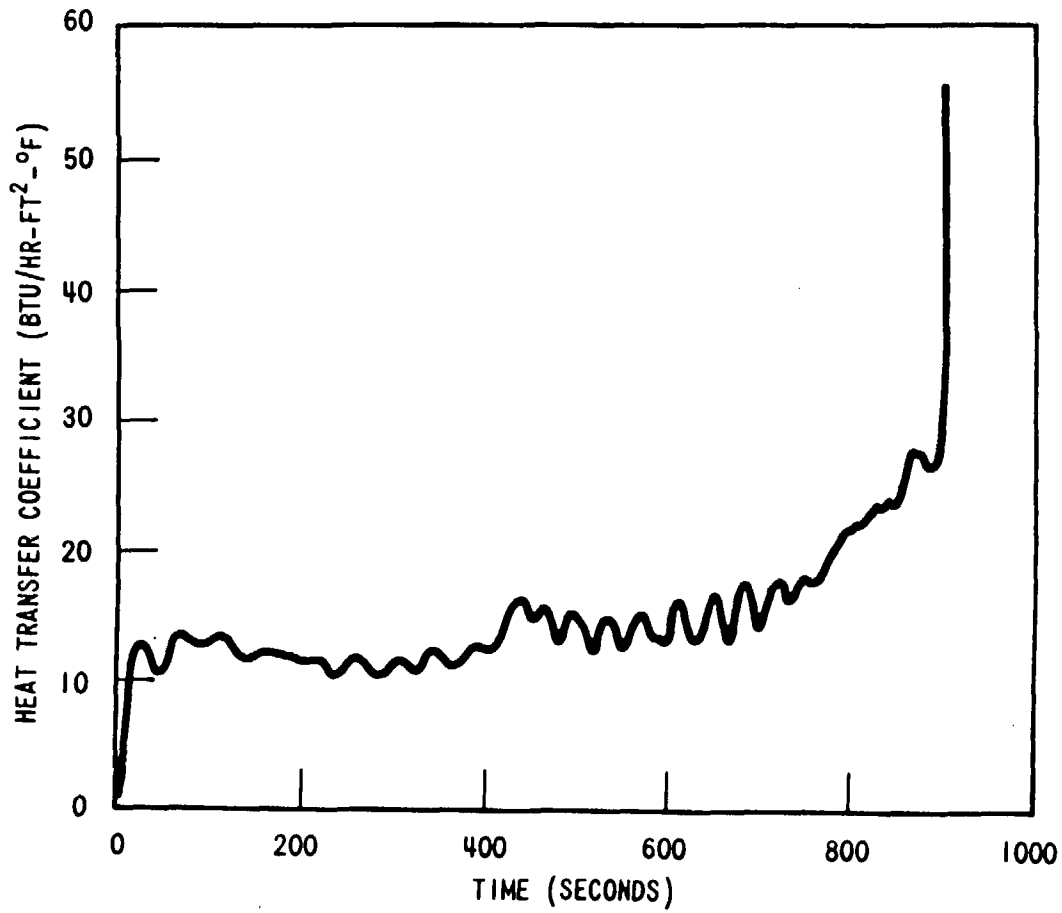

Figure 3-52. 10 FT Heat Transfer Coefficient for Low Subcooling and Low Pressure Test 13914

The second factor which probably contributed to increased heat transfer late in time for the variable subcooling test is the flooding rate. At about 200 seconds, the flooding rate for test (Run No. 17046 began to drift upward, reaching a value 12 percent higher than Run No. 16844 by 500 seconds.

Given the observed differences between the pressure transient test and the combined pressure and subcooling transient test, the temperature transients in figure 3-53 behave as expected. The absence of the initial heat transfer peak results in higher cladding temperatures early in time for Run No. 17046. Later in time, the higher heat transfer coefficient results in more rapid turnaround and decrease of cladding temperature with time.

No qualitative conclusions can be drawn concerning the effect of combined subcooling and pressure transients except that no unusual or unexpected heat transfer was observed.

3-15. SKEWED COSINE COMPARISON TESTS

Low flooding rate skewed data are evaluated in this report for the first time. Previous experiments simulating PWR core recovery after a LOCA have all been run with a cosine power shape. Correlations in current use, with the exception of the h versus $z\text{-}z_q$ correlation presented in this report, have all been developed using data from only one power shape, the cosine

Different analytical techniques have been employed to relate the reflood heat transfer for different power shapes. One commonly used technique among PWR vendors and analysts such as Westinghouse[1], Combustion Engineering[2] and Aerojet Nuclear Corporation[3] is to use the integral-of-power method. The statement of the integral of power method differs slightly among companies but the basic idea is that "for similar bundles, the heat transfer will at the same time be the same at elevations for which the axial integrated power is the same."[2]

All previous attempts at verification of this theory have relied soley upon differences among cosine tests having different peak powers. The present skewed power test series offers an alternative data source for evaluating techniques when applying cosine correlations among varying power shapes. The ten skewed comparison tests found in table 3-6 were designed such that flooding rate, pressure, subcooling and bundle radial power profile duplicate that of previous FLECHT cosine run. The only differences between skewed and cosine comparison

---

1. Bordelon, F. M. et. al., LOCTA IV Program, Loss-of-Coolant Transient Analysis WCAP-8305 June 1974
2. Combustion Engineering Power Systems Safety Analysis Group, Calculation Methods of the C. E. Large Break LOCA Evaluation Model, CENPD 132, REV 01, Vol 1, August 1974.
3. R. F. Jimenez "An Empirical Flooding Heat Transfer Coefficient Including Quench Time Prediction Applicable to a Modification for Variable Flooding Rates; Short Core; and Non-Symmetrical Power Profiles," Jim-6-71 Aeroject Nuclear Company, Idaho Falls, Idaho Interoffice Correspondence, Transmitted to Valerin by L. J. Ybarrondo, November 24, 1971.

RUN NUMBERS	16844-17046
PRESSURE	40→20 (RAMP) PSIA
INITIAL CLADDING TEMPERATURE	1600°F
PEAK POWER	0.7 KW/FT
SUBCOOLING	140-140→5 (RAMP) °F
INJECTION RATE	6.0 (5 SEC) 0.8 (ONWARD) IN./SEC

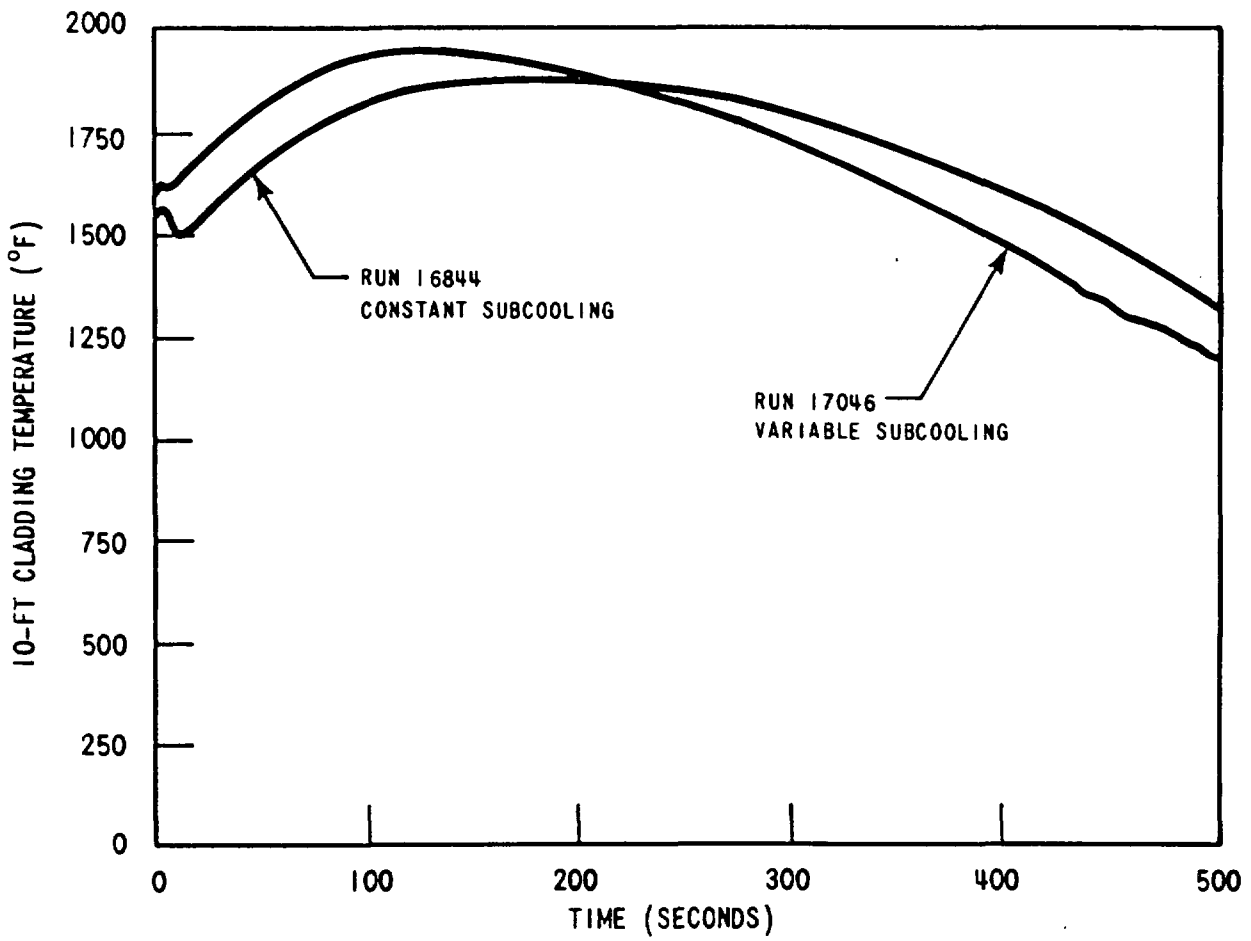

Figure 3-53. Comparison of Temperature Transients for Variable (17046) and Constant (16844) Subcooling Tests

TABLE 3-6

SKEWED COMPARISON TESTS

Comparison Test Matrix								
Run No.	Upper Plenum Pressure (psia)	Initial Cladding Temp At Peak Power Location (°F)	Rod Peak Power (kw/ft)	Flooding Rate (in/sec)	Coolant Temp (°F)	Bundle Radial Power Profile	Average Housing Temp (°F)	Test[a] Series
02223	40	1602	0.93	0.82	126	FLECHT	392	1
11524	40	837	0.373	0.8	126	FLECHT	265	2
5231	18	1603	1.24	5.9	169		478	3
12329	18	918	0.610	5.9	166	FLECHT	234	2
17529	18	917	0.552	6.0	167	Uniform	268	2
4225	59	1596	1.24	1.9	153		586	3
11326	60	950	0.608	2.0	152	FLECHT	290	2
04516	39	1601	0.95	6 (5 sec) 0.8 (onward)	131	FLECHT	625	1
13127	40	955	0.464	6.0 (5 sec) 0.8 (onward)	126	FLECHT	265	2
04641	20	1601	0.95	1.0	89	FLECHT	610	1
11428	20	916	0.464	1.0	90	FLECHT	227	2
04831	40	1600	0.95	1.5	125	FLECHT	502	1
11225	41	954	0.464	1.5	126	FLECHT	260	2

TABLE 3-6 (cont)

SKEWED COMPARISON TESTS

Overlap Test Matrix								
Run No.	Upper Plenum Pressure (psia)	Initial Cladding Temp At Peak Power Location (°F)	Rod Peak Power (kw/ft)	Flooding Rate (in./sec)	Coolant Temp (°F)	Bundle Radial Power Profile	Average Housing Temp (°F)	Test[a] Series
05132	40	1601	0.95	0.99	127	FLECHT	575	1
14548	41	1611	0.216	1.0	127	FLECHT	265	2
0183	21	1598	1.24B	1.0	84	FLECHT	556	4
14647	21	1610	0.47	1.0	89	FLECHT	269	2
3421 PHA	20	1098	1.0	11.78 lb/sec (14 sec) 1.20 lb/sec (onward)	161	FLECHT	632	5
16543	20	672	0.455	11.8 (lb/sec) (14 sec) 1.42 lb/sec (onward)	160	Uniform	266	2

a. Test Series

1) FLECHT Low Flooding Rate Cosine Test Series Data Report WCAP-8651
2) FLECHT Low Flooding Rate Skewed Test Series Data Report WCAP-9108
3) PWR Full Length Emergency Cooling Heat Transfer (FLECHT) Group I Test Report WCAP-7435
4) PWR Final Report Supplement WCAP-7931
5) PWR FLECHT Set Phase A Report WCAP-8238

tests are found in peak power and initial temperature, or equivalently stored and generated energy. Although initial temperature and peak power are nominally different, they were purposely chosen so that the total energy (i.e. the sum of stored and generated energy to a common quench time) up to the peak power location was equivalent for each axial profile in a given pair of comparison tests. Therefore, due to the philosophy behind choosing test conditions, these ten pairs of tests may be used to evaluate the following hypotheses.

- Heat transfer coefficients are suspected to be the same if the integrated power up to two different locations is equivalent[1]
- Peak power locations should quench at the same time if the integrated power up to the peak elevator is the same.
- Fluid conditions are expected to be similar for corresponding elevations having the same integrated power.

In examining these areas it is also useful to keep in mind that the comparisons generated later in this evaluation section may be beneficial toward developing other methods of using cosine correlations or in the development of advanced reflood models.

FLECHT Group I,[2] Supplement Data,[3] Phase A,[4] and Low Flooding Rate[5] cosine runs were selected to cover the range of test conditions as follows:

Pressure	18 – 60 psia
Flooding Rate	0.8 – 6.0 in./sec
Subcooling	50 – 140°F
Initial Temperature	1100 – 1600°F
Rod Peak Power	0.95 – 1.24 kw/ft

A comparison skewed power profile test was then paired with a given cosine run having the same flooding rate, subcooling, and pressure. Only initial temperature and rod peak power were changed according to the integral-of-power method to account for axial power profile differences (see figure 3-54). However the initial temperature, which is a measure of stored energy, and the peak power, which is a measure of generated energy, are not independent quantities if total energy below given locations is to be equated according to the integral-of-power

---

1. Combustion Engineering Power Systems Safety Analysis Group, Calculation Methods of the C. E. Large Break LOCA Evaluation Model, CENPD 132, REV 01, Vol 1, August 1974.
2. Cadek, F. F., et. al., PWR FLECHT Final Report WCAP-7665, April 1971.
3. Cadek, F. F., et. al., PWR FLECHT Final Report Supplement WCAP-7931, Oct. 1972.
4. Blaisdell, J. A., et. al. PWR FLECHT Set Phase A Report WCAP-8238, Dec. 1973.
5. Lilly, G. P., et. al. PWR FLECHT Cosine Low Flooding Rate Series Evaluation Report WCAP-8838, Mar. 1977.

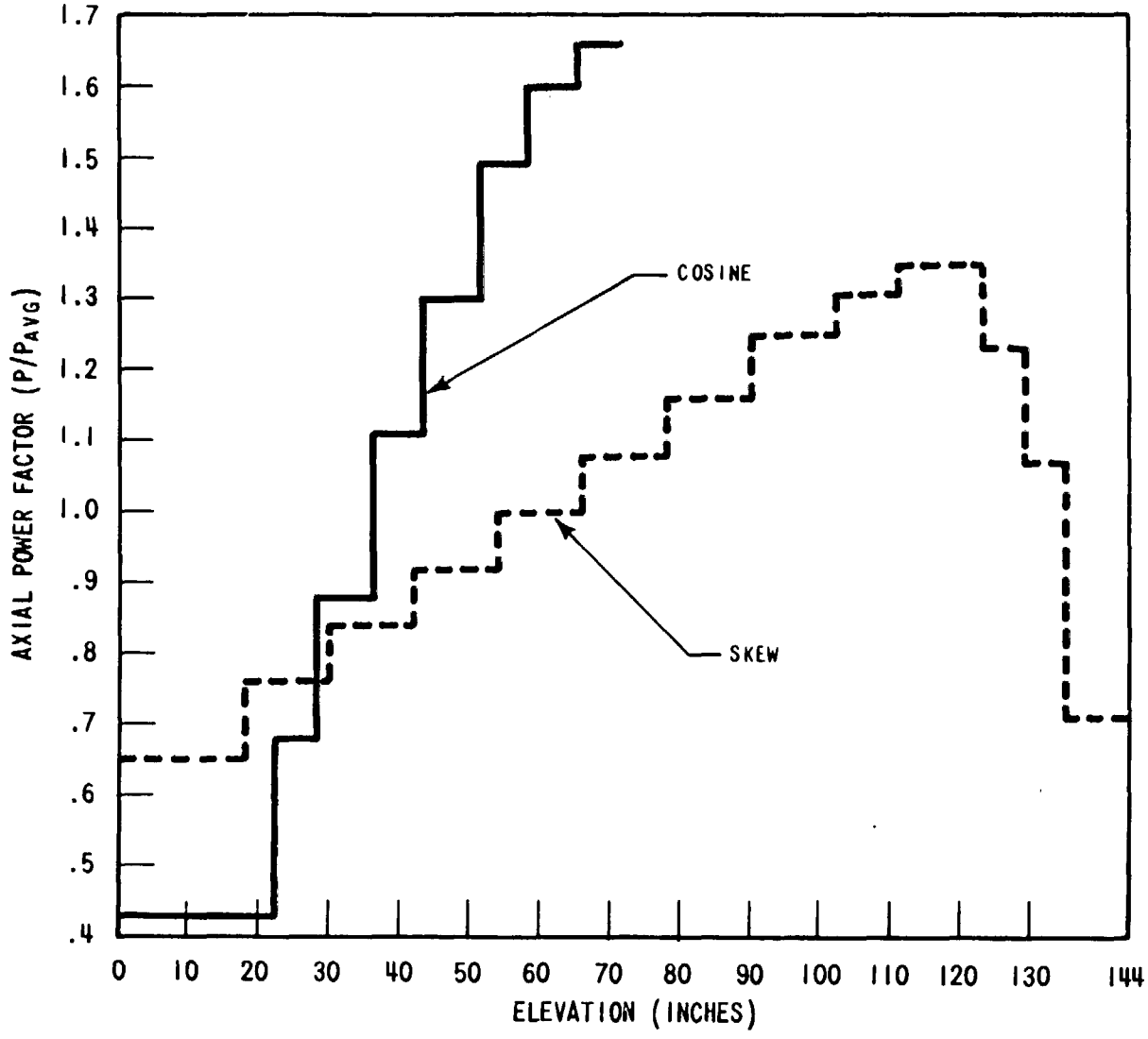

Figure 3-54. FLECHT – Low Flooding Rate Cosine and Skewed Axial Power Profile

method. For example, two skewed comparison tests were specified with a 1600°F initial temperature at the peak power location. The generated power at the peak location is necessarily much lower than any other of the comparison tests to compensate for increased stored energy due to the elevated temperatures. The general mathematical expressions relating stored and generated energy can be found in appendix A along with a more detailed explanation of the different ways in which total energy may be preserved below different elevations of different power profiles.

Use of the integral-of-power method as discussed in Appendix A and the six-foot cosine quench time to specify rod peak power and initial temperature for each of the skewed comparison tests permits experimental verification of the following hypothesis. If the sum of the integrated power and stored energy is the same up to the peak power location, then the peak power location quench times should be the same.

Previous experimentation has shown that quench times are approximately linear when plotted against energy supplied to the bundle.[1] This observation gives further credence to the integral of power hypothesis.

A plot of bundle average quench time data for each pair of comparison tests is shown in figure 3-55. Associated with each mean is an error band of approximately 10 percent representing the variation in quench time data found from repeatability experiments (see table 3-4, Data Repeatability).

Based on repeatability analysis, comparison tests should fall within 10 percent of the mean quench time if all of the assumptions regarding stored and generated energy used to calculate skewed T_{init} and Q_{max} are valid. Table 3-7 lists those pairs which do and do not coincide with the expected variation of mean bundle quench times.

The comparison between Phase A Runs No. 4321 and 16543 is not really meaningful. For example, at the peak power location, the cosine power profile quenched after 633 seconds, while the corresponding skewed profile quenched in only 46.2 sec. None of the other overlap test pairs have quench times which vary by an order of magnitude. Review of the comparison test matrix shows that Run No. 3421 was a relatively high power, low initial temperature test. When Run No. 4321 test conditions were rescaled to maintain equality between stored and generated energy independently, the corresponding skewed initial temperature was predicted to be 672°F. The maximum recorded temperature for Run No. 16543 of 739°F is well within the range of temperatures occurring at quench time. Therefore, it can be expected that Run No. 16543 may not be typical of its overlap cosine pair Run No. 3421. No further comparisons were made between Runs No. 16543 and 4321.

1. Lilly, G. P., et. al. PWR FLECHT Cosine Low Flooding Rate Series Evaluation Report WCAP-8838, Mar. 1977.

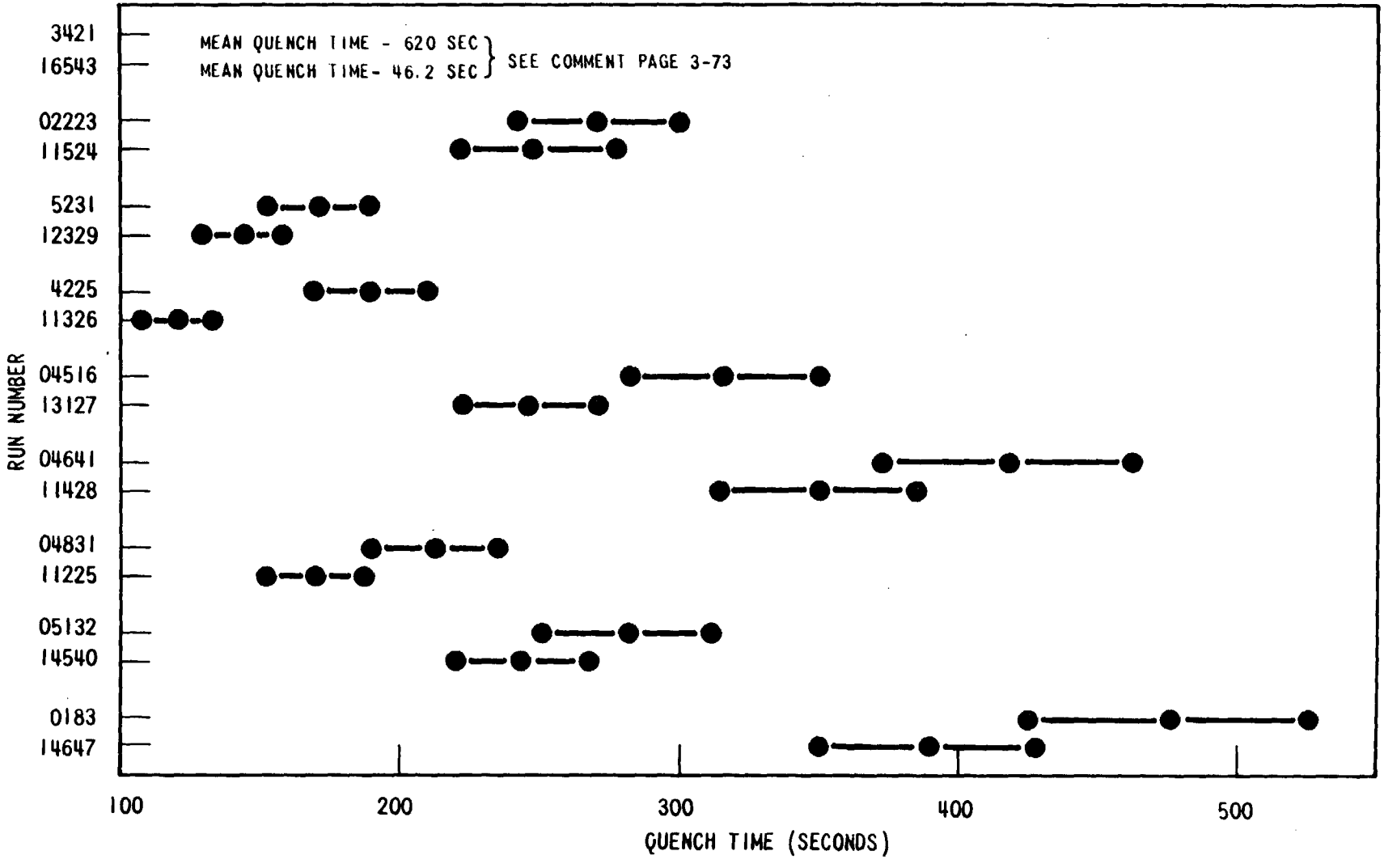

Figure 3-55. Average Bundle Quench Times for Overlap Tests Using Repeatability Average Variations in Data

11,863-53

Each skewed power shape test in the comparison pairs quenched before its comparable cosine tests, indicating either higher heat transfer or that the total energy in the skewed bundle may have been lower.

To examine this early quench behavior of the skewed data, plots of total energy release to the quench time for each particular test were made for four selected comparison pairs using average heat fluxes for the 1.1 rod in the inner 6 x 6 array. The energy release was integrated graphically to find the total energy liberated to the coolant up to quench time. Table 3-8 summarizes this analysis and shows that the cosine tests appear to release more energy than do the skewed tests with the exception of Runs No. 04641 and 11428.

However, graphical analysis can probably account for discrepancies of the order found in Table 3-8. In conclusion, the energy release appears the same for both power profiles up to their respective quench times.

Since the total energy supplied to each of the tests in a comparison pair is approximately the same up to the peak power location, differences in two-phase flow between skewed and cosine power profiles are suspected as the cause of the variations in quench times found in figure 3-55. Therefore, the fluid conditions and flow splits were analyzed for five pairs of comparison tests.

Data show that the differences in the amount of coolant supplied to each test for both constant and variable flooding rate experiments in a comparison pair at any given time is small. For example, total bundle coolant injection agrees within 10 percent at 200 sec for Runs No. 02223 and 11524.

Once injected into the test section, the coolant is stored in the bundle, or enters the upper plenum as a two-phase mixture. Bundle storage is typically larger for the skewed test than for the cosine test. This might be expected later in time, since the peak power location for the skewed profile is four feet above the cosine. However, the skewed storage is consistently larger shortly after the beginning of reflood. Reduced initial temperature and peak power imply that less energy must be removed before lower sections of the skewed bundle quench with a corresponding decrease in quality and increased water storage.

It was also observed that more liquid reaches the top of the bundle sooner in the skewed test with the exception of the high initial temperature comparison (Runs No. 14548 and 05132). Since entrained water acts as a sink for heat release from the rods, it acts to enhance the heat transfer mechanisms present in the bundle. This higher heat transfer should result in shorter quench times for the skewed test which is consistent with the data shown in figure 3-55.

TABLE 3-7

COMPARISON OF MEAN BUNDLE QUENCH TIMES

Test Pairs Considered to be Comparable	Test Pair Which Do Not Appear to be Comparable
02223 – 11524	4225 – 11326
5231 – 12329	04516 – 13127
04641 – 11428	04831 – 11225
05132 – 14548	4321 – 16543
0183 – 14647	

TABLE 3-8

COMPARISON OF HEAT RELEASE TO PEAK POWER LOCATION QUENCH TIME

Run	Ratio of Cosine Energy Release To Skewed Energy Release
02223 11524	1.09
04831 11225	1.04
04516 13127	1.05
04641 11428	0.98

By the time the effluent from the upper plenum reached the orifice meter, the total flow was dry steam. Typically, the cosine test emits significantly more vapor than the skewed overlap test which would help account for the discrepancy in bundle storage mentioned earlier.

A summary of five pairs of overlap tests has been compiled in table 3-9, showing the flow splits for each test at its respective quench time. In all cases the cosine injected mass was approximately the same as, or greater than, the corresponding skewed test. This observation agrees with the fact that cosine tests required a longer time to quench than did the skewed tests. Typically, the average quality calculated from total steam flow to total flow out the top of the bundle at quench time was higher for the cosine test than for the skewed test with the exception of the high temperature, low power pair, Runs No. 05132 and 14548. Again, this calculation indicates that a higher percentage of the total flow out of the bundle is in the liquid phase for the skewed power profile. In all cases, the skewed carryover tank captures more liquid over a shorter period of time than does the cosine. These results would indicate an improved heat transfer above the quench front for the skewed tests as compared to the cosine tests and hence a shorter quench time.

Evaluation of local heat release to the fluid is best done at the peak power location for several reasons. First, the comparison test conditions were determined such that the total of stored and generated energy integrated to the peak power location was the same for both profiles. Secondly, steam probes measuring vapor temperature are found only in the upper half of the bundle for both power profiles. These steam probes at 7 and 10 feet are the only means of obtaining steam temperature data necessary to evaluate local heat transfer using actual fluid conditions. The limiting factor in this analysis is clearly the availability of steam temperature data. From a rod viewpoint, heat flux released to the fluid was compared at the peak power elevation. The generated energy at the peak power location in the cosine shape is typically twice that for the 10-foot skewed profile peak location. Stored energy does not compensate for this difference and the time-dependent heat release to the fluid is greater for the cosine comparison test than for the skewed test.

From the fluid viewpoint, the appropriate quantity to be compared is the heat transfer coefficient. For the skewed test, this is easily done. Thermocouples measuring rod surface temperature are available at 10 feet, as is one steam probe. The real heat transfer coefficient can be computed from the FLECHT definition of the heat transfer coefficient based on saturation temperature using the following formula.

$$h_{real} = h_{FLECHT}\left[\frac{T_{wall} - T_{sat}}{T_{wall} - T_{steam}}\right] \qquad (3\text{-}3)$$

TABLE 3-9

INTEGRATED FLUID FLOWS FOR OVERLAP PAIRS
UP TO QUENCH TIME

Run No.	t_q (sec)	Total Mass Injected (lb)	Mass Diff (lb)	Effluent From Exhaust Orifice (lb)	Mass In Steam Sep (lb)	Mass In Carryover Tank (lb)	Mass Stored In Bundle (lb)	M_{out} Total (lb)
0183	476	–[a]	–	–	–	–	–	–
14647	389.8	–	–	–	–	–	–	–
05132	282.4	200.6	10.8	117.8	-0.1	27	45	144.7
14548	243.9	183.5	10.5	76.2	0.3	10.0	86.5	86.5
04831	213.1	229.2	20.7	110.7	-0.1	45.1	52.8	155.7
11225	170.7	207.9	26.4	53.6	0.1	48	79.9	101.6
04641	418.3	301.3	10.4	165.4	0.1	78.2	47.2	243.6
11428	349.3	261.4	25.8	82.6	0.1	81.4	71.6	164.1
04516	316.9	213.6	32.2	128.3	0	11.9	41.2	140.2
13127	246.7	169.9	5.3	78	0.1	20.5	66	98.6
4225	190.3	–	–	–	–	–	–	–
11326	121	–	–	–	–	–	–	–
5231	172	–	–	–	–	–	–	–
12329	144.5	–	–	–	–	–	–	–
02223	271.9	149.2	10.1	93.1	0	6.0	40.2	99
11524	247.4	150.6	15.7	55.8	0	7.4	71.7	63.2

a. Test not analyzed.

However, evaluation of the real heat transfer coefficient for a cosine test at six feet is not as straight-forward because six-foot steam temperature data do not exist. Several different methods were used to get a rough estimate of the steam temperature from available data at the quench front, 7 and 10 feet. The steam temperature profile (figure 3-56) has an assumed maximum at 6 feet. Furthermore, the steam temperature was assumed higher than saturation at the quench front and the average of wall temperature just prior to quench and saturation temperature was chosen as an appropriate estimate. Once the steam temperature was calculated at quench elevation, 7 and 10 feet in addition to the assumed maximum at 6 feet, the coefficients of a polynomial of the form

$$T_{steam} = a_0 z^3 + a_1 z^2 + a_2 z + a_3 \qquad (3\text{-}4)$$

were evaluated. The ESTIMATE of the six-foot steam temperature is then possible by evaluating the above polynomial at $z = 6$. Three different curves were tried. First, all four coefficients were evaluated in the cubic polynomial. Second, two parabolic approximations were made using the conditions

- T_{steam} (z quench), T_{steam} (7 feet) and maximum at 6 feet
- T_{steam} (7 feet), T_{steam} (10 feet) and maximum at 6 feet

Up to turnaround time, the calculated 6-foot steam temperatures using each method do not differ from one another, as shown in table 3-10. After turnaround time, the curve fits predicted negative heat transfer at the peak power location which is a physical impossibility since the highest steam temperature should occur at or above the peak power location. The calculated real heat transfer coefficients in the cosine test before that time are smaller than those calculated from skewed experimental data. Since calculation of real heat transfer coefficients uses the difference between two temperatures which are similar in magnitude, a small error in either minuend or subtrahend can result in a significant error in the difference and hence in the real heat transfer coefficient. The calculation above is only a rough estimate since the six-foot cosine steam temperature is not known. Either of two explanations, which cannot be resolved with available data, is possible.

- The cosine steam temperature may be underpredicted, resulting in a smaller heat transfer coefficient or
- The cosine heat transfer coefficient is in fact less than skewed at a given time at the peak power location.

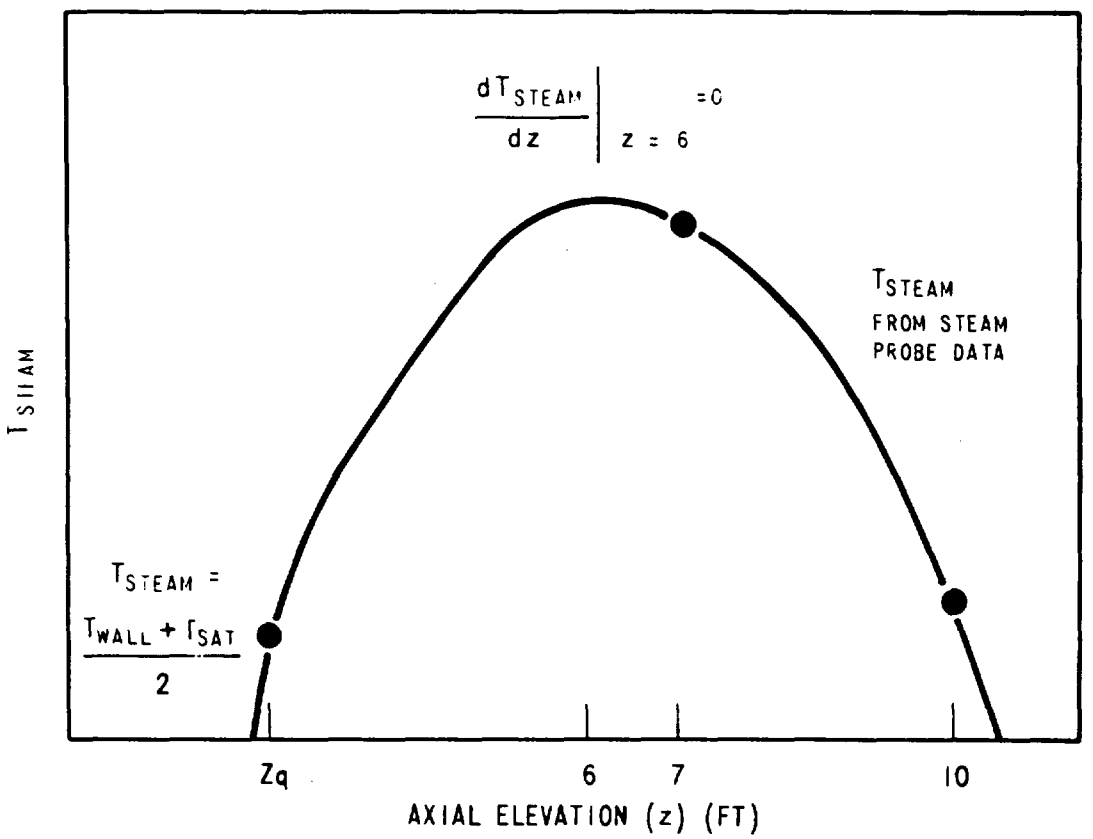

Figure 3-56. Schematic Diagram of Data Used to Calculate Cosine 6 FT Steam Temperature

TABLE 3-10

CALCULATED 6-FOOT COSINE STEAM TEMPERATURE AND REAL HEAT TRANSFER COEFFICIENT COMPARISON

Quench Time (sec)	Run No. 05132 Analytical Curve Fit Calculation					
	Parabola using: Z_{quench} 7′ steam probe 6′ max steam temp		Parabola using: 7′ steam probe 10′ steam probe 6′ max steam temp		Cubic using: Z_{quench} 7′ steam probe 10′ steam probe 6′ max steam temp	
	T_{steam} (°F)	h_{real} (Btu/hr-ft^2-°F)	T_{steam} (°F)	h_{real} (Btu/hr-ft^2-°F)	T_{steam} (°F)	h_{real} (Btu/hr-ft^2-°F)
27.8	1473	49.4	1478	50.2	1477	50.2
46.2	1639	83.6	1630	79.7	1634	83.5
94.3	1770	153.4	1700	101.1	1729	117.3
149.5	2021	-121.4	1688	167.5	1836	-3062
	Run No. 14548 Data					
28.2	1405	107.3				
49.8	1383	104.9				
99.6	1372	181.9				

FLECHT heat transfer coefficients based on (T_{wall} - T_{sat}) temperature differences have also been included for the two high temperature comparison tests as figures 3-57 and 3-58. Elevated rod temperatures in both tests should maintain roughly the same degree of non-equilibrium between vapor and saturation conditions. Therefore differences in the FLECHT h (at peak power locations) can be expected to be minimized using these two comparison groups. Note that Runs No. 14647 and 0183 heat transfer coefficients are approximately the same over the duration of the test. Agreement between Runs No. 14548 and 05132 is not as good.

FLECHT heat transfer coefficient comparisons for the lower temperature comparison tests do not agree as favorably as do the two pairs presented in figures 3-57 and 3-58. The poor agreement is believed to be caused by the lower initial temperature of the skewed profile comparison tests which results in lower entrainment and less nonequilibrium as compared to the cosine data. The difference in the thermal nonequilibrium is not reflected in the FLECHT definition of the heat transfer coefficient.

In conclusion, the data comparisons have shown:

- The energy release up to the quench time for each test in a comparison pair is the same, indicating that the integral of power method used to prescribe initial temperature and rod peak power is a viable means accounting for total energy in a rod bundle.

- Agreement between quench times of a given comparison pair is not entirely satisfactory. In all cases, the skewed power profile quenched prior to the cosine.

- The higher heat transfer found in a skewed test is probably due to differences in fluid flow. The skewed profile entrains much more water and generates less steam than does the cosine power profile for equivalent injected flow. The extra water in the bundle acts as a sink for heat transfer. In general, it is easier to cool a skewed power profile having the same total energy below peak elevation than it is a cosine profile.

- Two different integral-of-power methods were used to generate comparison test conditions to relate cosine power shapes to skewed power shapes:

    1. Maintain equivalence of stored and generated energy separately.

    2. Maintain the peak location initial temperature at the expense of a much lower peak power.

RUN NUMBERS	14548-05132
PRESSURE	40 PSIA
INITIAL CLADDING TEMPERATURE	1600°F
PEAK POWER	VARIABLE KW/FT
SUBCOOLING	140°F
INJECTION RATE	1.0 IN./SEC

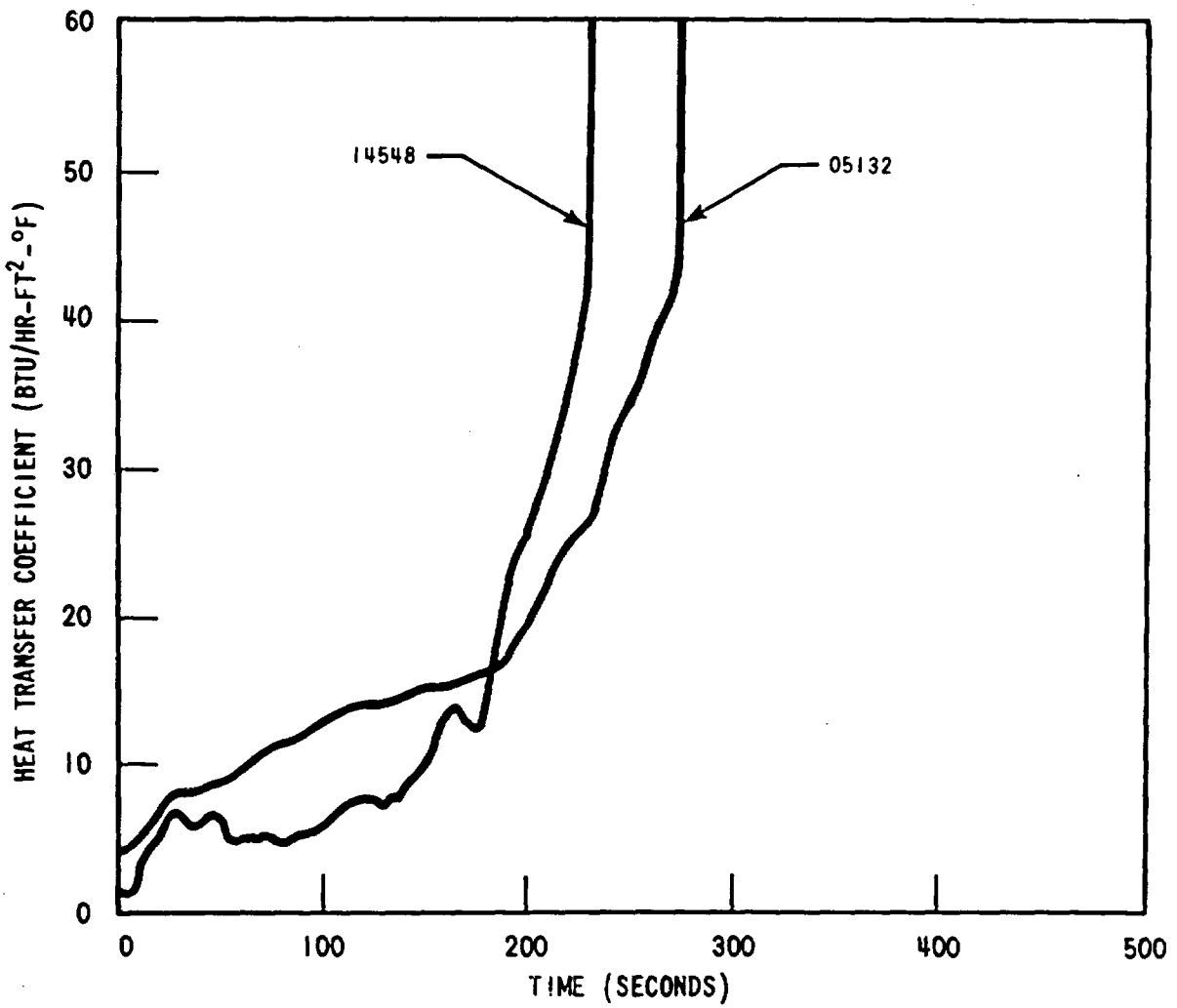

Figure 3-57. Heat Transfer Coefficient Versus Time for High Temperature Comparison Tests 14548-05132

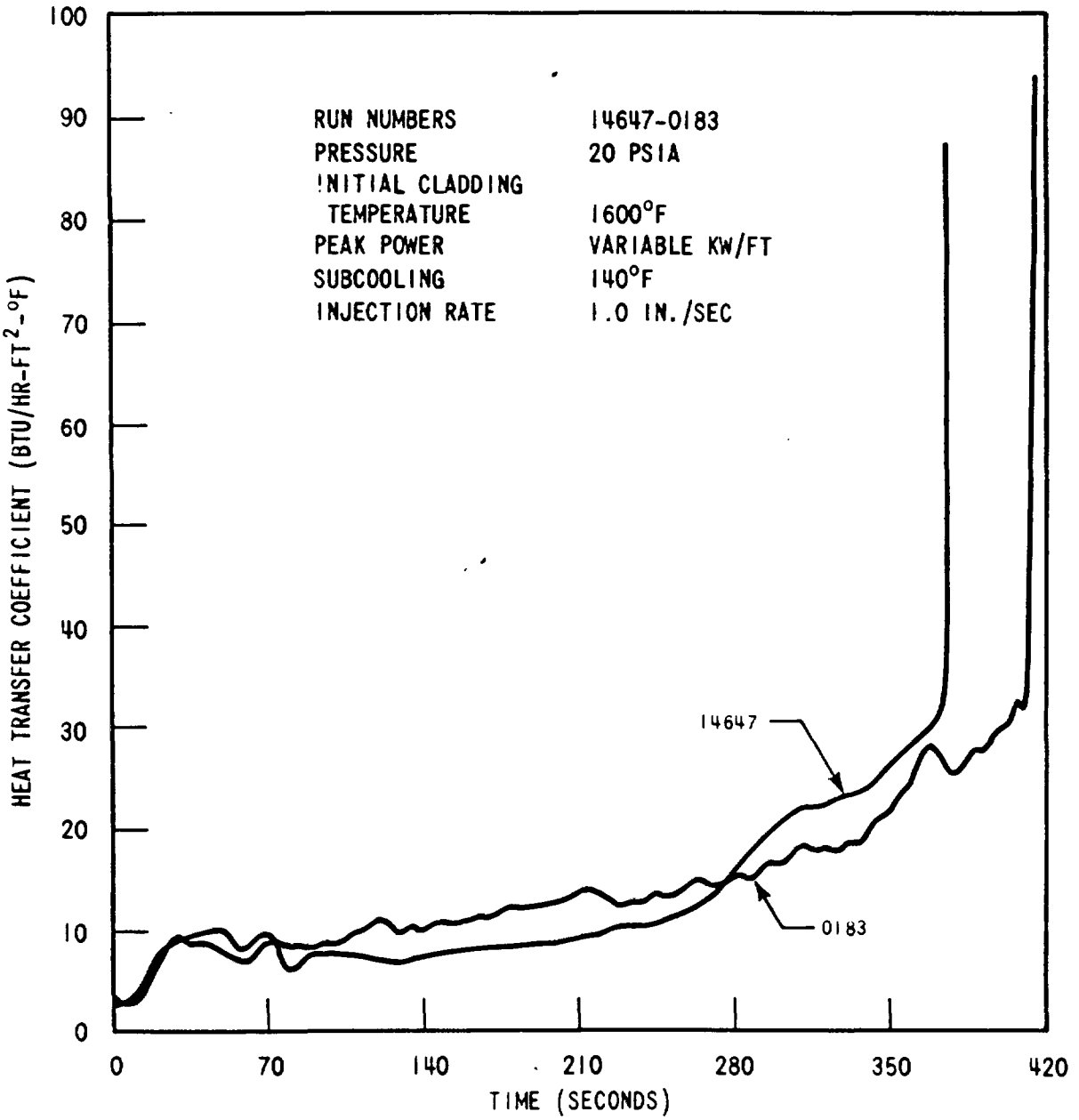

Figure 3-58. Heat Transfer Versus Time for High Temperature Comparison Test 14647-0183

Although neither method was perfect, it was found that preserving the peak initial temperature between the two power shapes would result in maintaining the same amount of non-equilibrium in the two-phase flow. This resulted in better agreement of both the real and FLECHT heat transfer coefficients. This method of using the integral-of-power method for scaling was found to be the better choice.

SECTION 4
BUNDLE FLOW CONDITIONS AND REFLOOD HEAT TRANSFER MECHANISMS

4-1. INTRODUCTION

An effort has been made in the present test series to extend the mass and energy balance methods developed and discussed in WCAP-8838.[1] The calculational procedure discussed in WCAP-8838 has been programmed and allows calculation of the mass velocity and nonequilibrium quality at different bundle cross sections where steam temperature measurements exist. These calculations, along with a radiation heat transfer model, allow the separation of the total wall heat flux into its basic components; radiation to surface, radiation to vapor, radiation to drops which are entrained in the flow, and forced convection of vapor. By examining the wall heat flux split for different test conditions, times, and elevations, various heat transfer models or correlations can be examined to see if they represent the same physical picture calculated from the data.

The method of analysis does have some limitations which should be recognized. Completely one-dimensional flow was assumed and all quantities calculated represent bundle averages. Many calculated values rest rather heavily on the three steam probe measurements at 7, 10, and 11.5 feet. One measurement at each of these two elevations is assumed to give the average vapor temperature for the whole cross section. Although the steam probes are probably good indicators of vapor temperature, they cannot be taken as precise measurements. A few other points are raised in the discussion of results.

4-2. AXIAL DEPENDENCE OF BUNDLE MASS FLOWS AND QUALITIES

A calculation applying a mass and energy balance to calculate bundle mass flow and quality was detailed in section 4 of WCAP-8838. The equations presented in that report have been programmed and the code, FLECMB, has been run for several key skewed and cosine runs. The results of the calculations for the cosine tests checked with the hand calculations for seven key runs presented in WCAP-8838.

The principal application of mass flow and quality information is in the area of model development and verification. This will be discussed in subsequent subsections of this section. Results of the quality and mass flow calculations will be presented for a couple of reference runs for illustration and comparison with the cosine test results.

1. Lilly, G. P., Yeh, H. C., Hochreiter, L. E., Yamaguchi, N., "PWR FLECHT Cosine Low Flooding Rate Test Series Evaluation Report", WCAP-8838, March 1977.

Reference test conditions for the skewed test series were as follows

Pressure	40 psia
Flooding Rate	0.8 - 1.5 in./sec
Initial Cladding Temp.	1600 °F
Peak Power	0.7 kw/ft
Subcooling	140 °F

Figures 4-1 and 4-2 present calculated axial dependence of quality and equilibrium quality for Run No. 15305 which was performed at the above test conditions and 0.8 inch/sec flooding rate.

Actual quality can only be calculated when a vapor temperature is known or assumed. These qualities are presented at the steam probe locations, (7, 10, and 11.5 feet) and test bundle outlet. Quality at the quench front assumes that the vapor temperature is the average of the wall temperature at that location and the saturation temperature. For the cosine series, the vapor temperature measurement at 12.5 feet was judged unreliable and quality is presented at only four locations.

From figure 4-1 the quality for Run No. 15305 is seen to start at a low value at the quench front and progressively increase with increasing elevation. Qualities at upper elevations decrease slowly with time. Equilibrium qualities are higher than the actual qualities early in time reflecting the highly superheated vapor. Before turnaround (150 seconds for this run), equilibrium qualities are very near unity at peak and upper elevations, but the actual quality indicates that a significant fraction (40 - 50%) of the total mass flow past the peak is made up of liquid. Figure 4-3 displays the vapor temperatures measured at the various elevations. Superheats of greater than 1000°F are typical of upper elevations up to and beyond turnaround time.

Figure 4-4 presents the mass effluent fraction Run No. 15305. Due to the very low storage rate the mass flow above the quench front is constant and proportional to the mass effluent fraction.

Figures 4-5 thru 4-8 present the same set of data for Run No. 13303, at 1.5 inches/sec, but otherwise with the same test conditions as Run No. 15305. The higher flooding rate results in lower qualities which decrease more rapidly with time, as could be expected. The vapor temperatures are still highly superheated, but less so than at the lower flooding rate. The mass effluent fraction curve has the same shape with time as the lower flooding rate, but rises more quickly to a value near unity. The principal effect of higher flooding rate on mass flow above the quench front is through the increased injection mass flow. The effluent fraction has a secondary influence.

RUN NUMBER	15305
PRESSURE	40 PSIA
INITIAL CLADDING TEMPERATURE	1603°F
PEAK POWER	0.7 KW/FT
SUBCOOLING	140°F
INJECTION RATE	0.8 IN./SEC

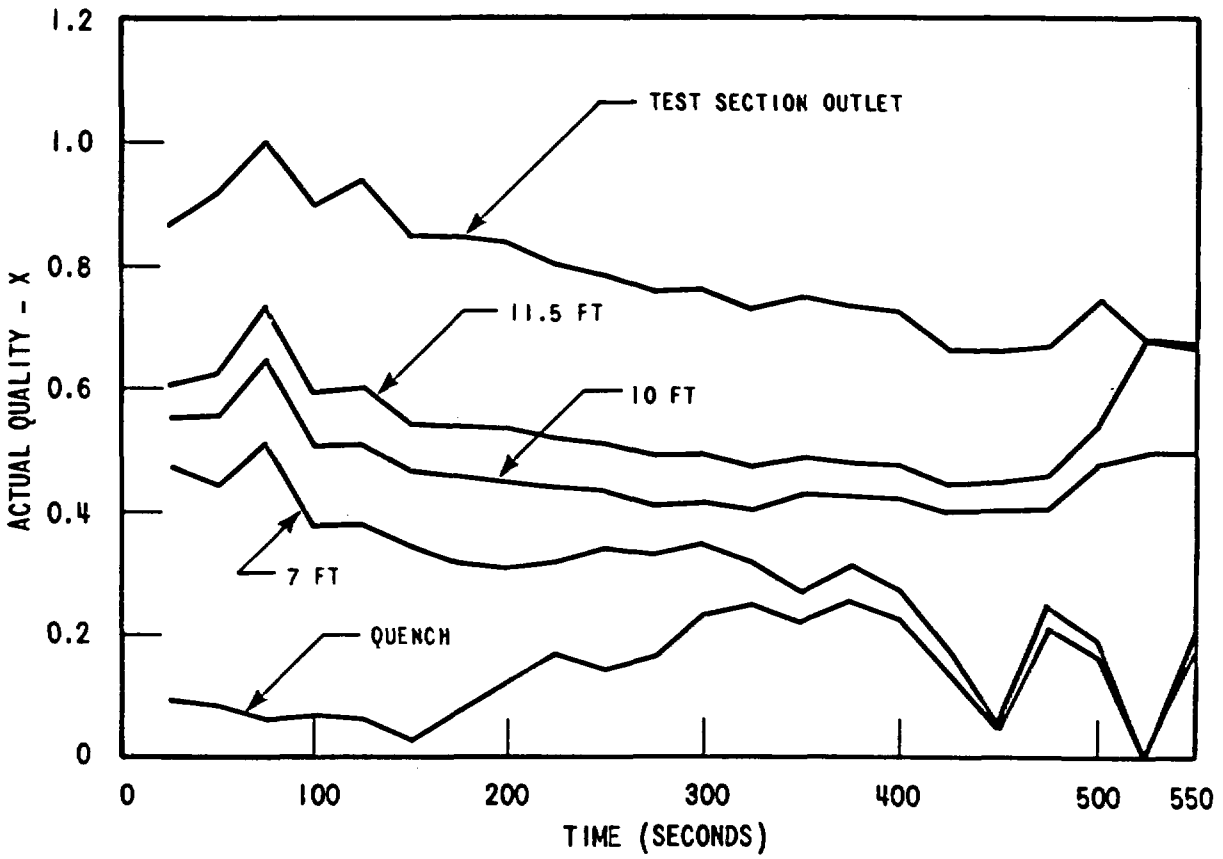

Figure 4-1. Actual Quality Versus Time and Elevation, Run Number 15305

RUN NUMBER	15305
PRESSURE	40 PSIA
INITIAL CLADDING TEMPERATURE	1603°F
PEAK POWER	0.7 KW/FT
SUBCOOLING	140°F
INJECTION RATE	0.8 IN./SEC

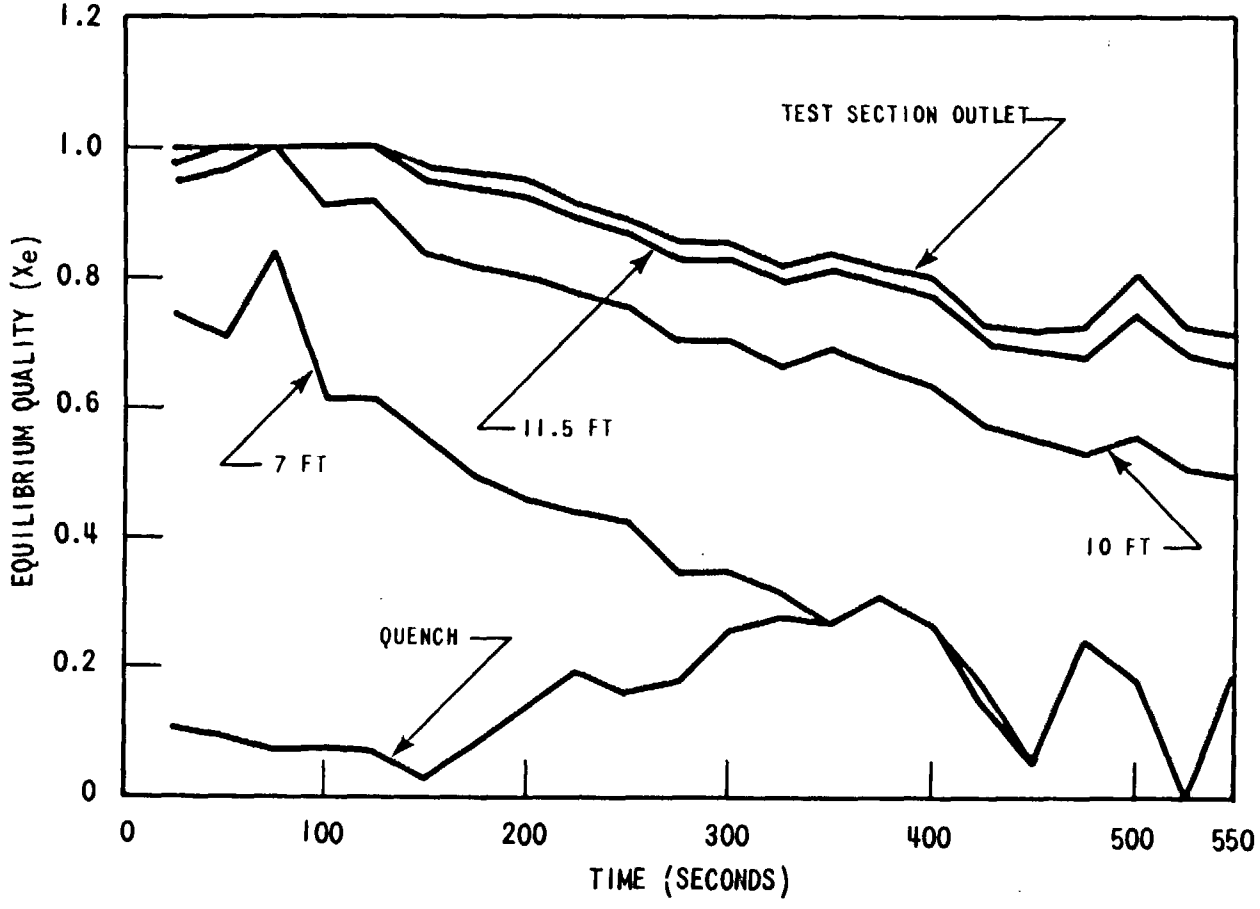

Figure 4-2. Equilibrium Quality Versus Time and Elevation, Run 15305

11,863-235

RUN NUMBER	15305
PRESSURE	40 PSIA
INITIAL CLADDING TEMPERATURE	1603°F
PEAK POWER	0.7 KW/FT
SUBCOOLING	140°F
INJECTION RATE	0.8 IN./SEC

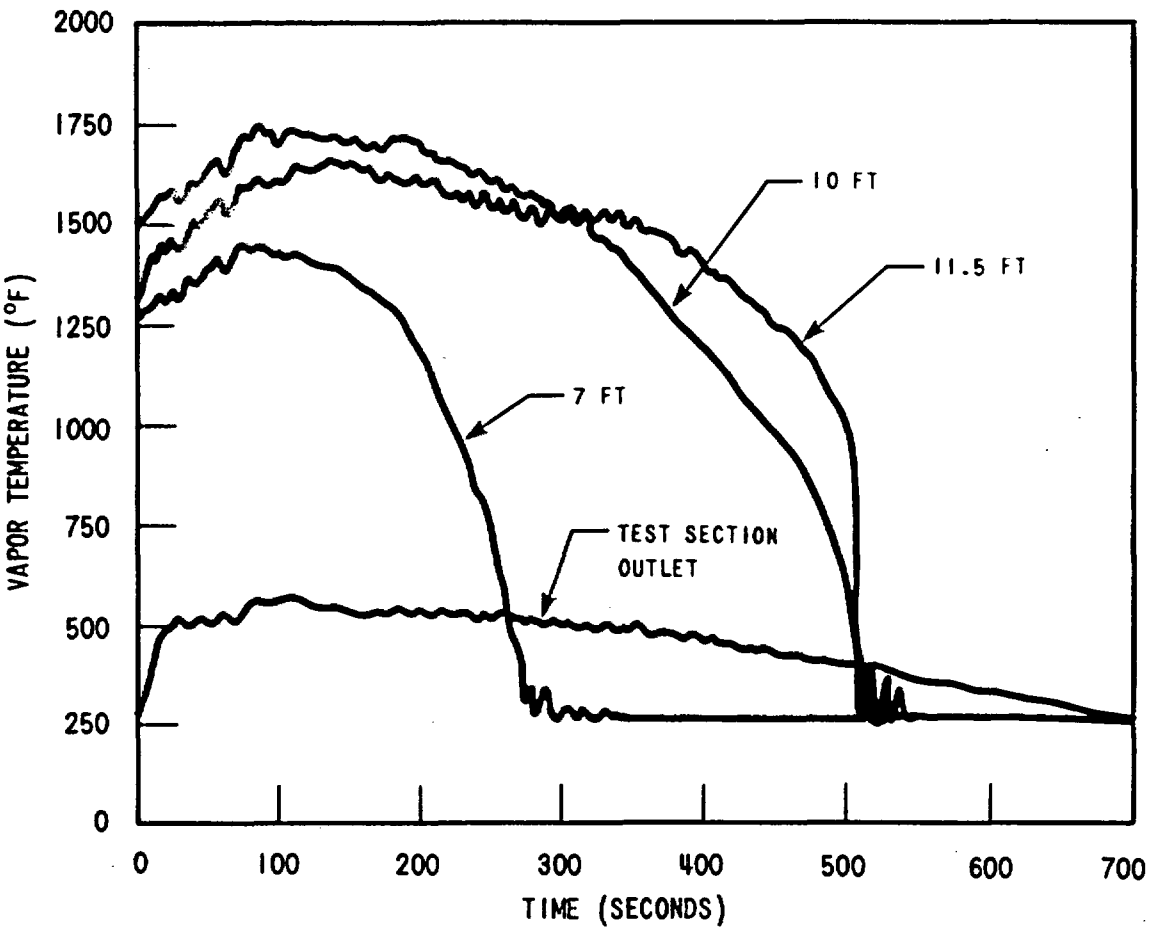

Figure 4-3. Vapor Temperatures Versus Time, Run 15305

RUN NUMBER	15305
PRESSURE	40 PSIA
INITIAL CLADDING TEMPERATURE	1603°F
PEAK POWER	0.7 KW/FT
SUBCOOLING	140°F
INJECTION RATE	0.8 IN./SEC)

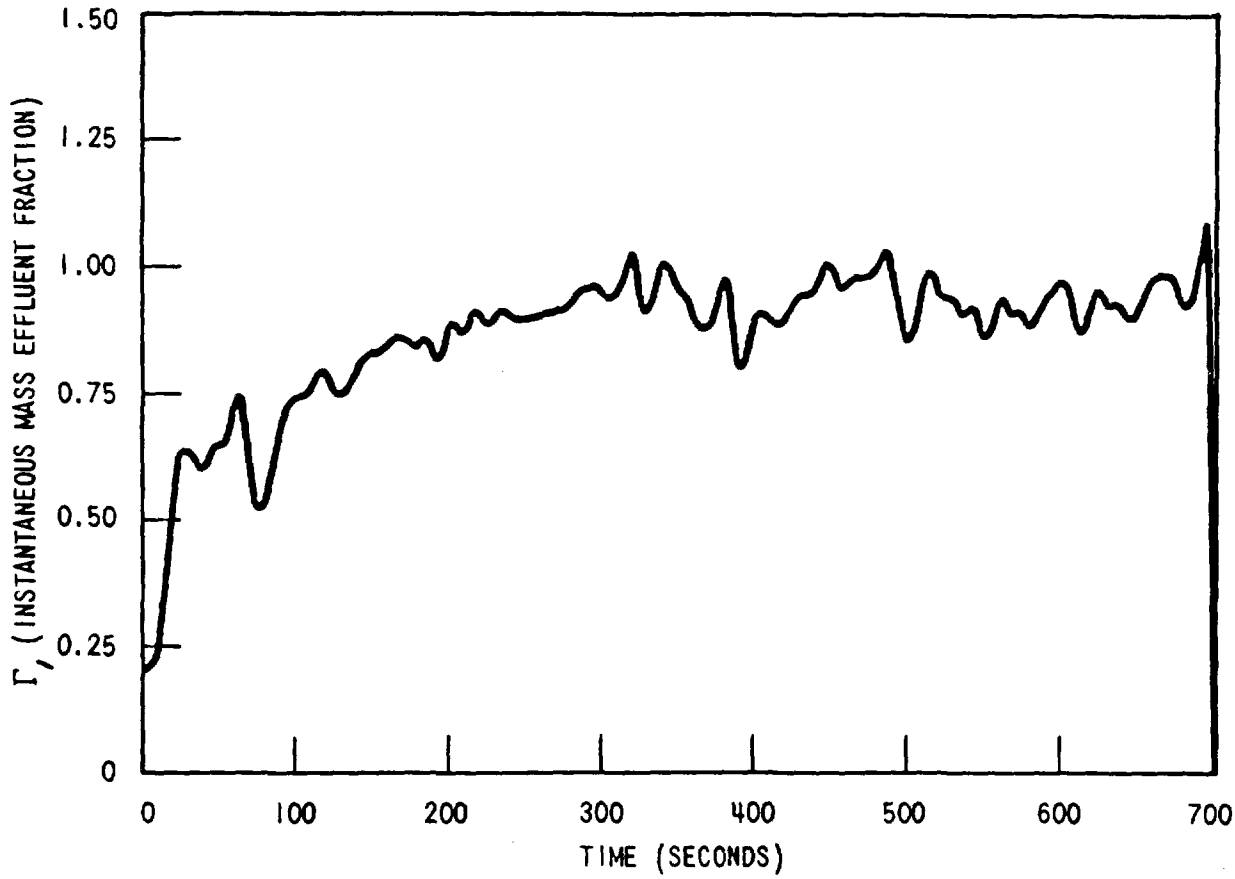

Figure 4-4. Mass Effluent Fraction Versus Time, Run Number 15305

RUN NUMBER	13303
PRESSURE	41 PSIA
INITIAL CLADDING TEMPERATURE	1600°F
PEAK POWER	0.7 KW/FT
SUBCOOLING	140°F
INJECTION RATE	1.5 IN./SEC

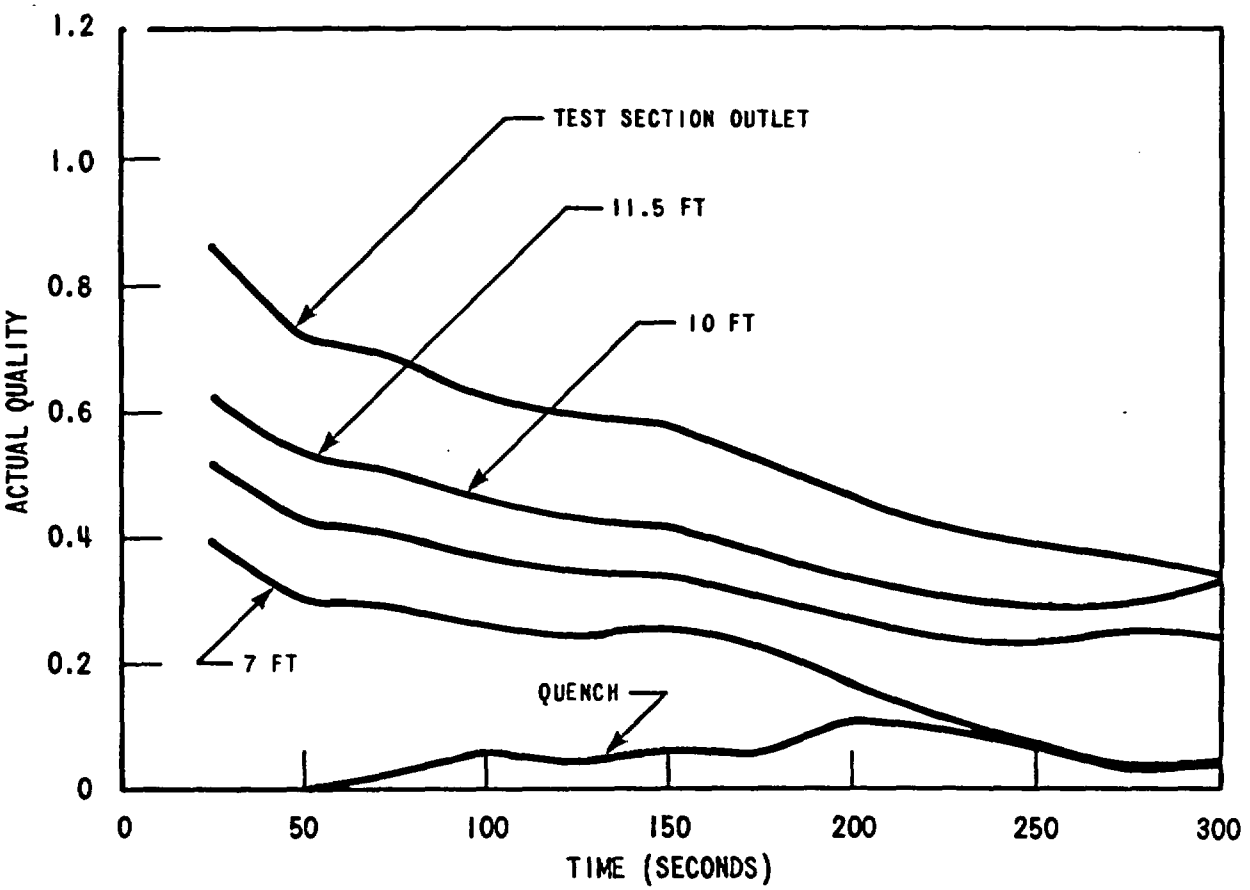

Figure 4-5. Actual Quality Versus Time and Elevation, Run Number 13303

RUN NUMBER	13303
PRESSURE	41 PSIA
INITIAL CLADDING TEMPERATURE	1600°F
PEAK POWER	0.7 KW/FT
SUBCOOLING	140°F
INJECTION RATE	1.5 IN./SEC

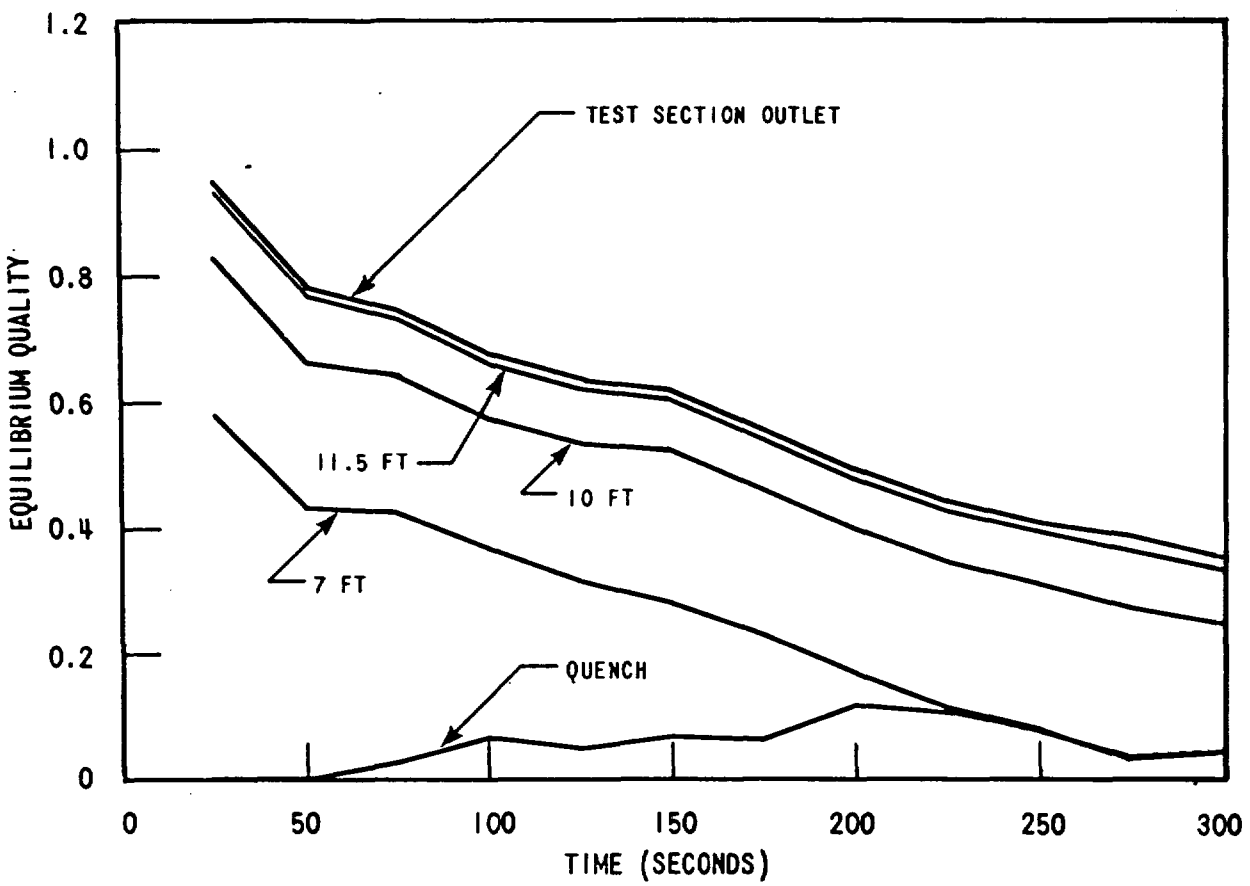

Figure 4-6. Equilibrium Quality Versus Time and Elevation, Run Number 13303

RUN NUMBER	13303
PRESSURE	41 PSIA
INITIAL CLADDING TEMPERATURE	1600°F
PEAK POWER	0.7 KW/FT
SUBCOOLING	140°F
INJECTION RATE	1.5 IN./SEC

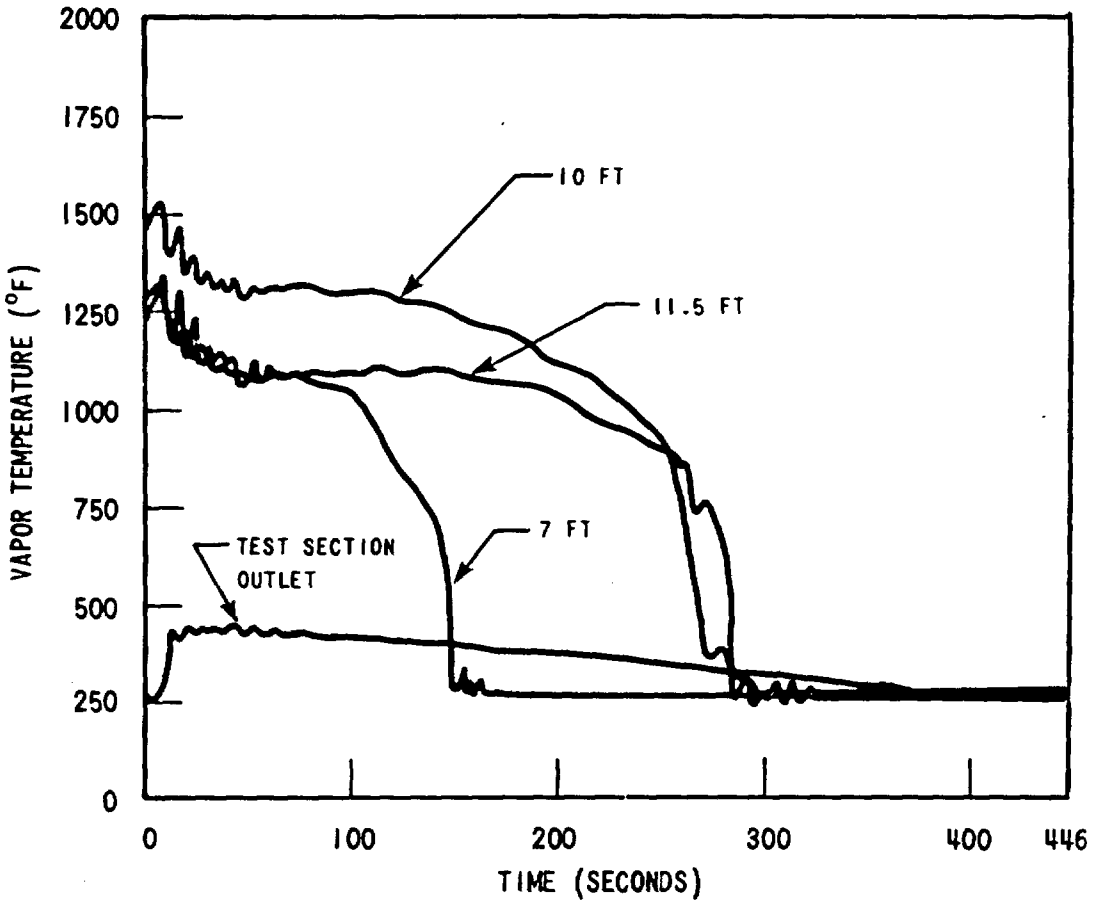

Figure 4-7. Vapor Temperatures Versus Time, Run 13303

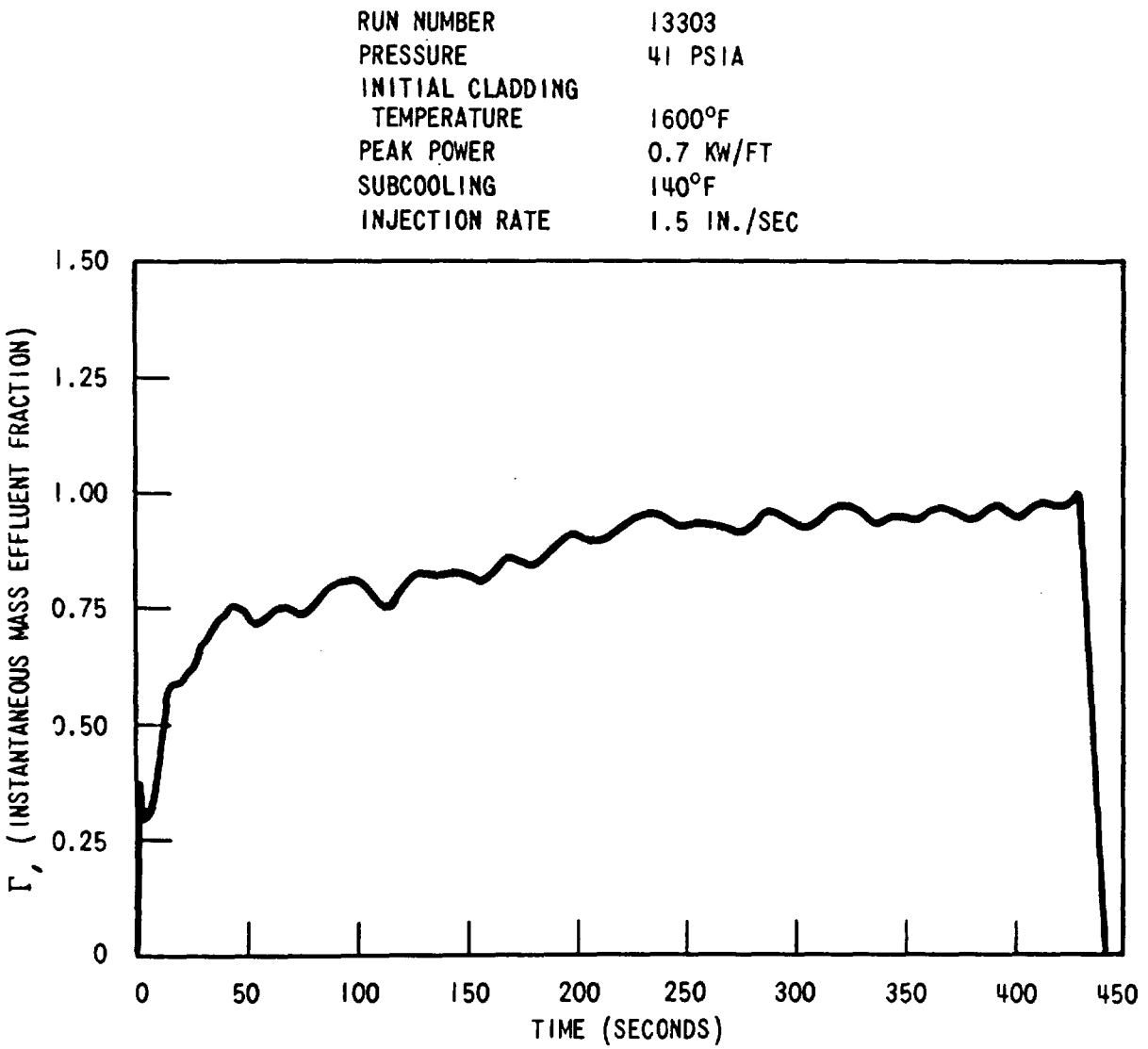

Figure 4-8. Mass Effluent Fraction Versus Time, Run Number 13303

Similar data for the cosine test series was presented in WCAP-8838. Those data were the result of hand calculations. The calculations have been repeated using the FLECMB code and the results are in agreement with the hand calculations. Results of the quality calculations, mass effluent fraction, and vapor temperatures are presented in figures 4-9 through 4-12 for cosine Run No. 02833. This run has the same conditions as Run No. 15305, except that the peak power was 0.9 kw/ft. The average bundle power was approximately equal for the two runs. Characteristics of the quality plots are quite similar for the skewed and cosine power shapes. Vapor temperatures and mass effluent fraction (figures 4-11 and 4-12) for the cosine tests also exhibit the same characteristics as the skewed power shape tests.

4-3. ENERGY ABSORPTION BY DROPLETS ABOVE THE QUENCH FRONT

Current safety analysis requirements state that cooling above the quench front be limited to single-phase steam when the flooding rate is below 1.0 inch/sec. In view of this requirement it is of interest to examine the role of droplets in heat transfer above the quench front. In WCAP-8838 a method for calculating energy flow to droplets was described. Results of this calculation for the cosine tests showed energy absorption by the droplets to be substantial although calculations were performed only for elevations above the peak power point on the rod where steam probes were located. The skewed tests had steam probes above and below the peak power location. Calculations for skewed tests showed energy absorption by drops to be significant both above and below the peak power elevation. Some typical results for skewed tests are presented below and compared with cosine results.

Section 4 of WCAP-8838 demonstrated that net energy flow to the droplets could be calculated between any two elevations where vapor temperature actual quality and mass flow were known. The integral energy flow to droplets between these two elevations can then be compared to the total heat release to the fluid (drops plus vapor) from the bundle and housing. This comparison reveals the relative importance of droplets in the overall heat transfer picture.

Figure 4-13 presents the comparisons of droplet-to-total-energy release for two skewed runs. Test conditions for these runs were given in the previous paragraph. At 0.8 inch/sec, droplet energy absorption accounts for about 40 percent of the total rod and housing heat release below the peak power location (integral 7 to 10 ft) and before turnaround time (150 sec). Above the peak power location (integral 10 to 11.5 ft), droplet absorption account for 70 to 80 percent of the total heat release before turnaround time.

At a flooding rate of 1.5 inches/sec the energy absorption by droplets represents an even larger percentage of the total rod and housing heat release. Above the peak power elevation, the droplet absorption energy exceeds the total rod and housing heat release. The droplets represent the lowest temperature heat sink in the bundle and absorb energy from both the bundle and the superheated vapor. Energy absorption by droplets, which is greater than the

RUN NUMBER	02833
PRESSURE	40 PSIA
INITIAL CLADDING TEMPERATURE	1602°F
PEAK POWER	0.89 KW/FT
SUBCOOLING	142°F
INJECTION RATE	0.8 IN./SEC

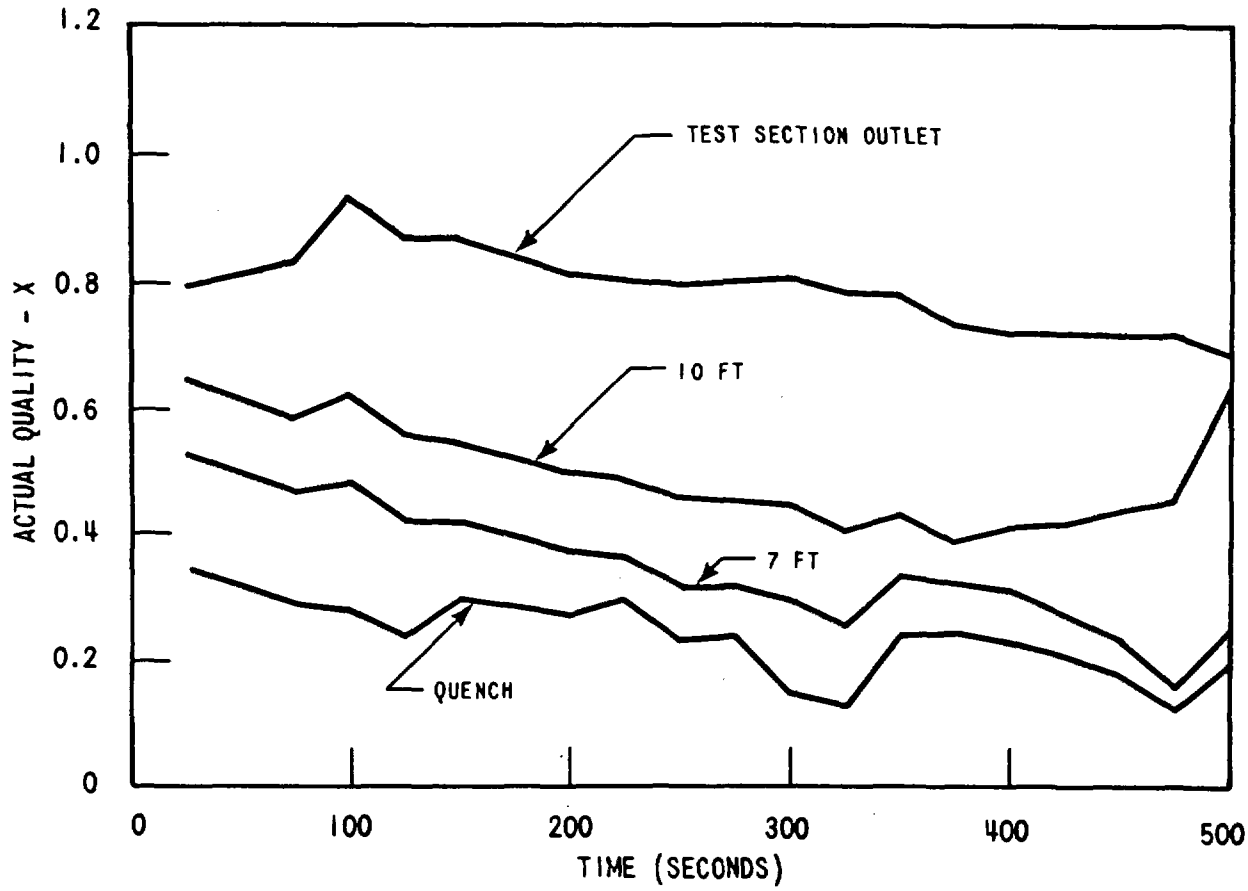

Figure 4-9. Actual Quality Versus Time, Run Number 02833

RUN NUMBER	02833
PRESSURE	40 PSIA
INITIAL CLADDING TEMPERATURE	1602°F
PEAK POWER	0.89 KW/FT
SUBCOOLING	142°F
INJECTION RATE	0.8 IN./SEC

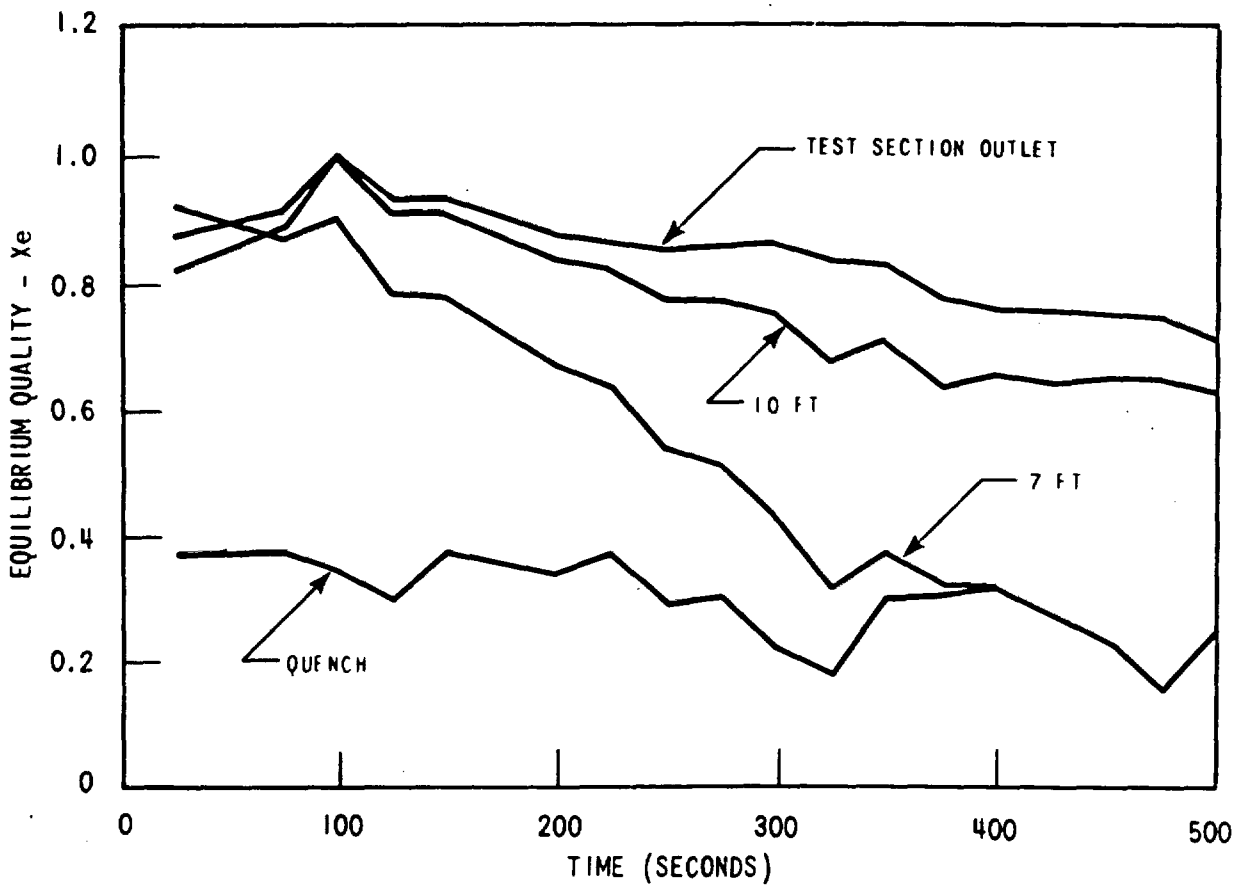

Figure 4-10. Equilibrium Quality Versus Time, Run 02833

RUN NUMBER	02833
PRESSURE	40 PSIA
INITIAL CLADDING TEMPERATURE	1602°F
PEAK POWER	0.89 KW/FT
SUBCOOLING	142°F
INJECTION RATE	0.8 IN./SEC

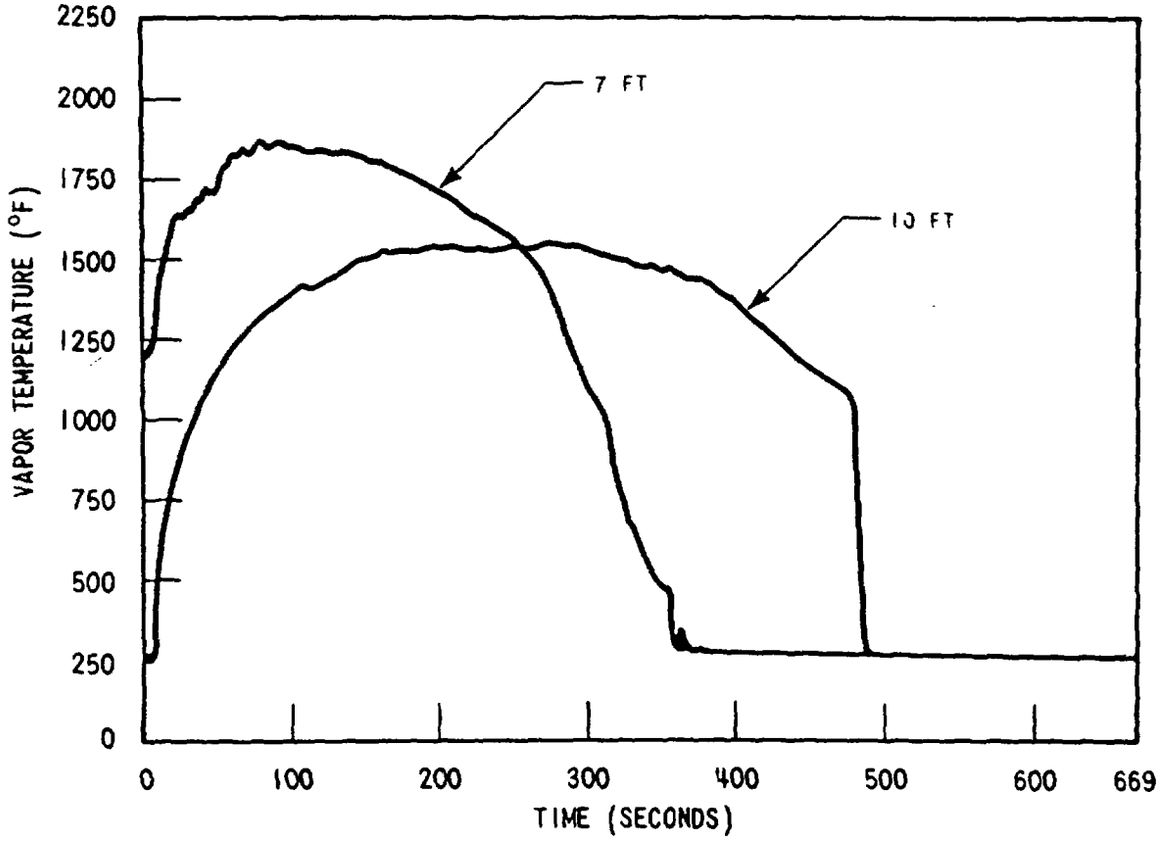

Figure 4-11. Vapor Temperatures Versus Time, Run 02833

RUN NUMBER	02833
PRESSURE	40 PSIA
INITIAL CLADDING TEMPERATURE	1602°F
PEAK POWER	0.89 KW/FT
SUBCOOLING	142°F
INJECTION RATE	0.8 IN./SEC

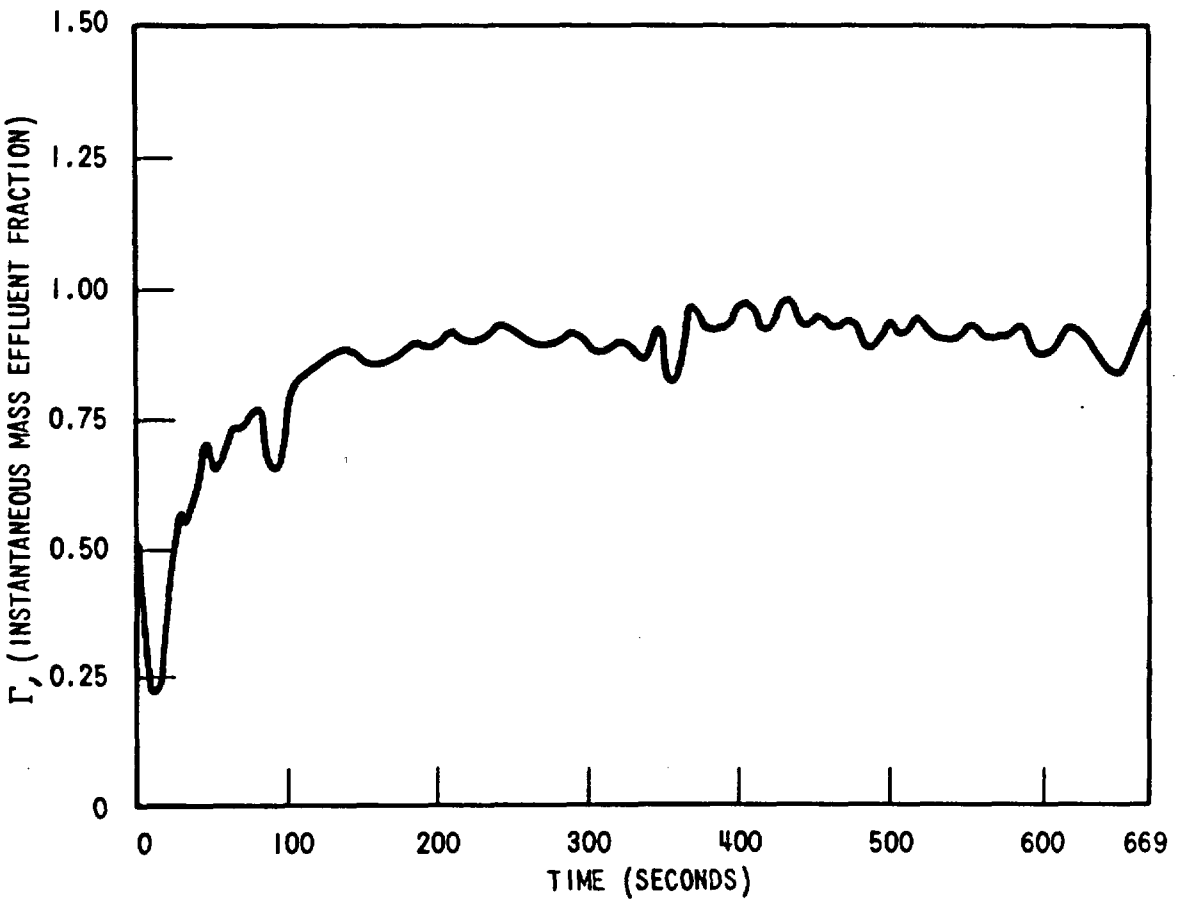

Figure 4-12. Mass Effluent Fraction Versus Time, Run Number 02833

RUN NUMBER	15305
PRESSURE	40 PSIA
INITIAL CLADDING TEMPERATURE	1603°F
PEAK POWER	0.7 KW/FT
SUBCOOLING	140°F
INJECTION RATE	0.8 IN./SEC

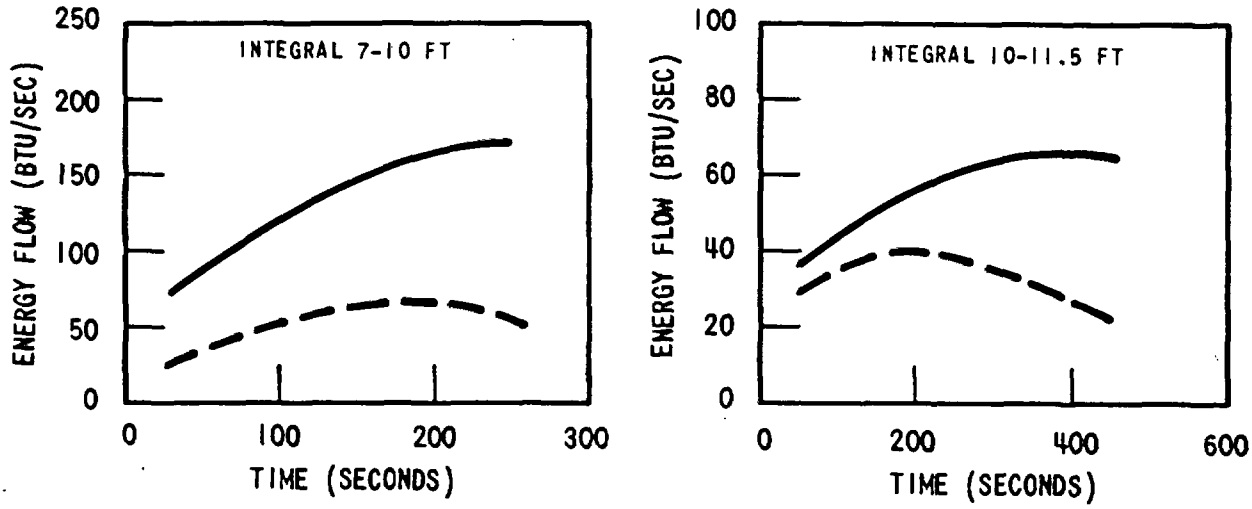

RUN NUMBER	13303
PRESSURE	40 PSIA
INITIAL CLADDING TEMPERATURE	1600°F
PEAK POWER	0.7 KW/FT
SUBCOOLING	140°F
INJECTION RATE	1.5 IN./SEC

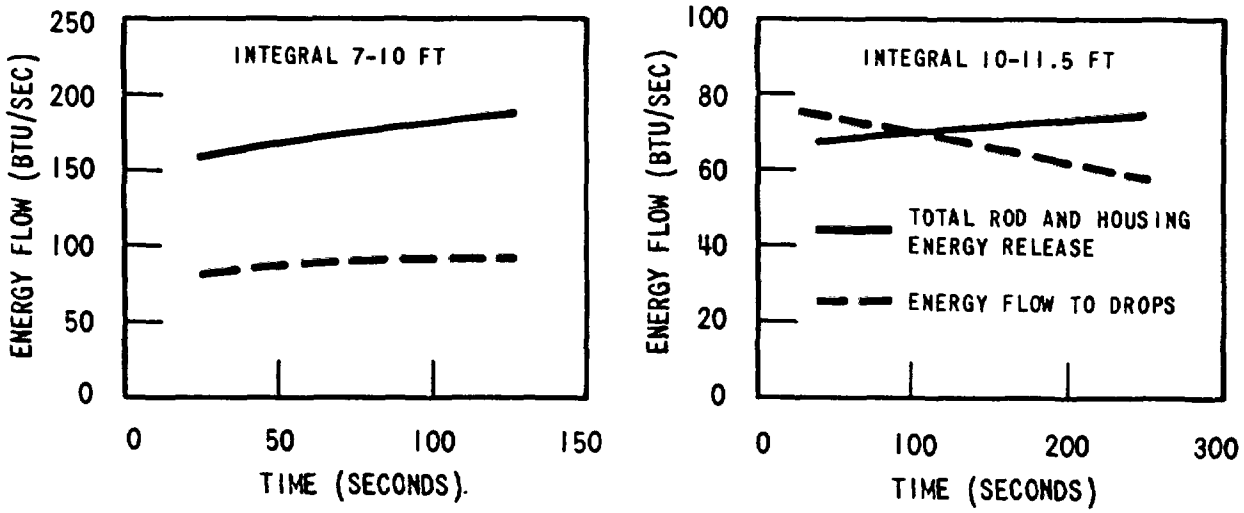

Figure 4-13. Integral Energy Flow to Drops Relative to Total Rod and Housing Heat Release, Run Numbers 15305, 13303

total rod and housing heat release, simply implies that the sum of energy flowing to the drops from both the vapor and bundle surfaces is greater than the total bundle surface heat release to the fluid (drops plus vapor). The following relation always applies

$$Q_T = Q_{NV} + Q_{ND} \tag{4-1}$$

Total Rod and Housing Heat Release	=	Net Energy Absorbed by Vapor	+	Net Energy Absorbed by Droplets

The condition $Q_{ND} > Q_T$ simply says $Q_{NV} < 0$, and the vapor desuperheats.

Figure 4-14 presents droplet absorption and total bundle release data for two cosine tests. These runs, No. 02833 and 04831, had the same test conditions as the skewed Runs No. 15305 and 13303, respectively, except that peak power for the cosine tests was 0.9 kw/ft. Average bundle powers for the corresponding tests were approximately the same. The integral from 7 to 10 feet for the cosine tests was well above the peak power location. This is significant, since in this region bundle heat release drops off and energy flow from superheated vapor to droplets begins to dominate. This is reflected in the low rod and housing heat release in relation to the energy absorbed by the droplets.

To summarize, droplets present at flooding rates below 1.0 inch/sec play a significant role in overall heat transfer and constitutes a significant heat sink for the rod heat flux.

Treatments of reflood heat transfer above the quench front have typically taken two approaches:

- The direct application of modified film boiling correlations
- Development or application of dispersed flow heat transfer models

Film boiling correlations are basically one-step heat transfer from wall to two-phase mixture. Dispersed flow models sometimes have a multi-step approach, separating heat transfer to drops and vapor. In most cases, however, these correlations are traceable to single-phase forced convection correlations.

Film boiling has been used with some success by Andreoni[1] for correlation of reflooding results in a tube. A modified version of the Ellion[2] correlation was used. Film boiling correlations of this type assume a thin film in inverted annular flow where the vapor film

1. Andreoni, D., Courtaud, M., Deruaz, P., "Heat Transfer During the Reflooding of a Tubular Test Section", European Two-Phase Flow Meeting, Harwell 3-7, June, 1974.
2. Ellion, M. E., "A Study of the Mechanism of Boiling Heat Transfer", Jet Propulsion Laboratory, CIT, Memorandum No. 20-88, Pasadena, 1974.

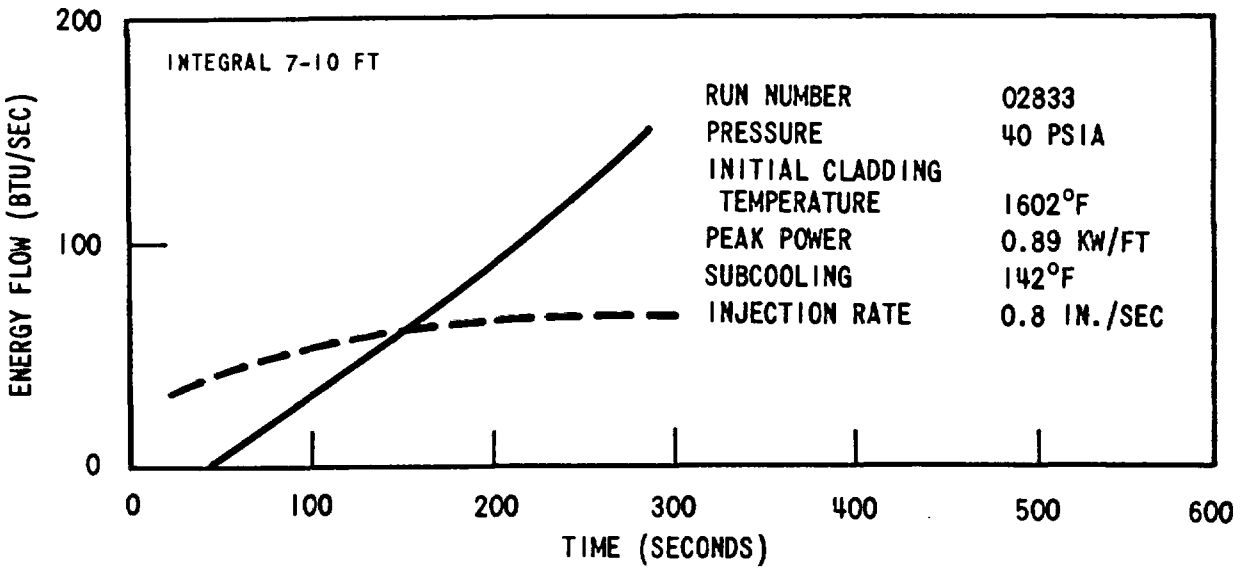

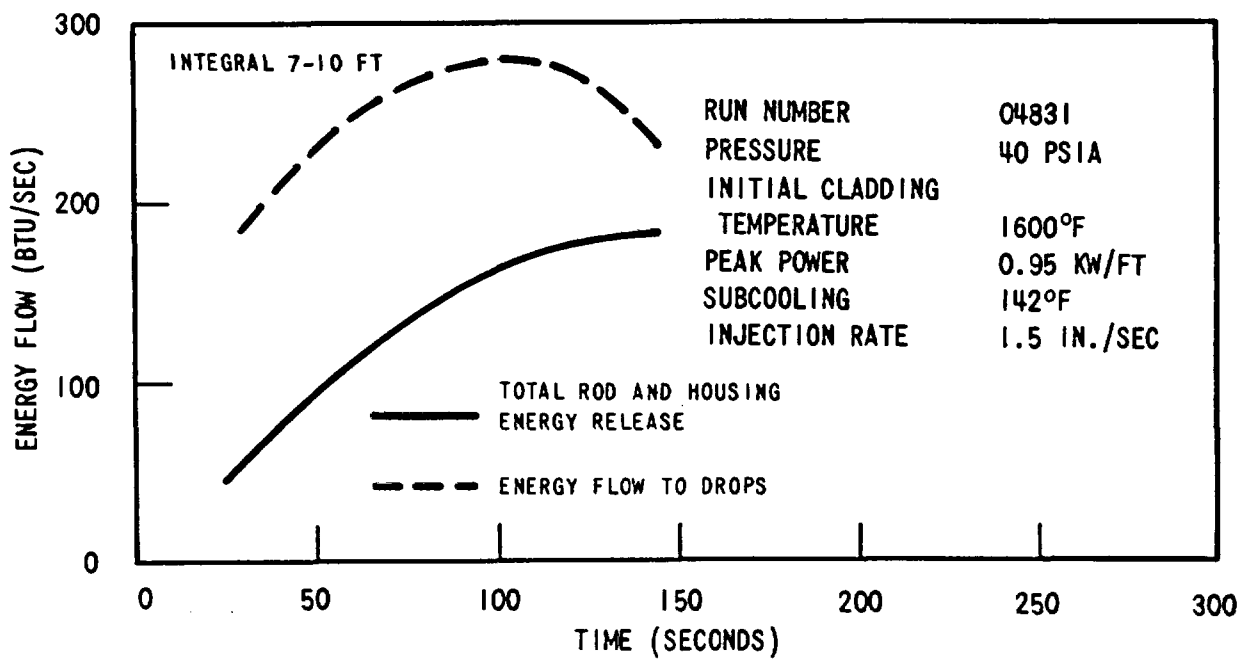

Figure 4-14. Integral Energy Flow to Drops Relative to Total Rod and Housing Heat Release, Run Numbers 02833, 04831

(laminar or turbulent) is driven by the static pressure drop generated by the liquid column. At high flooding rates, this flow regime may occur for a considerable length above the quench front. The main concern of the present study is low flooding rate tests where this flow regime does not appear. Application of this type of film boiling correlation is not consistent with what is known of the physics of the flow above the quench front at low flooding rates.

A variety of dispersed flow correlations and models have been developed to predict available data. Unfortunately, all of the available data and most of the models and correlations are for flow conditions much different than the FLECHT low flooding rate tests. Mass velocity, pressure, or both, are typically an order of magnitude above the FLECHT experiments. The models for dispersed flow range from essentially empirical correlations to models which propose and treat detailed droplet mechanics and vaporization.

At the empirical end of the spectrum Groeneveld[1] has correlated a large body post-dryout data. The correlation is not directed specifically at dispersed flow, but encompasses much data at the very high qualities which would be characteristic of dispersed flow. The correlation includes nonequilibrium effects, but assumes the total wall heat flux can be calculated as convective heat transfer to a superheated vapor. In fact, many of the dispersed flow heat transfer correlations stem from the basic turbulent forced-convection relation

$$Nu = Re^a \, Pr^b. \qquad (4\text{-}2)$$

Slaughterbeck[2] has summarized a number of these correlations and compared them with data.

The difficulty of applying the above correlations lies in the fact that the majority of available FLECHT data have vapor Reynolds numbers well below accepted fully developed turbulent values (Re = 6-10 x 10^3).

Iloeje[3] on the other extreme, examined in detail the behavior of each drop as it impacted and boiled or simply approached the wall and was driven away by pressure forces due to vapor generation. In the resulting model, heat flux is made up of three components: (1) heat flux due to droplets impacting the wall; (2) heat flux due to droplets approaching the wall; and (3) forced convection. At very high wall superheats typical of FLECHT, the first two components become small and the model is reduced to a form similar to those described above.

1. Groeneveld, D. C., "Prediction of Thermal Non-Equilibrium in the Post-Dryout Regime", Nuclear Engineering and Design 30, pp. 17-26, 1976.
2. Slaughterbeck, D. C., Ybarrondo, L. J., Obenchair, E. F., "Flow Film Boiling Heat Transfer Correlations Parametric Study with Data Comparisons", ASME-AIChE Heat Transfer Conference, Atlanta, Ga., August 5-8, 1973.
3. Iloeje, O. C., Rohsenow, W. M., Griffith, P., "Three-Step Model of Dispersed Flow Heat Transfer, "ASME Winter Meeting, Houston, Nov. 30-Dec. 4, 1975.

In the models and correlations reviewed above, the forced convection relations were applied without regard to the effect of droplets on velocity and temperature profiles. It is apparent from figures 4-15 to 4-18 that the vapor Reynolds numbers in the FLECHT low flooding experiments are in the laminar to transition range and preclude application of turbulent convection correlations with any degree of confidence. The effect of droplets on a turbulent flow field may indeed be negligible. Droplet evaporation and generation of turbulence by droplet slip are not negligible in a laminar flow. These effects should work to flatten significantly the velocity and temperature profiles which would otherwise be parabolic in fully developed laminar flow. In the transition range, the application of any forced convection correlation is somewhat equivocal.

A further deficiency of most dispersed flow models is the neglect of radiant heat transfer to drops and colder surfaces in the bundle. Preliminary estimates for the FLECHT conditions indicate these are potentially significant heat transfer mechanisms. One model which appeared to be most representative of the FLECHT experiments was that of Sun, Gonzales, and Tien.[1] This model solved the problem of laminar flow with dispersed droplets evaporating in the flow. Vapor superheat and radiation from walls to vapor and drops was permitted. A closer examination of the applicability of the model to the FLECHT experiments turned up a number of difficulties. Specifically, the model:

- Neglects surface to surface radiation
- Neglects turbulence caused by drops
- Neglects turbulence in the flow (transition regime)
- Uses tube geometry rather than a rod array[2]
- Assumes fully developed flow (neglects d/dz terms)
- Requires input drop size

These difficulties are of sufficient magnitude that the Sun, Gonzales, and Tien method could not be used in toto. A simple model described in the following section is being pursued and makes use of the radiation terms of the Sun, Gonzales, and Tien model but eliminates most of the above problems.

---

1. Sun, K. H., Gonzales, J. M., and Tien, C.L. "Calculations of Combined Radiation and Convection Heat Transfer in Rod Bundles under Emergency Cooling Conditions", ASME-AICHE 15th National Heat Transfer Conference, San Francisco, 1975.
2. Sparrow has shown that for the same hydraulic diameter, a triangular rod array has a fully developed laminar Nu number almost a factor of two higher than a tube. See Sparrow, E. M., Loeffler, A. L., Jr., Hubbard, H. A., "Heat Transfer to Longitudinal Laminar Flow Between Cylinders," ASME Trans., Journal of Heat Transfer, pp. 415-422, Nov. 1961.

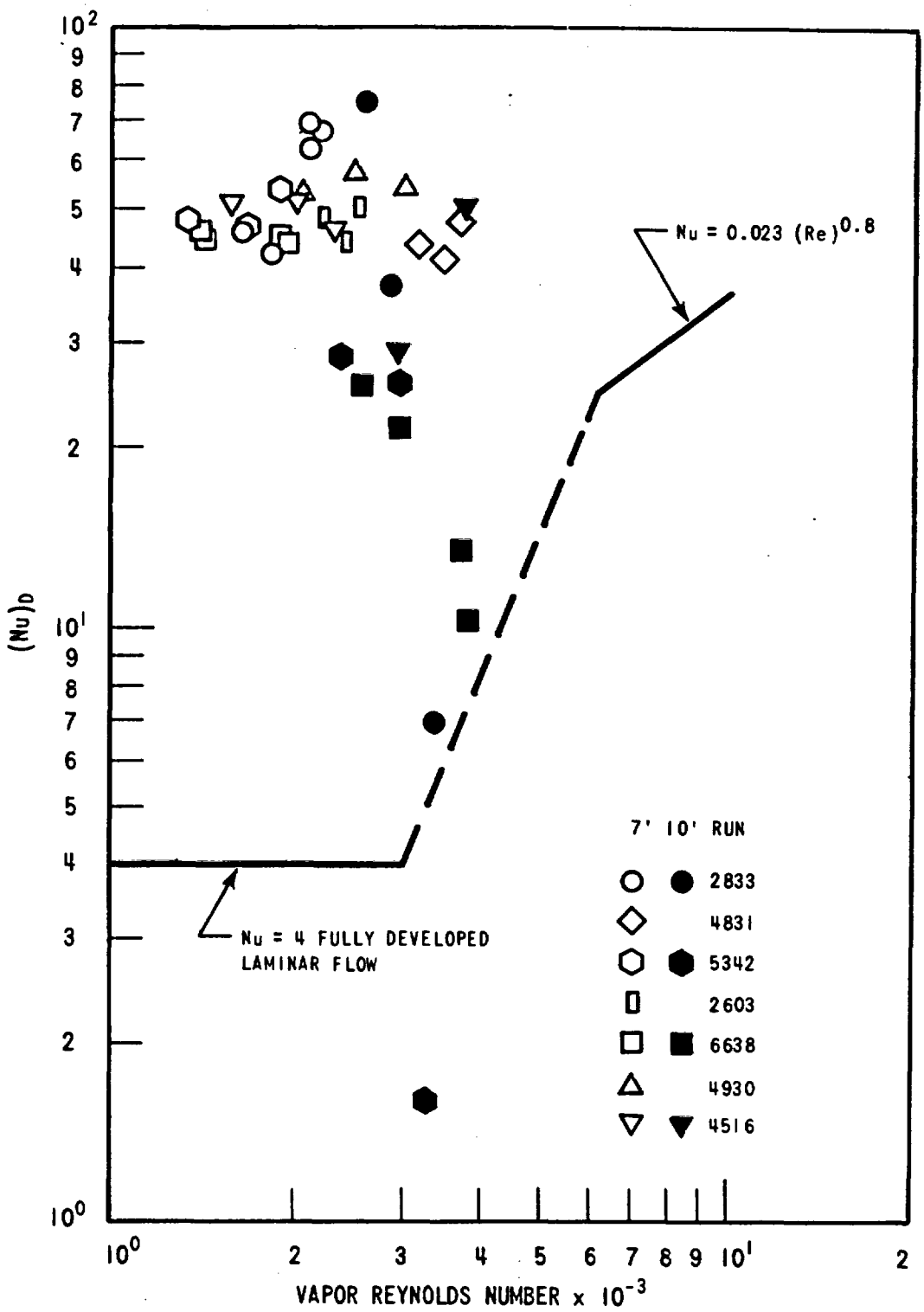

Figure 4-15. Data Based Nusselt Numbers Versus Reynolds Number for Cosine Data, 7 and 10 FT

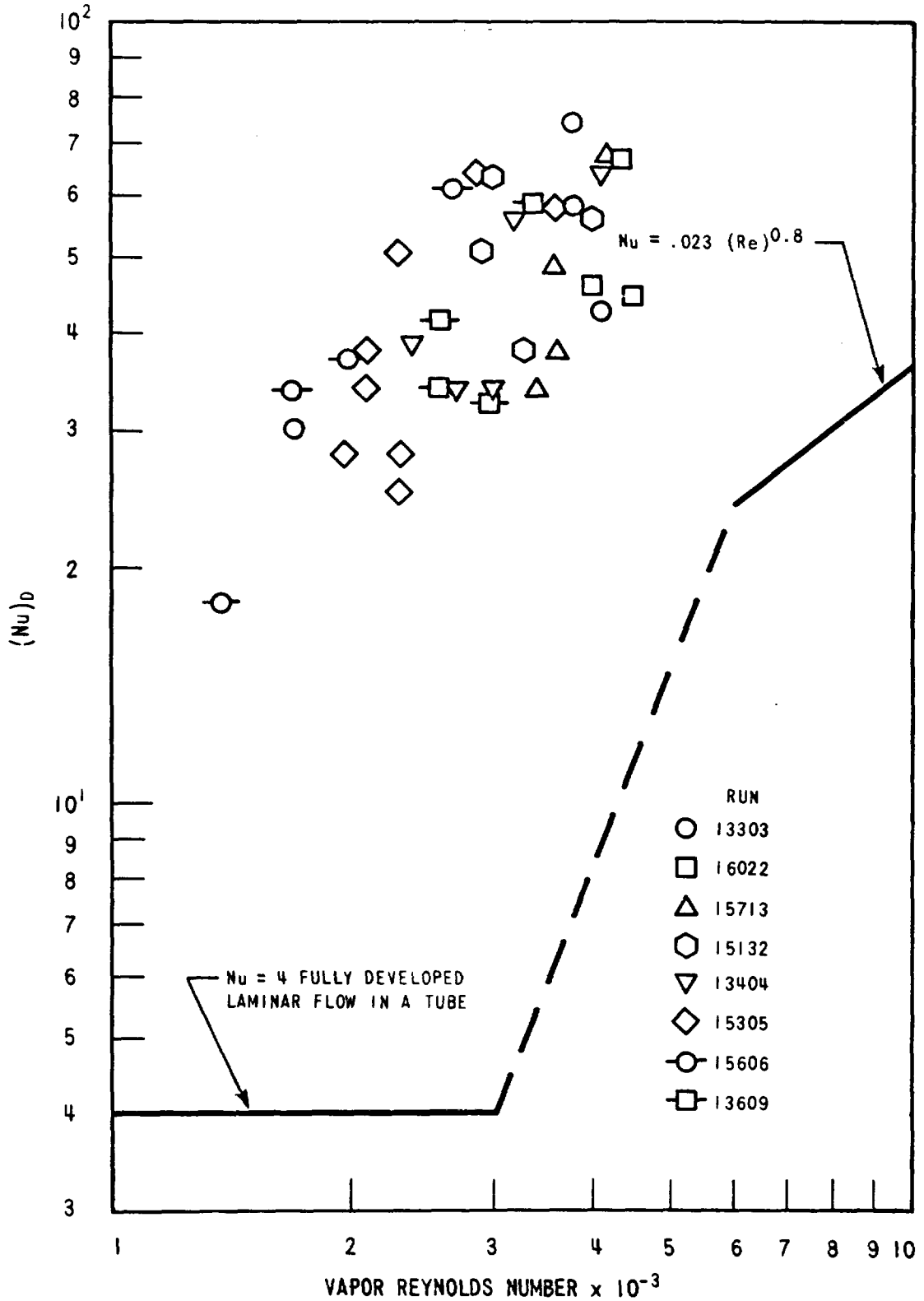

Figure 4-16. Data Based Nusselt Number Versus Reynolds Number for Skewed Data at 7 FT

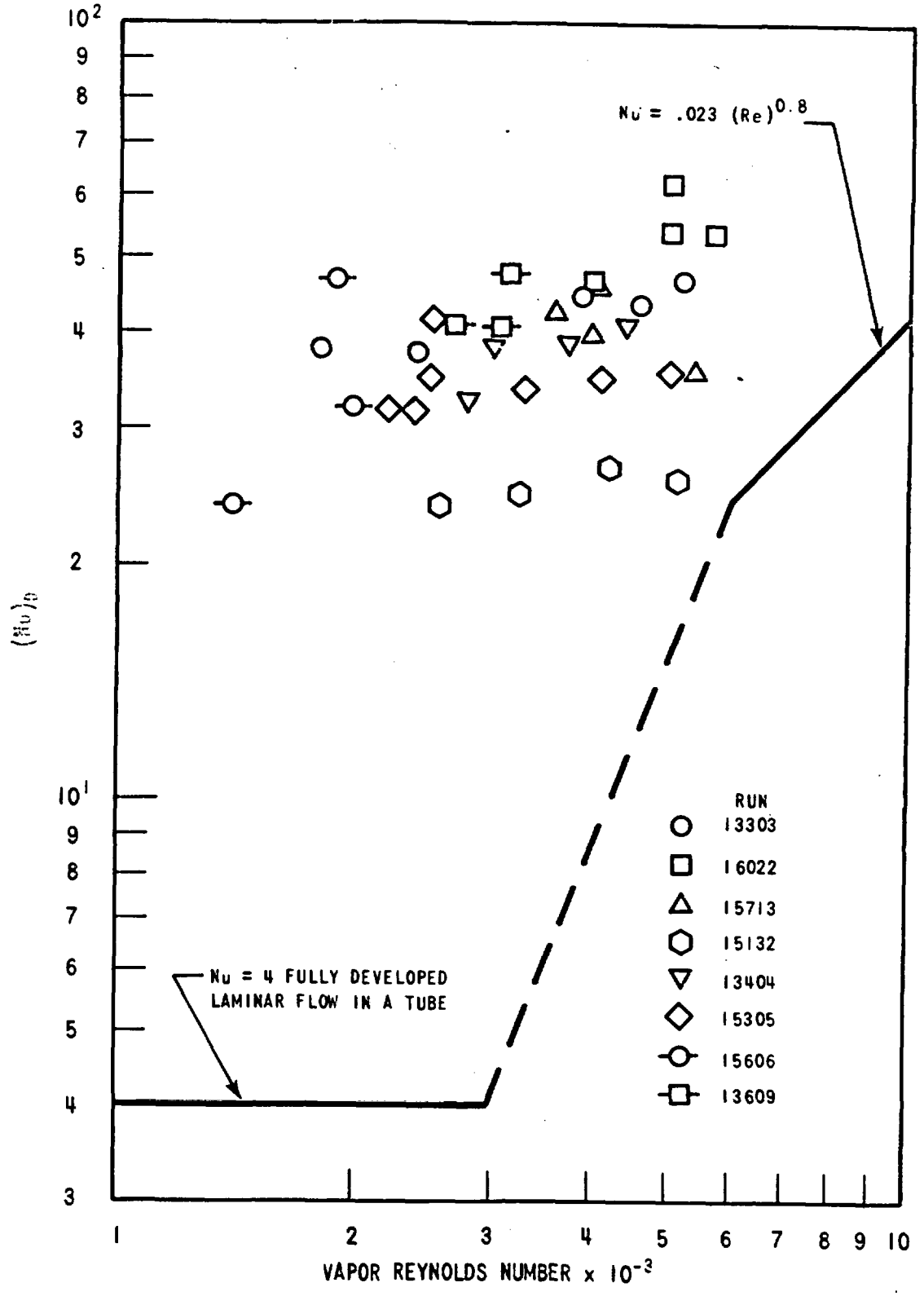

Figure 4-17. Data Based Nusselt Number Versus Reynolds Number for Skewed Data at 10 FT

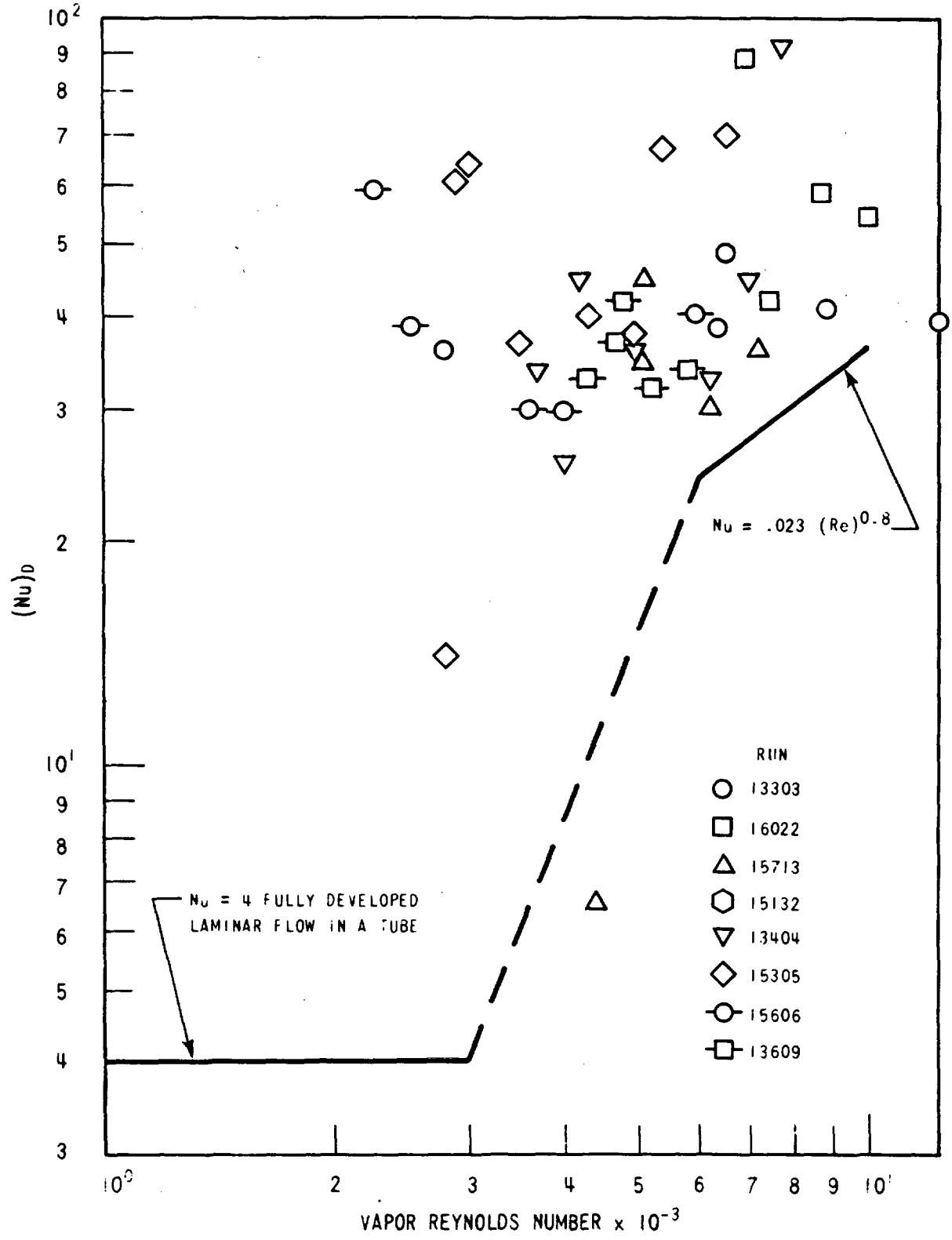

Figure 4-18. Data Based Nusselt Number Versus Reynolds Number for Skewed Data at 11.5 FT

Forslund[1] also used a multi-step approach to heat transfer. The model for heat transfer to drops simply uses an existing correlation for the evaporation of droplets falling by gravity on a highly superheated horizontal plate. Once again, however, as wall superheats become increasingly large, this contribution of droplet heat transfer becomes smaller.

Heat transfer in the models reviewed invariably is reduced to turbulent forced convection for very high wall superheats typical of FLECHT. The fraction of total wall heat flux made up by single phase forced convection was examined for the cosine data in WCAP-8838. Vapor Reynolds numbers are known from mass flow, quality, void fraction, and vapor temperature data. A Nusselt number can be formulated assuming that the measured wall heat flux is dominantly forced convection,

$$(Nu)_D = \frac{D}{k_v} \frac{(q''_t - q''_{rv})}{(T_w - T_v)} \tag{4-3}$$

Where q''_t is the total wall heat flux. The term q''_{rv} represents radiation to vapor which was calculated and subtracted from the total wall heat flux. Radiation to vapor was typically small, of the order of five percent of total wall heat flux.

The results of plotting $(Nu)_D$ versus Reynolds number were presented in WCAP-8838 for the cosine data. Figure 4-12 from that report is repeated (slightly modified) as figure 4-15. The commonly used fully developed laminar and turbulent correlations for forced convection are plotted for reference. It can be seen that the data bear little relation to the correlations. Figures 4-16, 4-17, and 4-18 present the skewed data for 7, 10, and 11.5 feet, respectively, in the same format. The relationship between the skewed data and the correlations is essentially equivalent, though vapor Reynolds numbers extend to higher values, particularly at the 11.5-foot level.

Some selectivity has been exercised in plotting the data on figures 4-15 to 4-18. The steam probes can only be expected to be effective when the thimbles which enclose them cannot be wetted by drops which will subsequently be ingested in the sampling ports. To prevent consideration of these types of data, only data with vapor temperatures >750°F were considered. Further, the elevations with negative axial wall temperature gradients (10 feet for cosine, 11.5 feet for skewed) occasionally had measured vapor temperatures greater than the rod temperature. Nusselt numbers for these were often quite erratic. Inclusion of these points with convective heat transfer from vapor to wall would probably confuse an already difficult problem. Consequently, these data will be ignored for the present.

1. Forslund, R. P., Rohsenow, W. M., "Dispersed Flow Film Boiling", ASME Trans. Journal of Heat Transfer, pp. 399-407, Nov. 1968.

4-4. HEAT TRANSFER ABOVE THE QUENCH FRONT

Alternatives for developing a mechanistic model of heat transfer above the quench front for the FLECHT Low Flooding Rate Series have been examined. Existing models and correlations have been considered for their potential applicability to the FLECHT experiments. A model which will permit calculation of the various heat transfer mechanisms contributing to heat transfer above the quench front is proposed.

The physics of the flow regime above the quench front has been deduced from the low flooding rate test data coupled with mass and energy balance calculations. The data indicates a high void fraction (0.95 to 1.0) of dispersed flow with a large degree of nonequilibrium. Typical vapor superheats range up to 1500 °F. Mass velocities are quite low (0.02×10^6 lbm/hr-ft^2). The low mass velocity and high vapor temperature results in calculated vapor Reynolds numbers in the laminar and transition ranges (1300 to 10,000).

Evaporation of drops represents a significant heat sink, particularly at upper elevations. This, coupled with slip between drops and vapor, can be expected to lead to relatively flat undeveloped) velocity and temperature profiles. In spite of significant droplet evaporation, wall superheats are so high that above the quench front 700 to 2000°F, droplet contract with the wall is not anticipated.

4.5. PROPOSED MODEL FOR IDENTIFICATION OF HEAT TRANSFER MECHANISMS

The model described below is designed to back out the individual heat transfer mechanisms maximizing the use of the FLECHT low flooding rate data. The basic form of the model is assumed to be as follows:

$$q''_t = q''_{cv} + q''_{rv} + q''_{rd} + q_r \qquad (4\text{-}4)$$

Total Wall Heat Flux	=	Convection to Vapor	+	Radiation to Vapor	+	Radiation to Drops	+	Radiation to Other Surfaces

This model is slightly different than the model proposed in WCAP-8838 in that no film boiling term is included. Film boiling is not a basic heat transfer mechanism. Most film boiling correlations are reduced to convection or conduction problems with the liquid simply establishing the temperature gradient. In the case of FLECHT above the quench front data, no droplet contact with the wall is expected. Evaporation of the droplets is assumed to modify the radial vapor temperature profile which becomes a factor in determining q''_{cv}.

Calculation of q_{cv} is the most problematical of the four terms on the right-hand side of equation (4-4). Complicating factors in calculation of convective heat transfer are the laminar-to-transition range Reynolds numbers, and evaporating droplets slipping with respect to the flow, thus generating turbulence. The approach used is to calculate the radiative terms on the right-hand side of equation (4-4) and then use the measured total wall heat flux, q''_t combined with equation (4-4) to calculate q''_{cv}.

Radiation to vapor and droplets is calculated using the method of Sun, Gonzales, and Tien. The calculation of q''_{rd} requires the knowledge of droplet size and volumetric number density. A tentative model has been developed for calculating these quantities from the axial mass velocity, quality and vapor temperature data available from the FLECHT program (FLECMB output).

Radiative heat transfer to other surfaces is estimated from the heat flux at time zero (q''_t, at t = 0). The variation of radiation to other surfaces with time has already been examined using the MOXY code. A correction for the presence of absorbing media (drops and vapor) has been added.

Details of the calculations of droplet size and slip and the radiative terms are presented in the subsequent sections and their associated appendices B and C.

4-6. CALCULATION OF RADIATION TO VAPOR AND DROPLETS

Radiation to vapor and droplet will be calculated using the method of Sun, Gonzales, and Tien. Assuming that the droplets and the vapor are optically thin media, we can then represent the system by an equivalent electrical network as shown in figure 4-19. The medium is said to be in the optically thin regime when the optical thickness is defined as:

$$\tau_o = (a_v + a_\ell + s_\ell)\, D_h \qquad (4\text{-}5)$$

and is much smaller than one.

where: a_v, a_ℓ = absorption coefficient of vapor and droplet, respectively

s_ℓ = scattering coefficient of droplet

This condition may not be fully satisfied in the dispersed flow regime above the quench front. The typical optical thickness above the quench front is of the order from 0.1 to 1, but it is believed that the model could still be used with confidence. A full list of model and calculational assumptions is given in appendix B. Each node in the network represents one

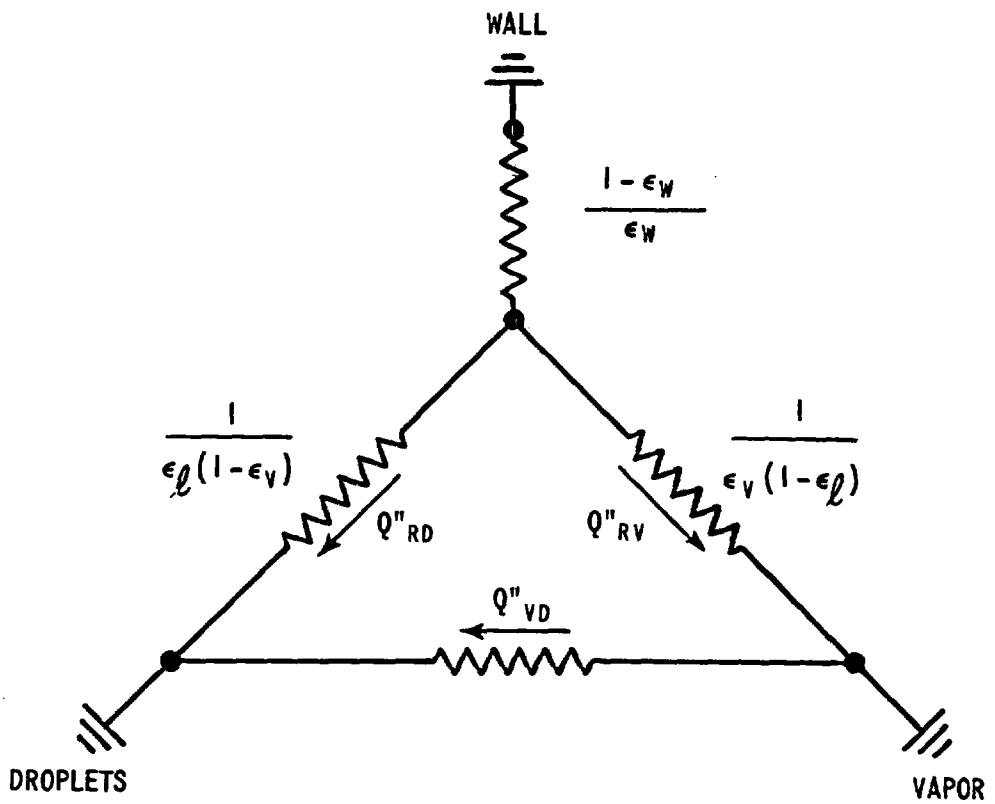

$\epsilon_W, \epsilon_\ell, \epsilon_V$ = EMISSIVITY OF WALL, DROPLET, VAPOR RESPECTIVELY

Figure 4-19. Radiation Network Used by Sun and Gonzales

medium (wall, vapor, and droplets). Calculation of the radiative components q''_{rd} and q''_{rv} can be made at any elevations where the wall, vapor, and droplet temperatures are known. Droplets are assumed to be at saturation temperature. The wall and vapor temperatures are known at steam probe locations.

Emissivity (absorptivity) of the vapor (ϵ_v) is calculated by integrating a vapor absorption coefficient over a mean beam length determined from the rod array geometry. Absorption coefficient is a property of the vapor. Droplet emissivity (absorptivity) is similarly determined, except that the absorption coefficient of the droplet medium is a function of droplet size and number density. For a given droplet size, number density can be determined from quality and slip. Although quality can be calculated from the data, droplet size and slip are unknown. Droplet size observed from the FLECHT movies were not used except as a guide because:

- The film speed was usually not fast enough to be able to capture the faster moving drops.
- The drops observed from the housing windows are believed to be much larger then the average drop size in the bundle. This is due to the larger gap between the housing and the bundle and the lower housing temperature in the cosine tests.
- In the skewed profile tests, the window tended to wet thereby obscuring the view of the droplet flow.

Lack of knowledge of droplet size and slip represents a gap in the FLECHT data which complicates calculations of the heat transfer mechanisms and requires the introduction of many somewhat arbitrary assumptions. The model developed for calculating droplet size and slip is described in the next section. Detailed equations for the application of the method of Sun, Gonzales, and Tien are given in appendix B.

4-7. CALCULATION OF DROPLET SIZE AND SLIP

Quasi-steady state is assumed in the following discussions. Assuming the droplets do not break up as they move up the bundle, one can compute the droplet diameter as a function only of quality and the initial droplet diameter by a simple mass balance. The equation of motion of the droplet is given by a balance of the drag and gravitation forces. Assuming that the initial conditions are known, droplet size and slip at the quench front, and using

the quality and vapor temperature given along the bundle, one can easily compute the droplet velocity and hence vapor velocity and slip at any elevation by integrating the equation of motion. That is,

$$u_\ell(z) = u_\ell(Z_Q) + \int_{Z_Q}^{z} \left(\frac{du_\ell}{dz}\right) dz \qquad (4\text{-}6)$$

where

u_ℓ = droplet velocity

Z_Q = quench front elevation

The quality and the vapor temperature along the bundle are obtained by linear interpolation between the steam probe elevations.

A computer program was written to study the effect of the initial slip or equivalently, initial void fraction on the droplet velocities along the bundle. The result of this study is given in appendix B. For a given initial droplet diameter, the droplet velocity, and hence vapor velocities and slip, at more than six inches from the quench front is essentially independent of the initial estimate of the slip. An overestimate (underestimate) of the slip is compensated for by an overestimate (underestimate) of the drag force. Hence, the initial droplet diameter is the critical assumption in the whole calculation.

A literature search was conducted to find a model or correlation that could predict the droplet diameter at the quench front. The search, however, seems to indicate that no existing literature would give a reasonable prediction of the droplet size. A study on the motion of the droplets at the quench front using typical FLECHT data shows the following peculiar behavior. At low quality, the droplets of a given diameter move with essentially constant speed with magnitude less than one foot/sec until the quality increases to a critical value beyond which the droplets start to accelerate rapidly. Conversely, for a given quality at the front, there exists a maximum droplet diameter above which the drops will move very slowly above the quench front with essentially no acceleration. The result of this study is based on calculations using typical FLECHT data. The equations used for the calculation are given in appendix B. Inspired by these observations, a simple model was developed to estimate the droplet diameter based on the physical arguments:

- The droplets entrained at the quench front must be moving at reasonable speed and acceleration.
- The Weber number of the droplet is smaller than the critical Weber number:

$$We \leq (We)_{cr} = 7.5$$

- The droplets are small enough to be entrained; that is, the equilibrium velocity of the droplet must be greater than zero.

Due to the uncertainty in the production of droplet size, it is important to study the resulting heat transfer components to see how they are affected by the choice of droplet diameters. It was found that the radiation to droplet component of the total wall heat flux was approximately 8 to 15 percent of the total wall heat flux, while the total radiation components were 25 to 35 percent of the total wall heat flux. Therefore, it is felt that the resulting convective portion of the total wall heat flux is not overly sensitive to the droplet size used. The detailed mathematical development of the model and the derivation of the equations used to determine the slip and droplet number density are given in appendix B.

4-8. CALCULATION OF SURFACE-TO-SURFACE RADIATION

Analysis of heat transfer mechanisms is being done for a group of central hot rods. The presence of colder rods and thimbles provides the source for surface-to-surface radiation. Estimates of surface-to-surface radiation have indicated that it is not a negligible quantity in the FLECHT experiments. Studies using the MOXY[1] code showed that radiation made up essentially 100 percent of the total heat flux at flood time, as expected. At turnaround time, radiation still constituted 20 to 35 percent of the hot rod heat flux. These estimates are high, since the MOXY code does not provide for an absorbing medium between the rods. A model is needed, however, to predict surface-to-surface radiation.

The model chosen for surface-to-surface radiation is quite simple.

$$q_r'' = q_t''\Big|_{t=o} A_r \qquad (4\text{-}7)$$

where

$q_t\Big|_{t=o}$ = Hot rod heat flux at flood (Btu/hr-ft^2)

A_r = Attenuation factor due to absorption by droplet/vapor medium

Surface-to-surface heat flux is assumed constant during the run except for the attenuation of the medium which varies with fluid conditions.

The MOXY analysis (no medium) indicated that surface-to-surface radiation heat flux increased as the bundle heated up after flood and then decreased as the bundle cooled. A model which

1. Evans, D. R., "MOXY, A Digital Computer Code for Core Heat Transfer Analysis", IN-1392, August 1970.

reproduced this expected trend was also developed. This model gave excessively high surface-to-surface radiation under some circumstances and is not used in the present heat transfer mechanism analysis.

The MOXY analysis results and the details of development of the two surface-to-surface radiation models are given in appendix C.

4-9. CALCULATED WALL HEAT FLUX RESULTS

The method of calculating each radiation wall heat flux component was programmed into a calculational technique called HEAT-II. The HEAT-II program read the output from the mass and energy balance calculation on the bundle and calculated each wall heat flux component. As indicated earlier, the radiation wall heat flux components were individually calculated, but the connective wall heat flux was obtained as a difference between the total measured value and the sum of the radiation components.

Examples of the calculated wall heat flux components are shown in figures 4-20 to 4-23 for Run No. 15305. The wall heat flux components normalized on the total wall heat flux are also shown in figures 4-24 and 4-25. It can be seen from the normalized fluxes, that the sum of the radiation terms is approximately 30 to 50 percent of the total, leaving the convective wall heat flux, which is calculated by the difference of the total, leaving the terms, to be approximately 50 to 70 percent of the total wall heat flux. These values are relatively constant over the transient. Since the convective wall heat flux is obtained by a difference method, it would have the largest error of any component. Therefore, care must be used in interpreting the results and probably differences of less than 10 percent of the convective heat flux values are with the uncertainty range of the calculation.

However, using the calculated convective wall heat flux value, a convective Nusselt number can be formed and should more accurately represent the convection process occurring in the bundle rather than the data Nusselt number given in paragraph 4-4. The convective Nusselt number can be calculated from q''_{cv} as

$$Nu_c = \frac{D}{k_v} \frac{(q''_T - q''_{rd} - q''_{rv} - q''_r)}{T_w - T_v} = \frac{D}{k_v} \frac{q''_{cr}}{(T_w - T_v)} \qquad (4\text{-}8)$$

Values of Nu_c were obtained for both the skewed and cosine profile tests at each location where steam probed information existed. Again, steam probe data with temperatures less than 750°F were not used. Examination of the values of Nu_c and the vapor Reynolds number were relatively constant from before turnaround to just before quench when the vapor temperature decreased sharply.

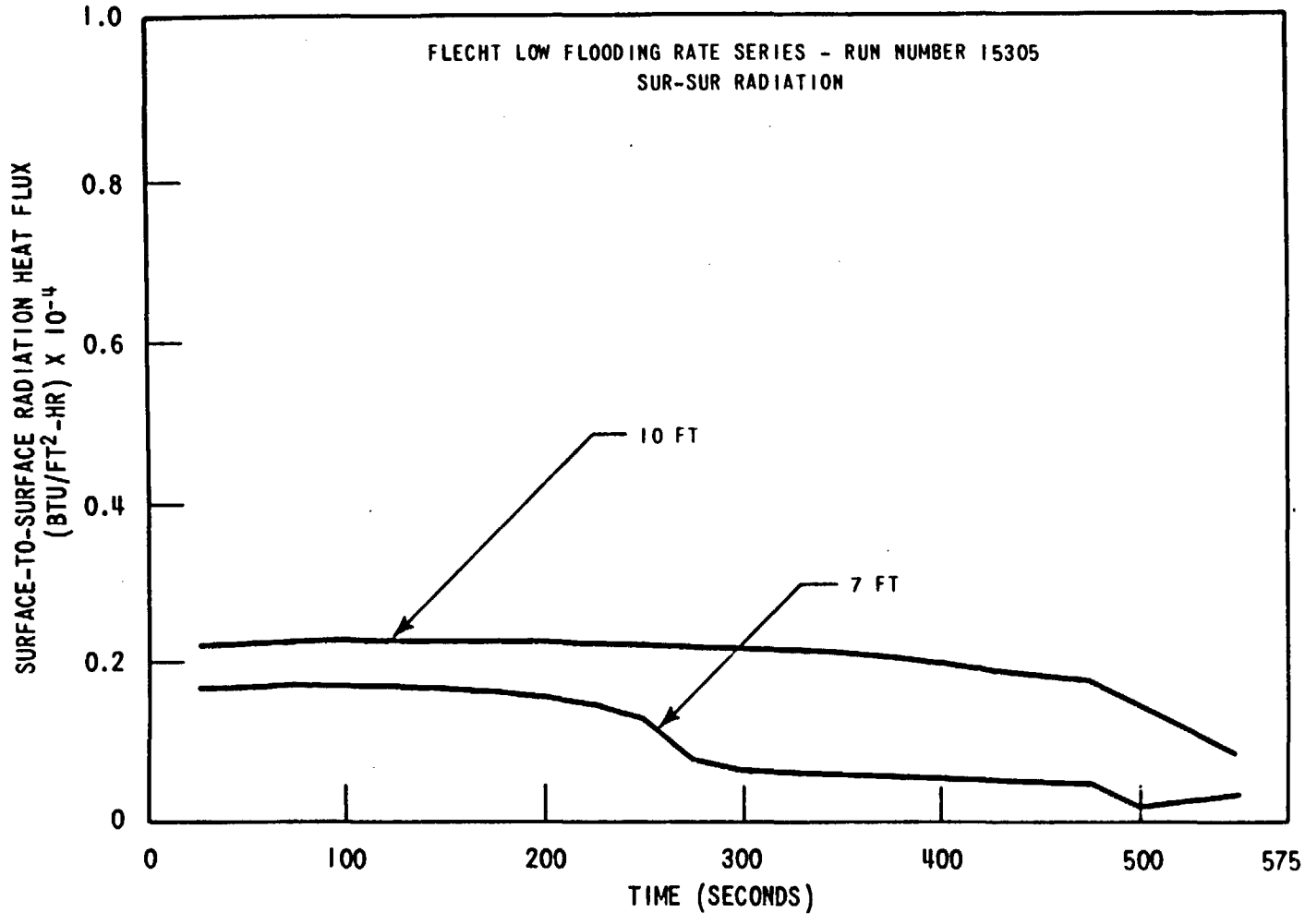

Figure 4-20. Calculated Surface-to-Surface Radiation Heat Flux Versus Time for Run No. 15305

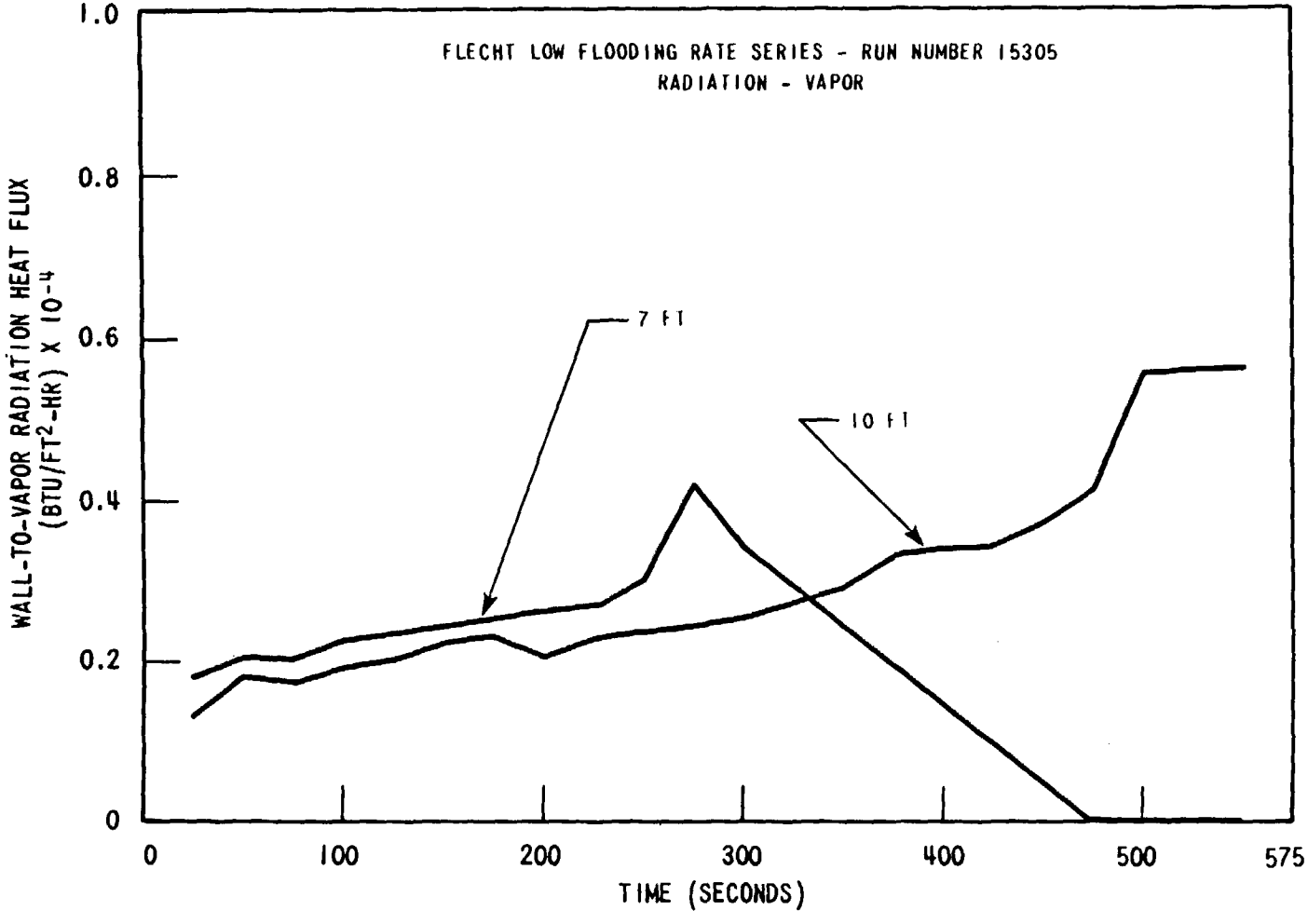

Figure 4-21. Calculated Wall-to-Vapor Radiation Heat Flux Versus Time for Run No. 15305

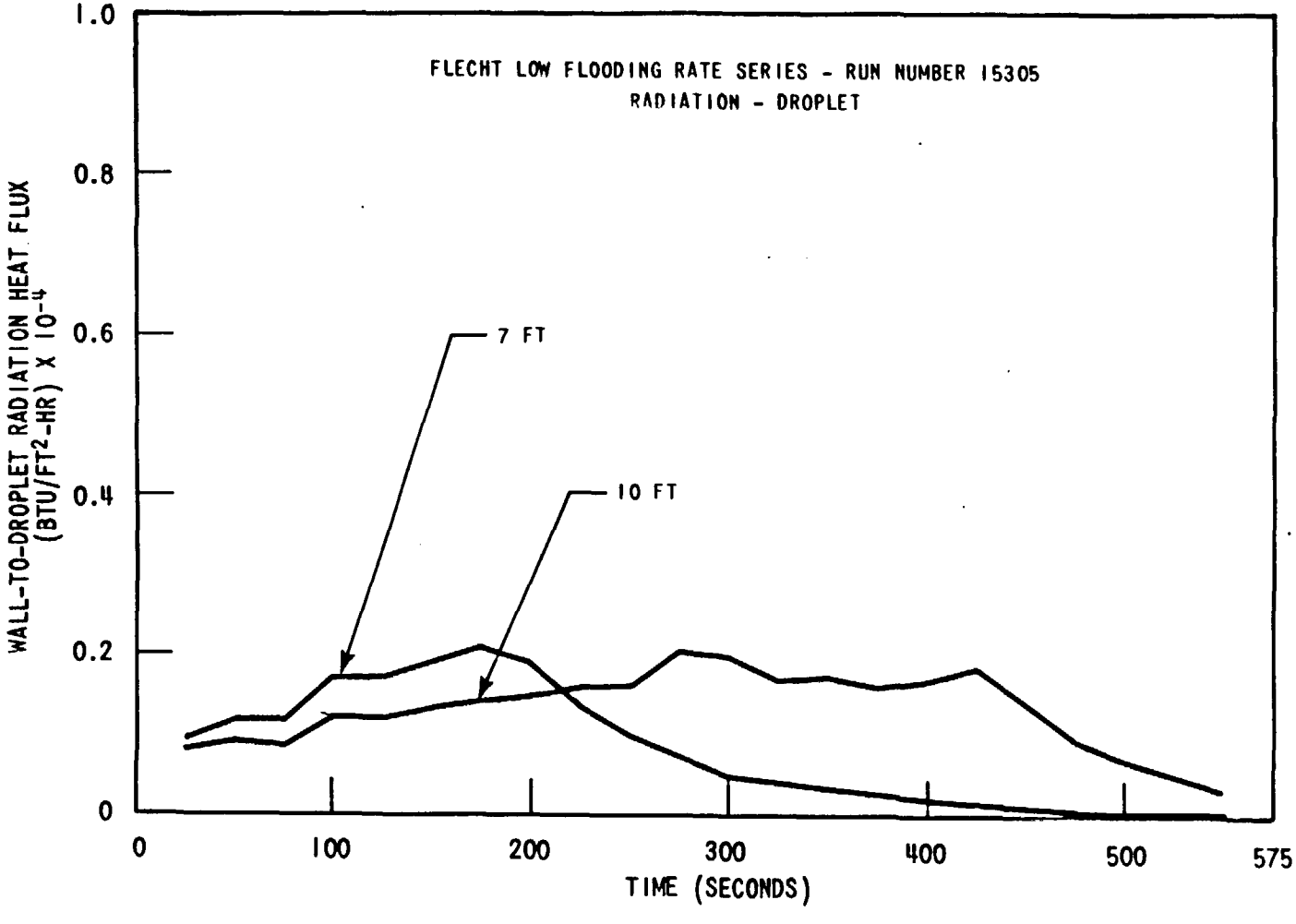

Figure 4-22. Calculated Wall-to-Droplet Radiation Heat Flux Versus Time for Run No. 15305

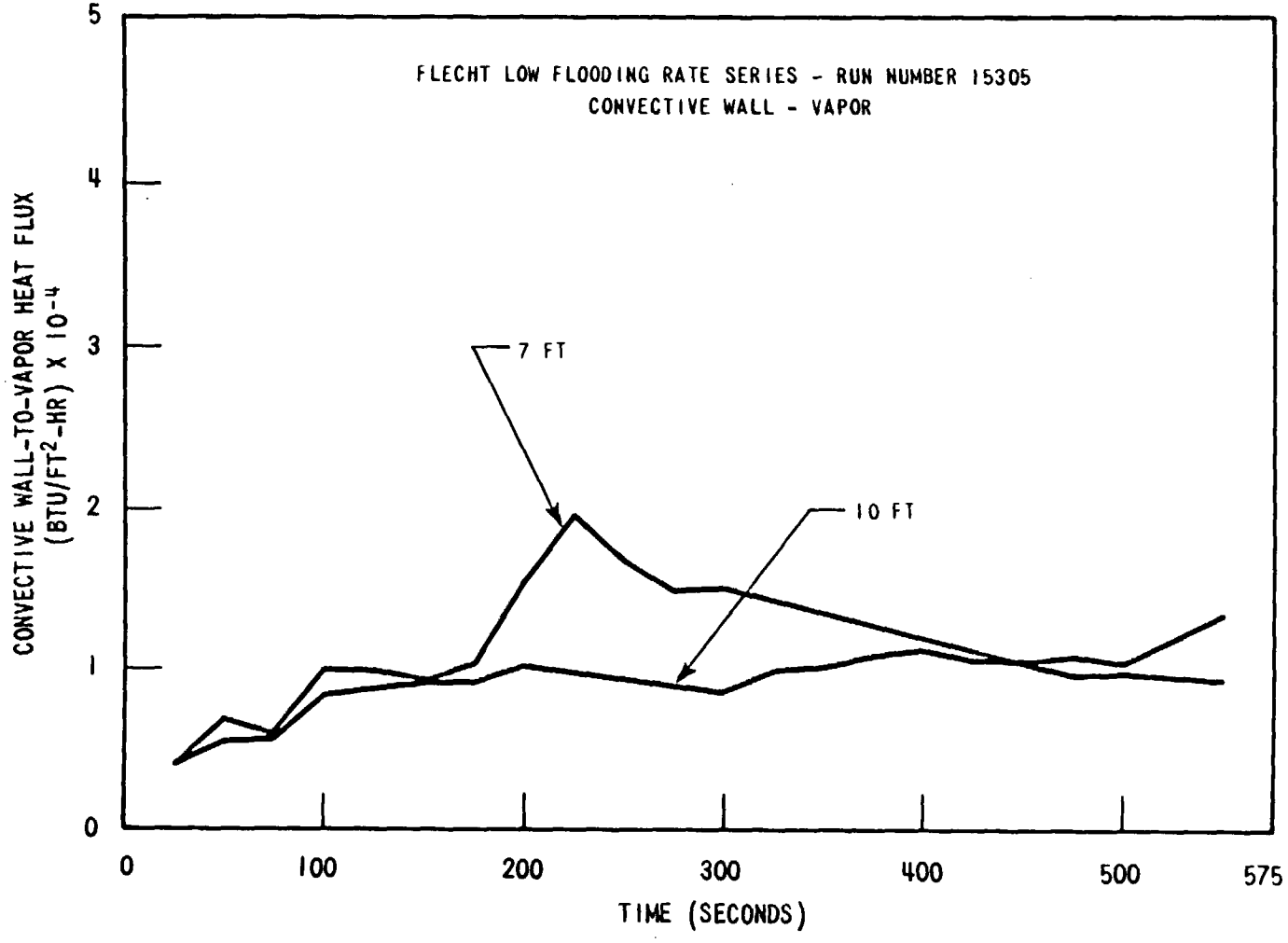

Figure 4-23. Calculated Convective Wall-to-Vapor Heat Flux Versus Time for Run No. 15305

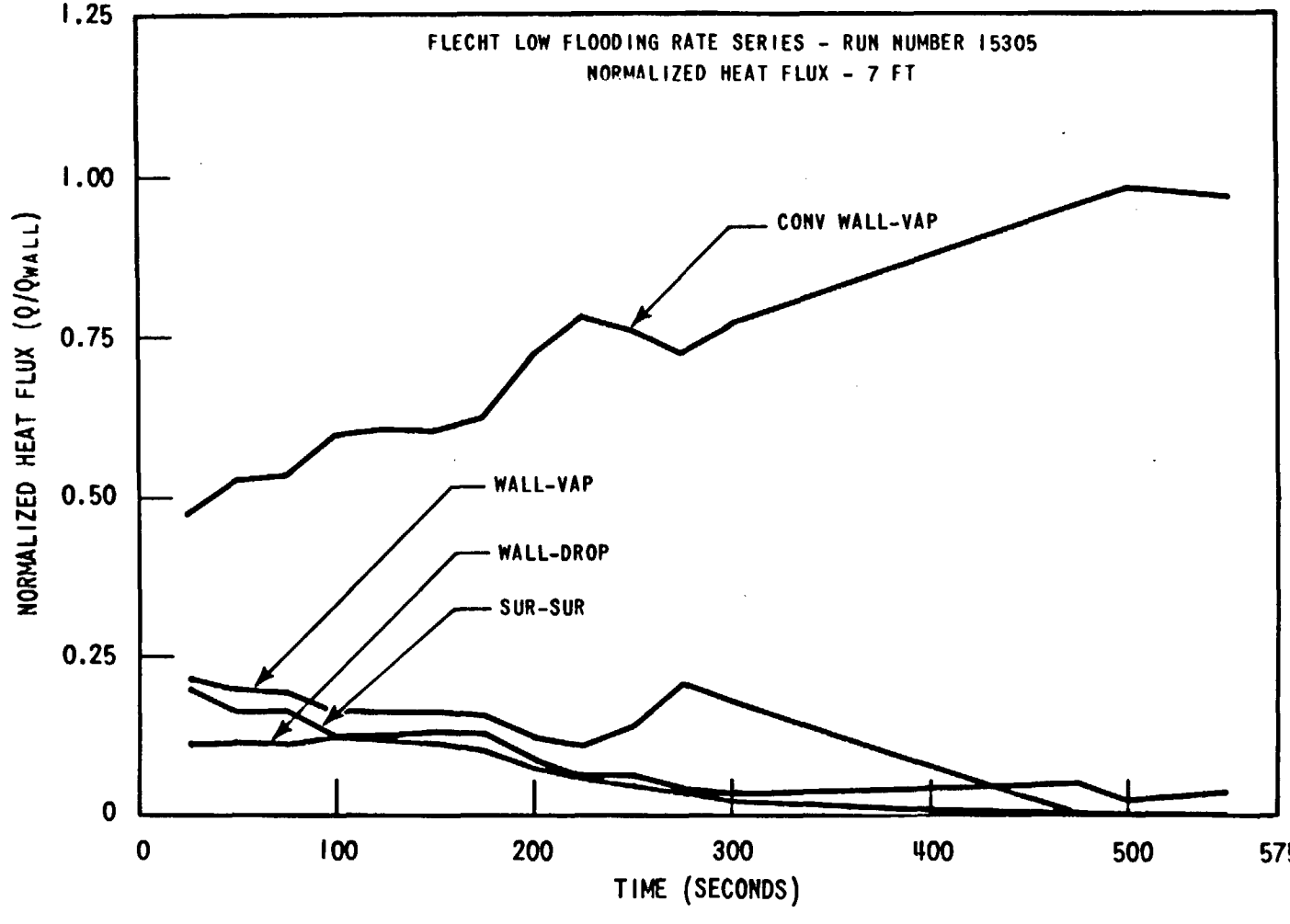

Figure 4-24. Components of Normalized Wall Heat Flux Versus Time at 7 FT for Run No. 15305

11,863-209

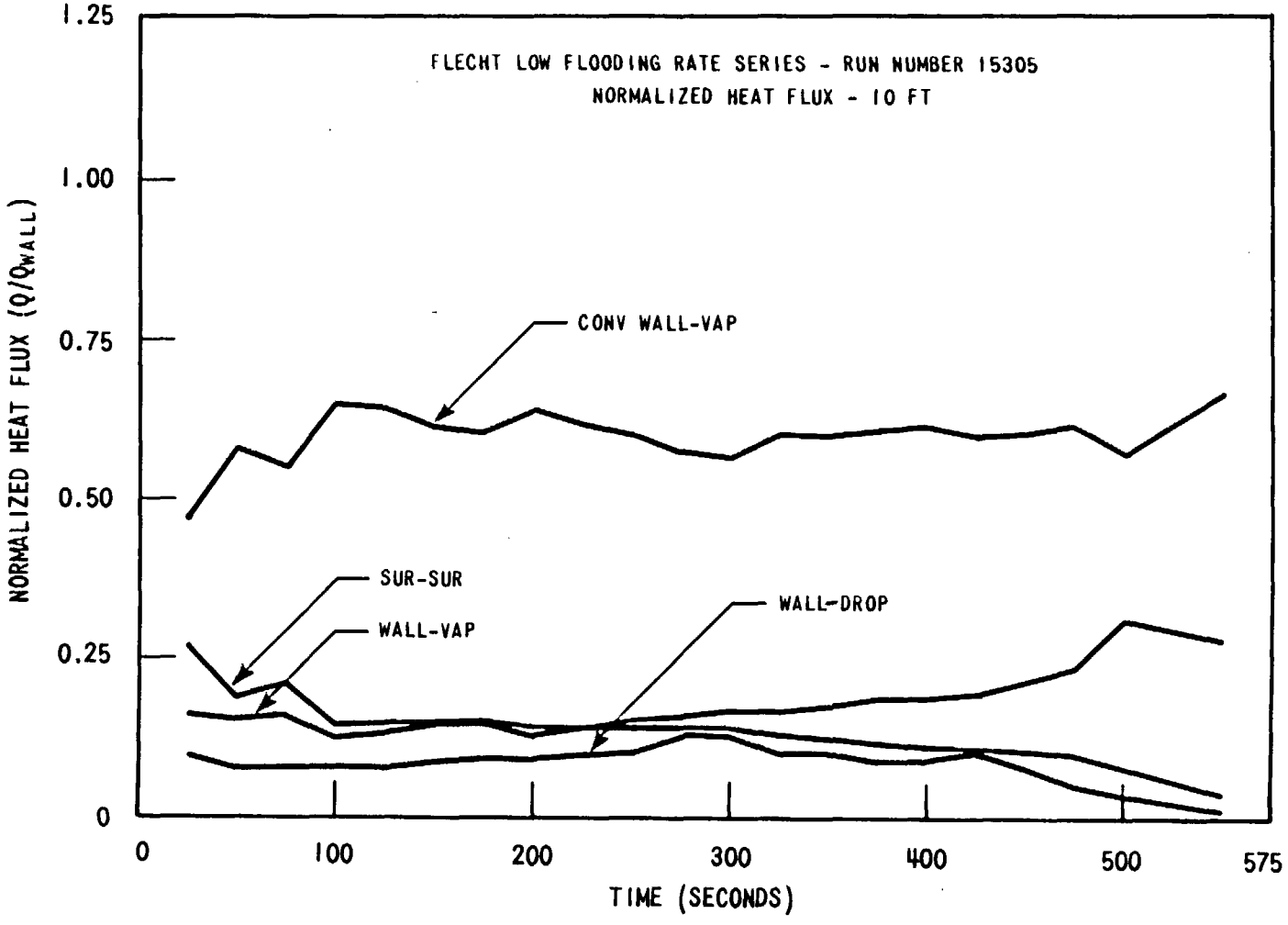

Figure 4-25. Components of Normalized Wall Heat Flux Versus Time at 10 FT Run No. 15305

The vapor Reynolds number was also calculated from the total mean flow, nonequilibrium quality, and the measured vapor temperature. It can be shown from the linear dependency of the steam viscosity on temperature, and the inverse dependency of the steam density on temperature that the vapor Reynolds number is proportional to

$$Re \propto \frac{u_g}{T_v^2} \tag{4-9}$$

Examination of the calculated steam flow rate and measured vapor temperature indicated that both peak early in the transient then decrease with time. However, the $1/T_v^2$ relationship for the vapor Reynolds number results in a near constant vapor Reynolds number as the test proceeds, until the quench front approaches. As the quench approaches, the vapor temperature quickly decreases toward the saturation temperature and the vapor Reynolds number correspondingly increases. This behavior is shown in figures 4-26 and 4-27.

The convective Nusselt numbers were also examined and found to be relatively constant from before turnaround to just before quench where the steam temperature is greater than 750°F. Both cosine and skewed power tests were analyzed to calculate the convective Nusselt number at 7 and 10 feet for the cosine and 7, 10, and 11.5 feet for the skewed power shapes. The resulting calculation for the convective Nusselt number is shown in figure 4-28. The same data with bands which indicate the vapor Reynold number and convective Nusselt number variation are shown in figure 4-29. Usually, the variation was approximately 25 percent or less.

As the data in figure 4-28 indicate, the vapor Reynolds number range is still in the transition region (3000 - 6000). The convective Nusselt number, however, is larger than one would calculate from single-phase vapor flow and lies above the extrapolation of the Dittus-Boelter[1] equation to lower vapor Reynolds numbers. It is believed that the convective Nusselt number at these low vapor Reynolds numbers is improved by the presence of drops in the dispersed two-phase flow. The drops would increase the low levels of turbulent mixing in the vapor flow by slipping relative to the vapor flow, generating low temperature steam by evaporation, and by interacting with the grids to form new size drops in the flow. All these effects would increase the convective capacity of the dispersed flow resulting in a larger convective Nusselt number.

1. McAdams, W. H., "Heat Transmission," McGraw Hill Book Co., Inc. 1954

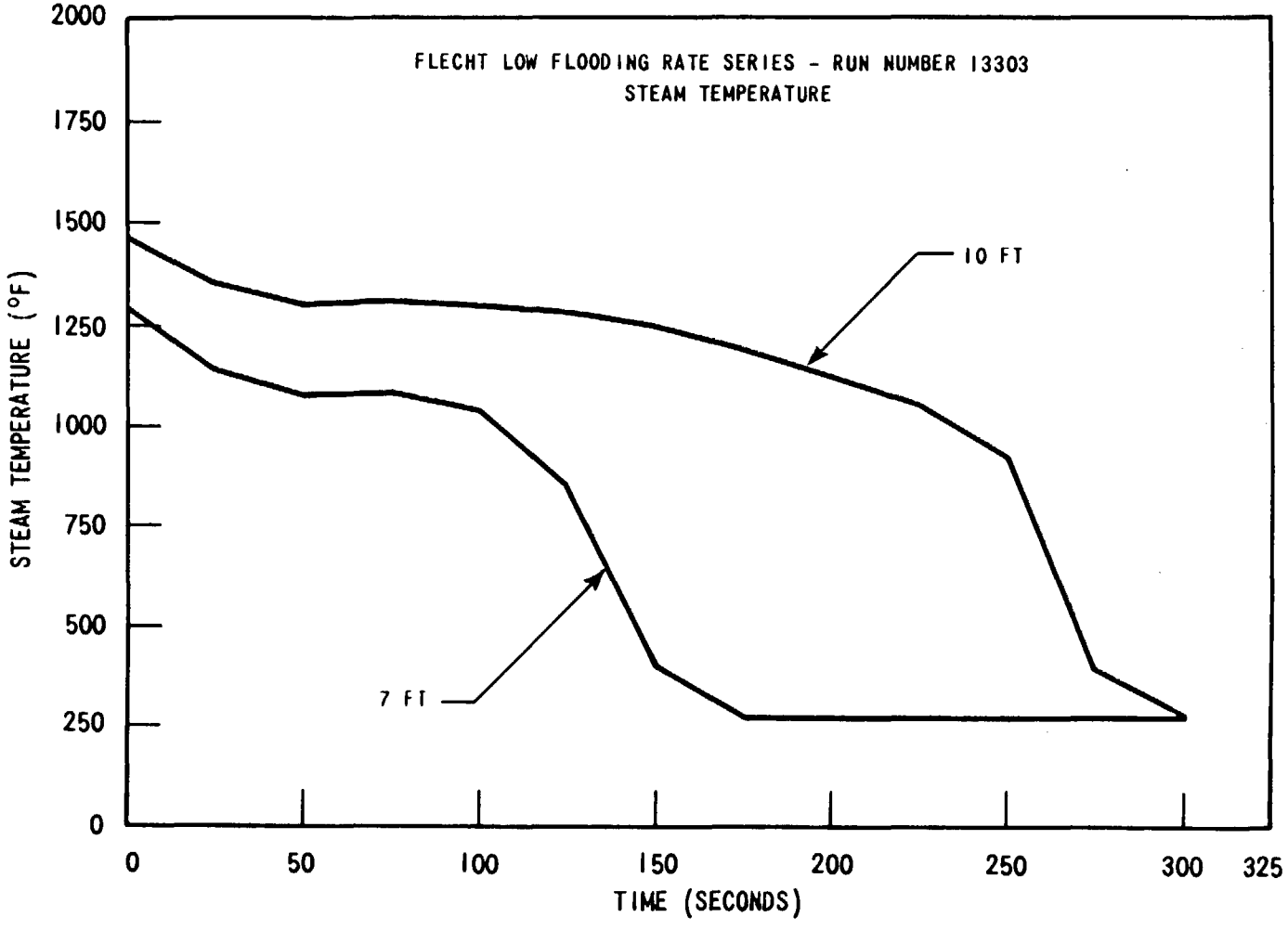

Figure 4-26. Steam Temperature Versus Time for Run No. 13303

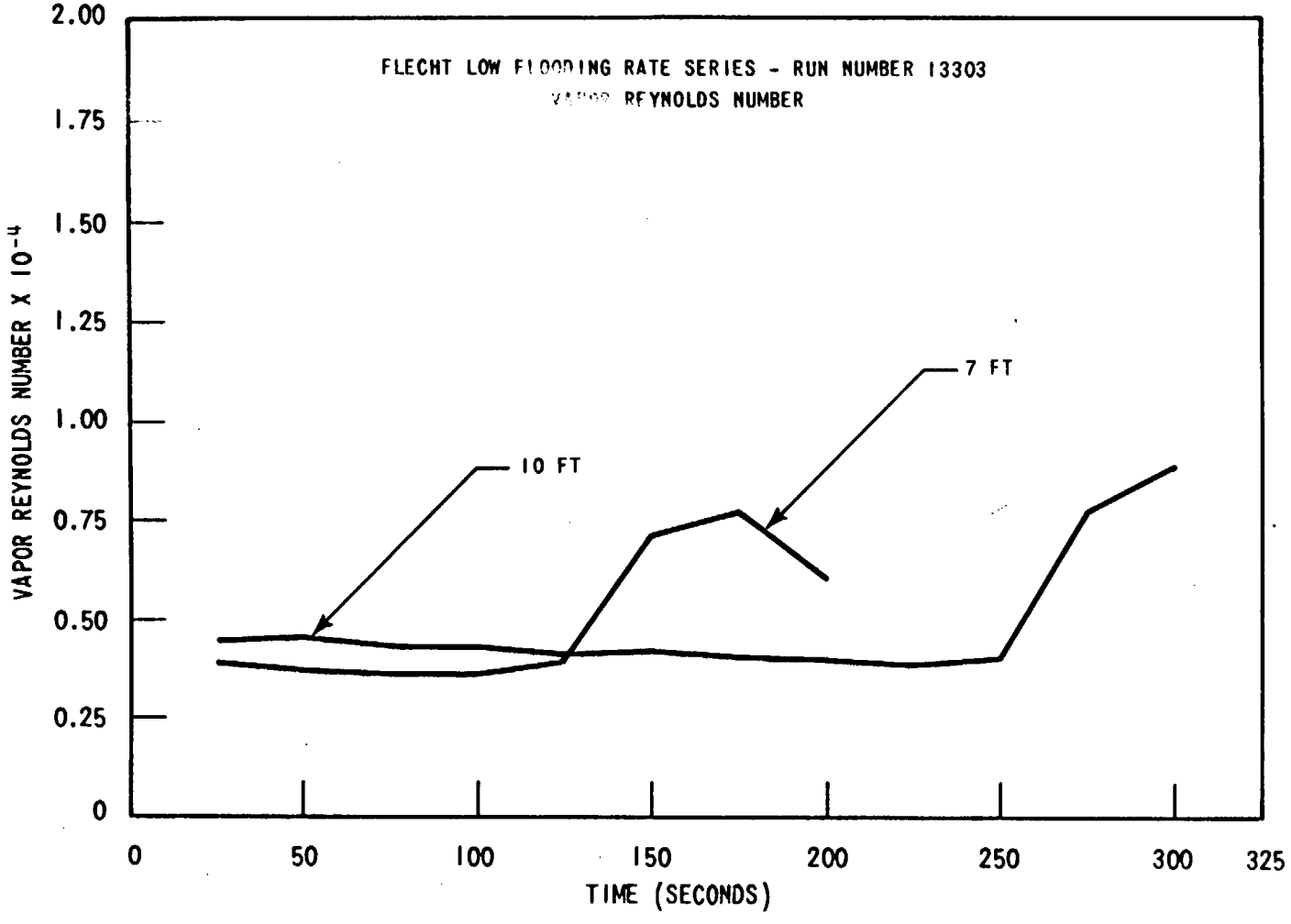

Figure 4-27. Vapor Reynolds Number Versus Time for Run No. 13303

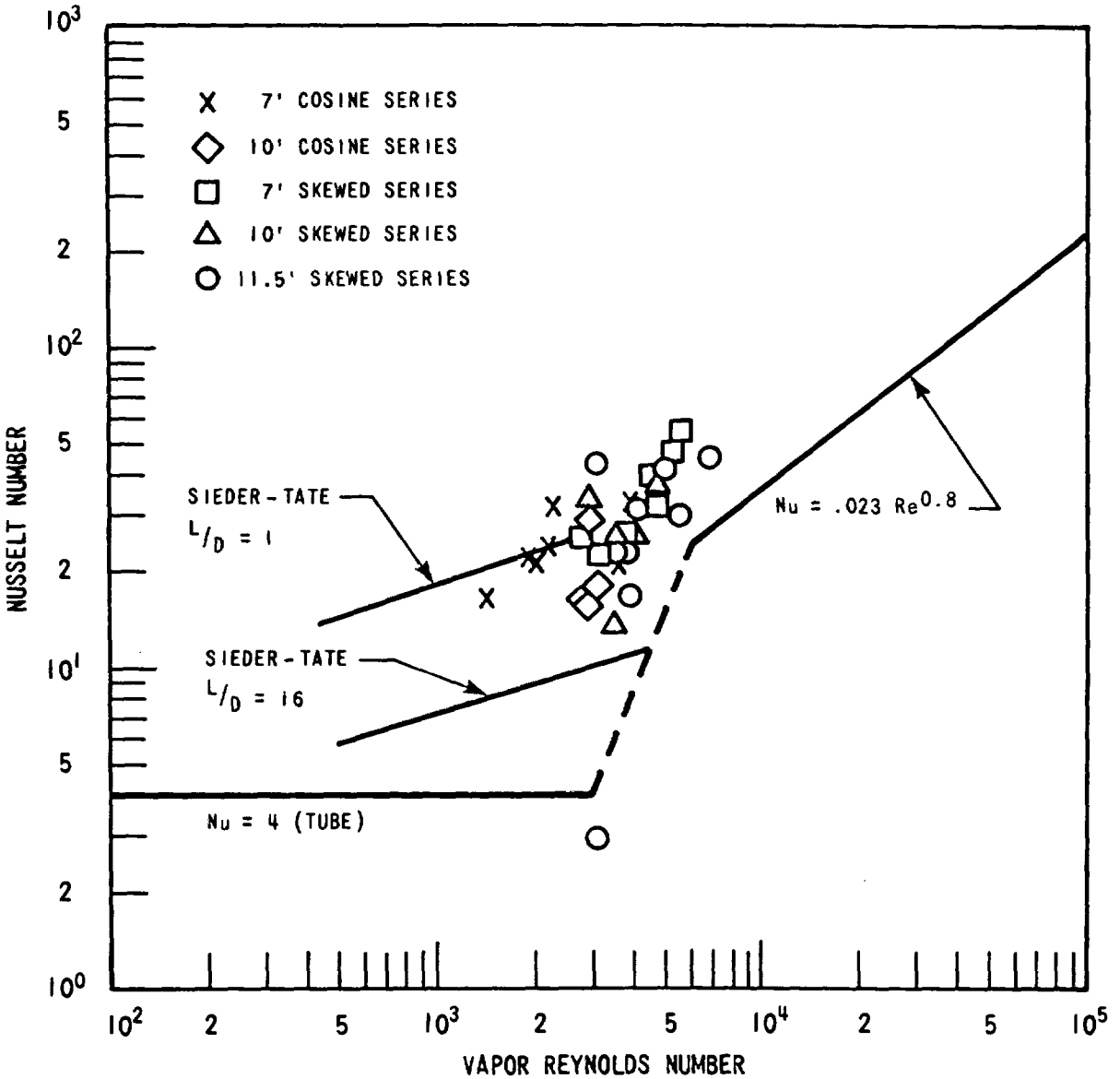

Figure 4-28. Average Nusselt Number Dependence on Average Vapor Reynold Number for Selected Cosine and Skewed Runs. (In Presence of Two-Phase Flow.)

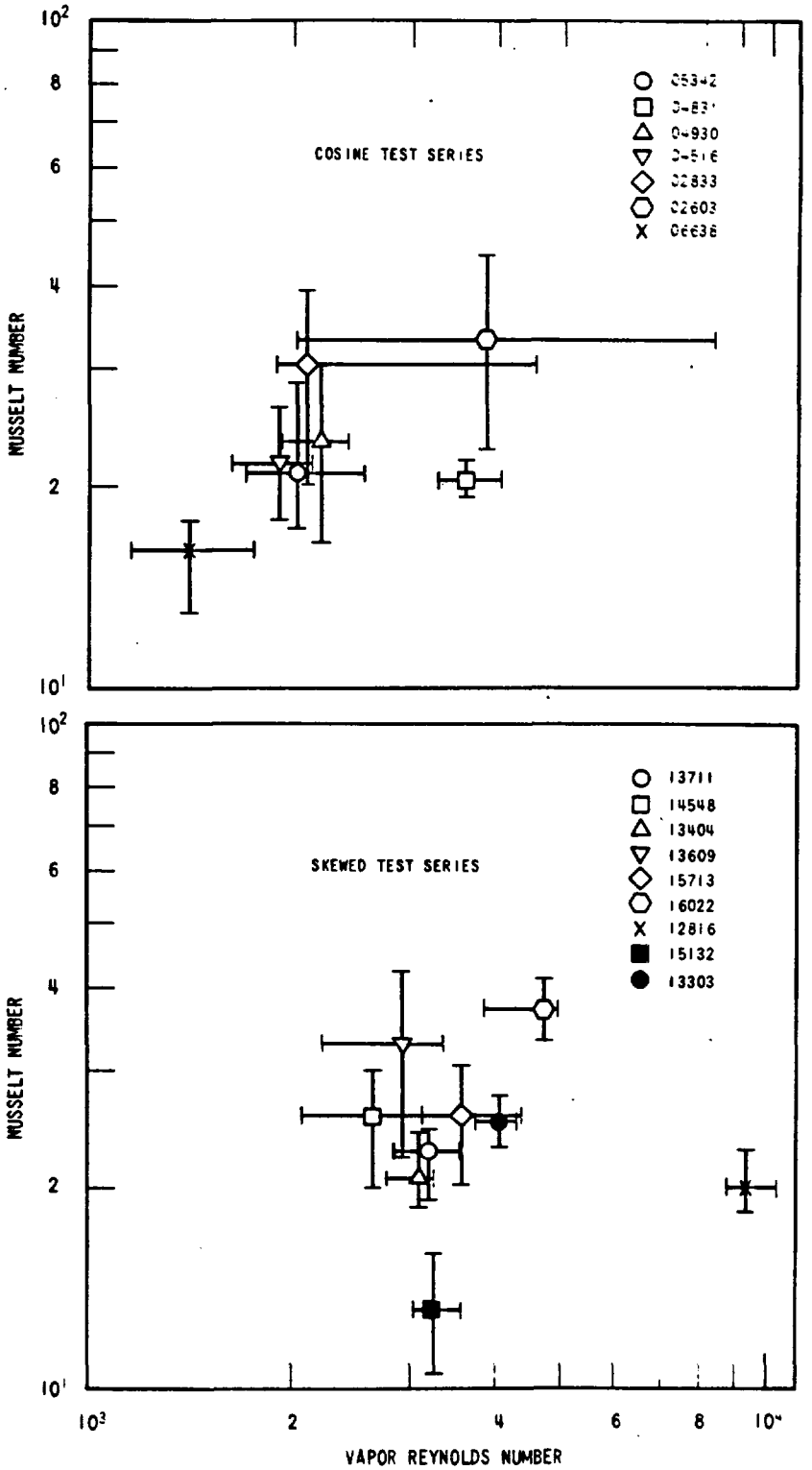

Figure 4-29. Mean and Range of Convective Nusselt Number Versus Vapor Reynolds Number for Selected (7 FT) Cosine and Skewed (10 FT) Runs

To further study the convective Nusselt number at these low vapor Reynolds numbers, the FLECHT data were examined at early times before liquid entrainment was observed in the tests. There were only a few tests which could be examined in this manner and for which good movies were available. Also, only those tests were examined in which the steam probe data indicated no significant lag time. The HEAT-II calculations were prepared using a quality of unity at each steam probe location and both the surface radiation and radiation-to-vapor terms were subtracted from the total wall heat flux to obtain the convective portion. The radiation-to-drops term was zero. All convective fluxes which were less than 10 percent of the total wall heat flux were ignored, since it was felt that they were within the accuracy of the calculation. The resulting Nusselt numbers for the pure steam case are shown in figure 4-30.

Each point for a given run represents a different time. As time increases, the calculated Nusselt numbers and vapor Reynolds numbers increase, and the points move upward toward the upper right-hand side of the figure. Comparing the points in this figure, and the data in figure 4-28 where the flow is two-phase, a significant improvement can be observed in the convective Nusselt number at the same vapor Reynolds number. Improvements of factors of 2 to 4 can be observed over the single-phase data. This improvement is believed to be due to the droplets which enhance the convective nature of the flow.

4-10. COMPARISON OF COSINE AND SKEWED PROFILE WALL HEAT FLUX RESULTS

The two most sensitive parameters which effect reflood heat transfer are the system pressure and the flooding rate into the bundle. Parametric comparisons of the calculated wall heat flux components for pressure and flooding rate variation for both the skewed and cosine test results are given in appendix A. These results should provide the reflood code developer with a larger data base with which he can compare his reflood model.

One trend which was observed in the skewed reflood tests was that the temperature rise was usually less than or equal to, the peak temperature rise for the cosine tests at the same conditions, even though the peak power zone for the skewed test was four feet higher in the bundle. Runs No. 05029 (cosine) and 15305 (skewed) were compared in detail in an attempt to find out why.

The test conditions for these two runs are given in table 4-1. Figures 4-31 to 4-33 show a side-by-side comparison of these two runs. The turnaround time for each is labeled on each graph. Note that the seven-foot elevation must be used for comparison with the cosine data since no six-foot steam probe was available. Therefore, the comparison is not as exact as one would wish it to be.

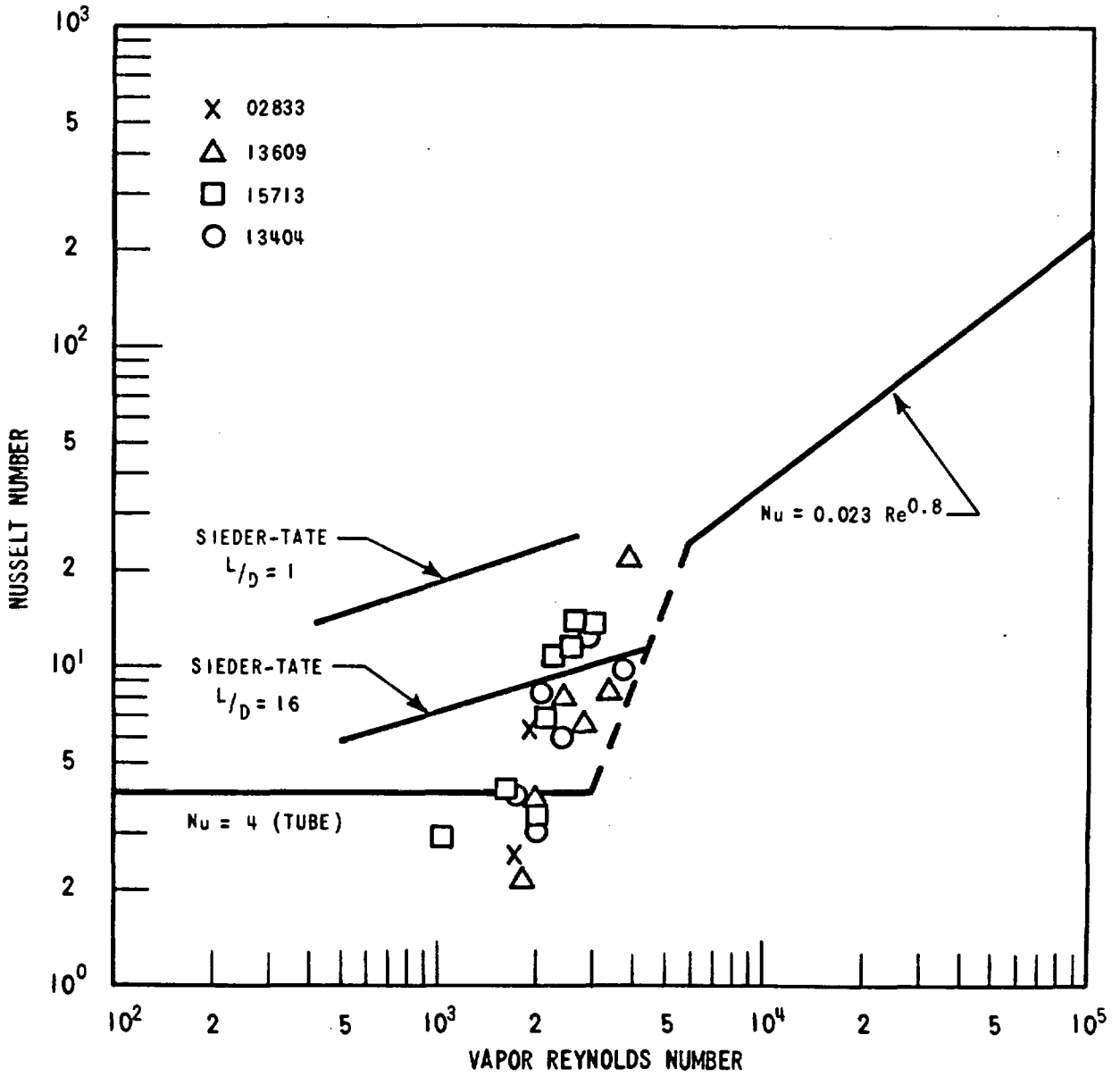

Figure 4-30. Nusselt Number Dependence on Vapor Reynolds Number for Selected Cosine and Skewed Runs. (In Presence of Steam Only.)

TABLE 4-1

COMPARISON OF SKEW TEST 15305 TO COSINE TEST 05029

Run No.	Pressure (psia)	Peak Power (kw/ft)	ΔT_{sub} (°F)	T_{clad} Initial (°F)	Flooding Rate (in/sec)	T_{max} at z (°F)	ΔT_{rise} (°F)	t_{turn} (sec)
15305	40	0.7	140	1603	0.8	2034	158	620
05029	40	0.73	141	1600	0.85	2075	475	102

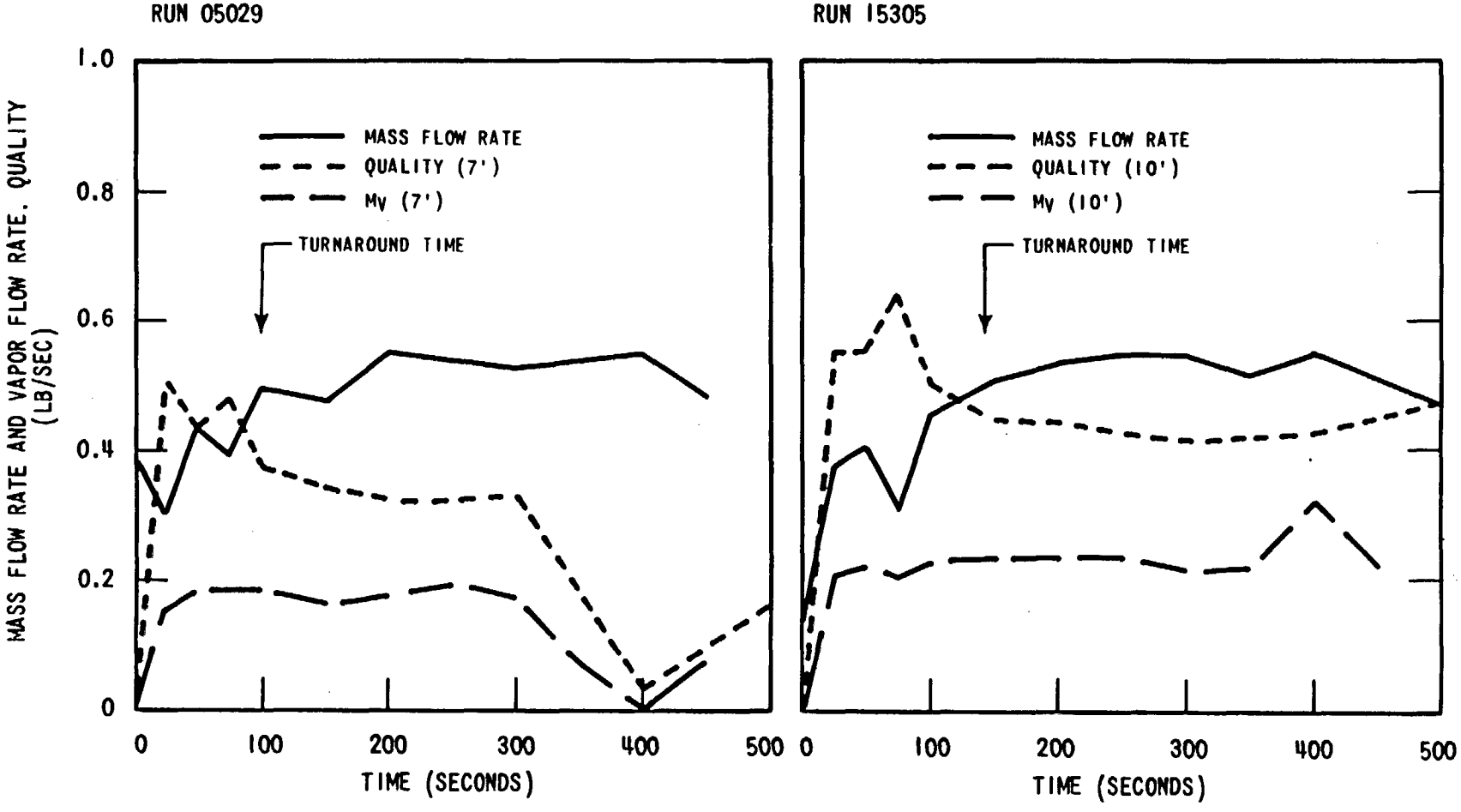

Figure 4-31. Mass Flow Rate, Vapor Flow Rate, and Quality Comparison Between Cosine Run No. 05029 and Skewed Run No. 15305

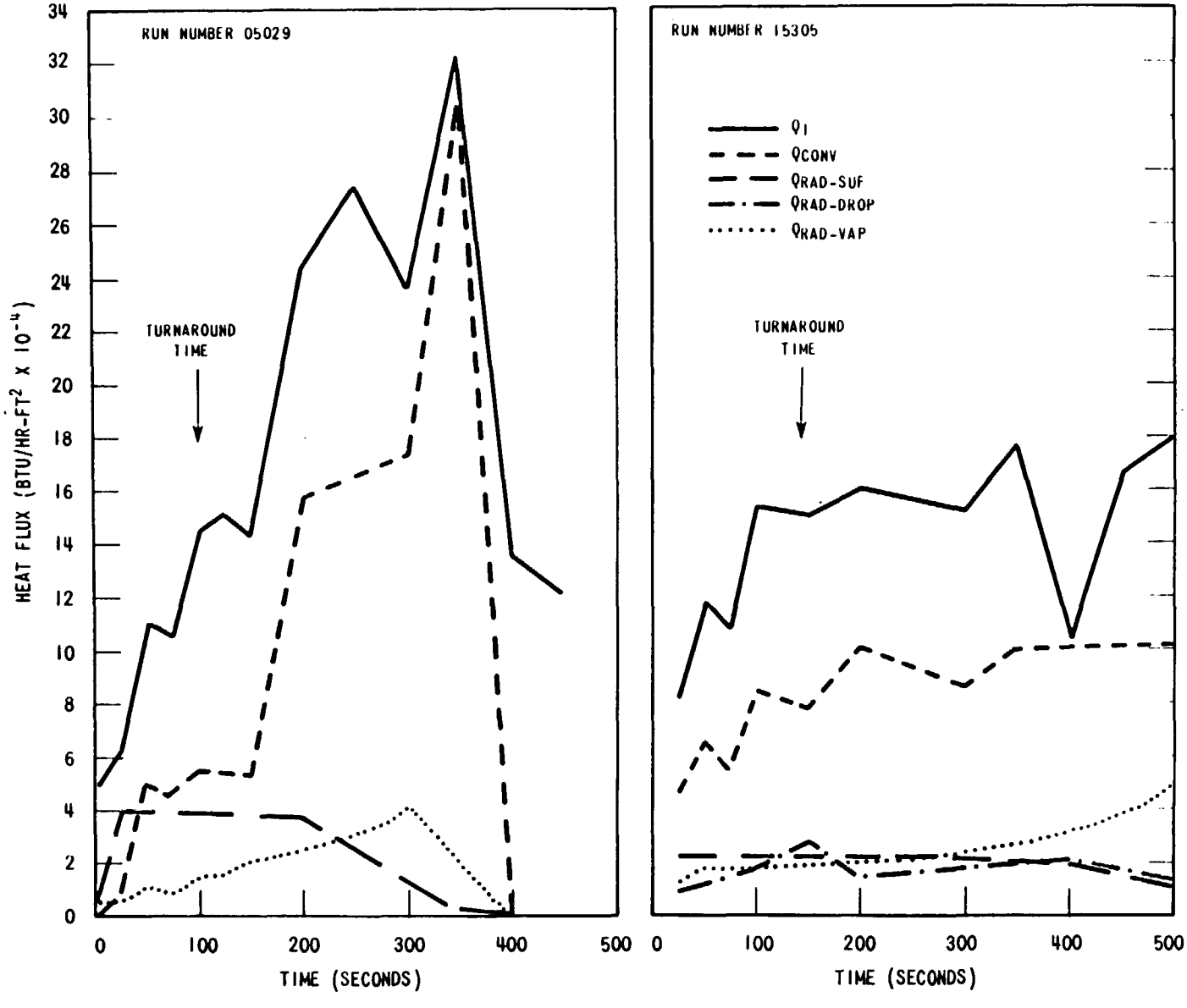

Figure 4-32. Mechanistic Breakdown of Wall Heat Flux Comparison Between Cosine Run No. 05029 and Skewed Run No. 15305

11,863-217

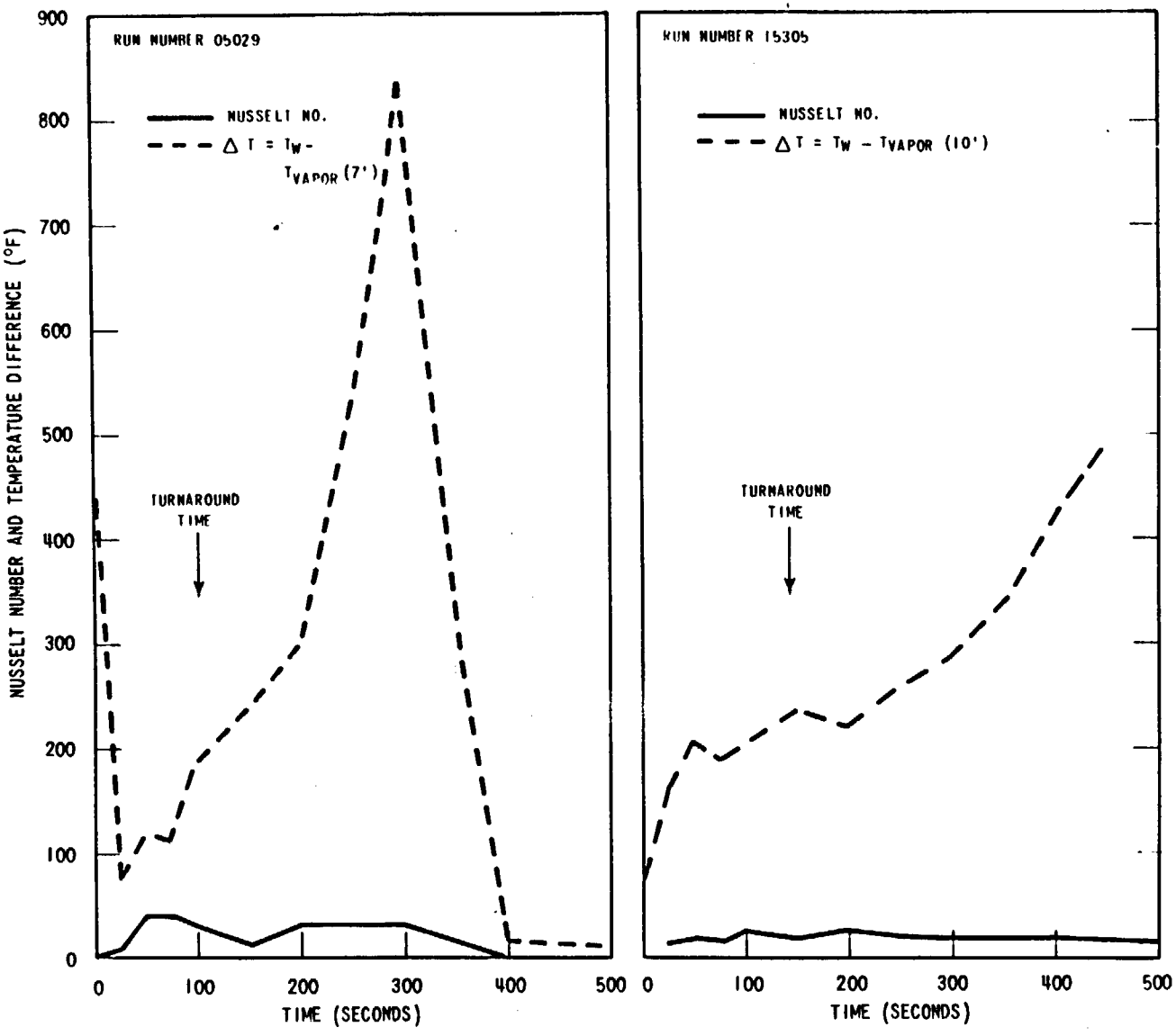

Figure 4-33. Nusselt Number and Temperature Difference Comparison Between Cosine Run No. 05029 and Skewed Run No. 15305

Since the concern is the maximum temperature rise, the discussion will primarily concern the heat transfer up to turnaround time. As figure 4-31 indicates, the mass flow is nearly the same for the two runs, but the quality is higher for the skewed test, resulting in a higher vapor flow.

Comparing the wall heat flux components in figure 4-32, the indication is that the average wall heat flux up to turnaround for the skewed test is larger. Also, both the rod-to-vapor and convective wall heat flux components are larger for the skewed case as compared to the cosine. The cosine did have a larger surface-to-surface radiation term than the skewed; however, the two larger skewed wall heat flux terms then offset the larger cosine surface radiation term.

The convective Nusselt number and $T_w - T_{vapor}$ plot given in figure 4-33 indicate nearly the same Nusselt numbers when the $T_w - T_{vapor}$ temperature difference is the same. The unusual $T_w - T_{vapor}$ plot for the skewed data indicates that the seven-foot steam probe was not initially bled and lagged the rod temperatures significantly for the first 25 seconds. This procedure was changed in the skewed tests and more accurate steam probe data were obtained earlier in time.

While these tests tend to indicate nearly the same results, it does appear that the higher quality for the skewed test does give a high vapor flow past the hot spot. The higher vapor flow apparently allows a larger rod-to-coolant ΔT as shown in figure 4-33, which helps to give a larger wall heat flux. A secondary effect is the larger droplet radiation component for the skewed test. Both of these effects help to limit the temperature rise of the skewed test relative to the cosine test.

SECTION 5
MASS FLOW ABOVE FROTH LEVEL

The model for calculating the mass flow above the froth level (mass effluence) has been formulated by Yeh et al[1] and Lilly et al.[2] The model utilizes the Lagrangian method of describing fluid motion to compute the fluid velocity and steam generation, and uses the Yeh void fraction correlation to compute the void fraction below the quench front. The rate of mass effluence, $\dot{m}_f$, is then computed by:

$$\dot{m}_f = \dot{m}_{in} \left[1 - \frac{1}{V_{in}} \frac{dZ_{Lf}(t)}{dt} \right] \equiv \dot{m}_{in} \Gamma_f \qquad (5\text{-}1)$$

where $\dot{m}_{in}$ and V_{in} are the inlet mass flow rate and velocity, respectively, $Z_{Lf}(t)$ is the collapsed liquid height (i.e., net liquid if all bubbles were collapsed) below the froth level. Froth level is defined as the interface between the region of continuous vapor phase (dispersed flow) and the region of continuous liquid phase (flow boiling), and $\Gamma_f \equiv \dot{m}_f/\dot{m}_{in}$ is the mass effluent ratio. In FLECHT cosine power low flooding rate tests, the froth level detected from the pressure drop data was found to be in the scattering band of the quench front data. Therefore the froth level and quench front elevation are assumed to be the same for the low flooding rate. The collapsed liquid level $Z_{Lf}(t)$ is obtained by computing the void fraction and integrating the liquid up to the froth level. The void fraction is obtained by computing superficial steam velocity (steam volumetric flux) and using Yeh's void fraction correlation. The superficial steam velocity is obtained by computing heat release from the heater rods. The calculated mass effluent ratio, Γ_f, and the void fraction for the FLECHT cosine power low flooding rate tests are in good agreement with data.[1,2]

The model can be applied to the recent FLECHT skewed power tests.[3] As in the cosine power tests, the froth level was found to be in the scattering band of the quench front data for the low flooding rate. Therefore, the froth level is assumed, to be the same as the quench

1. Yeh, H. C., and Hochreiter L. E., "Mass Effluence During FLECHT Forced Reflood Experiments", Trans. Am. Nucl. Soc., Vol. 24, 301 (1976).
2. Lilly, G. P., Yeh, H. C., Hochreiter L. E., and Yamaguichi N., "PWR FLECHT Cosine Low Flooding Rate Test Series Evaluation Report," WCAP-8838, March 1977.
3. Rosal, E. R., Conway, C. E., and Krepirevich, M. C., "FLECHT Low Flooding Rate Skewed Test Series Data Report," WCAP-9108, May 1977.

front elevation for a low flooding rate. Figure 5-1 plots the froth level as detected from pressure drop data, the quench front elevation, the collapsed liquid level, and the saturation line. Figure 5-2 shows that the calculated average void fraction for every one-foot interval is in good agreement with that reduced from pressure drop data.

To compare the calculated Γ_f we note that since the void fraction is high above the froth level and the mass storage, and hence the rate of mass storage, is small above the froth level, the mass flow ratio, Γ_f, above the froth level should be about the same as the ratio of mass flow out of the bundle, Γ_o. This is confirmed for the cosine power bundle by comparing the calculated Γ_f with the measured Γ_o.[1] Figure 5-3 shows that this is also true for the skewed power bundle.

The pressure drop data indicate that in runs in which the flooding rate is equal to or greater than 3 inches/sec, the froth level is higher than the quench front elevation, which means that there is film boiling above the quench front for these runs. Since an appropriate method for computing the void fraction is not available at present, the calculation for these runs was not made.

Appendix E contains additional comparisons of the collapsed liquid level, the void fraction, and the mass flow ratio, Γ_f, above the froth level for low flooding rate.

From the agreement of the above comparisons and the comparisons from WCAP-8838 with the calculational results of the model and the test data, for both the cosine and the skewed power shape it can be inferred that the model is applicable to any power shape.

1. Lilly, G. P., Yeh, H.C., Hochreiter L.E., and Yamaguichi N., "PWR FLECHT Cosine Low Flooding Rate Test Series Evaluation Report," WCAP-8838, March 1977.

RUN NUMBER	15305
PRESSURE	40 PSIA
INITIAL CLADDING TEMPERATURE	1603°F
PEAK POWER	0.7 KW/FT
SUBCOOLING	140°F
INJECTION RATE	0.8 IN./SEC

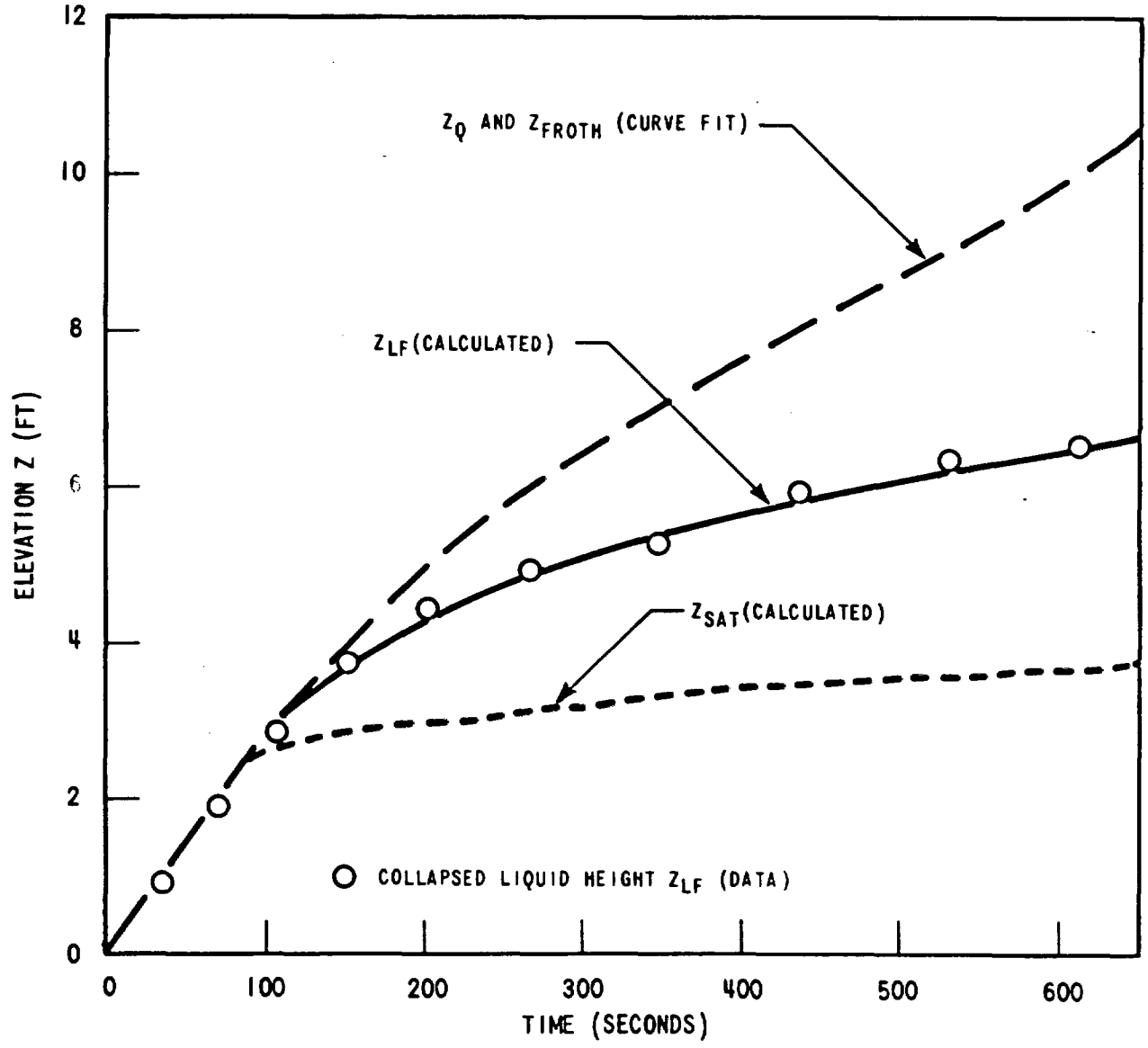

Figure 5-1. Comparison of the Measured Collapsed Liquid Height Z_{Lf} and That Calculated by Using Z_{froth} (= Z_q) Data

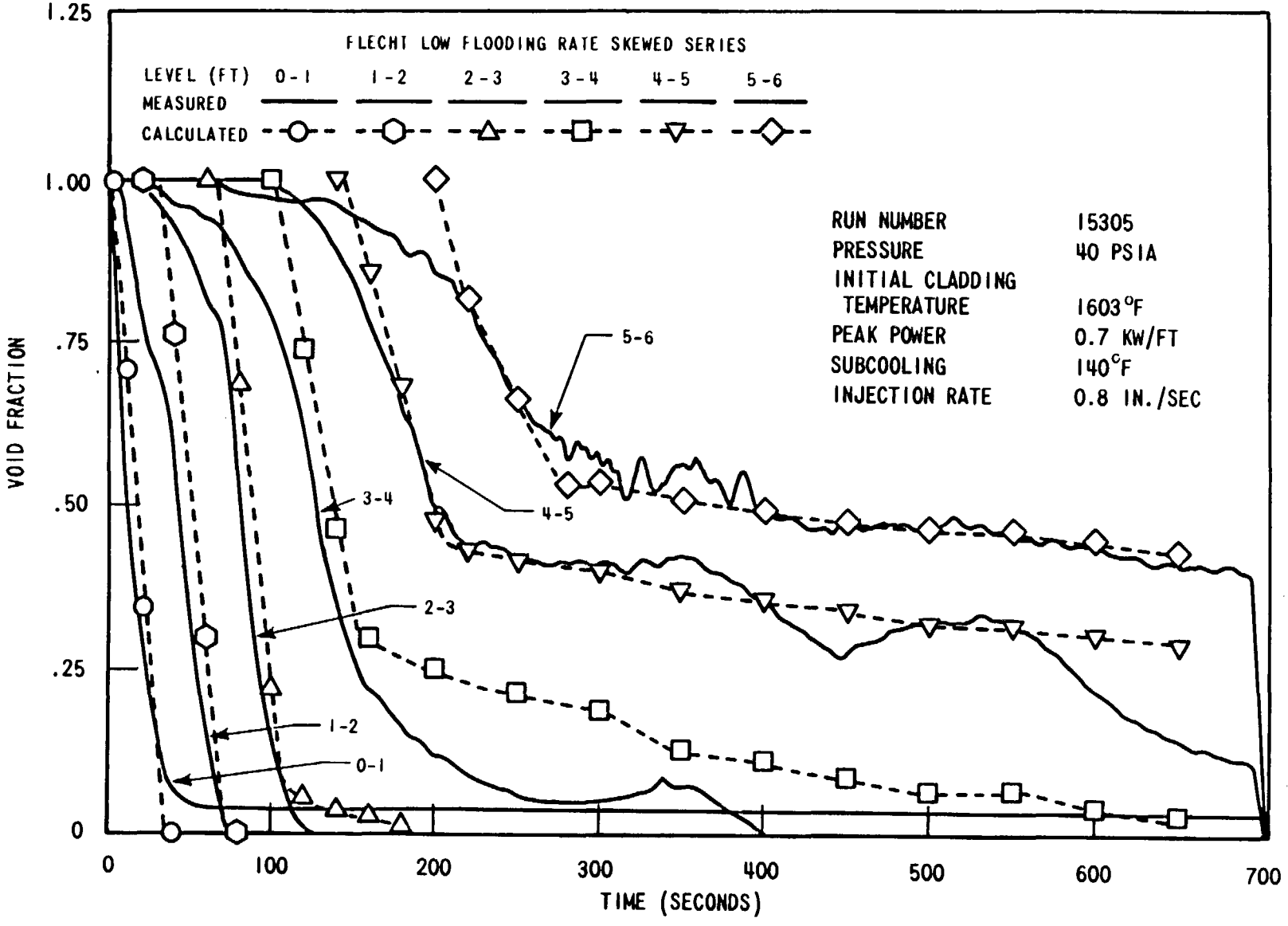

Figure 5-2(A). Comparison of the Calculated and the Measured Average Void Fraction in Every 1 FT Interval (Run Number 15305, 0-6 FT Level)

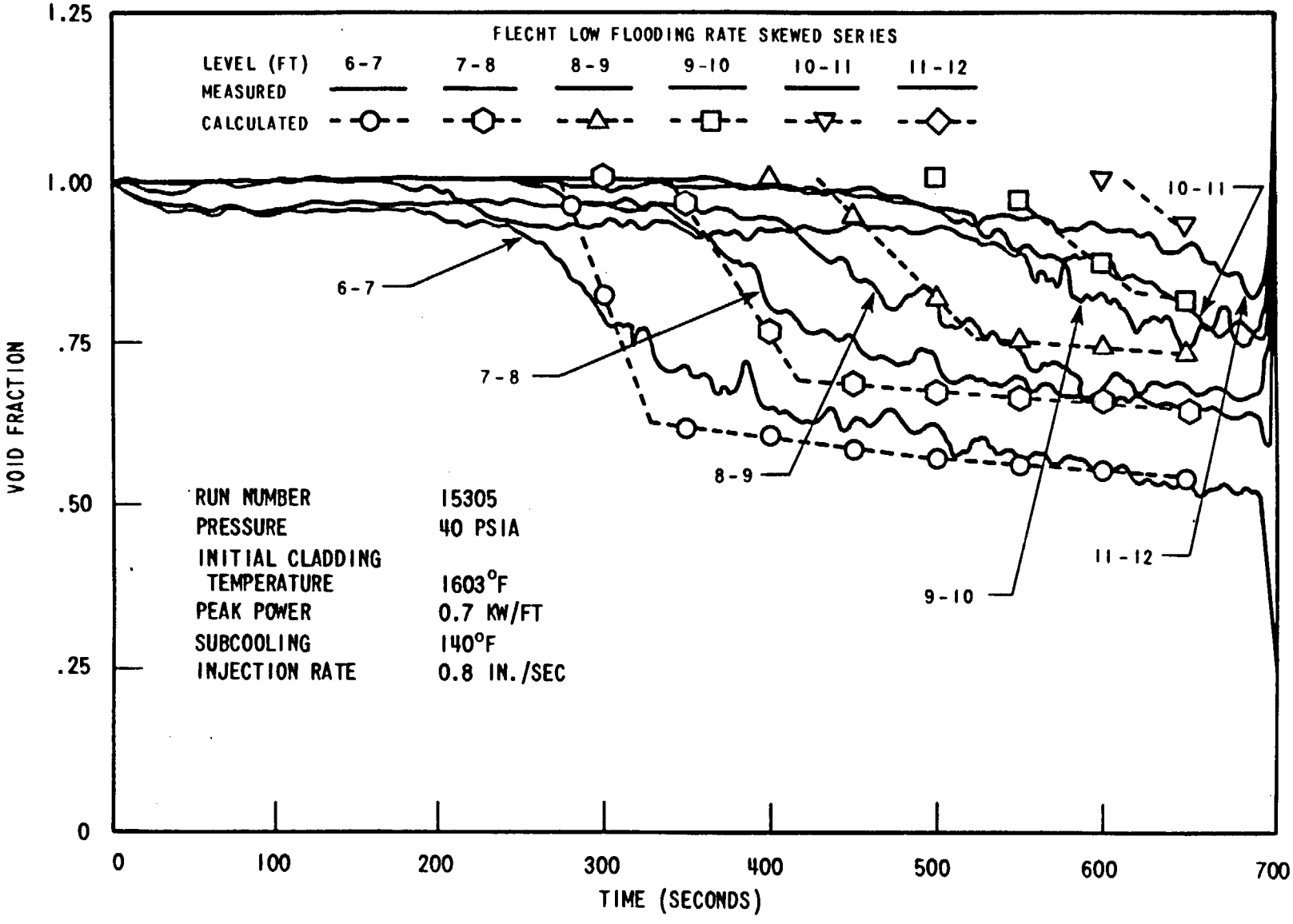

Figure 5-2(B). Comparison of the Calculated and the Measured Average Void Fraction in Every 1 FT Interval (Run Number 15305, 6-12 FT Level)

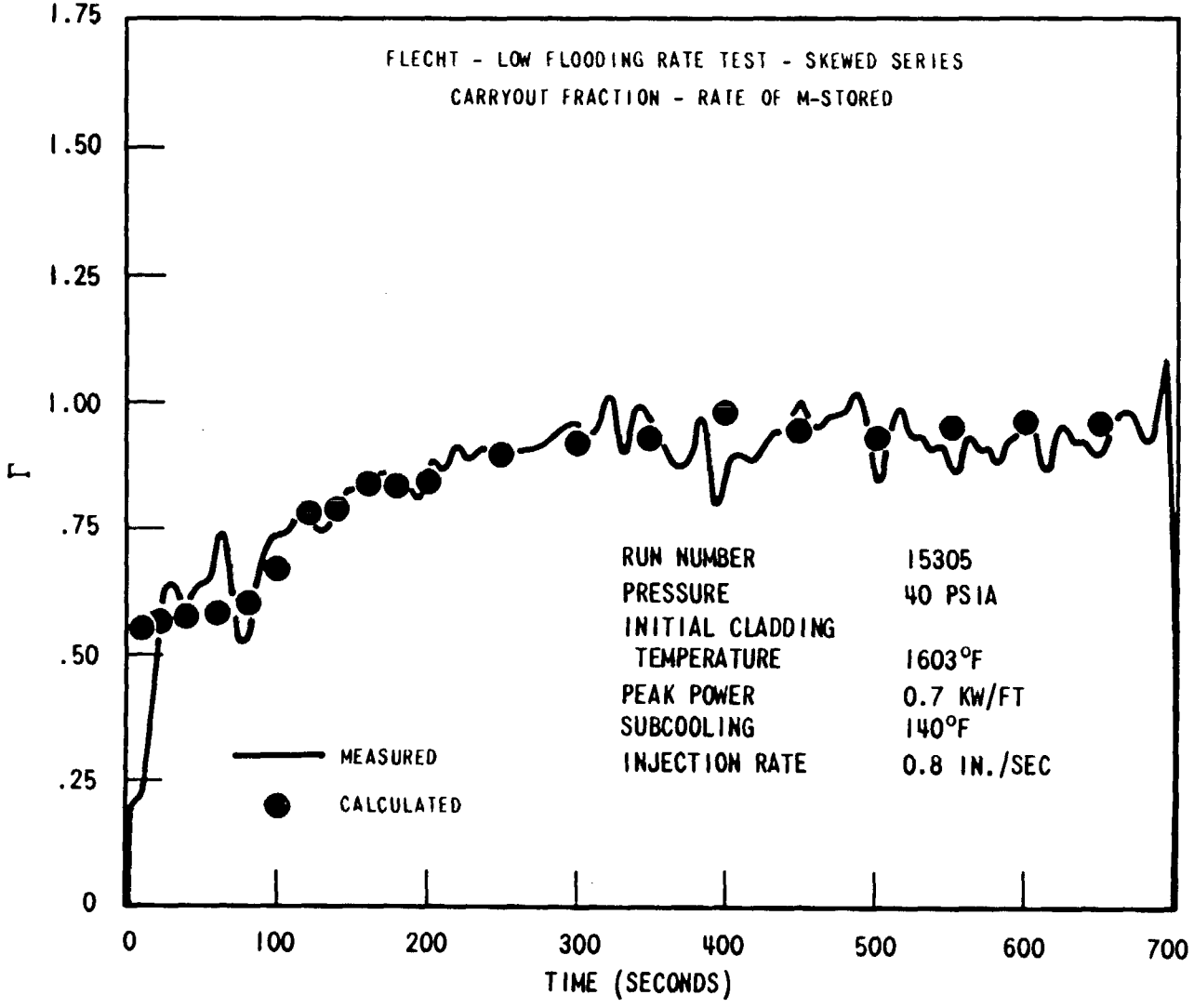

Figure 5-3. Comparison of the Calculated and the Measured Mass Effluent Ratio, Γ

SECTION 6
HEAT TRANSFER CORRELATION

6-1. INTRODUCTION

The existing FLECHT correlation[1] was derived from the data of FLECHT cosine power shape tests. It is desirable to have a heat transfer correlation which is derived from a more general basis and which can be used for any power shape. This is the motivation for the proposed correlation discussed in this section.

The rationale for the proposed correlation is that the heat transfer coefficient is primarily a function of the distance from the quench front. This idea was suggested from various references. In WCAP-7665[2] the higher heat transfer coefficient of the Zircaloy cladding tests over that of the stainless steel cladding tests was explained. Because the quench front velocity of the Zircaloy cladding is larger than that of the stainless steel cladding, the distance from a given elevation to the quench front at a given time is shorter for Zircaloy cladding than for stainless steel cladding. In an ASME paper,[3] the heat transfer coefficients of German reflood test data were plotted against the distance from the bundle water head as shown in figure 6-1. The plot seemed to collapse all test data within a reasonably narrow scattering band. Although the water head is in general somewhat smaller than the quench front elevation, the plot suggests that the heat transfer coefficient can be correlated with the distance of this sort. In WCAP-8838 there is a plot of heat transfer coefficient versus elevation which appears to be similar for all curves at all times. This also suggests that the heat transfer coefficient can be correlated with a distance of some kind.

The reason that the heat transfer coefficient is primarily a function of the distance from the quench front is because the heat transfer regime on unwetted cladding surface starts to develop from the quench front. For high flooding rates, (larger than 3 in./sec) the film boiling starts at the quench front. Immediately above the quench front the vapor film is very

1. Lilly, G. P., Yeh, H. C., Hochreiter, L. E. and Yamaguchi, N., "PWR FLECHT Cosine Low Flooding Rate Test Series Evaluation Report," WCAP-8838, March 1977.
2. Cadek, F. F., Dominicis, D. P. and Leyse, R. H., "PWR FLECHT (Full Length Emergency Cooling Heat Transfer) Final Report," WCAP-7665, April 1971.
3. Riedle, K., et al., "Reflood and Spray Cooling Heat Transfer in PWR and BWR Bundles", ASME paper 76-HD-10 (1976).

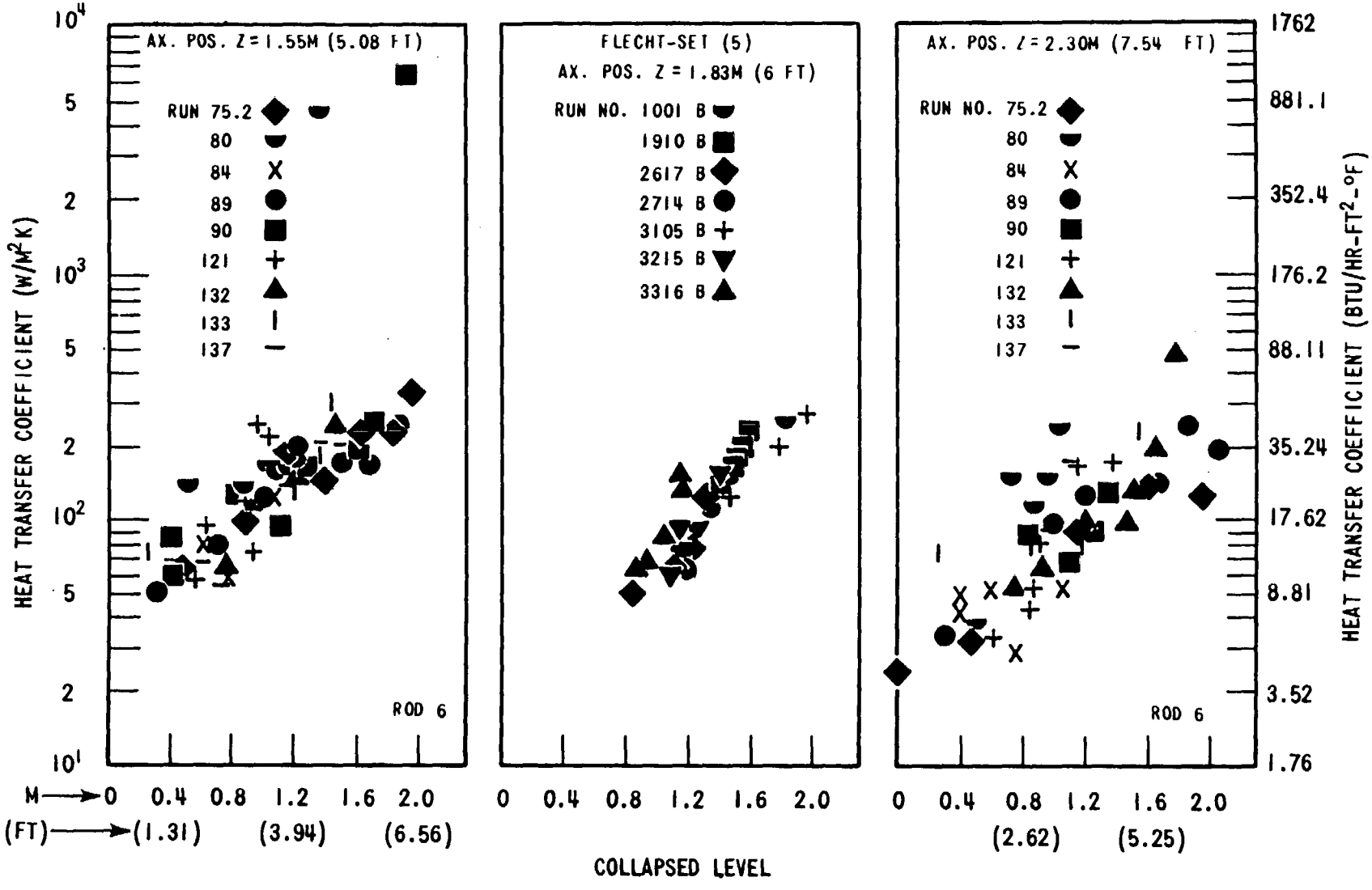

Figure 6-1. Heat Transfer in the Unwetted Region as a Function of Collapsed Level (Reference 3)

thin and stable. As the distance from the quench front increases, the thickness of the vapor film also increases due to increasing vapor generation. As the distance from the quench front further increases, the vapor film becomes so thick that it becomes unstable and the vapor-liquid interface appears to be in wavy motion. This is called unstable film boiling. As the distance from the quench front further increases, the vapor flow rate becomes so great that the water becomes very turbulent and the vapor breaks the water into pieces and carries them up. This is the dispersed flow region. The pattern of these heat transfer regimes moves up with the quench front. Therefore the heat transfer coefficient is expected to be primarily a function of the distance from the quench front. For low flooding rates (less than 3 in./sec), the film boiling regime above the quench front is either negligible or missing, and the flow regime above the quench front is essentially dispersed flow. The vapor comes out of the quench front at essentially the saturation temperature or slightly superheated. The vapor temperature increases with increasing elevation. According to the FLECHT definition of heat transfer coefficient, which uses the saturation temperature as a sink temperature, the FLECHT heat transfer coefficient h_{FLECHT} is related to the real heat transfer coefficient h_{real} by

$$h_{FLECHT} = \left(\frac{T_w - T_{vapor}}{T_w - T_{sat}}\right) h_{real} \qquad (6\text{-}1)$$

The vapor temperature T_{vapor} increases with elevation; the FLECHT heat transfer coefficient, h_{FLECHT}, decreases although the real heat transfer coefficient, h_{real}, may increase due to the increase of vapor velocity. This pattern of heat transfer regime also moves with the quench front elevation. Therefore the heat transfer coefficient also is expected primarily to be a function of the distance from the quench front.

An analytical expression of the heat transfer coefficient was obtained by Ellion[1] for film boiling which shows that the heat transfer coefficient is inversely proportional to the 1/4th power of the distance from the quench front. Although Ellion's equation underpredicts the FLECHT data, it does show the dependency of the heat transfer coefficient on the distance from the quench front.

The main feature of the proposed heat transfer correlation is that the integral of power and and the local initial temperature, are used rather than the peak power and the peak initial temperature. This is different from the correlation in WCAP-8838.

1. Ellion, M. E., "Study of the Mechanism of Boiling Heat Transfer", Jet Propulsion Laboratory, CIT, Memorandum No. 20-88.

As in the previous FLECHT correlation, (WCAP-7665) the present correlation consists of two independent sub-correlations:

- Quench correlation (the Z_q-correlation) which predicts the quench front elevation as a function of time.
- Heat transfer coefficient correlation (the h-correlation) which predicts the heat transfer coefficient as a function of the distance from the quench front, $Z\text{-}Z_q$.

Unlike the previous FLECHT correlation, in the present correlation the heat transfer coefficient is a function of the space variable, Z_q instead of the time variable, t. The heat transfer coefficient can be computed as a function of time using the quench correlation which bridges the space variable (Z_q) and the time variable (t).

6-2. QUENCH CORRELATION (THE Z_q-CORRELATION)

The quench front elevation Z_q can be computed from the t_{q6ft} correlation in WCAP-7665. The t_{q6ft} correlation is used to predict the quench time at the peak power elevation, 6 ft, of the FLECHT cosine power rod bundle. However, it can be used to predict the quench time of any power shape at any elevation by using the ratio of the integral of power, Q_r, defined below as a parameter.

$$Q_r = \int_0^{Z_q} Q'(Z)dZ \Big/ \int_0^{Z_{peak}} Q'(Z)dZ$$

where Q'(Z) is the linear power (kw/ft) at the elevation Z. It has been shown in WCAP-8838 and WCAP-8838[1] that the quench time is proportional to the heat input below the quench front. The heat input below the quench front can be reasonably approximated by the integral of power below the quench front.

1. Blaisdell, J. A., Hochreiter, L. E., and Waring, J. P., "PWR FLECHT-SET Phase A Report," WCAP-8838. December, 1973.

The t_{q6ft} correlation of WCAP-8838 is given by

$$
\begin{aligned}
t_{q6ft} = {} & 98.39\ [\exp(-0.0107\ \Delta T_{sub})\ \{1 - \exp(-0.667\ V_{in})\} \\
& \cdot \{1 + 0.5 \exp(-0.000037p^3 + 1.3 \exp(-0.111\ V_{in}{}^2) \\
& + 17.3 \exp(-0.000037p^3) \exp(-0.49\ V_{in}{}^2)\}\ (1.207\ Q'_{maxtq}{}^{1.5} - 0.667) \\
& + \{3.28/V_{in}{}^{1.1} - 2.8 \exp(-V_{in})\}\ \{1 + 0.5 \exp(-0.000037p^3)\}\ ] \\
& \cdot [1 + 0.0000588 T_{init} - 1.05 \exp(-0.0025\ T_{init})]\ [1 + 0.5/\ \{1 + \\
& 50^{**}\ (2 - 0.667\ V_{in})\}\ ]\ [1 + 0.32/\ \{1 + 50^{**}\ (5 - 0.1\ P)\}\ ]
\end{aligned}
\tag{6-2}
$$

where "**" denotes the exponentiaton to avoid possible confusion and

Q'_{maxtq} = equivalent peak power (kw/ft) obtained by multiplying Q'_{max} by the ratio of the time integrals of current power decay curve and power decay curve B, as given in WCAP-7665. If the radial power shape is uniform, Q'_{maxtq} is multiplied by the factor 1.1.

The quench time t_q (Z_q) at any elevation, Z_q, of any power shape can be computed from t_{q6ft} with Q_r as the parameter:

$$
t_q(Z_q) = \left[\frac{Z_q}{V_{in}} + \left\{ t_{q6ft}\ (Q_r + 0.8\ Q_r e^{-3.5Q_r}) - \frac{Z_q}{V_{in}} \right\} \Big/ \left(1 + 50^{**} \left\{ - \frac{T_{initeq}\ (Z_q) - 400}{400 - T_{sat}} \right\} \right] \right. f \tag{6-3}
$$

where t_{q6ft} is computed from equation (6-2) with Q'_{maxtq} replaced by Q'_{eq} and the peak initial cladding temperature T_{init} replaced by the local initial cladding temperature $T_{init}(Z_q)$, which are defined by:

$$
Q'_{eq} = Q'_{maxtq}\ Q_r \tag{6-4}
$$

$$T_{init}(Z_q) = (T_{init} - T_{sat})\ F(Z_q) + T_{sat} \tag{6-5}$$

where

T_{init} = initial cladding temperature at the peak power location.

$F(Z)$ = power at the elevation Z divided by peak power Q'_{max}

and f is given by

$$f = 1 + 1.5\ [1 - \exp\left\{-1.613\ (Q'_{eqmax} - 1.25)\right\}\ ]$$

$$/[1 + 50^{**}\ \left\{-80\ (Q'_{eqmax} - 1.25)\right\}\ ] \tag{6-6}$$

where

$Q'_{eqmax} = Q'_{maxtq}\ Q_r(Z_{max})$

Z_{max} = peak power elevation

In heat transfer calculation, it is necessary to compute the quench front elevation, Z_q, as a function of time, t. This can be accomplished by first computing the quench front velocity V_q

$$V_q = \frac{(Z_q+\Delta Z_q) - Z_q}{t_q(Z_q+\Delta Z_q) - t_q(Z_q)} \tag{6-7}$$

where $t_q(Z_q+\Delta Z_q)$ and $t_q(Z_q)$ are the quench time computed from equation (6-3). Then compute the quench front elevation Z_q by

$$Z_q = \int_o^t V_q dt \tag{6-8}$$

$$Z_q(t+\Delta t) = Z_q(t) + V_q \Delta t \tag{6-8a}$$

It should be noted that the time t in equation (6-8) is not necessarily the same as the quench time t_q which is computed from equation (6-3). For a constant flooding rate case, t and t_q are identical. For a variable flooding rate case, however, t and t_q are different. This can be illustrated by considering a variable flooding rate case with flooding rate V_{in1} at an early time and V_{in2} after time t_A (figure 6-2(a)). The Z_q versus t_q curve computed from equation (6-3) with the constant flooding rate V_{in1} is represented by the curve OAC; with constant flooding rate V_{in2} is represented by the curve OA'A''B', as shown in figure 6-2(b)). If we assume that for the variable flooding rate shown in figure 6-2(a) the actual time t is equal to t_q, then the Z_q versus t curve would be OAA''A'B' with a discontinuity of Z_q at the time t_A which is physically unrealistic.

The continuity of Z_q can be preserved by the method described above. At $t=t_A$, first compute the quench front velocity V_{qA} from equation (6-7).

$$V_{qA} = \frac{(Z_{qA}+\Delta Z_q) - Z_{qA}}{t_q(Z_{qA}+\Delta Z_q) - t_q(Z_{qA})} \tag{6-9}$$

then compute the quench front elevation by equation (6-8) or (6-8a)

$$Z_q(t_A+\Delta t) = Z_{qA} + V_{qA}\Delta t \tag{6-10}$$

This is equivalent to shifting the curve A'B' to AB (that is, to shift the curve O A'B' to O'AB). Thus, for the time larger than t_A, the actual time t is not equal to t_q, but t and t_q are related by

$$t = t_q - (\Delta t)_{shift} \tag{6-11}$$

where $(\Delta t)_{shift}$ is the time shift represented by O'O in figure 6-2(b). It is apparent from figure 6-2 that t_q is the effective quench time if the flooding rate is constant at $V_{in} = V_{in2}$ from time O' to time t. The time shift $(\Delta t)_{shift}$ (= O'O) is due to the extra mass of water, $V_{in1} - V_{in2}$, which is injected into the bundle during the time interval $0 \leqslant t \leqslant t_A$ as indicated by the shaded area in figure 6-2(a). Thus the computation with equations (6-7) and (6-8) or (6-8a) leads to a physically meaningful result.

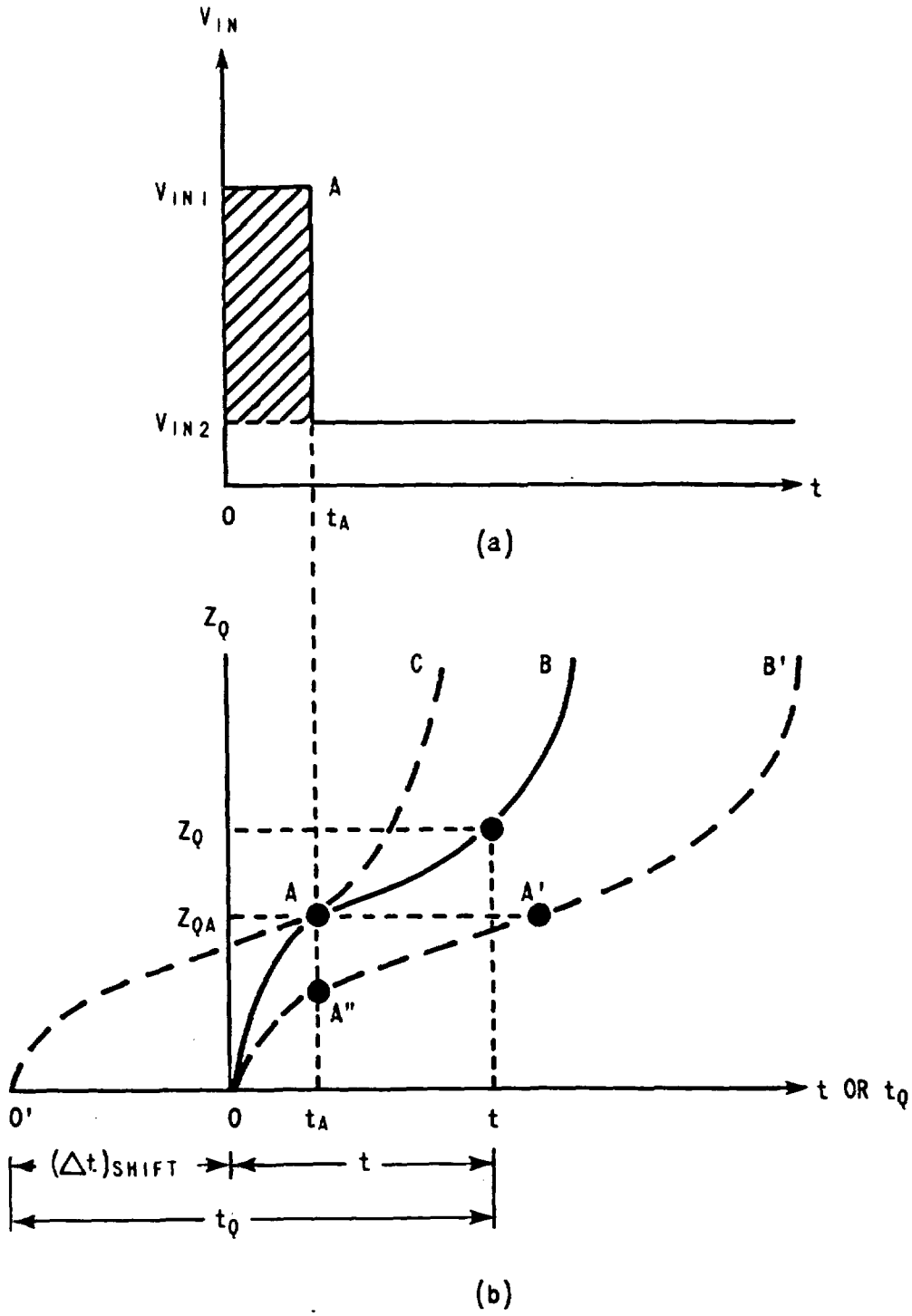

Figure 6-2. Schematic of the Quench Front Elevation Versus Time Curves

The quench correlation has been compared with both skewed and cosine data and satisfactory agreement has been obtained. Two such comparisons are illustrated for reference Runs 02833 (figure 6-3) and 15305 (figure 6-4). In general the correlation is more accurate at lower bundle elevations corresponding to earlier quench times. This is due partly to basic differences in measured quench data between skewed and cosine power profiles. For example, the 12-foot-elevation in the cosine test tends to quench prior to 10 and 11 feet. This trend is not as pronounced for the skewed profile run. Also the skewed quench curve is more linear than the corresponding cosine quench curve. This different behavior is due to the difference in power shape which has been handled properly in the correlation. Further samples of the quench correlation comparison with data are found in appendix E where fourteen figures illustrate changes in quench time for a given parametric variation in run conditions for both cosine and skewed tests.

6-3. HEAT TRANSFER COEFFICIENT CORRELATION (THE h-CORRELATION)

The heat transfer coefficient correlation is divided into three parts:

- The Early Developing Period

  This period extends from the beginning of flooding to the time when the heat transfer reaches a guasi-steady state (figure 6-5). During this developing period the heat transfer mechanism changes from the radiation-dominated prereflood condition to the single-phase steam flow. The mechanism then changes to the dispersed flow when the steam velocity becomes great enough to carry droplets up the bundle. These changes were indicated in the movies taken during the FLECHT test by the appearance of the first droplet. Figure 6-6 shows that the heat transfer coefficient starts to increase at the time of first droplets observed. Figure 6-7 shows that the time of first droplets is primarily a function of flooding rate. For low flooding rate (< 3 in./sec) the dispersed flow eventually becomes a quasi-steady state. For high flooding rate (> 3 in./sec) the heat transfer mechanism further develops into the unstable film boiling which becomes a quasi-steady state.

- The Quasi-Steady Period

  During this period the heat transfer is essentially in a quasi-steady state. This means that the heat transfer pattern moves with the quench front, that is, the heat transfer coefficient versus the distance from the quench front is essentially unchanged with time.

- Heat Transfer Coefficient Above the Peak Cladding Temperature Elevation

  The situation for the elevation above the peak cladding temperature elevation is different from that below the peak cladding temperature elevation and therefore must be treated separately. Above the peak cladding temperature elevation the steam temperature may be greater than the cladding surface temperature, and the heat may be transferred from the steam to heater

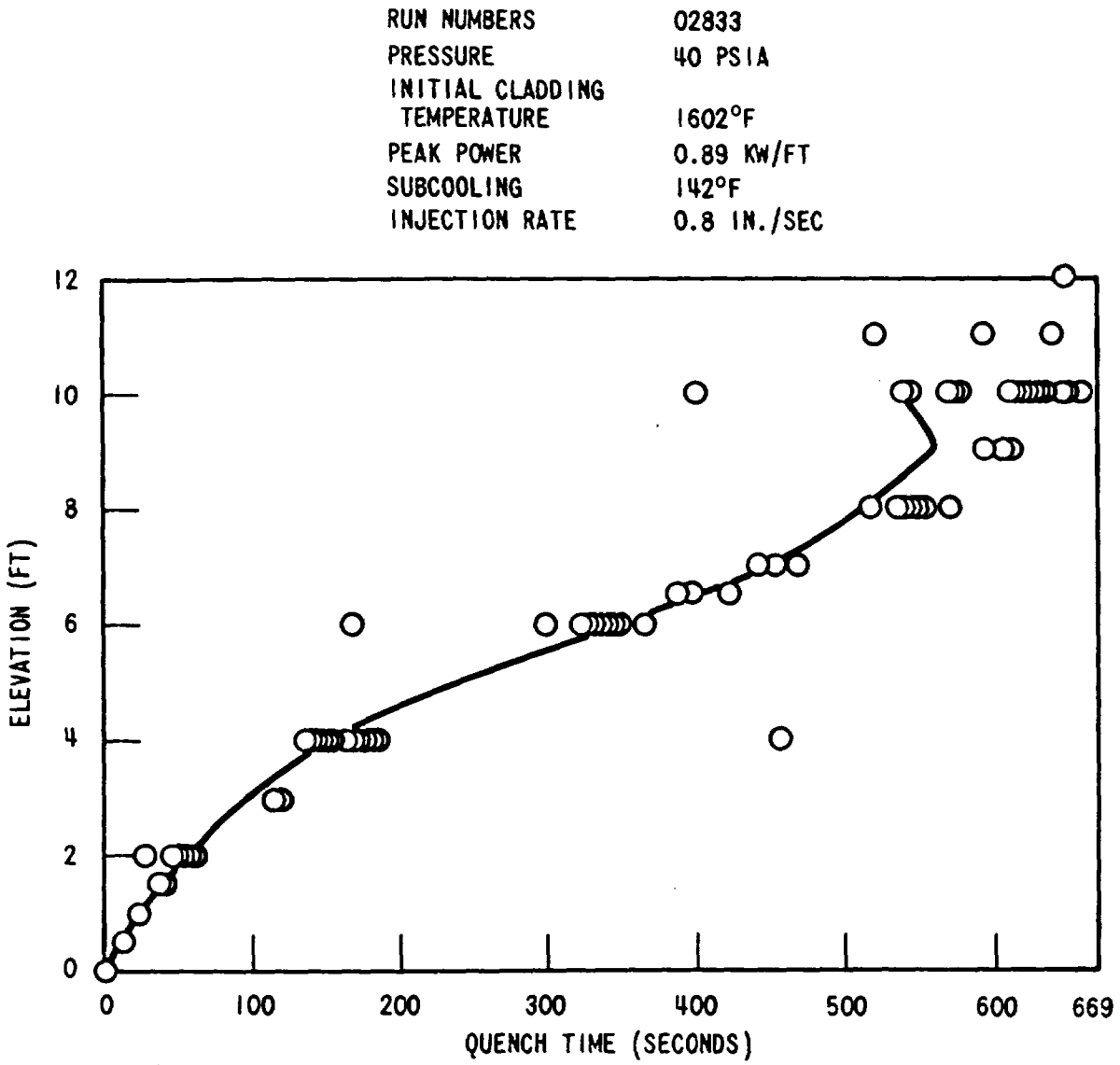

Figure 6-3. Comparison of Predicted and Measured Quench Elevation Versus Quench Time for Run Number 02833

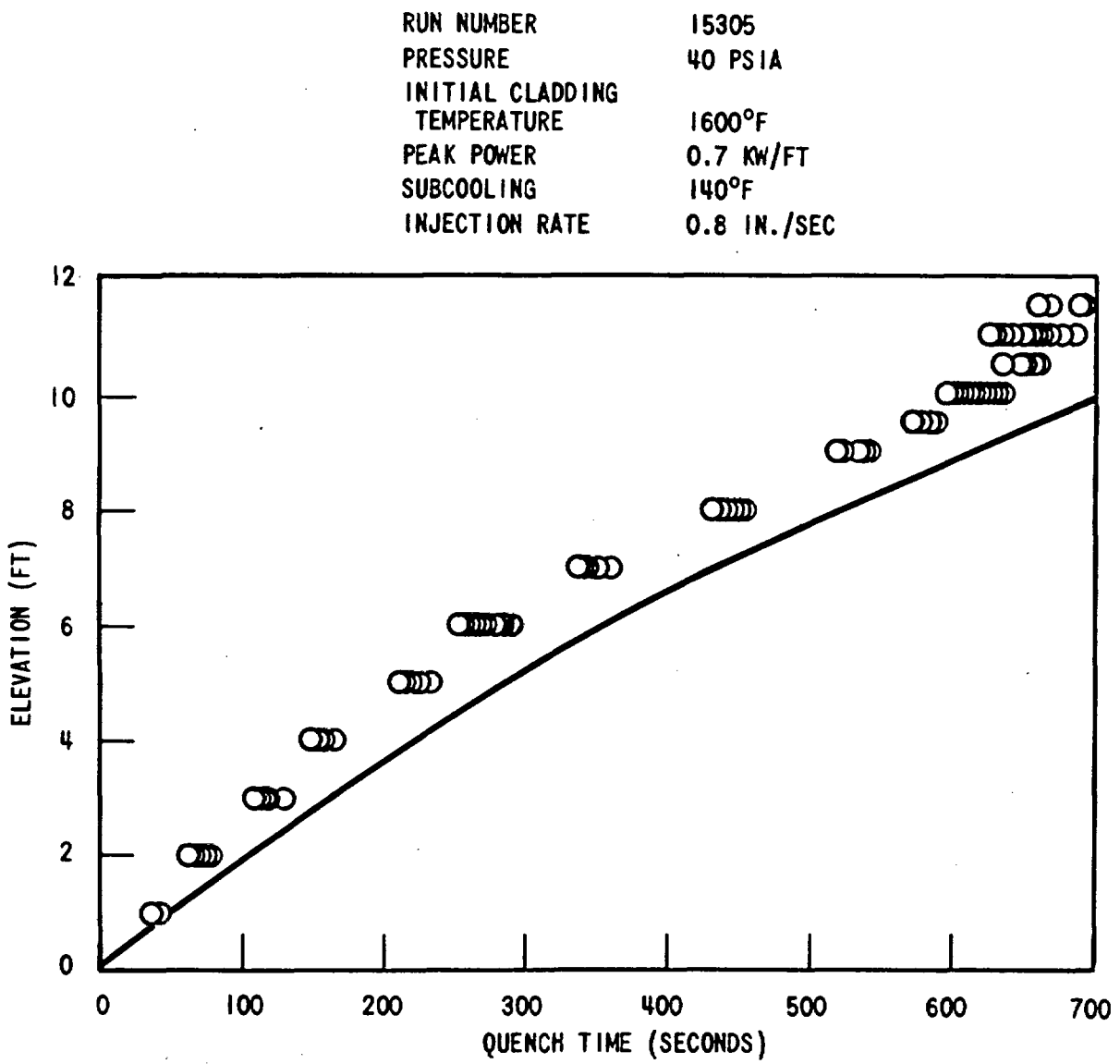

Figure 6-4. Comparison of Predicted and Measured Quench Elevation Versus Quench Time for Run Number 15305

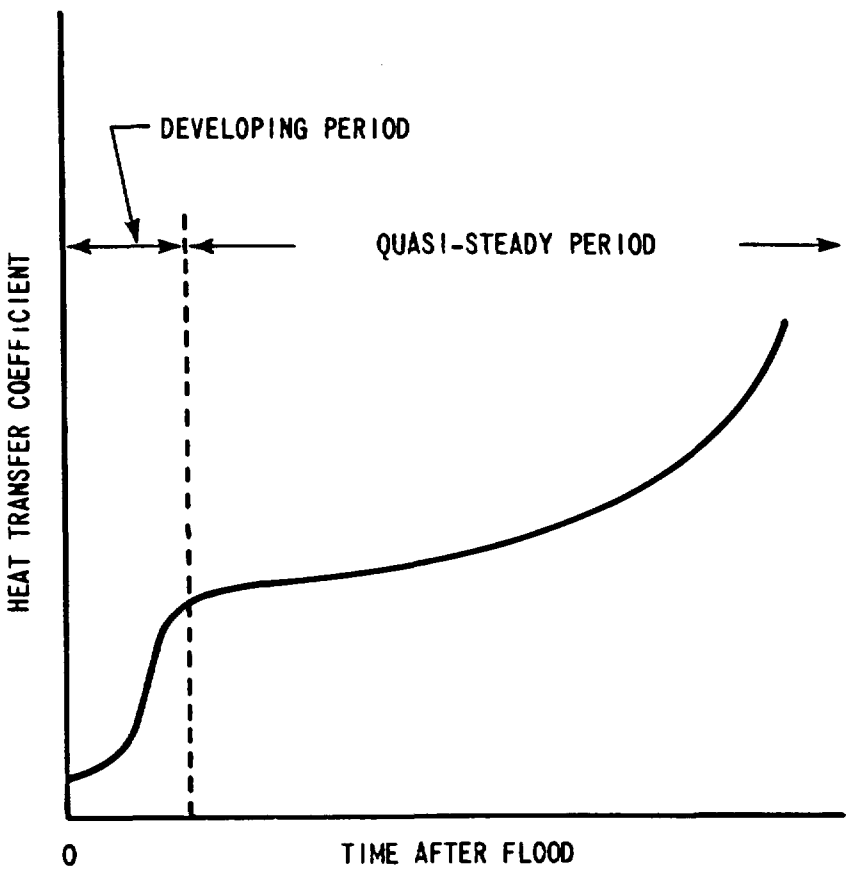

Figure 6-5. Graph Showing the Heat Transfer Coefficient in Developing Period and Quasi-Steady Period

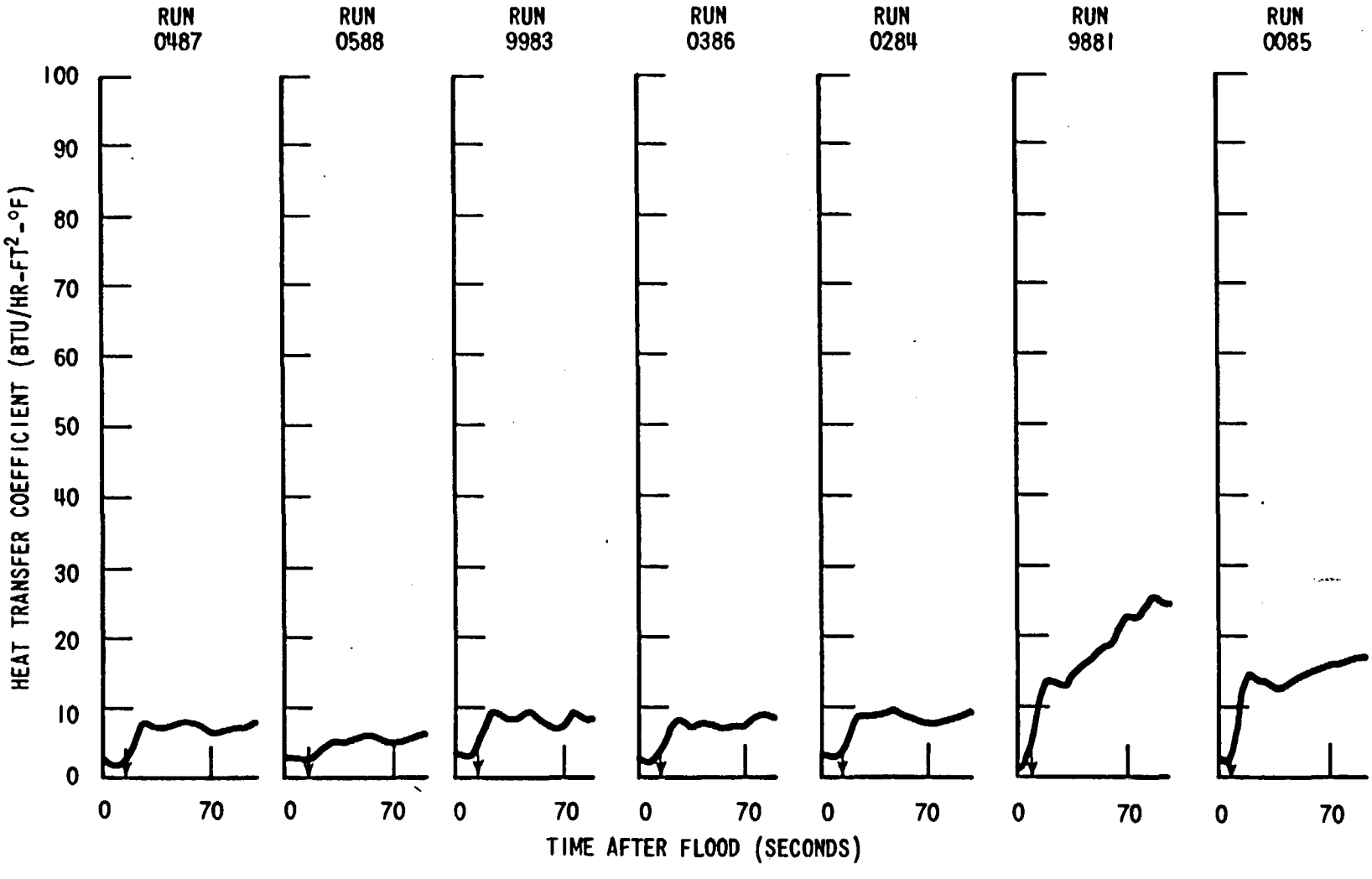

Figure 6-6. Comparison of the Time of First Droplet Observed in FLECHT Movies (Indicated by Arrows) and the Time When Heat Transfer Coefficient Starts to Increase (Sheet 1 of 2)

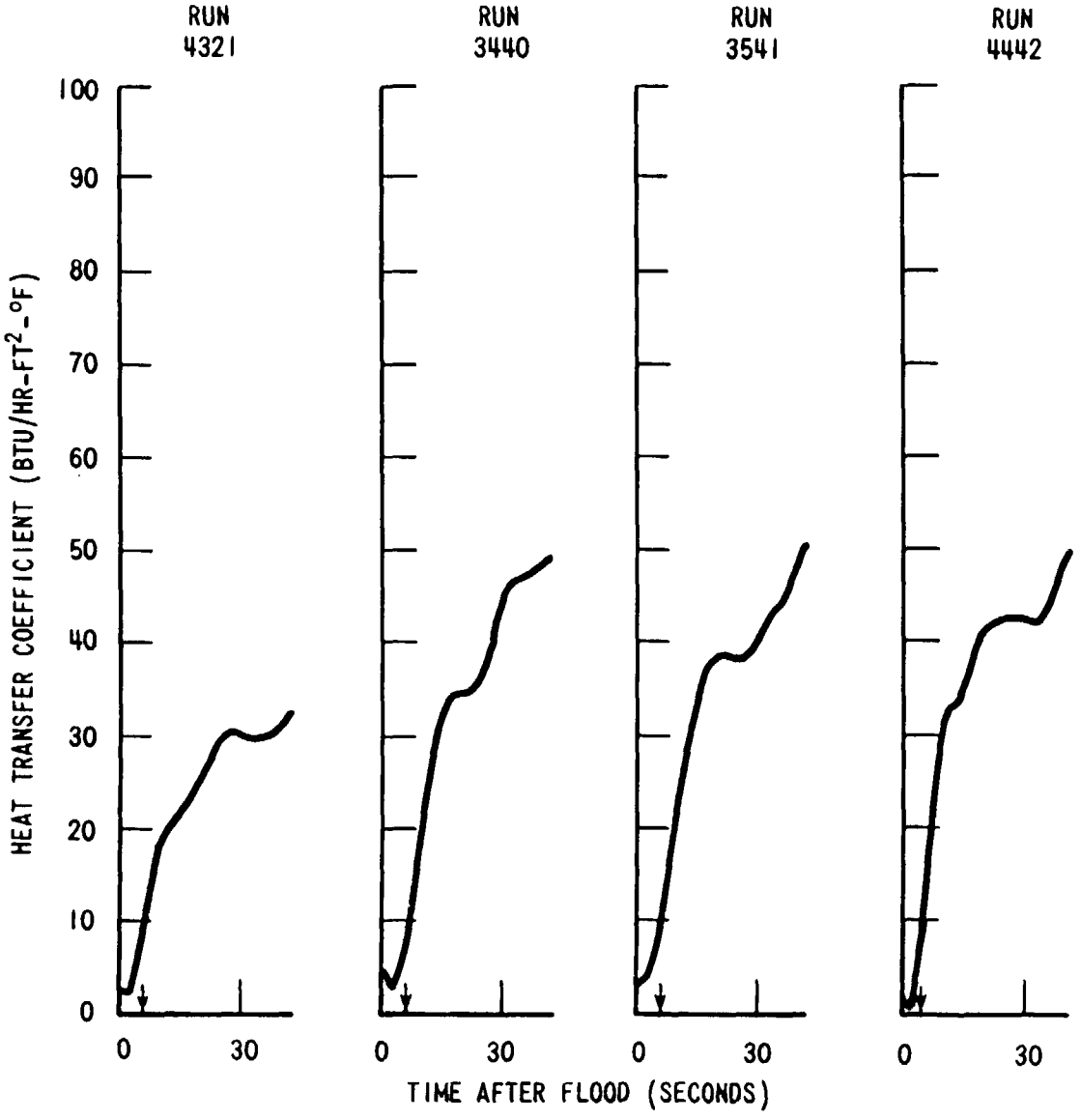

Figure 6-6. Comparison of the Time of First Droplet Observed in FLECHT Movies (Indicated by Arrows) and the Time When Heat Transfer Coefficient Starts to Increase (Sheet 2 of 2)

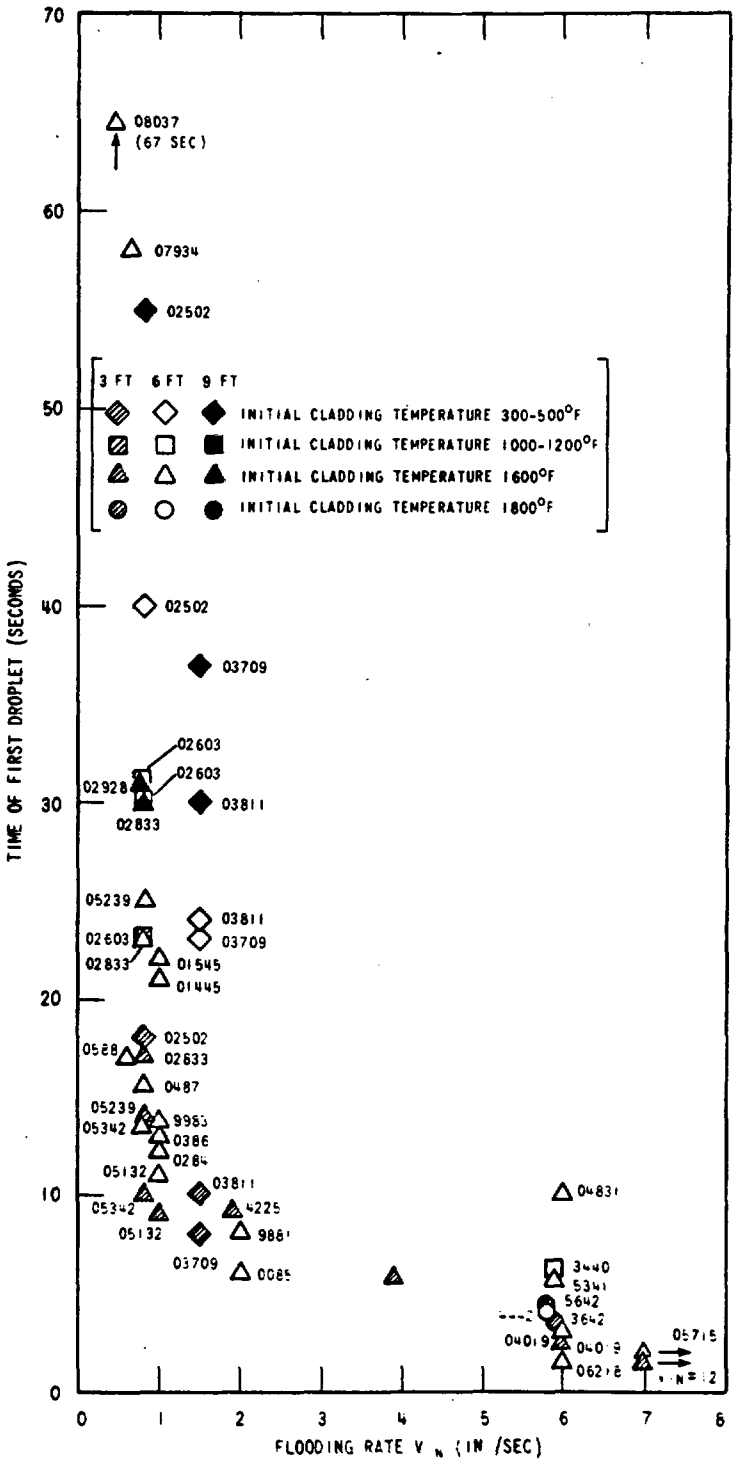

Figure 6-7. Time of First Droplet Observed in FLECHT Movies

rods. The FLECHT definition of heat transfer coefficient, (saturation temperature equal to sink temperature.) implies that the heat transfer coefficient is negative. Below the peak cladding temperature elevation the steam temperature never becomes greater than the cladding surface temperature. Therefore the heat transfer coefficient never becomes negative.

Figures 6-8 and 6-9 show that heat transfer coefficient increases with time during the early developing period. Figures 6-10 and 6-11 show that the heat transfer coefficient versus the distance from the quench front is practically unchanged during the quasi-steady period except above peak cladding temperature elevation. Figures 6-8 through 6-11 show that the heat transfer coefficient decreases as the distance from the peak cladding temperature elevation increases.

The three parts of the heat transfer correlation are as follows: (The transition between the developing period and the quasi-steady period occurs when Z_q is equal to Z_s, which is defined below.)

- Developing Period ($Z_q \leq Z_s$)

$$h = h_1 [1 - \exp(2.5\,x-10)] + [h_2 - h_1 \{1 - \exp(2.5\,x-10)\}] [1 - e^{-x} - 0.9\,xe^{-x^2}] \quad (6\text{-}12)$$

where

$$Z_s = 1.833\, V_{in}\ ^{**}\ (0.5466 - 0.426\, V_{in})$$

$$x = 4\, Z_q/Z_s$$

$$h_1 = 3.67\, Q'(Z) [1 - \exp - (T_{init}(Z) - 700)/435]$$

$$h_2 = h_3 + 38 \exp(-0.15\, V_{in}) \exp\{-1.2\,(Z-Z_q)\}$$

$$h_3 = 46 [1-\exp(-0.25\, V_{in})] [0.714 + 0.286 (1 - e^{-1.8P/V_{in}^2})]$$

and Z_q (ft) is the quench front elevation, V_{in} (in./sec) is the flooding rate, and $Q'(Z)$ (kw/ft) and T_{init} (Z) (°F) are the linear power and the initial cladding temperature at elevation Z at the beginning of reflood.

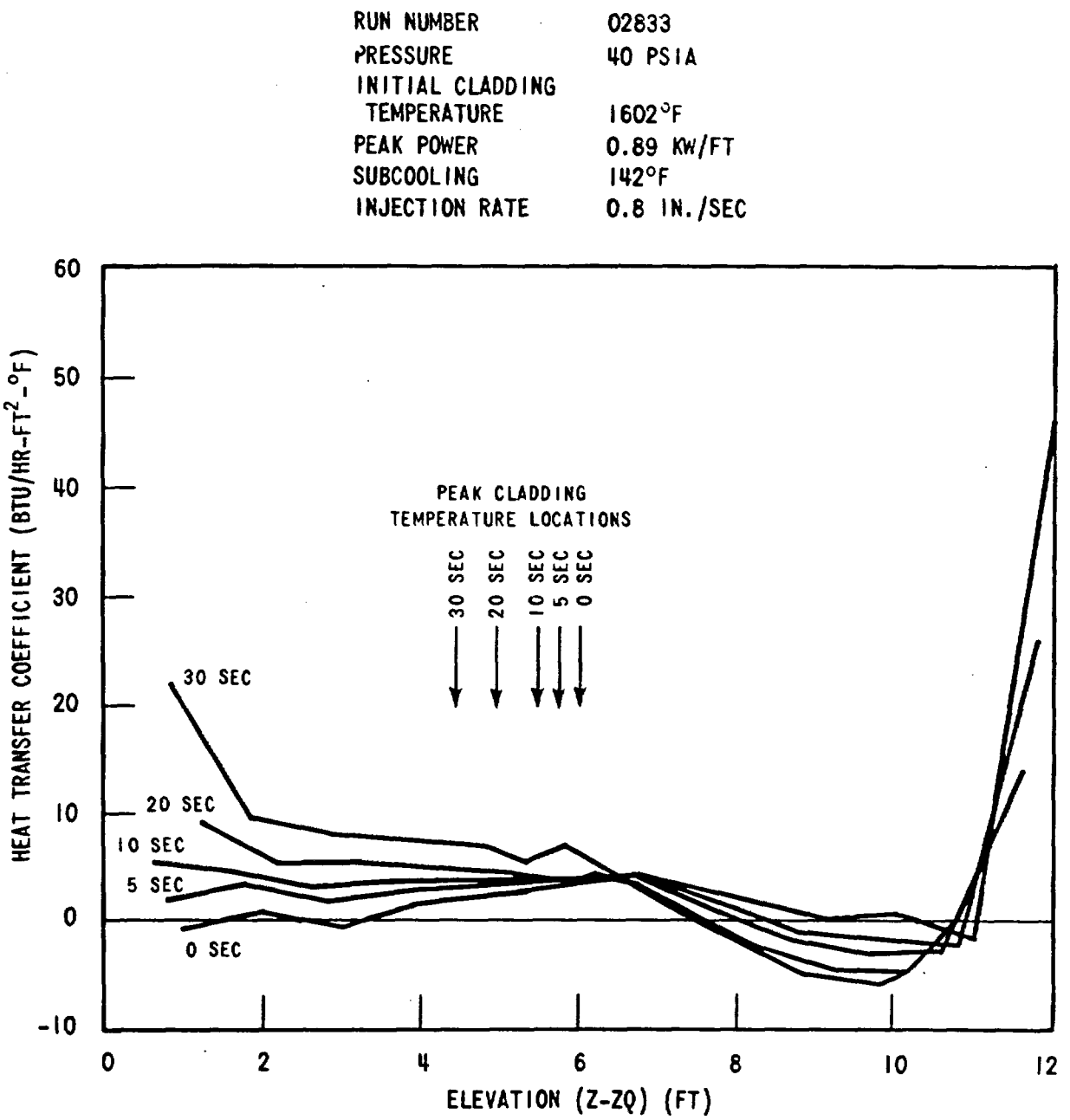

Figure 6-8. Heat Transfer Coefficient Versus Distance from Quench Front in Developing Period for Run Number 02833, the Peak Cladding Temperature Location is Shown by Arrows

RUN NUMBER	15305
PRESSURE	40 PSIA
INITIAL CLADDING TEMPERATURE	1603°F
PEAK POWER	0.7 KW/FT
SUBCOOLING	140°F
INJECTION RATE	0.8 IN./SEC

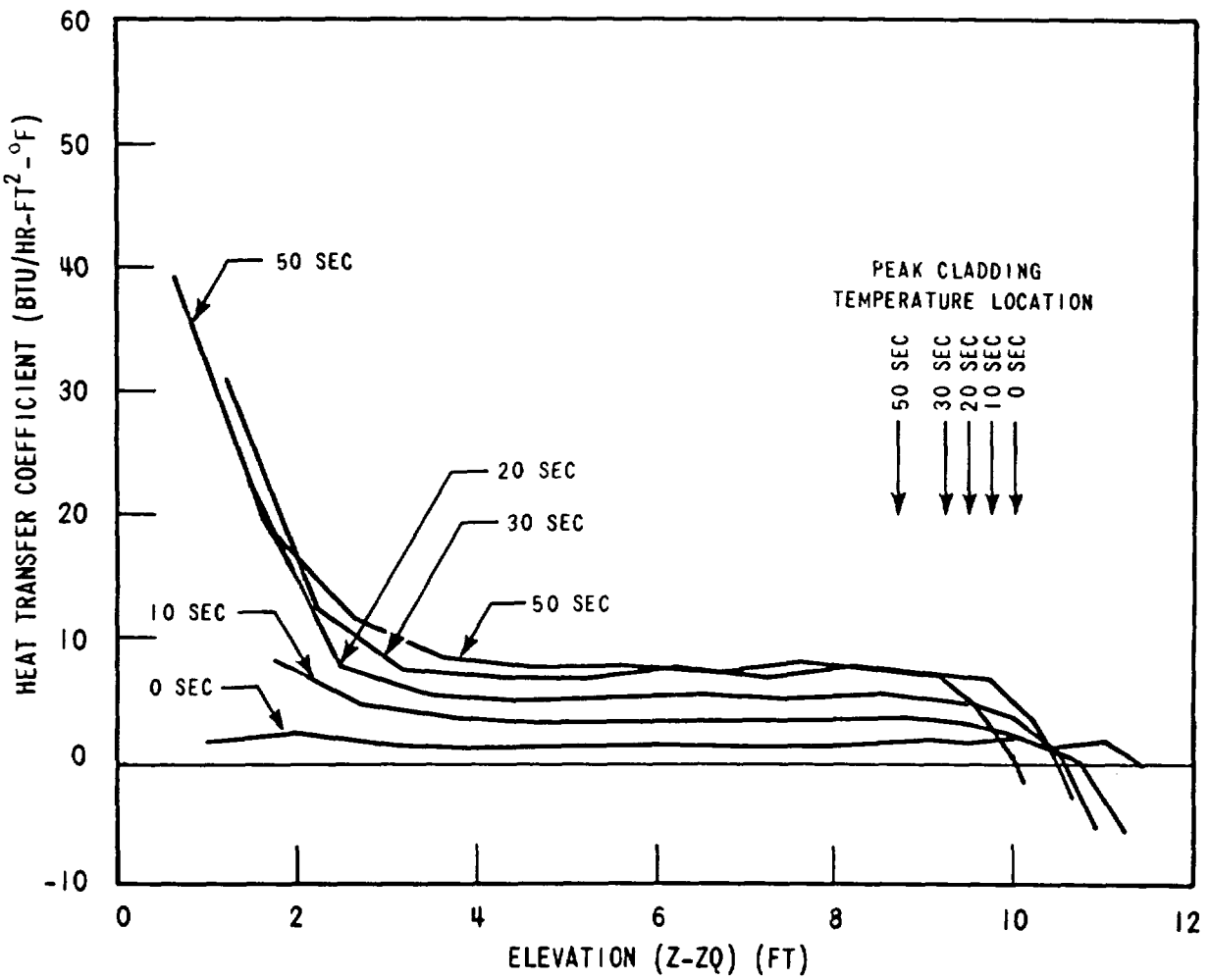

Figure 6-9. Heat Transfer Coefficient Versus the Distance from Quench Front Versus Developing Period for Run Number 15305, the Peak Cladding Temperature Location is Shown by Arrows

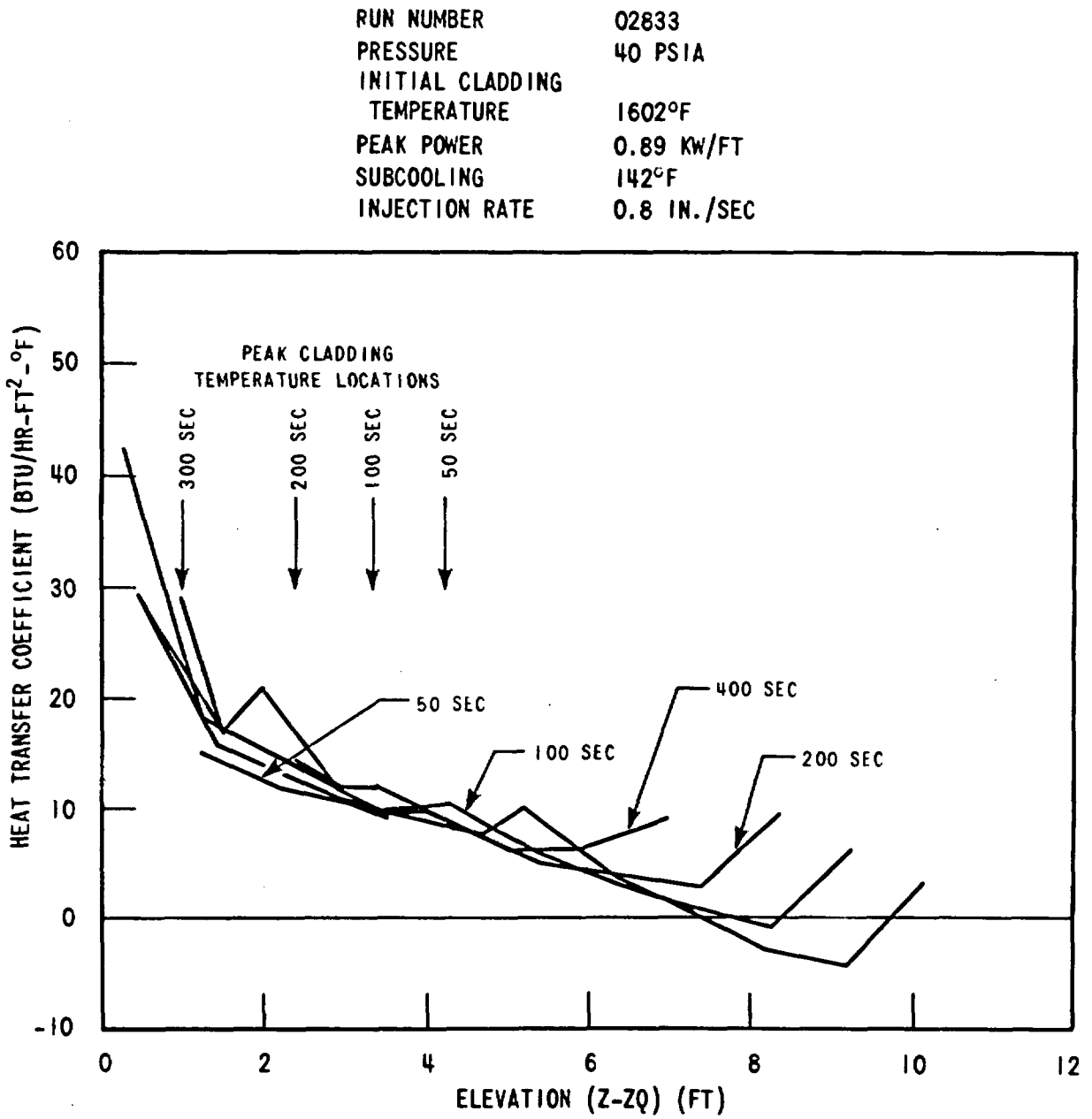

Figure 6-10. Heat Transfer Coefficient Versus the Distance from Quench Front in Quasi-Steady Period for Run Number 02833, the Peak Cladding Temperature Location is Shown by Arrows

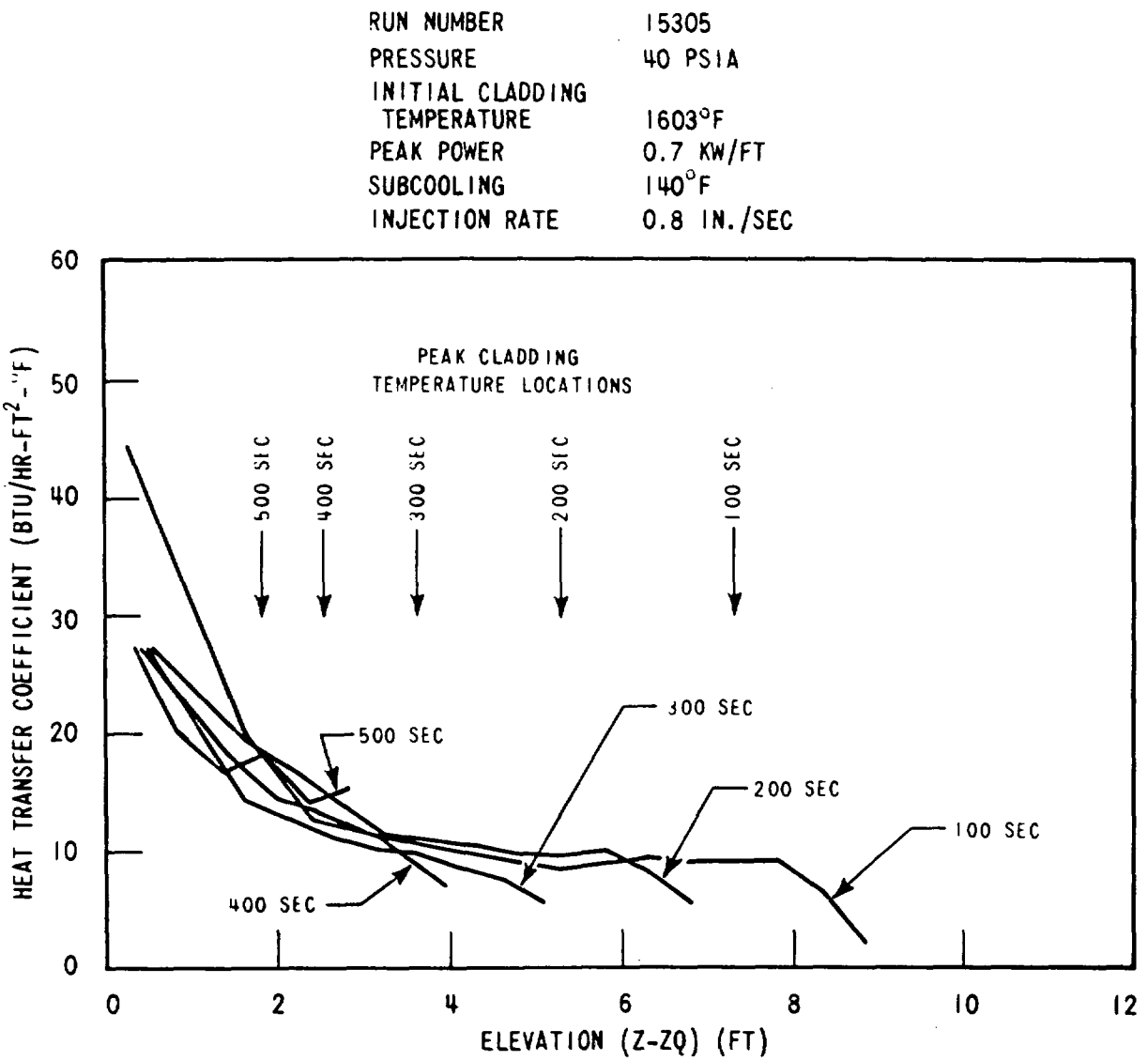

Figure 6-11. Heat Transfer Coefficient Versus the Distance from Quench Front in Quasi-Steady Period for Run Number 15305, the Peak Cladding Temperature Location is Shown by Arrows

- Quasi-steady Period ($Z_q > Z_s$)

$$h = h_2 \tag{6-13}$$

In the quasi-steady period the heat transfer coefficient is practically independent of time. Therefore the expression for the heat transfer coefficient is less complicated.

- Above Peak Elevation ($Z > Z_{peak}$)

$$h = h_4 - 15.594 \left[1 - \frac{Q'(Z)}{Q'(Z_{peak})}\right] \exp\left\{-0.0683 (Z - Z_{peak})\right\} \tag{6-14}$$

where h_4 is the heat transfer coefficient computed either from equation (6-11) or (6-12), depending on the period, at the peak cladding temperature elevation Z_{peak}.

A data reduction code, ALLTURN, was written to plot the average heat transfer coefficient and associated standard deviation as a function of distance from the quench front. The h versus $Z - Z_q$ correlation was also incorporated with this code to facilitate comparisons between data and correlation.

Two different groups of thermocouple data are used in ALLTURN depending upon the radial power profile. If the radial power profile is uniform then all good channels within the inner 6 x 6 array are used to calculate an average quench time and average heat transfer coefficient. In the case of the FLECHT radial power profile, the reduction scheme manipulates only the 1.1 power rod thermocouple data within the inner 6 x 6 array.

Figures 6-8 to 6-11 were included to show developing and quasi-steady state periods. Selected times have been extracted from these curves and replotted with the predicted heat transfer $Z - Z_q$ correlation as shown in figures 6-12 through 6-14 (Run 02833) and figures 6-15 through 6-17 (run 15305). Several oddities can be found in figures 6-12 to 6-14. First, the heat transfer rises abruptly at a large $Z - Z_q$. This effect is caused by a thermocouple at the 12-foot elevation (where the rod temperature is low) which quenches early. Secondly, the stepped nature of the correlation curve is due to the stepped axial power profile shape used in the FLECHT tests. In practical application to a reactor, the step change will not occur, as the axial power shape of the reactor is generally smooth.

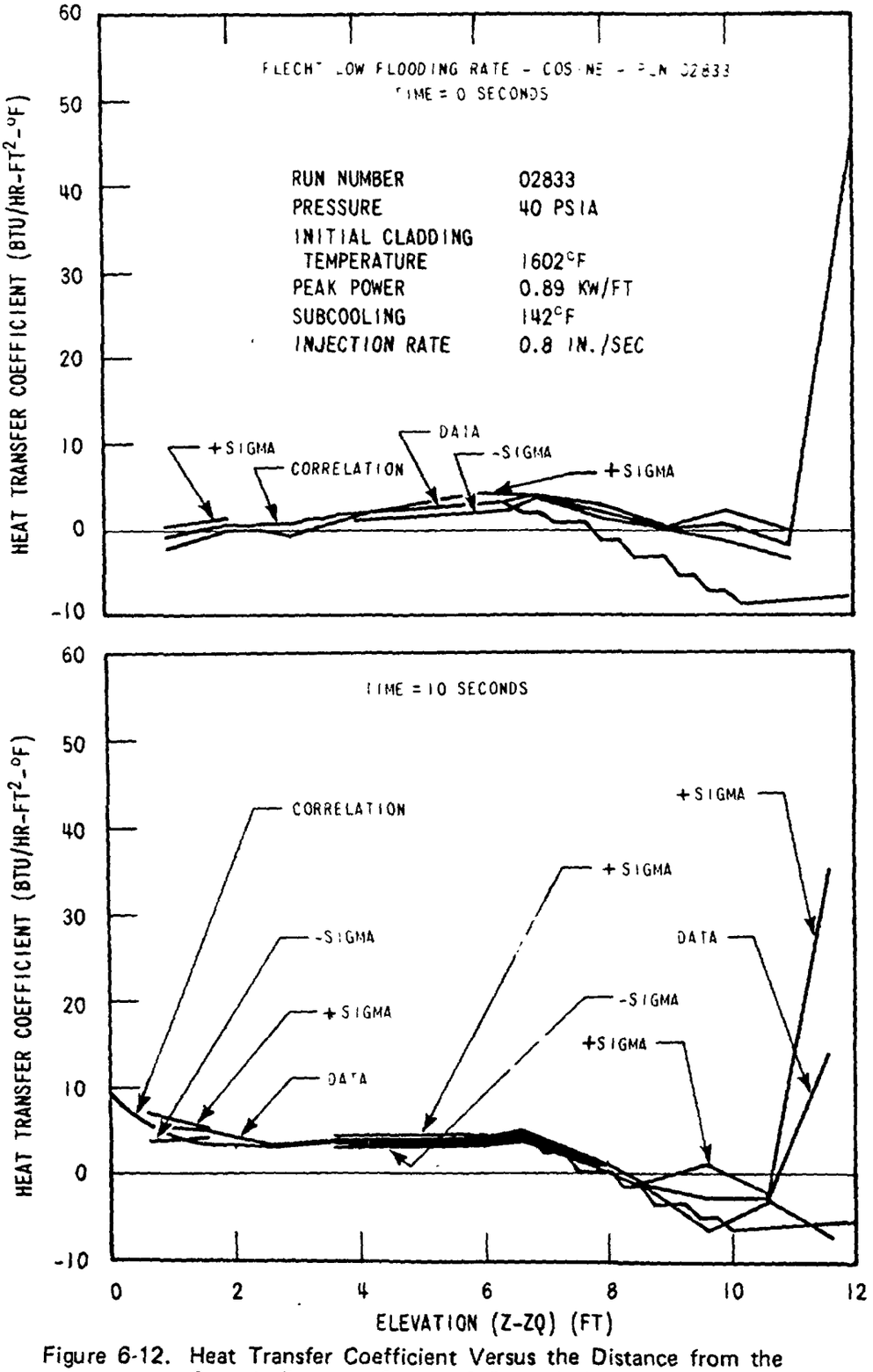

Figure 6-12. Heat Transfer Coefficient Versus the Distance from the Quench Front at 0 and 10 Seconds for Run Number 02833

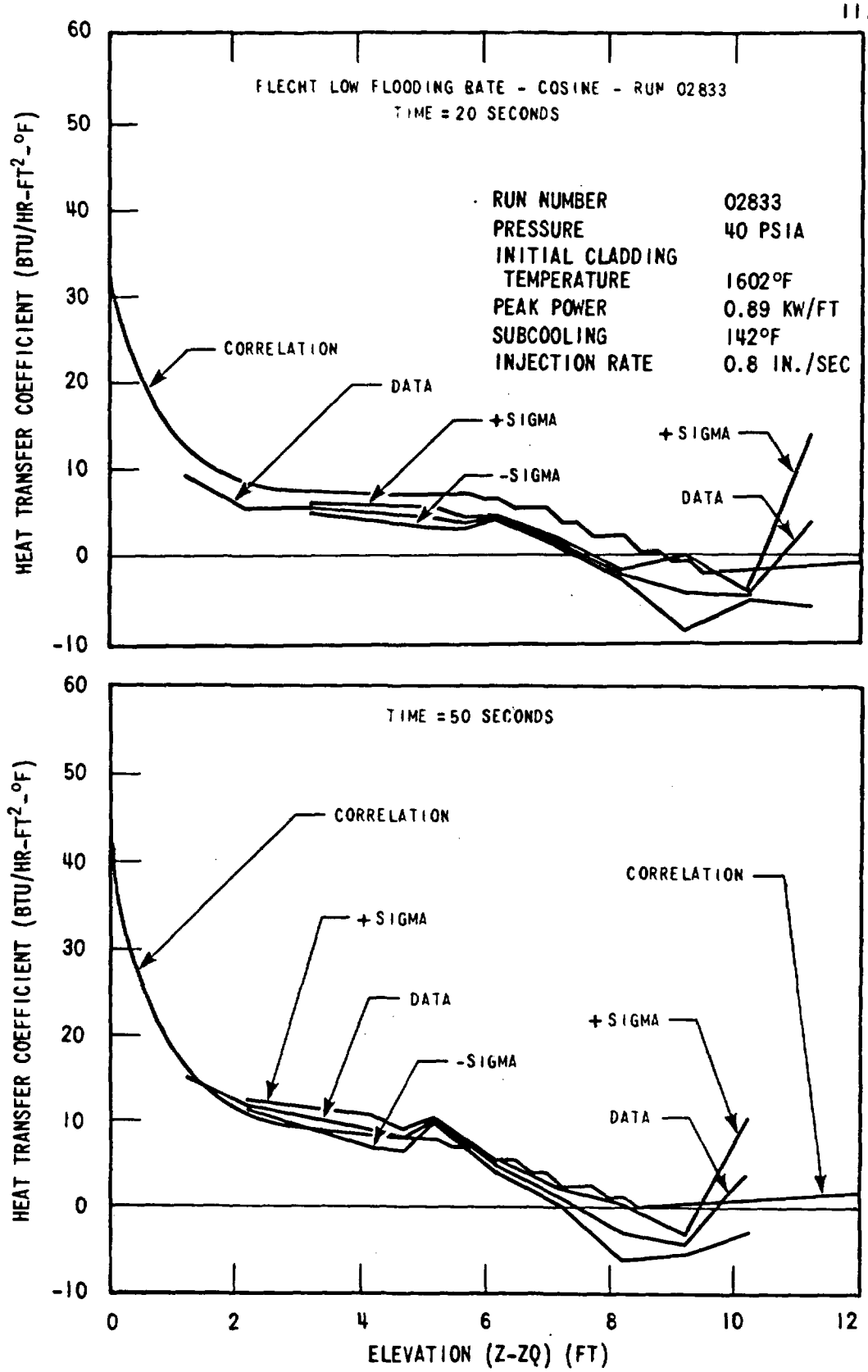

Figure 6-13. Heat Transfer Coefficient Versus the Distance from the Quench Front at 20 and 50 Seconds for Run Number 02833

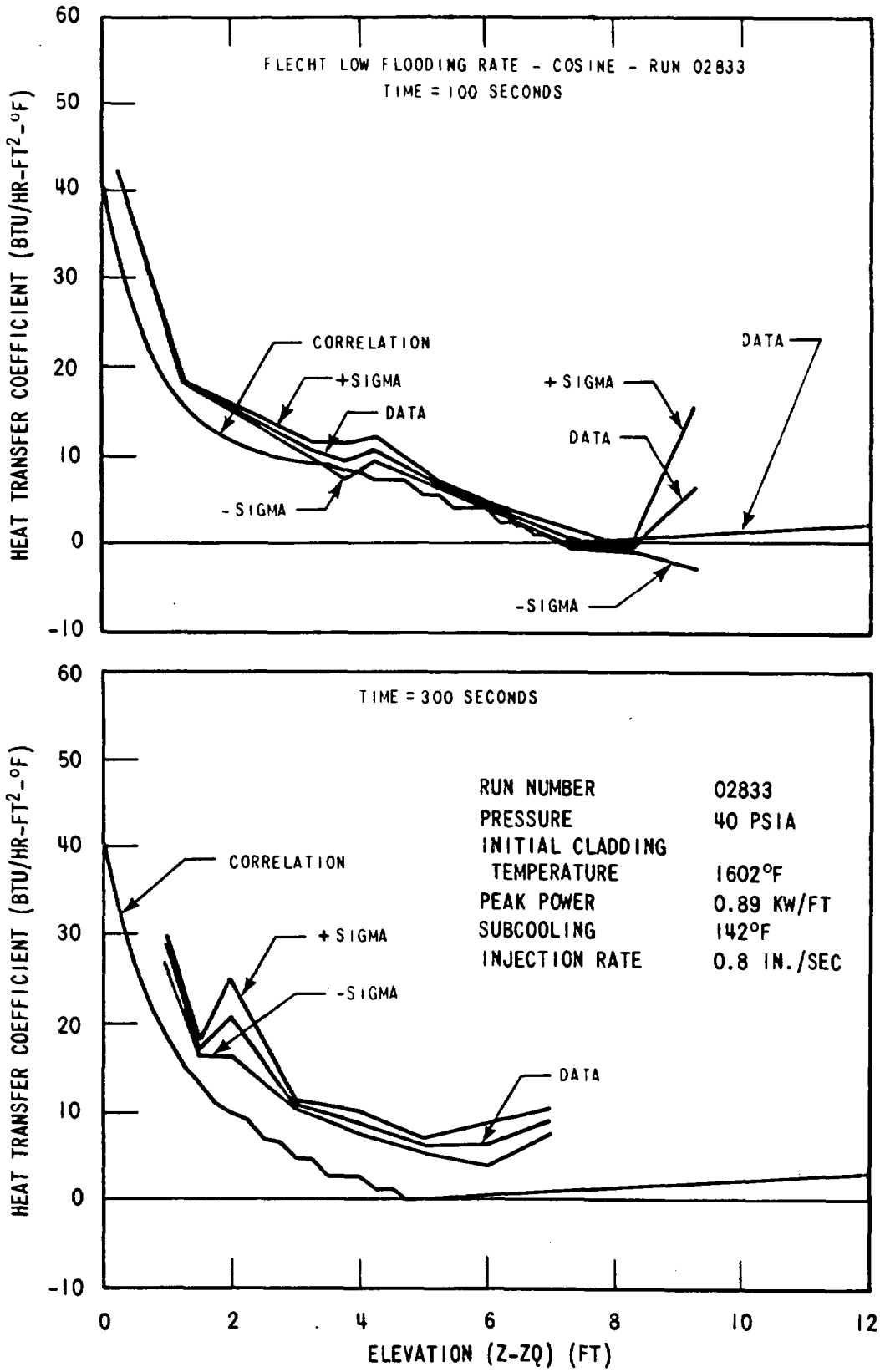

Figure 6-14. Heat Transfer Coefficient Versus the Distance from the Quench Front at 100 and 300 Seconds for Run Number 02833

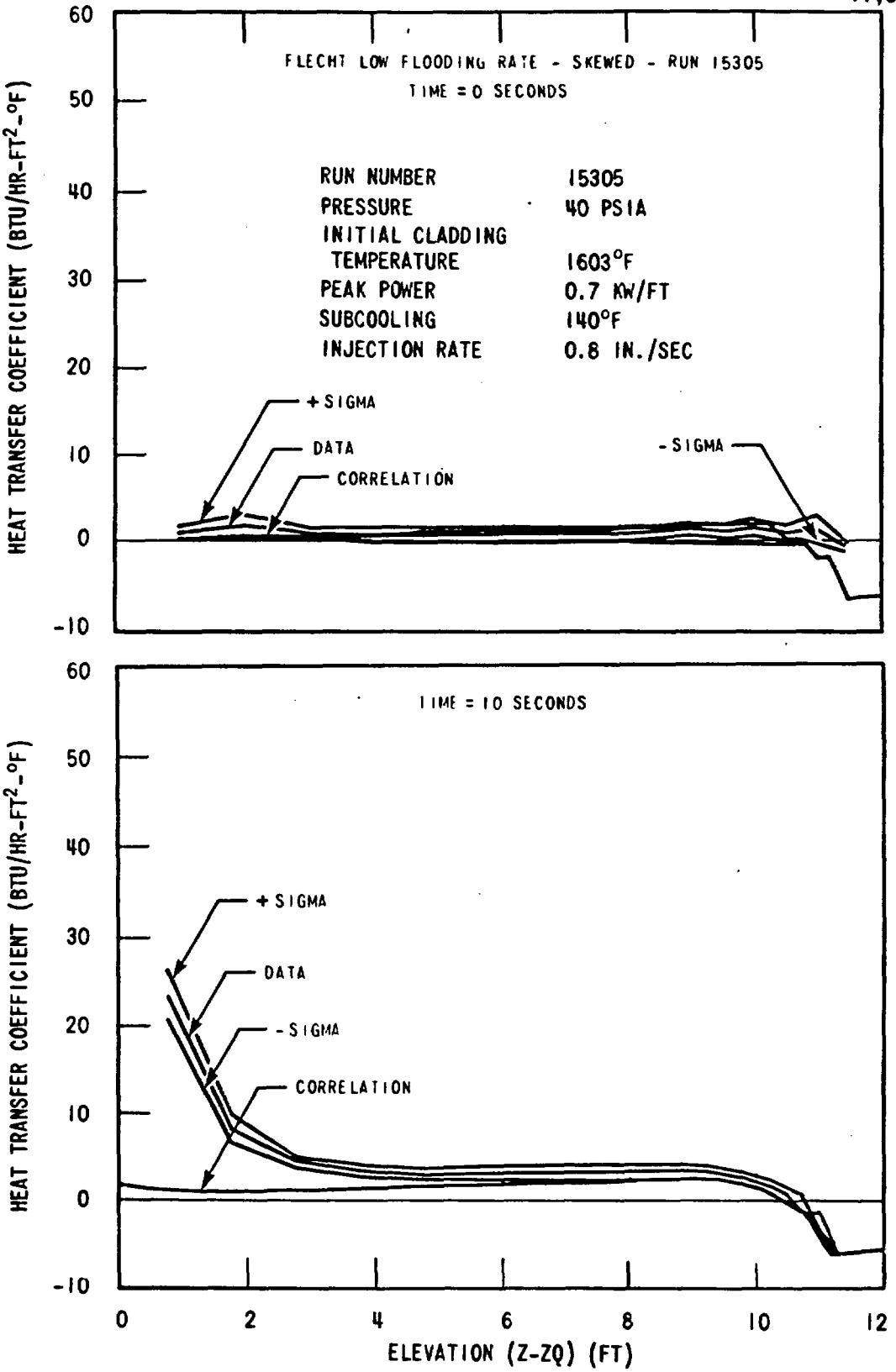

Figure 6-15. Heat Transfer Coefficient Versus the Distance from the Quench Front at 0 and 10 Seconds for Run Number 15305

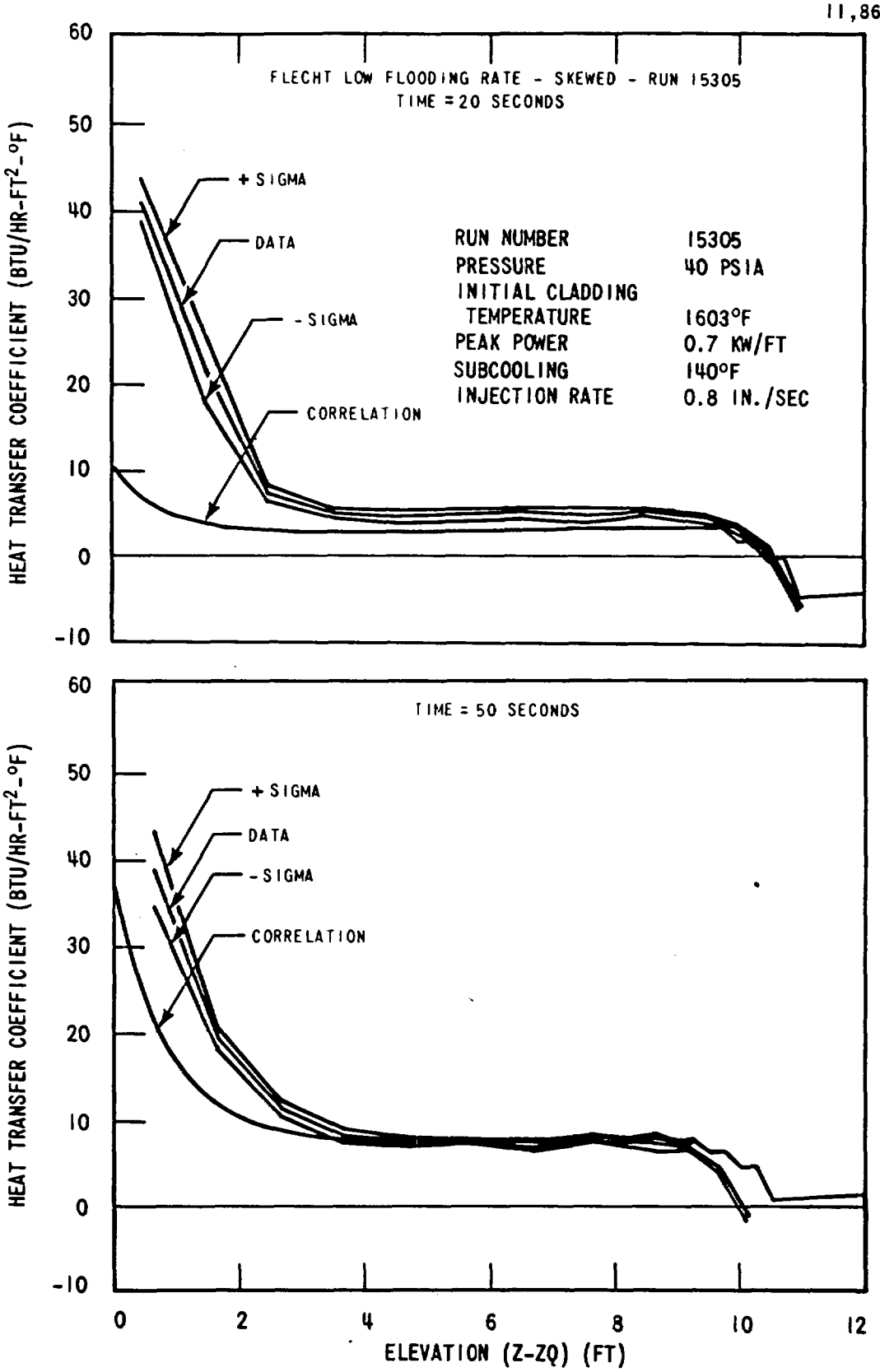

Figure 6-16. Heat Transfer Coefficient Versus the Distance from the Quench Front at 20 and 50 Seconds for Run Number 15305

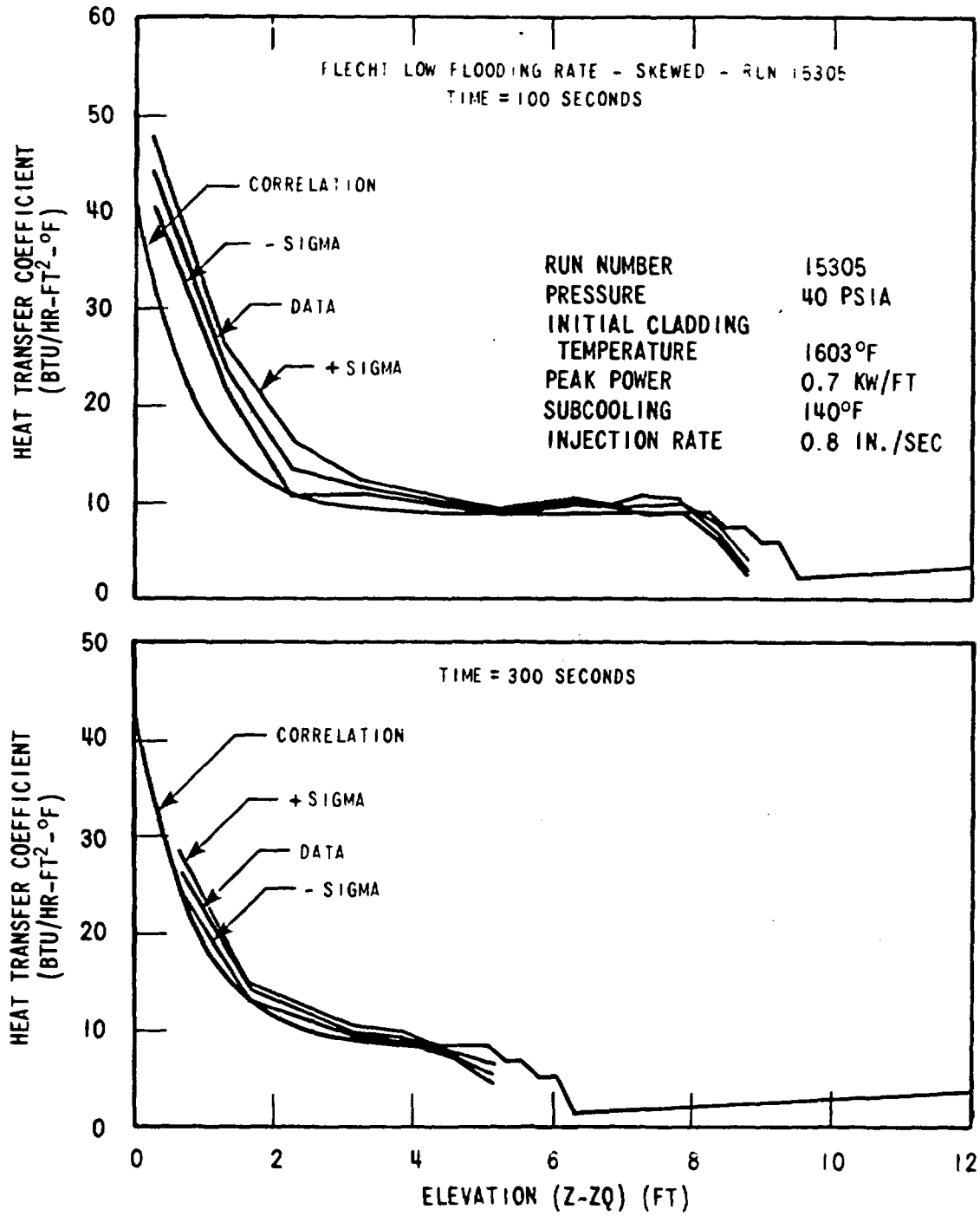

Figure 6-17. Heat Transfer Coefficient Versus the Distance from the Quench Front at 100 and 300 Seconds for Run Number 15305

Figures 6-12 through 6-17 show that the correlation can predict both skewed and cosine power heat transfer within reasonable accuracy. The correlation is generally conservative or falls within one standard deviation of the data. Further comparisons included in appendix E illustrate the effect of flooding rate, pressure, subcooling, initial temperature and power on correlation versus data agreement. Appendix E also contains two high flooding rate tests which show that the grids increase heat transfer significantly. Low flooding rate data do not show this trend.

Of more general interest and practical use is a heat transfer coefficient versus time-history at one elevation. The $Z - Z_q$ correlation, unlike previous FLECHT correlations, predicts heat transfer from space variables alone. However heat transfer versus time predictions can be easily obtained from the $Z - Z_q$ methodology if suitable quench data or quench time correlation is available. In figures 6-18 and 6-19, the quench correlation and $Z - Z_q$ correlation are combined to predict heat transfer as a function of time at the peak power elevation for Runs 02833 and 15305, respectively. The old FLECHT correlation was plotted for cosine Run 02833 and acceptable agreement was obtained.

A listing of the new correlation, which calculates h versus $Z - Z_q$, is given in appendix F. In addition, an example of the calculation for both a skewed profile test and a cosine test is given.

In case of any disagreement between the equations above and appendix F, the latter listing should be considered the correct version.

6-4. CONCLUSION

This section presents a new heat transfer correlation which is rather general and is applicable to all power shapes. The new heat transfer correlation is based on the idea that the heat transfer coefficient is primarily a function of the distance from the quench front. The development of the correlation is still in the preliminary stage, but the results of comparisons with test data seem to indicate that the present approach is quite promising. Some improvements which can be made in future work include:

- A sensitivity study such as that done in WCAP-8838.
- Fine adjustment for parameter effects, especially the effect of power, Q'_{max}, and initial cladding temperature.

RUN NUMBER	02833
PRESSURE	40 PSIA
INITIAL CLADDING TEMPERATURE	1602°F
PEAK POWER	0.89 KW/FT
SUBCOOLING	142°F
INJECTION RATE	0.80 IN./SEC

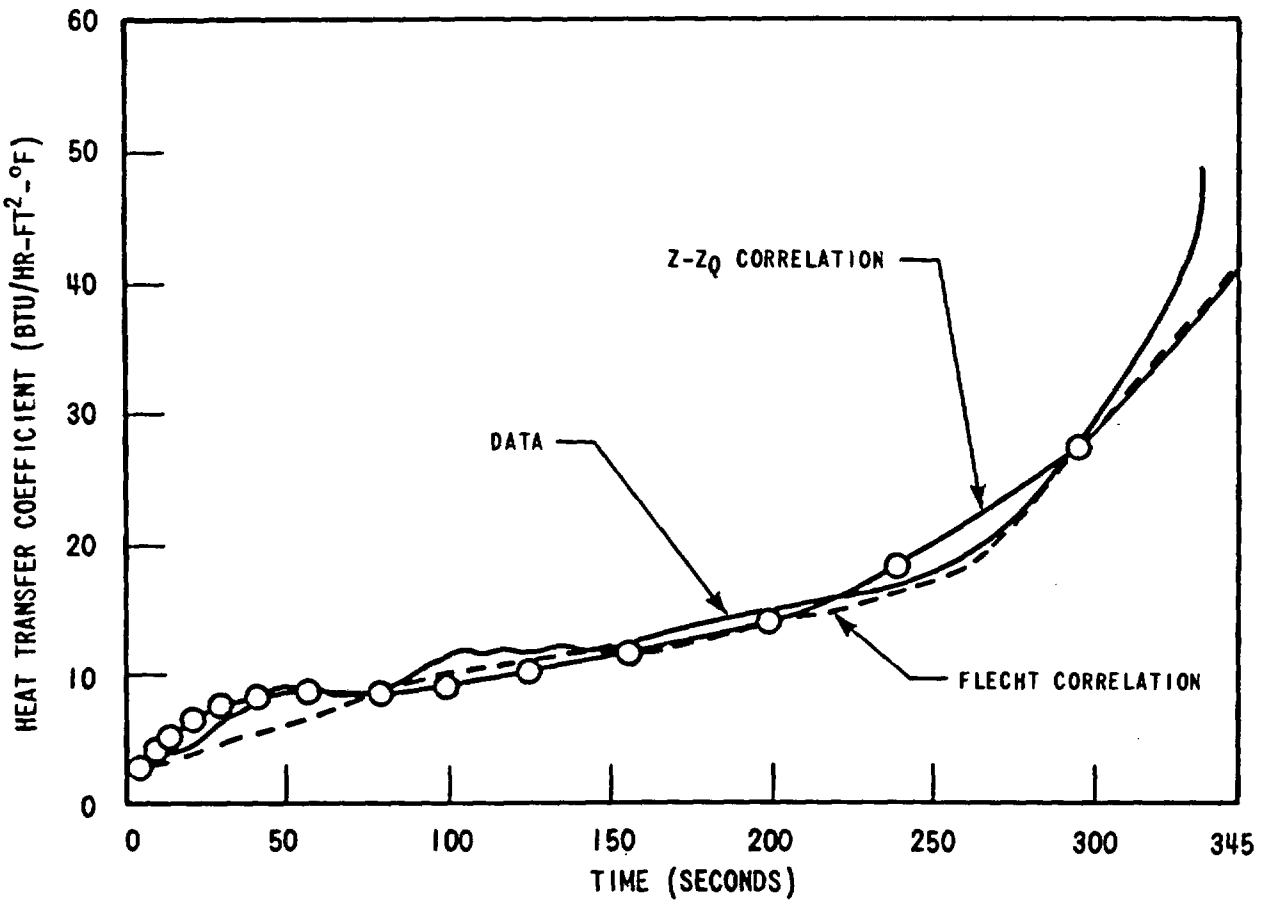

Figure 6-18. Comparison of Peak Power Location Heat Transfer Versus Time for Run 02833 Using Quench Correlation, Z-Zq Correlation and FLECHT Correlation

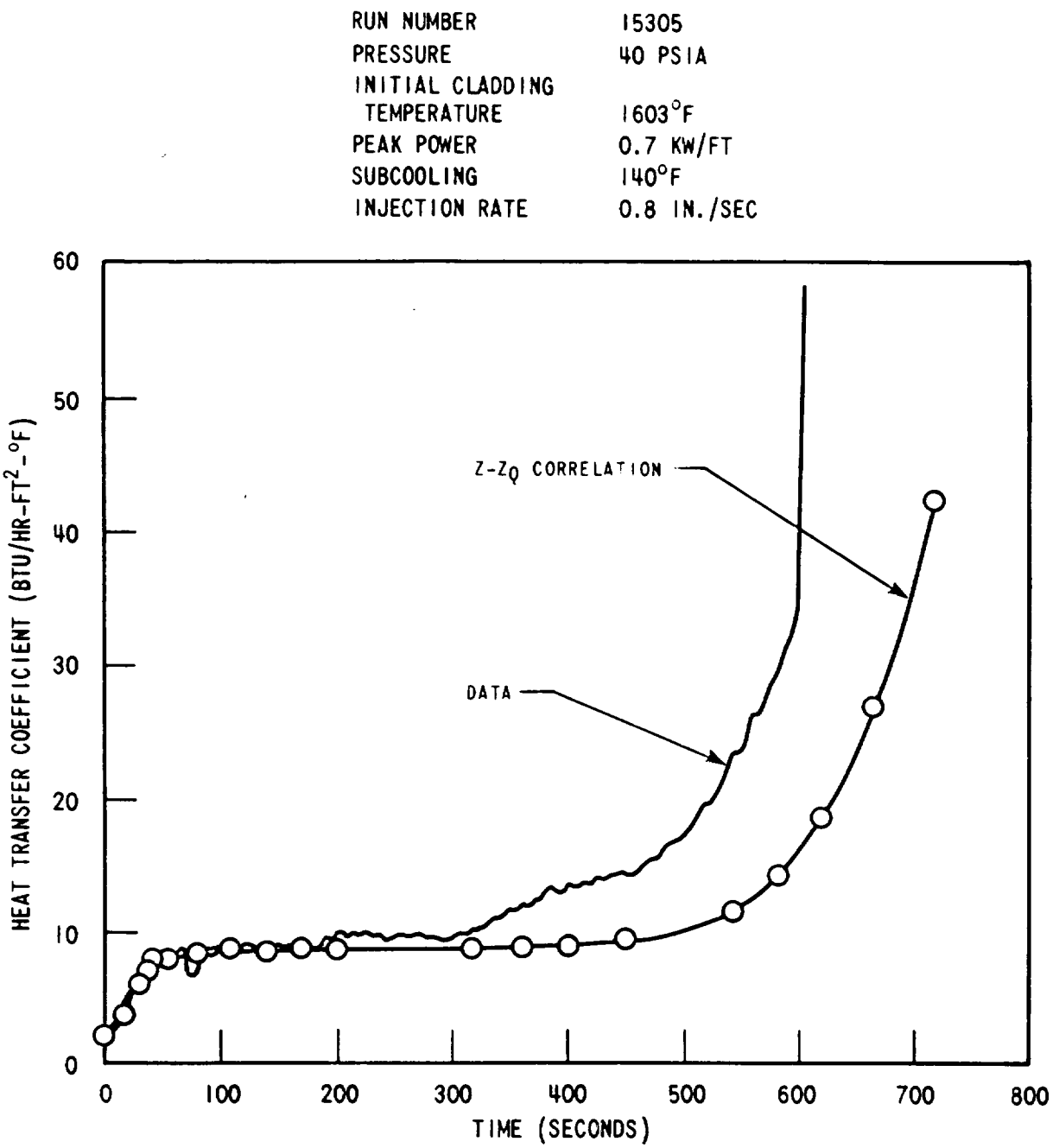

Figure 6-19. Comparison of Peak Power Location Heat Transfer Versus Time for Run 15305 Using Quench Correlation and Z-Zq Correlation

- Improvement of the heat transfer coefficient above the peak temperature elevation, which is underpredicted at the later time of flooding in the present correlation. The test data indicated that the heat transfer coefficient above the peak temperature elevation can be improved by shifting the peak temperature elevation upward with time.

- Improvement of the heat transfer coefficient in the developing period, which is underpredicted for high flooding rate with the present correlation.

It should be noted that since the quench correlation and the heat transfer coefficient correlation are independent of each other, the quench front calculation can be replaced by any other method, either a correlation method or an analytical method.

SECTION 7
CONCLUSIONS AND RECOMMENDATIONS

7-1 CONCLUSIONS

The evaluation of the skewed profile low flooding rate data indicated that the reflooding heat transfer for this power shape is not degraded because of the axial power shape with the peak power at the 10-foot elevation. Comparisons with cosine low flooding rate data with the same initial conditions, including local power, indicated that better heat transfer occurred in the skewed power shape as compared to the cosine power shape. The reason for the improved heat transfer for the skewed power shape is earlier entrainment and a larger vapor flow at the peak power elevation as compared to the cosine shape. The earlier entrainment is believed to be due to the larger power at the lower elevations for the skewed shape. This resulted in a larger convective component of the total wall heat flux. The improved heat transfer for the skewed profile compared to similar cosine tests extended to flooding rates below 1.0 inch/sec.

The pressure sensitivity at low pressures was also found to be different than the cosine power shape. The 20 psia tests had improved heat transfer and correspondingly smaller temperature rises than did either the higher pressure skewed profile tests or comparable 20 psia cosine tests. Again, this difference is believed to be due to the earlier entrainment and higher steam flow which occurred in the skewed tests as a result of the large amount of stored and generated energy in the first two feet of the bundle.

In terms of increased knowledge of the reflood phenomena, the following items represent the significant accomplishments of the skewed test series:

- Parameter effects and differences between the skewed profile and the cosine data were noted and explained.
- The heat transfer data at 1 inch/sec or less were not affected in any unexpected manner and no particular significance can be associated with a flooding rate of 1 inch/sec or below.
- An improved heat transfer correlation was provided to predict the heat transfer for different axial power shapes.

- The semiempirical mass effluent model which was developed from the cosine data was found to predict the skewed profile tests without any adjustment.

- Droplets were again found to be a significant heat sink both upstream and downstream of the peak power location.

- A method was advanced to permit the calculation of the different wall heat flux components during reflood and the local fluid parameters at selected bundle elevations. These calculations indicate that a droplet-enhanced convective mechanism is responsible for 50 to 70 percent of the total wall heat flux during the transient, even though the vapor Reynolds numbers are in the laminar-turbulent transition regime. The results of this analysis have helped clarify reflood heat transfer mechanisms. It is believed the resulting analysis performed on the cosine low flooding rate data will be very useful for reflood model development and verification. The calculation of local qualities, void fraction, flows, and the measurement of the vapor temperature will allow effective testing of nonequilibrium post CHF reflood heat transfer and entrainment models.

7-2. RECOMMENDATIONS

After reviewing the FLECHT low flooding rate data and the analysis performed on these data, a list of recommendations has been developed to serve as a guide for future FLECHT tests and analysis.

- The improved instrumentation used in the FLECHT low flooding rate tests has permitted the calculation of the local nonequilibrium qualities and flows in the post CHF region above the quench front. Improvement should continue to be made in this area by placing rod thermocouples in the rod bundle so that more accurate energy release values can be calculated. Also, additional steam probes should be added at more elevations to more accurately track vapor temperature and to investigate radial effects. Improved movies should be obtained to investigate the droplet size, velocity, and distribution in the FLECHT tests

- The new proposed heat transfer correlation should be improved such that it is a best estimate of all the FLECHT data. Sensitivity studies should be performed on the correlation.

- Examination of the rod heat transfer mechanisms have continued. This effort should continue in future FLECHT tests so that a thorough understanding of the reflood heat transfer process is completed. In this manner, model and code development people will have a clearer understanding of the processes they must represent in reflood calculation.

- A significant effort has been made formulating a mass effluent model which will accurately predict the mass inventory in the FLECHT bundle. This effort should continue and be extended to variable and high flooding rate tests.

- The modeling efforts initiated in the low flooding rate tests series should be combined to yield a predictive model based on local fluid conditions.

APPENDIX A
FLECHT COMPARISON TESTS FOR SKEWED AND COSINE POWER SHAPES

The integral-of-power method[1,2,3] in its most general sense preserves the sum of stored and generated energy liberated to the coolant below given elevations before a common quench time. Mathematically, the integral of power is expressed as follows:

$$\left[\left\{\int_0^{z_1} \rho CpA\,(T_{init} - T_{sat})\,dz + \int_0^{t_q}\int_0^{z_1} \text{Power}\,(z,t)\,dz\,dt\left\{\left(\frac{N}{A}\right)_{cos}\right]_{cos} = \right.$$

$$\left[\left\{\int_0^{z_2} \rho CpA\,(T_{init} - T_{sat})\,dz + \int_0^{t_q}\int_0^{z_2} \text{Power}\,(z,t)\,dz\,dt\left\{\left(\frac{N}{A}\right)_{skew}\right]_{skew} \right. \qquad \text{(A-1)}$$

1. Bordelon, F.M. et. al., LOCA IV Program Loss-of-Coolant Transient Analysis, WCAP-8305 Westinghouse Electric Corporation, 1974.
2. Combustion Engineering Power Systems Safety Analysis Group, "Calculative Methods for the C-E Large Break LOCA Evaluation Model," CENPD 132, Rev. 01 Volume 1 August, 1974.
3. Jimenez, R. F., "An Empirical Flooding Heat Transfer Coefficient Including Quench Time Prediction Applicable to a 12-foot-Long PWR Core and Including a Modification for Variable Flooding Rates; Short Core; and Non-symmetrical Power Profiles," Jim-6-71, Aerojet Nuclear Company Interoffice Correspondence, Transmitted to Valerin by L. J. Ybarrendo, November 24, 1971.

where

z_1 and z_2 = corresponding elevations for cosine and skew below which total energy is to be preserved

t_q = the common quench time for each power profile at z_1(cosine) and z_2 (skew)

Power(z,t) = the time and elevation power decay term

n = the equivalent number of active rods in the test section, including housing effects.

A_{cos}, A_{skew} = bundle cross-sectional flow areas for cosine and skew, respectively.

Several different methods which satisfy equation (A-1) are available;

1) Maintain the equivalence of stored energy (ρCpA ΔT) terms on both sides of the equation. This automatically forces the generated power up to the quench time to be the same for both power shapes. In this case, neither initial temperature nor peak power will be the same for two different power profiles.

2) Maintain the same initial temperature at the expense of reduced peak power

3) Maintain the same peak power at the expense of lower initial temperature.

Compensation for elevated housing temperature above saturation was possible using an analysis which showed that the subchannels near the wall had the same flow area as~16.8 heater rod unit cells. Therefore, stored and generated energy in the cosine bundle were increased by an effective ~16.8 rods in equation (A-1) for those cosine tests having a heat housing.[1]

With the exception of Runs No. 14548 and 14647, the skewed overlap test peak power and initial temperature were calculated according to Method 1. That is, stored and generated energy were equated separately. Runs No. 14548 and 14647 satisfy Method 2 above (i.e., a specification of 1600°F initial temperature significantly reduces the skewed the peak power.)

Evaluation of equation (A-1) is not a straightforward process. As written, the skewed initial temperature profile must be known before the stored energy term can be computed. Since equation (A-1) is being used to specify run conditions, another solution technique is needed to calculate stored energy before taking data. The power profile curve can be used if axial conduction, radiation, and natural convection losses from the rods can be neglected during heatup. This assumption implies that the axial power input to the rods is proportional to

1. Blaisdell, J. A. et. al., PWR FLECHT-SET Phase A Report, WCAP-8238, December, 1973.

stored energy or, equivalently, initial temperature. Therefore, the total initial stored energy is proportional to the integral of the generated power profile up to the location of interest. Figure 3-54 can be used to evaluate the stored energy if the integral expressions in equation (A-1) are nondimensionalized by average quantities.

$$\left(\frac{N}{A}\right)_{cos}\left[\rho CpA\,(T - T_{sat})_{avg}\int_0^6 \frac{\rho CpA\,(T_{init} - T_{sat})}{\rho CpA\,(T - T_{sat})_{avg}}\,dz\right]_{cos} =$$

$$\left(\frac{N}{A}\right)_{skew}\left[\rho CpA\,(T - T_{sat})_{avg}\int_0^{10} \frac{\rho CpA\,(T_{init} - T_{sat})}{\rho CpA\,(T - T_{sat})_{avg}}\,dz\right]_{skew} \qquad \text{(A-2)}$$

or

$$\frac{\left[\int_0^6 \frac{\rho CpA\,(T_{init} - T_{sat})}{\rho CpA\,(T - T_{sat})_{avg}}\right]_{cos}}{\left[\int_0^{10} \frac{\rho CpA\,(T_{init} - T_{sat})}{\rho CpA\,(\ - T_{sat})_{avg}}\right]_{skew}} =$$

$$\frac{\left[\left(\frac{N}{A}\right)\rho CpA\,(T - T_{sat})_{avg}\right]_{skew}}{\left[\left(\frac{N}{A}\right)\rho CpA\,(T - T_{sat})_{avg}\right]_{cos}} \qquad \text{(A-3)}$$

The left-hand side is a nondimensionalized stored energy ratio which was shown to be approximately equal to the integral of the generated power curve.

$$\frac{\left[\int_0^6 \left(\frac{\text{Power }(z,t)}{\text{Power}_{avg}}\right) dz\right]_{cos}}{\left[\int_0^{10} \left(\frac{\text{Power }(z,t)}{\text{Power}_{avg}}\right) dz\right]_{skew}} \approx 0.6 \qquad \text{(A 4)}$$

(See page A-15 for more details concerning equation (A-4). The right-hand-side can be rewritten in terms of the peak initial temperature if one further assumption is made. The peak-to-average ratios for generated power are

$$\left(\frac{\text{Power}_{peak}}{\text{Power}_{avg}}\right)_{cos} = 1.66 \qquad \text{(A 5)}$$

$$\left(\frac{\text{Power}_{peak}}{\text{Power}_{avg}}\right)_{skew} = 1.35 \qquad \text{(A 6)}$$

Since the initial stored and generated power profiles are similar, their peak-to-average ratios should also be similiar. This assumption reduces the right-hand side to yield the following result

$$0.6 \approx \frac{\left[\frac{N}{A}\left\{\frac{\rho CpA\ (T_{peak} - T_{sat})}{1.35}\right\}\right]_{skew}}{\left[\frac{N}{A}\left\{\frac{\rho CpA\ (T_{peak} - T_{sat})}{1.66}\right\}\right]_{cos}} \qquad \text{(A 7)}$$

or assuming ρCpA to be constant

$$\left(T_{peak} - T_{sat}\right)_{skew} \approx 0.5 \left(\frac{N}{A}\right)_{cos} \left(\frac{A}{N}\right)_{skew} \left(T_{peak} - T_{sat}\right)_{cos} \qquad \text{(A-8)}$$

This methodology was compared with experimental data. Initial temperatures from four pairs of comparison tests were multiplied by the appropriate weighted ρCpA to account for the Kanthal heater element, boron nitride filler and stainless steel cladding materials taken from figure A-1. Curves of stored energy shown in figures A-2 to A-9, were drawn and integrated using a planimeter up to the peak power location.

Results of this analysis shown in table A-1 indicates, that the stored energy in the cosine overlap test was generally 10 percent higher than that for the comparable skewed test.

TABLE A-1
COMPARISON OF INITIAL STORED ENERGY

Run No.	Ratio of Cosine Stored Energy to Skewed Stored Energy
02223 11524	1.23
04831 11225	1.02
04516 13127	1.08
04641 11428	1.10

Although the data analysis technique is uncertain to the extent that a smoothed curve was drawn through somewhat irregular data points and integrated graphically, the conclusion to be drawn is this: the cosine tests appear to have more stored energy than do the skewed tests at the onset of flooding.

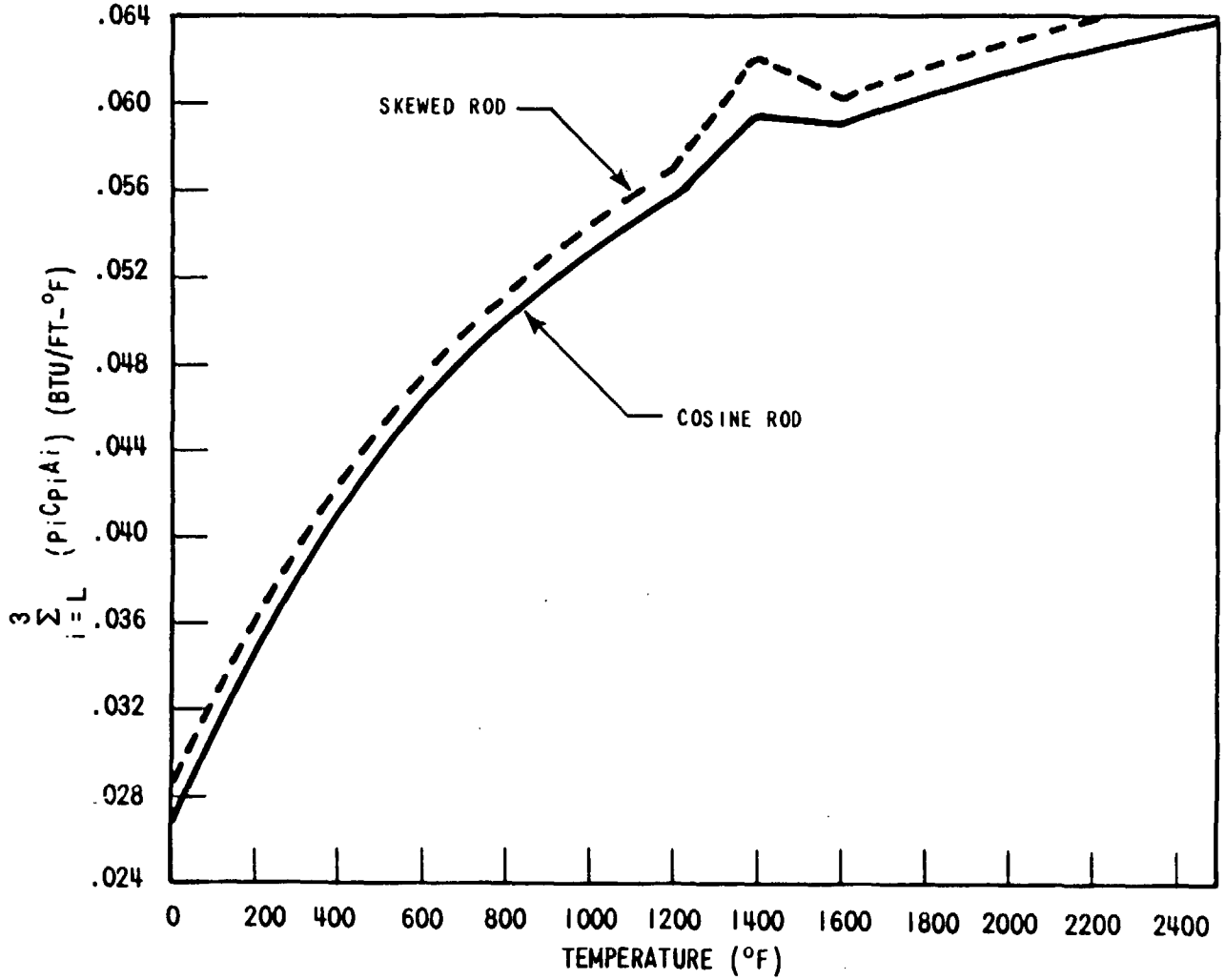

Figure A-1. $\sum_{i=1}^{3} (\rho_i C_{Pi} A_i)$ Versus Temperature for a FLECHT Heater i=1 Rod Calculated From the Properties in DATARH

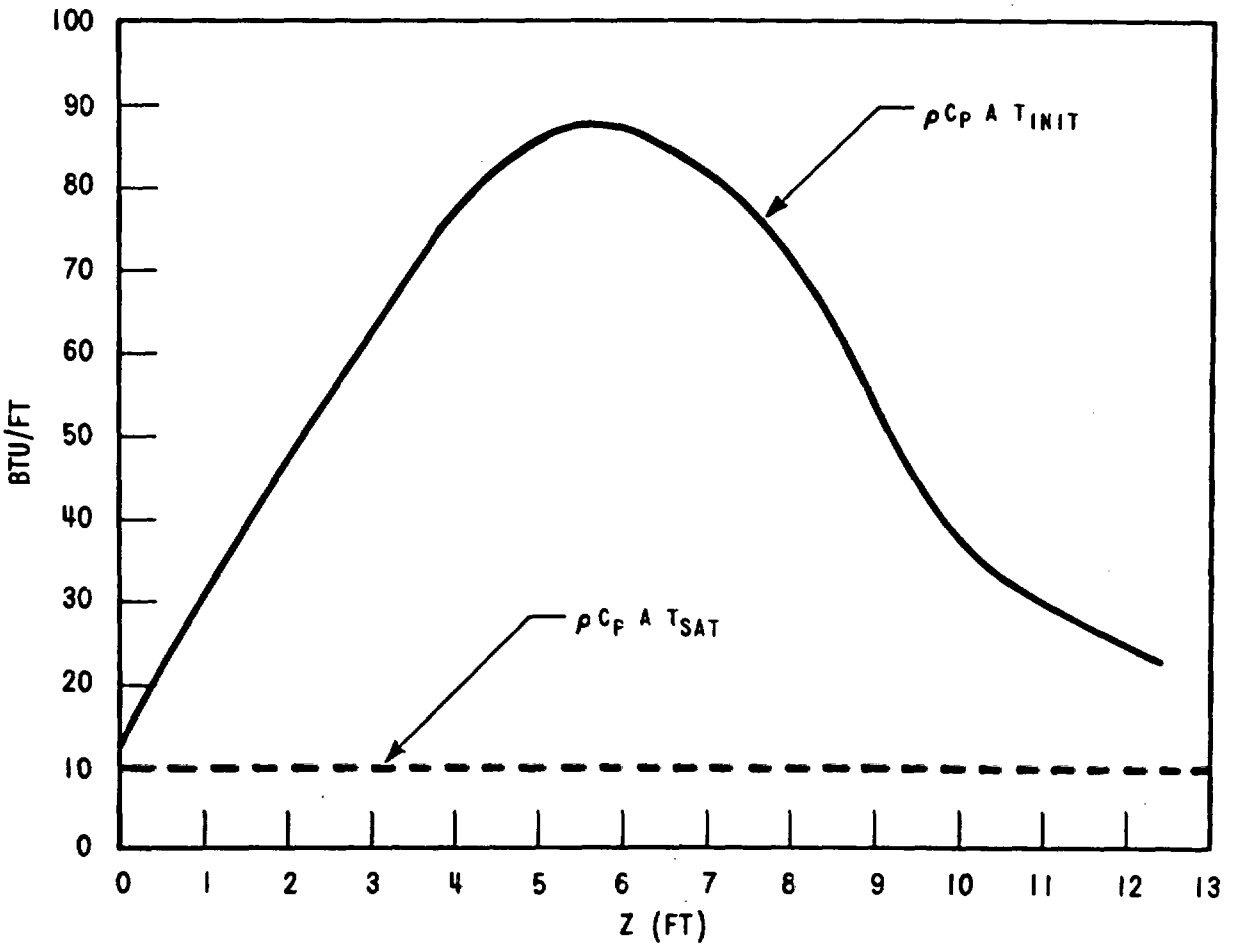

Figure A-2. Initial Stored Energy Distribution in Run 04831 as a Function of Elevation

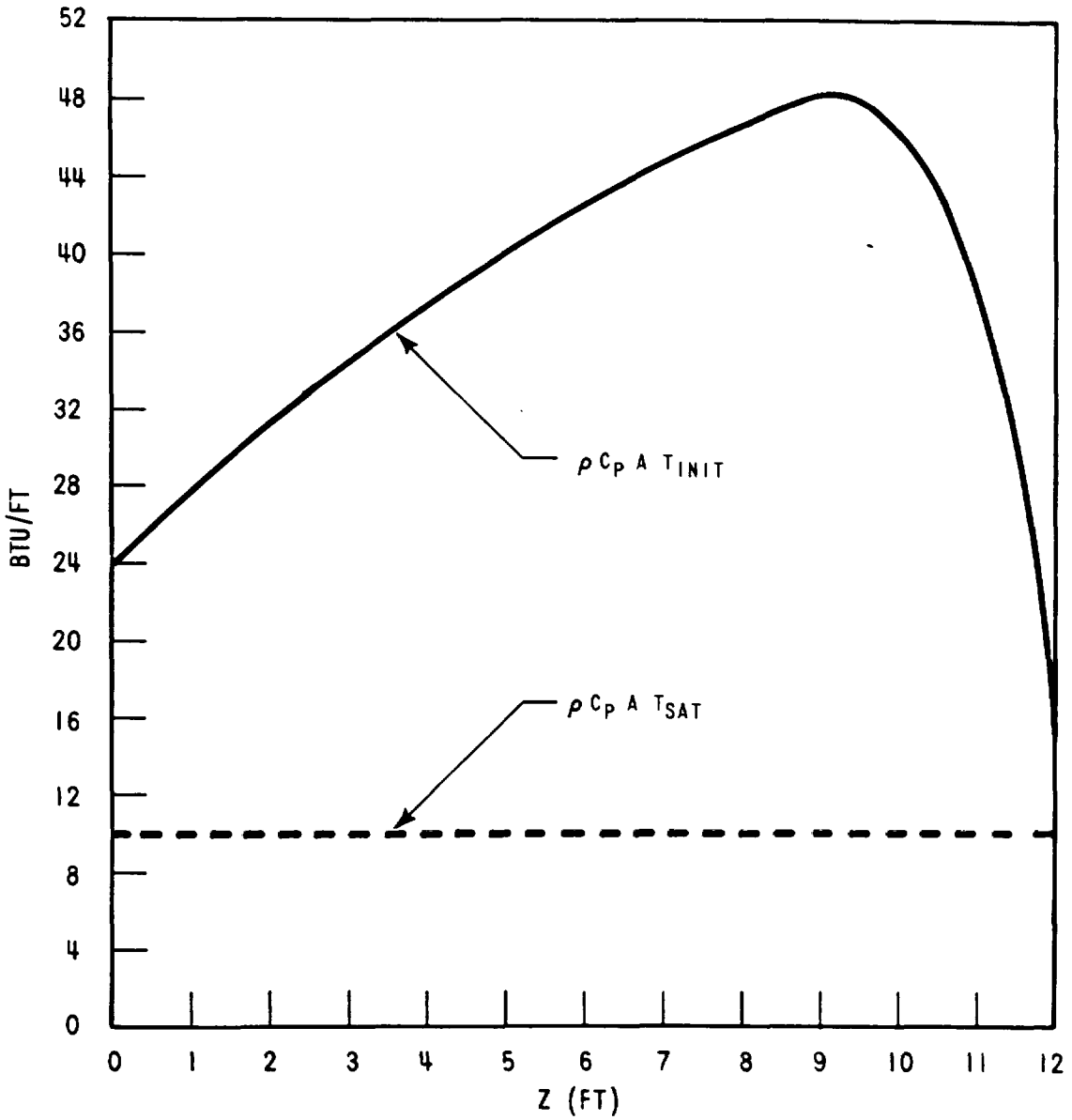

Figure A-3. Initial Stored Energy Distribution in Run 11225 as a Function of Elevation

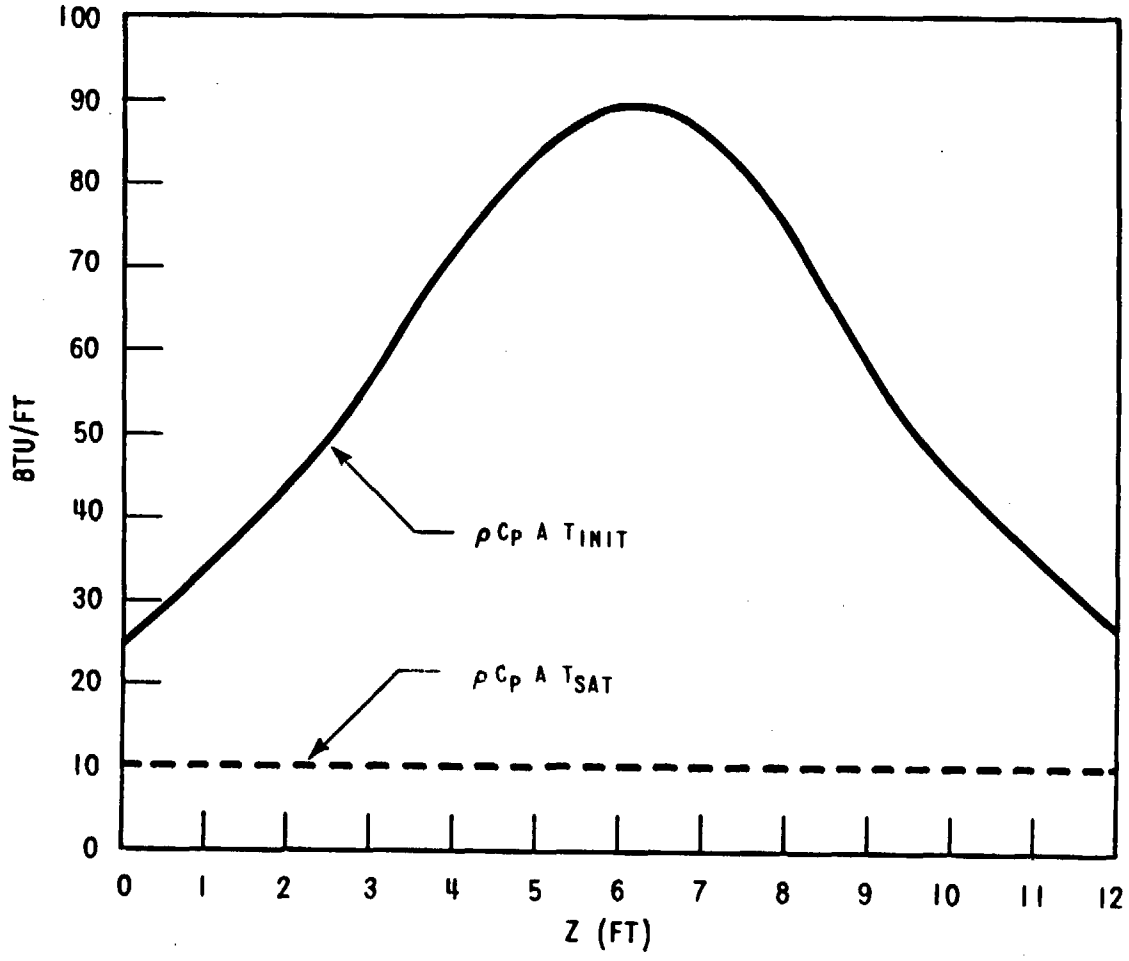

Figure A-4. Initial Stored Energy Distribution in Run 02223 as a Function of Elevation

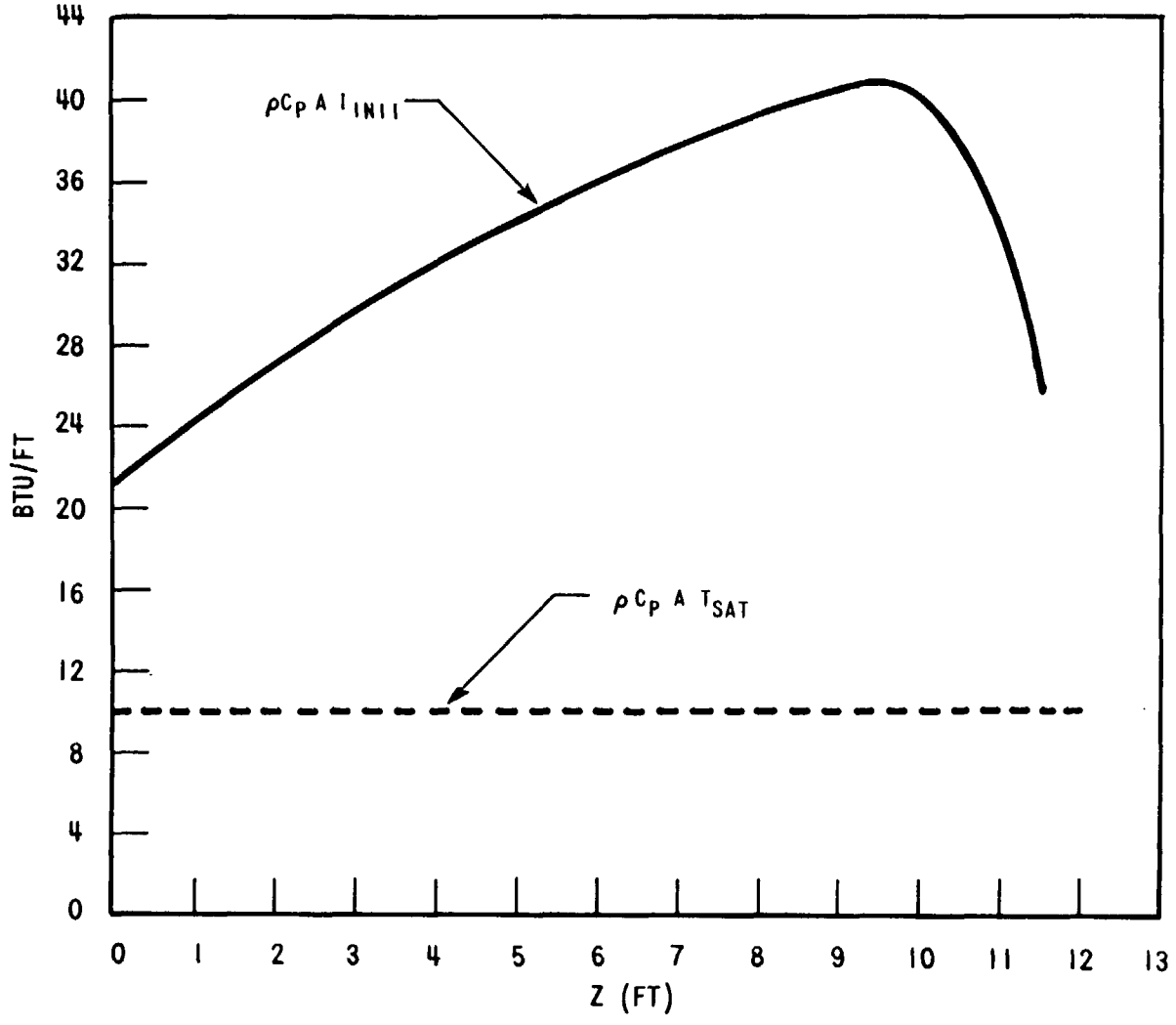

Figure A-5. Initial Stored Energy Distribution in Run 11524 as a Function of Elevation

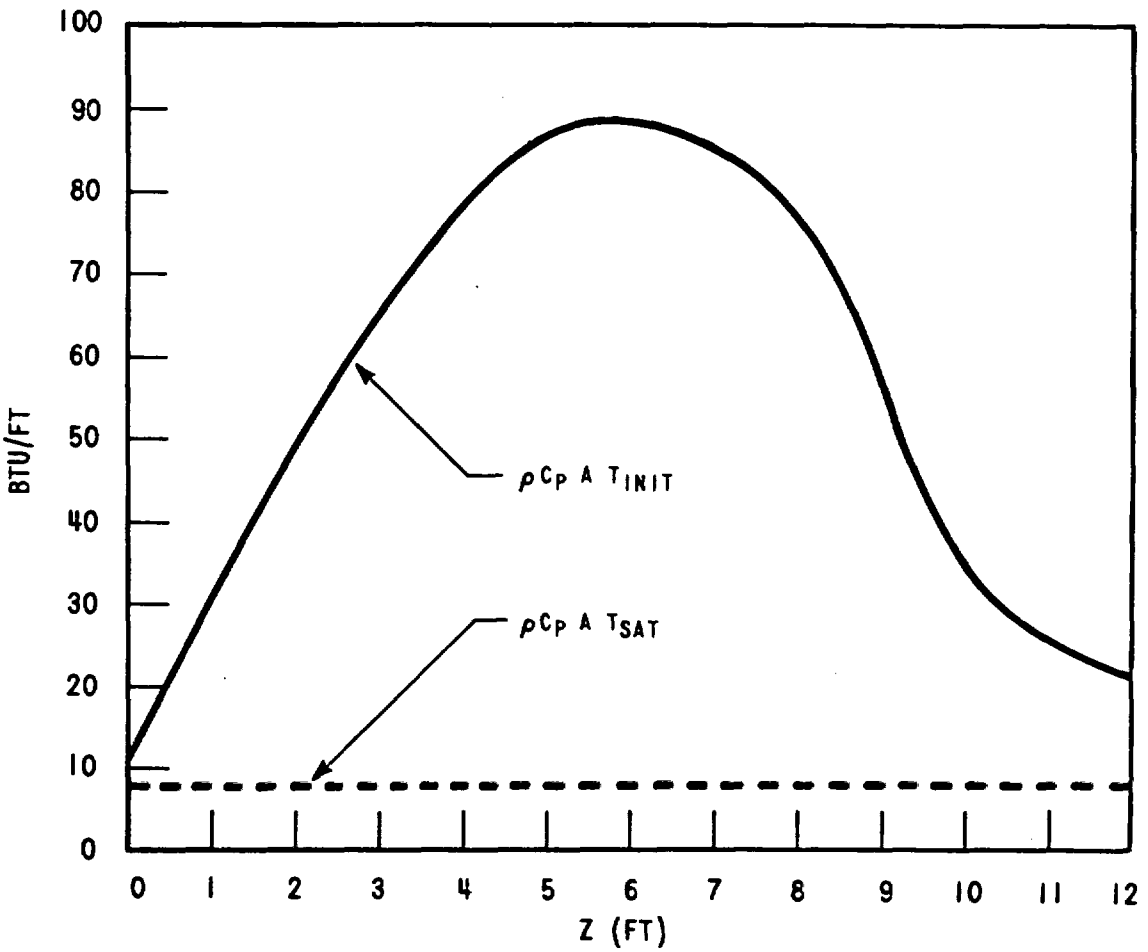

Figure A-6. Initial Stored Energy Distribution in Run 04641 as a Function of Elevation

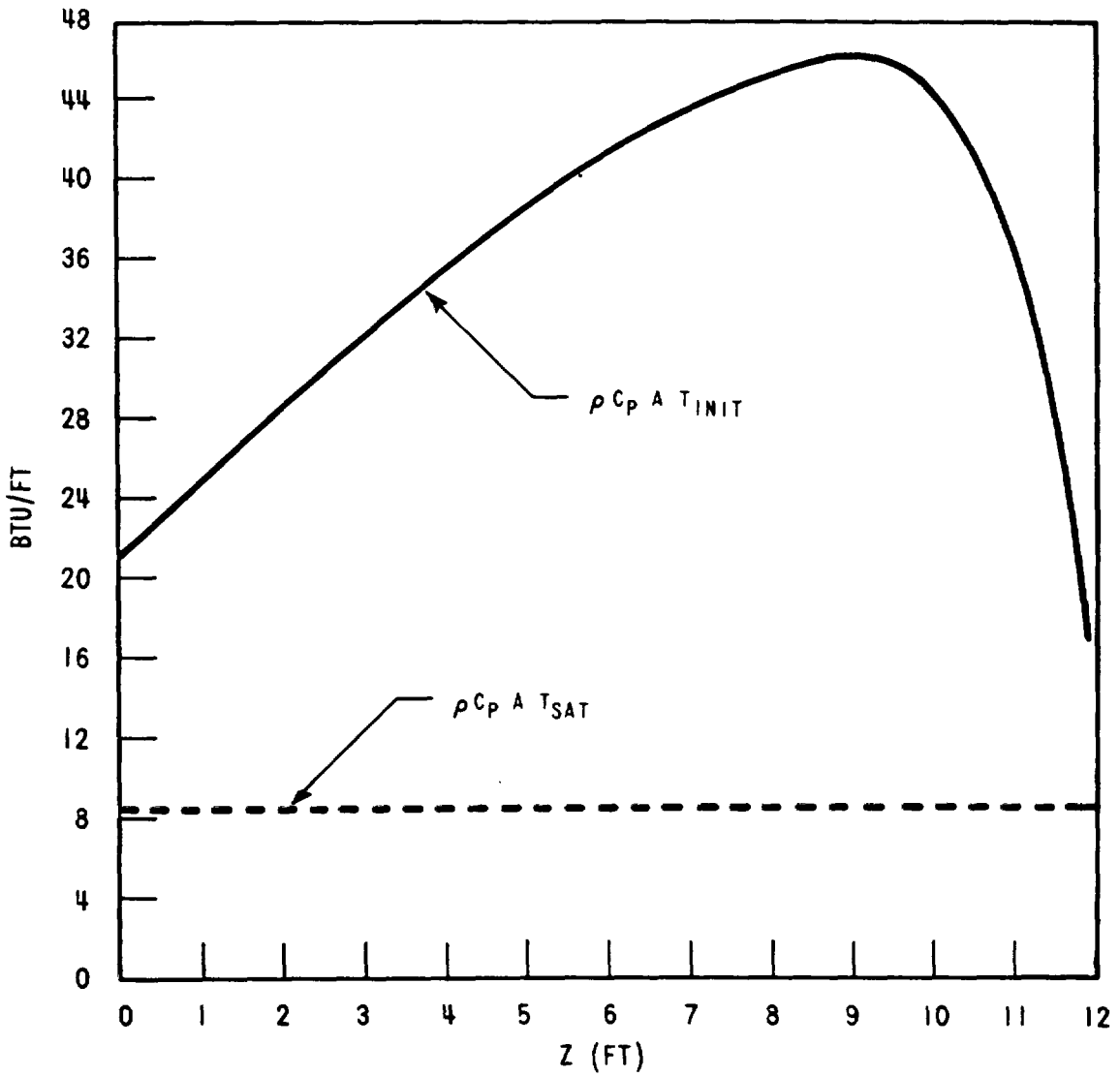

Figure A-7. Initial Stored Energy Distribution in Run 11428 as a Function of Elevation

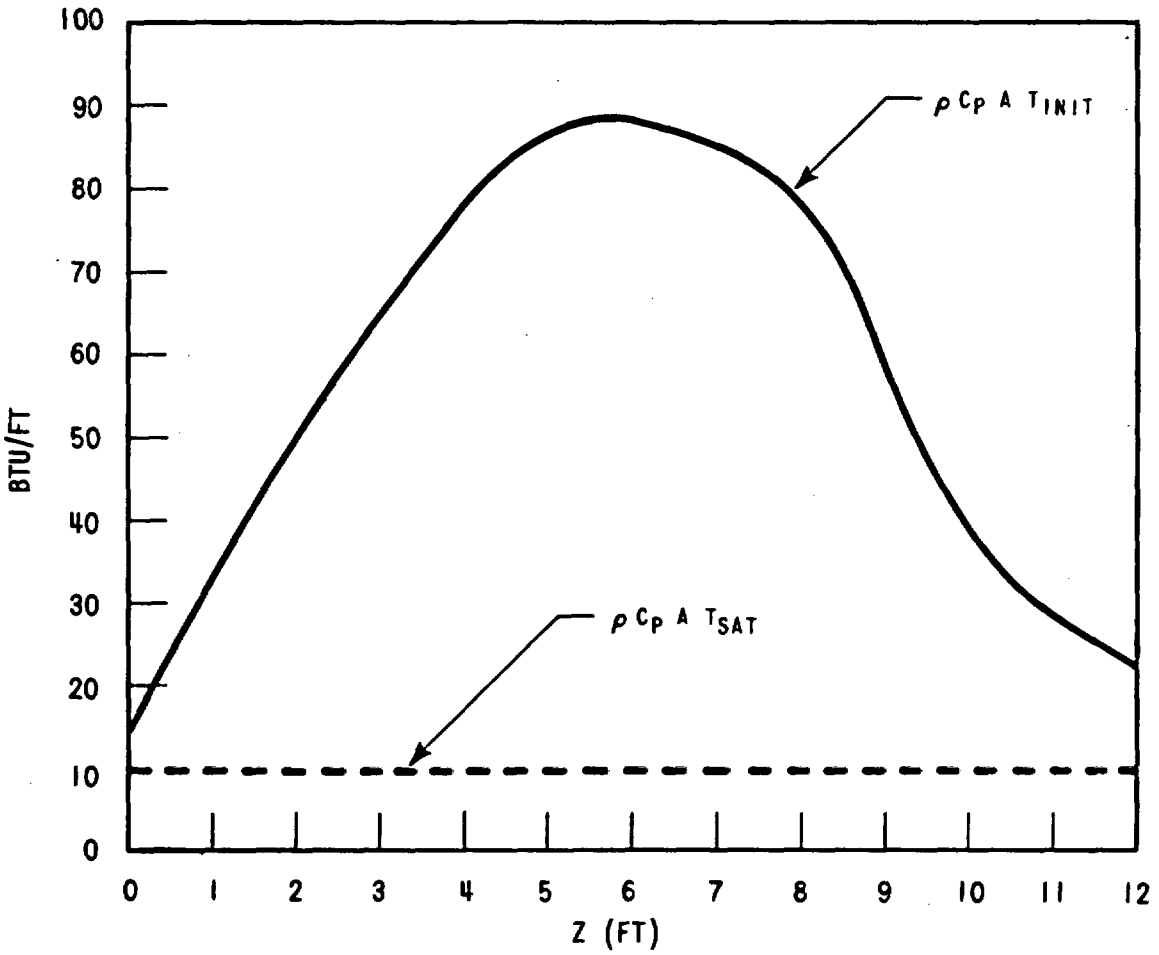

Figure A-8. Initial Stored Energy Distribution in Run 04516 as a Function of Elevation

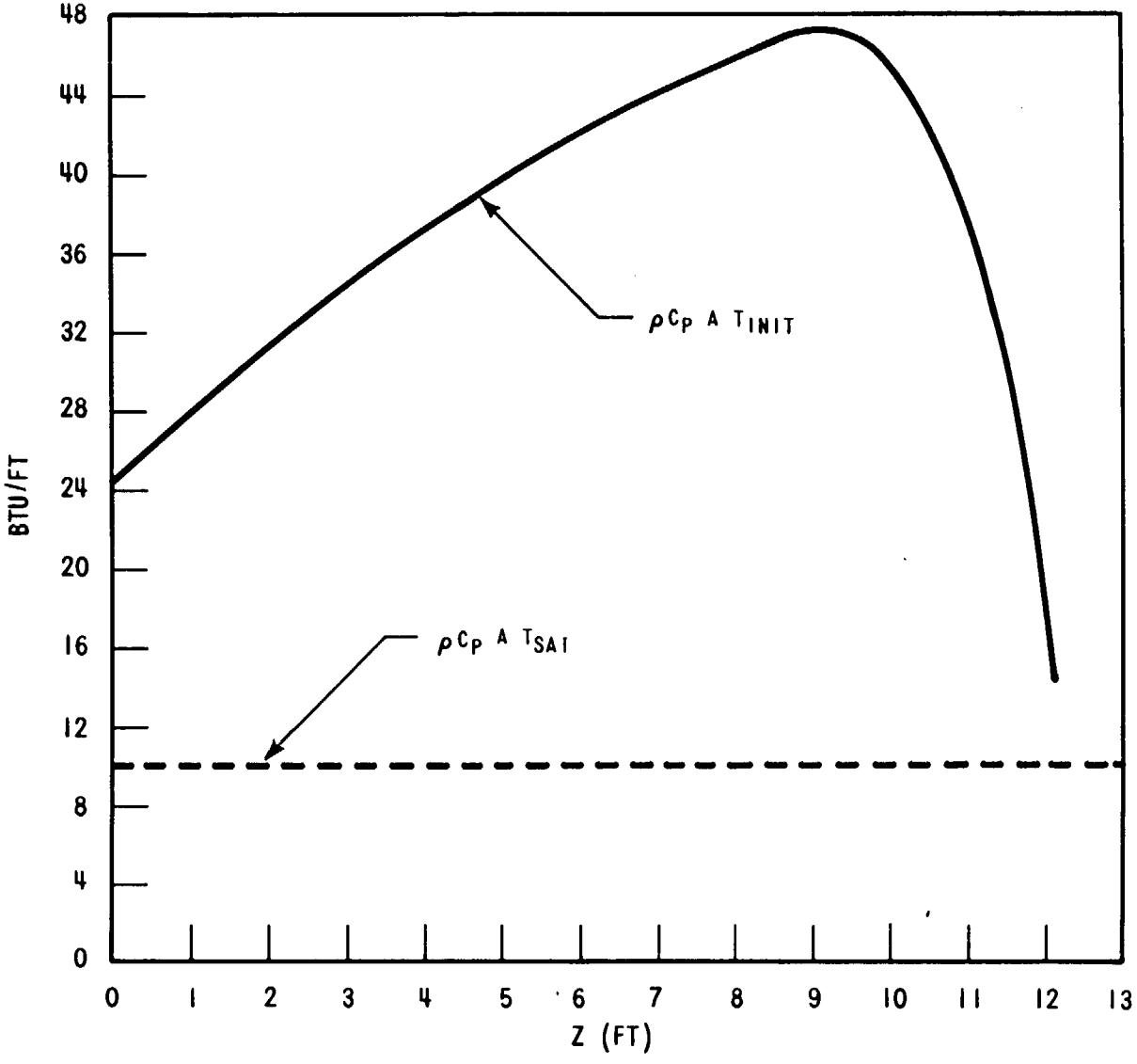

Figure A-9. Initial Stored Energy Distribution in Run 13127 as a Function of Elevation

Evaluation of the power decay generation term in Method 1 proceeds as follows

$$\left[\frac{N}{A}\int_0^{t_q}\int_0^{6} \text{Power } (z,t)\ dz\ dt\right]_{cos} =$$

$$\left[\frac{N}{A}\int_0^{t_q}\int_0^{10} \text{Power } (z,t)\ dz\ dt\right]_{skew} \qquad \text{(A-9)}$$

If the same time-dependent power decay curve is used for both skewed and cosine series and the same peak power, location, and quench time is assumed, then

$$t_q\ cos = t_q\ skew \qquad \text{(A-10)}$$

$$\text{Power } (t)_{cos} = \text{Power } (t)_{skew} \qquad \text{(A-11)}$$

Equation (A-9) can be reduced to

$$\left[\text{Power}_{avg}\left(\frac{N}{A}\right)\int_0^{6}\frac{\text{Power } (z,t)\ dz}{\text{Power}_{avg}}\right]_{cos} =$$

$$\left[\text{Power}_{avg}\left(\frac{N}{A}\right)\int_0^{10}\frac{\text{Power } (z,t)\ dz}{\text{Power}_{avg}}\right]_{skew} \qquad \text{(A-12)}$$

after the integrand is nondimensionalized by Power_{avg} and the results of equations (A-10) and (A-11) have been used.

Then, after substitution of peak-to-average power ratios, equations (A-5) and (A-6) and equation (A-12) can be rearranged as follows

$$\text{Power}_{\text{peak skew}} =$$

$$\left(\frac{N}{A}\ \frac{\text{Power}_{\text{peak}}}{1.66}\right)_{\cos}\left(\frac{A}{N}\ 1.35\right)_{\text{skew}}\ \frac{\left[\int_0^6 \frac{\text{Power (z) dz}}{\text{Power}_{\text{avg}}}\right]_{\cos}}{\left[\int_0^{10} \frac{\text{Power (z) dz}}{\text{Power}_{\text{avg}}}\right]_{\text{skew}}} \qquad \text{(A-13)}$$

The integral ratio can be evaluated from the local-to-average power curve shown in figure 3-54.

$$\text{Power}_{\text{peak,skew}} \approx 0.5\left(\frac{N}{A}\right)_{\cos}\left(\frac{A}{N}\right)_{\text{skew}}\ \text{Power}_{\text{peak,cos}} \qquad \text{(A-14)}$$

Equations (A-8) and (A-14) were used to prescribe initial temperature and rod peak power for all overlap tests, except for Runs No. 14548 and 14647.

Since Runs No. 14548 and 14647 were performed with the same initial temperature at the peak power location, neither equations (A-8) nor (A-14) apply. To prescribe peak power for these two runs, similar power and temperature profiles were assumed the stored energy for each test was evaluated from the following equation.

$$Q_{\text{stored}} = \rho CpA\ (\text{distance to peak power})\ x$$

$$\frac{(T_{\text{initial, peak}} - T_{\text{sat}})}{\text{peak-to-average ratio}} \qquad \text{(A-15)}$$

Evaluation of the generated energy terms requires specification of a power decay curve and a given quench time ($t_{q6ftcosine} = t_{q10ftskew}$) from the cosine overlap test. Once these two quantities are known, the equation for generated energy becomes

$$Q_{generated} = \frac{\text{(Peak power) x (distance to peak power)}}{\text{(Peak-to-average ratio)}} \quad \text{(A-16)}$$

x (integrated power decay term from known t_q and figure A-10)

The total energy equation

$$\left(Q_{stored} + Q_{generated}\right)_{cosine} = \left(Q_{stored} + Q_{generated}\right)_{skewed} \quad \text{(A-17)}$$

can be solved for the only unknown, skewed peak power.

In general then, two techniques were used to generate peak power and initial conditions for the overlap tests according to either equation (A-8) and (A-14) or equations (A-15), (A-16), and (A-17). Equations (A-8) and (A-14) maintain the equality of stored and generated energy to quench time independentlv, while equations (A-15), (A-16) and (A-17) maintain the sum of stored and generated energy, given an initial temperature.

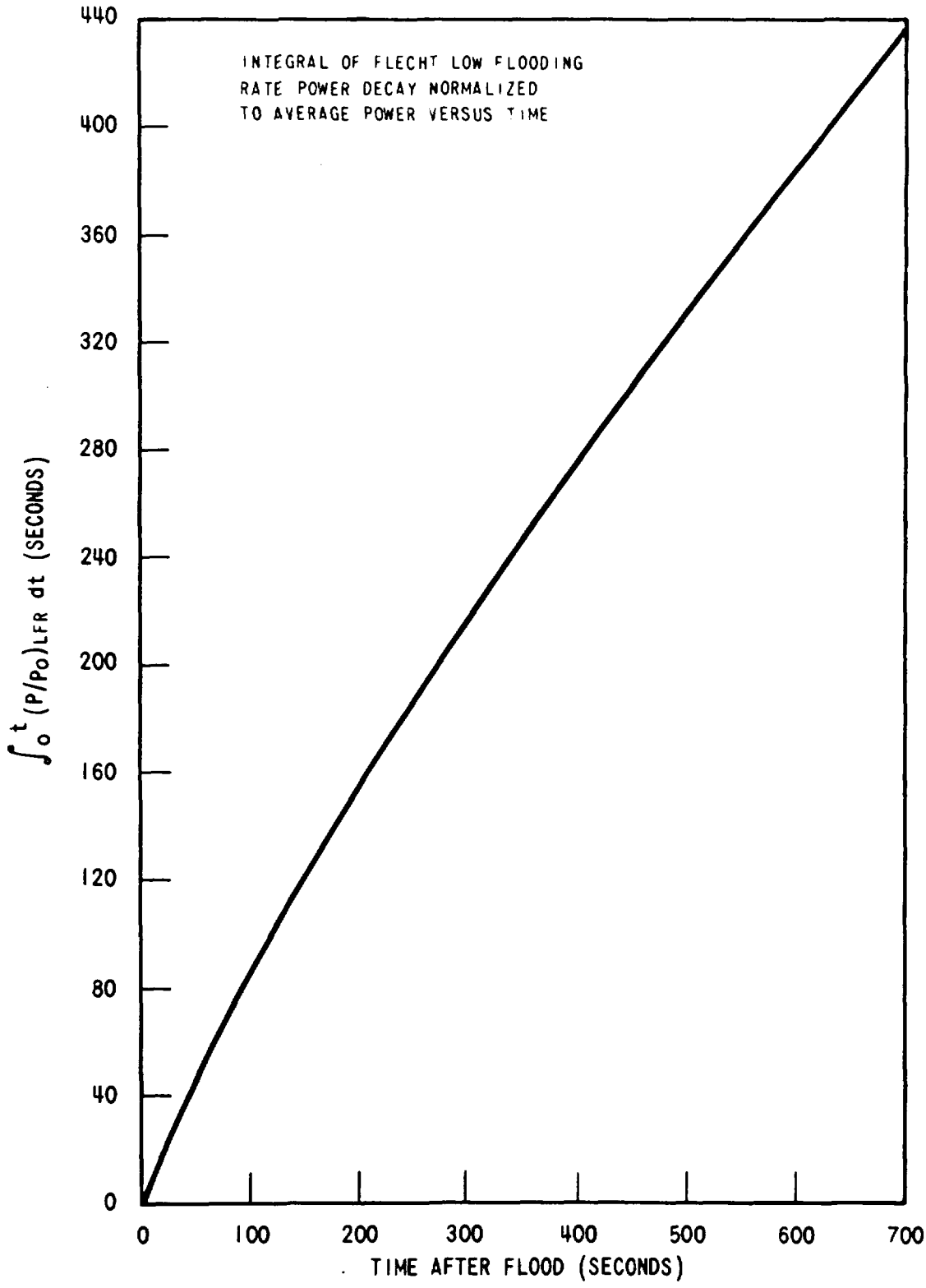

Figure A-10. Integral of FLECHT Low Flooding Rate Power Decay Normalized to Average Power Versus Time

APPENDIX B
DEVELOPMENT OF THE DROPLET MODEL FOR THE WALL HEAT FLUX CALCULATIONS

B.1 INTRODUCTION

Appendix B discusses the following items:

- Equations used to calculate radiation heat transfer to vapor and droplets
- The model used to choose initial drop size
- The effect of initial (quench front) void fraction on droplet slip
- Calculation of droplet slip and droplet volumetric density
- Dependence on resulting wall heat flux components or droplet size.

The radiation heat transfer to the entrained liquid droplets and the steam was calculated using the approach given by Sun, Gonzalez and Tien[1] along with a dynamic droplet model developed using the FLECHT data. The calculations used in this appendix have been programmed into a computer program called HEAT-II. The following assumptions were used in developing the models and calculation given in this appendix.

- The total wall heat flux is composed of a convection-to-vapor term, q''_{cv} a radiation-to-vapor term, q''_{rv}, a radiation-to-droplet term, q''_{rd} and a radiation-to-other-surfaces term, q''_{r}.

  Therefore, the total wall heat flux is expressed as

$$q''_T = q''_{cv} + q''_{rv} + q''_{rd} + q''_r \qquad \text{(B-1)}$$

- The q''_r is assumed to be given by q''_T at time t=0 and is modified by an attenuation coefficient due to the presence of vapor and drops.
- The q''_{rd} and q''_{rv} are calculated using the Sun and Gonzalez approach which also assumes:

  a. The mediums are optically thin

1. Sun K.H., Gonzalez J.M., and Tren C.L., "Calculations of Combined Radiation and Connection Heat Transfer in Rod Bundles Under Emergency Cooling Conditions" ASME-AICHE, 15 National Heat Transfer Conference (August 1975).

b. The medium is in the geometric scattering regime

c. The drop size and slip are given

- FLECHT data are used as input for the calculations. Quality and vapor temperature are obtained by linear interpolation between the steam probe elevations.
- In performing the calculations, the following assumptions are made:

  a. Quasi-steady state

  b. Constant system pressure

  c. Liquid is at saturation

  d. The droplet velocity and the droplet acceleration is always positive

  e. Slip (or void fraction) is given at the quench front.

- Droplet size is supplied by a proposed model discussed in this appendix.

B.2 RADIATION TO VAPOR AND DROPLETS

Radiation to vapor and droplets will be calculated following the method of Sun, et. al. The equations used are summarized below:

$$q''_{rd} = F_{w\ell}\ \sigma\ (T_w^4 - T_{sat}^4) \tag{B-2}$$

$$q''_{rv} = F_{wv}\ \sigma\ (T_w^4 - T_v^4) \tag{B-3}$$

$$q''_{rvd} = F_{v\ell}\ \sigma\ (T_v^4 - T_{sat}^4) \tag{B-4}$$

where:

q''_{rd}, q''_{rv}, q''_{rvd} = Radiation heat flux from wall to droplets, wall to vapor, and vapor to droplet, respectively.

$F_{w\ell}$, F_{wv}, $F_{v\ell}$ = gray-body factors

T_w, T_{sat}, T_v = Wall, droplet, vapor temperature, respectively (°R)

σ = Stefan-Boltzmann constant

The gray-body factors $F_{w\ell}$, F_{wv}, $F_{v\ell}$ are defined as:

$$F_{w\ell} = \frac{1}{R_2\left(1 + \frac{R_3}{R_1} + \frac{R_3}{R_2}\right)} \tag{B-5}$$

$$F_{wv} = \frac{1}{R_1\left(1 + \frac{R_3}{R_1} + \frac{R_3}{R_2}\right)} \tag{B-6}$$

$$F_{v\ell} = \frac{1}{R_2\left(1 + \frac{R_1}{R_2} + \frac{R_1}{R_3}\right)} \tag{B-7}$$

$$R_1 = \frac{1 - \epsilon_v}{\epsilon_v\,(1 - \epsilon_v \epsilon_\ell)} \tag{B-8}$$

$$R_2 = \frac{1 - \epsilon_\ell}{\epsilon_\ell\,(1 - \epsilon_v \epsilon_\ell)} \tag{B-9}$$

$$R_3 = \frac{1}{1 - \epsilon_v \epsilon_\ell} + \frac{1 - \epsilon_w}{\epsilon_w} \tag{B-10}$$

where

ϵ_v, ϵ_ℓ, ϵ_w = Vapor, droplet, wall emissivity, respectively

The wall emissivity is taken to be 0.9. Assuming an optically thin vapor and droplet medium, the vapor and droplet emissivity can be expressed as per Sun, et. al:

$$\epsilon_w = 0.9 \tag{B-11}$$

$$\epsilon_v = 1 - e^{-a_v L_m} \tag{B-12}$$

$$\epsilon_\ell = 1 - e^{-a_\ell L_m} \tag{B-13}$$

where:

a_v, a_ℓ = absorption coefficient for vapor and droplets, respectively

L_m = mean beam length

Based on a survey of a variety of geometries, the mean beam length can be taken to be 0.9 of the hydraulic diameter (D_h) for a rod array.

$$L_m = 0.9\ D_h \tag{B-14}$$

The vapor absorption coefficient is computed from:

$$a_v = p\left[5.6 \times \left(\frac{1000}{T_v}\right)^2 - 0.3\left(\frac{1000}{T_v}\right)^4\right](ft)^{-1}\ [1] \tag{B-15}$$

$$a_\ell = X_a \frac{\pi d^2}{4}\ N_\ell\ (ft)^{-1} \tag{B-16}$$

where:

p = system pressure in atmospheres

X_a = absorption efficiency

N_ℓ = droplet number density (No. of droplets/ft^3)

1. Abu-Romia M. M. and Tien C. L., "Appropriate Mean Absorption Coefficients for Infrared Radiation of Gases," J. Heat Transfer (ASME), 321-327 (1907).

Assuming the droplets are in the geometric scattering regime, it can then be shown that X_a is equal to 0.74. The geometric scattering regime is defined as one in which:

$$\pi d >> \lambda$$

where:

d = droplet diameter

λ = characteristic length of radiation

For a wall temperature of 1800°F, Wien's[1] displacement law gives $\gamma \approx 2.3\mu$ (7.6×10^{-6} ft). During reflooding, the typical diameter ranges from 0.005 to 0.01 foot. Hence, the assumption is justified that the droplets are in a geometric scattering regime. The calculation of the droplet diameter and the droplet volumetric density will be described in the following sections.

B.3 MODEL TO PREDICT INITIAL DROP SIZE

As mentioned in section 4, the model used to predict the initial drop size was inspired by a study of the droplet motion above the quench front. In the following sections, the equation of motion of the droplets will be derived first. A quantitative illustration of the droplet motion as a function of drop size using typical FLECHT data will then be given followed by the detailed description of the model and the mathematical determination of the initial droplet size.

The force on the droplet is given by a balance of drag, gravitation and buoyancy forces.

$$F = \frac{1}{2} C_d A_d \rho_g (u_g - u_\ell)^2 - g (\rho_\ell - \rho_g) V \qquad \text{(B-17)}$$

where,

$$V = \frac{1}{6} \pi d^3 \qquad \text{(B-18)}$$

$$A_d = \frac{1}{4} \pi d^2 \qquad \text{(B-19)}$$

$$Re_d = \frac{(u_g - u_\ell)\, d \rho_g}{\mu_g} \qquad \text{(B-20)}$$

$$C_d = \frac{24}{Re_d} + \frac{6}{1 + \sqrt{Re_d}} + 0.4 \text{[2]} \qquad \text{(B-21)}$$

1. Holman, J. P. Heat Transfer Third edition, p. 240 McGraw-Hill Book Co., New York, 1972.
2. White, F., Viscous Fluid Flow, p. 209 McGraw-Hill Book Co., New York, 1974.

u_g, u_ℓ = vapor, droplet velocity, respectively

ρ_g, ρ_ℓ = vapor, droplet density respectively

Re_d = droplet Reynold's number

μ_g = dynamic viscosity of vapor

C_d = drag coefficient

V = drop volume

A_d = drop cross sectional area

The equation of motion of the droplet is given by Newton's Second Law of Motion:

$$\frac{du_\ell}{dt} = \frac{F}{M} \tag{B-22}$$

and

$$M = V\rho_\ell \tag{B-23}$$

such that

$$\frac{du_\ell}{dz} = \frac{1}{u_\ell}\frac{du_\ell}{dt} \tag{B-24}$$

The vapor velocity can be obtained from:

$$\dot{m}_g = A_g \rho_g u_g \tag{B-25}$$

$$\dot{m}_\ell = A_\ell \rho_\ell u_\ell \tag{B-26}$$

$$A_c = A_g + A_\ell \tag{B-27}$$

where:

$\dot{m}_g$, $\dot{m}_\ell$ = vapor, liquid mass flow rate, respectively

A_g, A_ℓ = vapor, liquid flow area

A_c = total flow area

solving for the vapor velocity, one obtains:

$$u_g = \frac{\dot{m}_g \rho_\ell u_\ell}{\rho_g \left[A_c \rho_\ell u_\ell - \dot{m}_\ell\right]} \tag{B-28}$$

and, therefore,

$$\Delta u \equiv u_g - u_\ell = \frac{m_g \rho_\ell u_\ell}{\rho_g [A_c \rho_\ell u_\ell - \dot{m}_\ell]} - u_\ell \tag{B-29}$$

Simplifying and solving for u_ℓ, yields:

$$u_\ell = \frac{-B + \sqrt{B^2 - 4AC}}{2A} \tag{B-30}$$

where:

$$A = A_c \rho_g \rho_\ell \tag{B-31}$$

$$B = A_c \rho_g \rho_\ell \, (\Delta u) - \dot{m}_g \rho_\ell - m_\ell \rho_g \tag{B-32}$$

$$C = - \dot{m}_\ell \rho_g \, (\Delta u) \tag{B-33}$$

Assuming the droplets are at equilibrium,[1] for a given droplet diameter d, we can readily solve for (Δu) from equations (B-17) through (B-21) by iteration. We can then solve for the equilibrium droplet velocity as a function of quality (and hence z), using equation (B-30).

For the sake of quantitative illustration, we shall use typical FLECHT data and assume the following to be constants:

$$A_c = 0.0015 \text{ ft}^2$$

$$\rho_g = 0.005 \text{ lb/ft}^3$$

$$\rho_\ell = 50 \text{ lb/ft}^3$$

$$u_g = 1.5 \times 10^{-5} \text{ lb/ft-sec}$$

$$\dot{m}_T = 0.01 \text{ lb/sec}$$

1. Equilibrium is defined here as the "local" net force (drag, gravitation, and buoyancy force) acting on the drop being zero. Note that the equilibrium velocity is a function of diameter, pressure, and vapor temperature and is not a constant along the bundle.

The results are plotted in figure B-1. Note the peculiar behavior of the droplets as mentioned in section 4. This can be understood mathematically as explained in the following paragraph.

An order of magnitude estimation of equation (B-30) shows that B^2 is much greater 4AC. Thus, for B greater than zero, u_ℓ is very small and is approximately a constant. When B is negative, the two terms in the numerator of equation (B-30) are additive. Thus, u_ℓ increases much more rapidly as the quality increases. The "turning point" on the curves, as indicated by the arrows in figure B-1, is then defined as the point where B is equal to zero.

Figure B-2 illustrates a proposed mechanism of droplet entrainment at the quench front which fits the mathematical interpretation of equation (B-30). The water vapor breaks a "sheet" of water with "diameter" greater than d_5 (see figure B-1) as shown in figure B-2. This "drop" is too big to be entrained and moves at essentially constant speed with the quench front. The "sheet" then breaks up into smaller drops with diameter equal to d_4; these drops are still too big to be entrained. The drops break up further into drops with a diameter equal to d_3, which then accelerates rapidly up the bundle. Note that drops with a diameter smaller than d_3 will also be created at the quench front and be entrained. An analytical model to predict the droplet size distribution is not necessary for the present calculations. Hence d_3 is simply taken as the average initial droplet size. Note also that in this model, the onset of droplet entrainment does not necessarily coincide with the quench front as shown in figure B-2d and can be above the quench front.

To solve for d_3, we simply solve equation (B-32) for (Δu) by putting B equal to zero. d_3 is then obtained from equations (B-17) through (B-21) by iteration and equating the force acting on the droplet to zero.

The droplet diameter above the quench front is computed as follows. Assuming the droplets do not break up, the number of droplets passing any particular elevation per second will then be a constant; that is;

$$N = \frac{6\dot{m}_T\,(1-x)}{\pi d^3 \rho_\ell} = \frac{6\dot{m}_T\,(1-x_i)}{\pi d_i^3 \rho_\ell} = \text{constant} \qquad \text{(B-34)}$$

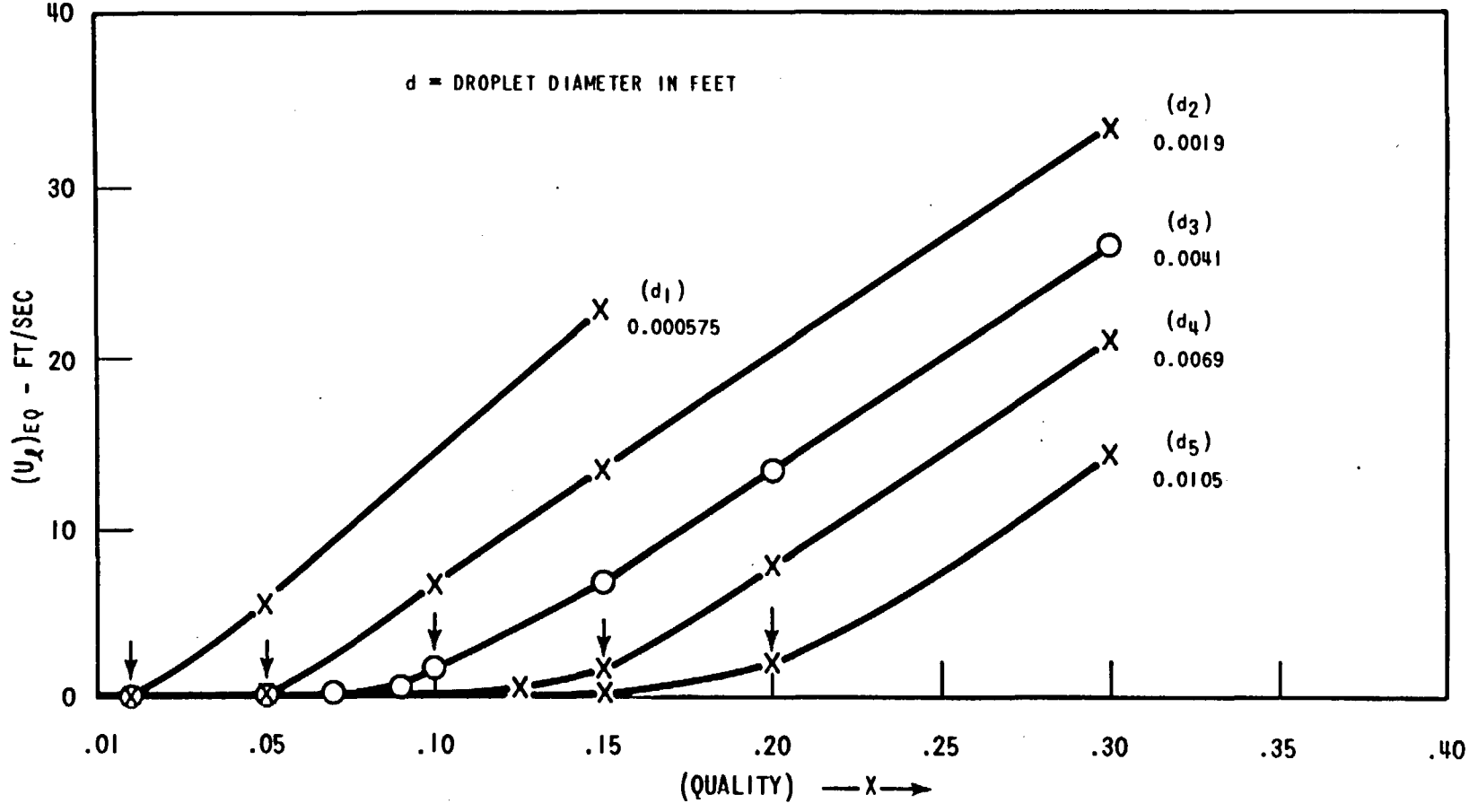

Figure B-1. Droplet Sizes Needed for Entrainment

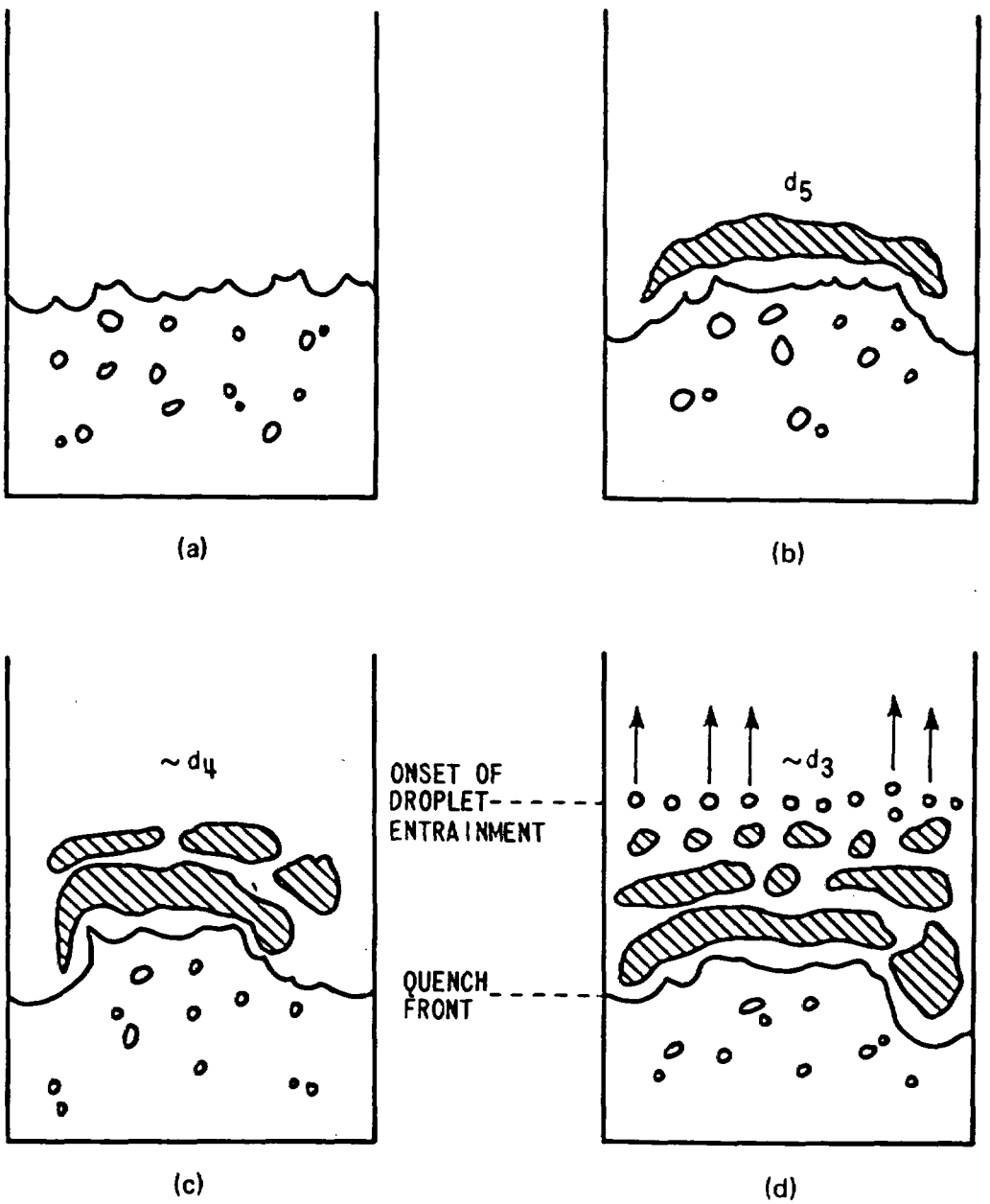

Figure B-2. Proposed Model for Droplet Entrainment

The droplet diameter is then a function only of quality and the initial droplet diameter

$$d = d_i \left[\frac{1-x}{1-x_i} \right]^{\frac{1}{3}} \tag{B-35}$$

where:

The subscript i refers to the quench front

$\dot{m}_T$ = total max flow rate (lb/sec)

x = quality

ρ_ℓ = liquid density (lbm/ft^3)

N = No. of droplets passing any particular elevation per second.

Finally, to allow for droplet breakup, the critical Weber number was defined as 7.5; that is,

$$We \equiv \frac{d\,(u_g - u_\ell)^2\,\rho_g}{6} \tag{B-36}$$

$$(We)_{critical} \equiv 7.5 \tag{B-37}$$

where

d = droplet diameter

σ = surface tension

If the initial Weber number exceeds 7.5, the initial drop size will be computed by equation (B-36). If the Weber number exceeds 7.5 along the bundle, we simply split a drop into two.

Figures B-3 and B-4 show typical initial drop size as computed by the model. The solid line in the figure represents the droplet size computed by the model without allowing for droplet breakup. The dotted line represents droplet size computed by allowing for droplet breakup.

B.4 EFFECT OF INITIAL VOID ON SLIP

As mentioned in section 4, the slip ratio or droplet velocity (for a given drop size) above the quench front is independent of initial slip value. An overestimate (underestimate) of slip is compensated for by an overestimate (underestimate) of the drag force (hence, acceleration of the drop which will then reduce the slip ratio).

RUN NUMBER	02833
PRESSURE	40 PSIA
INITIAL CLADDING TEMPERATURE	1602°F
PEAK POWER	0.89 KW/FT
SUBCOOLING	142°F
INJECTION RATE	0.8 IN./SEC

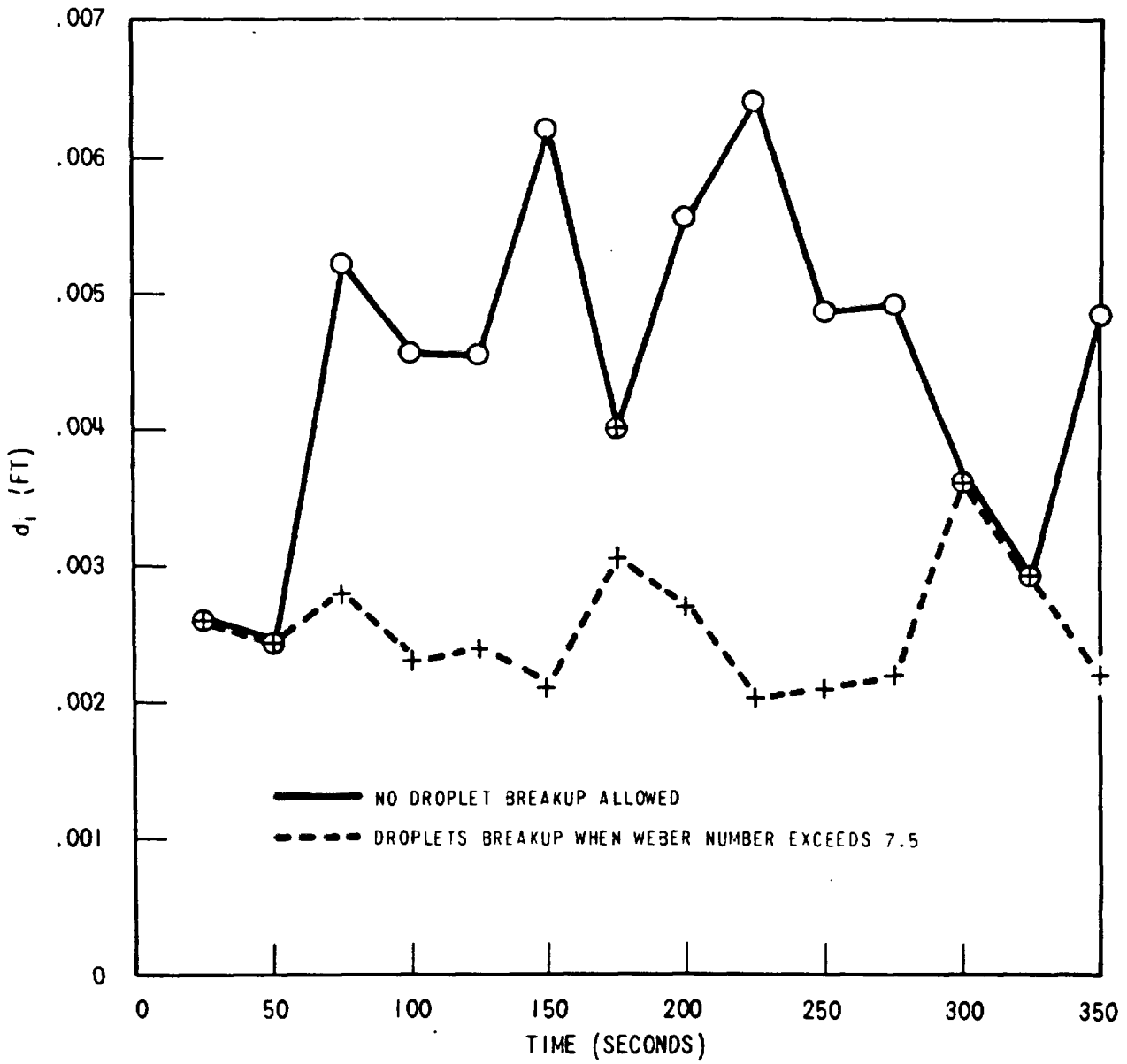

Figure B-3. Initial Drop Size Computed by Model

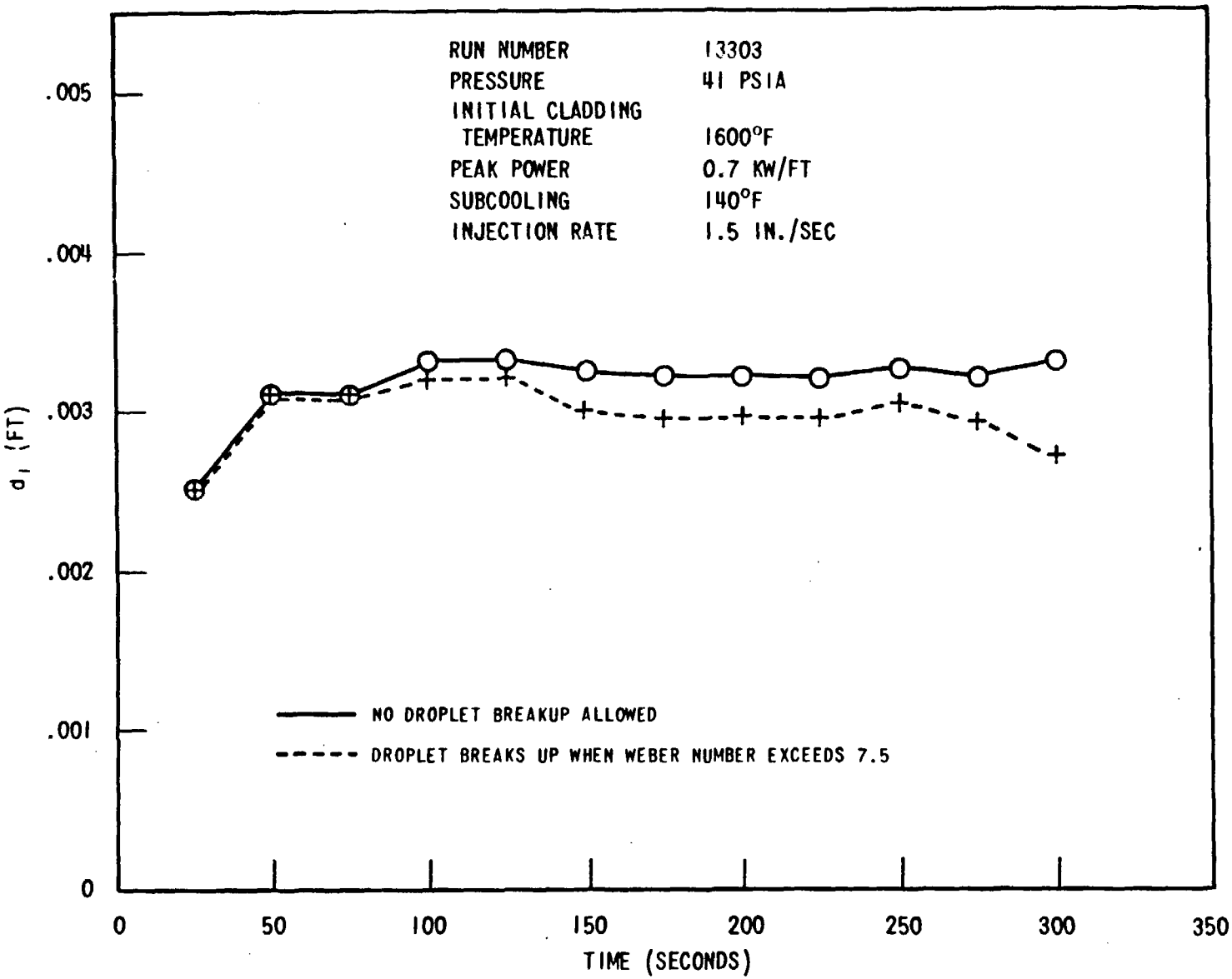

Figure B-4. Initial Droplet Size Computed by Model

Figures B-5 and B-6 show that for an initial void fraction of 0.5 and 0.9, respectively, the slips approach each other very rapidly. At about one fifth of a foot above the initial elevation, the slips are essentially identical.

B.5 CALCULATION OF SLIP AND DROPLET VOLUMETRIC DENSITY

As the result of the preceding section shows, slip is independent of its initial value. Since in the dispersed flow regime, the void fraction is approximately one, an initial void fraction of 0.99 was arbitrarily chosen. The initial droplet and vapor velocity can then be computed from:

$$S = \left(\frac{x}{1-x}\right)\left(\frac{1-\alpha}{\alpha}\right)\frac{\rho_\ell}{\rho_g} \tag{B-38}$$

$$u_\ell = \frac{1}{A_c\rho_\ell}\left[\frac{\dot{m}_g}{S}\frac{\rho_\ell}{\rho_g} + \dot{m}_\ell\right]^{[1]} \tag{B-39}$$

$$u_g = Su_\ell \tag{B-40}$$

where:

S = slip ratio

α = void fraction

The droplet velocity above the quench front is then obtained by numerically integrating the equation of motion, equation (B-24). The numerical procedure consists of dividing the bundle into small intervals with length (Δz). The droplet velocity in the k^{th} interval is then obtained from:

$$(u_\ell)_k = (u_\ell)_{k-1} + \left.\frac{du_\ell}{dz}\right|_{k-1}(\Delta z)_{k-1} \tag{B-41}$$

The vapor velocity and slip is given by

$$(u_g)_k = \frac{(\dot{m}_g)_k\,\rho_\ell\,(u_\ell)_k}{(\rho_g)_k\,[A_c\rho_\ell(u_\ell)_k - (\dot{m}_\ell)_k]} \tag{B-42}$$

$$(S)_k \equiv \frac{(u_g)_k}{(u_\ell)_k} \tag{B-43}$$

1. Equation (B-39) is obtained from equation (B-28), remembering that the slip is defined as the ratio of vapor velocity to droplet velocity.

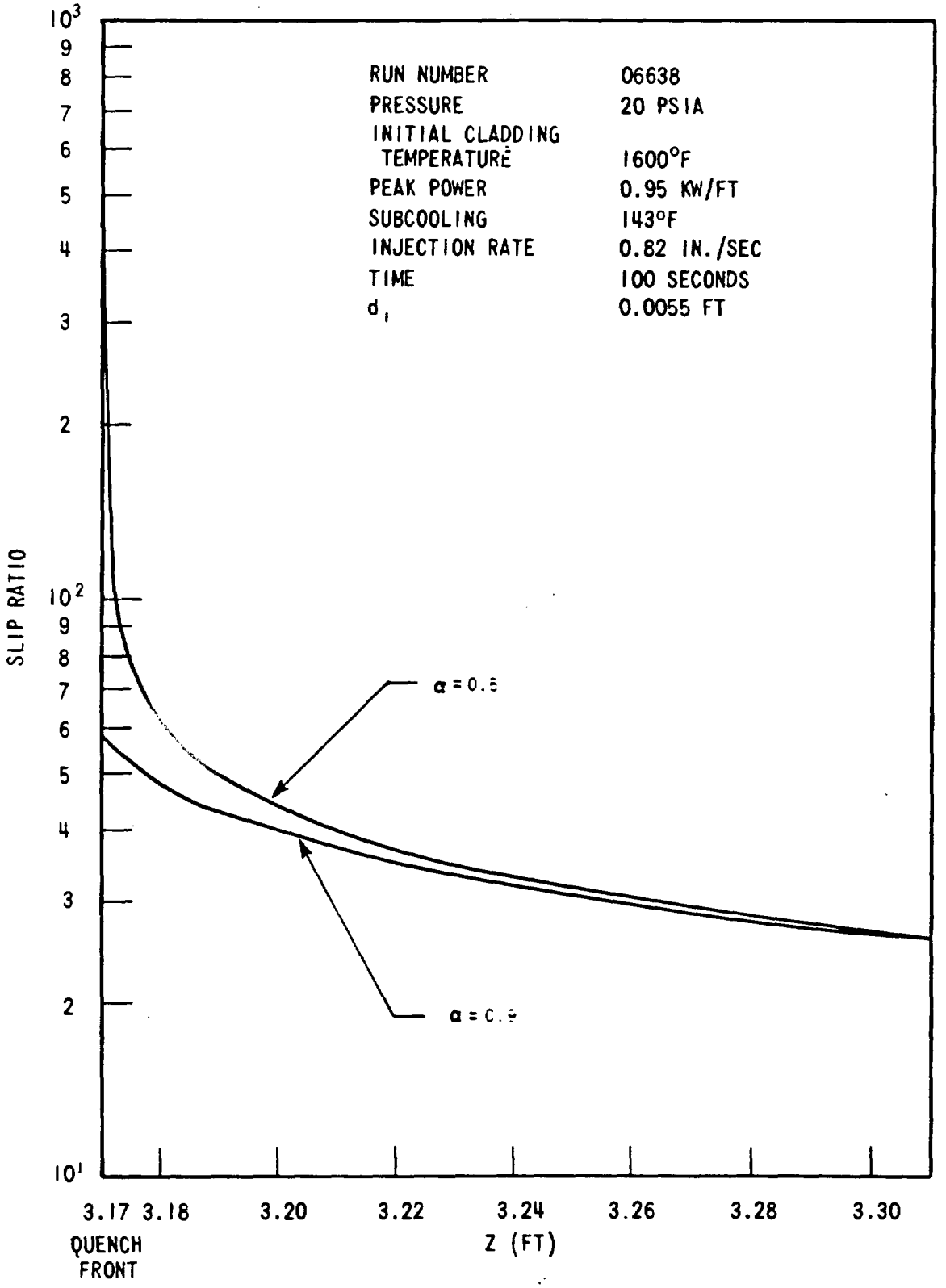

Figure B-5. Slip Versus Elevation for Different Initial Voids

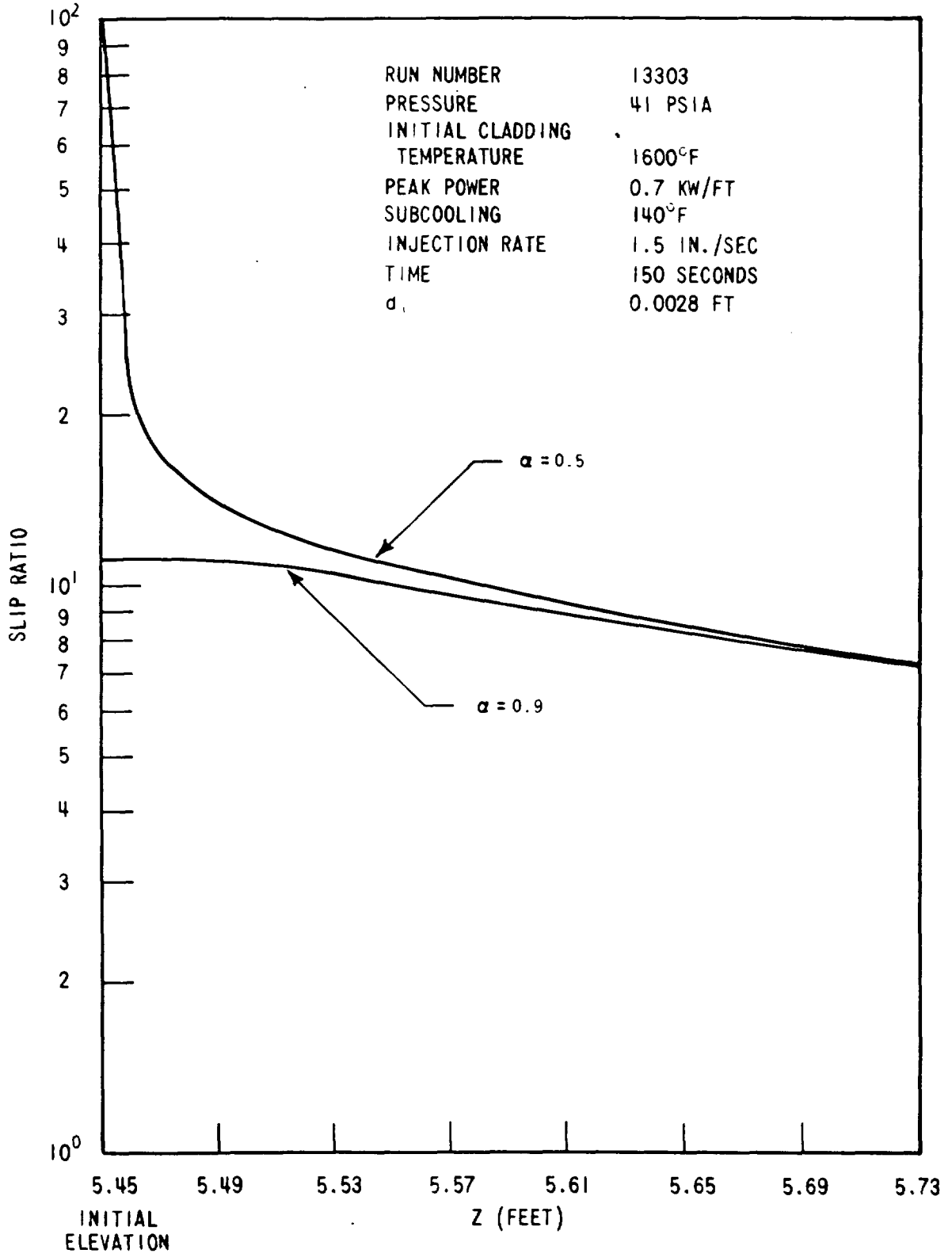

Figure B-6. Slip Versus Elevation for Different Initial Voids

Finally, the droplet number density is obtained from:

$$N_\ell = \frac{N}{A_c u_\ell} \tag{B-44}$$

where

N_ℓ = droplet number density (No. of droplets/ft^3)

B.6 DEPENDENCE OF HEAT FLUXES (q''_{cv}, q''_{rd}, q''_{rv}, q''_{ru}) ON DROPLET SIZE

As mentioned in section 4, droplet size is the most uncertain assumption in the whole calculation. The drop size, computed by the model described above is of the order of 0.012 inches while those observed from the FLECHT movies are of the order of 0.12 inches. It is believed that the actual size of the droplet lies within this range 0.01, to 0.1 inch. Note that under identical flow conditions (ie, pressure, fluid and wall temperature, quality, and total mass flow rate), the heat flux is a function only of drop size and slip (which is in turn affected by the drop size). Hence, it is important to study how the results are affected by the drop size.

To study the effect of droplet size, four different input initial drop diameters (0.005, 0.001, 0.005, 0.01 feet) were used. The heat flux and slip were then calculated and compared.[1]

Figures B-7 and B-8 show how the slip ratio varies with the initial droplet size. The result is to be expected. The droplet acceleration[2] (hence droplet velocity) decreases as the droplet diameter increases. Hence, the slip ratio increases as drop size increases since the vapor velocity is essentially a constant and approximately equal to the superficial vapor velocity.

Figures B-9 and B-10 show the normalized heat fluxes (heat flux/total heat flux) versus the initial drop size. Note that the radiative heat fluxes only account for a small fraction of total heat flux (0-30%). Hence, in the range of drop size (0.01 - 0.1 inch) that we are interested in, the convective heat flux varies only by 5 to 10 percent. Note also that:

- q''_r and q''_{rv} are essentially constant
- As drop size increases, q''_{rd} falls rapidly, and then remains essentially a constant.

---

1. To isolate the effect of droplet size, the calculation was modified as follows:
   The flow conditions are identical; the initial void fraction (or slip) is identical; no droplet breakup allowed in the calculation.
2. The initial drop velocities (void fraction) are identical.

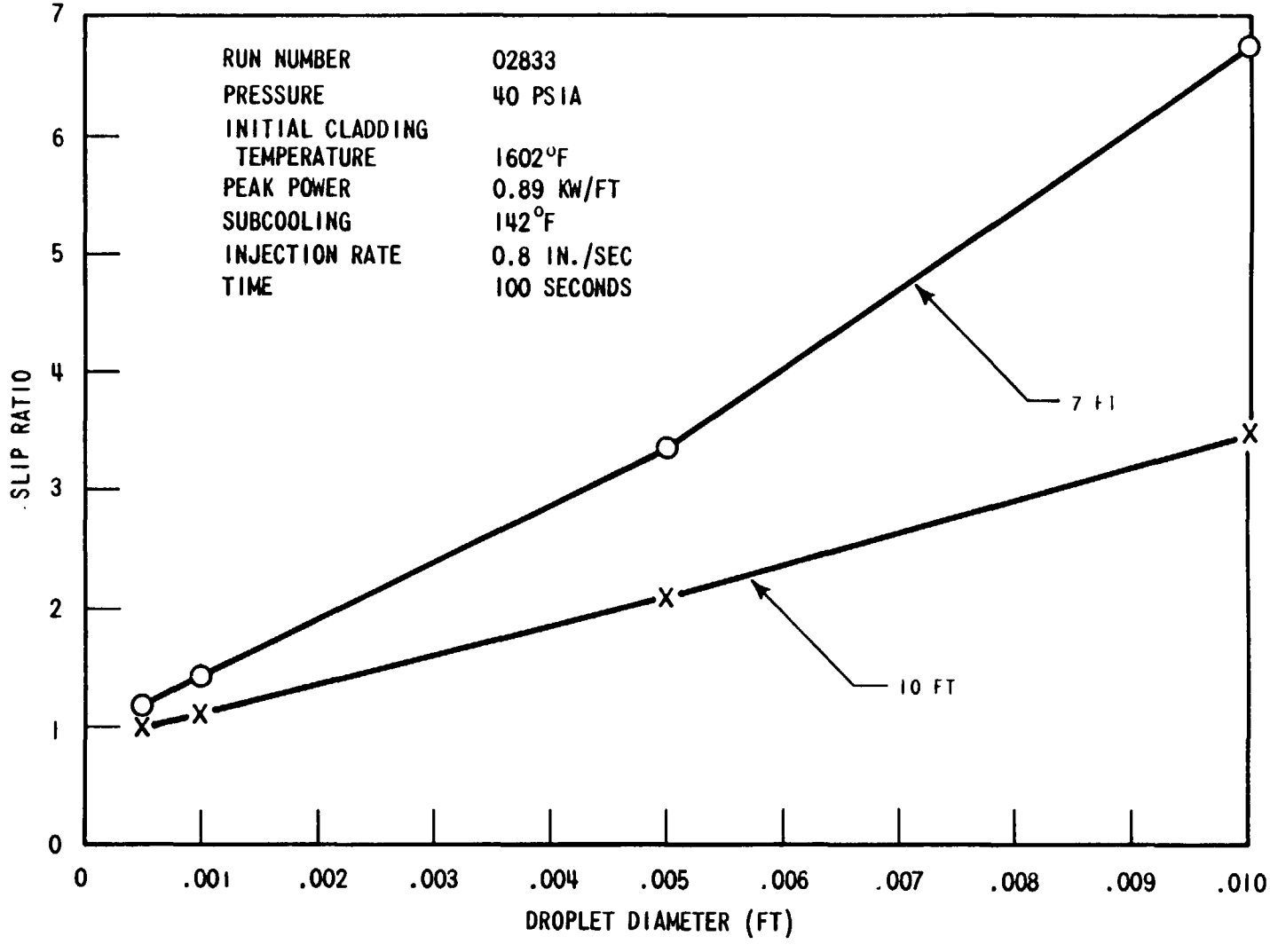

Figure B-7. Slip Ratio Versus Droplet Size

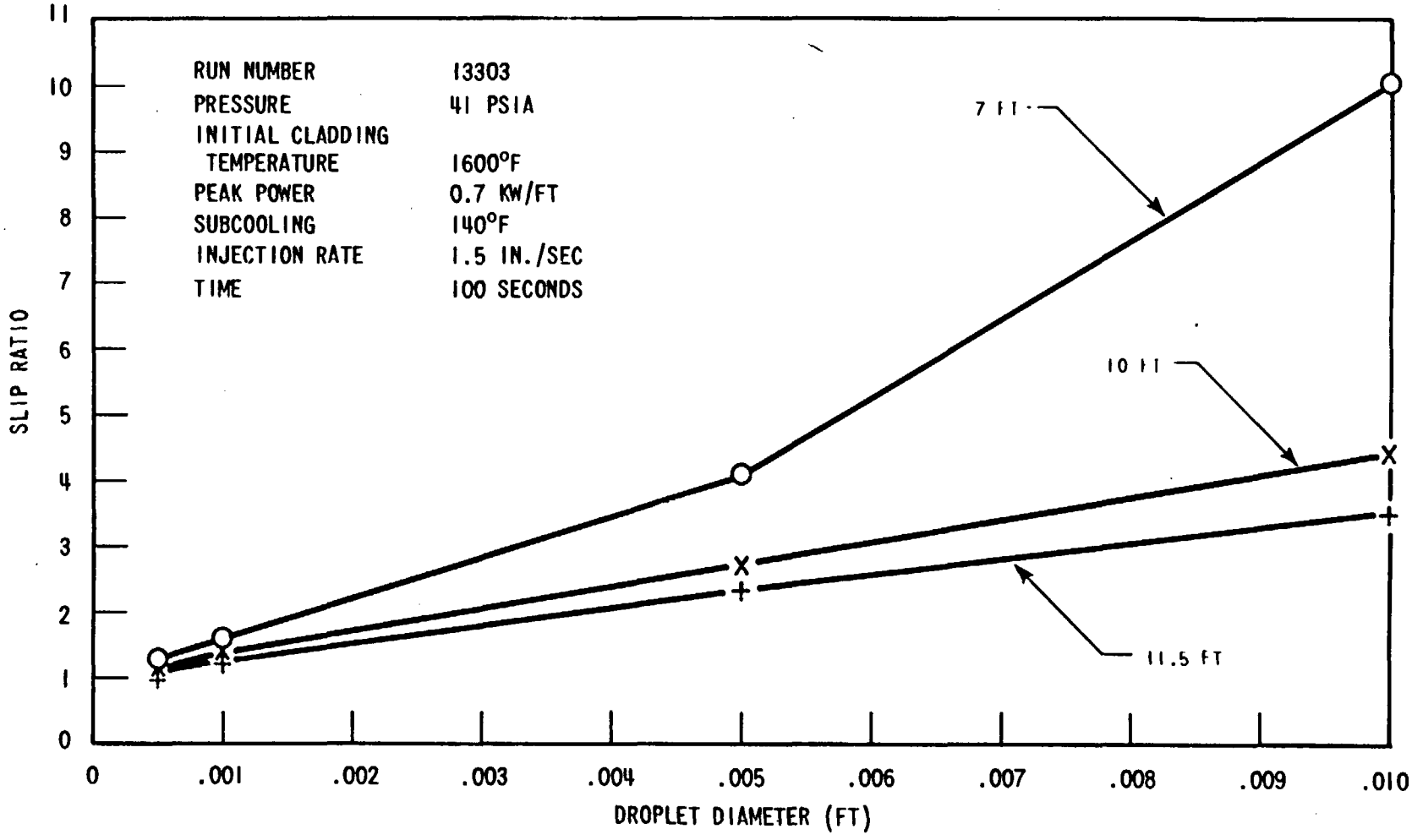

Figure B-8. Slip Ratio Versus Droplet Size

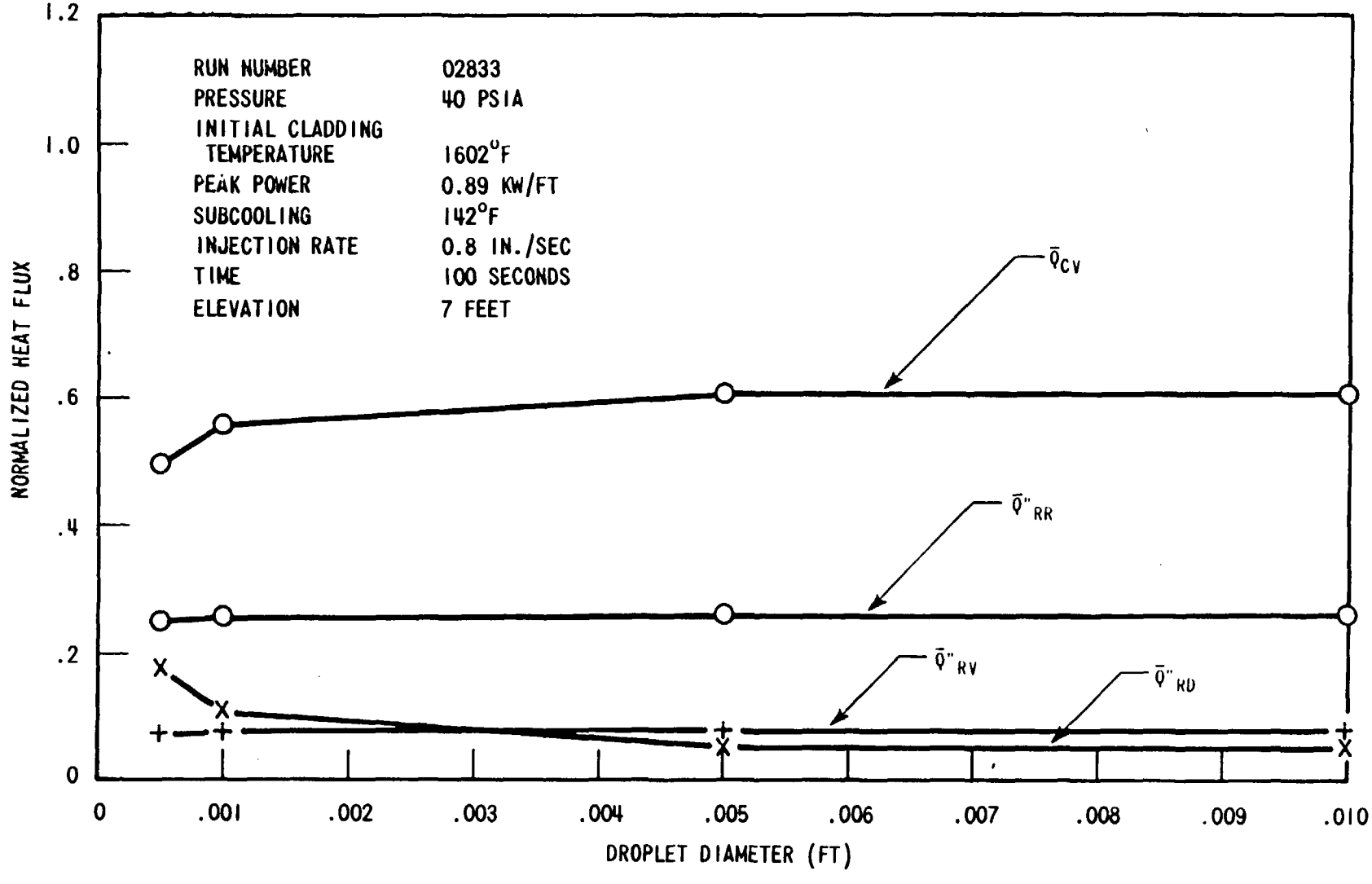

Figure B-9. Normalized Heat Flux Versus Droplet Size

11,863-90

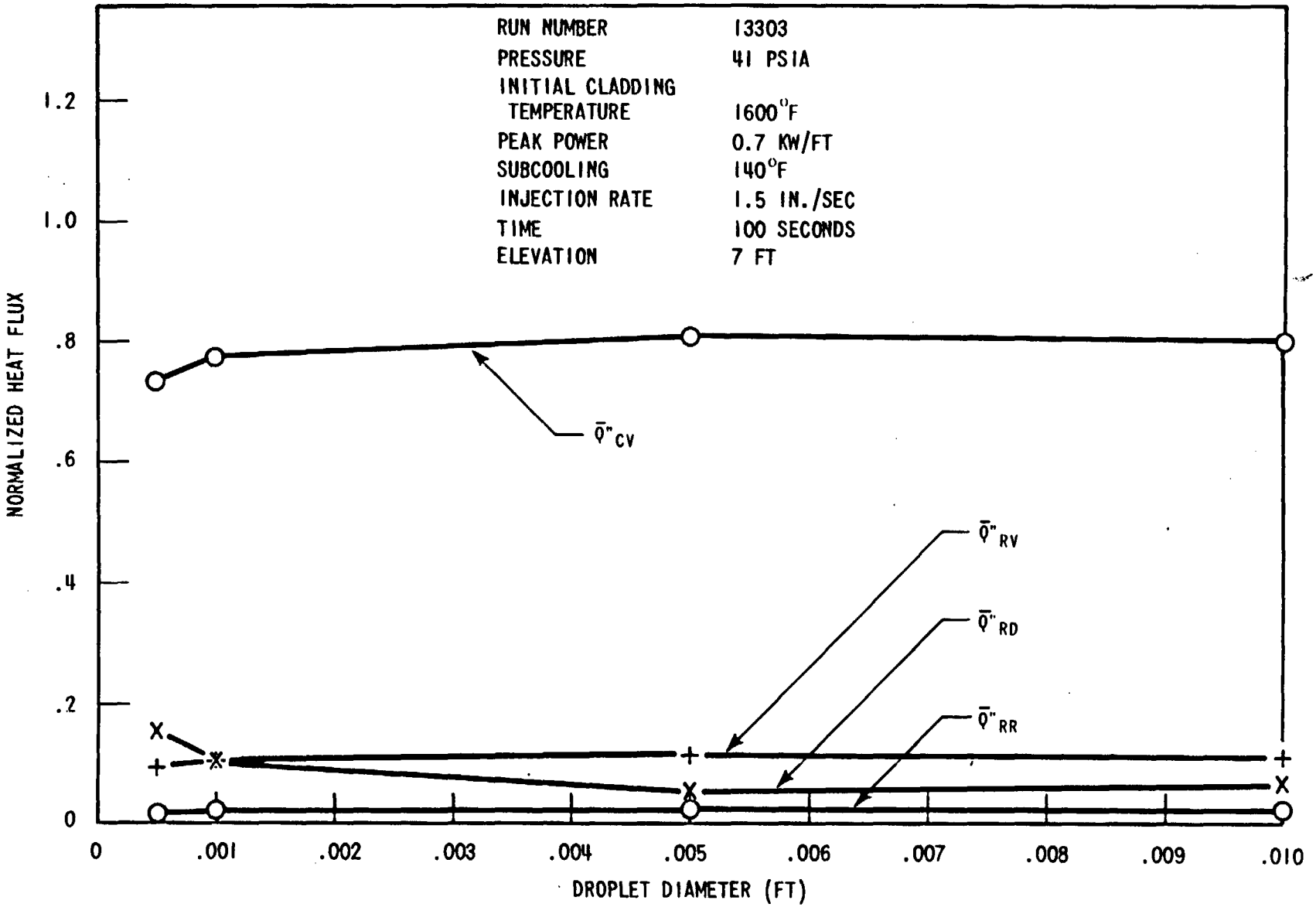

Figure B-10. Normalized Heat Flux Versus Droplet Size

11,863-89

The variation of the radiation heat flux with droplet size can be explained as follows:

$$q''_r \propto A_r = e^{-kL_m} \tag{B-43}$$

and from equations (B-2) and (B-3)

$$q''_{rv} \propto F_{wv} \tag{B-44}$$

$$q''_{rd} \propto F_{w\ell} \tag{B-45}$$

For an optically thin medium, we have:

$$1 >> a_v L_m,\ a_\ell L_m,\ kL_m \tag{B-46}$$

Then

$$A_r \approx 1 \tag{B-46}$$

and from equations (B-12) and (B-13):

$$\epsilon_v \approx a_v L_m = \text{constant}^{[1]} \tag{B-47}$$

$$\epsilon_\ell \approx a_\ell L_m \tag{B-48}$$

From equations (B-8), (B-9), (B-10) and remembering that ϵ_v and ϵ_ℓ are small quantities:

$$R_3 \approx 1 + \frac{1 - \epsilon_w}{\epsilon_w} \approx 1 = \text{constant} \tag{B-49}$$

$$R_1 \approx \frac{1}{\epsilon_v} = \text{constant} \tag{B-50}$$

$$R_2 \approx \frac{1}{\epsilon_\ell} \tag{B-51}$$

and

$$1 >> \frac{1}{R_1},\ \frac{1}{R_2}$$

1. Constant here means independent of droplet size.

Equations (B-5) and (B-6) can then be approximated by:

$$F_{w\ell} \approx \frac{1}{R_2} \quad . \tag{B-52}$$

$$F_{wv} \approx \frac{1}{R_1} = \text{constant} \tag{B-53}$$

Equations (B-43) and (B-44), together with equations (B-46) and (B-53) explain why q''_r and q''_{rv} are independent of the droplet size.

From equations (B-16), (B-34) and (B-42), we have:

$$a_\ell \propto \frac{1}{u_\ell d} \tag{B-54}$$

Since the vapor velocity is essentially a constant and equal to the superficial steam velocity, we then have:

$$a_\ell \propto \frac{\text{slip}}{d} \tag{B-55}$$

Combining equation (B-45), (B-52), (B-51), (B-48), and (B-55):

$$q''_{rd} \propto \frac{\text{slip}}{d} \tag{B-56}$$

Figures B-11, B-12, B-13 and B-14 show that the curves for q''_{rd} and $\frac{\text{slip}}{d}$ are essentially parallel, which confirms equation (B-56).

Finally, there remains to be explained why q''_{rd} or $\frac{\text{slip}}{d}$ drops rapidly as d increases and then stays almost a constant. This is done below for small and large drop diameters:

- Small drop (diameter $\lesssim$ 0.01-inch)

  For small drops, the acceleration is large and the drop velocity approaches that of the vapor velocity rapidly, hence:

  $$\text{Slip} \approx 1 \tag{B-57}$$

  and

  $$\frac{\text{Slip}}{d} \approx \frac{1}{d} \tag{B-58}$$

  The $\frac{"1"}{d}$ behavior for small drops can actually be observed from figures B-11 through B-14.

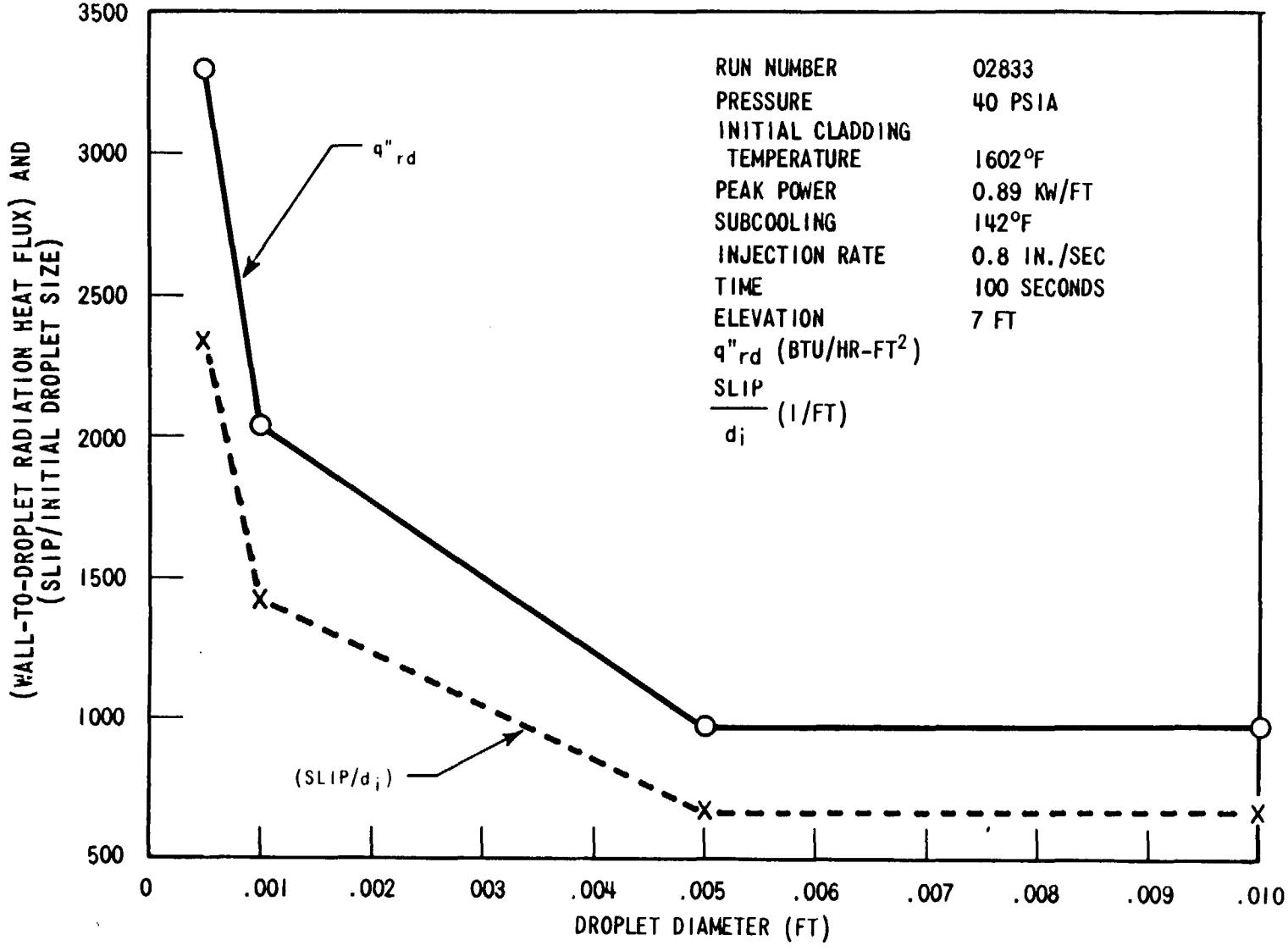

Figure B-11. q''_{rd} and $(\frac{Slip}{d_i})$, Versus Droplet Size

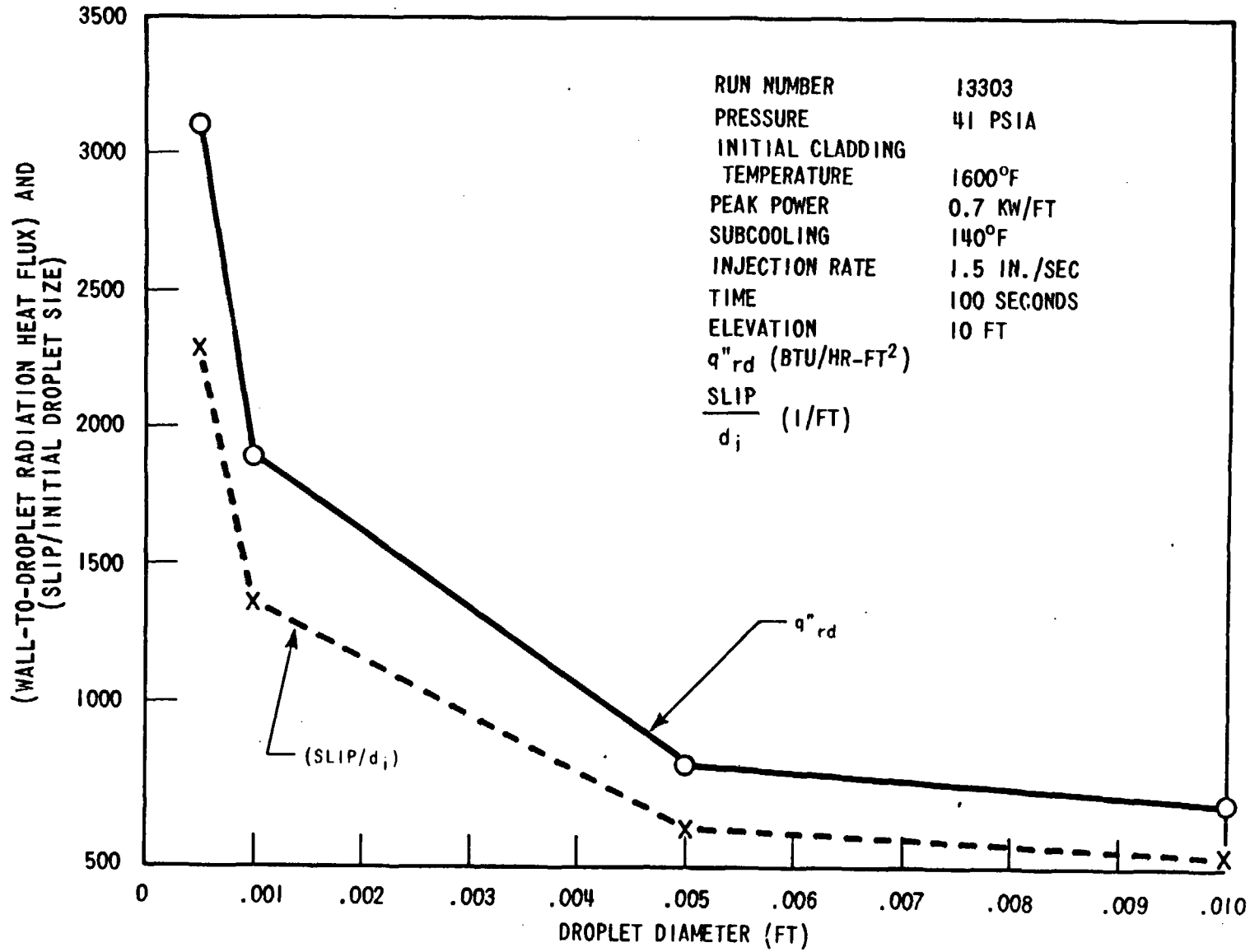

Figure B-12. q''_{rd} and $(\frac{Slip}{d_i})$, Versus Droplet Size

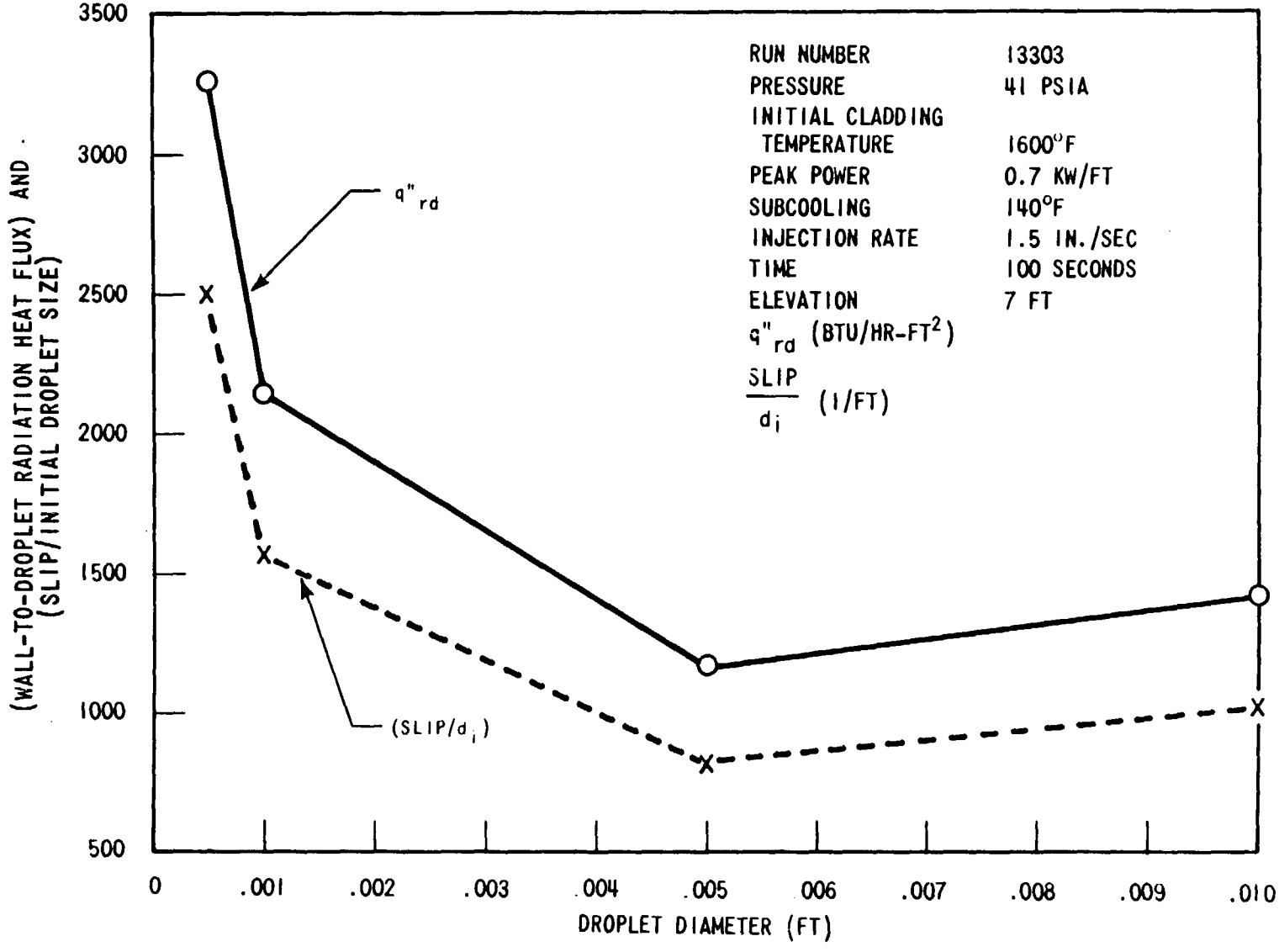

Figure B-13. q''_{rd} and $(\frac{Slip}{d_i})$, Versus Droplet Size

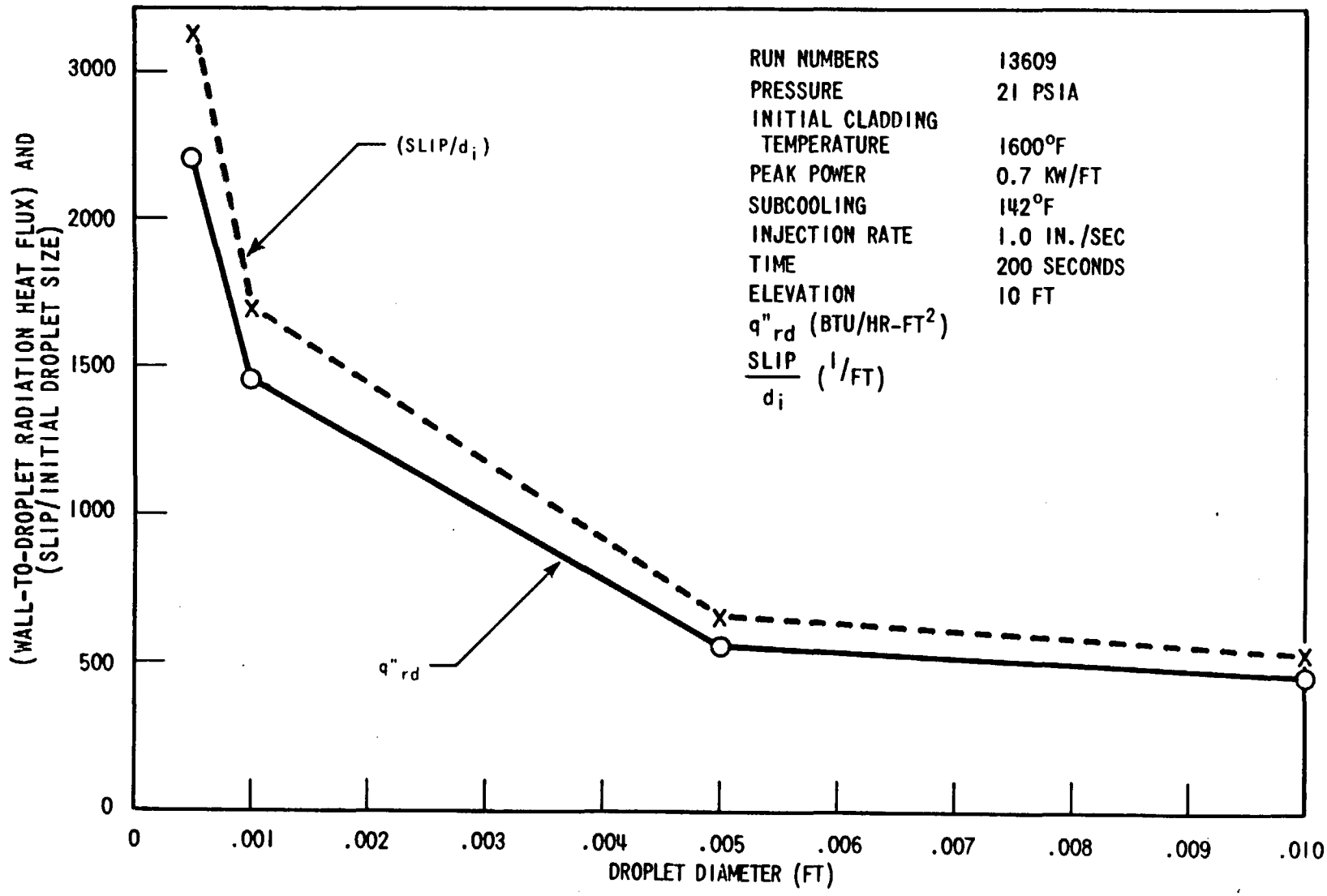

Figure B-14. q''_{rd} and $(\frac{Slip}{d_i})$, Versus Droplet Size

- Large drops (diameter $\gtrsim$ 0.005 foot)

To simplify the analysis, the drops are assumed to be at equilibrium and the drag coefficient is taken to be a constant. From equation (B-17), we have:

$$(u_g - u_\ell)^2 = k' d \tag{B-59}$$

where

$$k' \equiv \frac{4}{3} \frac{g}{C_D} \frac{\rho_\ell - \rho_g}{\rho_g} = \text{constant} \tag{B-60}$$

For large drops, acceleration is small and

$$u_g >> u_\ell$$

Therefore, equation (B-59) can be simplified to:

$$1 - \frac{2}{(\text{slip})} = k\, d \tag{B-61}$$

where

$$k \equiv \frac{k'}{u_g^2} = \text{constant} \tag{B-62}$$

Rearranging equation (B-61), we have:

$$\text{Slip} = \left[\frac{2}{1 - kd}\right] \tag{B-63}$$

and

$$\left(\frac{\text{slip}}{d}\right) = 2\left[\frac{1}{d} + \frac{k}{(1 - kd)}\right] \tag{B-64}$$

As d increases, the first term on the right-hand side of equation (B-64) decreases. The second term, however, increases with d and tend to offset the effect of the first term. This explains the relatively "flat" behavior of $\frac{slip}{d}$ (or q''_{rd}) for large drops.

An order of magnitude estimation will help to illustrate this point:

Let

$$u_g = 50 \text{ ft/sec}$$

$$u_\ell = 20 \text{ ft/sec}$$

From equation (B-59) and for a drop diameter of 0.005 foot:

$$k' = 180{,}000 \text{ ft/sec}^2$$

$$k = 72 \text{ ft}^{-1}$$

From equation (B-64), we have:

$$\left(\frac{slip}{d}\right)_{d=0.005 \text{ ft}} = 2\left[\frac{1}{0.005} + \frac{72}{(1 - 0.36)}\right] = 625 \text{ ft}^{-1}$$

$$\left(\frac{slip}{d}\right)_{d=0.01 \text{ ft}} = 2\left[\frac{1}{0.01} + \frac{72}{(1 - 0.72)}\right] = 714 \text{ ft}^{-1}$$

Therefore, for a factor of two change in drop size, the ratio $\frac{slip}{d}$ only changed 15 percent.

APPENDIX C
DEVELOPMENT OF A SURFACE-TO-SURFACE RADIATION MODEL

One of the inputs into the total wall heat flux equation is the amount of surface-to-surface radiation which is occurring in the FLECHT bundle. This component of the wall heat flux must be known or estimated to be able to calculate the convective wall heat flux as a difference between the total wall heat flux and the sum of radiation to surfaces, droplets, and vapor.

Several methods were investigated to develop a model which would predict the amount of surface radiation. The model finally chosen was one which assumed that the wall heat flux due to surface radiation was equal to the initial wall heat flux at flood time, measured in the test. Although indications are that this is correct at early times when there is little steam or entrained liquid flow in the bundle, it also appears that this model will over-estimate the radiation surface wall heat flux at later times. A discussion of the calculations and different models which were examined is attached.

C-1 MOXY ANALYSIS FOR ESTIMATING SURFACE RADIATION WALL HEAT FLUX

The MOXY code[1] was used to calculate radiation heat flux using experimental rod, thimble, and housing temperatures from the low flooding rate cosine test series (WCAP-8838).[2] No transients were run. The experimental temperatures were inserted in the program at each time during the run for which a heat flux calculation was desired. Only the output prior to the first time step of MOXY was used. This procedure eliminated the uncertainties of estimating convective heat transfer.

The six-foot elevation was used for the estimate since it is the most instrumented elevation. Even so, there are many uninstrumented rods and thimbles for which temperatures had to be estimated. Rod temperatures were determined using AVGSD output, which divides the rods into six groups according to power zone and proximity to the housing. All rods in each group in the MOXY array were assigned the average temperature of their respective groups. This

1. Evans, D. R., "MOXY, A Digital Computer Code for Core Heat Transfer Analysis", IN-1392, August 1970.
2. Lilly, G. P., Yeh, H. C., Hochrieter, L. E., and N. Yamaguchi, "PWR FLECHT Cosine Low Flooding Rate Test Series Evaluation Report", WCAP-8838, March 1977.

was done for each time considered. Only one or two thimble temperatures were available at six feet. All central thimbles were assigned a temperature equal to the average of the six-foot thimble thermocouples.

The procedure described above caused a step change in rod temperatures between rods two and three rows from the housing. This was the dividing line between rods near the housing and central rods for the cosine tests. To eliminate this as a factor, only rods more than three rows from the housing were used to estimate heat flux. Also, radiation to the housing can be neglected for these rods.

Radiation heat fluxes were calculated at five different times for three low flooding rate cosine series runs No. 02833, 04831, and 02603. Run No. 02833 was the reference run for the series, with the following test conditions:

Pressure	40 psia
Initial Cladding Temperature	1600°F
Peak Power	0.9 kw/ft
Subcooling	140°F
Flooding Rate	0.8 in./sec

Run No. 04831 had the same test conditions, except that the flooding rate was 1.5 in./sec. Run No. 02603 also had the same test conditions, except for an initial cladding temperature of 1000°F.

In addition to the above set of runs, an identical sequence was run with the thimble temperatures set equal to the hot rod temperatures. With the radiation to thimbles reduced to zero, these runs yield rod-to-rod radiation heat flux. Substracting this heat flux from the total radiation gives rod-to-thimble radiation.

Total radiation heat flux and rod-to-thimble heat flux are plotted versus time for the three runs investigated in figures C-1a, C-2a, and C-3a. Total rod heat flux and turnaround time are also indicated for reference. The difference between total radiation and rod-to-thimble radiation is the rod-to-rod radiation. Figure C-1b, C-2b, and C-3b present the radiation heat fluxes as a fraction of the total rod heat flux. At time zero, when there is not convection and most of the rod heat flux can be expected to be radiation, the calculated values for radiation heat flux for Runs No. 02833 and 04831 are 110 percent and 121 percent of total rod heat flux, respectively. For Run No. 02603 both total radiation and measured heat flux are small numbers. These points represent a check on the method used to estimate radiation

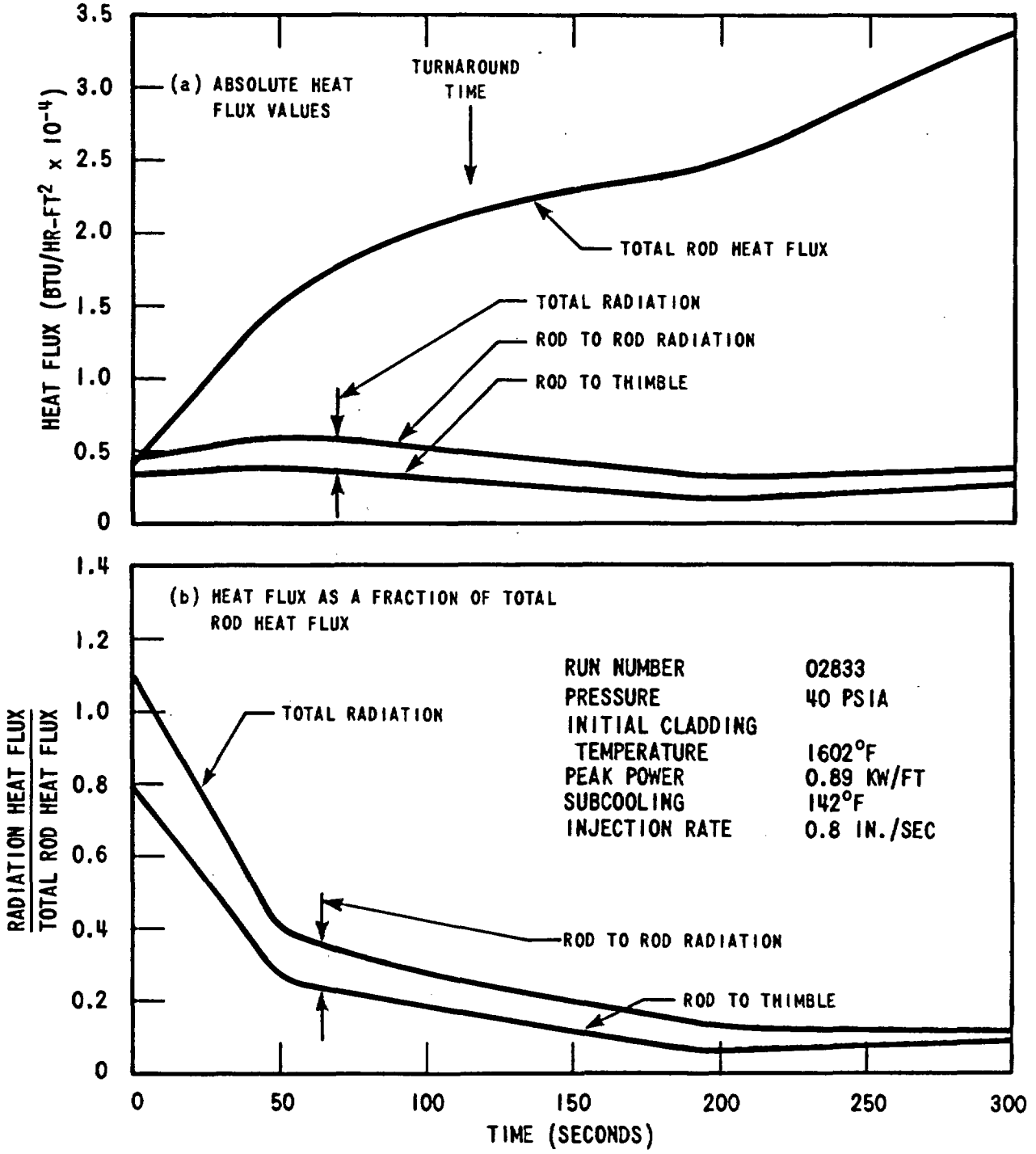

Figure C-1. Estimate of Hot Rod Radiation to Other Rods and Thimbles Run 02833 6 FT Elevation (No Absorbing Medium Considered)

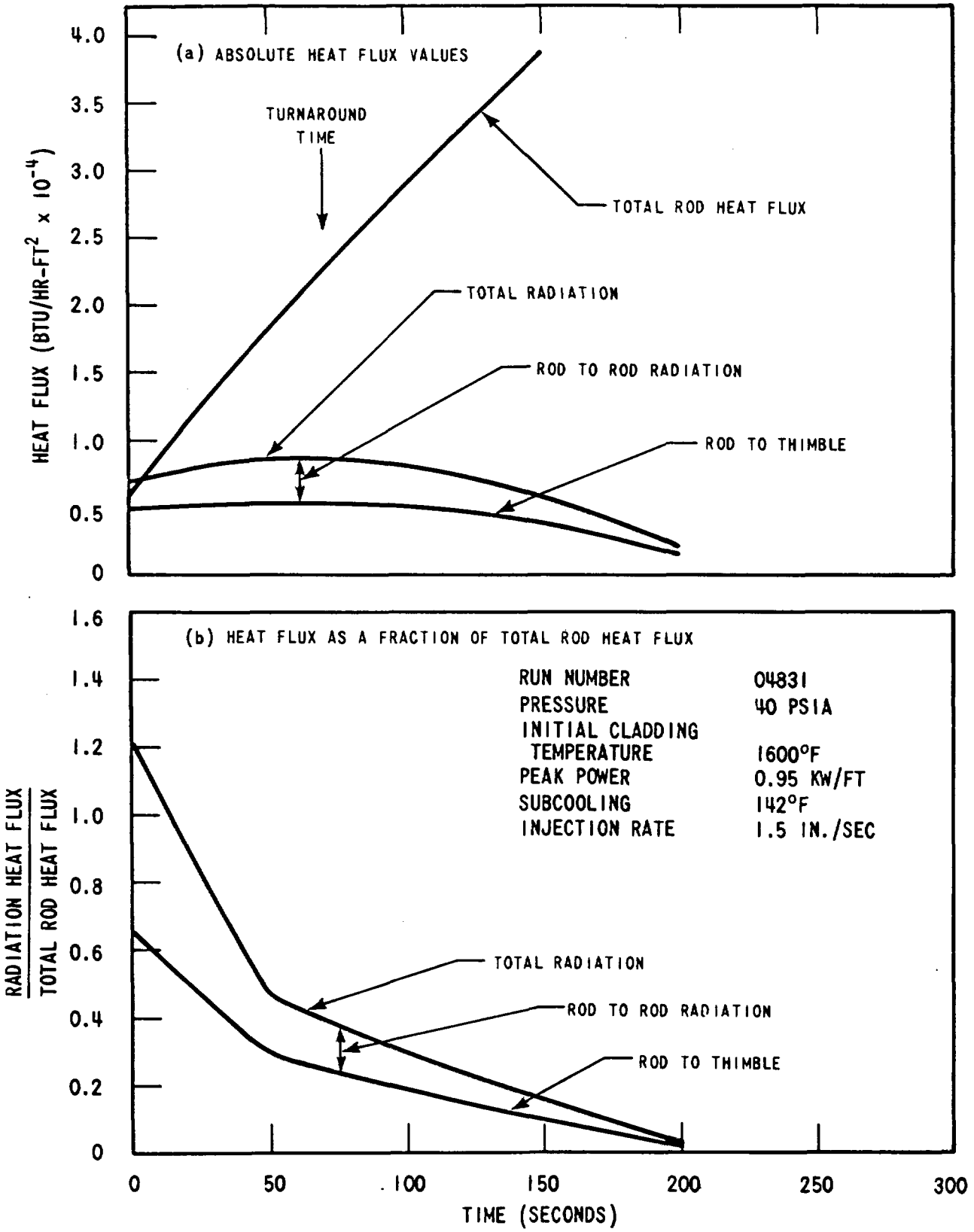

Figure C-2. Estimate of Hot Rod Radiation to Other Rods and Thimbles Run 04831 6 FT Elevation (No Absorbing Medium Considered)

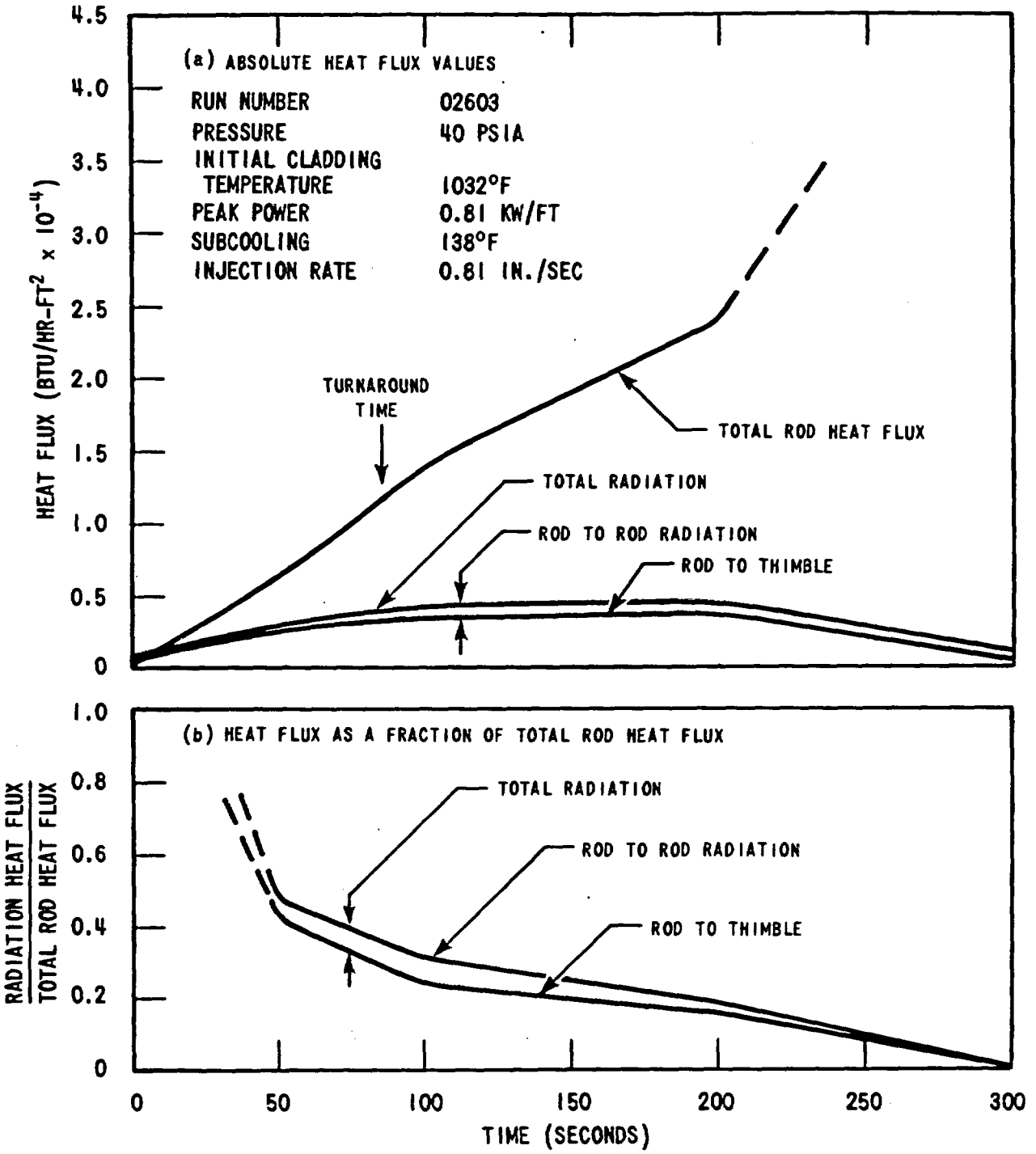

Figure C-3. Estimate of Hot Rod Radiation to Other Rods and Thimbles Run 02603 6 FT Elevation (No Absorbing Medium Considered)

heat flux and indicate that numbers are accurate to within 0.1 x 10^4 Btu/hr-ft^2. The calculated results are given in table C-1 at flood time.

With increasing time after flood, radiation increases for some time as the bundle continues to heat up, and then it decreases. Radiation as a fraction of the total heat flux decreases for all times, though at turnaround time it is still a significant fraction, 25 to 35 percent.

Numbers presented have been described as estimates of radiation heat transfer. A significant amount of temperature instrumentation is lacking and this precludes an accurate calculation to be performed. In particular, there are only two thimble thermocouples on which thimble temperature must be based. For Run No. 04831, one of these was not functioning.

In addition, no absorbing medium between the rods was assumed. If the absorbtion effects of the flowing vapor and two-phase mixture were accounted for, the surface radiation heat fluxes would in fact be lower. However, the calculations do show that at flood time, the calculated wall heat flux and that measured do agree indicating that surface radiation is significant at these times.

TABLE C-1

COMPARISON OF INITIAL RADIATION HEAT FLUX CALCULATED WITH MOXY AND MEASURED INITIAL HOT ROD HEAT FLUX AT FLOOD TIME

Run	Measured Heat Flux (Btu/hr-ft^2 x 10^{-4})	Predicted With MOXY (Btu/hr-ft^2 x 10^{-4})
02833	0.42	0.46
04831	0.57	0.69
02603	0.03	0.08

C-2 DIFFERENT SURFACE-TO-SURFACE RADIATION MODELS

The simplest model assumes surface-to-surface radiation heat flux is constant at the initial value for the entire run. MOXY results show that surface-to-surface radiation increases as the bundle heats up after flooding, then decreases as the bundle cools. This effect can be modeled by assuming that the effective temperature difference for radiation remains contant for the whole run. The effective temperature difference is the ΔT needed to match the hot rod initial heat flux. Models with constant surface-to-surface radiation heat flux and constant effective temperature difference are proposed and compared with the MOXY results.

Two simple models were examined to predict the surface-to-surface radiation;

$$\text{Model I} \qquad q_r'' = q''\Big|_{t=o} = \text{constant} \tag{C-1}$$

$$\text{Model II} \qquad q_r'' = \sigma\epsilon\left[T_{HR}^4 - \left(T_{HR} - \Delta T_o\right)^4\right] \tag{C-2}$$

where

T_{HR} = average hot rod temperature or (1.1 zone, central 6 x 6 rods)

ΔT_o = effective temperature difference at t=0 calculated from equation (C-3). (Assumed constant for entire run.)

$$\Delta T_o = T_{HR}\Big|_{t=0} - \left[T_{HR}^4\Big|_{t=0} - \frac{q''\Big|_{t=0}}{\sigma\epsilon}\right]^{1/4} \tag{C-3}$$

Equation (C-3) is obtained from equation (C-2) by setting t=0 and solving for ΔT_o, values of $q''|_{t=0}$ and $T_{HR}|_{t=0}$ are available from DATARH tape and FLECMB tape if t=0 is input as a time.

Figure C-4 compares the results of both model calculations with the estimates of surface-to-surface radiation produced using MOXY.

Except in the low initial cladding temperature test, both models agree with the qeneral level of radiative heat transfer, but can differ by as much as 4000 Btu/hr-ft^2. It should be kept in mind that MOXY numbers are estimates based on sometimes sketchy data. Model II better predicts the variation of radiation heat flux during the run and might be preferable for that reason. However, in preliminary analyses of heat transfer mechanisms, this model yielded excessively high surface-to-surface radiation. It was found that this model would overestimate the surface wall heat flux for some cases, resulting in very small or negative convective wall heat flux components. This was judged unrealistic.

The question of surface-to-surface radiation heat transfer models does require further work before this heat flux component is known more accurately.

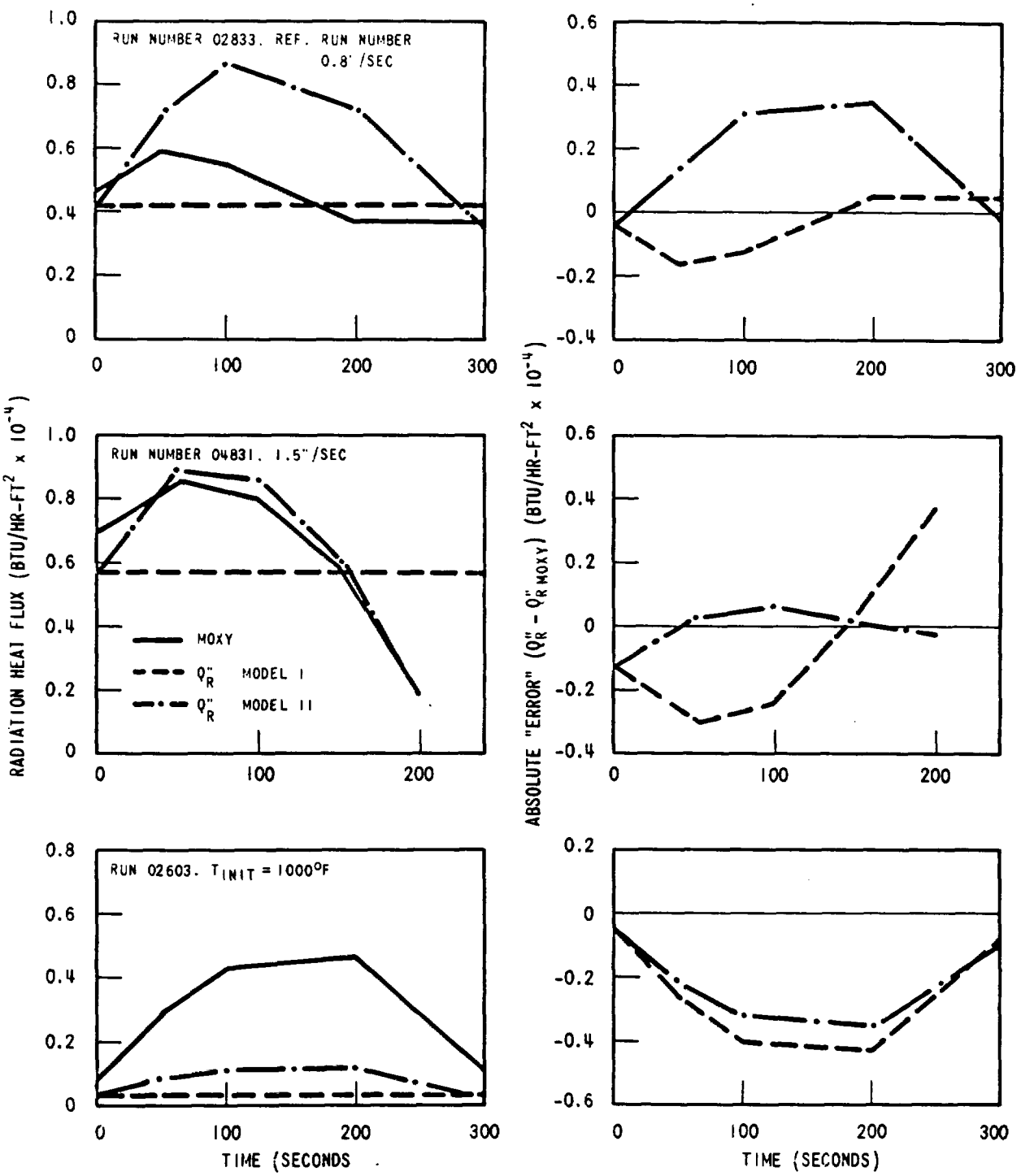

Figure C-4. MOXY Radiation Heat Transfer Results and Simple Radiation Models

APPENDIX D
FURTHER COMPARISON OF MASS FLOW CALCULATION WITH DATA

In this appendix, further comparisons are made of the mass flow calcuations of section 5 with data.

Figures D-1 to D-7 show the froth level, Z_{froth}, and the collapsed liquid height, Z_{Lf}. The froth level was reduced from the pressure drop data and was found to be in the quench front data band. The calculated collapsed liquid height is in good agreement with the collapsed liquid height reduced from the pressure drop data except for high flooding rate runs (flooding rate larger than 1.5 inches/sec.).

In these calculations, the quench front is assumed to be the same as the froth level.

Figures D-8 to D-14 compare the calculated mass flow rate ratio, Γ_f, above the froth level and the measured ratio of mass Γ_o, flowing out of the bundle. These two quantities should be the same if the rate of mass storage above the froth level is negligible. Figures D-8 to D-14 show that the agreement of comparison is excellent.

Figures D-15 to D-28 compare the calculated and the measured average void fraction in every one-foot interval. The agreement is good except for certain elevations.

RUN NUMBER	13404
PRESSURE	41 PSIA
INITIAL CLADDING TEMPERATURE	1603°F
PEAK POWER	0.7 KW/FT
SUBCOOLING	141°F
INJECTION RATE	1.0 IN./SEC

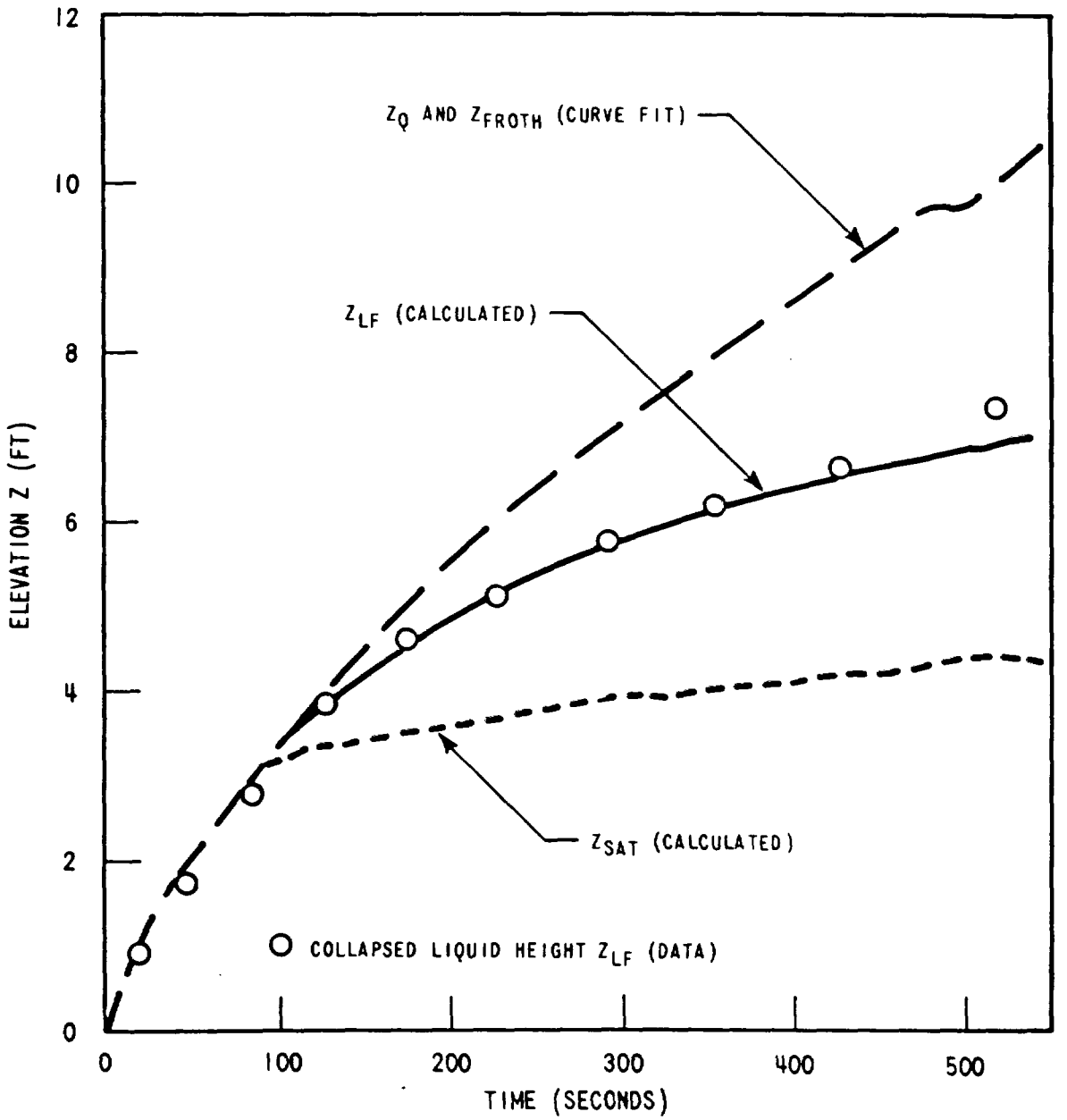

Figure D-1. Comparison of the Measured Collapsed Liquid Height Z_{Lf} and That Calculated by Using Z_{froth} (= Z_q) Data

RUN NUMBER	13303
PRESSURE	41 PSIA
INITIAL CLADDING TEMPERATURE	1600°F
PEAK POWER	0.7 KW/FT
SUBCOOLING	142°F
INJECTION RATE	1.5 IN./SEC

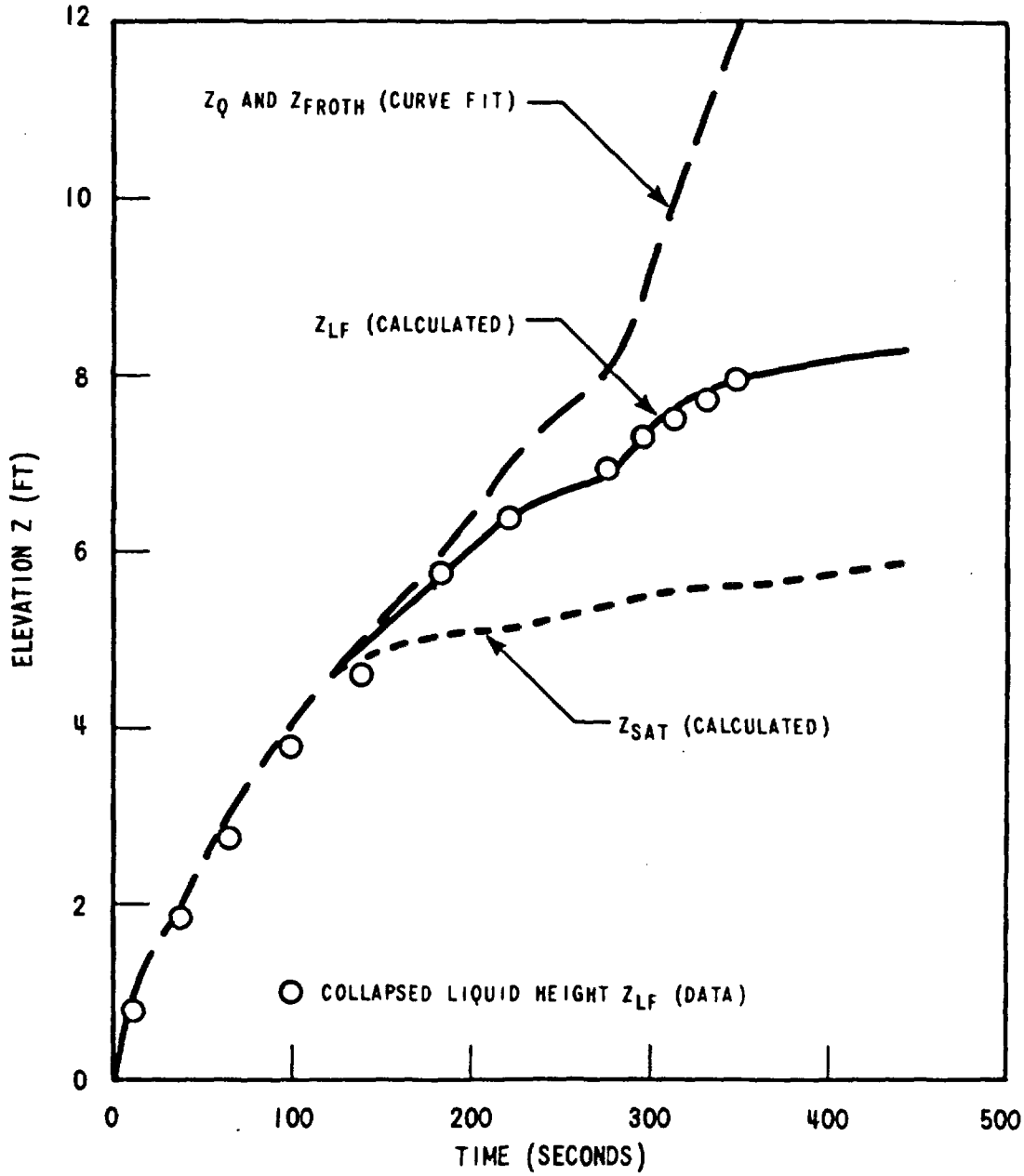

Figure D-2. Comparison of the Measured Collapsed Liquid Height Z_{Lf} and That Calculated by Z_{froth} (= Z_q) Data

RUN NUMBER	15606
PRESSURE	40 PSIA
INITIAL CLADDING TEMPERATURE	1528°F
PEAK POWER	0.7 KW/FT
SUBCOOLING	140°F
INJECTION RATE	0.7 IN./SEC

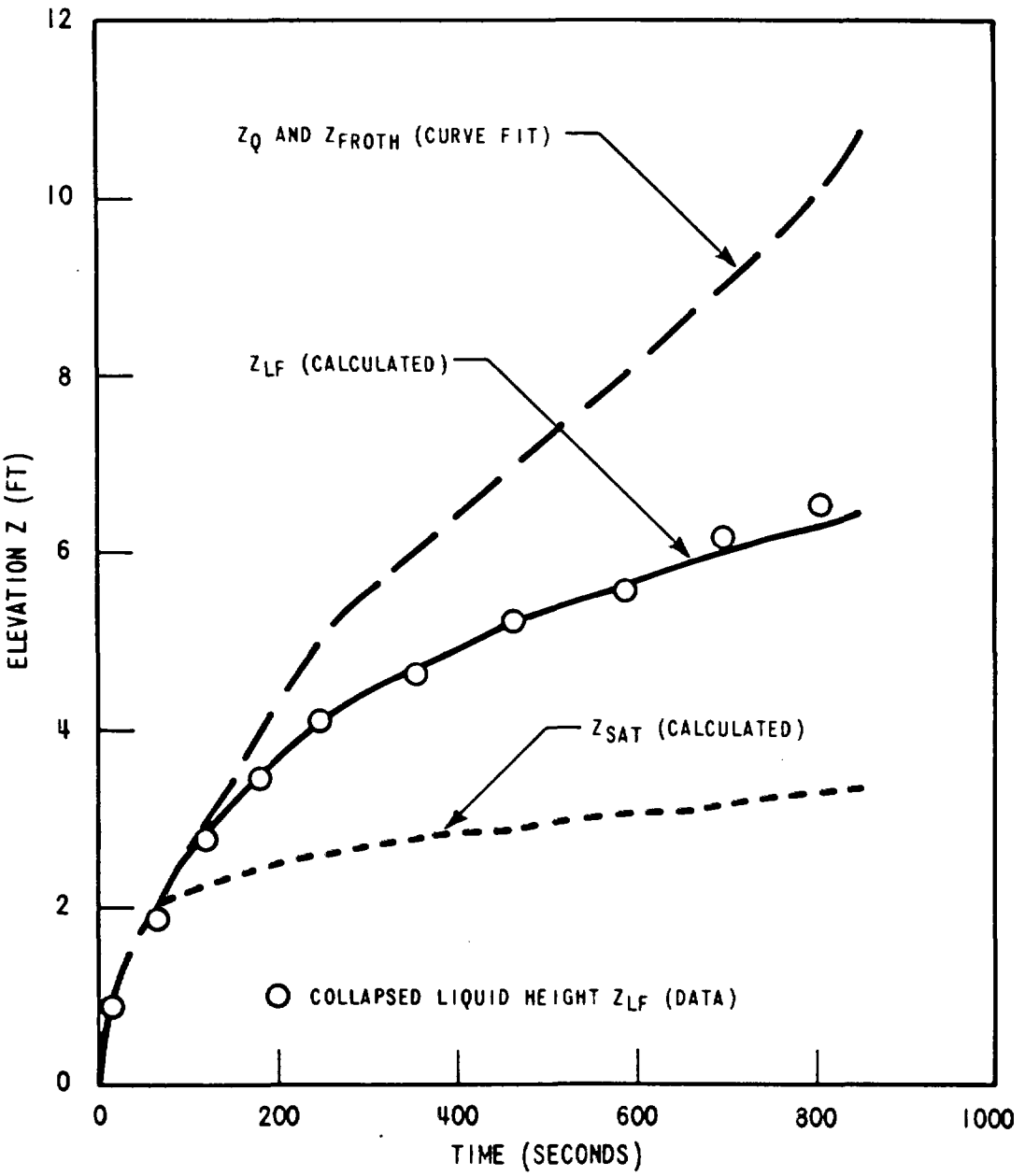

Figure D-3. Comparison of the Measured Collapsed Liquid Height Z_{Lf} and That Calculated by Z_{froth} (= Z_q) Data

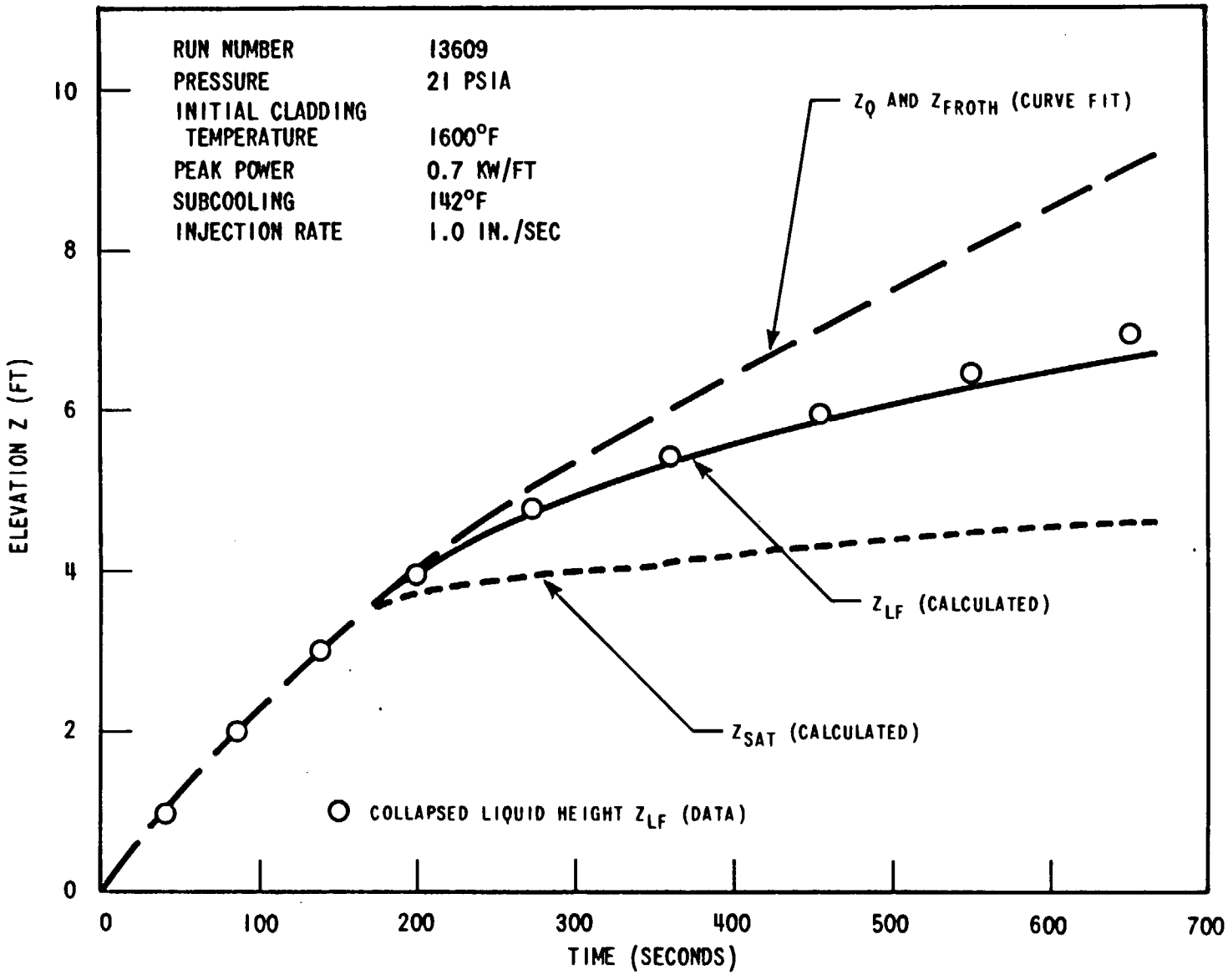

Figure D-4. Comparison of the Measured Collapsed Liquid Height Z_{Lf} and That Calculated by Z_{froth} (= Z_q) Data

11,863-81

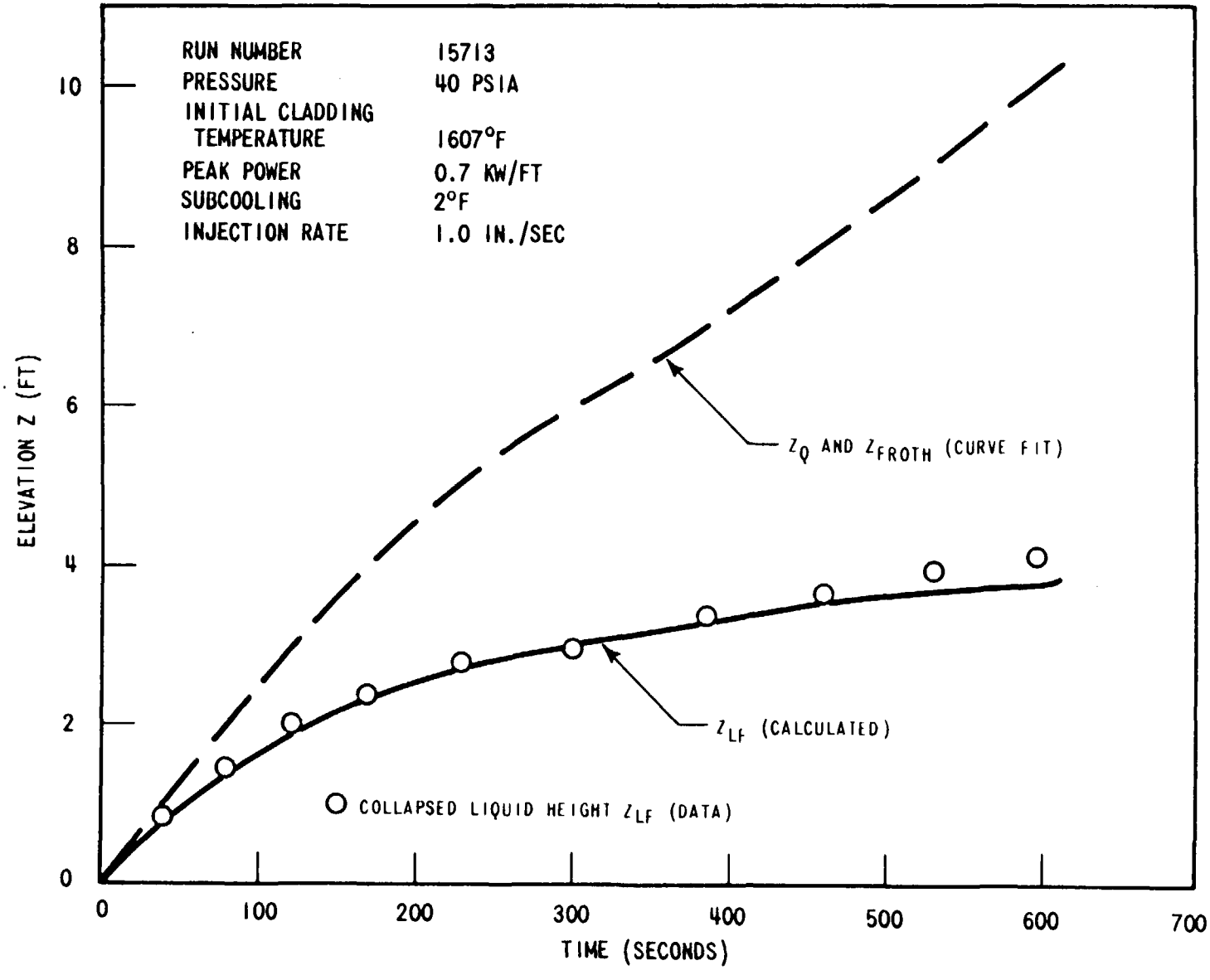

Figure D-5. Comparison of the Measured Collapsed Liquid Height Z_{Lf} and That Calculated by Z_{froth} (= Z_q) Data

11.863-80

RUN NUMBER	12816
PRESSURE	40 PSIA
INITIAL CLADDING TEMPERATURE	507°F
PEAK POWER	0.7 KW/FT
SUBCOOLING	141°F
INJECTION RATE	1.5 IN./SEC

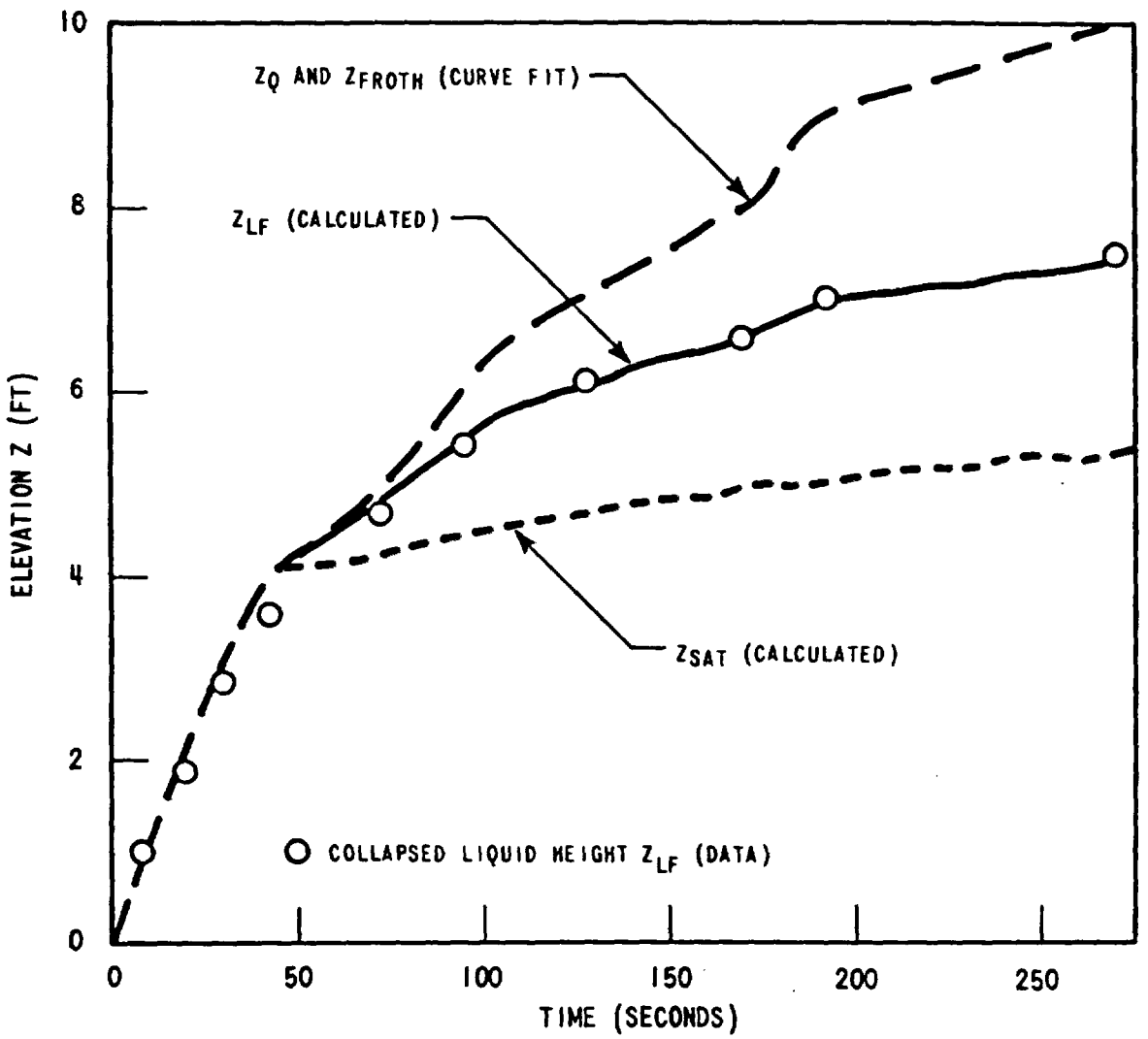

Figure D-6. Comparison of the Measured Collapsed Liquid Height Z_{Lf} and That Calculated by Using Z_{froth} (= Z_q) Data

RUN NUMBER	16022
PRESSURE	40 PSIA
INITIAL CLADDING TEMPERATURE	1636°F
PEAK POWER	1.0 KW/FT
SUBCOOLING	139°F
INJECTION RATE	1.5 IN./SEC

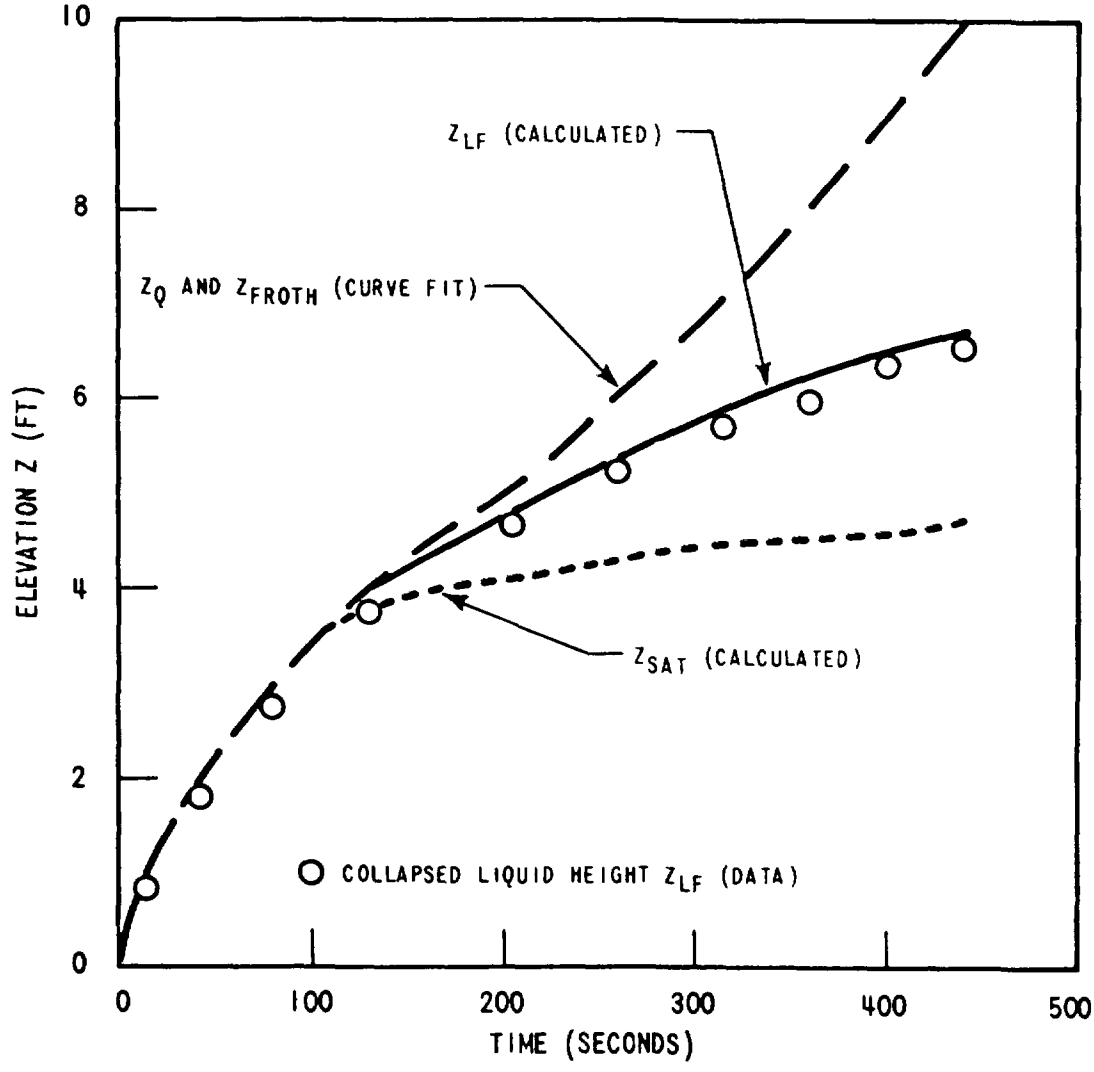

Figure D-7. Comparison of the Measured Collapsed Liquid Height Z_{Lf} and That Calculated by Using Z_{froth} (= Z_q) Data

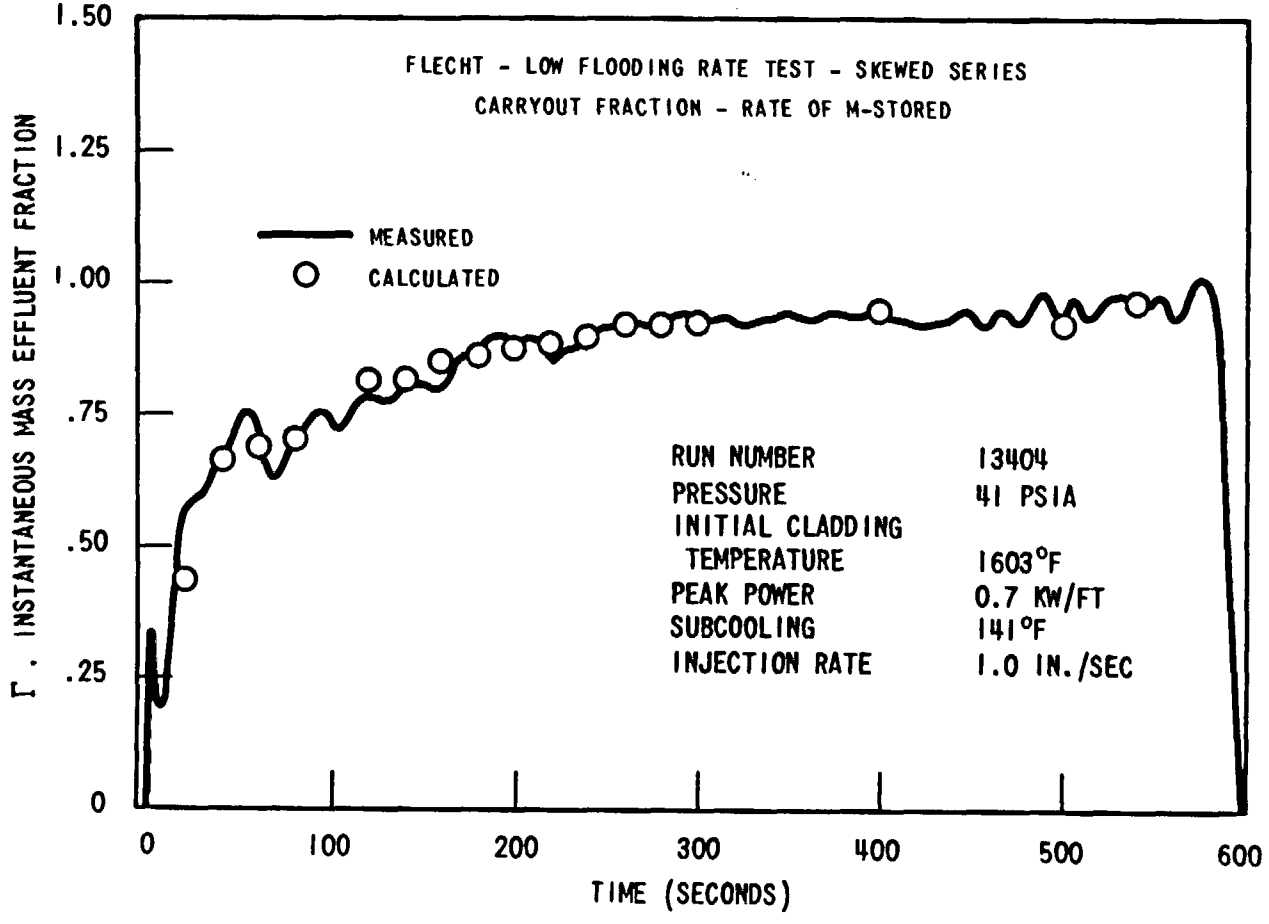

Figure D-8. Comparison of the Calculated and the Measured Mass Effluent Ratio, Γ

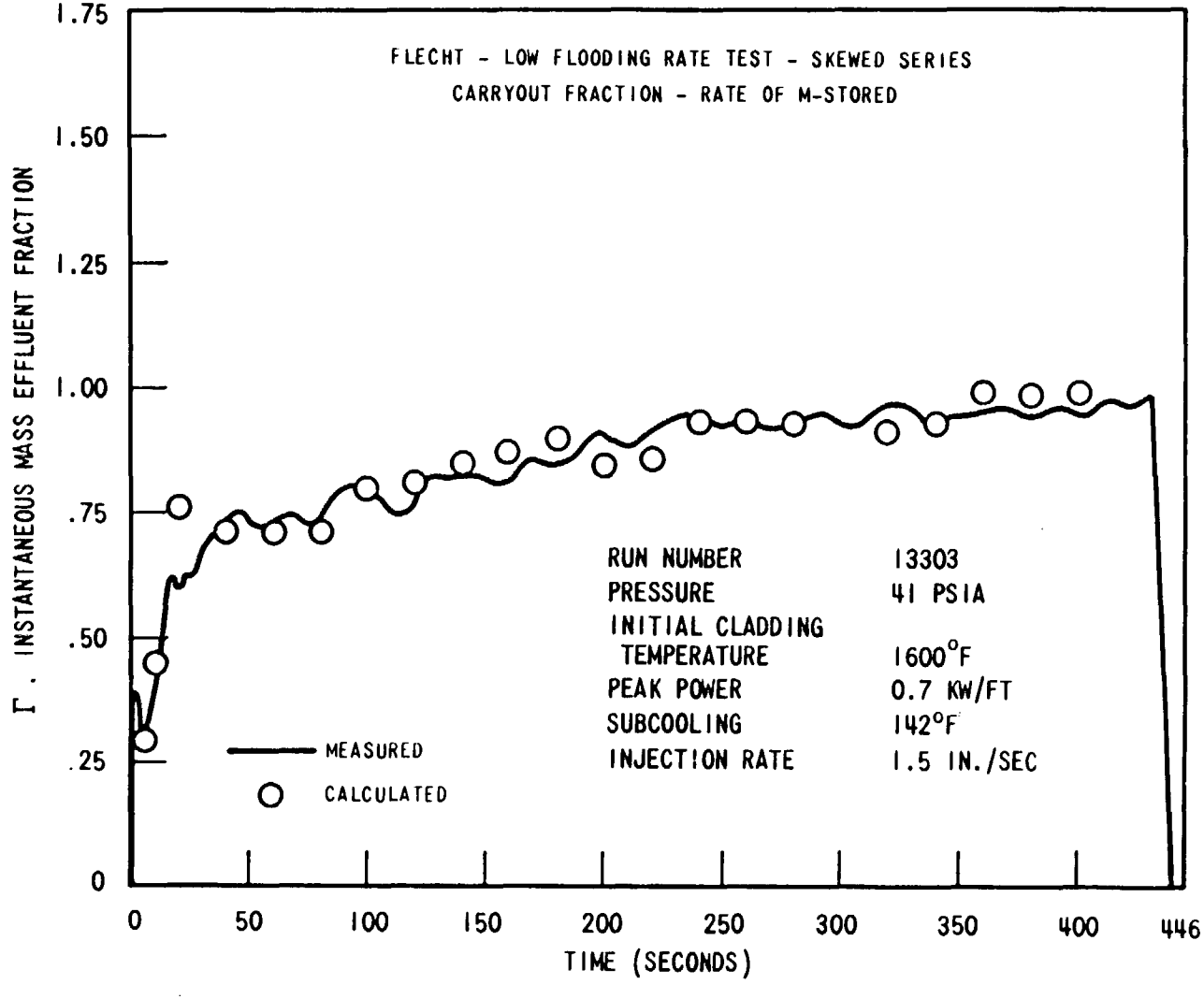

Figure D-9. Comparison of the Calculated and the Measured Mass Effluent Ratio, Γ

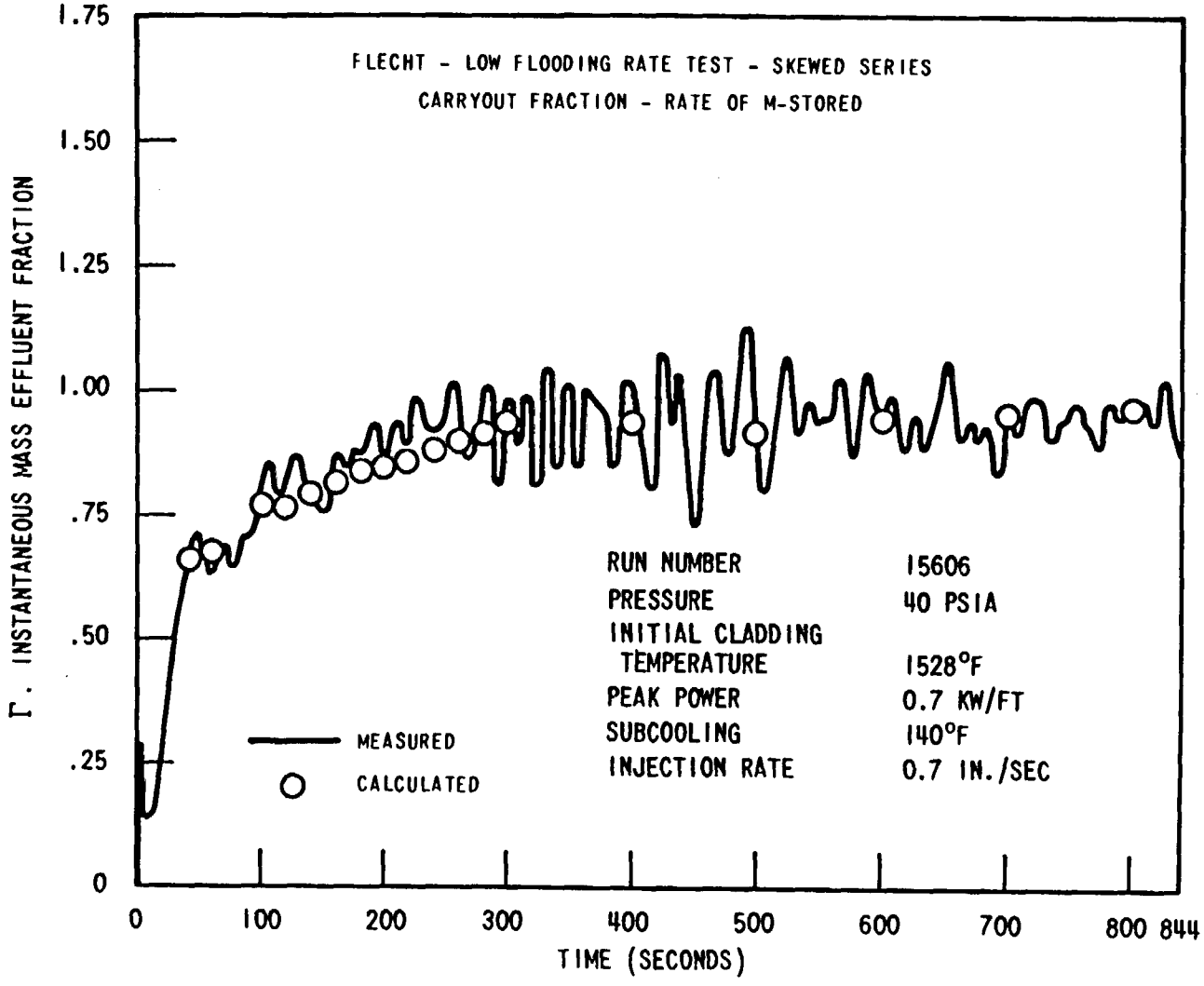

Figure D-10. Comparison of the Calculated and the Measured Mass Effluent Ratio, Γ

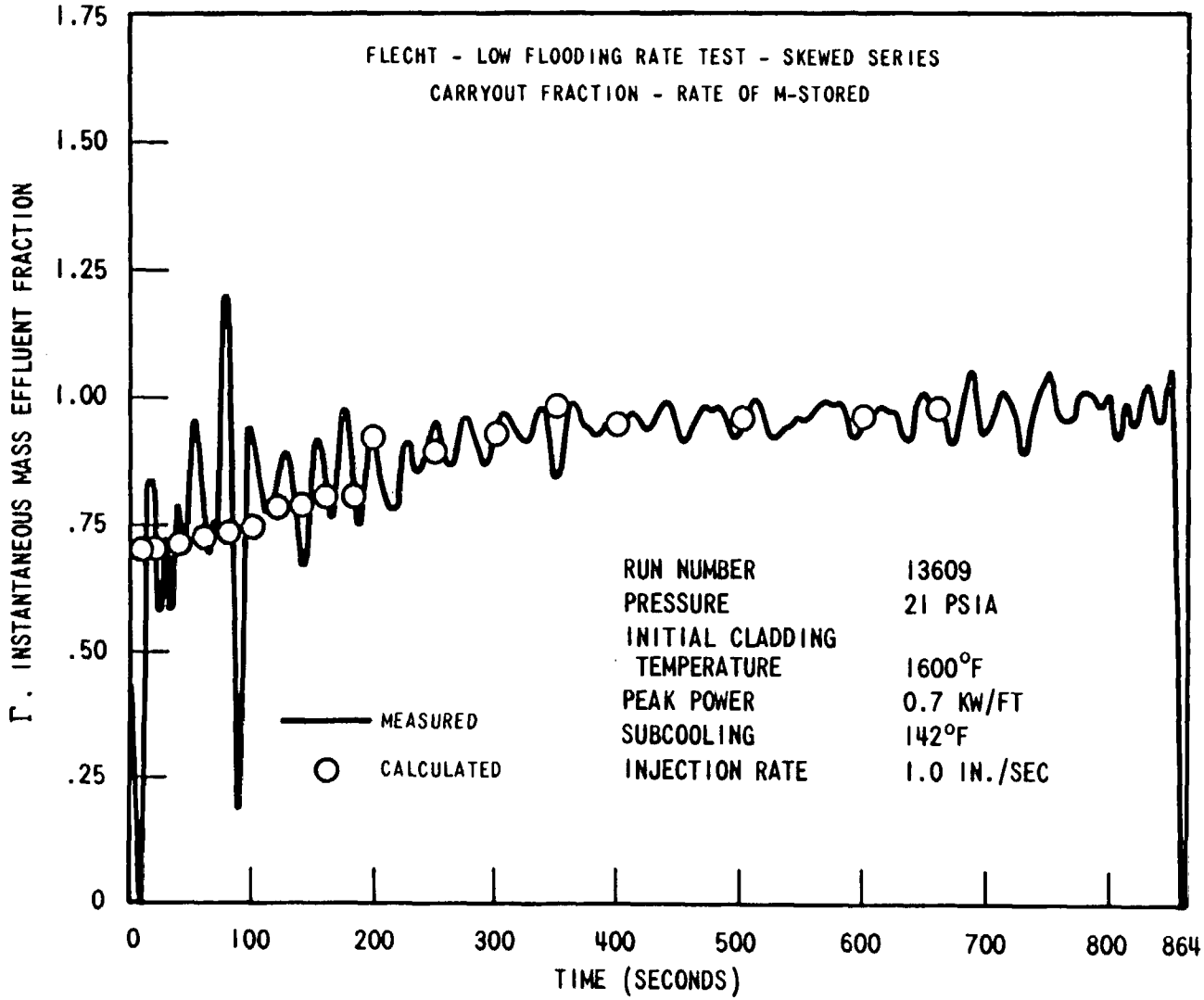

Figure D-11. Comparison of the Calculated and the Measured Mass Effluent Ratio, Γ

11.863-74

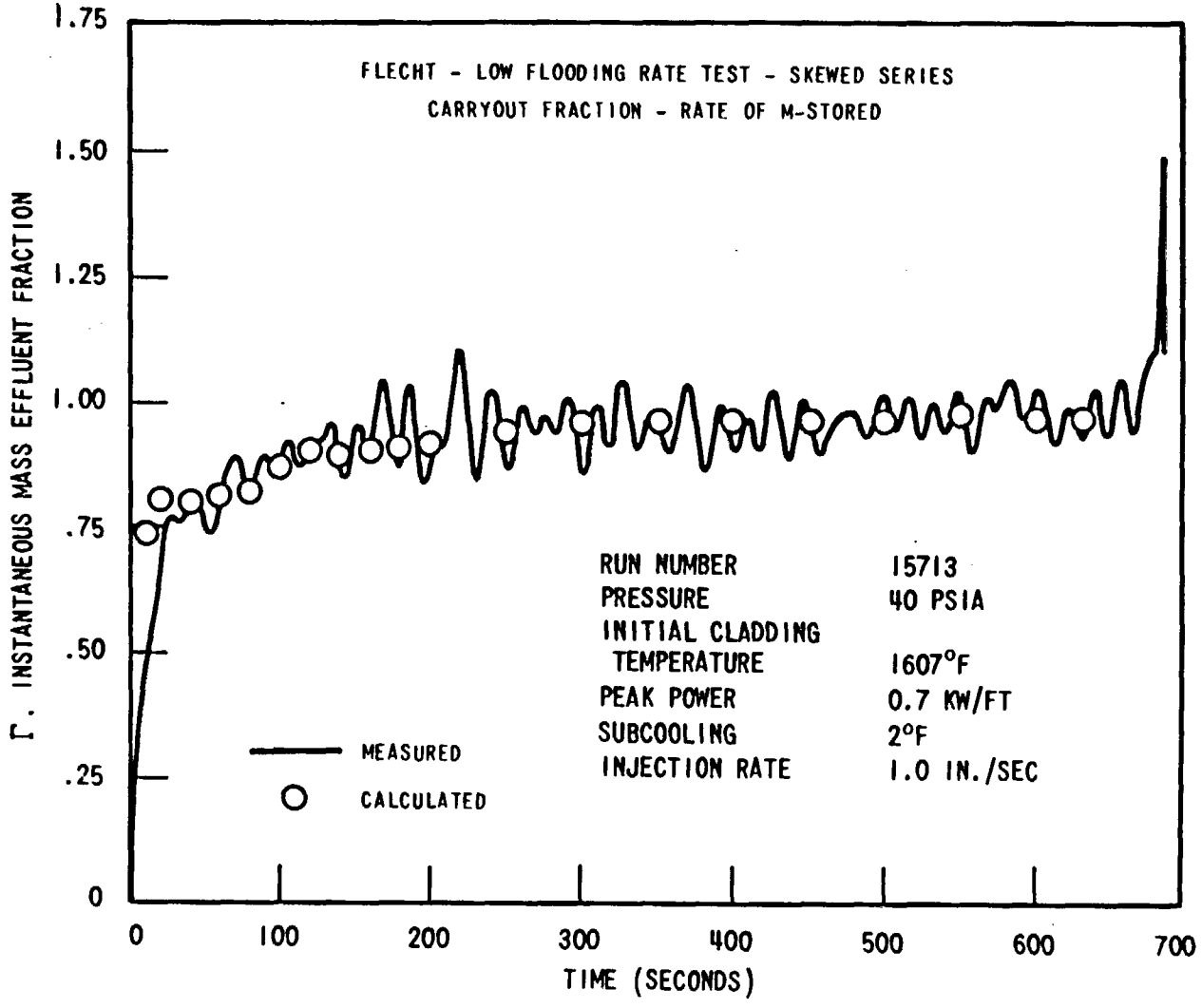

Figure D-12. Comparison of the Calculated and the Measured Mass Effluent Ratio, Γ

11,863-73

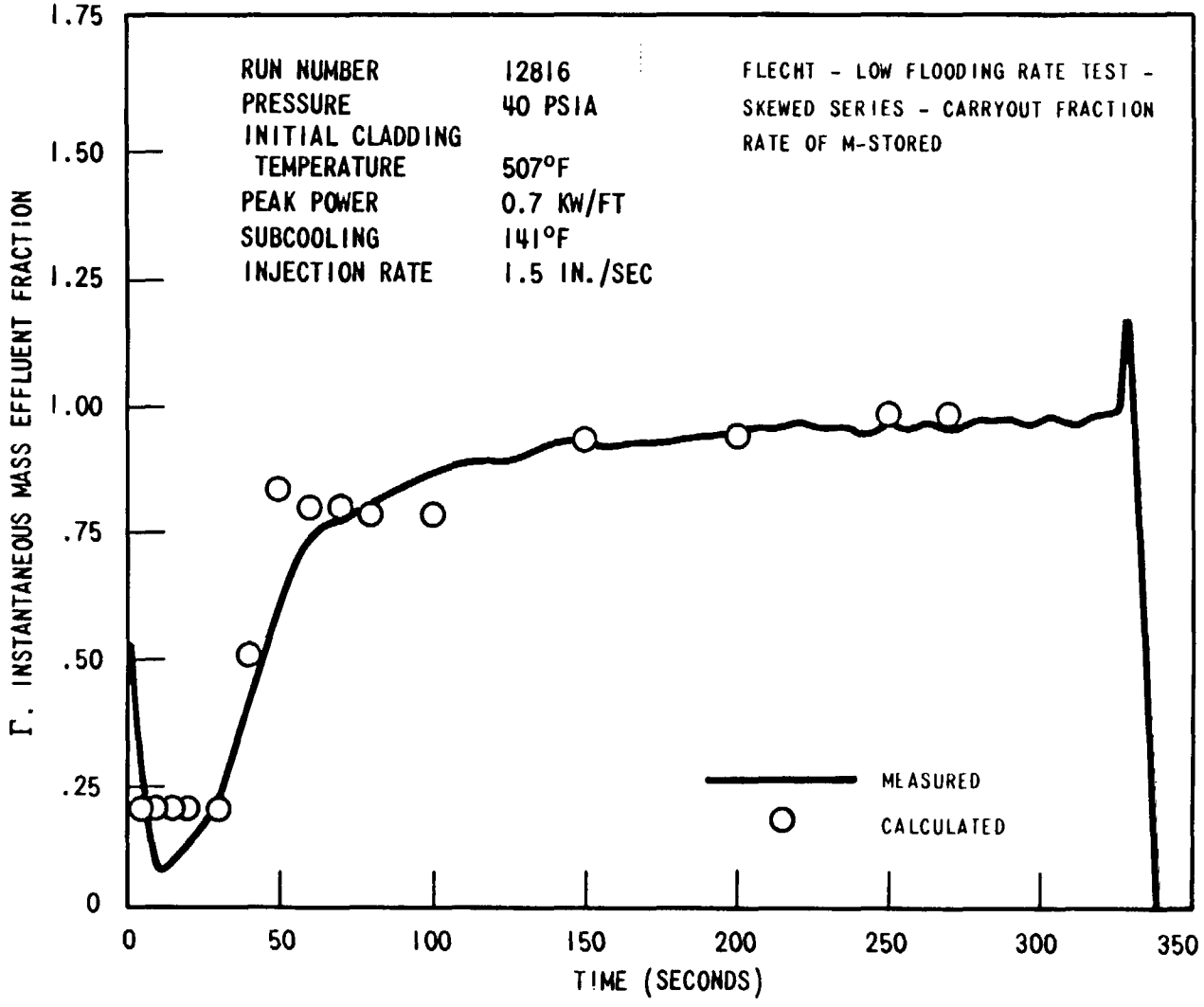

Figure D-13. Comparison of the Calculated and the Measured Mass Effluent Ratio, Γ

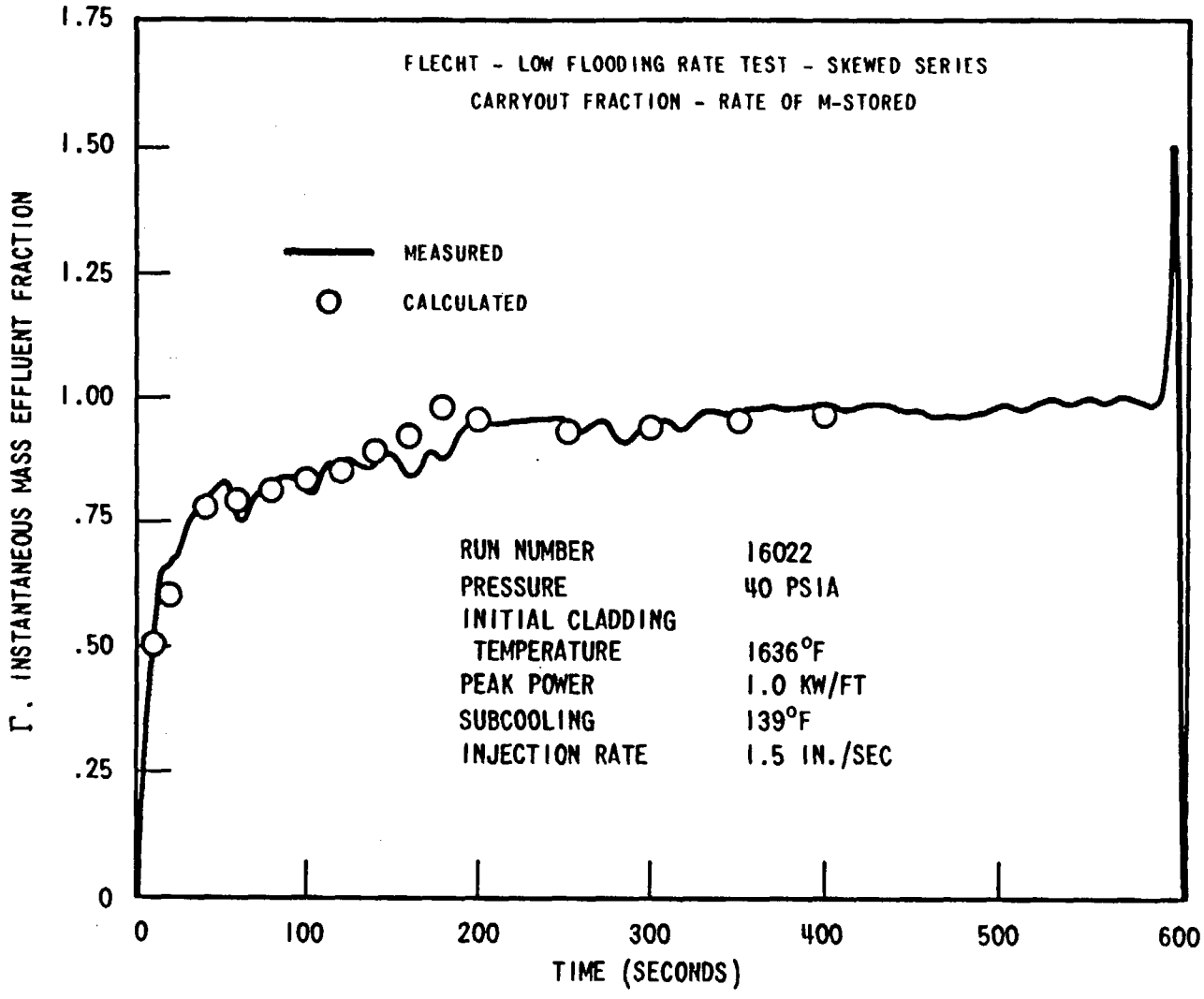

Figure D-14. Comparison of the Calculated and the Measured Mass Effluent Ratio, Γ

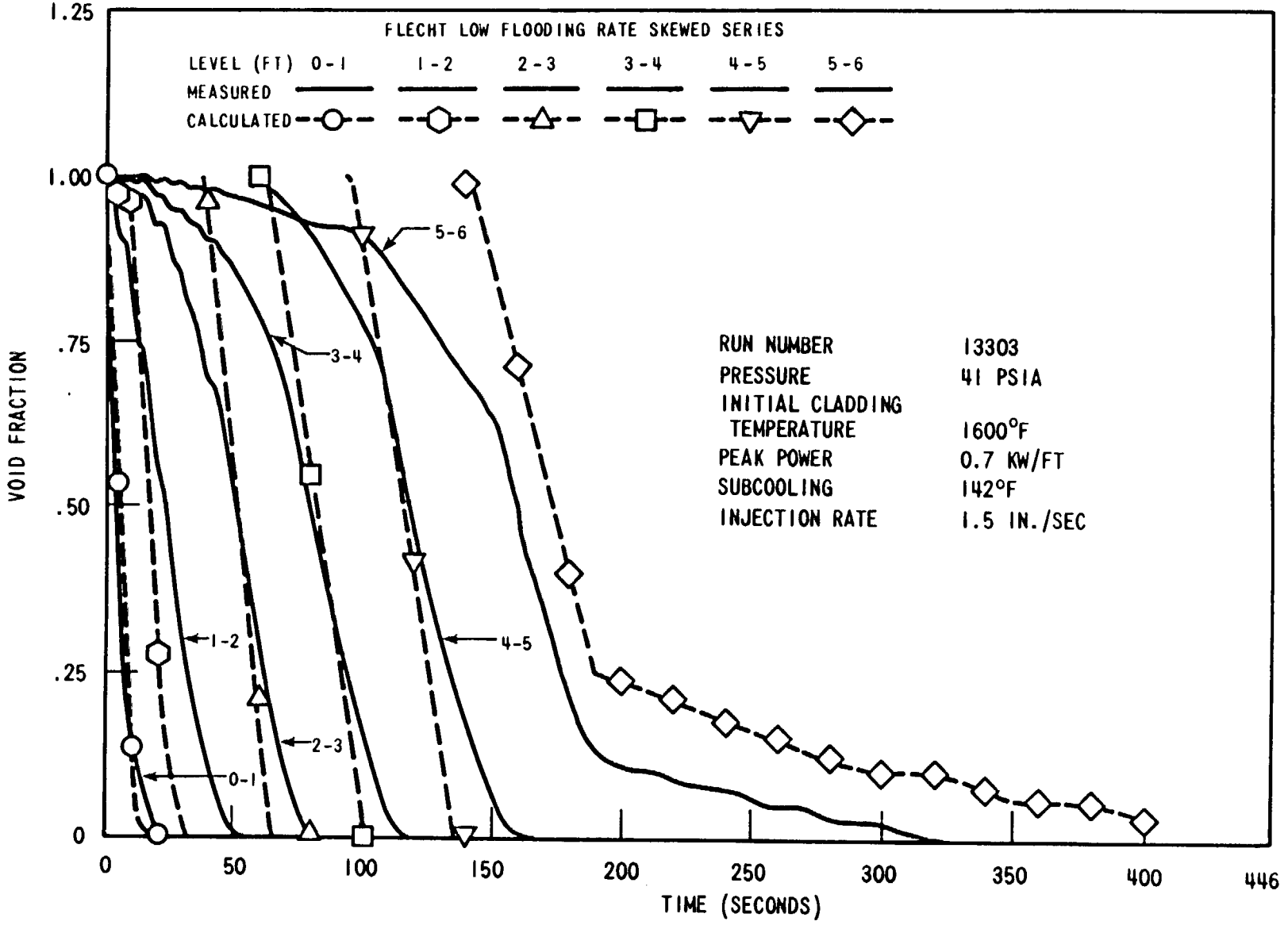

Figure D-15. Comparison of the Calculated and the Measured Average Void Fraction in Every 1 FT Interval (Run Number 13303, 0-6 FT Level)

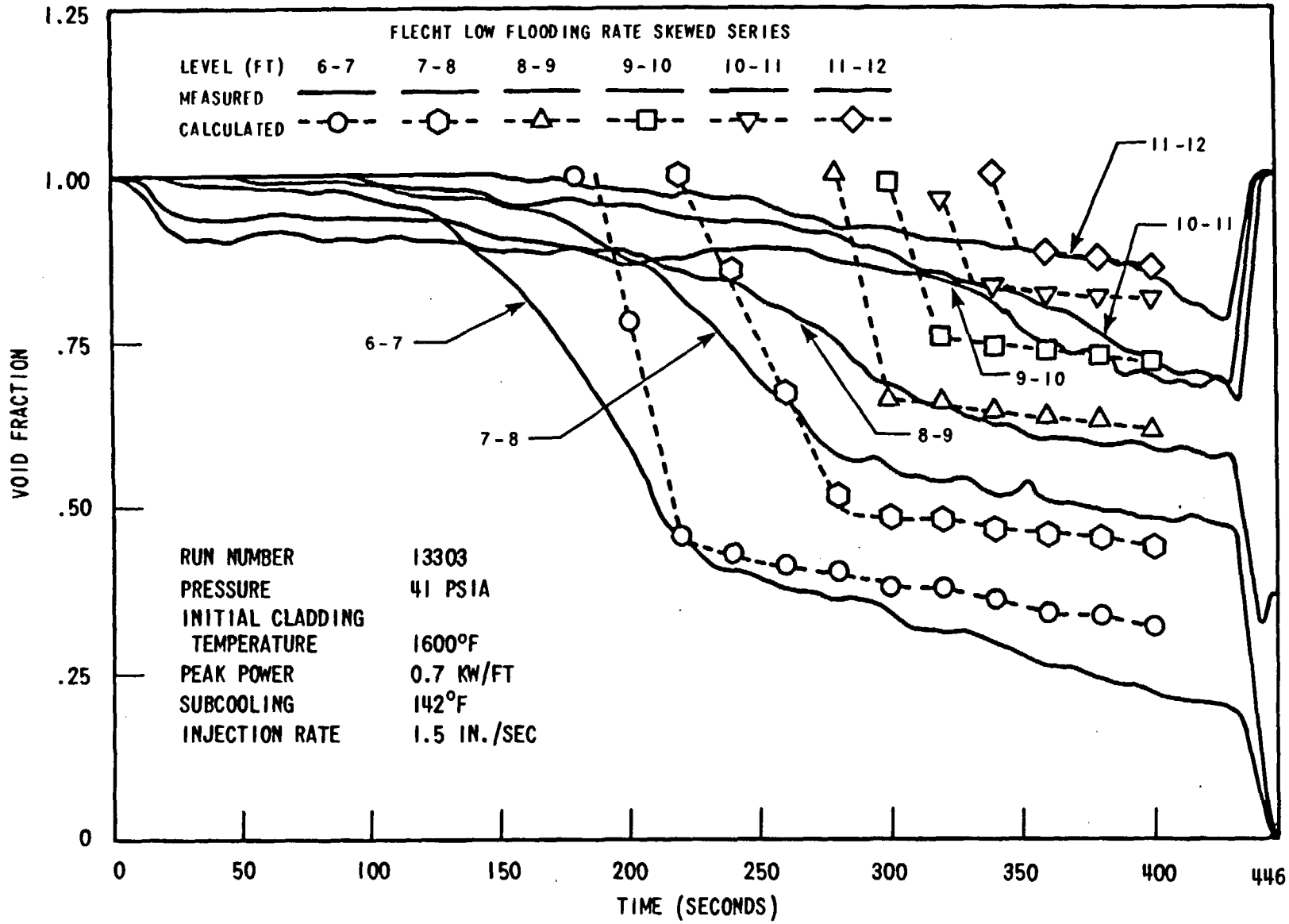

Figure D-16. Comparison of the Calculated and the Measured Average Void Fraction in Every 1 FT Interval (Run Number 13303, 6-12 FT Level)

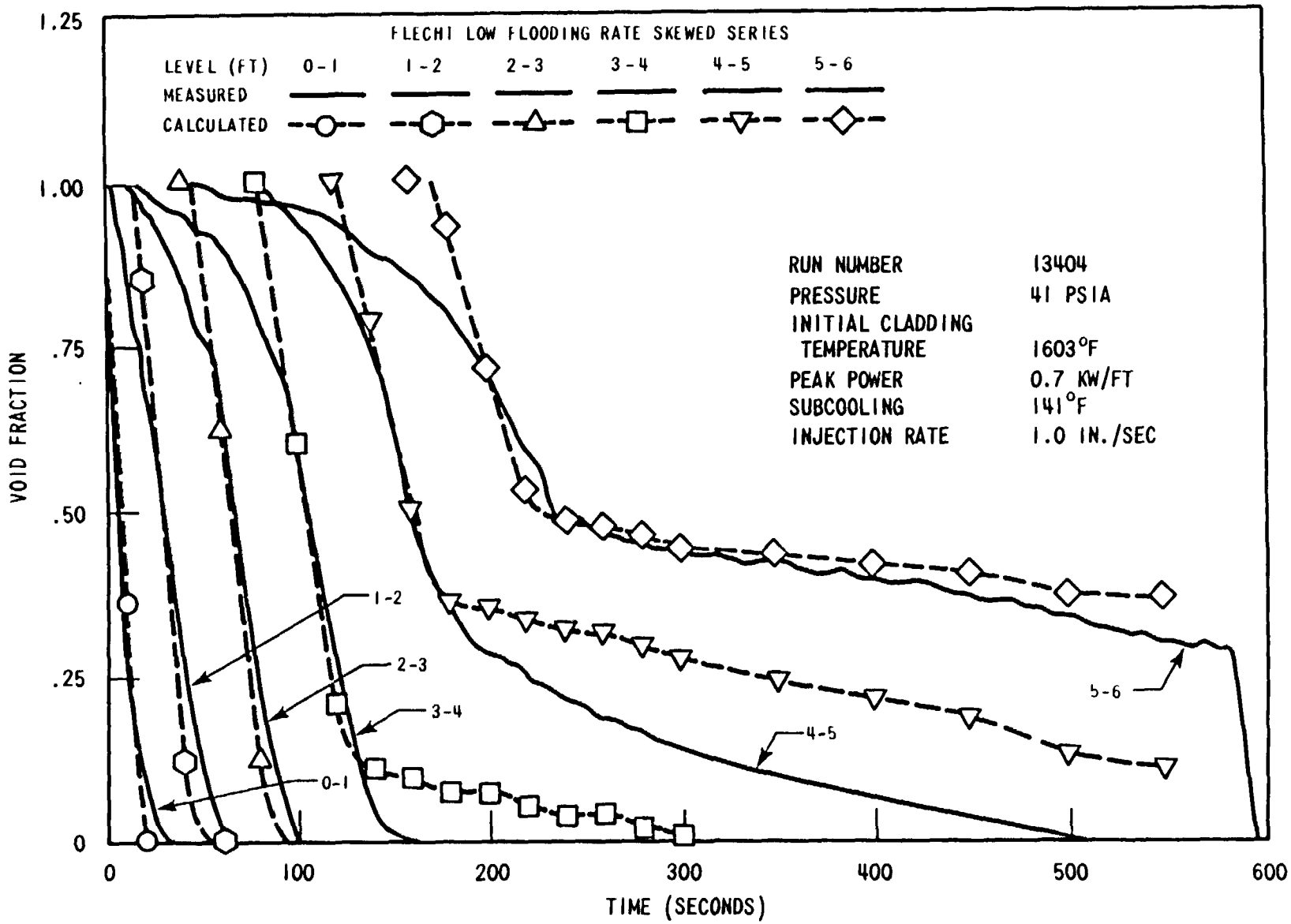

Figure D-17. Comparison of the Calculated and the Measured Average Void Fraction in Every 1 FT Interval (Run Number 13404, 0-6 FT Level)

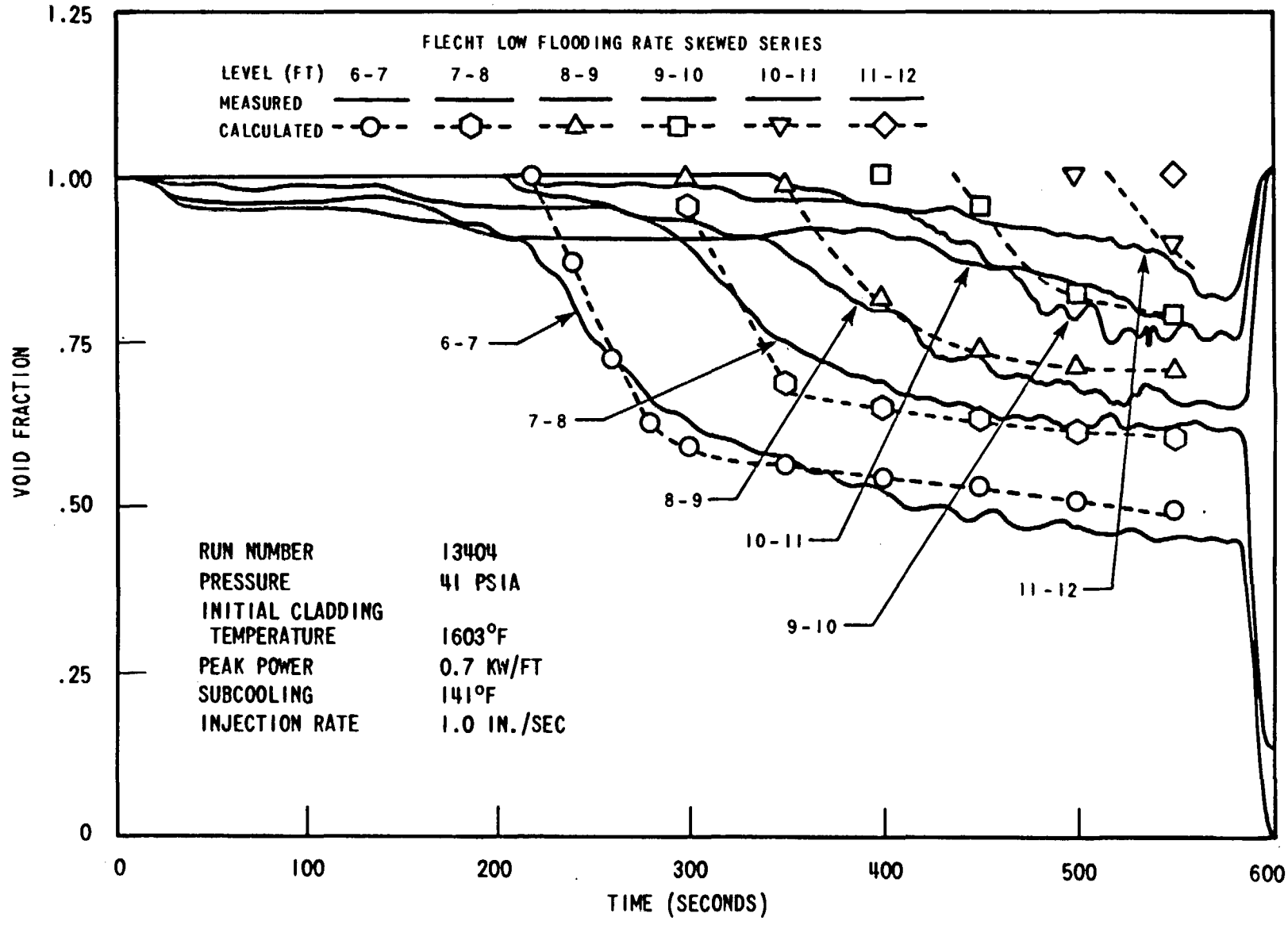

Figure D-18. Comparison of the Calculated and the Measured Average Void Fraction in Every 1 FT Interval (Run Number 13404, 6-12 FT Level)

11,863-67

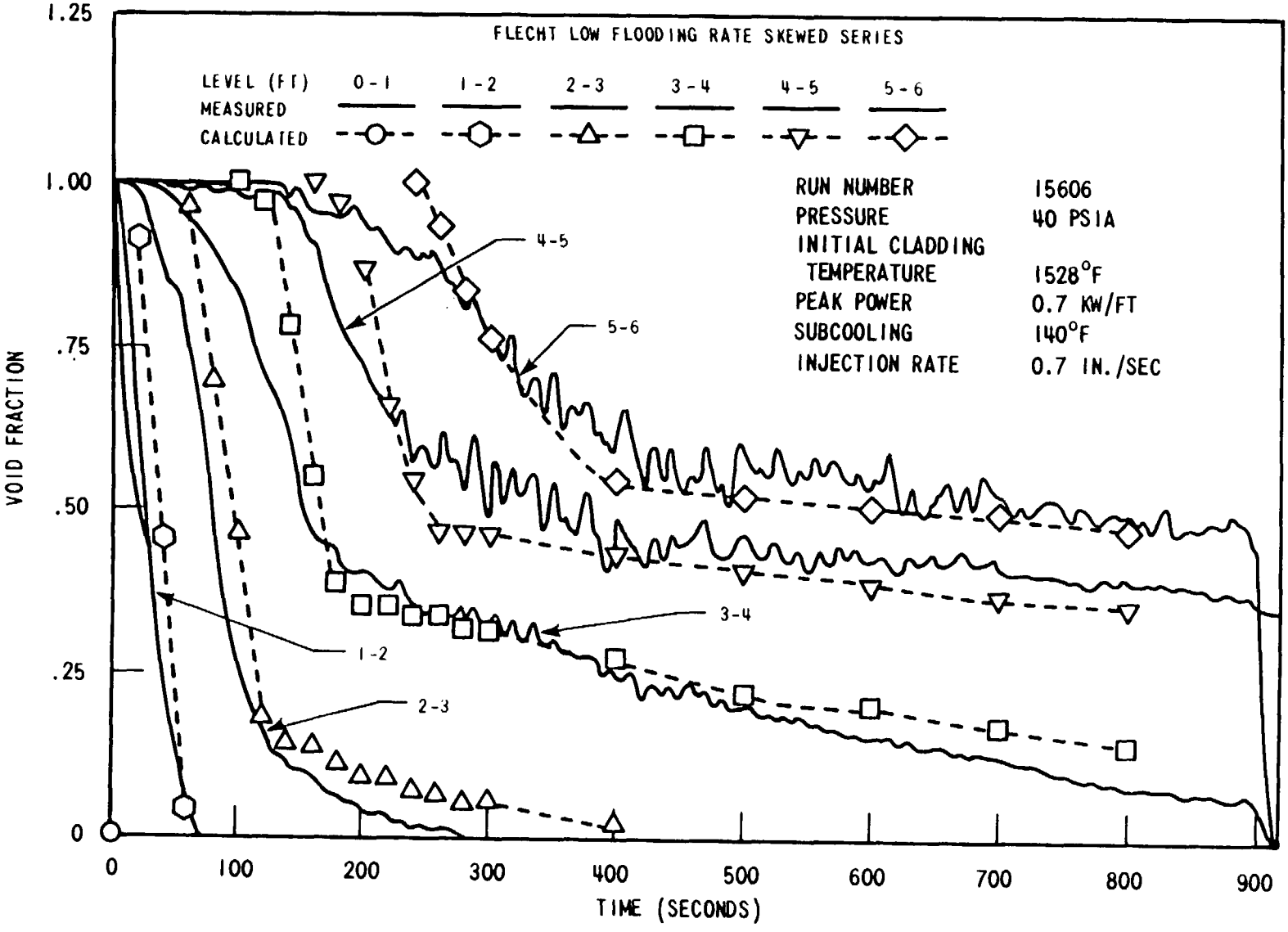

Figure D-19. Comparison of the Calculated and the Measured Average Void Fraction in Every 1 FT Interval (Run Number 15606, 0-6 FT Level)

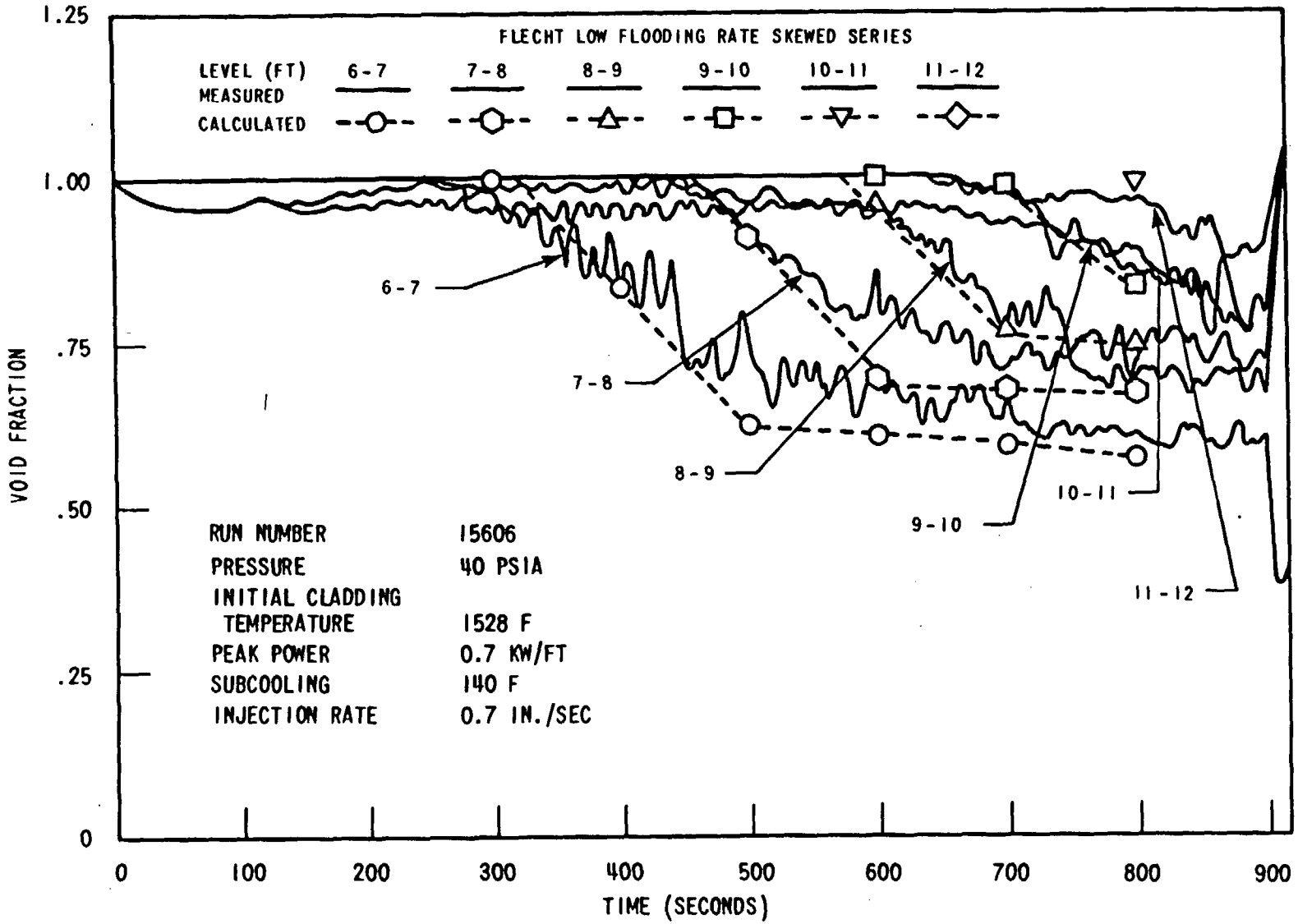

Figure D-20. Comparison of the Calculated and the Measured Average Void Fraction in Every 1 FT Interval (Run Number 15606, 6-12 FT Level)

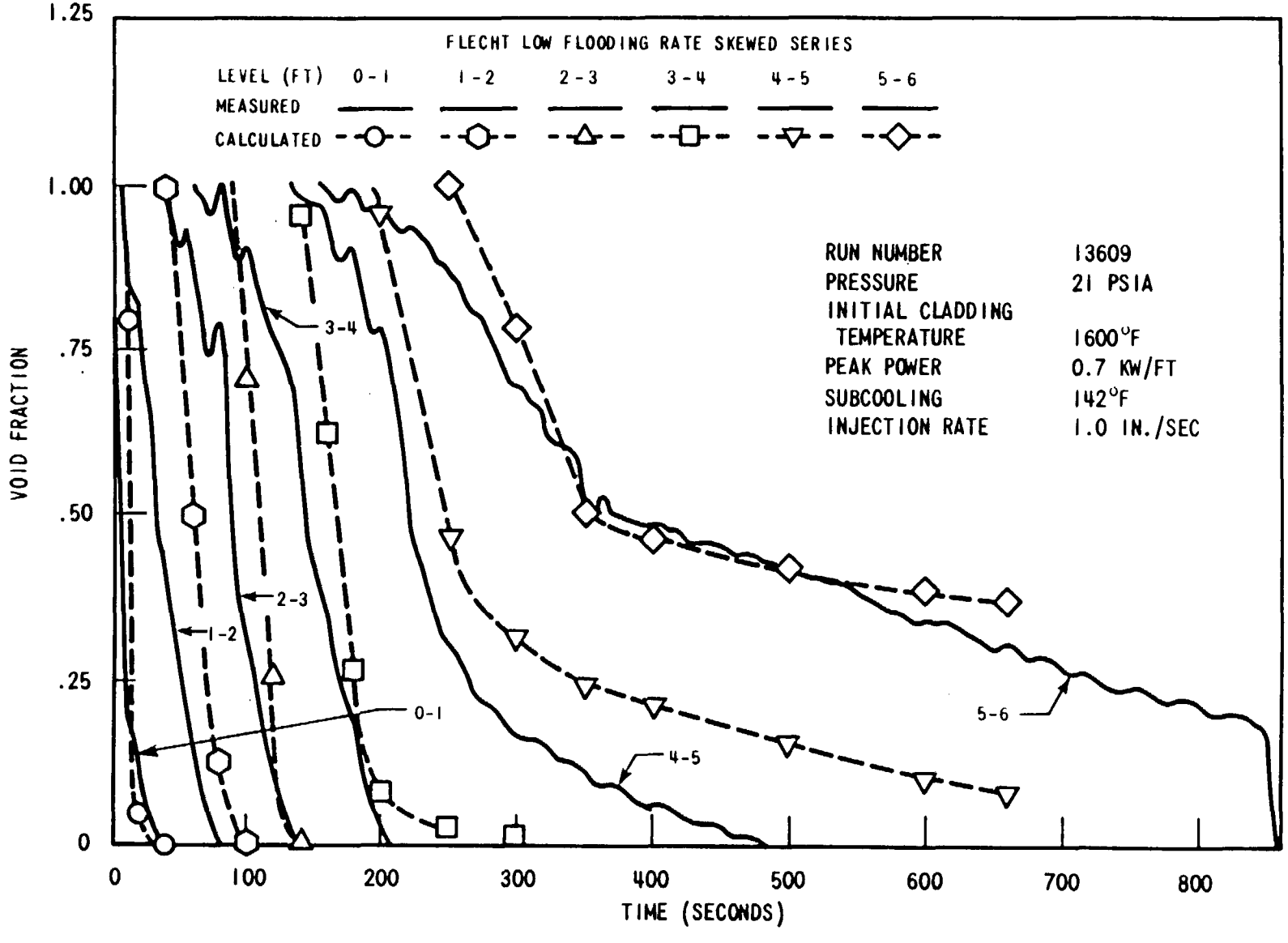

Figure D-21. Comparison of the Calculated and the Measured Average Void Fraction in Every 1 FT Interval (Run Number 13609, 0-6 FT Level)

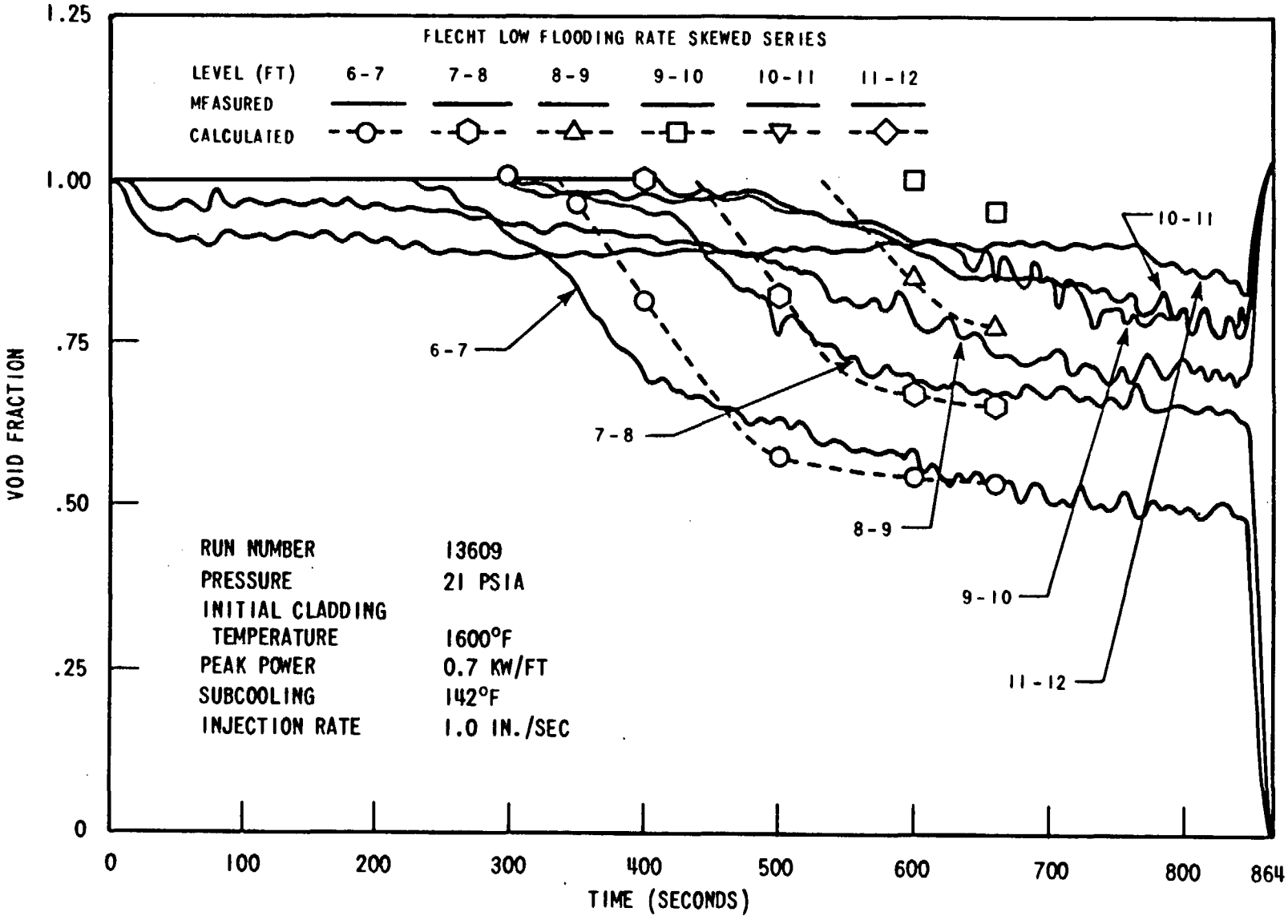

Figure D-22. Comparison of the Calculated and the Measured Average Void Fraction in Every 1 FT Interval (Run Number 13609, 6–12 FT Level)

11.863-63

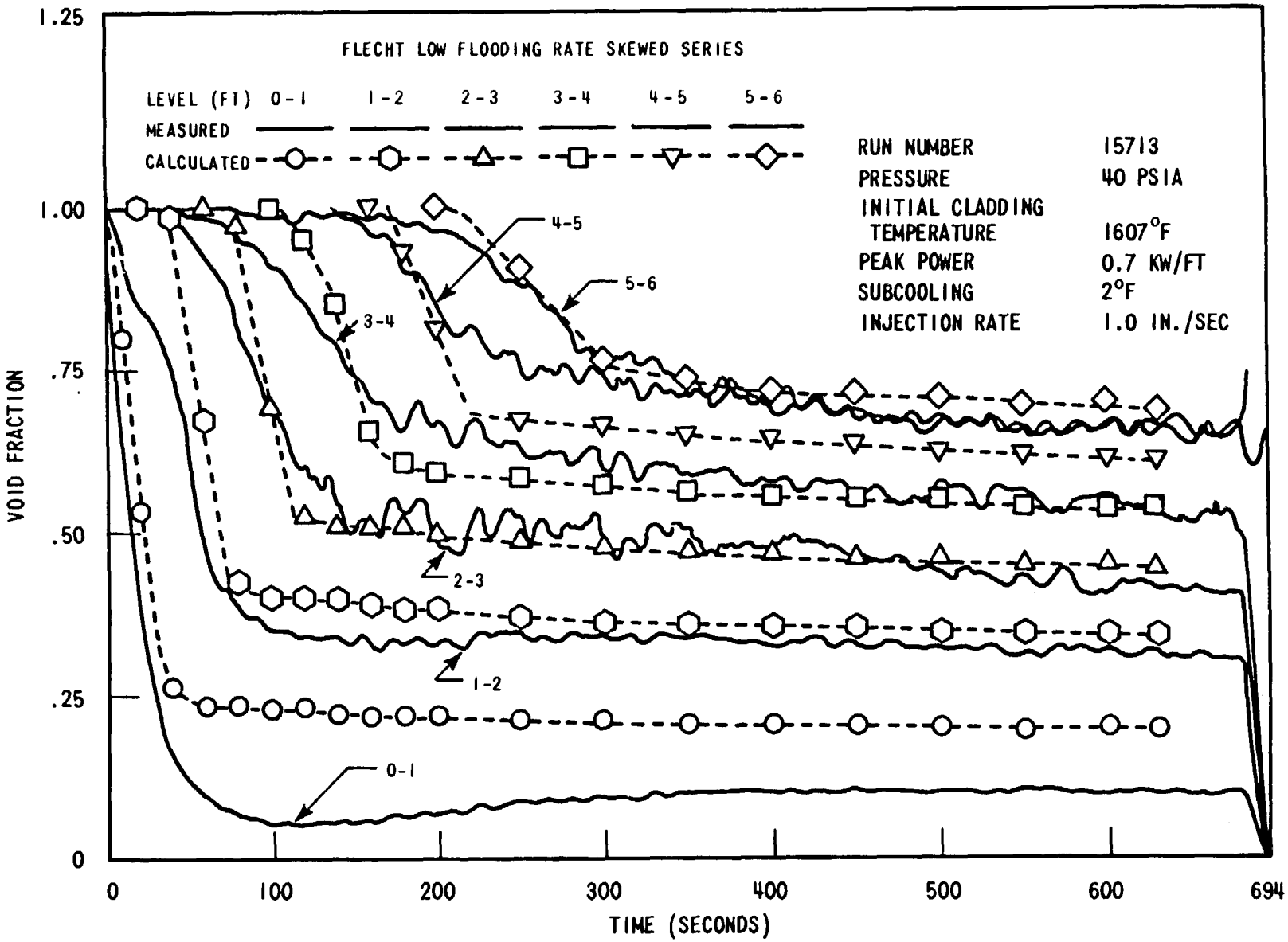

Figure D-23. Comparison of the Calculated and the Measured Average Void Fraction in Every 1 FT Interval (Run Number 15713, 0-6 FT Level)

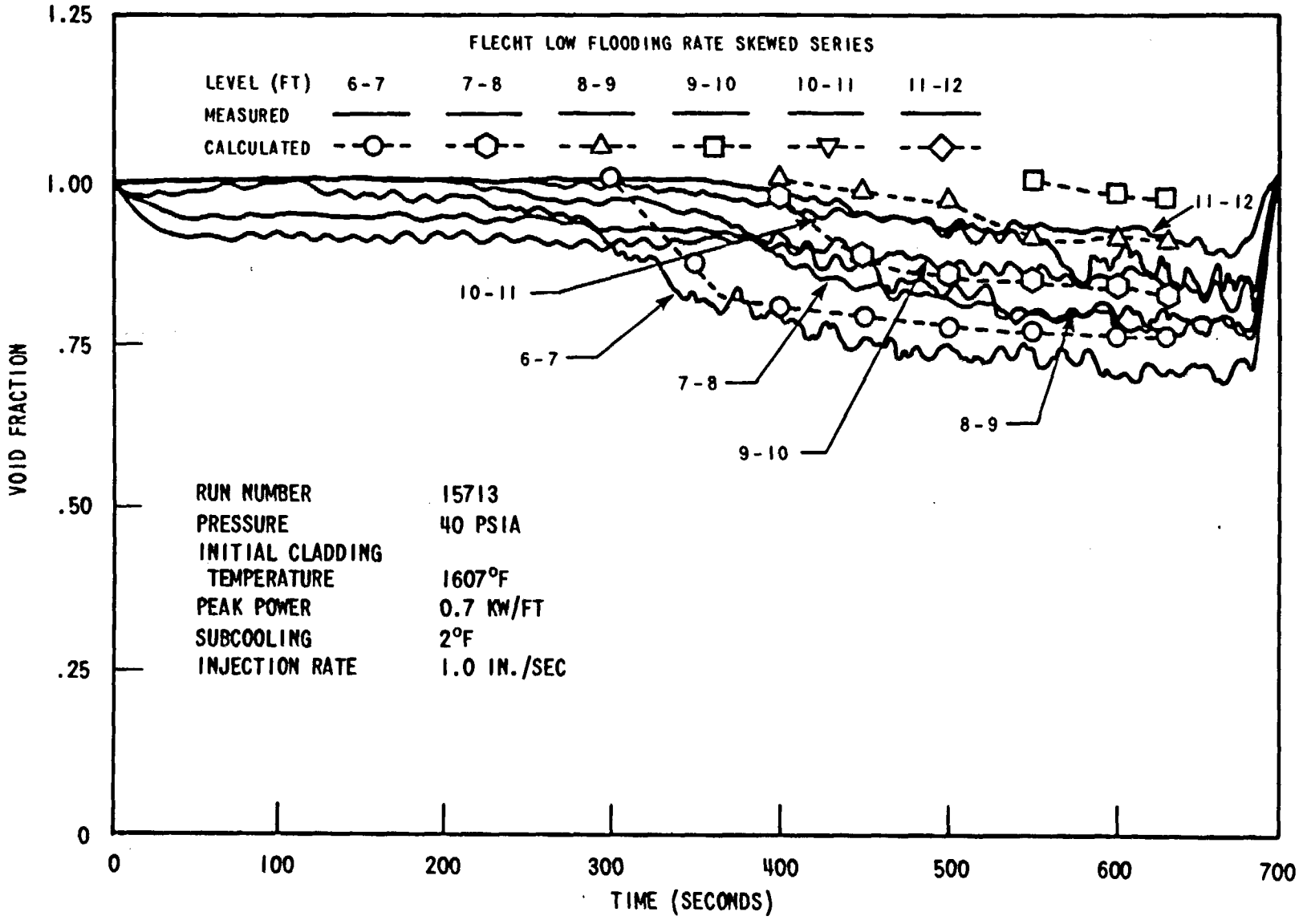

Figure D-24. Comparison of the Calculated and the Measured Average Void Fraction in Every 1 FT Interval (Run Number 15713, 6-12 FT Level)

11,863-61

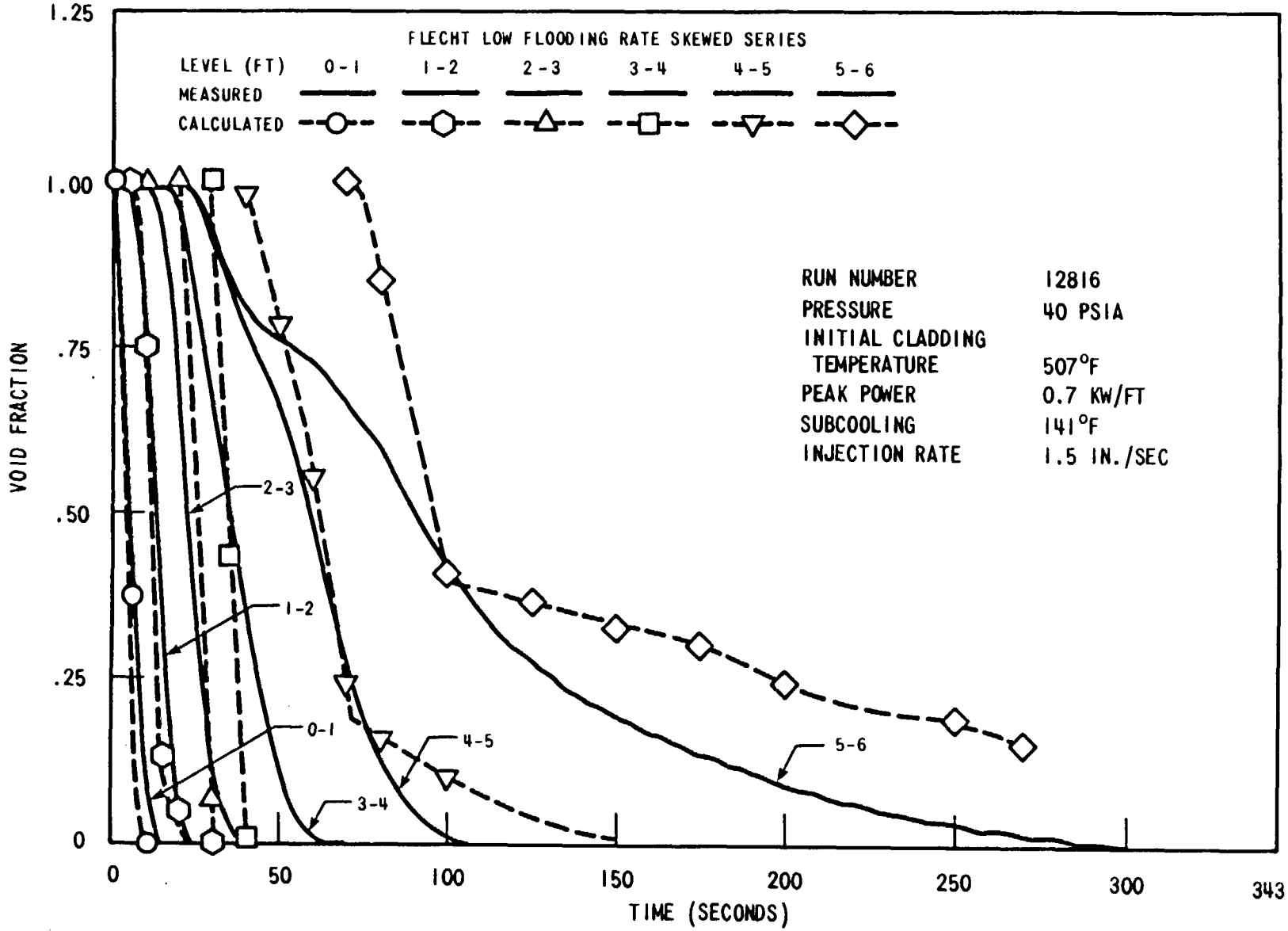

Figure D-25. Comparison of the Calculated and the Measured Average Void Fraction in Every 1 FT Interval (Run Number 12816, 0-6 FT Level)

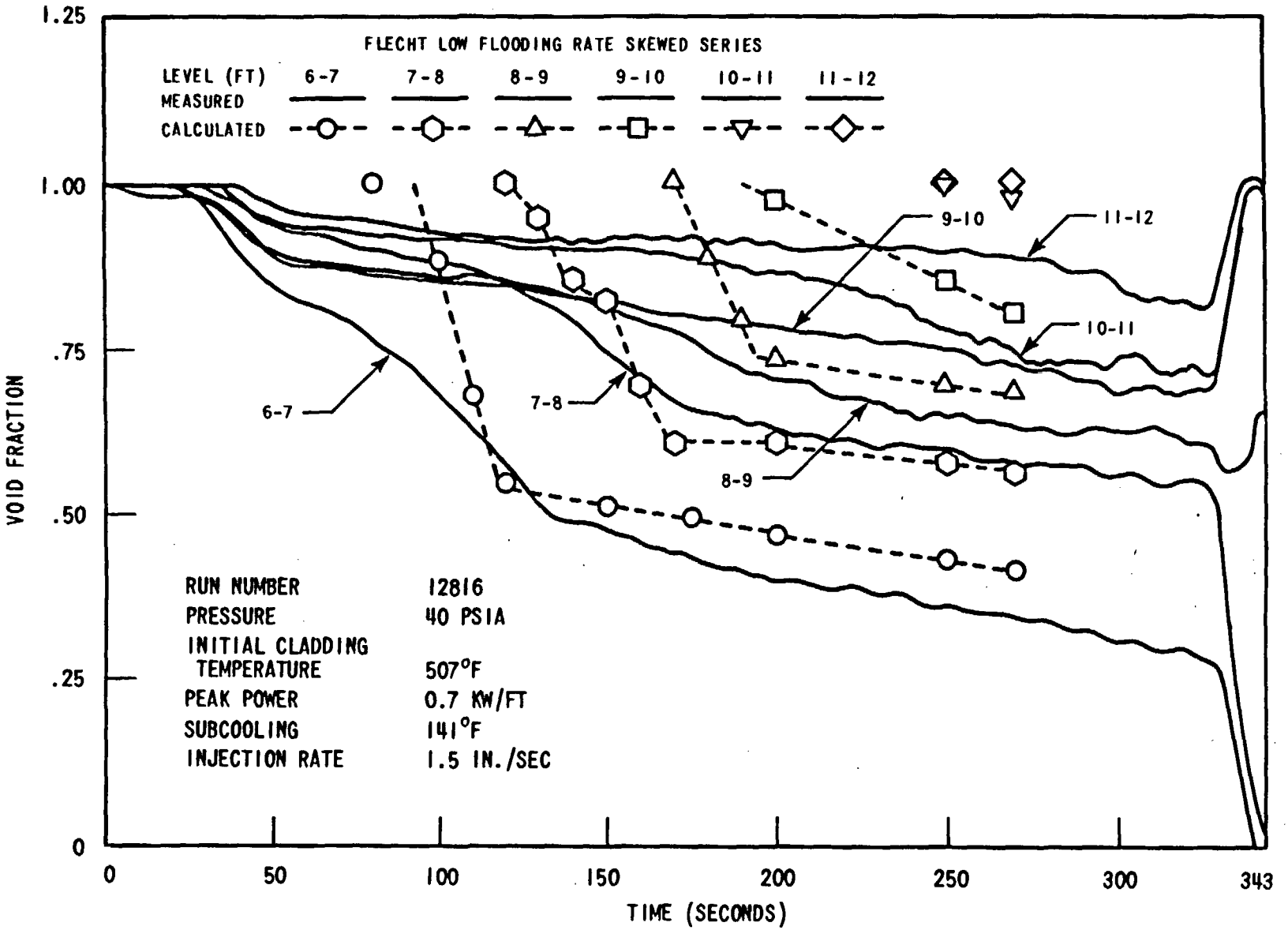

Figure D-26. Comparison of the Calculated and the Measured Average Void Fraction in Every 1 FT Interval (Run Number 12816, 6-12 FT Level)

11,863-59

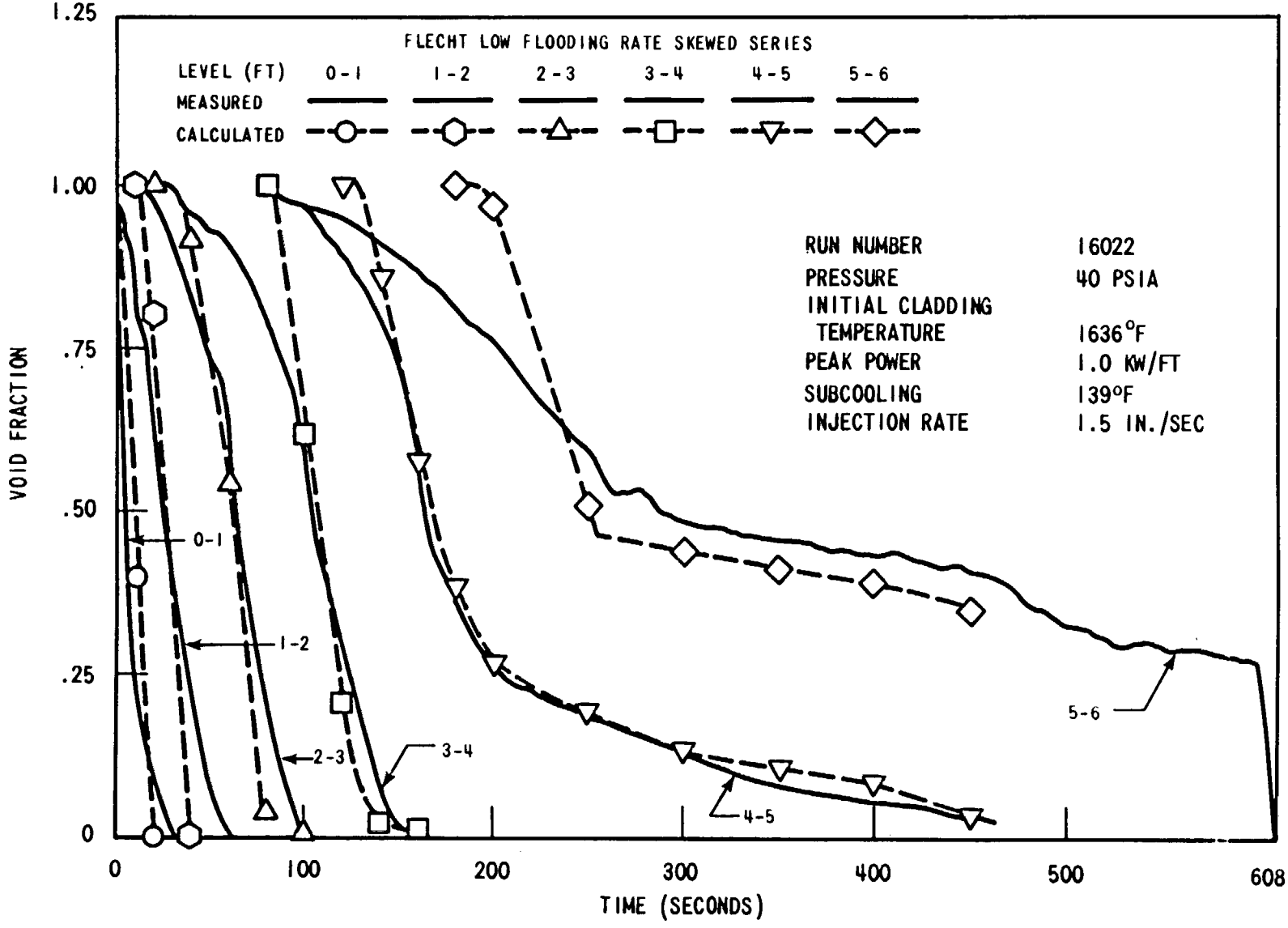

Figure D-27. Comparison of the Calculated and the Measured Average Void Fraction in Every 1 FT Interval (Run Number 16022, 0-6 FT Level)

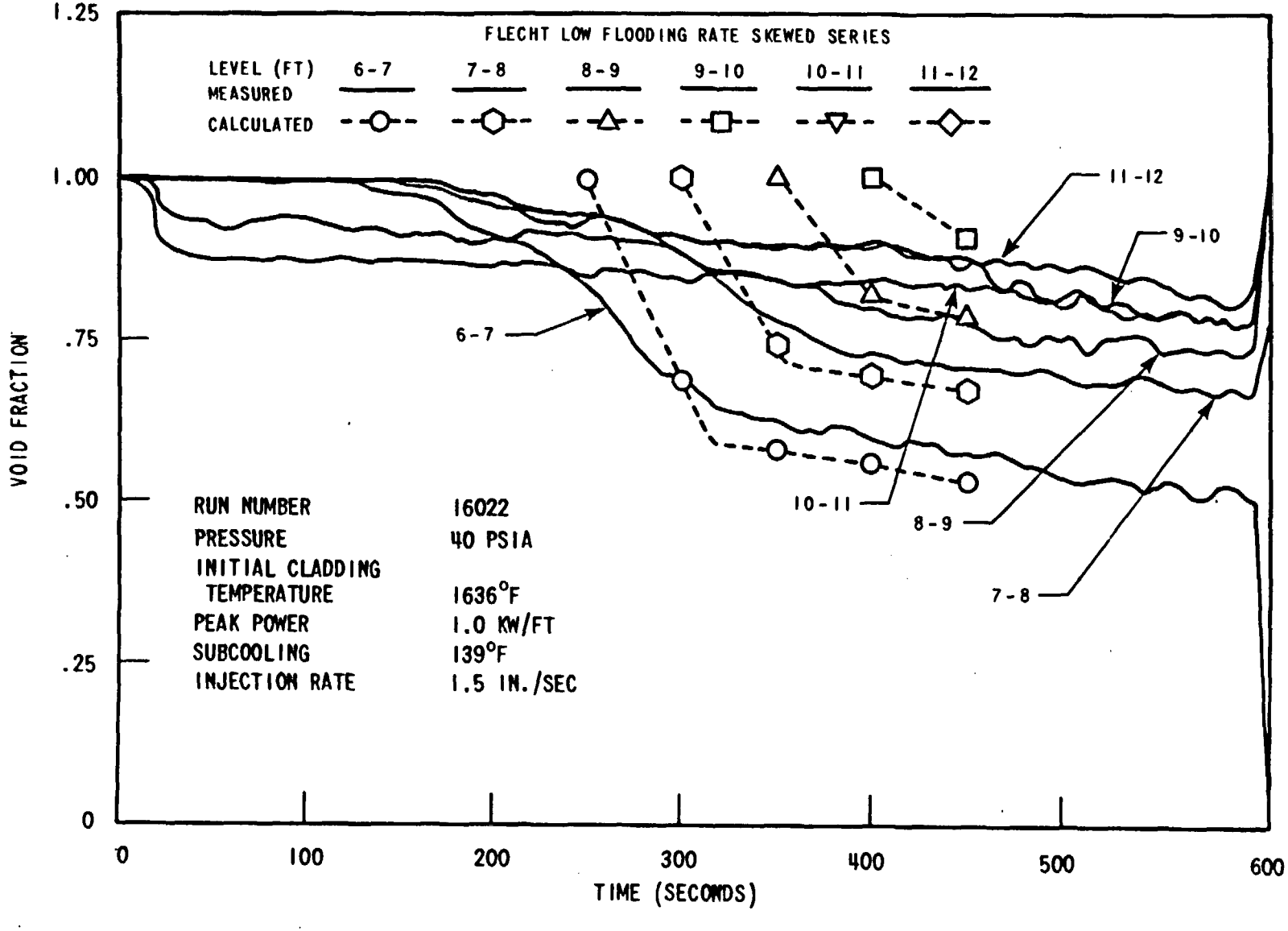

Figure D-28. Comparison of the Calculated and the Measured Average Void Fraction in Every 1 FT Interval (Run Number 16022, 6-12 FT Level)

APPENDIX E
DATA COMPARISON WITH QUENCH AND HEAT TRANSFER CORRELATIONS

Additional data comparisons for both quench time and heat transfer correlations have been included in appendix E to illustrate the effects each run parameter has on the correlation. Table E-1 lists both skewed and cosine runs along with the parameter being varied. Figures E-1 through E-7 compare cosine quench correlation results with data. Figures E-8 through E-14 compare skewed quench correlation results against data. Likewise, figures E-15 through E-21 and E-22 through E-28 illustrate the agreement between cosine and skewed heat transfer data and the $Z\text{-}Z_q$ correlation, respectively.

The last entry in table E-1, entitled "Grid Effect on Heat Transfer," is included to illustrate the pronounced effect that bundle grids have in increasing the heat transfer coefficient at high flooding rate. The high spikes in figures E-21 and E-28 correspond to thermocouple data located several inches either upstream or downstream of a grid.

TABLE E-1
RUN CONDITIONS FOR TESTS PRESENTED

Skewed Run Number	Upper Plenum Pressure (psia)	Rod Initial Cladding Temp (°F)	Rod Peak Power (kw/ft)	Flooding Rate (in./sec)	Coolant Temp (°F)	Bundle Radial Power Profile	Parameter Variation
15305	40	1603	0.7	0.8	127	Uniform	Reference See figures 6-4, 6-14 to 16
13303	41	1600	0.7	1.5	126	Uniform	Reference; Flooding rate
16110	20	1617	0.7	0.8	96	Uniform	Pressure
15713	40	1607	0.7	1.0	265	Uniform	Subcooling
12816	40	507	0.7	1.5	126	Uniform	Initial temperature
16022	40	1636	1.0	1.5	128	Uniform	Power
15132	39	1555	0.7	6.0 (5 sec) 0.8 (onward)	127	Uniform	Variable flooding rate
13001	39	1600	0.7	5.7	126	Uniform	Grid effect
Cosine Run Number							
02833	40	1602	0.89	0.80	125	FLECHT	Reference See figures 6-3, 6-12 to 13
04831	40	1600	0.95	1.50	125	FLECHT	Reference; Flooding rate
06638	40	1600	0.95	0.82	85	FLECHT	Pressure
05342	40	1601	0.95	0.80	248	FLECHT	Subcooling
02502	40	523	0.81	0.81	125	Uniform	Initial temperature
04930	40	1601	0.51	0.80	129	FLECHT	Power
04516	39	1601	0.95	6 (5 sec) 0.8 (onward)	131	FLECHT	Variable flooding rate
04444	58	1815	1.22	5.8	155	FLECHT	Grid effect

RUN NUMBER	04831
PRESSURE	40 PSIA
INITIAL CLADDING TEMPERATURE	1600°F
PEAK POWER	0.95 KW/FT
SUBCOOLING	142°F
INJECTION RATE	1.5 IN./SEC

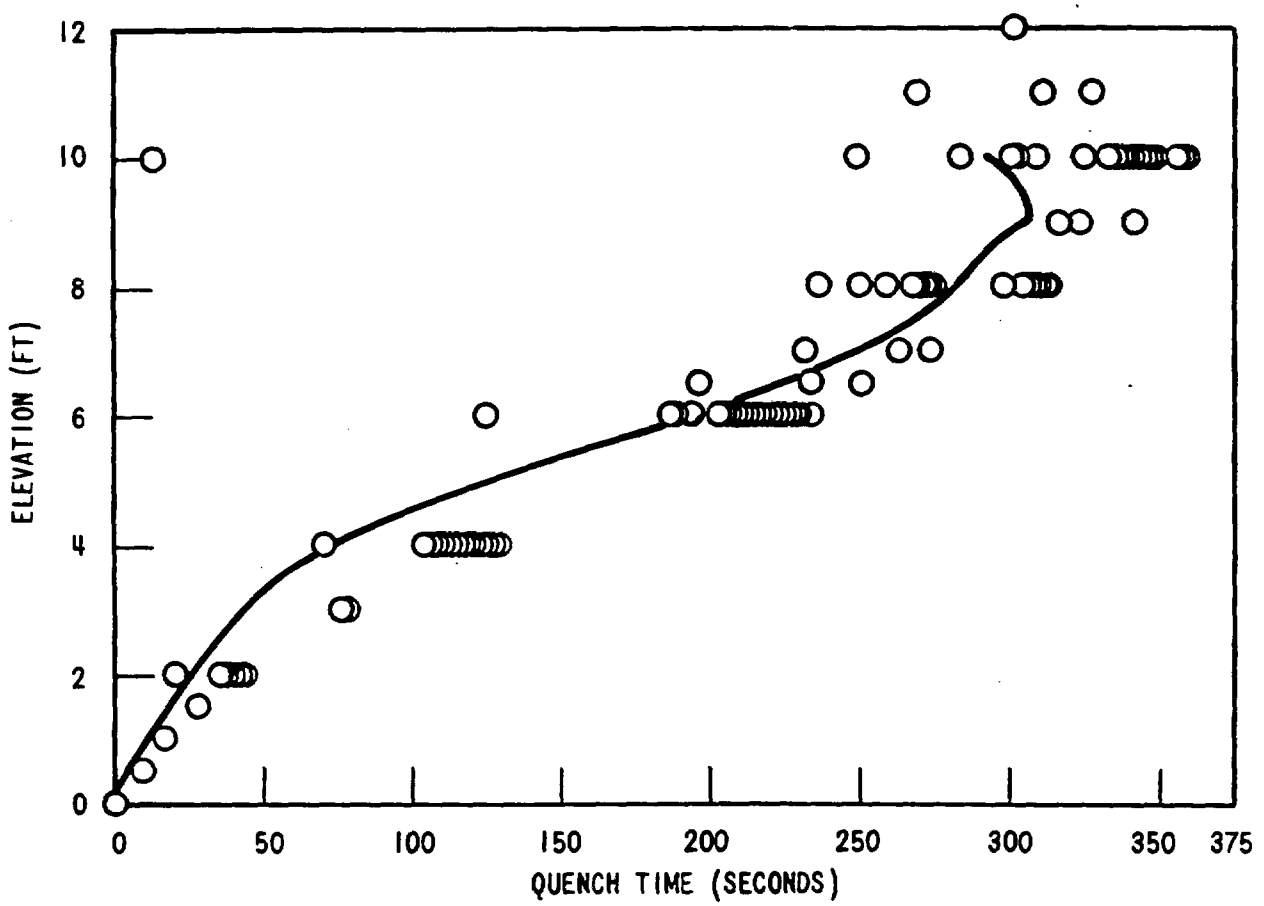

Figure E-1. Comparison of Predicted and Measured Quench Elevation Versus Quench Time for Run Number 04831

RUN NUMBER	06638
PRESSURE	20 PSIA
INITIAL CLADDING TEMPERATURE	1600°F
PEAK POWER	0.95 KW/FT
SUBCOOLING	78°F
INJECTION RATE	0.82 IN./SEC

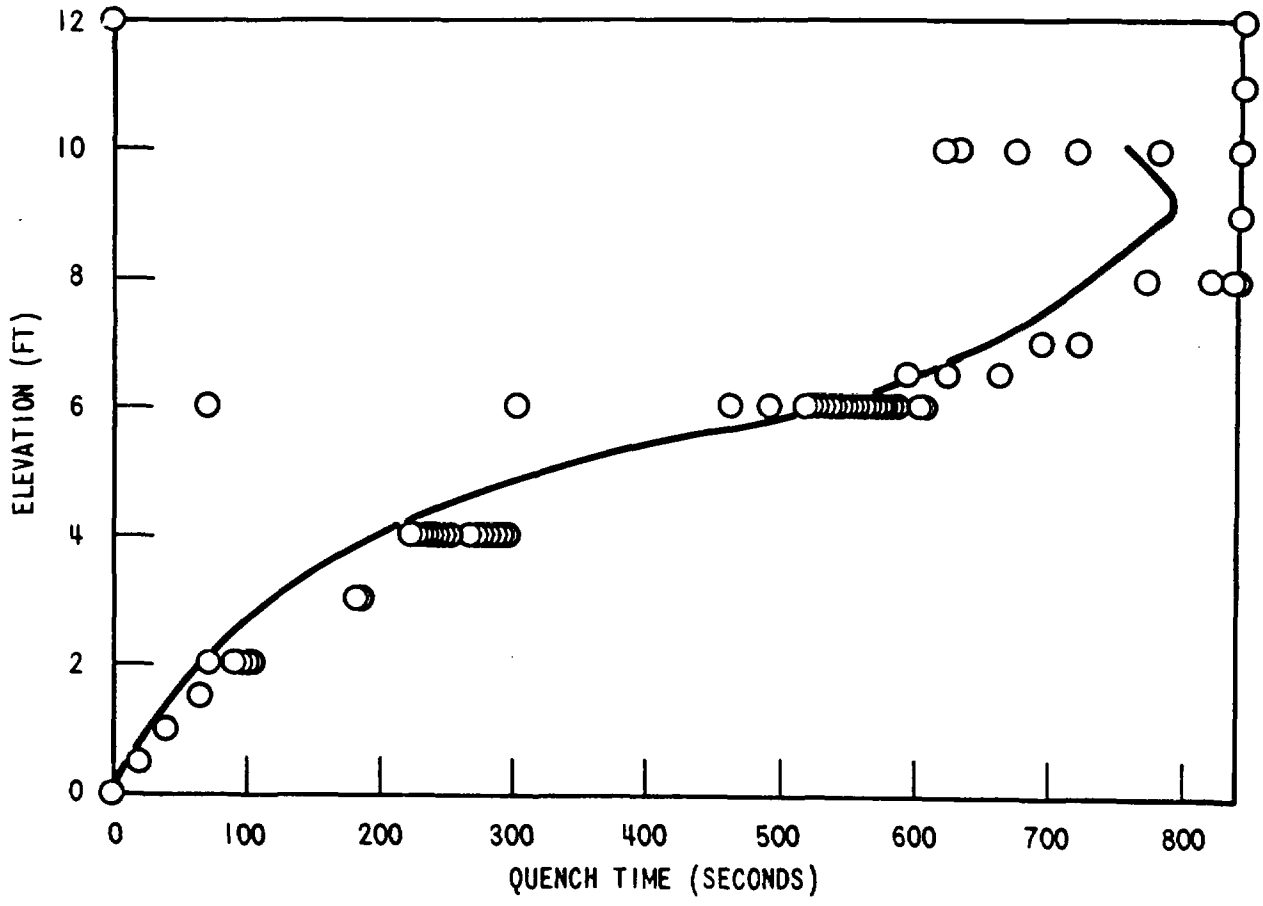

Figure E-2. Comparison of Predicted and Measured Quench Elevation Versus Quench Time for Run Number 06638

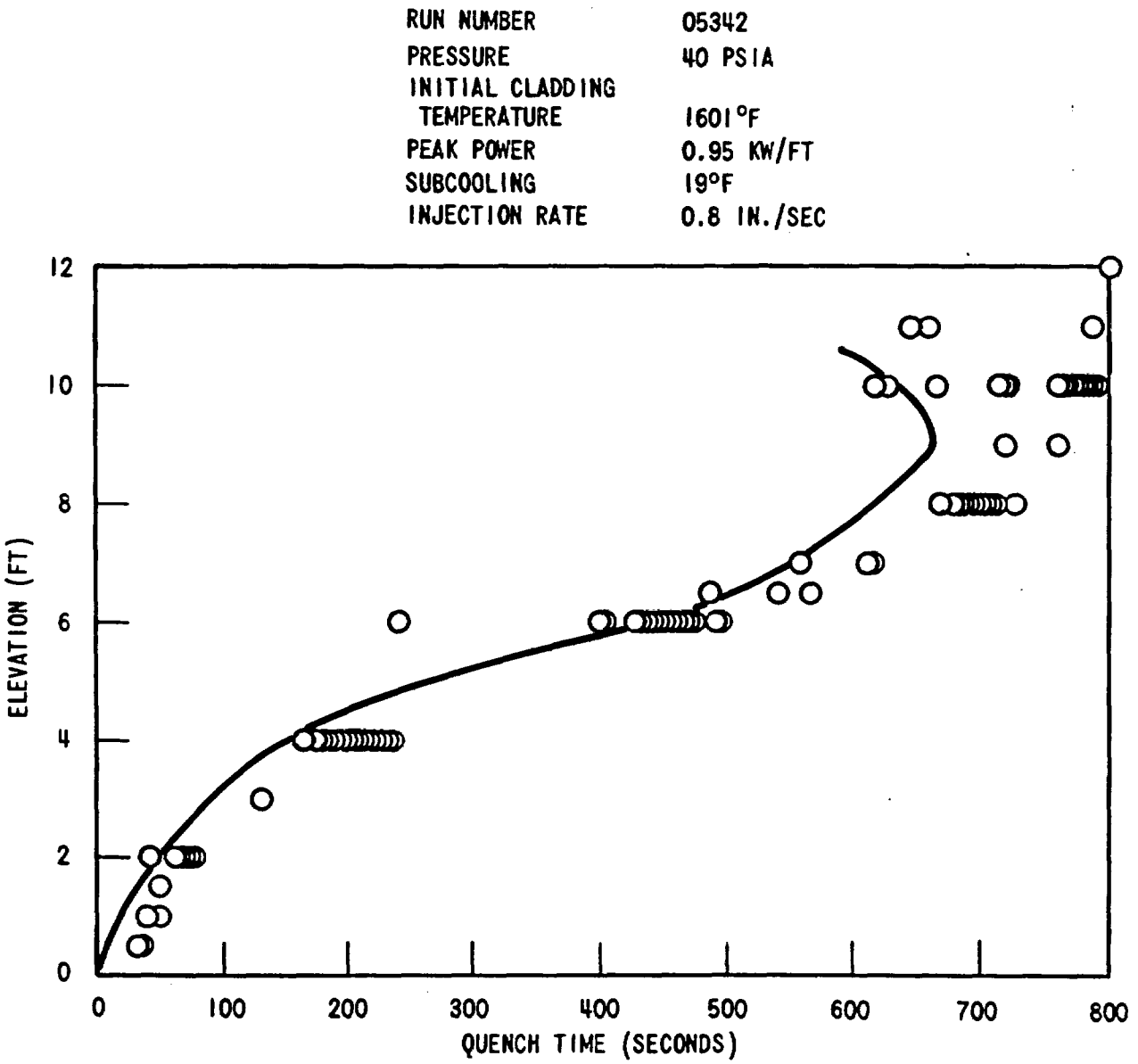

Figure E-3. Comparison of Predicted and Measured Quench Elevation Versus Quench Time for Run Number 05342

RUN NUMBER	02502
PRESSURE	40 PSIA
INITIAL CLADDING TEMPERATURE	445°F
PEAK POWER	0.81 KW/FT
SUBCOOLING	142°F
INJECTION RATE	0.81 IN./SEC

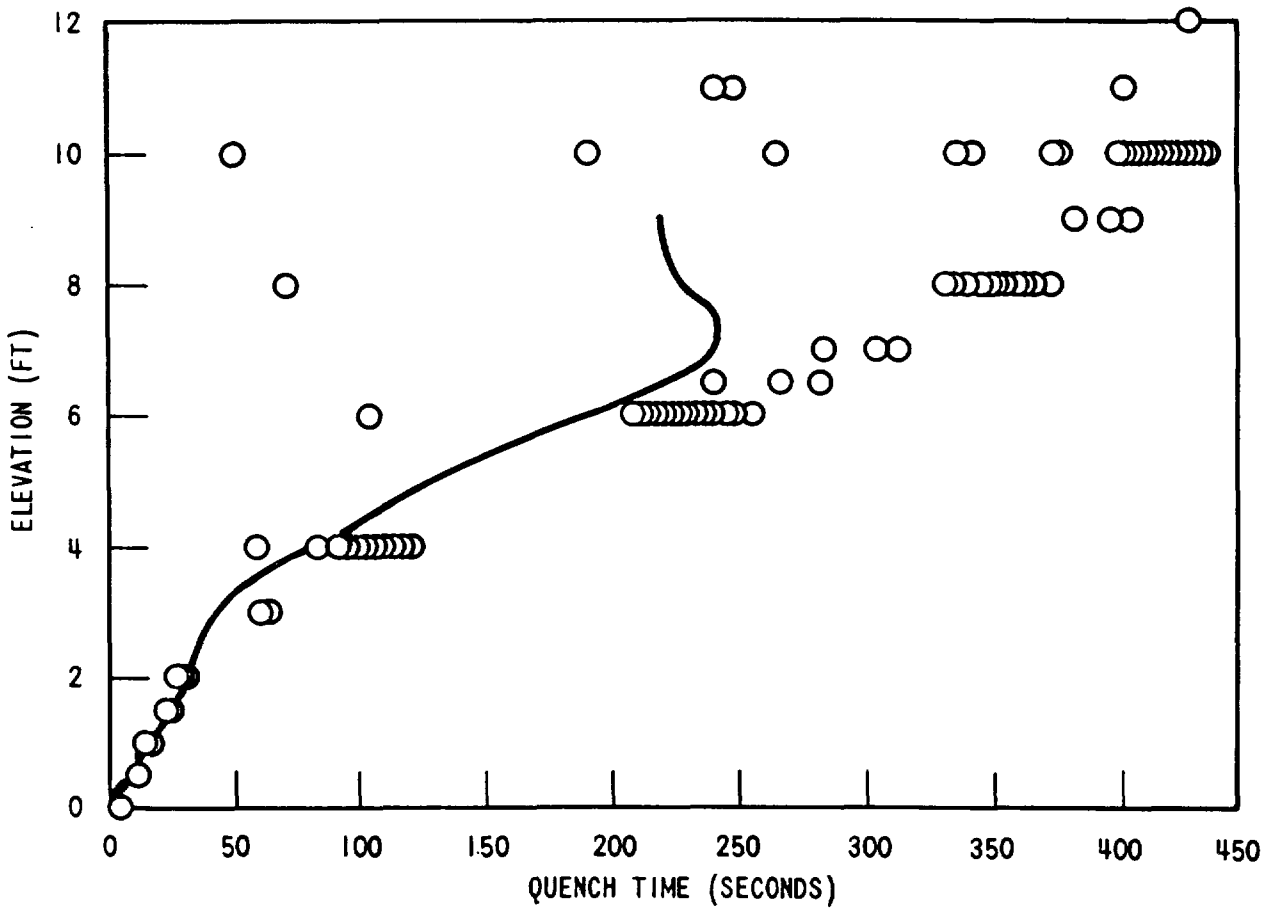

Figure E-4. Comparison of Predicted and Measured Quench Elevation Versus Quench Time for Run Number 02502

RUN NUMBER	04930
PRESSURE	40 PSIA
INITIAL CLADDING TEMPERATURE	1601°F
PEAK POWER	0.51 KW/FT
SUBCOOLING	138°F
INJECTION RATE	0.8 IN./SEC

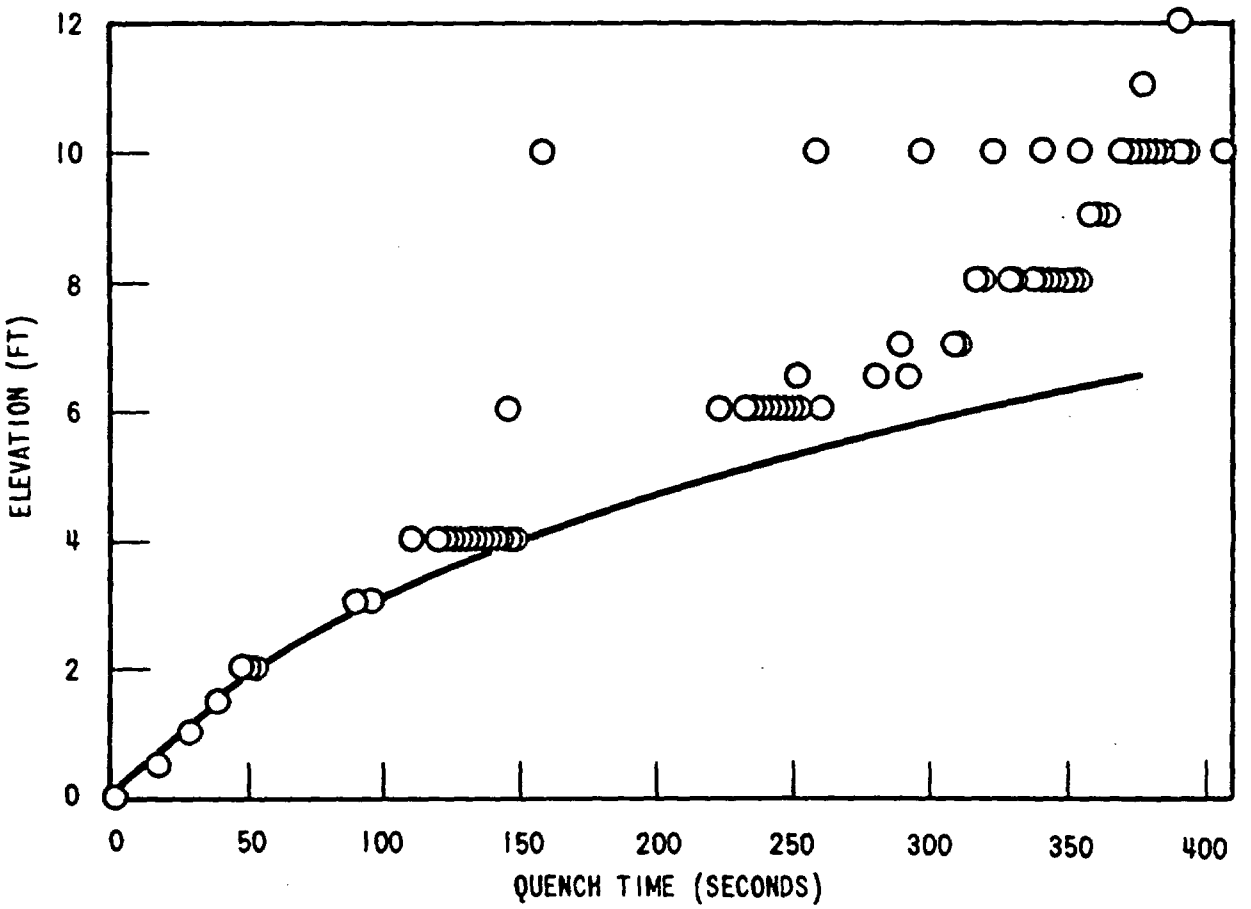

Figure E-5. Comparison of Predicted and Measured Quench Elevation Versus Quench Time for Run Number 04930

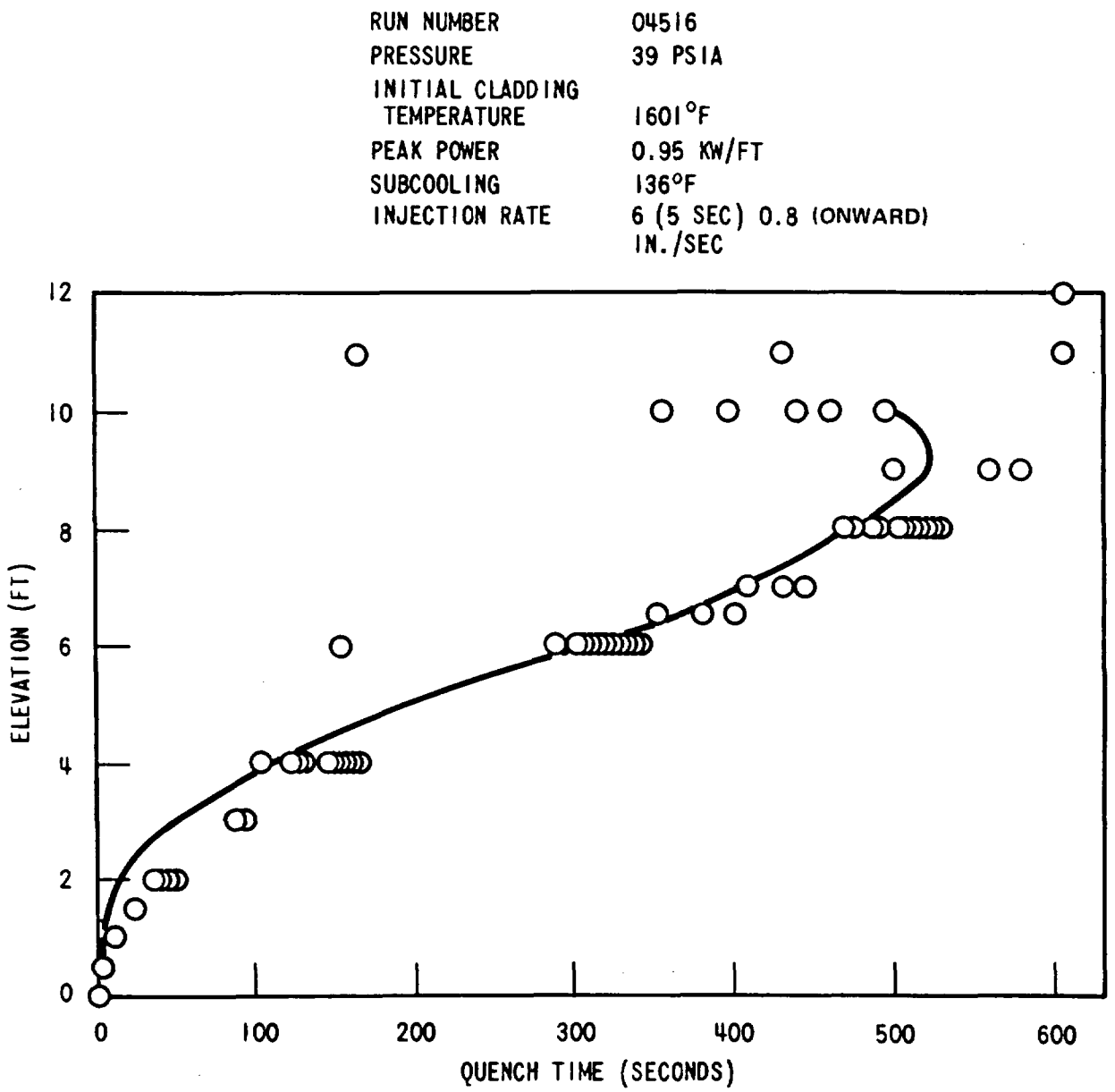

Figure E-6. Comparison of Predicted and Measured Quench Elevation Versus Quench Time for Run Number 04516

RUN NUMBER	04444
PRESSURE	58 PSIA
INITIAL CLADDING TEMPERATURE	1815°F
PEAK POWER	1.22 KW/FT
SUBCOOLING	136°F
INJECTION RATE	5.8 IN./SEC

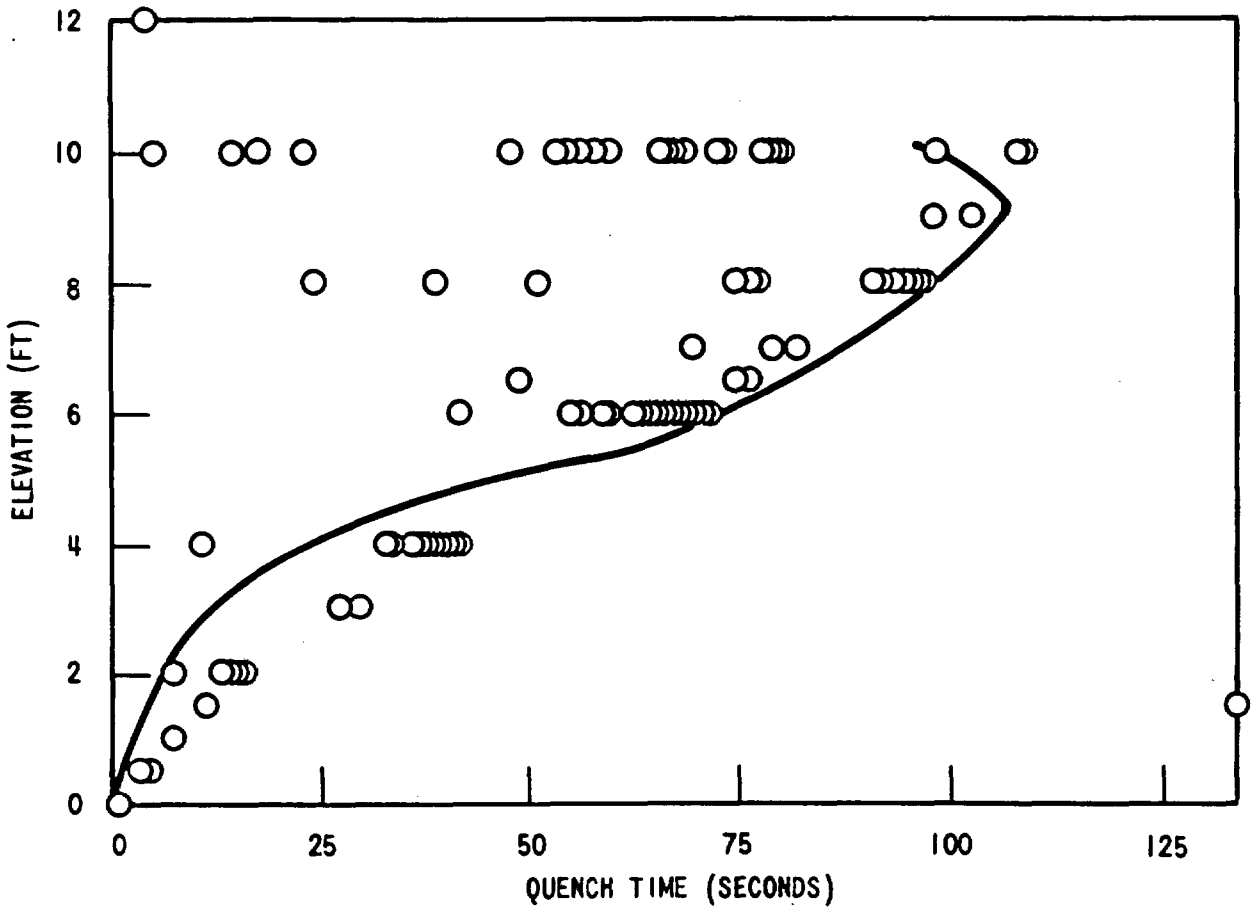

Figure E-7. Comparison of Predicted and Measured Quench Elevation Versus Quench Time for Run Number 04444

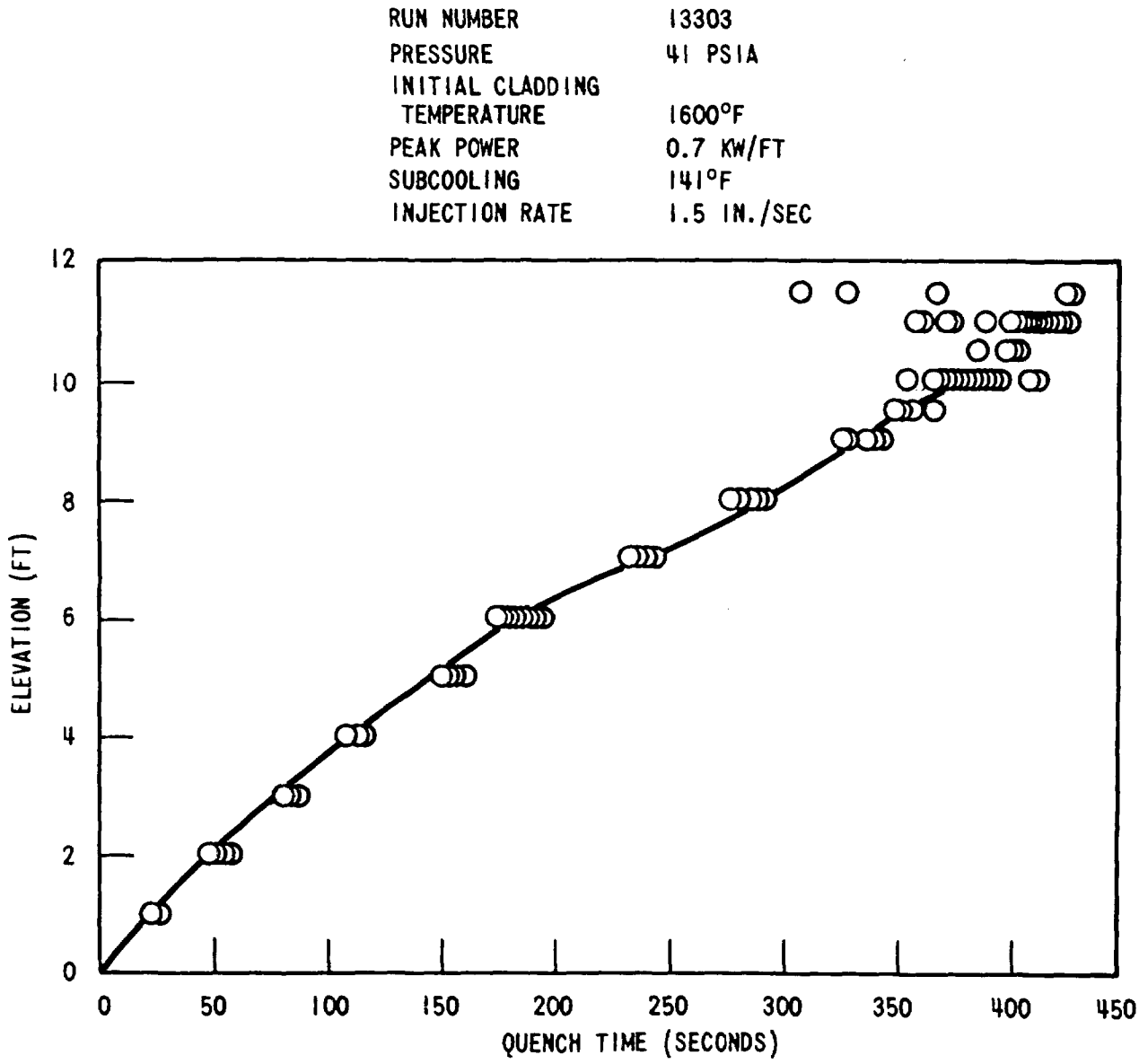

Figure E-8. Comparison of Predicted and Measured Quench Elevation Versus Quench Time for Run Number 13303

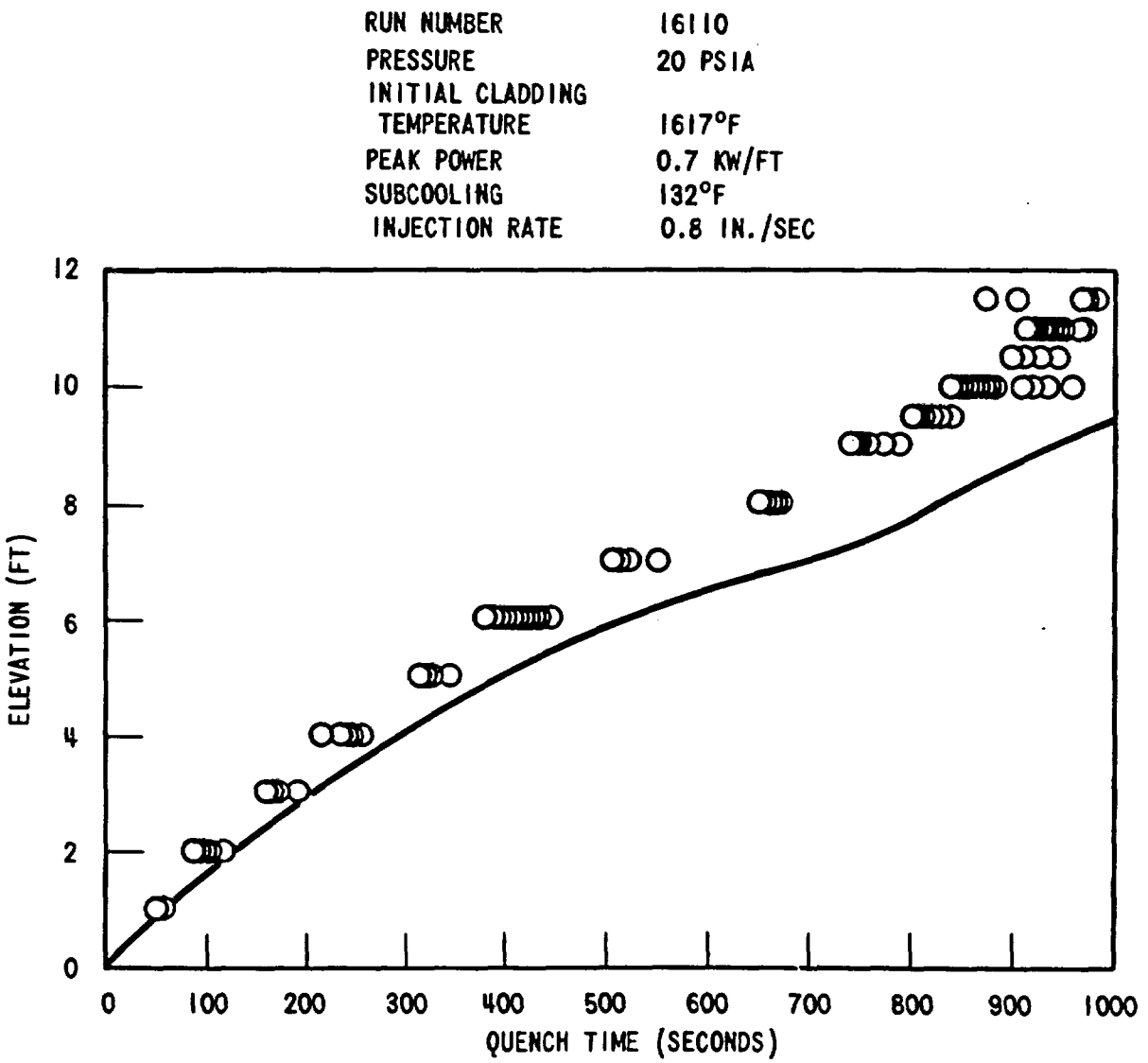

Figure E-9. Comparison of Predicted and Measured Quench Elevation Versus Quench Time for Run Number 16110

RUN NUMBER	15713
PRESSURE	40 PSIA
INITIAL CLADDING TEMPERATURE	1607°F
PEAK POWER	0.7 KW/FT
SUBCOOLING	2°F
INJECTION RATE	1.0 IN./SEC

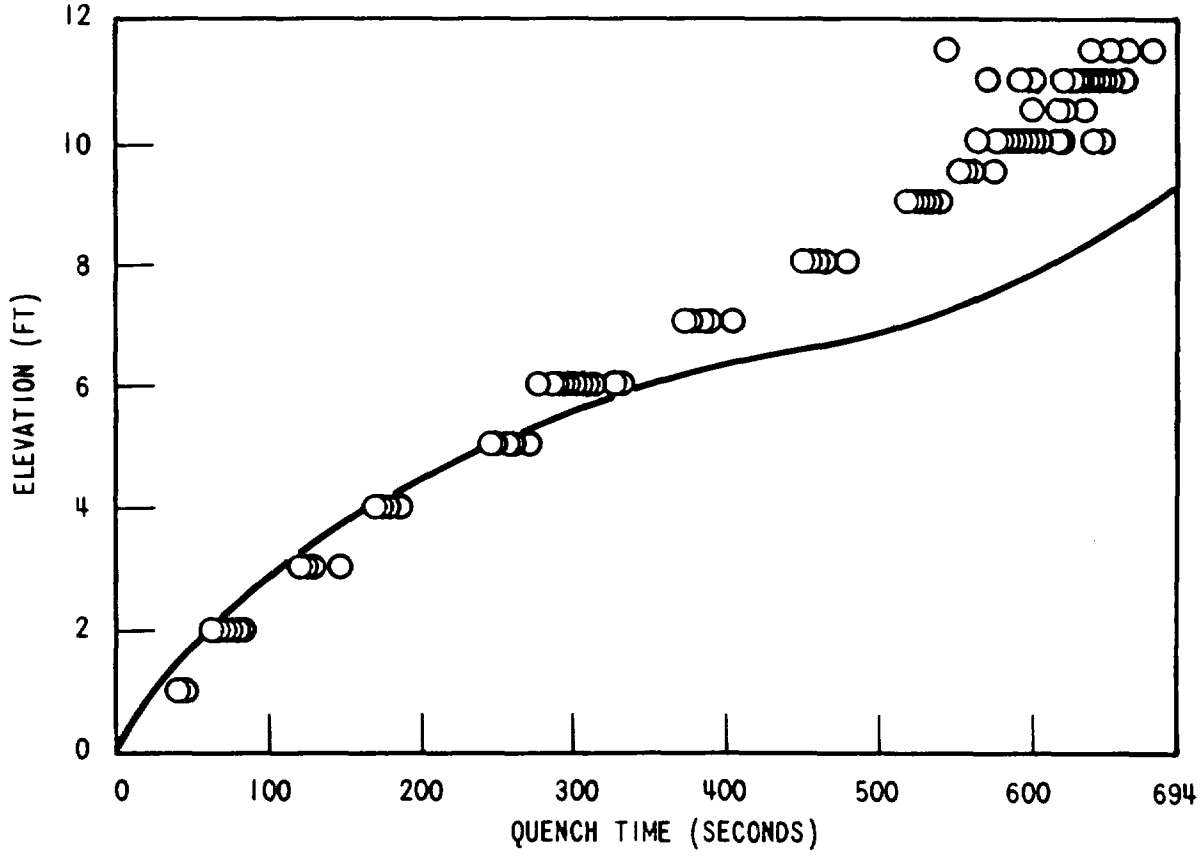

Figure E-10. Comparison of Predicted and Measured Quench Elevation Versus Quench Time for Run Number 15713

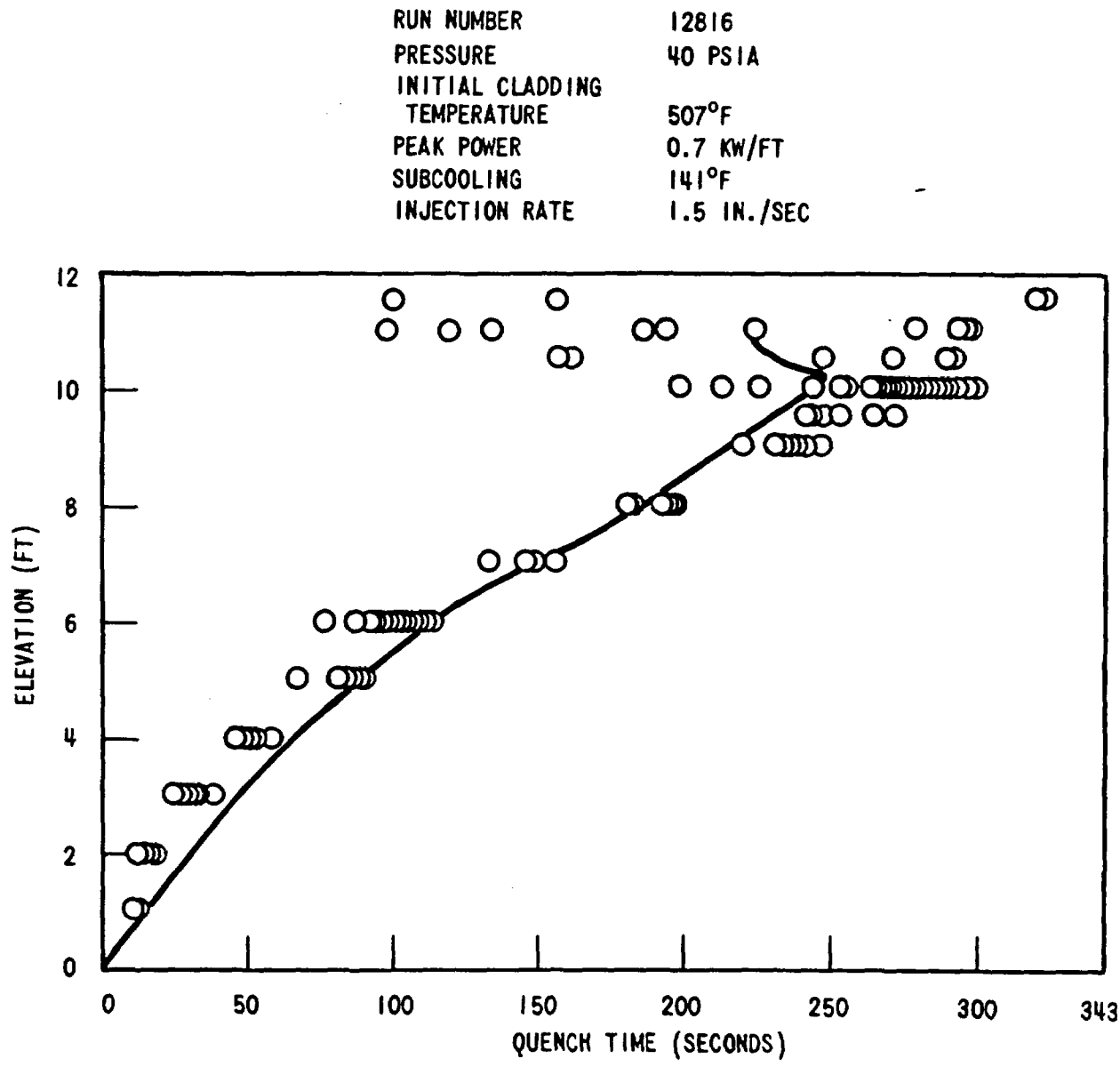

Figure E-11. Comparison of Predicted and Measured Quench Elevation Versus Quench Time for Run Number 12816

RUN NUMBER	16022
PRESSURE	40 PSIA
INITIAL CLADDING TEMPERATURE	1636°F
PEAK POWER	1.0 KW/FT
SUBCOOLING	139°F
INJECTION RATE	1.5 IN./SEC

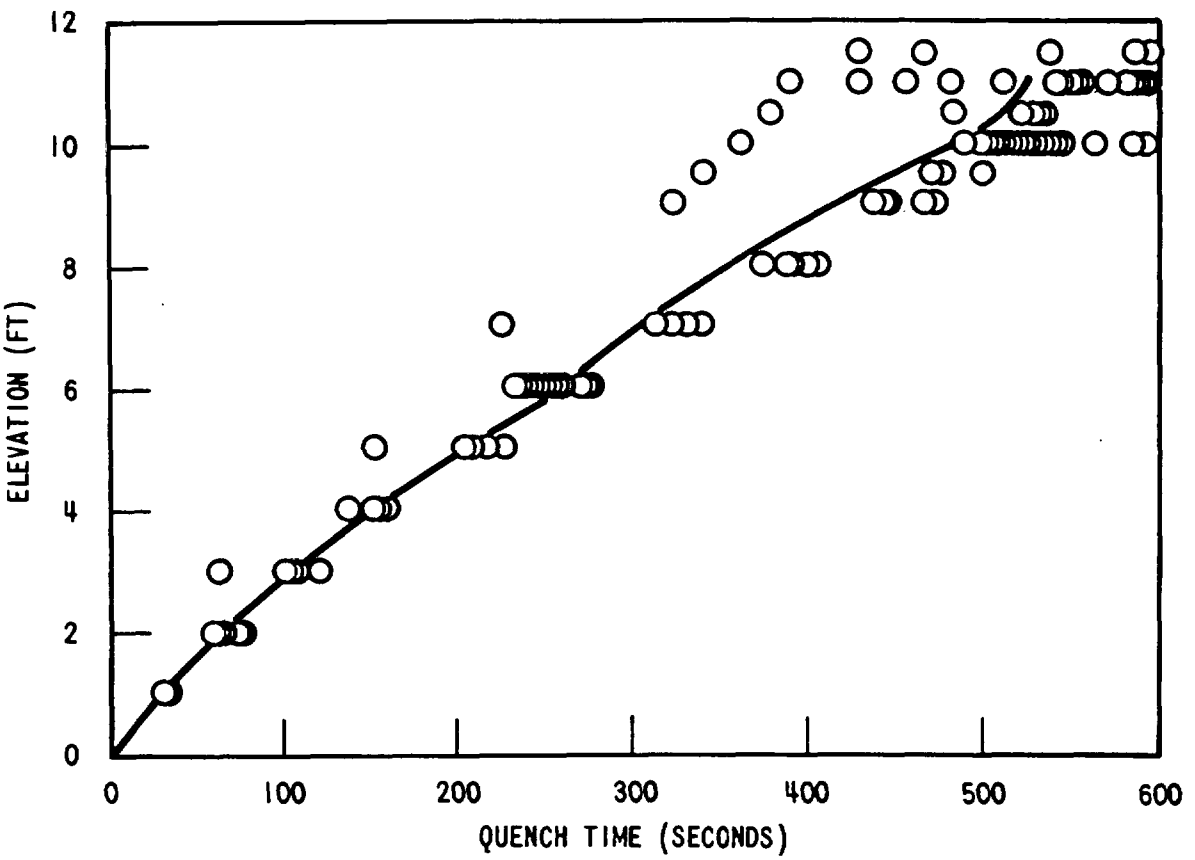

Figure E-12. Comparison of Predicted and Measured Quench Elevation Versus Quench Time for Run Number 16022

RUN NUMBER	15132
PRESSURE	39 PSIA
INITIAL CLADDING TEMPERATURE	1555°F
PEAK POWER	0.7 KW/FT
SUBCOOLING	139°F
INJECTION RATE	6 (5 SEC) 0.8 (ONWARD) IN./SEC

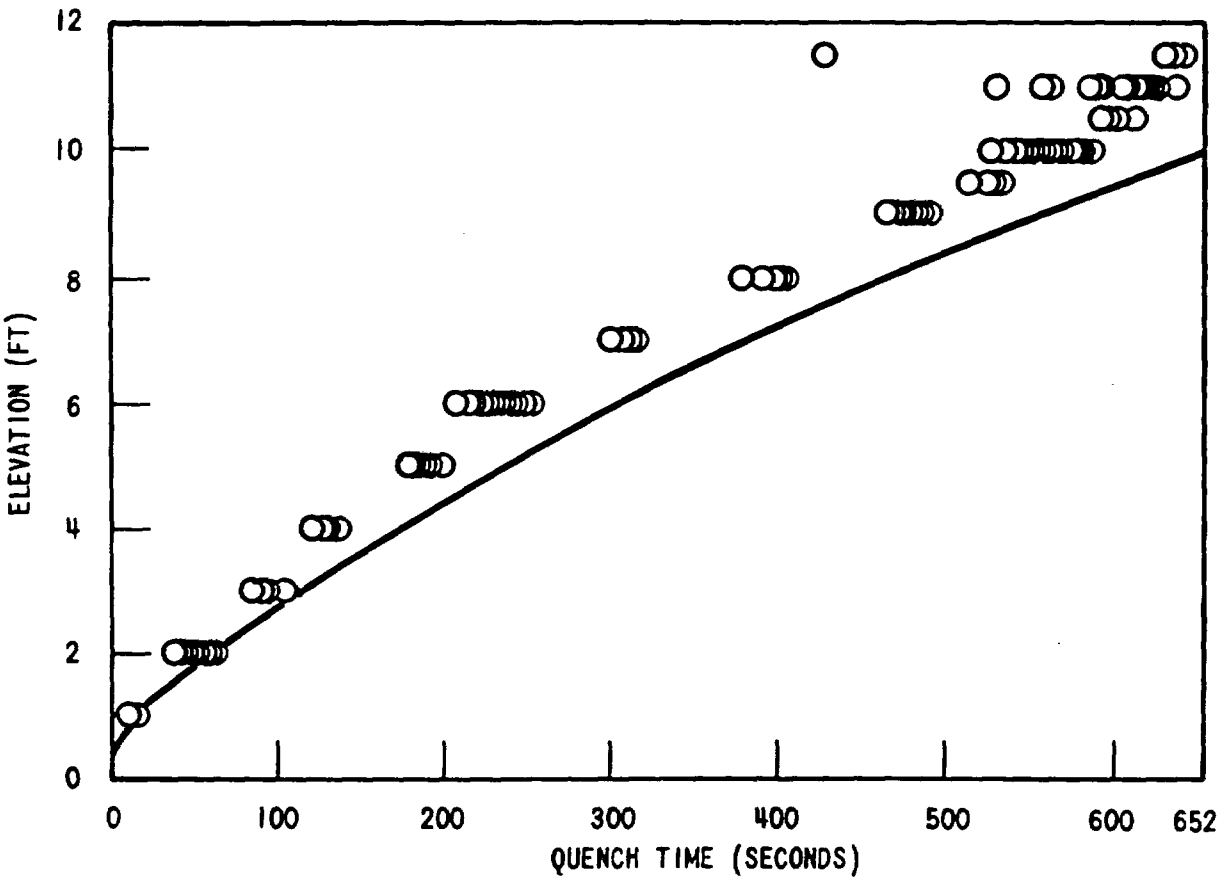

Figure E-13. Comparison of Predicted and Measured Quench Elevation Versus Quench Time for Run Number 15132

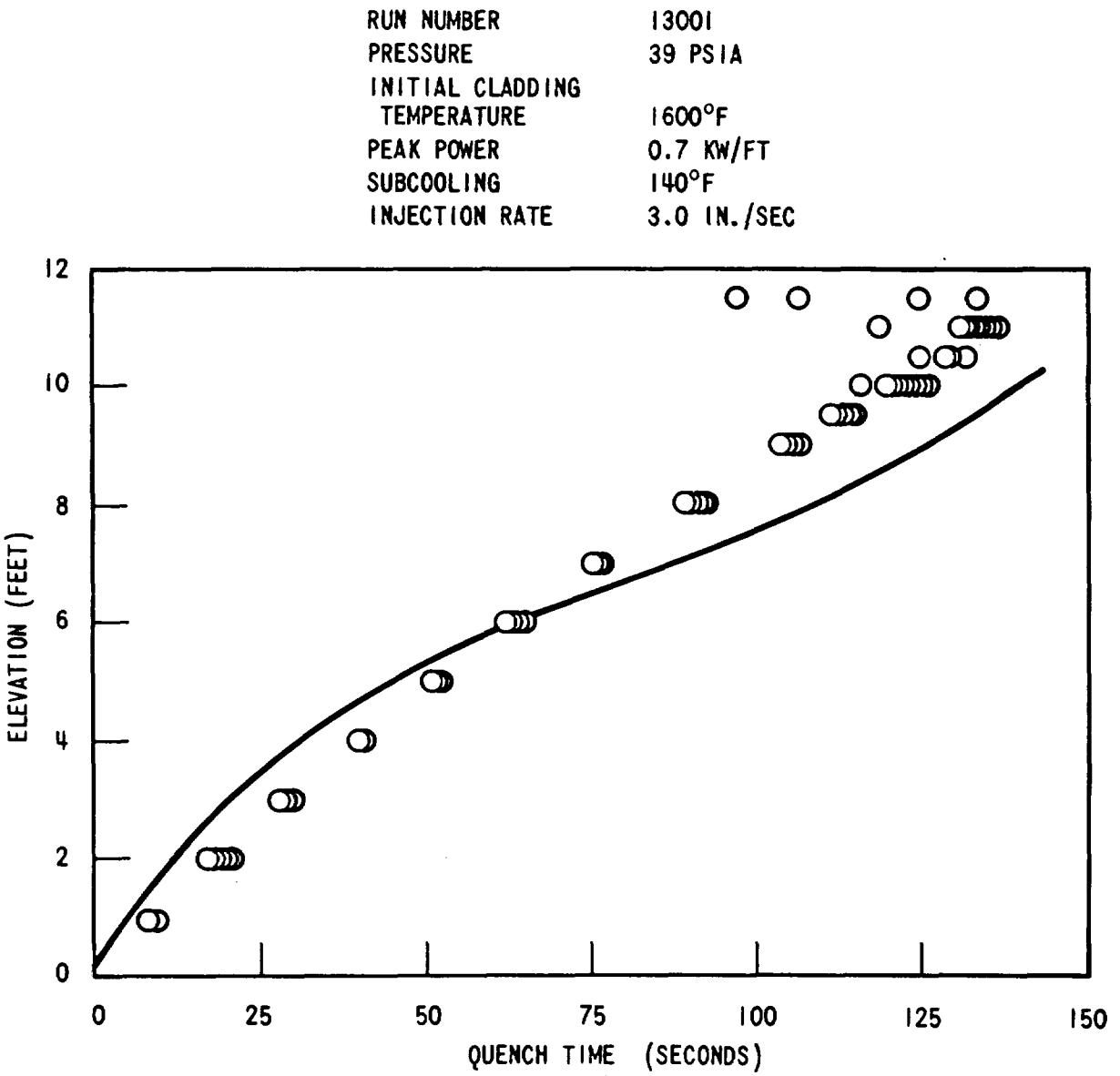

Figure E-14. Comparison of Predicted and Measured Quench Elevation Versus Quench Time for Run Number 13001

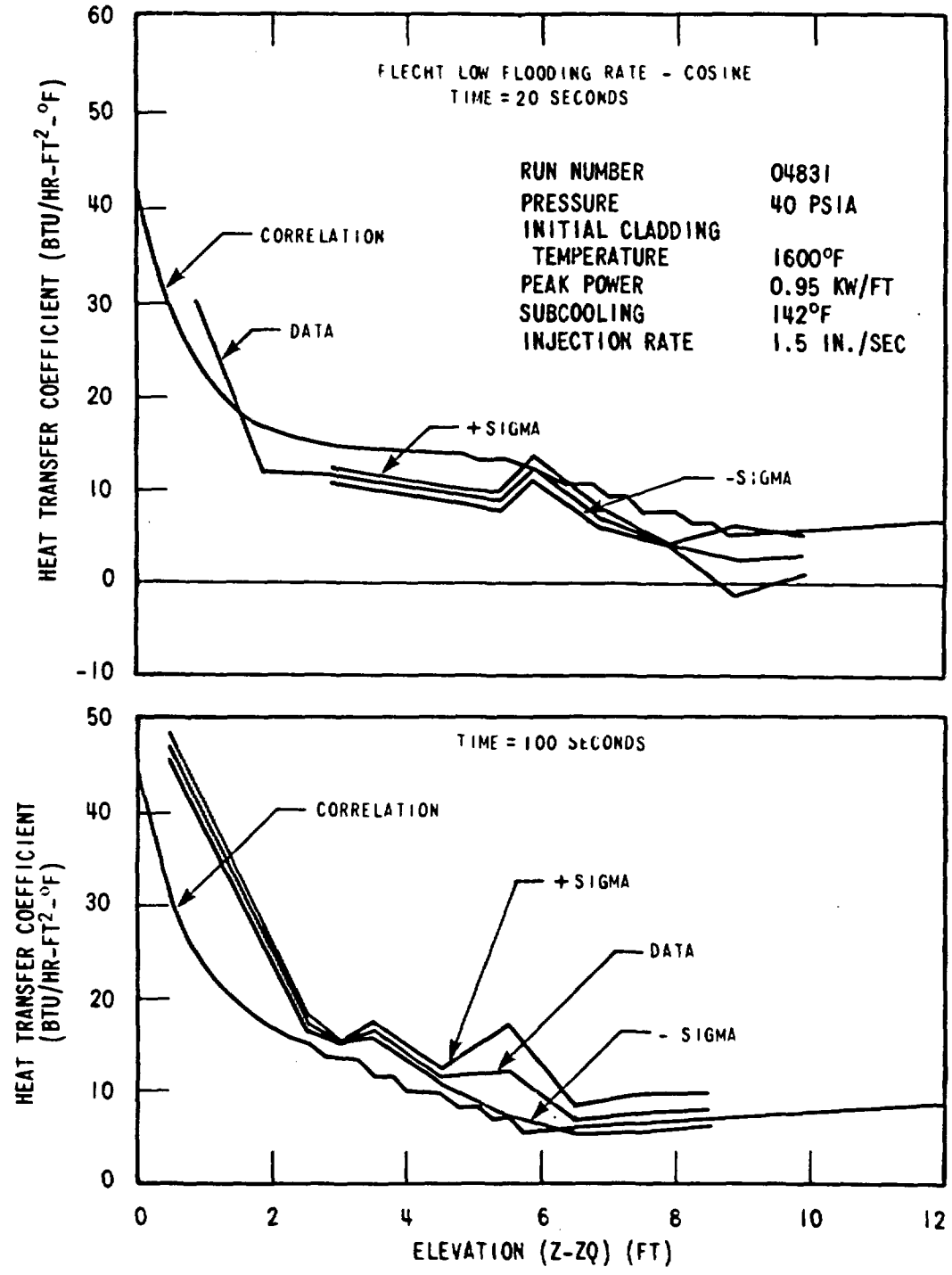

Figure E-15. Heat Transfer Coefficient Dependence on Distance From Quench Front at 20 and 100 Seconds for Run Number 04831

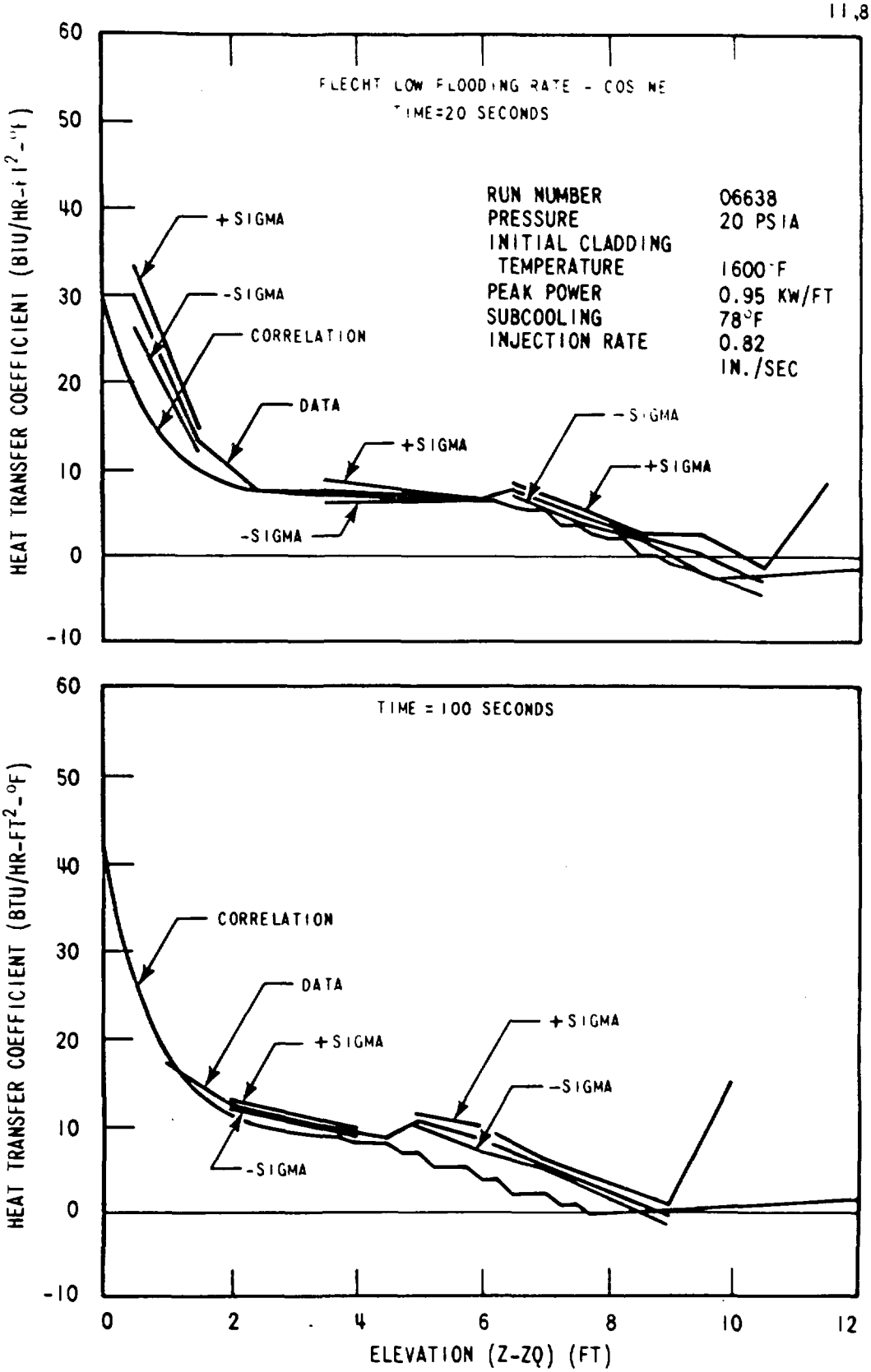

Figure E-16. Heat Transfer Coefficient Dependence on Distance From Quench Front at 20 and 100 Seconds for Run Number 06638

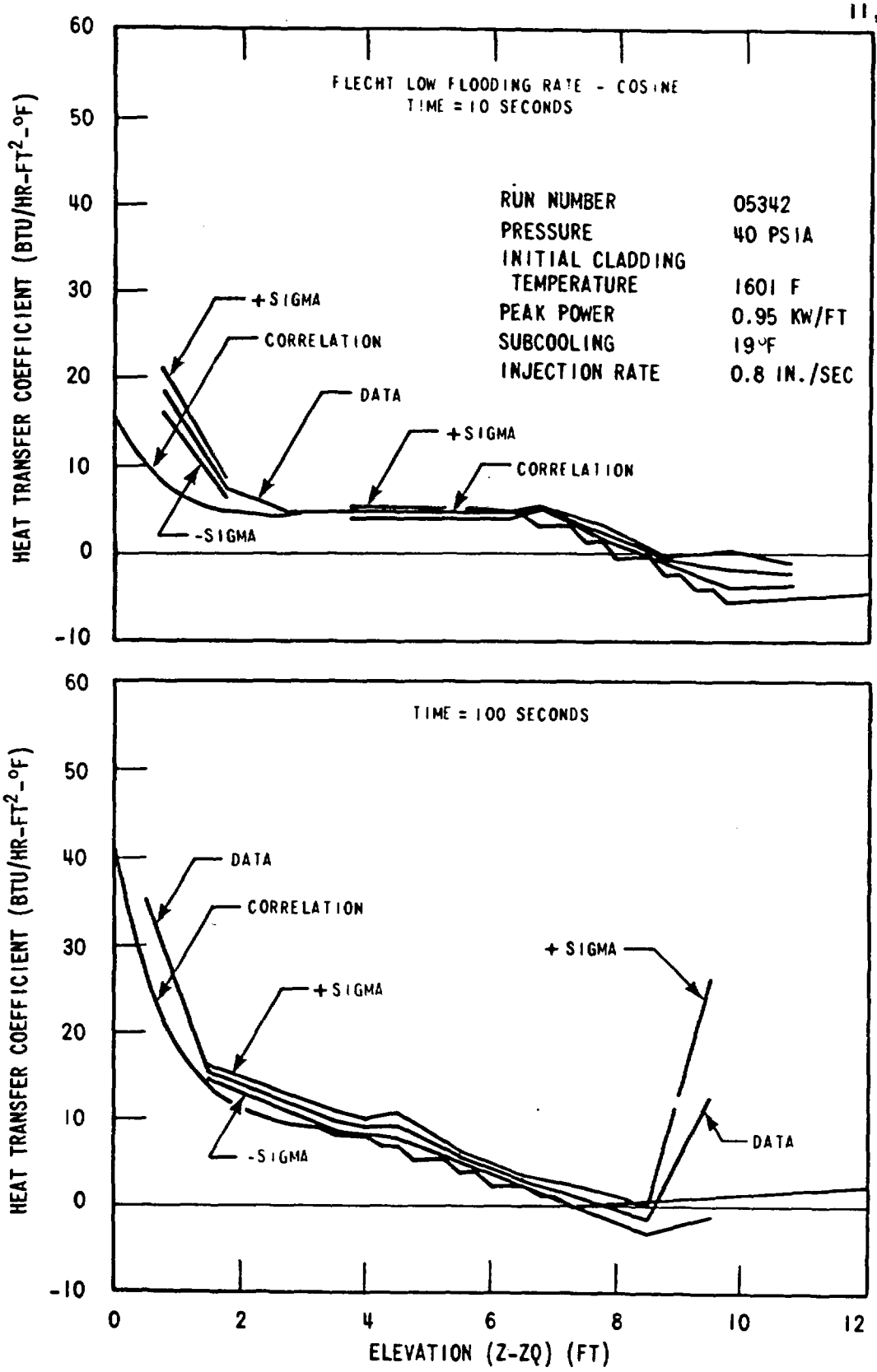

Figure E-17. Heat Transfer Coefficient Dependence on Distance From Quench Front at 10 and 100 Seconds for Run Number 05342

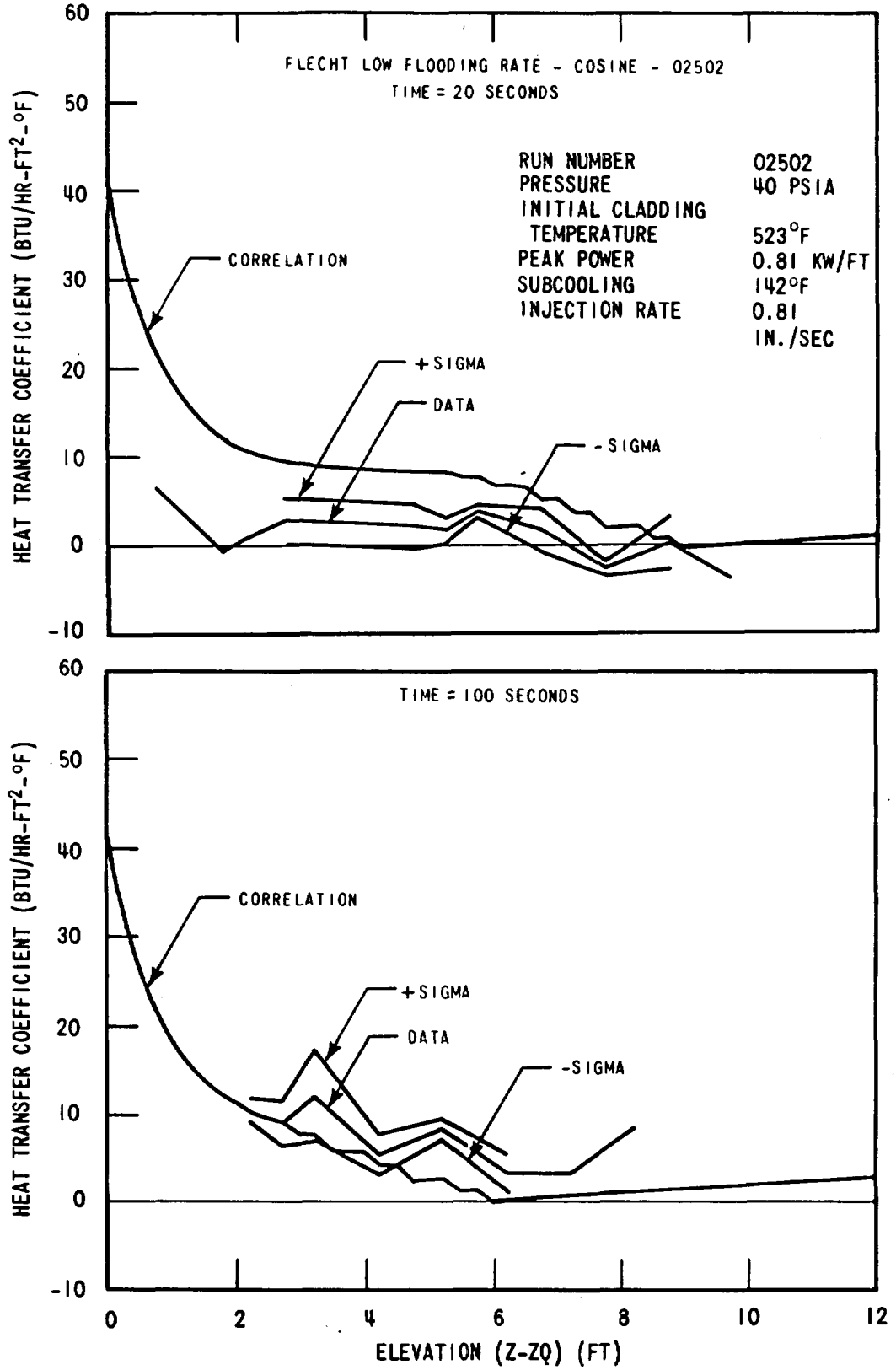

Figure E-18. Heat Transfer Coefficient Dependence on Distance From Quench Front at 20 and 100 Seconds for Run Number 02502

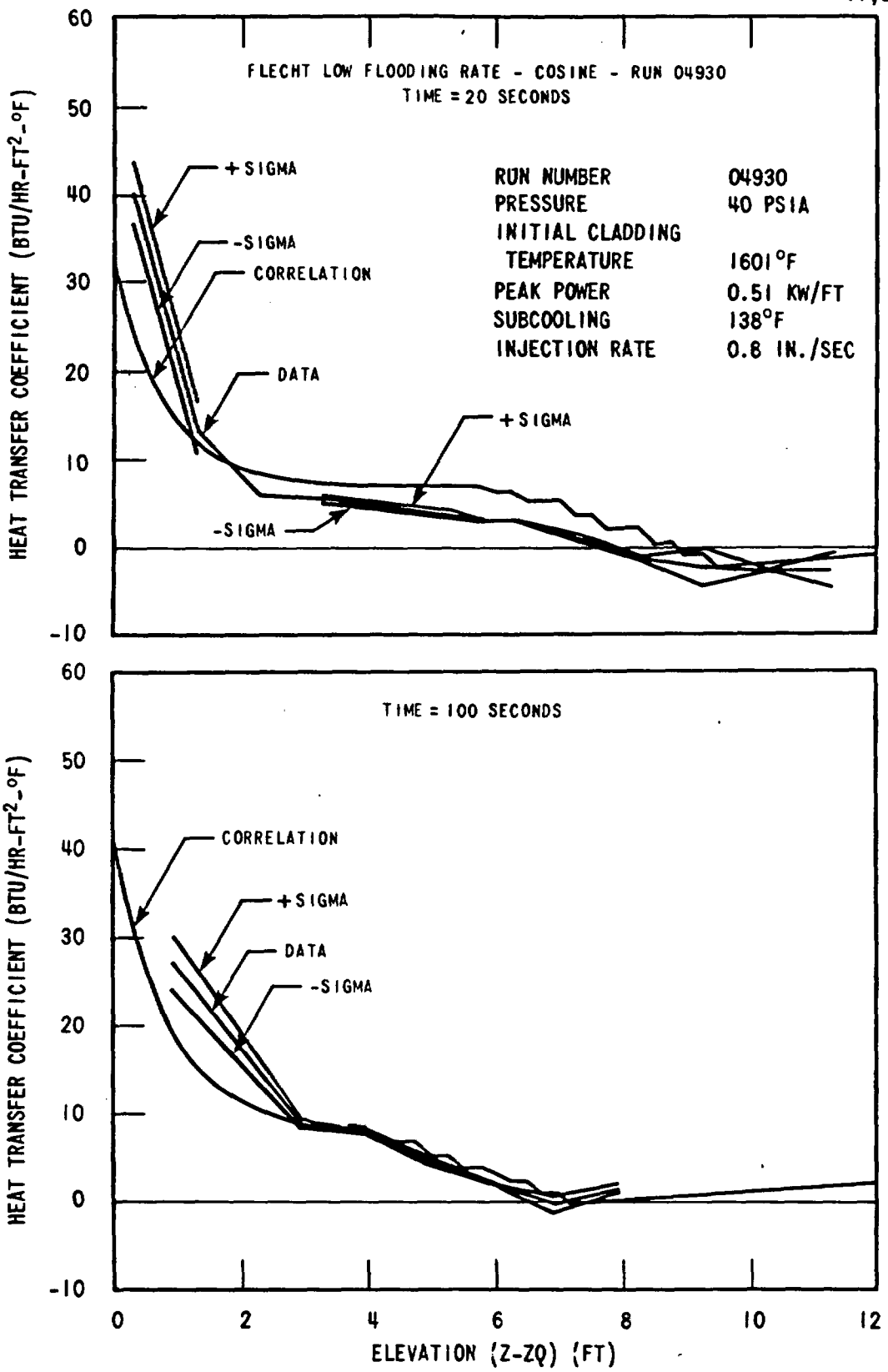

Figure E-19. Heat Transfer Coefficient Dependence on Distance From Quench Front at 20 and 100 Seconds for Run Number 04930

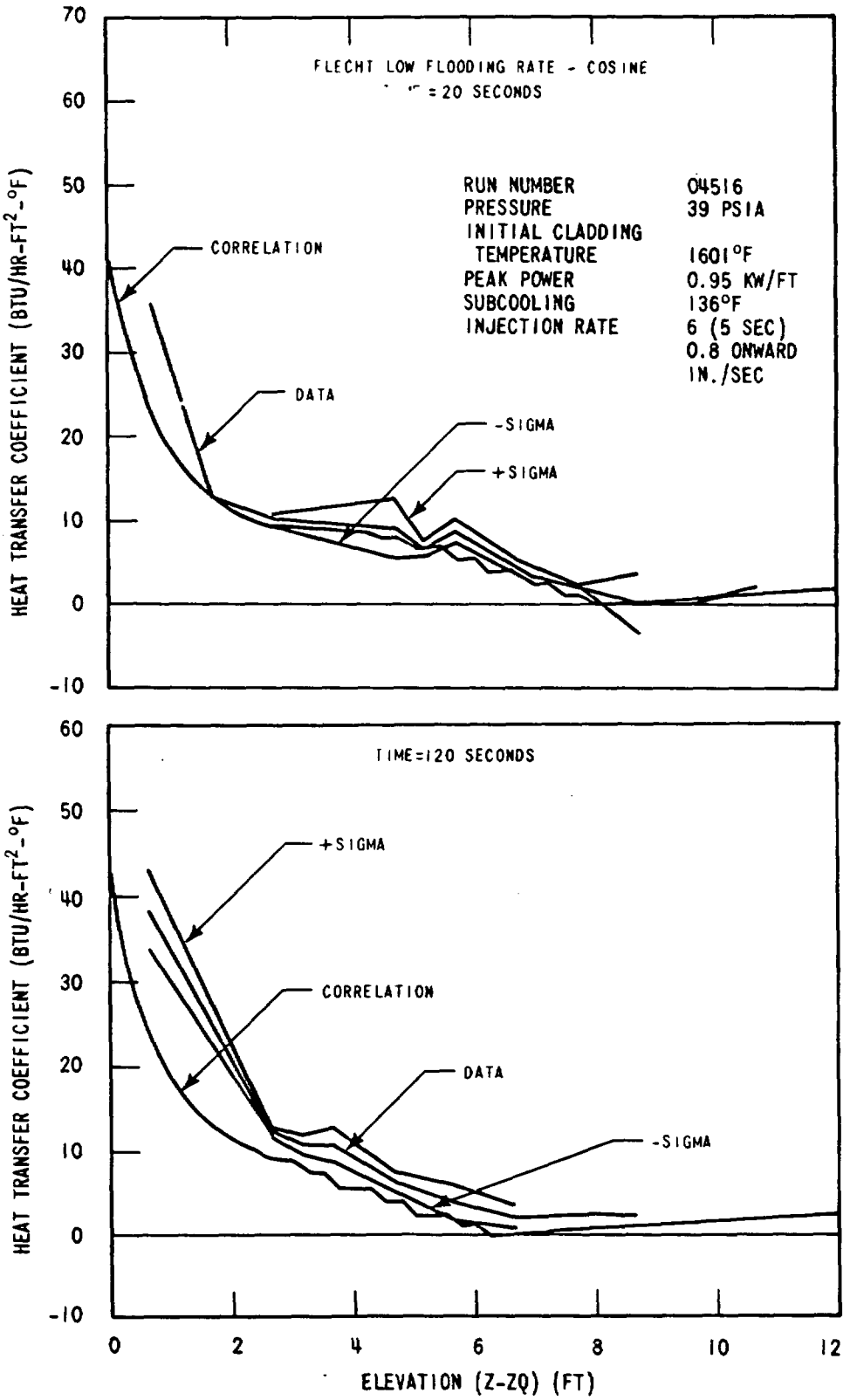

Figure E-20. Heat Transfer Coefficient Dependence on Distance From Quench Front at 20 and 100 Seconds for Run Number 04516

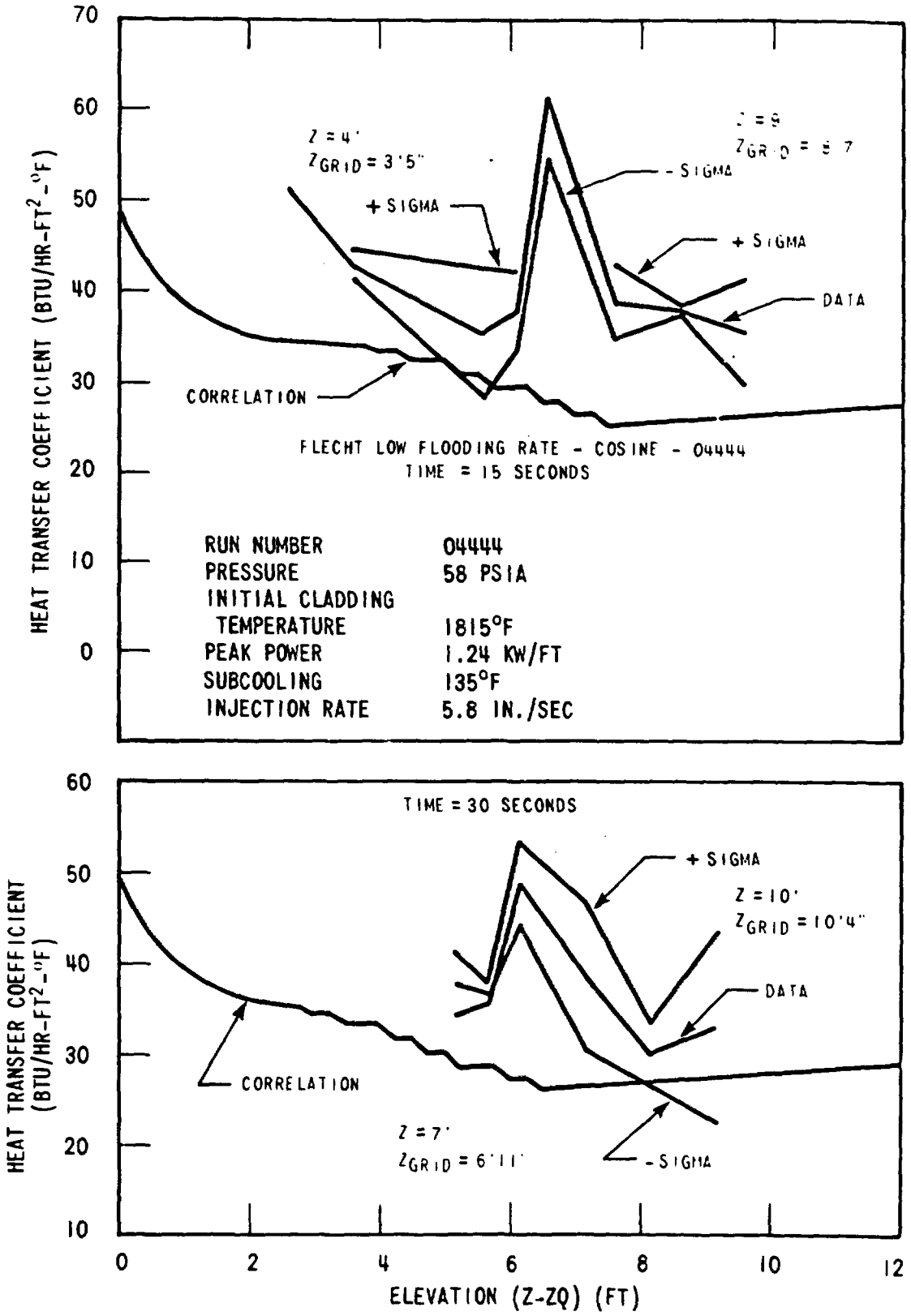

Figure E-21. Heat Transfer Coefficient Dependence on Distance From Quench Front at 15 and 30 Seconds for Run Number 04444

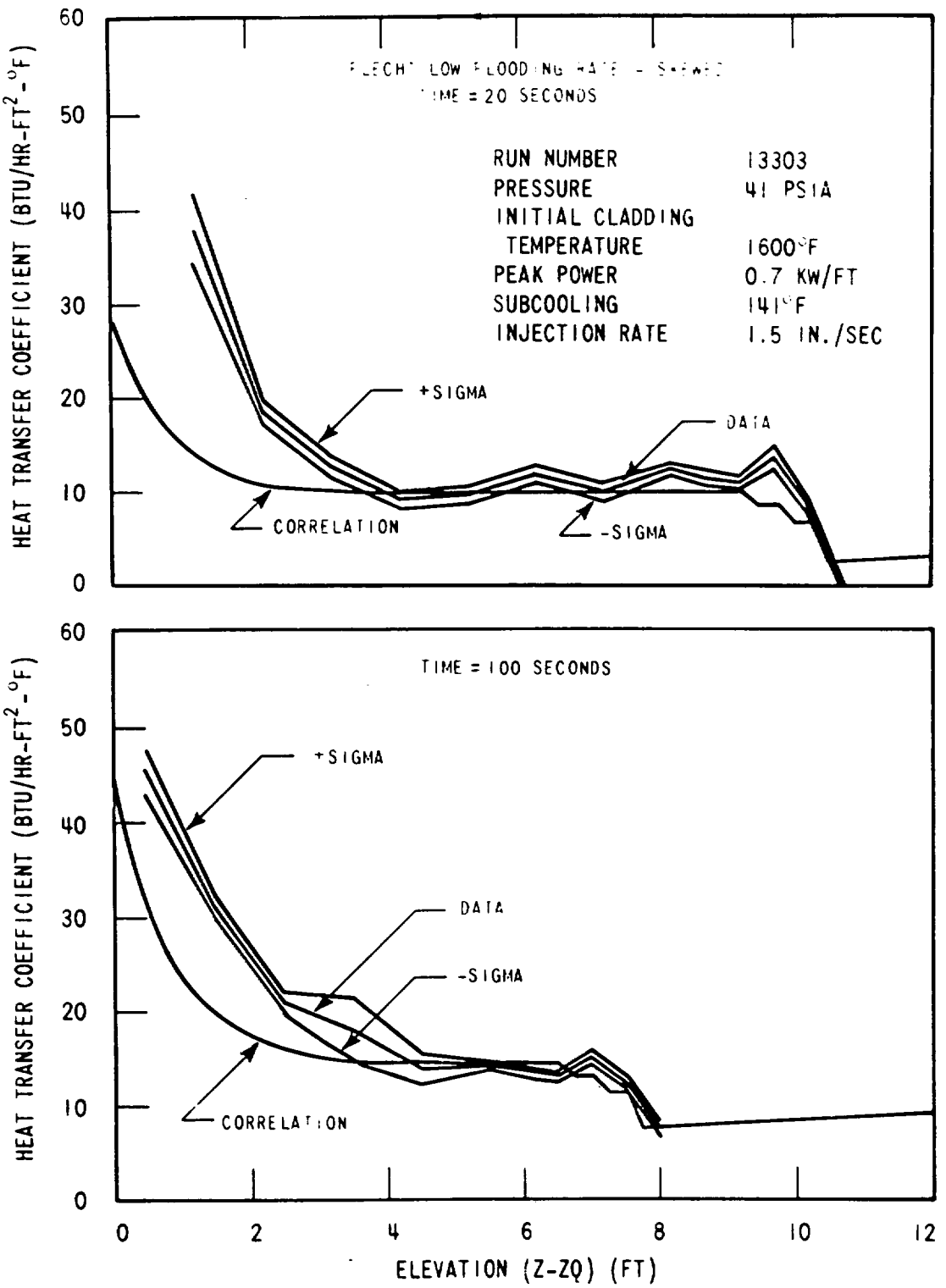

Figure E-22. Heat Transfer Coefficient Dependence on Distance From Quench Front at 20 and 100 Seconds for Run Number 13303

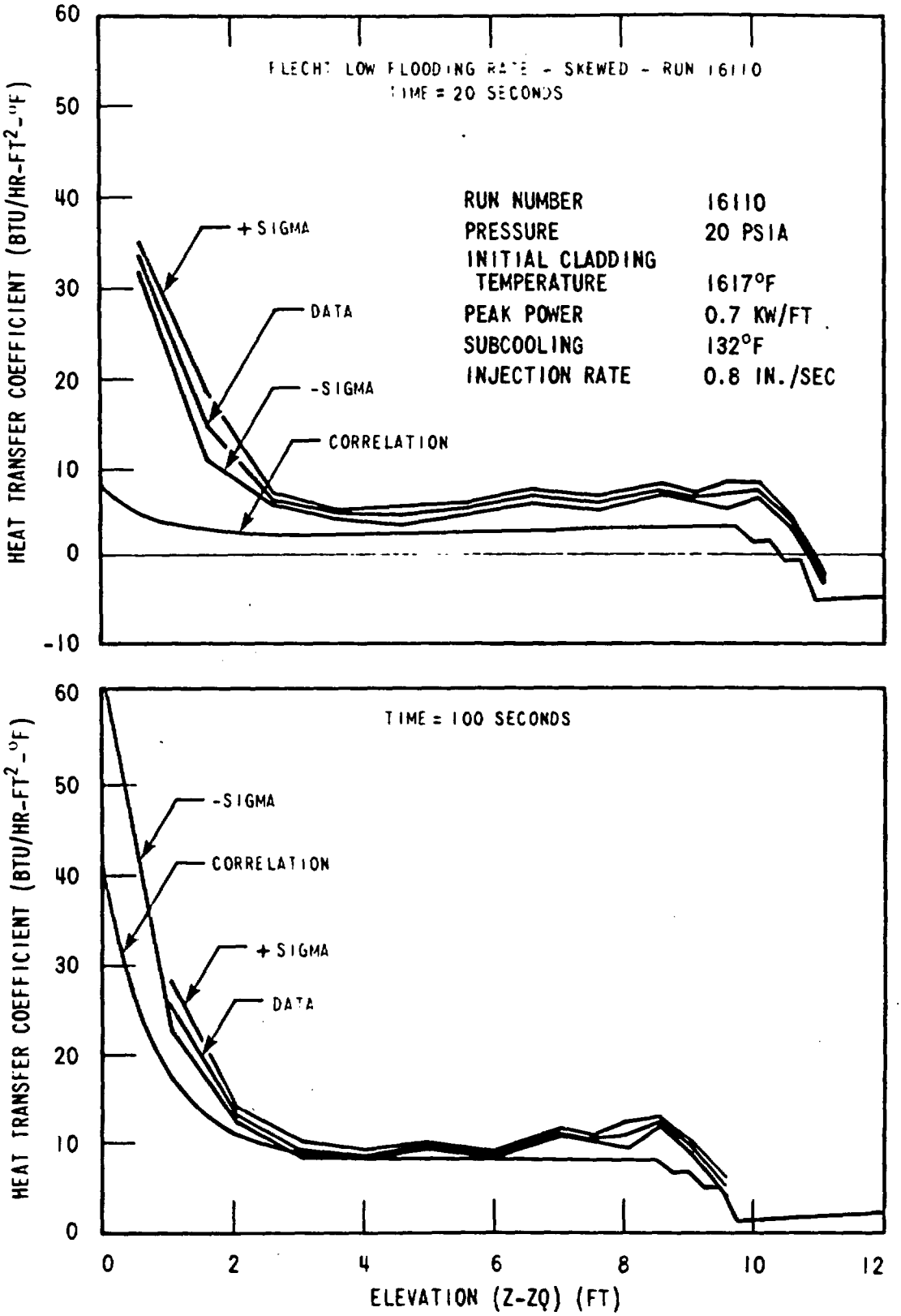

Figure E-23. Heat Transfer Coefficient Dependence on Distance From Quench Front at 20 and 100 Seconds for Run Number 16110

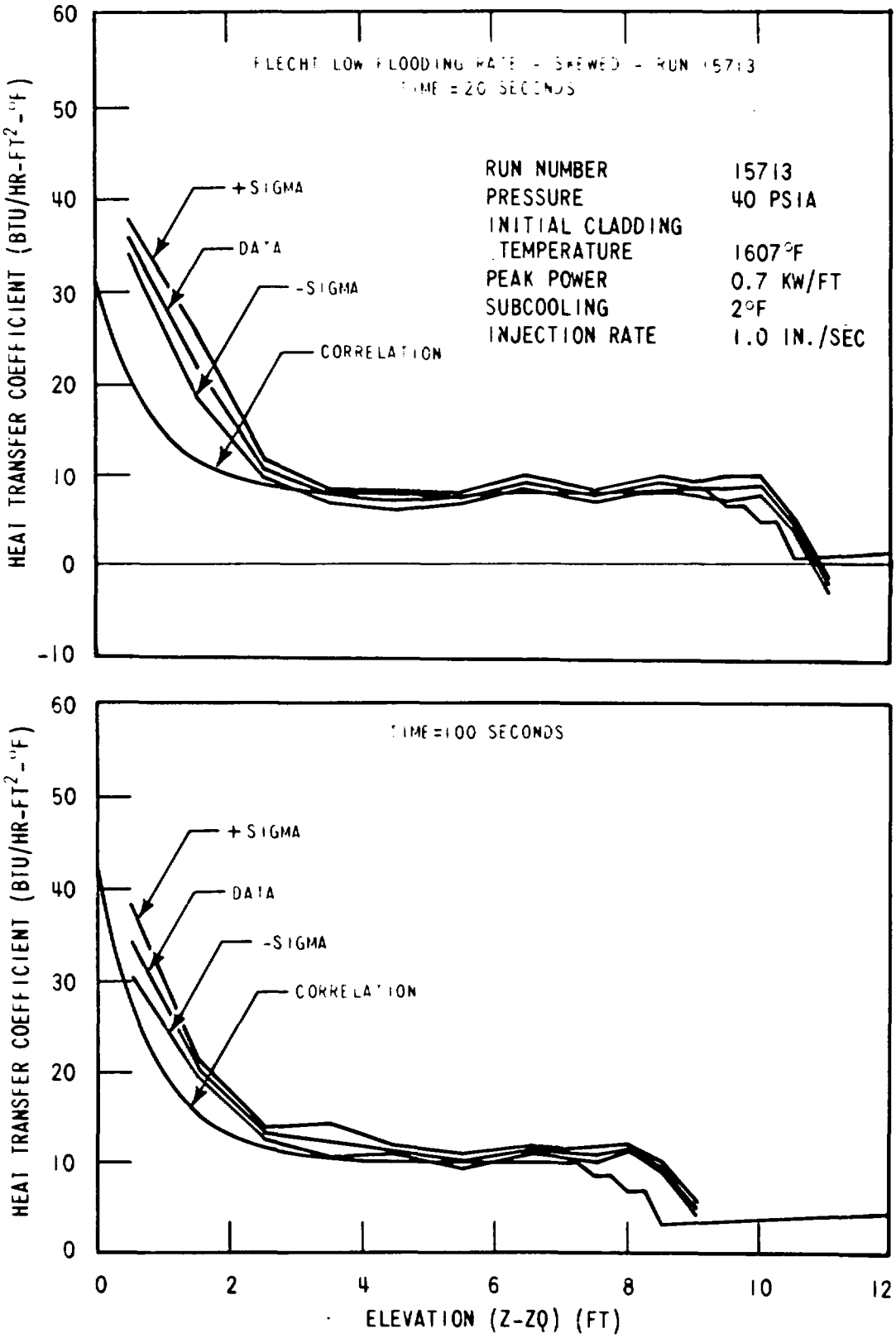

Figure E-24. Heat Transfer Coefficient Dependence on Distance From Quench Front at 20 and 100 Seconds for Run Number 15713

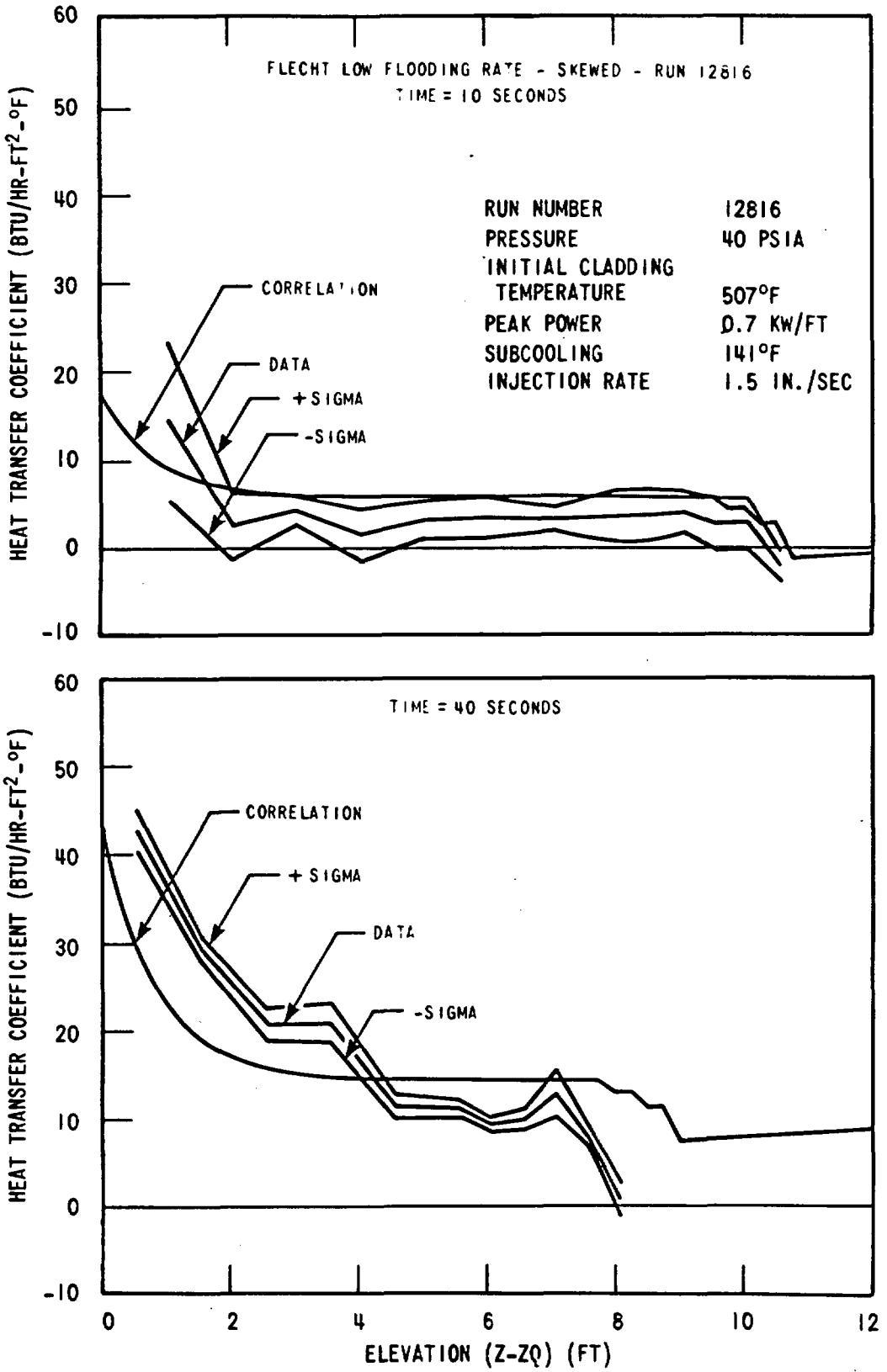

Figure E-25. Heat Transfer Coefficient Dependence on Distance From Quench Front at 10 and 40 Seconds for Run Number 12816

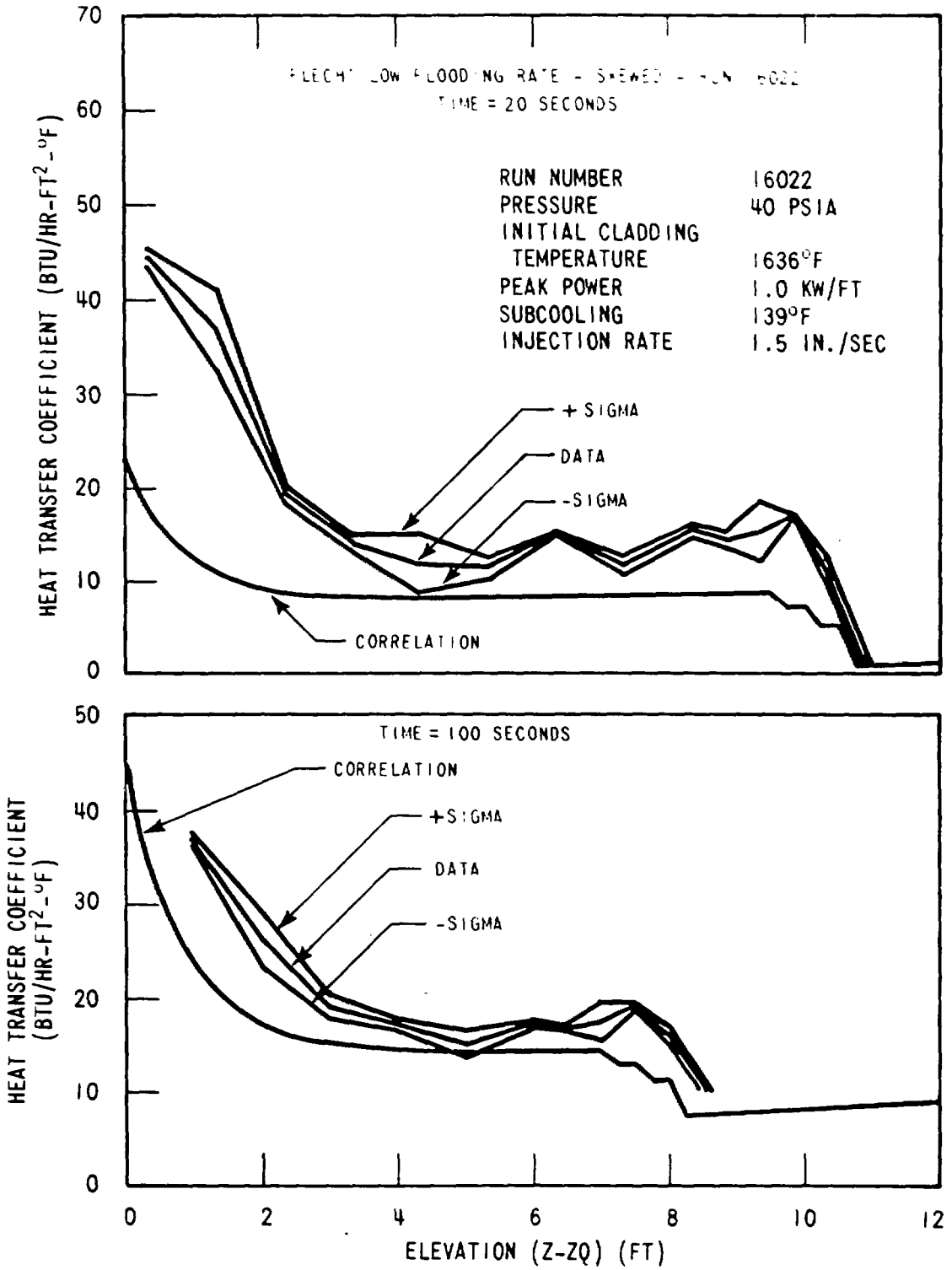

Figure E-26. Heat Transfer Coefficient Dependence on Distance From Quench Front at 20 and 100 Seconds for Run Number 16022

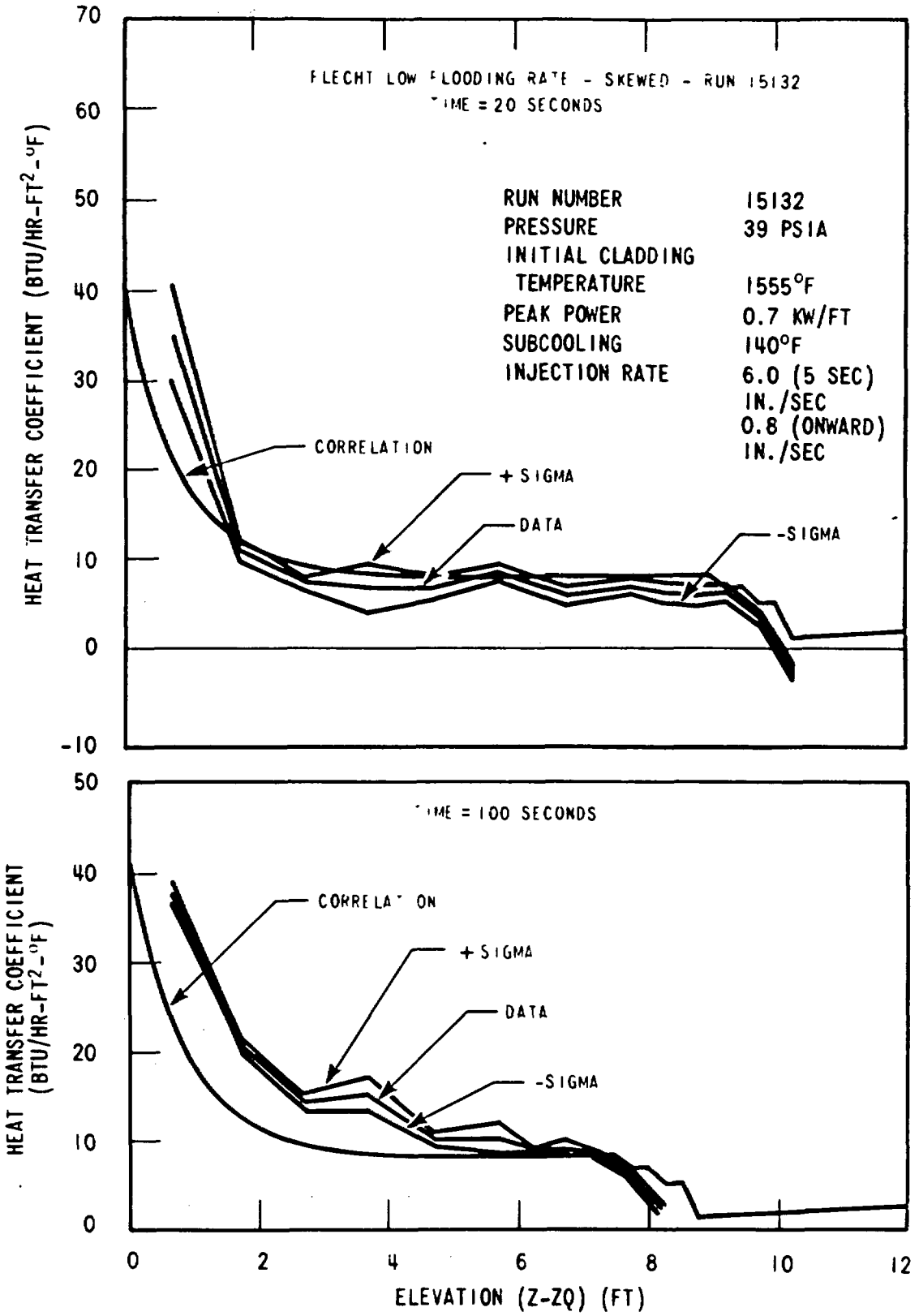

Figure E-27. Heat Transfer Coefficient Dependence on Distance From Quench Front at 20 and 100 Seconds for Run Number 15132

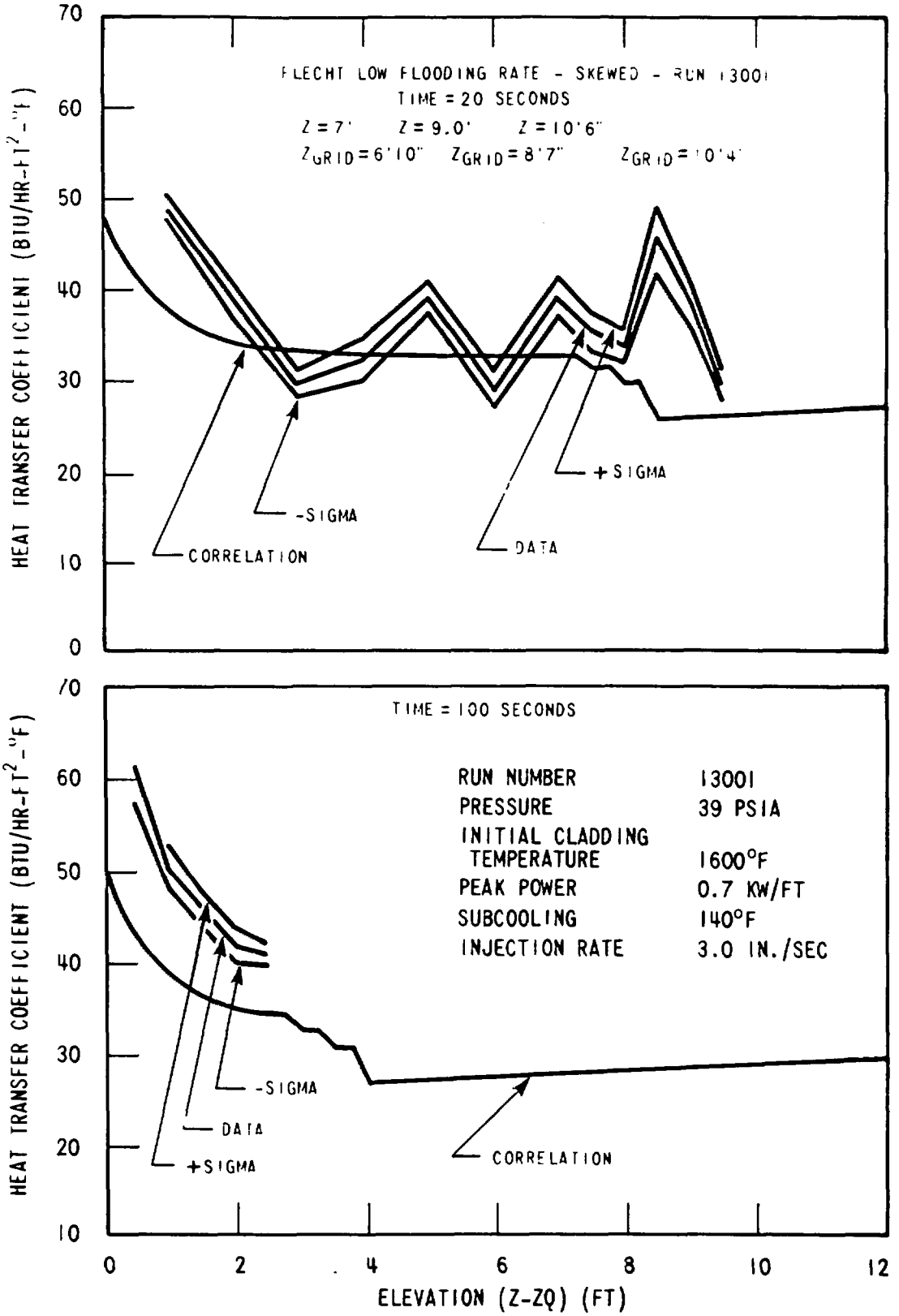

Figure E-28. Heat Transfer Coefficient Dependence on Distance From Quench Front at 20 and 100 Seconds for Run Number 13001

APPENDIX F
COMPUTER PROGRAM OF HEAT TRANSFER CORRELATIONS

The computer program for calculating the quench front elevation and the heat transfer, coefficient correlation of section 6 is listed in this appendix. Two examples of calculation for Run No. 15305 and 02833 are also given at the end of this appendix. The inputs and outputs for the program are described below.

NRUN = run number

DTSUB = inlet subcooling (°F)

VIN = flooding rate (in./sec.)

P = pressure (psia)

TINIT = initial cladding temperature at peak power elevation (°F)

QMAX = peak power (kw/ft)

TSAT = saturation temperature (°F)

Z = elevation at which the heat transfer coefficient is to be computed

ZPEAK = peak temperature elevation (ft)

T = time (sec)

H = heat transfer coefficient (Btu/hr-°F-ft^2)

ZQ = quench front elevation (ft)

VQ = quench front velocity (in./sec)

$$\text{PDCAY} = \int_o^t \frac{Q'(Z,\,t)}{Q'(Z,\,o)}\,dt \Bigg/ \int_o^t \left(\frac{Q'(Z,\,t)}{Q'(Z,\,o)}\right)_{\text{decay curve B}} dt$$

PDCT = time

$$\text{QAXTB} = \int_o^z \frac{Q'(Z,O)}{Q'_{max}}\,dz \qquad \text{for FLECHT cosine power}$$

QAXZQ = elevation Z for FLECHT cosine power

FAXTB = $Q'(Z,o) / Q'_{max}$ for FLECHT cosine power

FAXZ = elevation Z for FLECHT cosine power

QAXTBS, QAXZQS, FAXTBS, FAXZS = same as above for FLECHT skewed power

COMPUTER PROGRAM OF HEAT TRANSFER CORRELATION

```
 TYPE YHTCOR.F4
00100    C  FLECHT SKEWED POWER EVALUATION REPORT
00200    C  THIS PROGRAM COMPUTES THE FLECHT HEAT TRANSFER COEFFICIENT
00300    C  AS A FUNCTION OF TIME BY H VS Z-ZQ CORRELATION
00500          DIMENSION QAXZQ(92),QAXTB(92),FAXTB(93),FAXZ(93)
00600         1,PDCAY(111),PDCT(111),QAXTBS(99),QAXZQS(99),FAXTBS(99),
00700         2 FAXZS(99),VINTM(111),VINTB(111)
00800    10    CONTINUE
00900          TYPE 950
01000    950   FORMAT(' MR=1 FOR FLECHT POWER, MR=2 FOR UNIFORM POWER')
01100          TYPE 900
01200    900   FORMAT (' M=1 FOR COSINE, M=2 FOR SKEW')
01300          TYPE 1000
01400    1000  FORMAT(' ENTER  RUN    DTSUB    P    TINIT   QMAX  TSAT
01500         1 M   MR    Z    ZPEAK'/)
01600          ACCEPT 1002,NRUN,DTSUB,P,TINIT,QMAX,TSAT,M,MR
01700         1,Z,ZPEAK
01800    1002  FORMAT (11G)
01900          TYPE 1100
02000    1100  FORMAT(' ENTER VIN TABLE BELOW')
02100          TYPE 1110
02200    1110  FORMAT(' ENTER NO. OF POINTS'/)
02300          ACCEPT 1112, NVIN
02400    1112  FORMAT(I)
02500          TYPE 1102
02600    1102  FORMAT(' ENTER TIME(10/LINE)'/)
02700          ACCEPT 1104, (VINTM(J),J=1,NVIN)
02800    1104  FORMAT((10G),
02900          TYPE 1106
03000    1106  FORMAT(' ENTER VIN(10/LIN)'/)
03100          ACCEPT 1108, (VINTB(J),J=1,NVIN)
03200    1108  FORMAT((10G))
03300    C
03400    C  TABLE OF NORMALIZED POWER DECAY
03500    C
03600          DATA (PDCAY(J),J=1,16)/1., 1.085, 1.153, 1.198, 1.226
03700         1, 1.244, 1.255, 1.262, 1.27, 1.28, 1.298, 1.311, 1.319
03800         2, 1.324, 1.327, 1.328/
03900          DATA (PDCT(J),J=1,16)/0., 20., 40., 60., 80.
04000         1, 100., 120., 140., 160., 200., 280., 360., 440.
04100         2, 520., 600., 680./
04200          IF (M .EQ. 2) GO TO 12
04300    C
04400    C  TABLE OF NORMALIZED INTEGRAL OF POWER FOR FLECHT COSINE
04500    C  POWER BUNDLE.
 4600    C
```

```
04700           DATA (QAXZQ(J),J=1,17)/0., 1.83, 2.34, 3., 3.58,
04800          1 4.17, 4.83, 5.42, 6., 6.58, 7.17, 7.83, 8.42, 9.,
04900          2 9.66, 10.17, 12./
05000           DATA (QAXTB(J),J=1,17)/0., .53, .735, 1.088,
05100          11.478, 1.935, 2.534, 3.096, 3.6795, 4.263, 4.825,
05200          2 5.424, 5.881, 6.271, 6.624, 6.829, 7.359/
05300     C
05400     C    TABLE OF AXIAL POWER SHAPE FACTOR FOR FLECHT COSINE POWER
05450     C    BUNDLE.
05500     C
05600           DATA (FAXTB(J),J=1,30)/.289, .289, .41, .41, .53, .53
05700          1, .669, .669, .783, .783, .898, .898, .964, .964, 1., 1.
05800          2, .964, .964, .898, .898, .783, .783, .669, .669, .53, .53
05900          3, .41, .41, .289, .289/
06000           DATA (FAXZ(J),J=1, 30)/0., 1.83, 1.84, 2.33, 2.34, 3.
06100          1, 3.01, 3.58, 3.59, 4.17, 4.18, 4.83, 4.84, 5.42, 5.43
06200          2, 6.58, 6.59, 7.17, 7.18, 7.83, 7.84, 8.42, 8.43
06300          3, 9., 9.01, 9.67, 9.68, 10.17, 10.18, 12./
06400           GO TO 13
06500     12    CONTINUE
06600     C
06700     C    TABLE OF NORMALIZED INTEGRAL OF POWER FOR FLECHT SKEWED
06800     C    POWER BUNDLE.
06900     C
07000           DATA (QAXZQS(J),J=1,14)/0., 1.5, 2.5, 3.5, 4.5, 5.5
07100          1, 6.5, 7.5, 8.5, 9.25, 10.25, 10.75, 11.25, 12./
07200           DATA (QAXTBS(J),J=1,14)/0., .722, 1.285, 1.907, 2.589
07300          1, 3.33, 4.13, 4.989, 5.915, 6.643, 7.643, 8.098
07400          2, 8.494, 8.845/
07500     C
07600     C    TABLE OF AXIAL POWER SHAPE FACTOR FOR FLECHT SKEWED POWER
07650     C    BUNDLE.
07700     C
07800           DATA (FAXZS(J),J=1,26)/0., 1.5, 1.51, 2.5, 2.51, 3.5
07900          1, 3.51, 4.5, 4.51, 5.5, 5.51, 6.5, 6.51, 7.5, 7.51
08000          2, 8.5, 8.51, 9.25, 9.26, 10.25, 10.26, 10.75, 10.76
08100          3, 11.25, 11.26, 12./
08200           DATA (FAXTBS(J),J=1,26)/.4815, .4815, .563, .563, .622
08300          1, .622, .681, .681, .741, .741, .8, .8, .859, .859
08400          2, .926, .926, .97, .97, 1., 1., .911, .911, 793, .793
08500          3, .5259, .5259/
08600     13    CONTINUE
08700     2100  FORMAT (3X,4HTIME,4X,1HH,4X,6HZQ(FT),2X,10HVQ(IN/SEC))
08800           IX=30
08900           IF (M .EQ. 1) CALL INTERP(FAXZ,FAXTB,IX,Z,FAX,FAXVZQ)
09000           IX=26
09100           IF (M .EQ. 2) CALL INTERP(FAXZS,FAXTBS,IX,Z,FAX,FAXVZQ)
09200           TINITZ=(TINIT-TSAT)*FAX+TSAT
09300           H1=3.67*QMAX*FAX*(1.-EXP(-(TINITZ-700.)/435.))
```

COMPUTER PROGRAM OF HEAT TRANSFER CORRELATION (cont)

```
09400           H=H1
09500           T=0.
09600           ZQ=0.
09700           CQ=2.
09800           QMAXCO=QMAX
09900           IF (M .EQ. 2) QMAXCO=QMAX*7.393/3.6795
10000           DZQ=.005
10100           CALL INTERP(VINTM,VINTB,NVIN,0., VIN,VINSL)
10200     C   J=1---COMPUTE MULTIPLIER FTQ.
10400           JTYPE=0
10500           JSTYPE=0
10600           J=1
10700     15    CONTINUE
10800           IF (J .EQ. 1) GO TO 17
10900     19    CONTINUE
11000     C
11100     C   COMPUTE QUENCH FRONT ELEVATION
11200     C
11300           ZQ=ZQ+DZQ
11400           DO 40 IVQ=1,2
11500           IF (IVQ .EQ. 1) ZQ=ZQ-.0005
11600           IF (IVQ .EQ. 2) ZQ=ZQ+.0005
11700           IX=17
11800           IF (M .EQ. 1) CALL INTERP(QAXZQ,QAXTB,IX,ZQ,QAX,QAXSLP)
11900           IX=14
12000           IF (M .EQ. 2) CALL INTERP(QAXZQS,QAXTBS,IX,ZQ,QAX,QAXSLP)
12100           QSK=QMAX*QAX
12200           QCOS=QSK
12300           IF (M .EQ. 1) MAXCO=QMAX
12400           IF (M .EQ. 2) QMAXCO=QMAX*7.393/3.6795
12500           QAXCOS=QCOS/QMAXCO
12600           IXCOS=17
12700           CALL INTERP(QAXTB,QAXZQ,IXCOS,QAXCOS,ZQCOS,ZQCSL)
12800           QEQ1=QMAXCO*QAXCOS/3.6795
12900           IF (MR .EQ. 2) QEQ1=QEQ1*1.1
13000     17    CONTINUE
13100           IF (J .EQ. 1) QEQ1=QMAXCO
13200           IF (J .EQ. 1 .AND. MR .EQ. 2) QEQ1=QEQ1*1.1
13300           IX=30
13400           IF (M .EQ. 1) CALL INTERP(FAXZ,FAXTB,IX,ZQ,FAX,FAXVZQ)
13500           IX=26
13600           IF (M .EQ. 2) CALL INTERP(FAXZS,FAXTBS,IX,ZQ,FAX,FAXVZQ)
13700           QEQ=QEQ1
13800           TINITE=(TINIT-TSAT)*FAX+TSAT
13900           CALL INTERP(VINTM,VINTB,NVIN,T,VIN,VINSL)
14000           ZS=1.833*VIN**(.5466-.0426*VIN)
14100           F1=EXP(-.0107*DTSUB)*(1.-EXP(-.667*VIN))
```

```
14200          F4=1.+.5*EXP(-.000037*P*P*P)
14300          F2=F4+1.3*EXP(-.111*VIN*VIN)+17.3*EXP(-.000037
14400         1*P*P*P)*EXP(-.49*VIN*VIN)
14500          F3=3.28/VIN**1.1-2.8*EXP(-VIN)
14600          F5=1.+.0000588*TINITE-1.05*EXP(-.0025*TINITE)
14700         1*(1.+.5/(1.+50.**(2.-.667*VIN)))
14800         2*(1.+.32/(1.+50.**(5.-.1*P)))
14900          DO 20 K=1,3
15000          F61=1.207*QEQ**1.5-.667
15100          IF (J .NE. 1) F61=F61-2.8*(QEQ-1.3)/(1.+100.**(130.
15200         1-100.*QEQ))
15300          TQ=98.39*(F1*F2*F61+F3*F4)*F5
15400          IF (J .EQ. 1) GO TO 18
15500          FR1=0.5
15600          FR2=9.
15700          QR=QAXCOS/3.6795
15800          FQ=QR+FR1*QR*EXP(-FR2*QR*QR)
15900          TQ=TQ*FQ
16000          TQ=ZQ/VIN*12.+(TQ-ZQ/VIN*12.)/(1.+50.**(-(TINITE-400.)
16100         1/(400.-TSAT)))
16200          TQ=TQ*FTQ
16300    18    CONTINUE
16400          IX=16
16500          CALL INTERP(PDCT,PDCAY,IX,TQ,PDECAY,PDCP)
16600          QEQ=QEQ1*PDECAY
16700    20    CONTINUE
16800          IF (J .NE. 1) GO TO 50
16900          QMAXEQ=QEQ
17000          FTQ=1.+1.5/(1.+50.**(104.-80.*QEQ))*
17100         1(1.-EXP(-1.613*(QEQ-1.25)))
17200    C
17300    C  COMPUTE HEAT TRANSFER COEFFICIENT
17400    C
17500          TYPE 2100
17800          J=2
17900          GO TO 19
18000    50    CONTINUE
18100          IF (IVQ .EQ. 1) ZQ1=ZQ
18200          IF (IVQ .EQ. 1) TQ1=TQ
18300          IF (IVQ .EQ. 2) ZQ2=ZQ
18400          IF (IVQ .EQ. 2) TQ2=TQ
18500    40    CONTINUE
18600          VQ=(ZQ2-ZQ1)/(TQ2-TQ1)
18610          VQINCH=VQ*12.
18630    C
18640    C  COMPUTE HEAT TRANSFER COEFFICIENT
18650    C
18660          IF (J .EQ. 2) TYPE 2200, T,H,ZQ,VQINCH
```

COMPUTER PROGRAM OF HEAT TRANSFER CORRELATION (cont)

```
18700           T= T+DZQ/VQ
18800           FHP=.714+.286*(1.-EXP(-1.8*P/VIN/VIN))
18900           X=4.*ZQ/ZS
19000           HZS=46.*(1.-EXP(-.25*VIN))*FHP
19100          1+38.*EXP(-.15*VIN)*EXP(-1.2*(Z-ZQ))
19200           IF (ZQ .LT. ZS) H=H1*(1.-EXP(2.5*X-10.))+(HZS-
19300          1H1*(1.-EXP(2.5*X-10.)))*(1.-EXP(-X)-.9*X*EXP(-X*X))
19400           IF (ZQ .GE. ZS) H=HZS
19500           IF (Z .GT. ZPEAK) H=H-15.594*(1.-FAX)*EXP(-.0683*(Z-
19600          1ZPEAK))
19800           JTYPE=JTYPE+1
19900           JSTYPE=JSTYPE+1
20000           IF (ZQ .LE. ZS .AND. JSTYPE .EQ. 40 .AND. JTYPE .NE. 100)
20100          1TYPE 2200, T,H,ZQ,VQINCH
20200           ZMZQ=Z-ZQ
20300           IF (JTYPE .EQ. 100) TYPE 2200, T,H,ZQ,VQINCH
20400    2200   FORMAT(F7.0,F7.2,F7.1,F10.3)
20500           IF (JSTYPE .EQ. 40) JSTYPE=0
20600           IF (JTYPE .EQ. 100) JTYPE=0
20700           IF (ZQ .GE. 12.) GO TO 30
20800           J=J+1
20900           GO TO 15
21000    30     CONTINUE
21100           GO TO 10
21200           STOP
21300           END
21400           SUBROUTINE INTERP(X,Y,L,X1,Y1,SLOPE)
21500           DIMENSION X(100),Y(100)
21600           DO 100 K=1,L
21700           K1=K
21800           IF (X(K1)-X1) 100,100,200
21900    100    CONTINUE
22000    200    Y1=Y(K1-1)+((X1-X(K1-1))/(X(K1)-X(K1-1)))
22100          1*(Y(K1)-Y(K1-1))
22200           SLOPE=(Y(K1)-Y(K1-1))/(X(K1)-X(K1-1))
22300           RETURN
22400           END
```

```
 RUN YHTCOR


MR=1 FOR FLECHT POWER, MR=2 FOR UNIFORM POWER
M=1 FOR COSINE, M=2 FOR SKEW
ENTER   RUN     DTSUB     P     TINIT    QMAX   TSAT     M    MR     Z     ZPEAK
      15305,    140.,   40.,   1603.,    .7,    267.,    2,    2,    10.,    10.

ENTER VIN TABLE BELOW
ENTER NO. OF POINTS
2

ENTER TIME(10/LINE)
0., 1000.

ENTER VIN(10/LIN)
.8, .8

  TIME     H      ZQ(FT)   VQ(IN/SEC)
    0.    2.25     0.0       0.223
   11.    2.49     0.2       0.223
   22.    3.99     0.4       0.224
   27.    5.04     0.5       0.224
   32.    6.00     0.6       0.225
   43.    7.24     0.8       0.226
   53.    7.77     1.0       0.228
   64.    8.00     1.2       0.231
   74.    8.12     1.4       0.234
   79.    8.16     1.5       0.235
   88.    8.18     1.6       0.197
  112.    8.34     2.0       0.205
  140.    8.34     2.5       0.219
  173.    8.35     3.0       0.210
  200.    8.35     3.5       0.225
  232.    8.36     4.0       0.214
  260.    8.38     4.5       0.219
  294.    8.42     5.0       0.196
  326.    8.49     5.5       0.186
  366.    8.62     6.0       0.158
  406.    8.84     6.5       0.145
  457.    9.26     7.0       0.123
  498.   10.02     7.5       0.166
  543.   11.40     8.0       0.147
  584.   13.91     8.5       0.145
  632.   18.49     9.0       0.135
  680.   26.83     9.5       0.129
  727.   42.04    10.0       0.127
  762.   69.75    10.5       0.140
  901. .120.23    11.0       0.016
  968.  212.23    11.5       0.292
  988.  379.85    12.0       0.289
```

```
 RUN YHTCOR

MR=1 FOR FLECHT POWER, MR=2 FOR UNIFORM POWER
M=1 FOR COSINE, M=2 FOR SKEW
ENTER  RUN     DTSUB     P     TINIT    QMAX   TSAT     M    MR     Z     ZPEA
       02833,   142.,   40.,   1602.,   .89,   267.,    1,    1,    6.,     6.

ENTER VIN TABLE BELOW
ENTER NO. OF POINTS
2

ENTER TIME(10/LINE)
0., 1000.

ENTER VIN(10/LIN)
.8, .8

  TIME     H      ZQ(FT)   VQ(IN/SEC)
    0.    2.86     0.0      0.434
    6.    3.08     0.2      0.435
   11.    4.44     0.4      0.437
   14.    5.39     0.5      0.439
   17.    6.27     0.6      0.441
   22.    7.41     0.8      0.447
   27.    7.90     1.0      0.455
   32.    8.13     1.2      0.464
   38.    8.27     1.4      0.475
   40.    8.32     1.5      0.482
   43.    8.35     1.6      0.489
   58.    8.62     2.0      0.346
   81.    8.84     2.5      0.280
  100.    9.26     3.0      0.324
  128.   10.02     3.5      0.264
  158.   11.40     4.0      0.207
  197.   13.91     4.5      0.150
  243.   18.49     5.0      0.126
  295.   26.83     5.5      0.109
  352.   42.04     6.0      0.102
  409.   69.75     6.5      0.133
  450.  120.24     7.0      0.142
  486.  212.23     7.5      0.150
  512.  379.85     8.0      0.179
  530.  685.28     8.5      0.210
  559.1241.80      9.0      0.209
  553.2255.84      9.5      0.272
  536.4103.56     10.0      0.382
  497.7470.31     10.5      0.577
  507.*******     11.0      0.574
  518.*******     11.5      0.571
  529.*******     12.0      0.567
```

APPENDIX G

EXAMINATION OF LIQUID FALLBACK IN THE SKEWED PROFILE TESTS

G.1 LIQUID FALLBACK MODELS

In the skewed power tests, since the peak power location is at high at the 10-foot elevation, some concern was expressed about the effect of the possible liquid fallback on the heat transfer at the peak power elevation. Analysis of the test data showed that liquid fallback did not occur.

Three models for liquid fallback were examined.

G.2 Wallis Flooding Correlation

Flooding occurs in the counterflow of liquid and gas when the gas flow rate is large enough to prevent the liquid from falling down. The critical gas flow rate and liquid flow rate are correlated by Wallis[1] in the following equation.

$$\sqrt{j_g^*} + m\sqrt{j_f^*} = C \qquad \text{(G-1)}$$

where

$$j_g^* = \frac{j_g\sqrt{\rho_g}}{\sqrt{gD\,(\rho_f - \rho_g)}}$$

$$j_f^* = \frac{j_f\sqrt{\rho_f}}{\sqrt{gD(\rho_f - \rho_g)}} \qquad \text{(G-2)}$$

j_g, j_f = superficial velocities of steam and water, respectively (ft/sec)

ρ_g, ρ_f = densities of steam and water, respectively (lbm/ft^3)

D = hydraulic diameter (ft)

g = gravitational acceleration (ft/sec^2)

and m, C can be obtained from figures 11.14 and 11.15, respectively, from Wallis' book.

1. Wallis, G., "One-Dimensional Two-Phase Flow" McGraw-Hill Book Company, New York, 1969.

The same idea can be applied to the FLECHT tests. That is, if the measured dimensionless superficial steam velocity, j_g^*, is larger than the critical superficial steam velocity as calculated from equation (G-1), then the fallback cannot occur. The diameter D can be computed by

$$D = \text{hydraulic diameter} = \frac{4 \times (\text{Flow Area})}{\text{Wetted Perimeter}} \qquad \text{(G-3)}$$

Two kinds of flow channels are investigated: (1) the regular flow channel formed by four heater rods, which has the value of D = 0.0445 foot; (2) the largest possible channel formed by two outer rods and the housing wall or window, which has the value of D = 0.0608 foot.

The required superficial steam velocity V_g is computed by

$$j_g = \left(\frac{m_g}{A\rho_g}\right) \qquad \text{(G-4)}$$

where A is the flow area of the bundle and the steam flow rate m_g is measured at the exhaust orifice, the density of steam is calculated by using the steam temperature measured at 11.5 feet.

Three runs have been chosen for this study:

- Run No. 12720, which has the lowest steam flow rate, m_g, and the lowest initial cladding temperature of 500°F.
- Run No. 11719, which has the same run conditions as Run No. 12720, except that the initial temperature is 1000°F.
- Run No. 15305, which is the reference run in the skewed power test series.

Figures G-1 to G-3 plot the steam flow rate, m_g, for these three runs.

Figures G-4 to G-6 plot $j_g^{*1/2}$ against time. The horizontal line marked $\left(j_g^{*1/2}\right)_{\text{critical, max}}$ is the maximum critical value of $j_g^{*1/2}$ computed from equation (G-1), that is, when $j_f^{*1/2} = 0$ or

$$\left(j_g^{*1/2}\right)_{\text{critical, max}} = C \qquad \text{(G-5)}$$

In the actual case, $j_f^{*1/2}$ is not zero, and according to equation (G-1) $\left(j_g^{*1/2}\right)_{\text{critical}}$ should be smaller than that given by equation (G-5). Therefore, equation (G-5) is conservative.

Figure G-4 shows that for the worst case of Run No. 12720, the flooding might have occurred in the window before 45 seconds and after 110 seconds. However, movie observation at the 10-foot window indicates that flooding has not occurred. This is because there

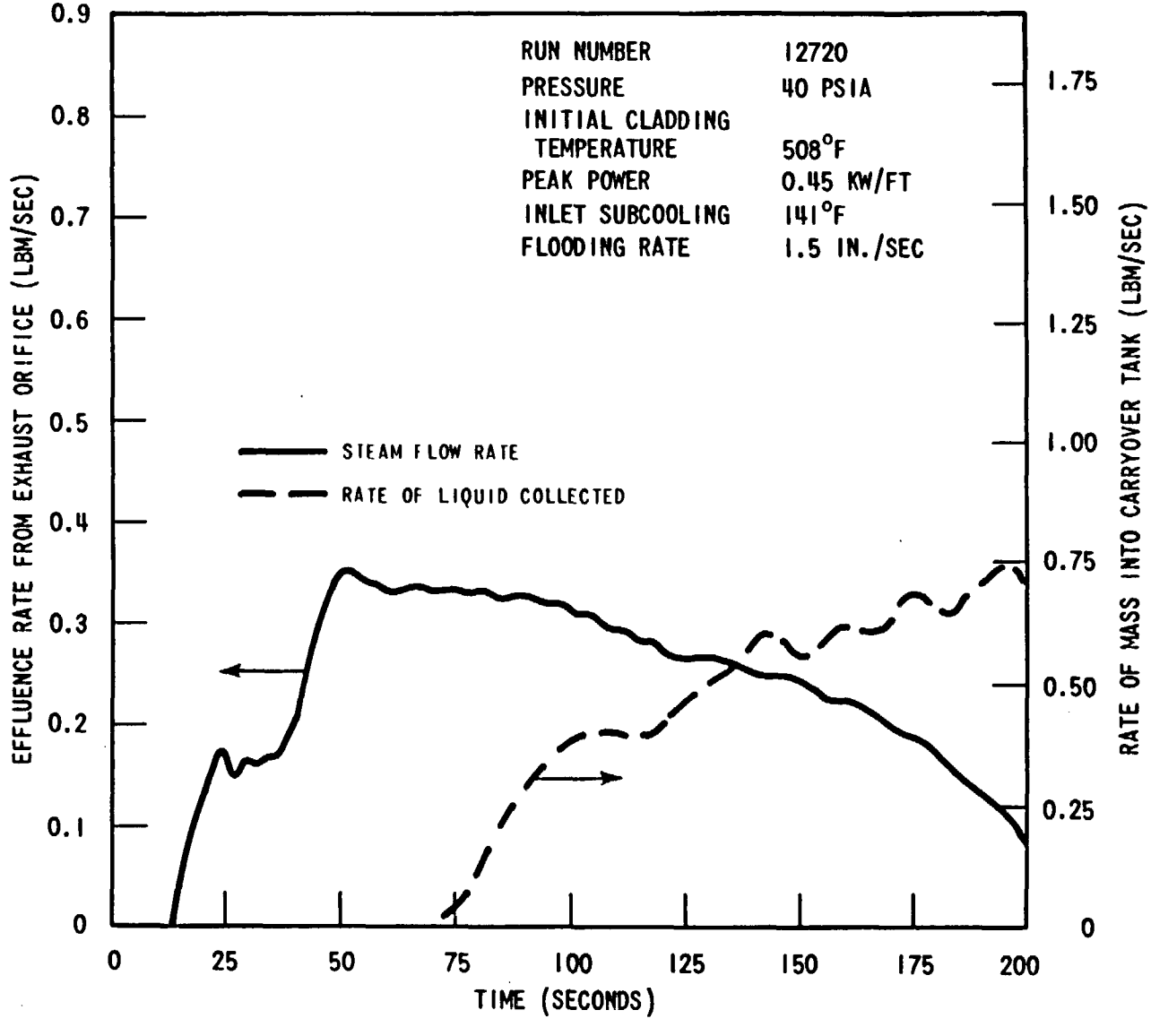

Figure G-1. Steam Flow Rate from Exhaust Orifice and Rate of Liquid Collected for Run 12720

11,863-113

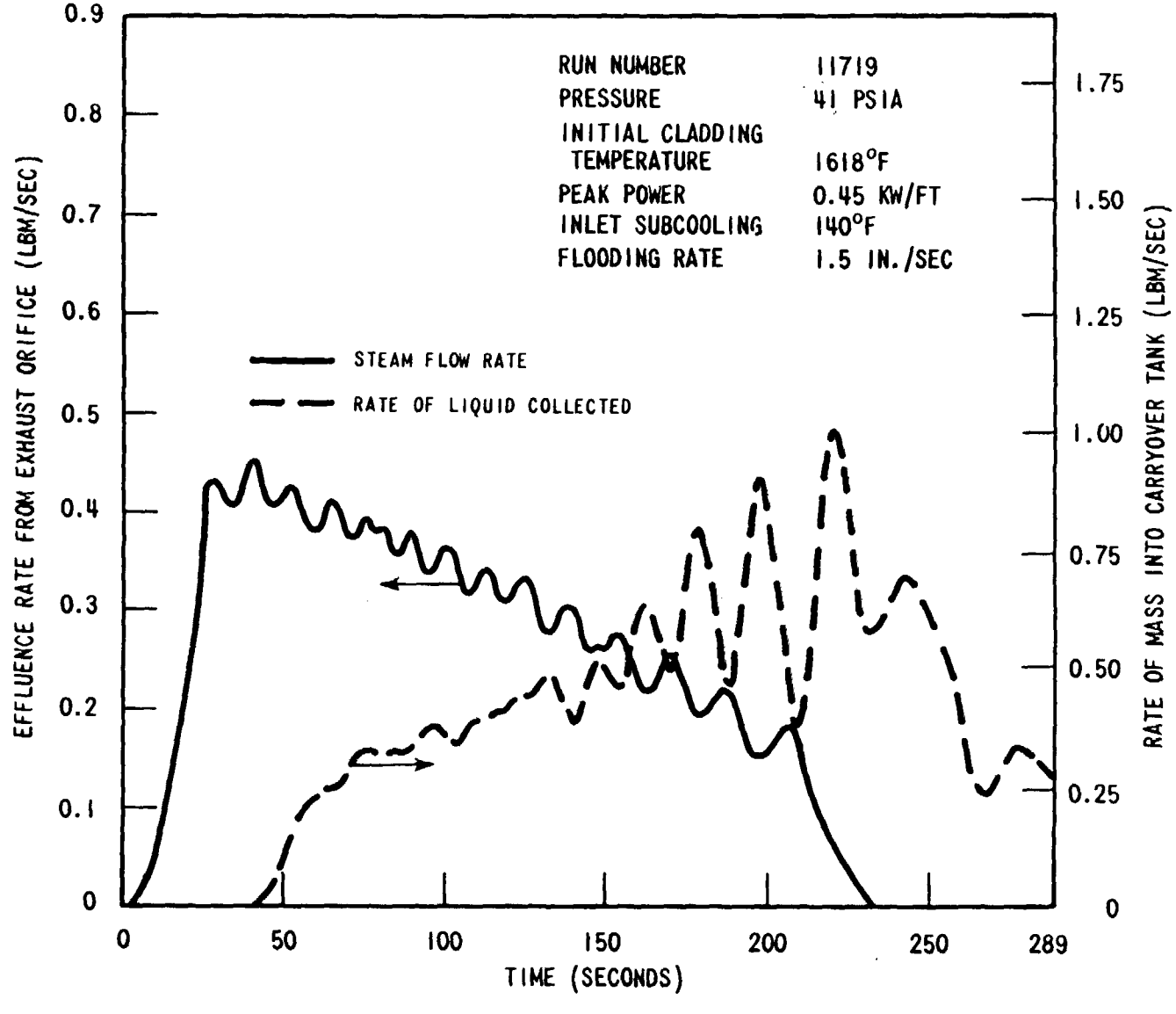

Figure G-2. Steam Flow Rate from Exhaust Orifice and Rate of Liquid Collected for Run 11719

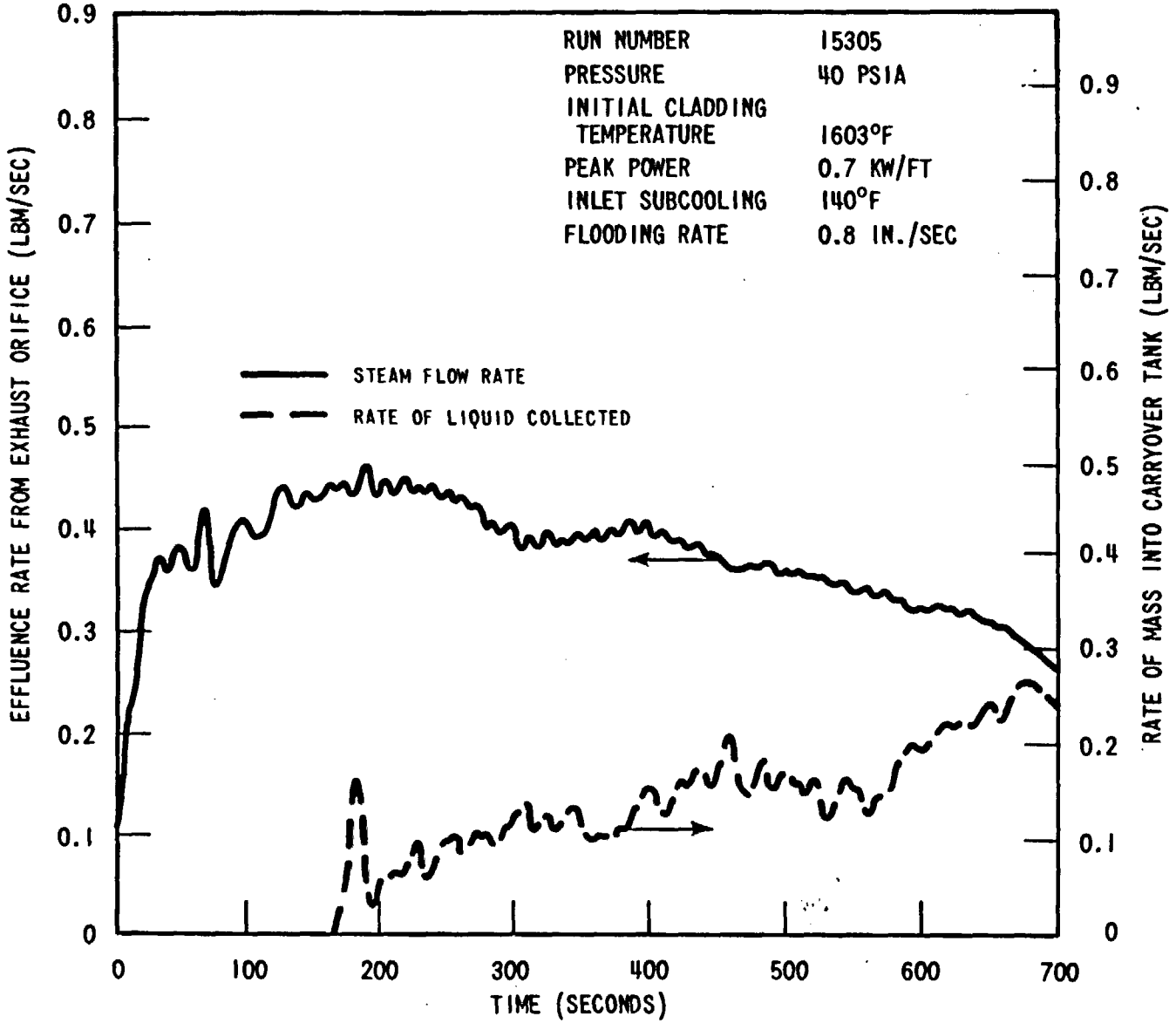

Figure G-3. Steam Flow Rate from Exhaust Orifice and Rate of Liquid Collected for Run 15305

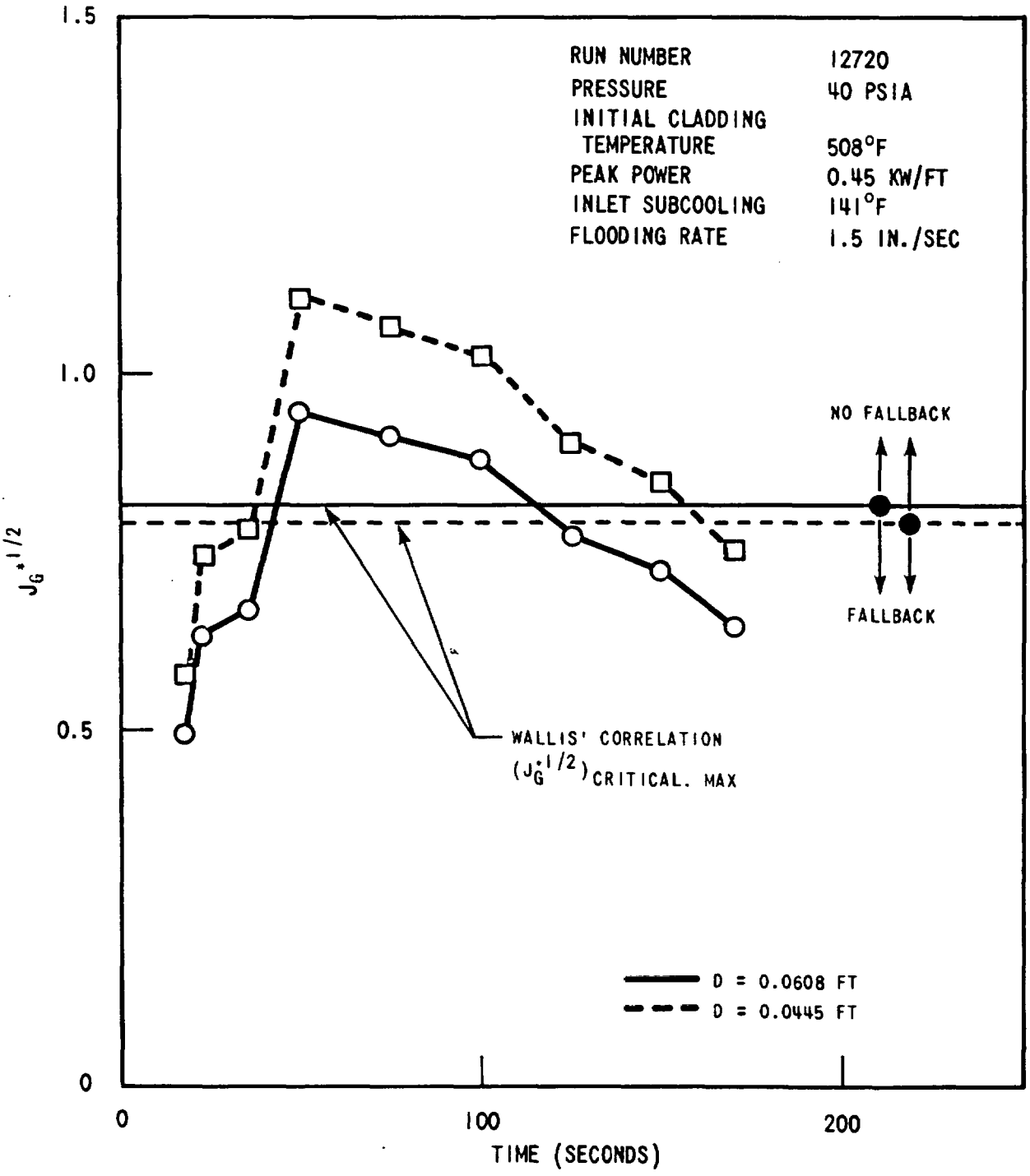

Figure G-4. Wallis' Flooding Correlation and the Computed Volumetric Flow Velocity for Run Number 12720

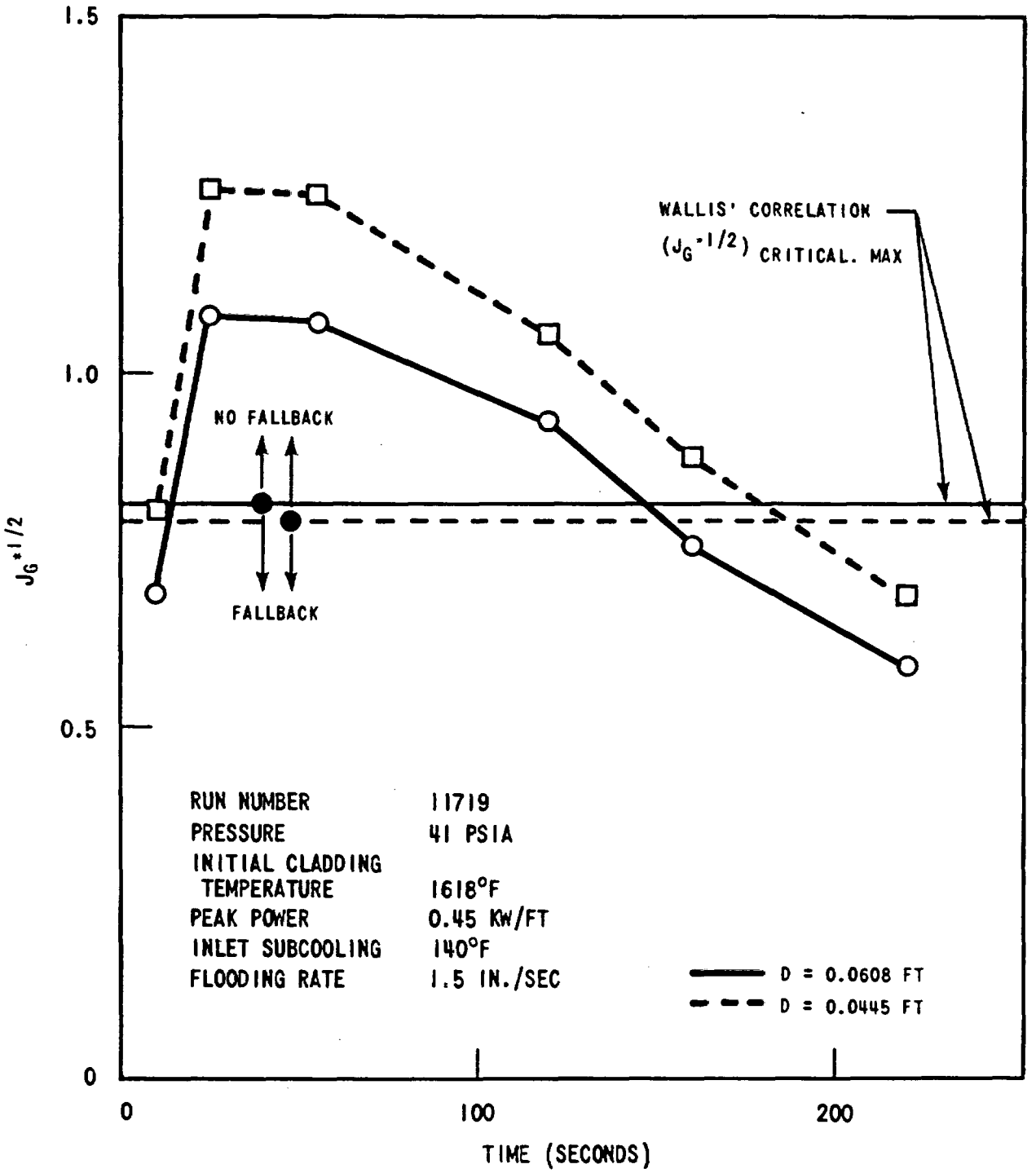

Figure G-5. Wallis' Flooding Correlation and the Computed Volumetric Flow Velocity for Run Number 11719

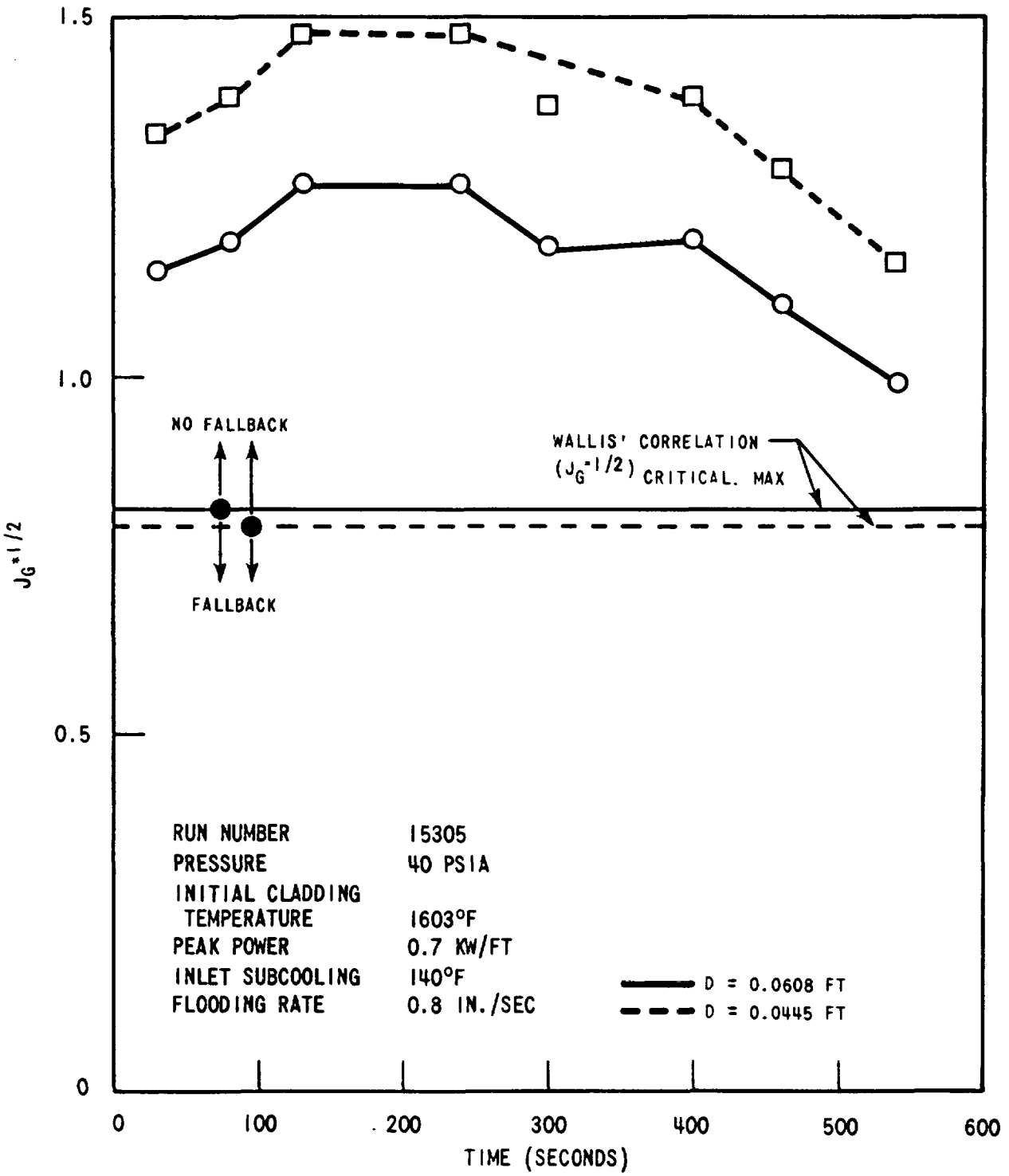

Figure G-6. Wallis' Flooding Correlation and the Computed Volumetric Flow Velocity for Run Number 15305

was not enough water to cause flooding. Movies show that at the six-foot window the liquid front (froth front) moved up at about 40 seconds and that at the 10-foot window the liquid front moved up at about 50 seconds. This liquid front movement is also confirmed by the pressure drop data which show that $\Delta\rho$ between six and seven feet started to increase from zero at about 40 seconds, and that $\Delta\rho$ between 10 and 11 feet started to increase at about 50 seconds, indicating that the froth front had just entered the one-foot interval at these times. At any rate, flooding due to the falling liquid was not observed.

Figure G-5 shows that in Run No. 11719, by increasing initial cladding temperature, $j_g^{*1/2}$ increases significantly. Figure G-6 shows that for the reference Run No. 15305, the flooding could not occur both on the window (or housing) and inside the bundle. This was confirmed by the movie observation.

The liquid collection rate, shown in figures G-1 to G-3, provides another justification that the liquid water has been indeed forced out of the bundle instead of falling back into the bundle.

G.3 Droplet Fallback

Another possible mechanism of liquid fallback is by water droplets. In examining droplet fallback, two drop diameters are of interest; the critical drop diameter determined by the critical Weber number for a given steam flow and the maximum diameter which the steam flow prevents from falling back. The argument is that if the steam flow is large enough, the critical drop size will always be smaller than the maximum drop size which the steam flow can force out of the bundle. This being the case, no drops can fall back into the bundle since they will break up and be carried out by the steam flow.

It is known that a water droplet will become unstable and break into pieces when the Weber number is larger than a critical value. The critical Weber number, W_{cr}, is expressed as

$$W_{cr} = \frac{\rho_g (V_g - V_d)^2 d}{\sigma} = 3.7 \qquad \text{(G-6)}$$

where

V_g, V_d = velocities of steam and droplet, respectively, ft/sec

d = diameter of droplet, ft

σ = surface tension, lbm/sec^2

For conservatism the steam velocity V_g can be assumed to be equal to one superficial steam velocity j_g. The value of 3.7 for W_{cr} was obtained from a FLECHT movie study by MIT.[1]

Therefore, the critical diameter size of a stable droplet that can exist is the diameter computed from equation (G-6). Let this critical diameter be d_{cr}. Then

$$d_{cr} = \frac{3.7\sigma}{\rho_g (V_g - V_d)^2} \tag{G-7}$$

On the other hand, there is a maximum diameter of a droplet that can be carried by the steam. Let this maximum diameter of droplet be d_{max}. Then

$$d_{max} = \frac{3}{4} C_D \frac{\rho_g}{g\rho_\ell} (V_g - V_d)^2 \tag{G-8}$$

where

C_D = drag coefficient of a droplet

Fallback will occur when $d_{cr} > d_{max}$, that is, when the maximum diameter of a droplet that can exist without being broken by the steam is larger than the maximum diameter of a droplet that can be carried out by the steam; then the droplet will fall.

In computing d_{cr} and d_{max} from equations (G-7) and (G-8), respectively, it is appropriate to set $V_d = 0$ for our study of fallback since it is the boundary between fallback ($V_d < 0$) and nonfallback ($V_d > 0$). It is postulated that the droplets will either decelerate and stop and then fall back, or the droplets will coalesce in the upper plenum then begin to fall back. In either case, the condition for fallback is when $V_d \leq 0$, therefore, cases with $V_d > 0$ need not be considered. Whether the droplets have fallen back into the bundle in the skewed power tests can be investigated by computing d_{cr} and d_{max} with $V_d = 0$ at the exit of the bundle and comparing the magnitudes of d_{cr} and d_{max}.

Figure G-7 shows that for the worst case of Run No. 12720 the droplet fallback could not occur during the period $43 < t < 115$ seconds, since $d_{max} > d_{cr}$. During other periods, the droplet fallback might possibly occur, since $d_{max} < d_{cr}$. However, the actual droplet diameter might be smaller than the critical diameter d_{cr}, and might be even smaller than d_{max}, since no droplet fallback was observed in the movie taken during the test. Figure G-8 shows that

1. Letter from Professor Petter Griffith, MIT, to Dr. Y. Y. Hsu, Reactor Safety Research Division NRC, dated January 3, 1975.

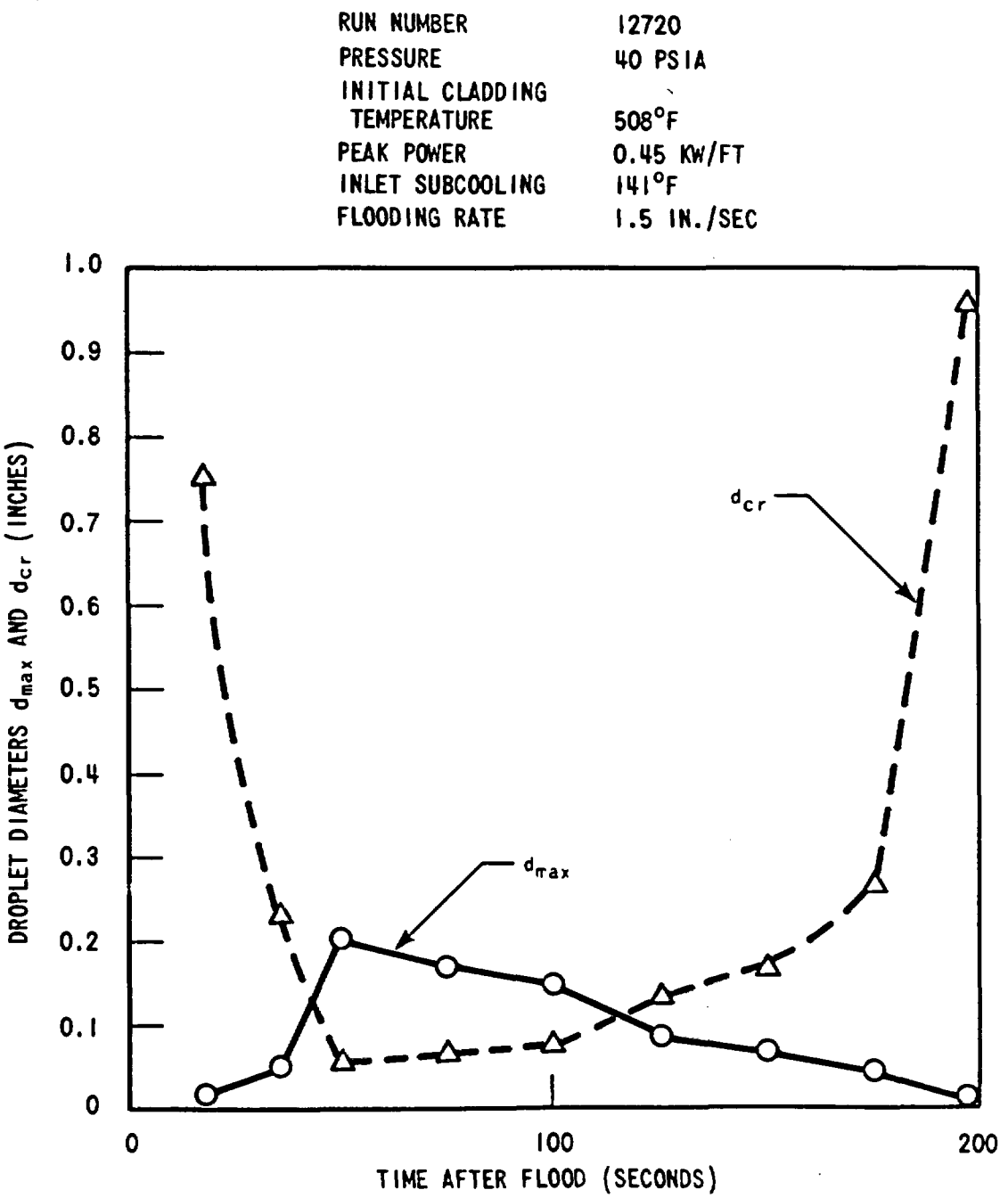

Figure G-7. Comparison of the Critical Droplet Diameter, d_{cr}, and the Maximum Droplet Diameter, d_{max}, for Run 12720

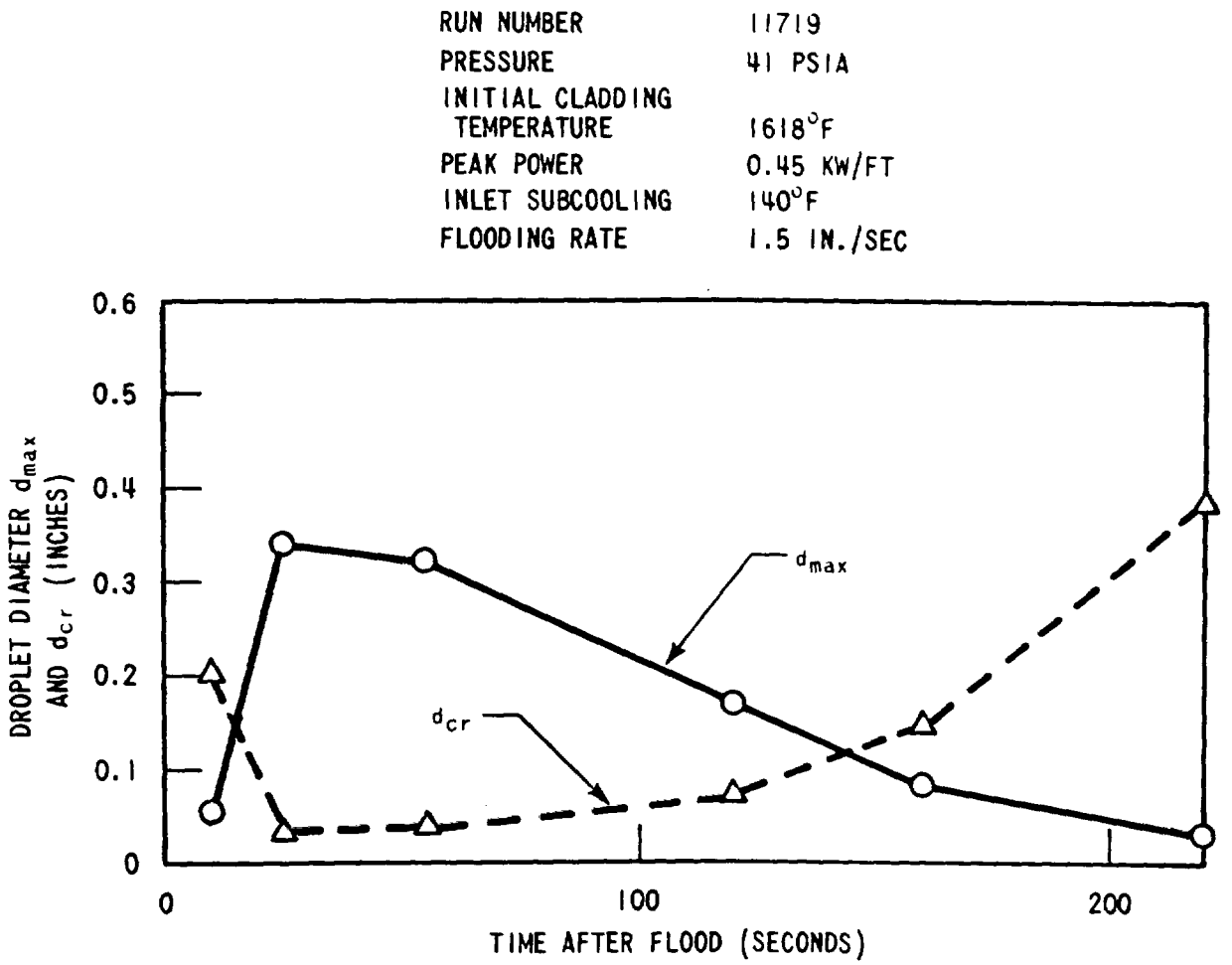

Figure G-8. Comparison of the Critical Droplet Diameter, d_{cr}, and the Maximum Droplet Diameter, d_{max}, for Run 11719

in Run No. 11719, by increasing the initial cladding temperature, and hence the steam temperature, the period in which fallback could not occur was extended to $15 < t < 145$ sec. Figure G-9 shows that for the reference run, Run No. 15305, the droplet fallback could not occur.

G.4 Falling Liquid Film

The last model to be examined is that in which the liquid film falls on the housing wall. Suppose that the film thickness is δ (see figure G-10). If the gravitational force of the film is larger than the interfacial shear force plus the pressure force, then the liquid film will fall. At the critical condition where these forces balance each other, the following equation is approximately valid:

$$(\tau_w + \tau_i)\ \Delta ZL + \frac{dp}{dZ}\ \Delta ZL\delta = \delta \Delta ZL\ \rho_f\ \frac{g}{g_c} \qquad \text{(G-9)}$$

where

τ_i = interfacial shear stress (lb_f/ft^2)

τ_w = wall shear stress (lb_f/ft^2)

L = width of wall (ft)

g_c = dimensional conversion factor, 32.2 ft lb_m/lb_f sec^2

The shear stress is given in p. 320 of Wallis' book[1] as:

$$\tau_i = (C_f)_i\ \frac{1}{2}\ \frac{\rho_g}{z_c}\left(\frac{j_g}{\alpha}\right)^2 \qquad \text{(G-10}$$

$$(C_f)_i = 0.005\left(1 + 300\ \frac{\delta}{D}\right) \qquad \text{(G-11)}$$

where α is the void fraction and $(C_f)_i$ is the interfacial friction factor. The last term of equation (G-11) corresponds to the interfacial surface roughness. With the substitution of equations (G-10) and (G-11), and neglecting the wall shear stress, pressure drop, and interfacial surface roughness, equation (G-9) can be reduced to

$$\delta_{max} = 0.0025\ g\ \frac{\rho_g}{\rho_f}\left(\frac{j_g}{\alpha}\right)^2 \qquad \text{(G-12)}$$

1. Wallis, G., "One-Dimensional Two-Phase Flow" McGraw-Hill Book Company, New York, 1969.

RUN NUMBER	15305
PRESSURE	40 PSIA
INITIAL CLADDING TEMPERATURE	1603°F
PEAK POWER	0.7 KW/FT
INLET SUBCOOLING	140°F
FLOODING RATE	0.8 IN./SEC

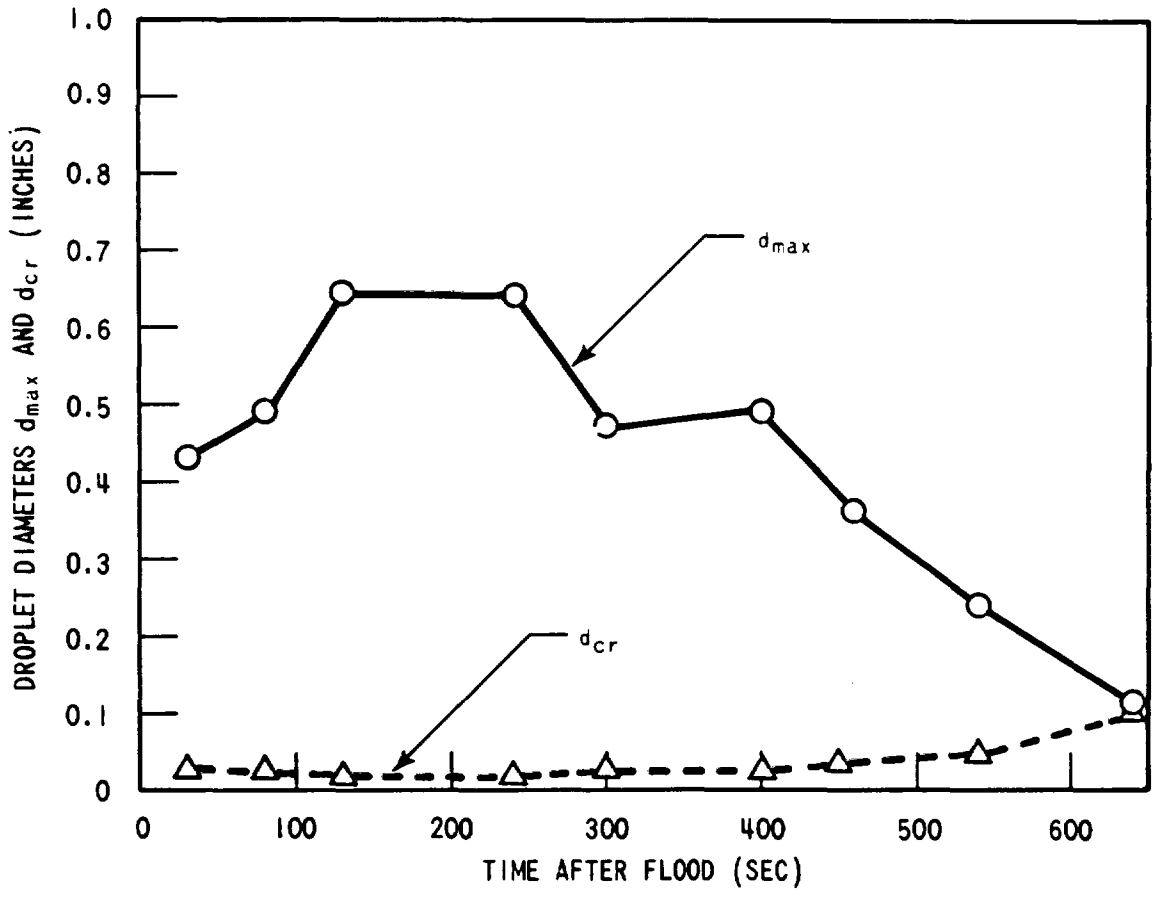

Figure G-9. Comparison of the Critical Droplet Diameter, d_{cr}, and the Maximum Droplet Diameter, d_{max}, for Run Number 15305

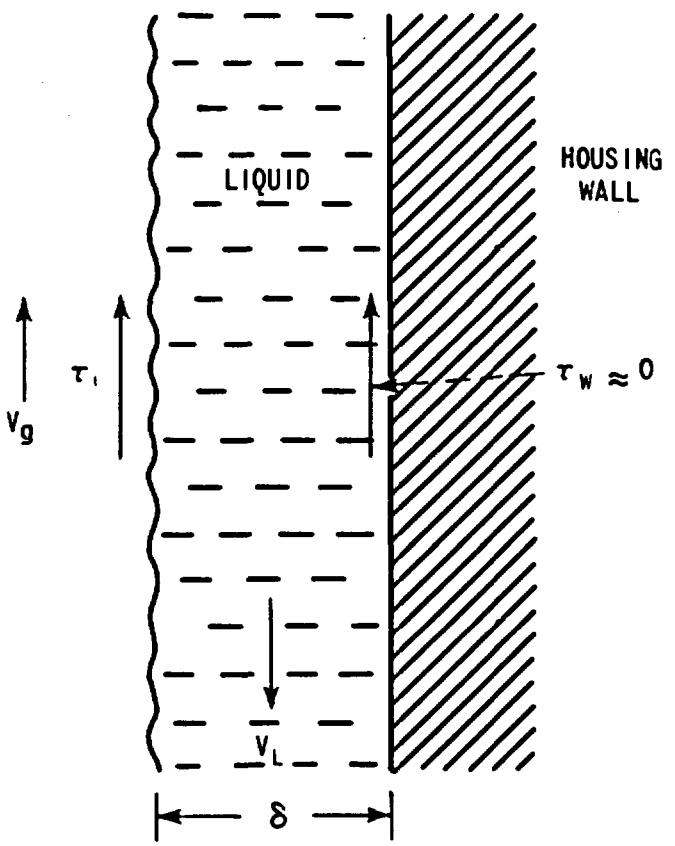

Figure G-10. Model of Falling Film

For conservatism, the void fraction α can be taken to be one. Equation (G-12) gives the maximum film thickness δ_{max} that can be held by the steam without falling. If the film thickness is smaller than that given by equation (G-12), the liquid film will be dragged up by the steam. The inclusion of the wall shear stress, the pressure drop, and interfacial surface roughness will yield a maximum film thickness much larger than that given by equation (G-12).

Figure G-11 plots δ_{max} for three runs. It is seen that for the worst case of Run No. 12720, δ_{max} is larger than 0.5 inch, except before 35 seconds, where liquid entrainment is negligible (the first droplet was observed at 35 seconds in the movie taken at the 10-foot window for this run, and later times, where the froth front had already moved to the 10-foot elevation). The movie reveals that there was no such thick liquid film. Therefore, all liquid on the wall must be dragged upward. This is confirmed by the movie in which it was observed that some of the droplets deposited on the window were dragged upward by the steam. For Runs No. 11719 and 15305, the possibility that the maximum film thickness, δ_{max}, is much larger than that of Run 12720 is an impossibility because there is no falling film.

It is concluded that the liquid fallback did not occur in any of the three mechanisms investigated; flooding, droplet fallback, and falling liquid film.

RUN NUMBERS	12720-11719-15305
PRESSURE	40-41-40 PSIA
INITIAL CLADDING TEMPERATURE	508-1618-1603°F
PEAK POWER	0.45-0.45-0.7 KW/FT
INLET SUBCOOLING	141-140-140°F
FLOODING RATE	1.5-1.5-0.8 IN./SEC

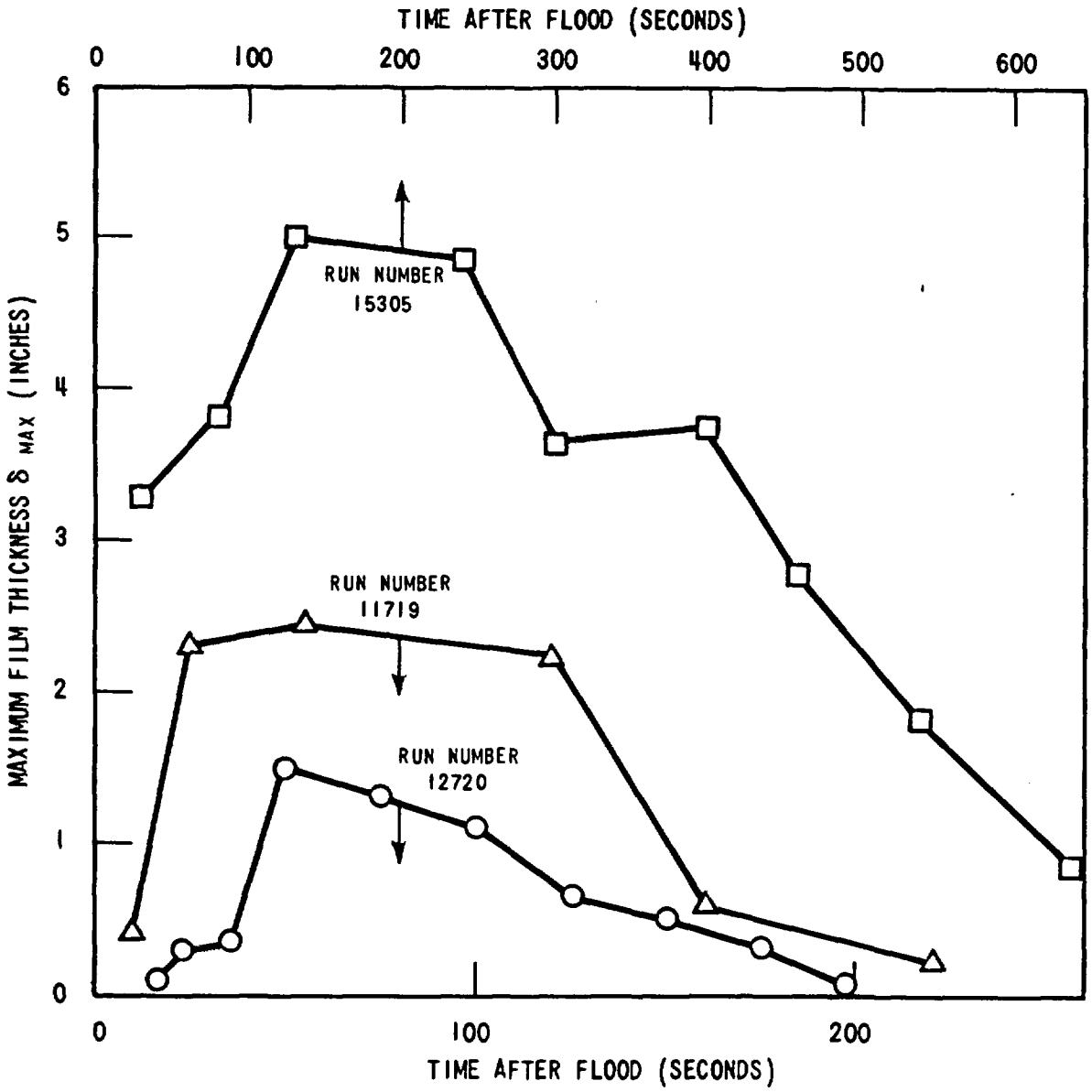

Figure G-11. Computed Maximum Film Thickness

APPENDIX H
TEST BUNDLE EXAMINATION

Upon completion of the skewed profile tests, the test bundle was removed from the housing and both were examined in detail.

The test section was rotated to the horizontal postion and the upper and lower seal plates were removed. Rods 2K and 07 were stuck in the lower seal plate and had to be cut off to remove the seal plate. Rods 2E, 5B, 6J and 9F were removed from the bundle and replaced with the four bundle-lifting rods. The support plate was placed back over the bottom end of the bundle and connected to the lifting rods. The test section and bundle were moved to remove the bundle in the vertical postion. As the bundle was being removed, the support plate stuck in the housing approximately one foot above the six-foot window. The support plate was disconnected from the lifting rods and the bundle was removed from the housing. The support plate was then tapped out and removed through the bottom end of the housing.

The heater rod bundle was transferred to the bundle assembly area for disassembly and inspection. Photographs were taken of the intact bundle and then it was photographed row by row during disassembly from the beginning of the heated length to the end of the heated length. The distortion of the heater rods, thimbles, steam probes, and fillers is listed in table H-1. The location and identification of the bundle components is shown on figure H-1. Surface roughness measurements were taken on rods 5G, 7F, 8C, 2H, and 8B.

The measurements are shown in table H-2 along with the surface roughness measurements taken on these rods before the test series began. Rod 8B was sandblasted two inches on each side of its thermocouple locations before bundle assembly. Examination of table H-2 indicates that the roughness of rod 8B did not increase during the testing.

Oxide thickness measurements were taken at the ten-foot elevation of rods 5D, 5F, 5G, and 7F. The rods were sectioned, plated with copper to preserve the oxide layer, cast in an epoxy mold, polished and examined under a microscope to measure the oxide thickness. Table H-3 lists the results of the measurements and figures H-2 to H-5 show the pictures of the cross sections.

TABLE H-1
DISTORTION OF THE SKEWED BUNDLE
(Refer to Figure H-1 for Location of Components)

1. Fillers: #1 – Slight distortion between 8' and 10' elevations.
   - #2 – Bowed between 8' and 10' elevation.
   - #3 – Bowed between 8' and 10' elevation.
   - #4 – Bowed between 8' and 10' elevation.
   - #5 – Bowed between 7" and 12' elevation.
   - #6 – Slight distortion between 8' and 10' elevation.
   - #7 – Slight distortion between 8' and 10' elevation.
   - #8 – Slight distortion between 8' and 10' elevation.
   - #9 – Slight bow into space between Rods 1B and 2A at the 9' 6" elevation.
   - #10 – Bowed between Rods 1J and 2K and touching Rod 2J at 9' 6" elevation.
   - #11 – Bowed between Rods 9K and 10J and touching Rod 9J at 9' 6" elevation.
   - #12 – Slight bow into space between Rods 9A and 10B at 9' 6" elevation.
2. Row 0: Rod 0G – Bowed at 9' 6" elevation – caused by bow in filler #2.
3. Row 1: Rod 1F – Failed rod – sheath is split open with the heater element exposed at the 8' 2" and 10' elevations. The length of the slits in the sheath are both 1.8".
   - Rod 1J – Bowed at 9' 6" elevation – caused by bow in filler #10.
4. Row 2: Rod 2J – Pushed between Rods 2H and 3J by the bow in filler #10 at the 9' 6" elevation.
   - Rod 2K – Bowed at 9' 6" elevation – caused by bow in filler #10.
5. Row 3: Rod 3G – 7' steam probe – bowed and touching Rod 3F at the 11' elevation.
   - Rod 3H – Bowed at 9' 5" elevation.
   - Rod 3J – Bowed at 9' 5" elevation.
   - Rod 3C – Instrument thimble – slight bow at 9' 5" elevation.
6. Row 4: Rod 4A – Failed rod – sheath is split open with the heater element exposed at the 10' 9" elevation. Length of split in sheath approximately 1.75".
7. Row 5: Rod 5H – Instrument Thimble – bowed at 9' 6" elevation and touching Rod 5J.

TABLE H-1 (cont)

DISTORTION OF THE SKEWED BUNDLE

(Refer to Figure H-1 for Location of Components)

8.	Row 6:	Rod 6F –	Instrument Thimble – bowed and touching 6E at 7' 10", 9' 10" and 10' 5" elevations.
		Rod 6K –	Slight bow at 7' 10" elevation.
9.	Row 7:	Rod 7C –	10' Steam Probe – bowed and touching Rod 7D at 9' 6" elevation.
			Bowed at 11' elevation.
10.	Row 8:	Rod 8G –	Level detector – bowed at 9' 3" elevation and 11' elevation.
		Rod 8J –	Bowed at 9' 5" elevation.
		Rod 8E –	11' Steam Probe – bowed at 7' 6" and 11' elevations.
11.	Row 9:	Rod 9A –	Bowed at 9' 6" elevation – caused by bow in #12 filler.
		Rod 9J –	Pushed between Rods 8J and 9H by filler #11 at the 9' 6" elevation.
12.	Row 10:	Rod 10J –	Bowed at 9' 6" elevation – caused by bow in filler #11.
		Rod 10B –	Bowed at 9' 6" elevation – caused by bow in filler #12.

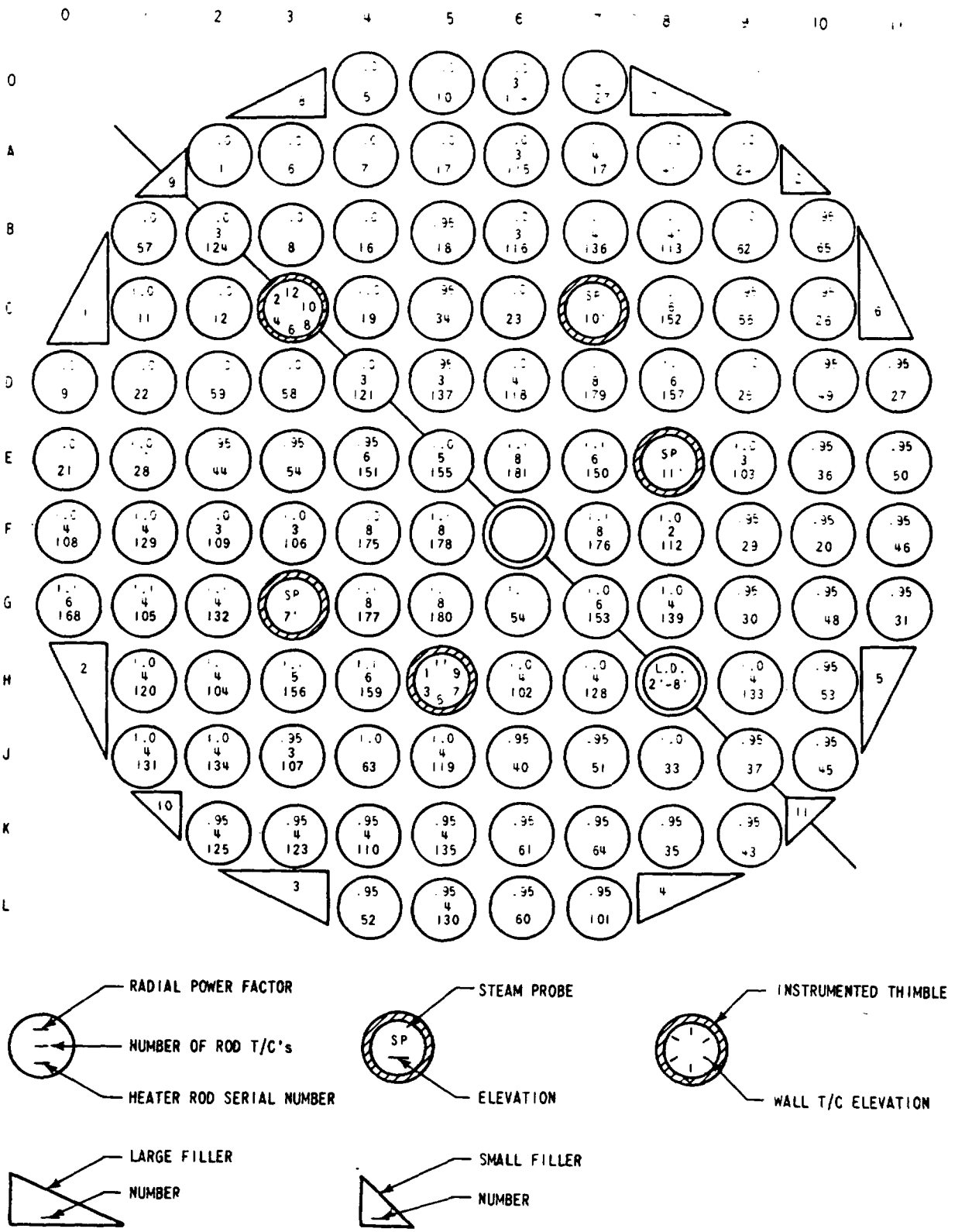

Figure H-1. FLECHT–LFR Skewed Heater Rod Bundle

TABLE H-2
FLECHT–LFR SKEWED HEATER ROD SURFACE ROUGHNESS MEASUREMENTS (μin.)

Inches From S/N End	Heater Rod									
	5G – S/N 180		7F – S/N 176		8C – S/N 152		2H – S/N 104		8B – S/N 113	
	Before Test	After Test	Before Test	After Test	Before Test	After Test	Before Test	After Test	Before Test	After Test
35 3/4					18	18				
47 1/8									80	65
47 1/2							15	19		
59 3/8	4 1/2	7	6 1/2	11						
71 5/8					21	15				
79 1/4										
83 1/2	5 1/2	15	5 1/2	12						
95 1/4							12	20		
95 3/8					27	22				
95 1/2									85	65
107 1/8	6	70								
107 1/4			15	35						
119 3/8					25	85				
131	15	35	7 1/2	95						
137	8 1/2	50	7	75						
142 7/8	5									
143 1/8			15	70						
143 1/4					16	47			85	60
143 1/2							17	90		
148 3/4	5	65								
149			6	70						
154 1/2	25	35								
155			6 1/2	80						
155 1/4							20	50	80	80
161 1/4					16	17				

NOTE: The beginning of the heated length starts 24 inches from the serial number (S/N) end.

TABLE H-3

FLECHT SKEWED HEATER RODS

(Oxide Thickness Measurements on OD of Rods at 10-foot Elevation)

Heater Rod No.		0°	90°	180°	270°	Average
7B S/N 136	Min.	0.0005	0.0001	0.0004	0.0004	0.0004
	Max.	0.0014	0.0011	0.0013	0.0013	0.0013
5G S/N 180	Min.	0.0006	0.0005	0.0009	0.0005	0.0006
	Max.	0.0016	0.0015	0.0017	0.0015	0.0016
5D S/N 137	Min.	0.0004	0.0011	0.0009	0.0010	0.0009
	Max.	0.0015	0.0018	0.0018	0.0017	0.0017
5F S/N 137	Oxide Thickness taken at one location only, ~ 0.00005"					

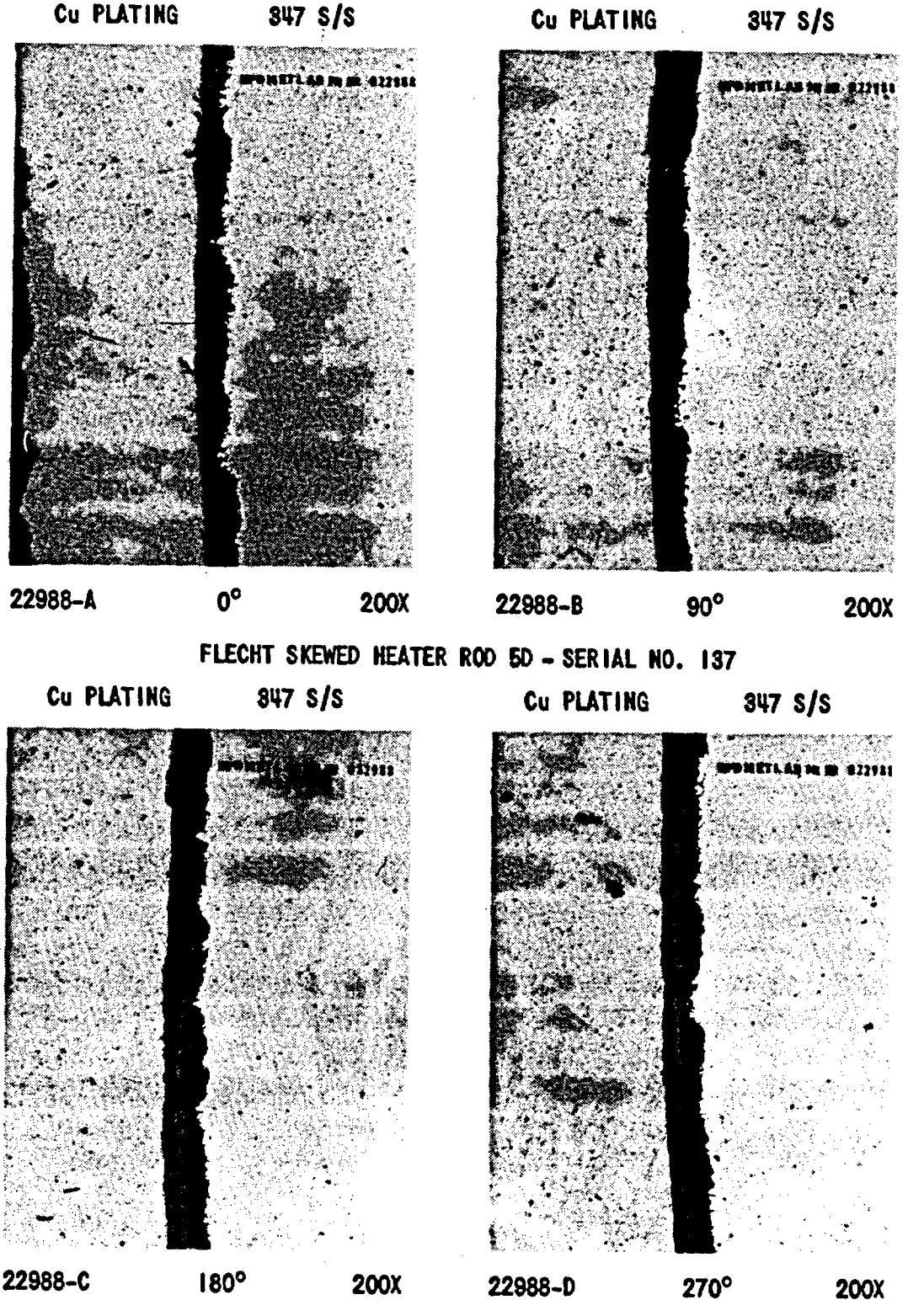

Figure H-2. Oxide Thickness for Rod 5D

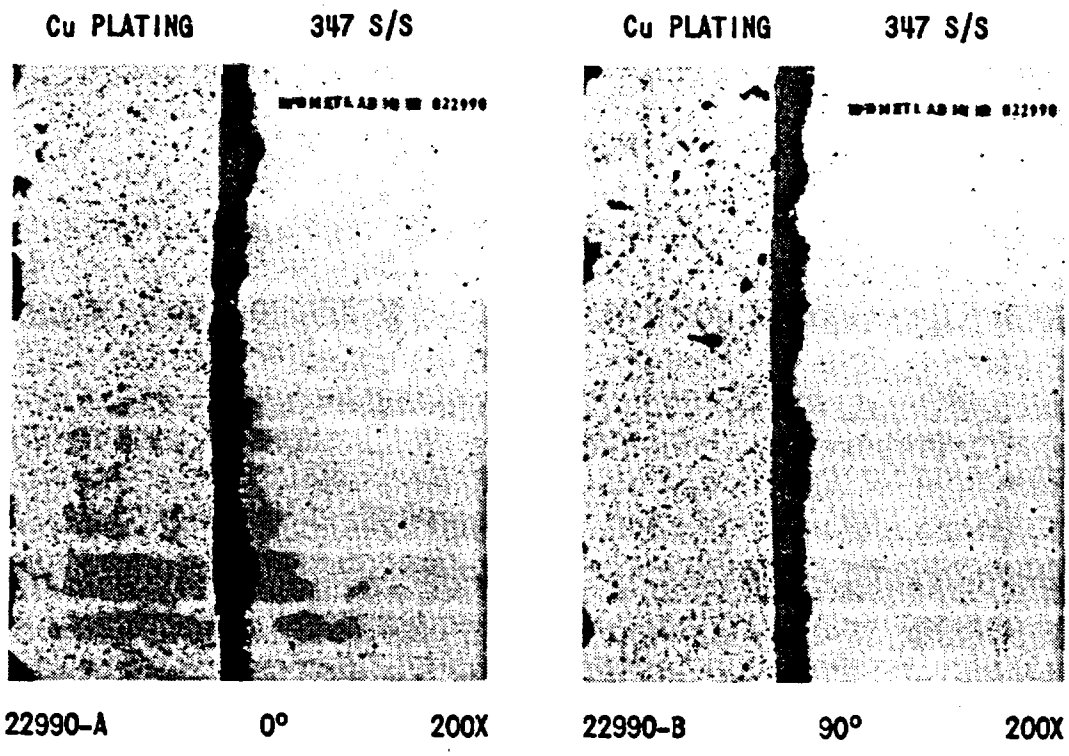

FLECHT SKEWED HEATER ROD 5G - SERIAL NO. 180

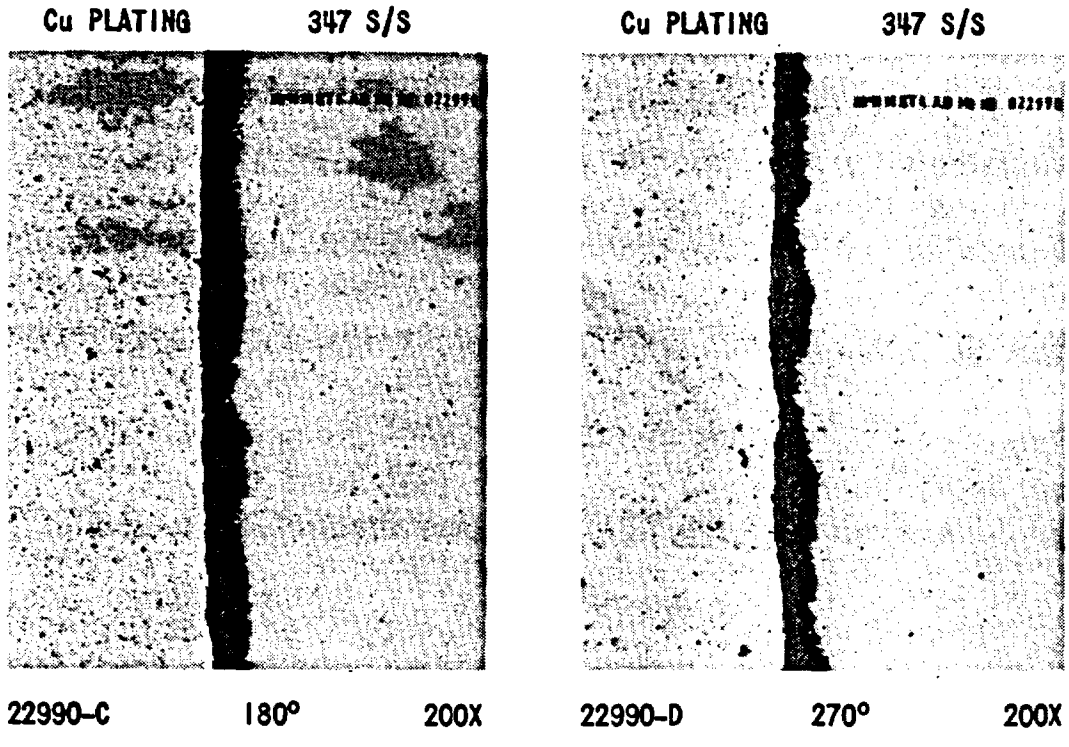

Figure H-3. Oxide Thickness for Rod 5G

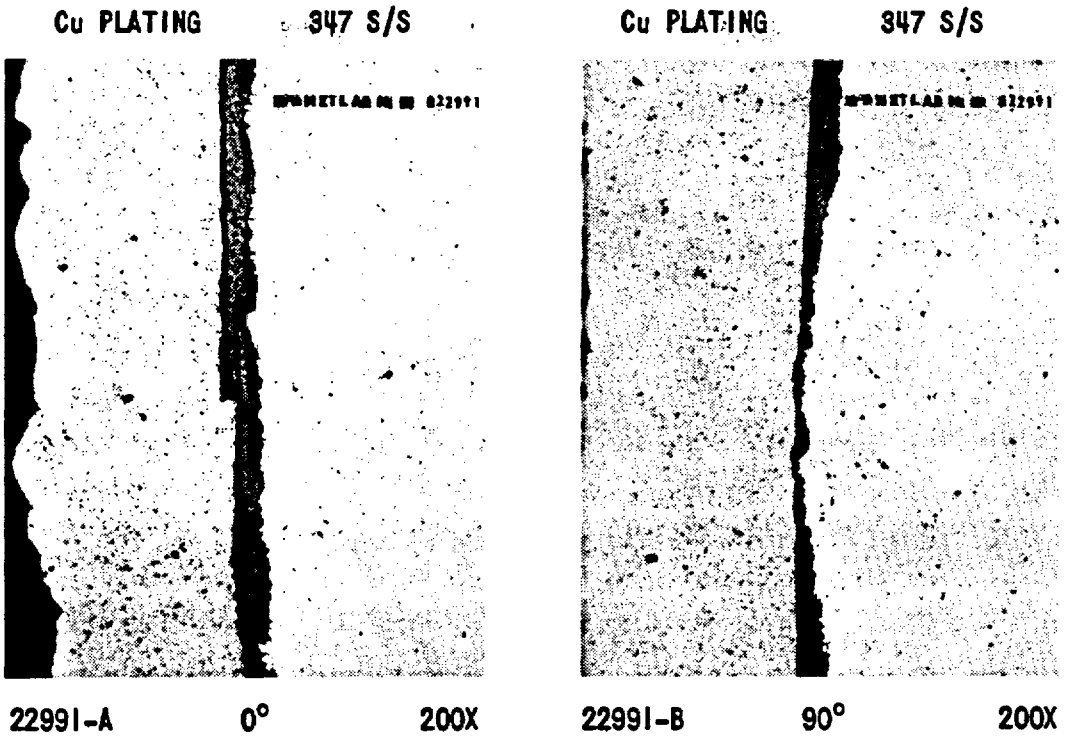

FLECHT SKEWED HEATER ROD 7B - SERIAL NO. 136

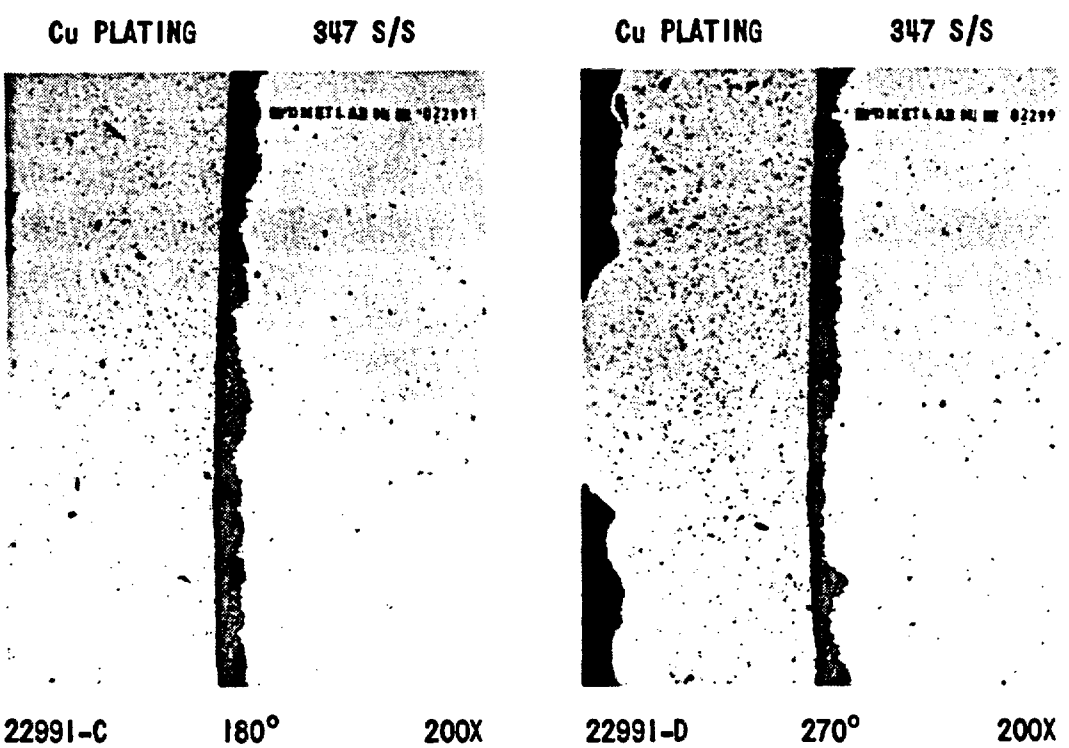

Figure H-4. Oxide Thickness for Rod 7B

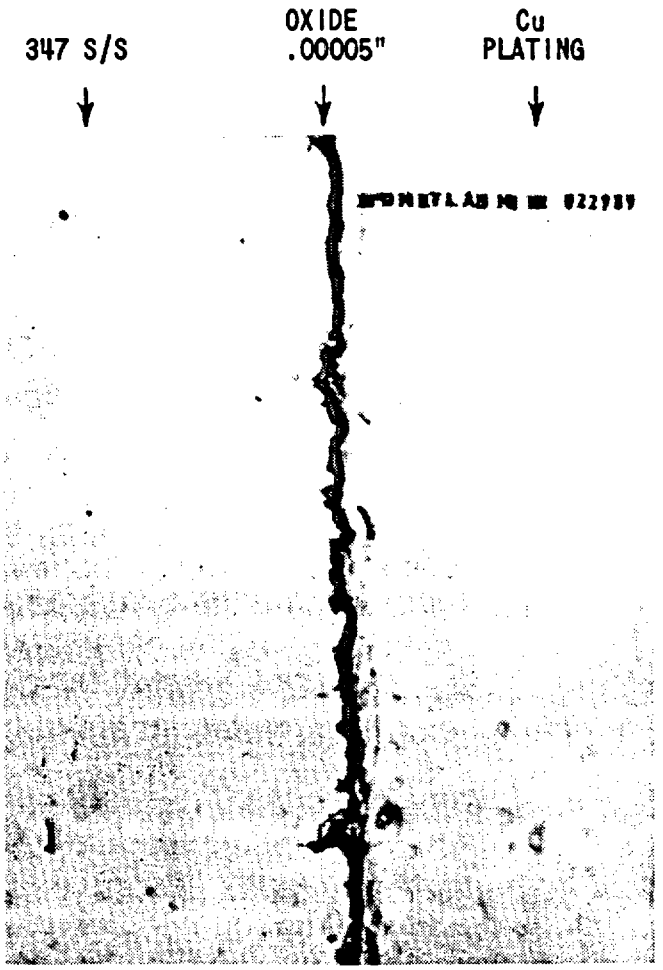

22989 TYPICAL 1000X

FLECHT SKEWED HEATER ROD 5F - SERIAL NO. 178

Figure H-5. Oxide Thickness for Rod 5F

The heat transfer coefficient was examined for a series of repeated tests which were conducted during the test series such that they reflected different periods during the bundle life. Rod 5G was examined at the 5, 7, 9.5, and 10.5-foot elevations. The roughness change was largest at the 7-foot elevation. The heat transfer coefficient was observed to be essentially the same, and easily within the test repeatibility discussed in section 3. This degree of repeatibility indicates that the surface roughness increase during the test series does not affect the heat transfer coefficient.

The quench times for rod 5G at the different elevations were also examined and are given in table H-4. A quick examination of the data indicated that two of the later tests gave longer quench times than their earlier counterparts, while the two later tests gave longer quench times. There does not seem to be a trend in this information that would indicate that as the rods aged, they would quench differently.

TABLE H-4

QUENCH TIMES FOR ROD 5G DURING BUNDLE LIFE USING REPEAT TESTS

Thermocouple Location	Test 13404 t_q (sec)	Test 17136 t_q (sec)	Test 11003 t_q (sec)	Test 13303 t_q (sec)	Test 12907 t_q (sec)	Test 17407 t_q (sec)	Test 12102 t_q (sec)	Test 17302 t_q (sec)
5G5	194	171	145	157	47	46	84	86
5G7	304	266	212	237	77	76	122	126
5G9.5	481	383	299	350	120	116.5	153	166
5G10.5	548	464	339	399	141	134	174	177

APPENDIX I

ADDITIONAL WALL HEAT FLUX COMPARISONS FOR SKEWED AND COSINE TESTS

Both skewed and cosine tests were analyzed using HEAT II described in appendix B to ascertain the importance of each radiation component as a function of the two variables of primary importance in reflood heat transfer, flooding rate, and pressure. Before flooding, at time zero, the primary modes of heat transfer are natural convection to the steam in the test section and surface-to-surface radiation. At the onset of flooding, the surface-to-surface radiation component normalized by the total wall heat flux should be close to 1.0, as indicated by figures I-1 and I-5. Note however, that the skewed surface-to-surface radiation heat flux drops off to less than 25 percent of the total wall heat flux much more rapidly than do comparable cosine flooding rate tests. In the case of the skewed series, the wall-to-wall radiation is found to increase with decreasing flooding rate, while the opposite trend is found in the cosine series.

Wall-to-vapor radiation (figures I-2 and I-6) is relatively constant for both skewed and cosine tests and accounts for 10 to 15 percent of the total wall heat flux. Late in time, this component increases but, in general, accounts for less than 25 percent of the total.

Normalized wall-to-droplet radiation heat transfer accounts for 10 to 15 percent of the total wall heat flux, as shown in figures I-3 and I-7. Both the cosine and skewed tests indicate that the wall-to-droplet radiation component rises to a maximum and then decreases to quench, with the higher flooding rate tests decreasing earlier. This result would be expected since tests with higher flooding rates do quench earlier.

Similar trends are also seen in surface-to-surface radiation. The importance of surface-to-surface radiation decreases earlier in time with increasing flooding rate (figures I-1 and I-5).

Convective heat transfer (figures I-4 and I-8) accounts for the major portion (~50 percent) of the total wall heat flux. The effects of increasing flooding rate are seen later in time as the percentage of wall heat flux removed by droplet-enhanced convection increases as quench time approaches.

RUN NUMBERS	02833-04831-05132
PRESSURE	40-40-40 PSIA
INITIAL CLADDING TEMPERATURE	1602-1600-1601°F
PEAK POWER	0.89-0.95-0.95 KW/FT
SUBCOOLING	142-138-141°F
INJECTION RATE	0.80-1.50-0.99 IN./SEC

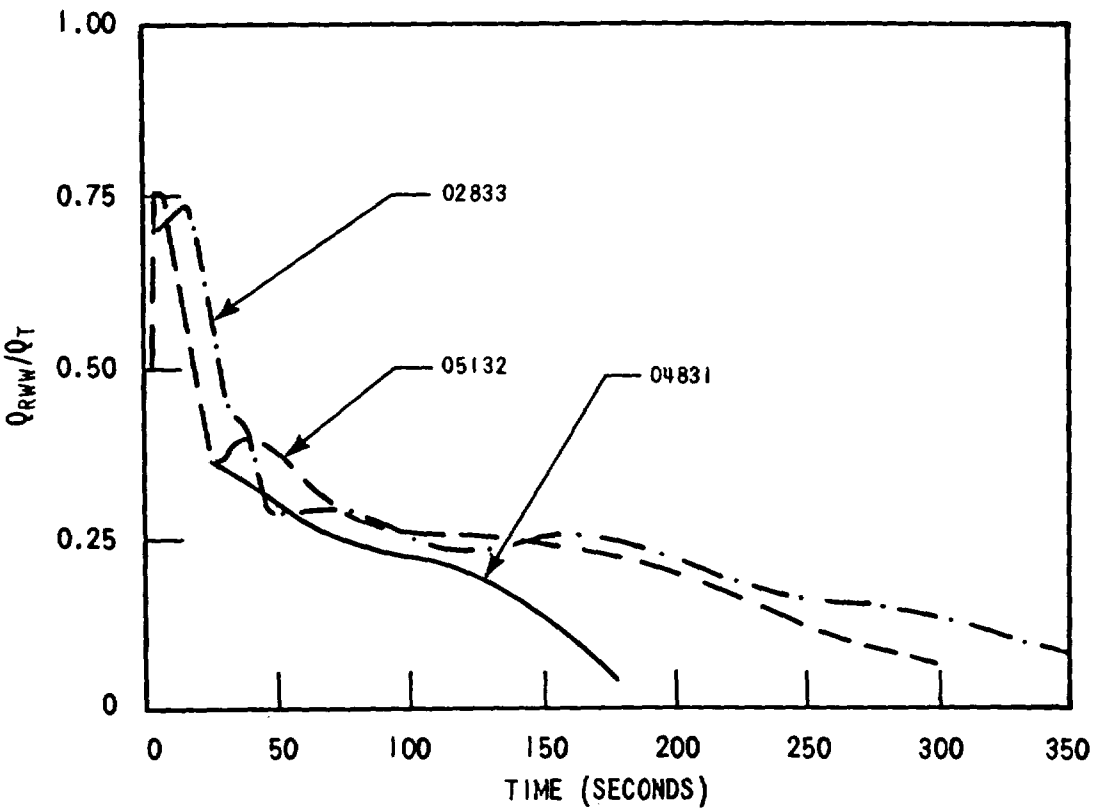

Figure I-1. Effect of Flooding Rate on Surface-to-Surface Radiation Heat Flux Normalized by Wall Heat Flux

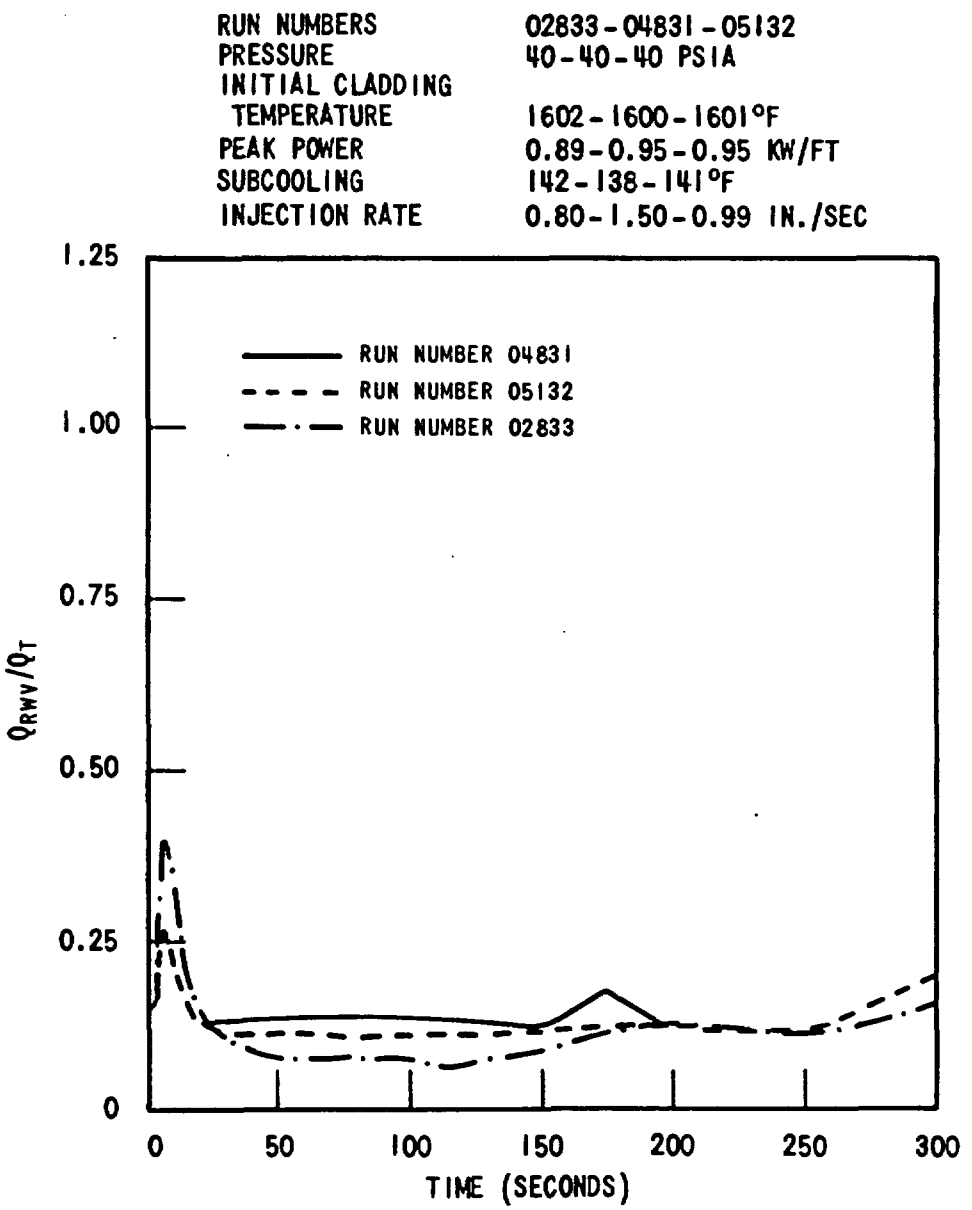

Figure I-2. Effect of Flooding Rate on Wall-to-Vapor Radiation Heat Flux Normalized by Wall Heat Flux

RUN NUMBERS	02833-04831-05132
PRESSURE	40-40-40 PSIA
INITIAL CLADDING TEMPERATURE	1602-1600-1601°F
PEAK POWER	0.89-0.95-0.95 KW/FT
SUBCOOLING	142-138-141°F
INJECTION RATE	0.80-1.50-0.99 IN./SEC

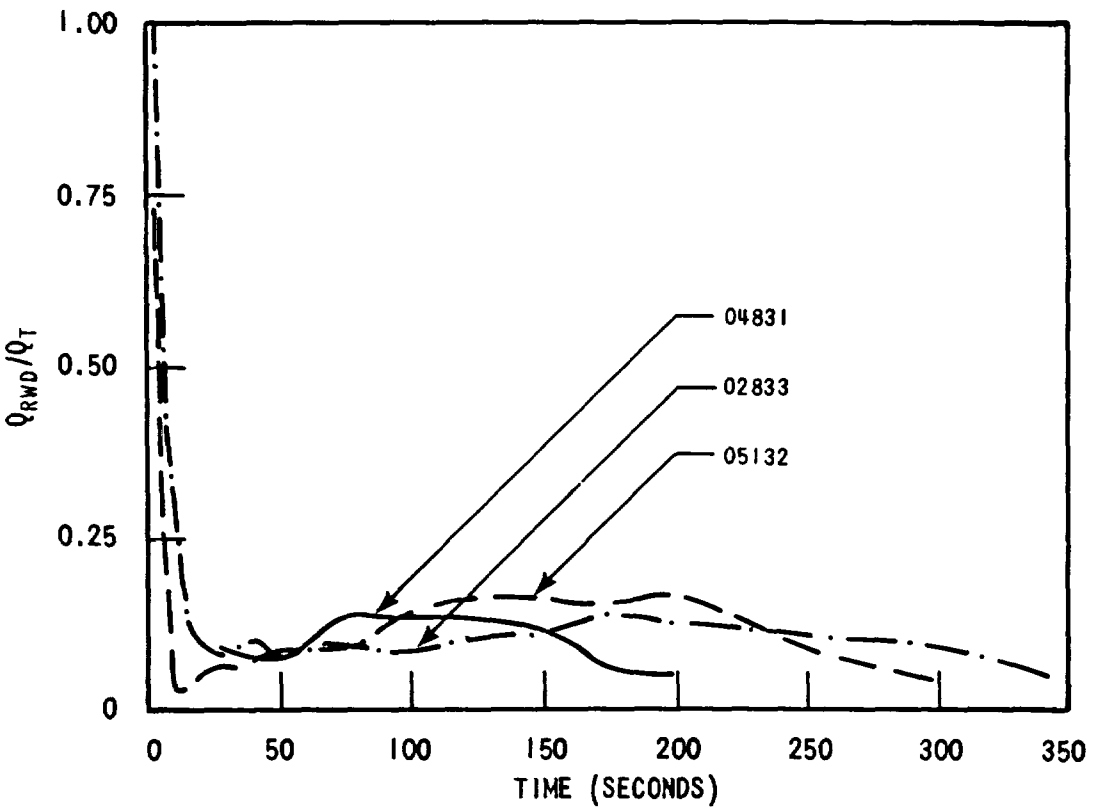

Figure I-3. Effect of Flooding Rate on Wall-to-Drop Radiation Heat Flux Normalized by Wall Heat Flux

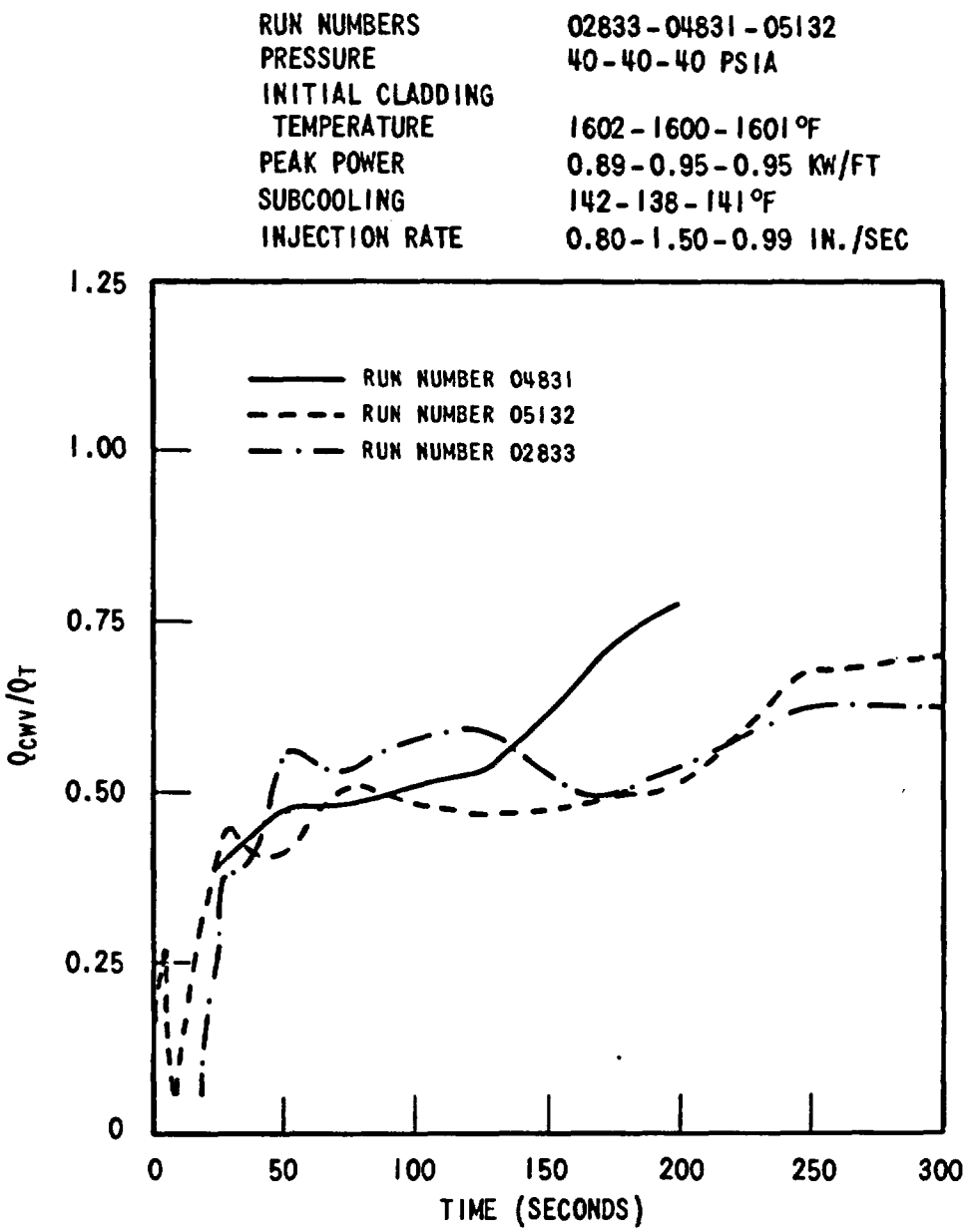

Figure I-4. Effect of Flooding Rate on Wall-to-Vapor Convection Heat Flux Normalized by Wall Heat Flux

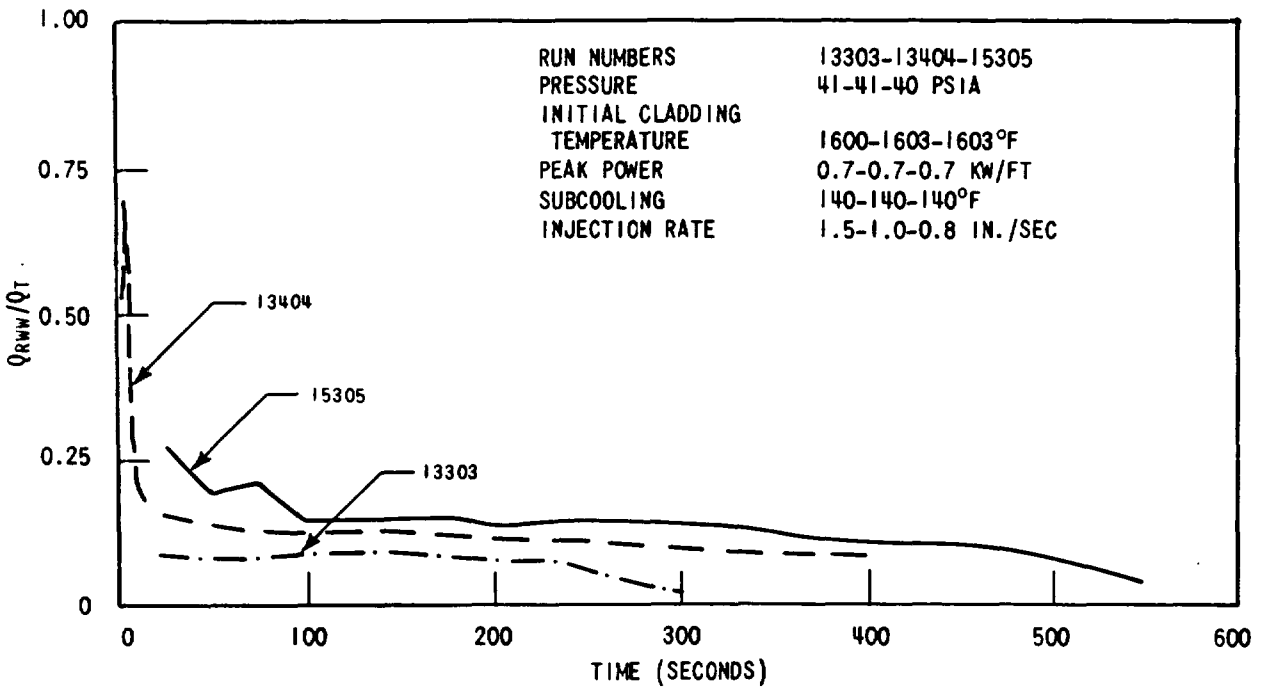

Figure I-5. Effect of Flooding Rate on Wall-to-Wall Radiation Flux Normalized by Wall Heat Flux

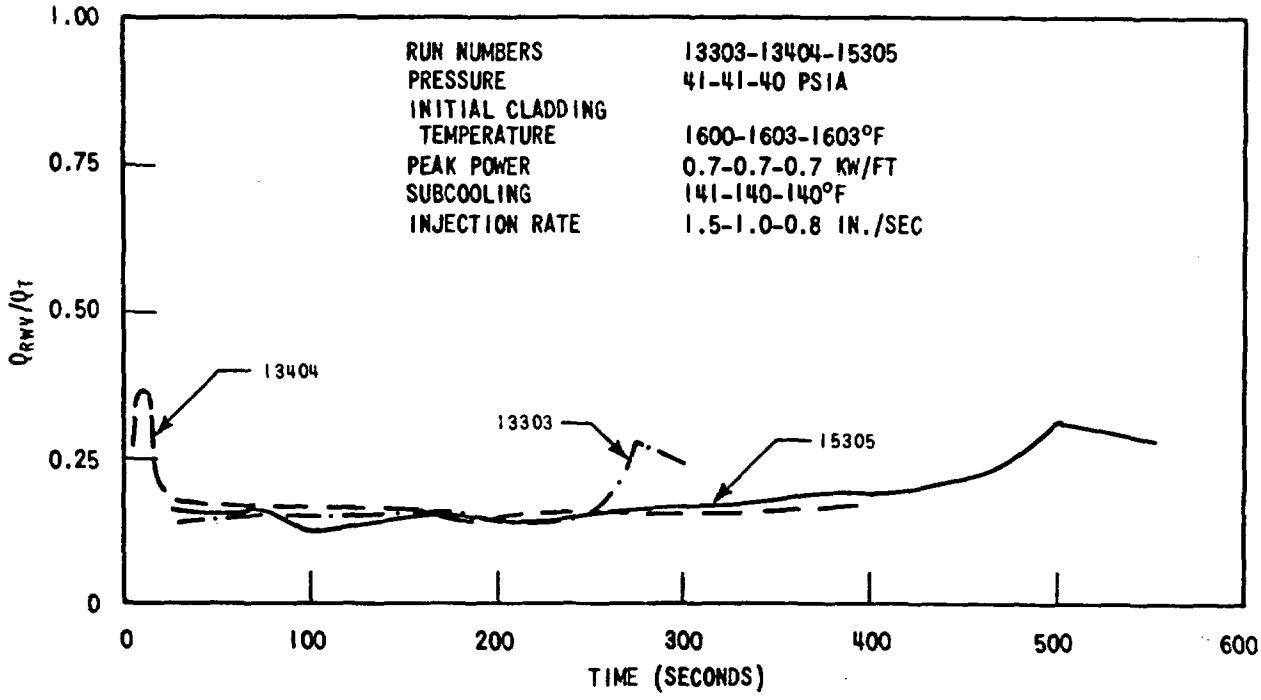

Figure I-6. Effect of Flooding Rate on Wall-to-Vapor Radiation Heat Flux Normalized by Wall Heat Flux

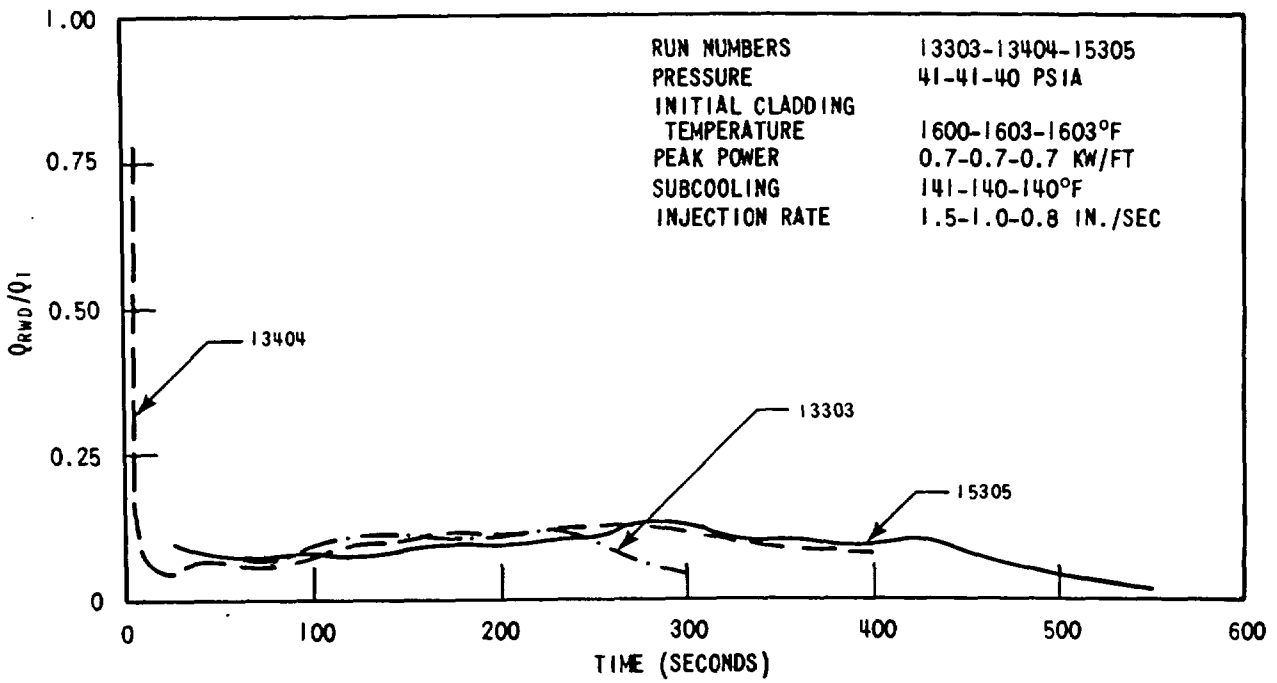

Figure I-7. Effect of Flooding Rate on Wall-to-Drop Radiation Heat Flux Normalized by Wall Heat Flux

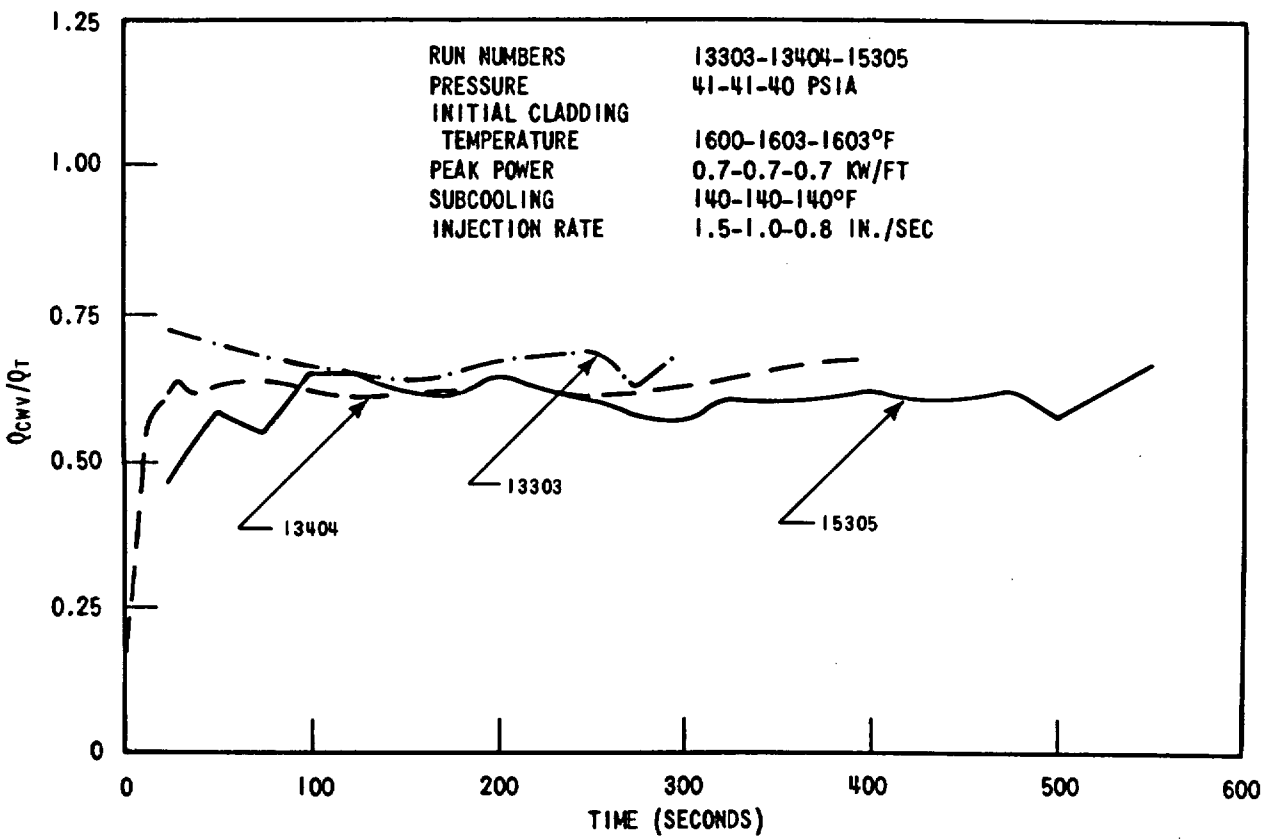

Figure I-8. Effect of Flooding Rate on Wall-to-Vapor Convection Heat Flux Normalized by Wall Heat Flux

In conclusion, increasing flooding rate does not shift the primary mode of heat transfer from one mechanism to another, nor are there large changes within the same mechanism. Near quench time, small changes are noticed, but are not of great significance. Early time shows the most fluctuation, but here the mass balance is inaccurate and differences are not to be totally believed.

Normalized heat flux dependence on pressure variations was also investigated using the HEAT II code. Note that two different flooding rates were used in drawing these comparisons (skew-1.0 in./sec and cosine 0.8 in./sec). Consistent trends are found for surface-to-surface radiation between the different power profiles (figures I-9 and I-13). As the pressure increases, radiation between surfaces decreases.

However, the differences between 60 and 20 psi for the skew profile test are much smaller than those found in the cosine test comparison and the cosine normalized surface-to-surface radiation flux is calculated to be roughly twice that of the skew test. Trends in the calculation of normalized wall-to-vapor radiation (figures I-10 and I-14) are not clear. For example, the skew 20 psi case is roughly half of the 40-60 value (~ 15 to 20%). In comparison, the cosine 20 psi test 06638 increases with time until at 350 seconds, radiation from wall-to-vapor accounts for approximately 25 percent of the total wall heat flux. The 40 and 60 psi cases are considerably less than 25 percent.

Consistancy returns to the calculation of wall-to-droplet radiation (figures I-11 and I-15), especially later in time. Initially the skew profile tests indicate 10 percent of the wall heat flux is transmitted to the drops through this radiation mechanism while 10 to 20 percent is typical for the cosine profile. Later in time, (200 sec) the curves begin to separate with the 60 psi droplet radiation flux dropping to near 0 and the 20 psi flux either maintains its former value or increases slightly.

Again figures I-12 and I-16 show that 50 percent or more of the total wall heat flux is transmitted through convective means after 50 seconds of testing with the exception of 20 psi cosine test. In general the convective mechanism is more significant in the skewed profile than the cosine by roughly 20 percent.

As quench time approaches, the difference in convective transport due to pressure is pronounced in the cosine profile; that is, the higher the pressure the higher the convective flux on a percentage basis.

The differences in normalized heat fluxes were greater due to pressure than due to flooding rate. While flooding curves tended to reflect differences in quench time more strongly, pressure effects tended to alter the proportion of wall heat flux allotted to each mechanism more significantly.

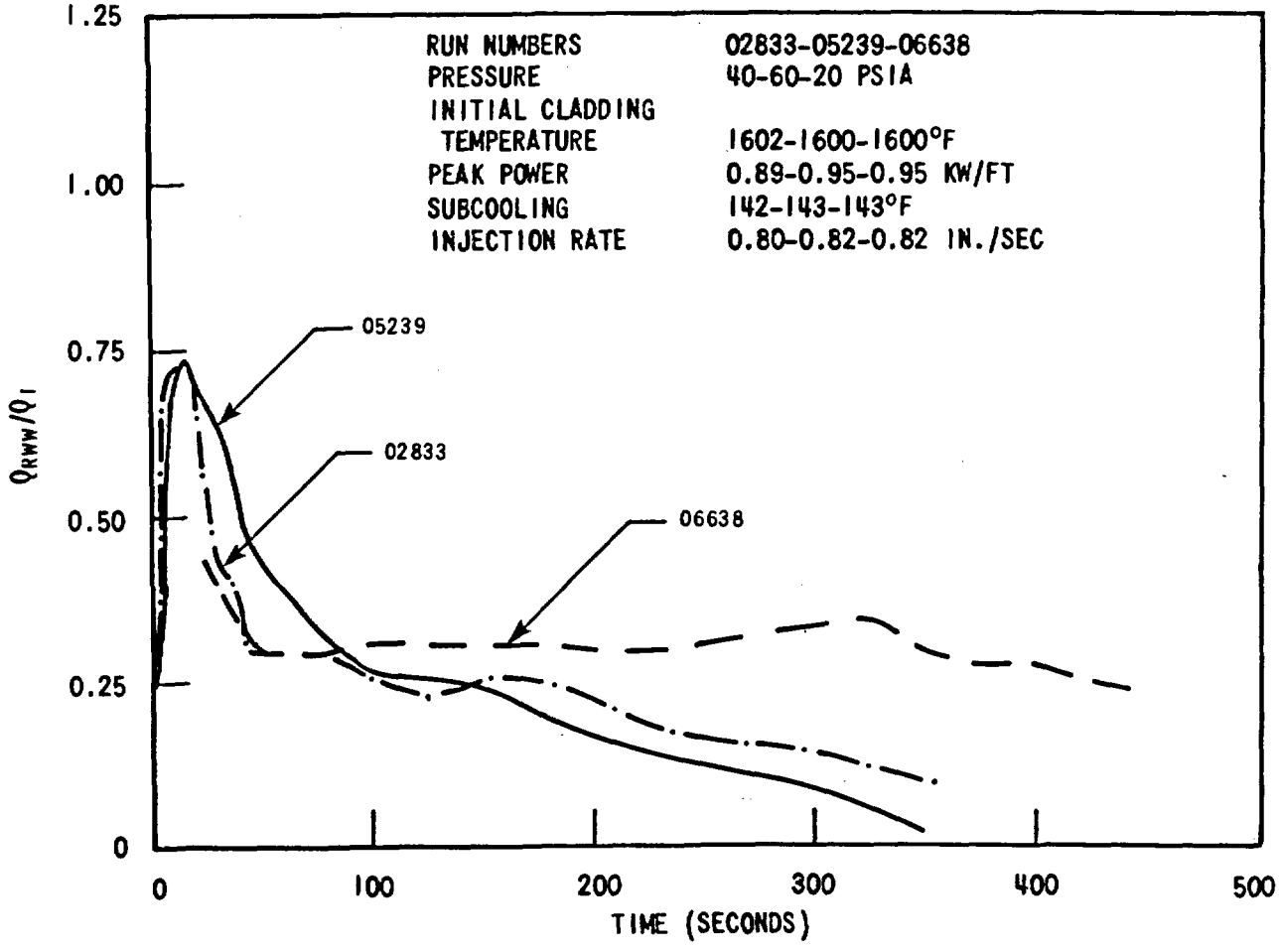

Figure I-9. Effect of Pressure on Surface-to-Surface Radiation Heat Flux Normalized by Wall Heat Flux

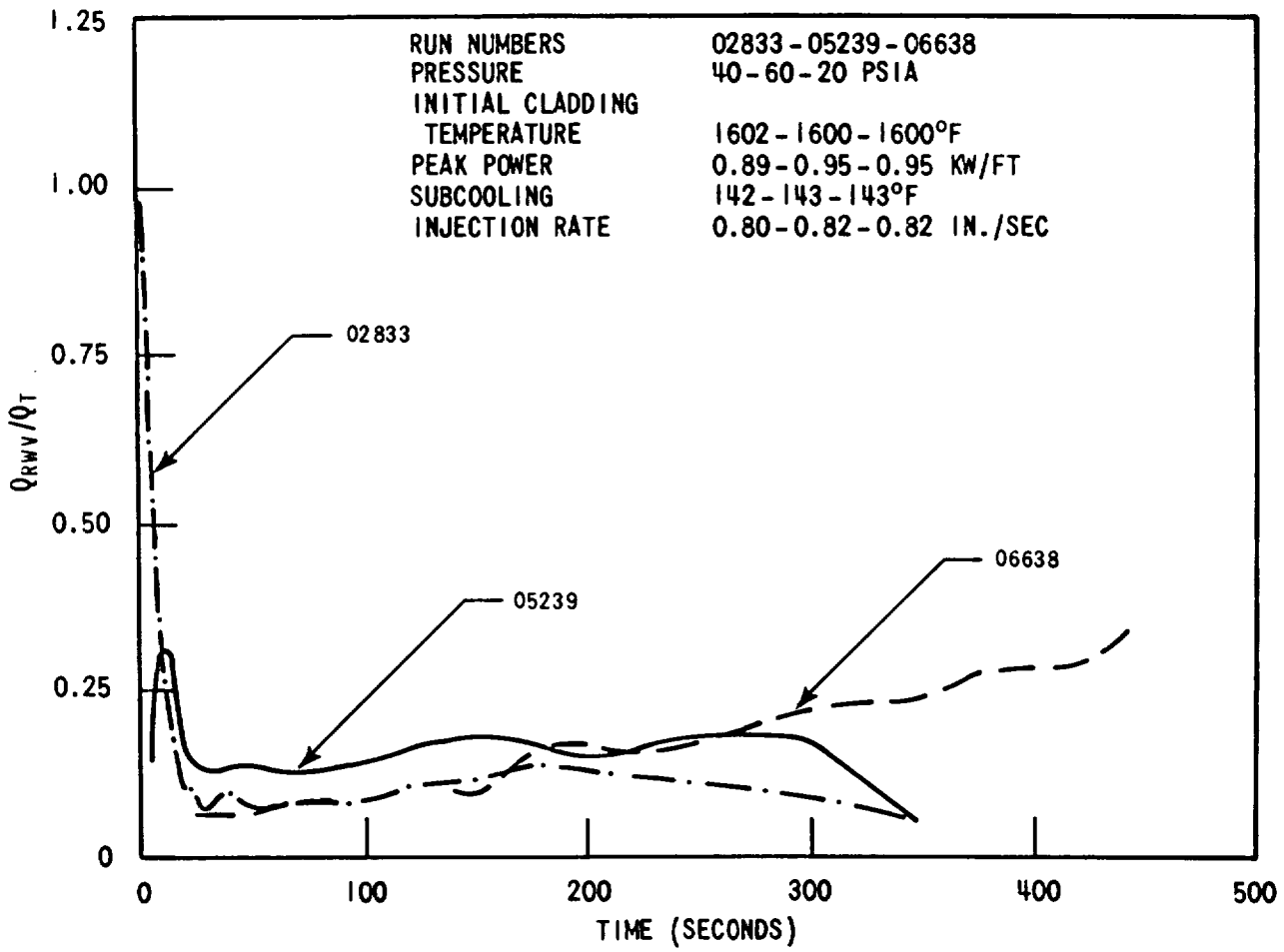

Figure I-10. Effect of Pressure on Wall-to-Vapor Radiation Heat Flux Normalized by Wall Heat Flux

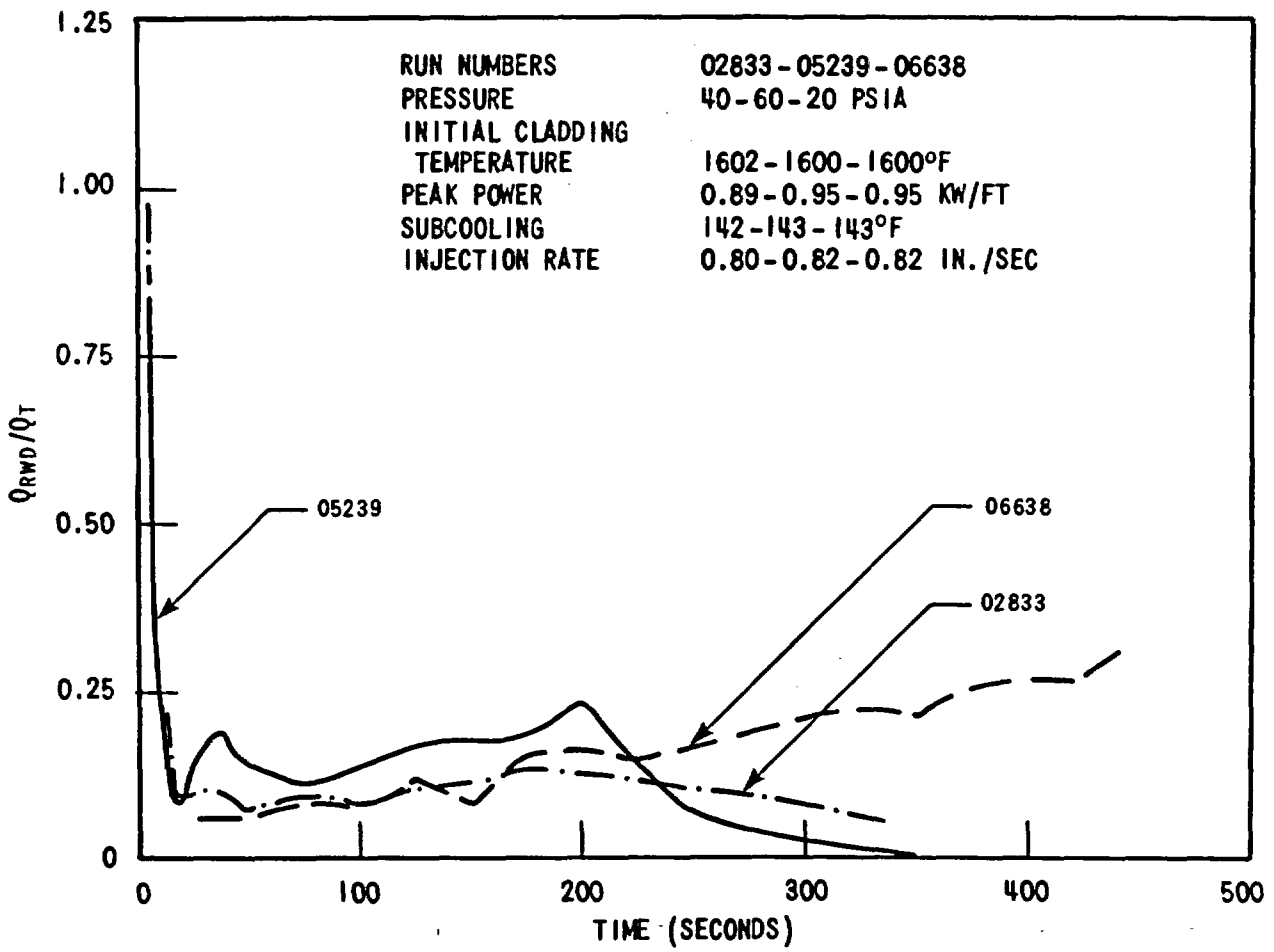

Figure I-11. Effect of Pressure on Wall-to-Droplet Radiation Heat Flux Normalized by Wall Heat Flux

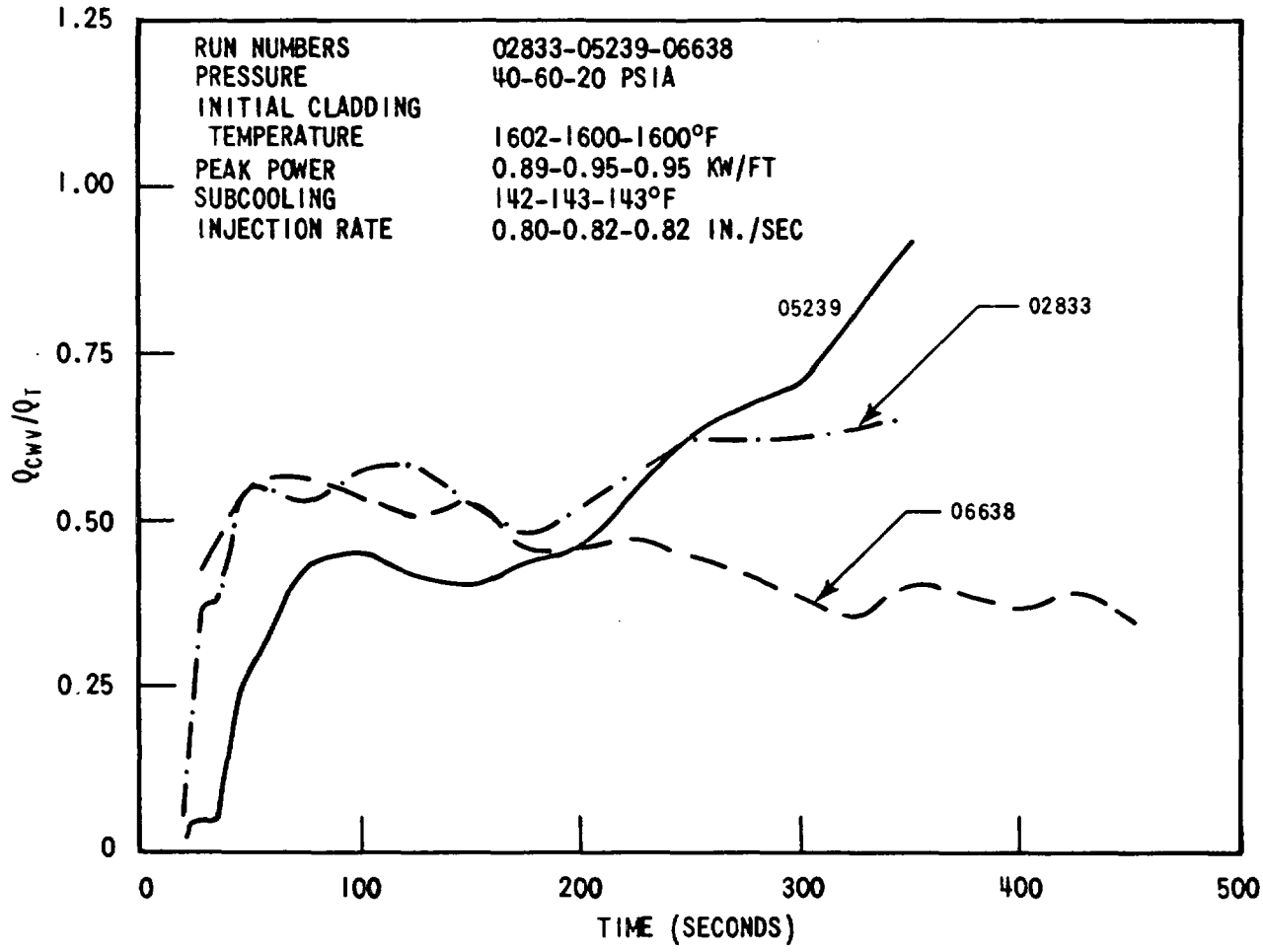

Figure I-12. Effect of Pressure on Wall-to-Vapor Convection Heat Flux Normalized by Wall Heat Flux

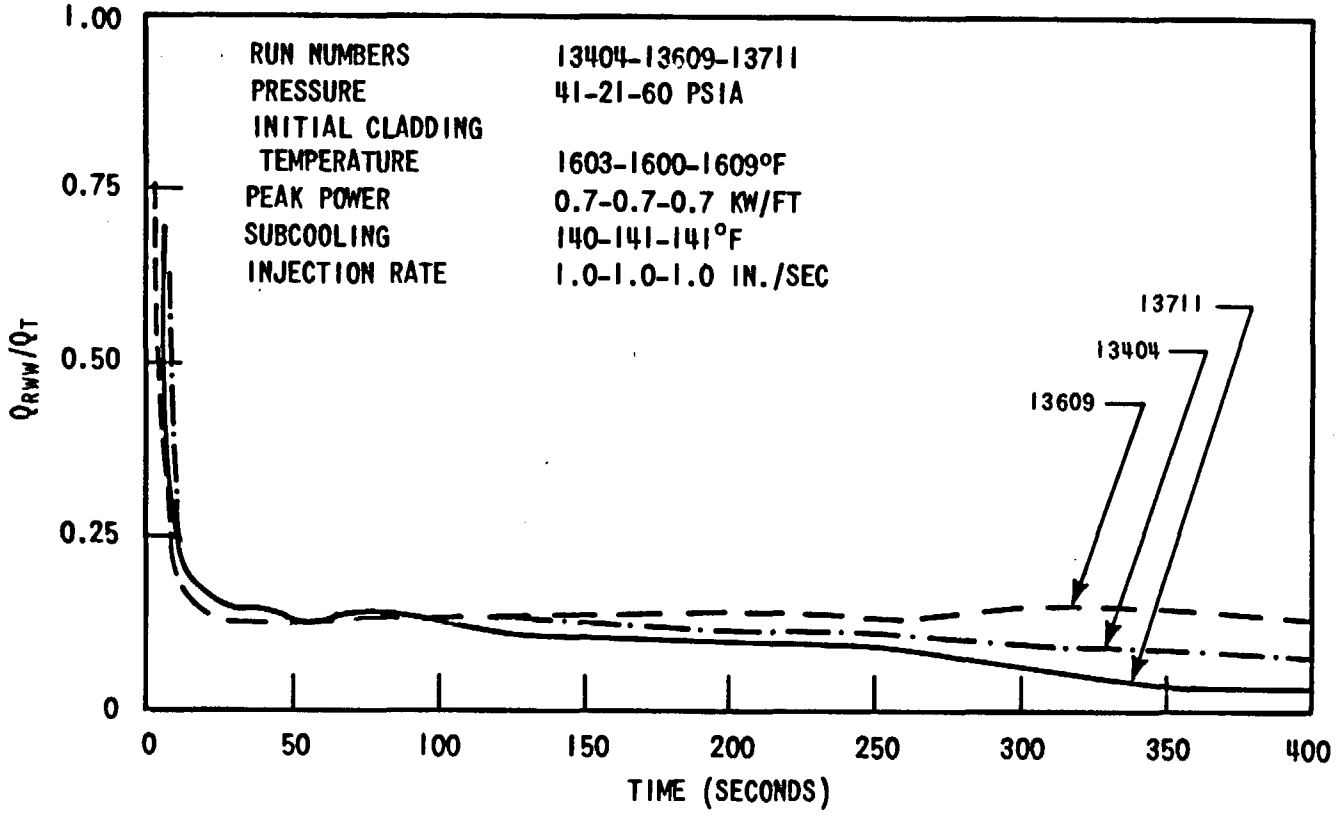

Figure I-13. Effect of Pressure on Surface-to-Surface Radiation Heat Flux Normalized by Wall Heat Flux

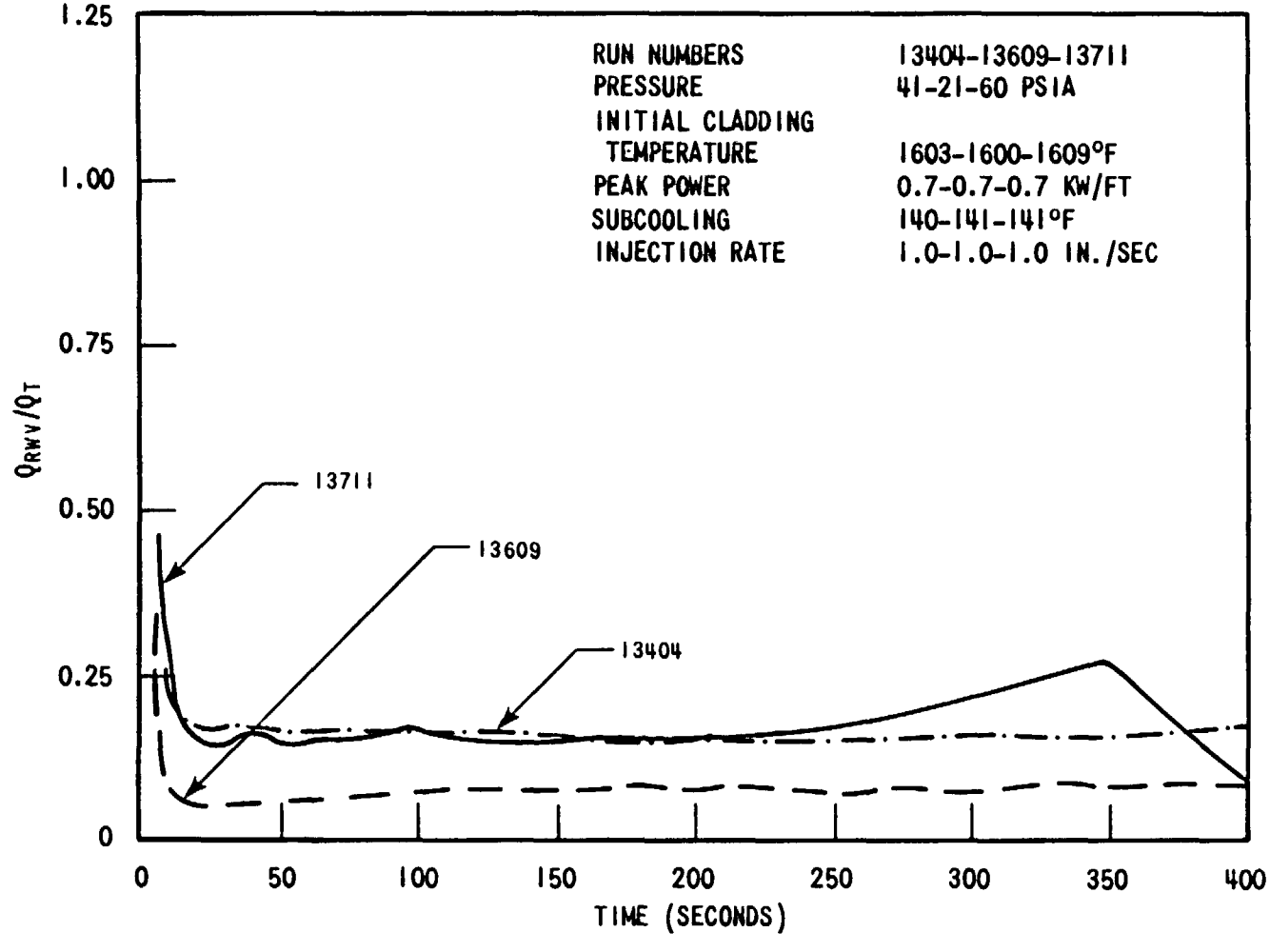

Figure I-14. Effect of Pressure on Wall-to-Vapor Radiation Heat Flux Normalized by Wall Heat Flux

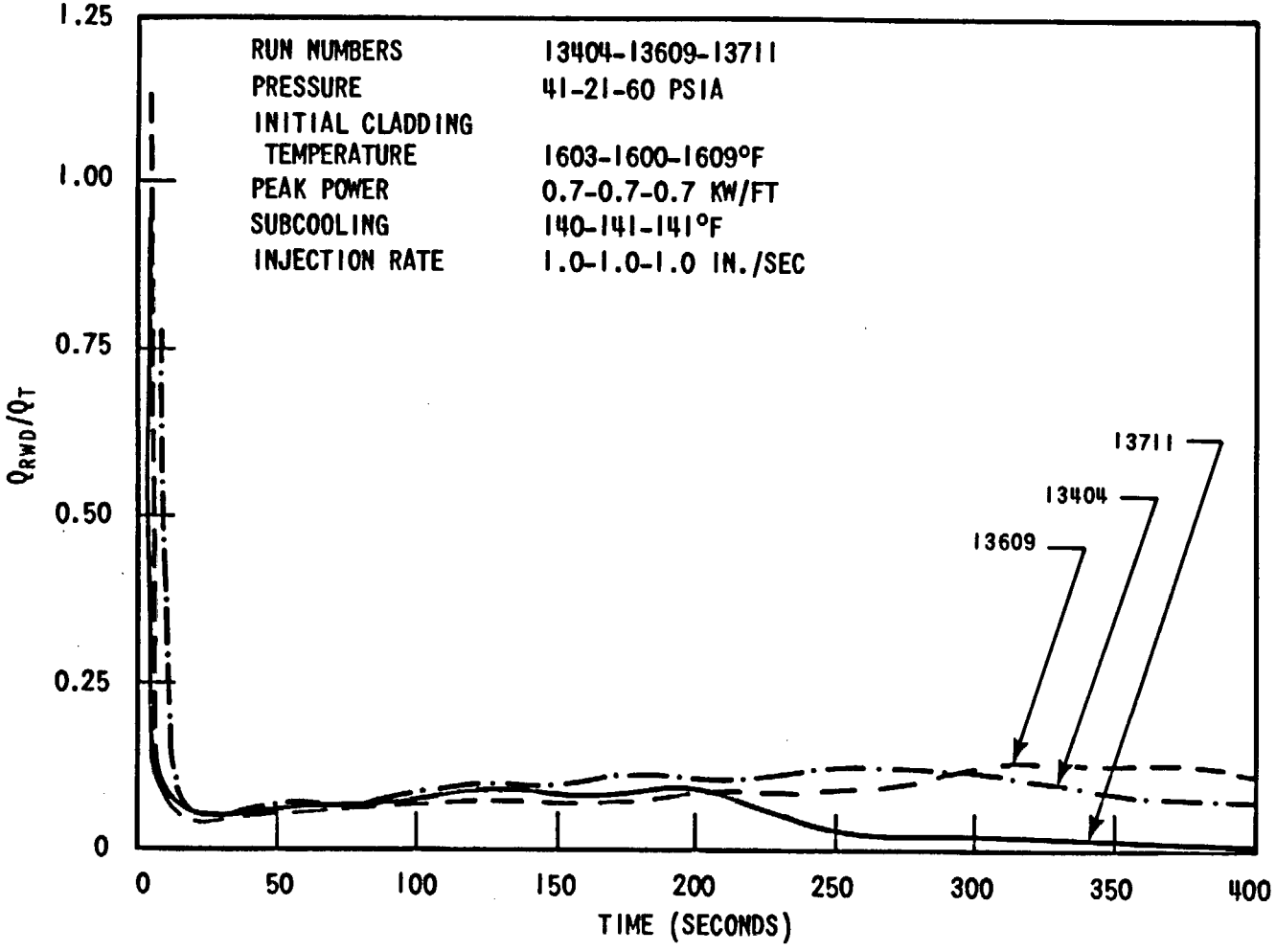

Figure I-15. Effect of Pressure on Wall-to-Droplet Radiation Heat Flux Normalized by Wall Heat Flux

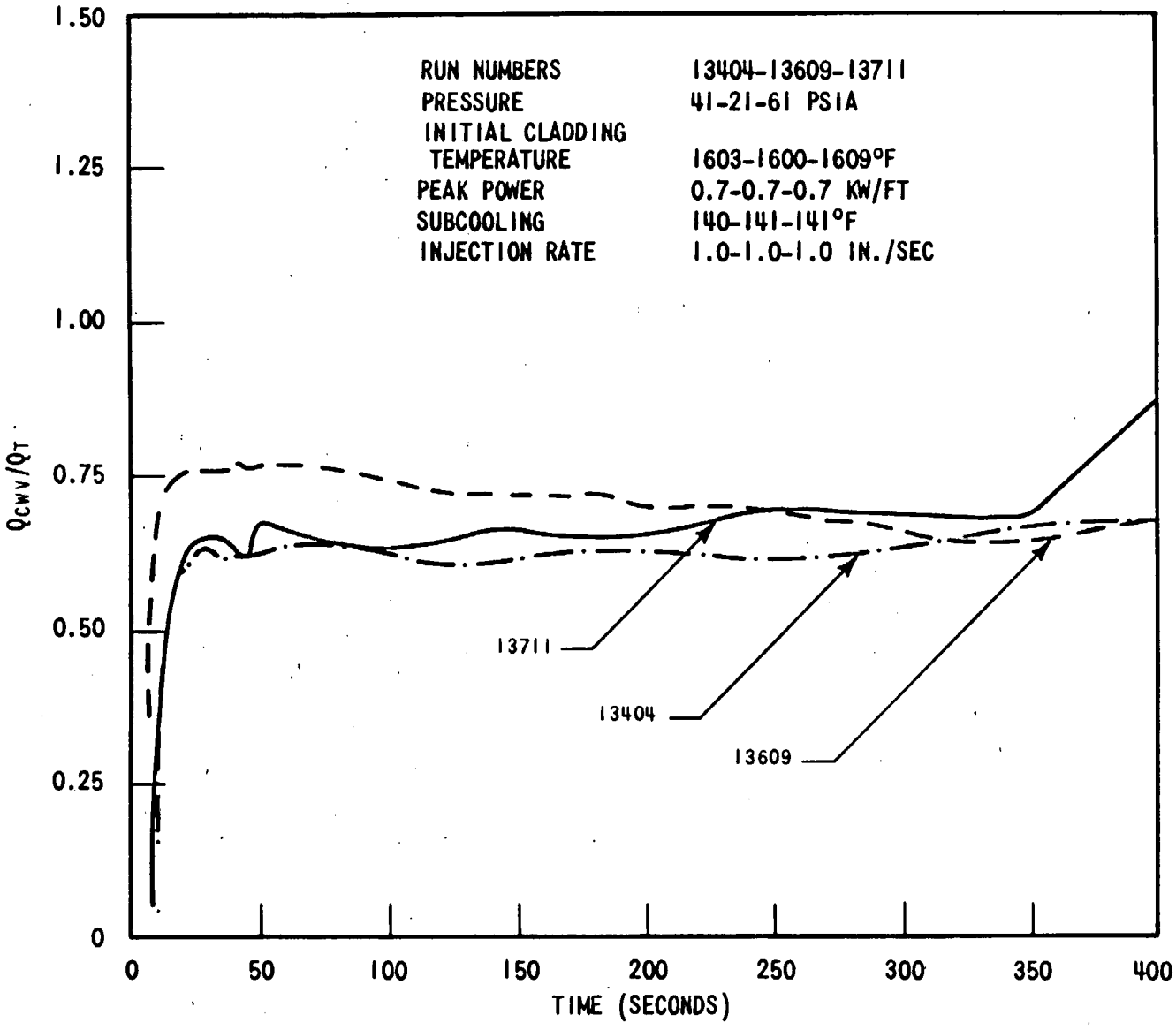

Figure I-16. Effect of Pressure on Wall-to-Vapor Convection Heat Flux Normalized by Wall Heat Flux